ResearchOnline@JCU

This file is part of the following reference:

**Alao, Abdur-Rasheed (2016)** ***Fabrication and characterization of lithium metasilicate/disilicate glass ceramics and yttria tetragonal zirconia polycrystals for dental restorations.*** **PhD thesis, James Cook University.**

Access to this file is available from:

http://researchonline.jcu.edu.au/46591/

*The author has certified to JCU that they have made a reasonable effort to gain permission and acknowledge the owner of any third party copyright material included in this document. If you believe that this is not the case, please contact ResearchOnline@jcu.edu.au and quote* **http://researchonline.jcu.edu.au/46591/**

JAMES COOK UNIVERSITY AUSTRALIA

**JAMES COOK UNIVERSITY**

## COLLEGE OF SCIENCE & ENGINEERING

# FABRICATION AND CHARACTERIZATION OF LITHIUM METASILICATE/DISILICATE GLASS CERAMICS AND YTTRIA TETRAGONAL ZIRCONIA POLYCRYSTALS FOR DENTAL RESTORATIONS

Abdur-Rasheed Alao (BEng, MSc)

Thesis submitted to the College of Science & Engineering for the degree of

Doctor of Philosophy

(Mechanical Engineering)

2nd September, 2016

# DECLARATION

I declare that this thesis is my own work and has not been submitted in any form for another degree or diploma at any university or other institute of tertiary education. Information derived from the published and unpublished work of others has been acknowledged in the text, and a list of references is given.

_____

Abdur-Rasheed Alao

September, 2016

# STATEMENT OF ACCESS TO THIS THESIS

I, the undersigned, the author of this work, understand that James Cook University will make this work available for use within the University Library, and via the Australian Digital Thesis Network, for use elsewhere.

I understand that as an unpublished work, a thesis has significant protection under the Copyright Act. I do not wish to place any restriction on access to this thesis. However, any use of its content must be acknowledged and could potentially be restricted by future patents.

_____

Abdur-Rasheed Alao

September, 2016

# Acknowledgements

I give praises to Allah for giving me the strength, patience and wherewithal to carry out this research and complete it successfully. I acknowledge the James Cook University (JCU) International Research Scholarship awarded for my PhD program. Equally, I acknowledge the JCU Graduate Research Scheme granted to support my research project in 2013 and conference attendance in Sydney in 2014.

My profound appreciation goes to my advisory team, A/Prof. Ling Yin of Mechanical Engineering at JCU Townsville and Prof. Richard Stoll of Restorative Dentistry at JCU Cairns, for their assistance, guidance and supervision throughout the research project. They have been a source of inspiration for me. Though this research really strained me, I learnt a lot from it. I also very much appreciate the JCU Collaboration Grants Scheme (2013–14), the Australia-China Science and Research Fund (Grant No. ACSRF GMB 12029) and the National Natural Science Foundation of China (Grant No. 51375335) for funding support.

My sincere appreciation goes to Drs. Shane Askew and Kevin Blake, JCU Advanced Analytical Center for nanoindentation training and SEM images; Dr Rosalind Gummow of JCU Chemical Engineering for sintering nanoindentation samples; Mr. Kevin Cheong of JCU Dental Laboratory for clinical preparation of samples; Mr. Warren Donnell, Mr. Tony Skalecki and Dr. Amy Lovisa of JCU Engineering Laboratory for their technical support in fatigue testing; and Prof John Abbott of JCU Dental for providing the dental CAD/CAM machine.

I also appreciate the clinical sintering offered by Drs. John and Betty-Ann Griffiths at John Griffiths Dental Laboratory, Cairns. I must not fail to acknowledge Mr. Jim Judy, Ivoclar Vivadent Australia, for the generous donation of emax CAD and Zenostar samples; Mr. Matthew Batty, Sirona Australia, for providing the CAD/CAM technical support; and Mr. Phillip McGuire, Northern Petrographics, Townsville, for preparing nanoindentation samples.

I am also grateful to Prof. Takashi Miyazaki, A/Prof. Yasuhiro Hotta and Dr. Yo Shibata, Showa University of Dentistry, Japan, for their assistance in the CAD/CAM-milling conducted at DIPRO, Japan. My gratefulness also goes to A/Prof. Xiao-Fei Song, School of Mechanical Engineering, Tianjin University, China, who collaborated with the Analytical Center of the university to painstakingly perform the x-ray diffraction testing and analyses.

I also appreciate Dr. Liz Tynan, JCU Graduate Research School for the academic writing training and Mrs. Melissa Norton, JCU College of Science & Engineering for her unparalleled administrative support. Mr. Asif Baloch, College of Science & Engineering, JCU, Townsville, is thanked for accommodating my family on our arrival in Australia.

Finally, I give kudos to my parents, Alhaji Usman G. Alao and Mrs. Salamot Idowu Alao, my spouse, Mrs. Ramata Omowumi Alao and my kids, Barakat Alao, Mujeedat Alao and Muhammad Alao for their patience, perseverance and encouragements while this PhD program lasted. I hereby dedicate to these people this thesis.

.

# Statement of the Contribution of Others

| Contributor | Role |
|---|---|
| A/Prof. Ling Yin, Mechanical Engineering, College of Science & Engineering, JCU Townsville. | Project management, primary supervision, editorial assistance and collaboration coordination. |
| Prof. Richard Stoll, Restorative Dentistry, College of Medicine & Dentistry, JCU Cairns. | Clinical supervision, CAD/CAM milling of emax CAD blocks (Chapter 5) and surface roughness measurements (Chapters 5 & 6). |
| Dr. Shane Askew, Advanced Analytical Center, JCU Townsville. | Nanoindentation training and performance of SEM morphologies in Chapters 5, 6 & 7. |
| Dr. Kevin Blake, Advanced Analytical Center, JCU Townsville. | SEM technical assistance. |
| Dr. Rosalind Gummow, Chemical Engineering, College of Science & Engineering, JCU Townsville. | Sintering of nanoindentation samples in Chapter 3. |
| Mr. Kevin Cheong, Dental Laboratory, College of Medicine & Dentistry, JCU Cairns. | Clinical preparation (polishing, sintering and sandblasting) of samples (Chapters 5 & 6). |
| Prof. John Abbott, JCU Dental, Cairns. | Offering of the dental CAD/CAM machine for the milling of emax CAD blocks in Chapter 5. |
| Dr. John & Mrs. Betty-Ann, John Griffiths Dental Laboratory, Cairns. | Clinical sintering of CAD/CAM-milled Y-TZP samples at high temperature in Chapter 6. |
| Prof. Takashi Miyazaki, A/Prof. Yasuhiro Hotta and Dr. Yo Shibata, Dentistry, Showa University of Dentistry, Japan. | Collaboration with DIPRO, Japan for CAD/CAM-milling of the Zenostar disc (Chapter 6). |
| A/Prof. Xiao-Fei Song, School of Mechanical Engineering, Tianjin University, China. | In collaboration with the Analytical Center, Tianjin University, China to perform X-ray diffraction testing and analyses in Chapters 5 & 6. |

# Abstract

Lithium disilicate glass-ceramics (LDGC) and yttria-stabilized tetragonal zirconia polycrystals (Y-TZP) are state-of-the-art materials for monolithic dental restorations. This is due to their excellent mechanical, chemical, optical and biocompatible properties. These ceramics are shaped either in pre-sintered or sintered states by computer aided design/manufacturing (CAD/CAM) abrasive machining which inevitably induces surface/sub-surface damage to the ceramic structures increasing their susceptibility to property degradation and shortening their lifespans. Addressing this fundamental fabrication issue to minimize machining-induced damage requires a comprehensive understanding of their mechanical behavior which, in turn, provides scientific insights into their responses to machining and mechanical loadings. Nanoindentation tests were conducted on lithium metasilicate glass-ceramic (LMGC), sintered and pressable LDGC, pre-sintered and sintered Y-TZP at a peak load of 10 mN and 0.1–0.2 mN/s loading rates to probe the rate effect on their mechanical properties and behavior. The Oliver-Pharr model was used to extract their contact hardness values and Young's moduli. Indentation responses of these ceramics from their force-displacement curves were related to different mechanically-induced deformations assisted by the *in situ* scanning probe microscopy and contact mechanics models including strain rate sensitivity, pressure-sensitive idealized yield criterion and continuum models.

Compared to other materials investigated, the highest and the lowest intrinsic contact hardness values were revealed by LMGC and pre-sintered Y-TZP respectively. Also, pre-sintered Y-TZP showed the smallest Young's modulus while sintered Y-TZP was the stiffest. In addition, several mechanisms of plasticity were revealed including compaction and kink bands for pre-sintered Y-TZP; densification, shear bands and strain hardening for LMGC, sintered and pressable LDGC, and strain- and pressure-hardening, and dislocations for sintered Y-TZP. Based on these deformations, different mechanisms were proposed to minimize brittle fractures during their abrasive machining. The deformations were further partitioned into elasticity and plasticity using Sakai and Sakai-Nowak models to reveal the dominant deformation mechanisms. Resistances to plasticity, normalized indentation absorbed energies and resistances to machining-induced cracking were also extracted providing a quantitative basis to rank their machinability. Pre-sintered Y-TZP exhibited the most quasi-plastic behavior ranking it more machinable than others; LMGC was least resistant to machining-induced cracking.

Fabrication of LDGC restorations is accomplished by CAD/CAM machining of LMGC followed by sintering, glazing and polishing processes conducted in an arbitrary manner. This

research also investigated the surface quality of CAD/CAM-milled and subsequent surface-treated LMGC/LDGC with respect to phase transformation, surface roughness and morphology, and removal mechanisms. CAD/CAM machining induced extensive brittle cracks and crystal pulverization indicating the dominant fracture mode material removal mechanism for LMGC. Subsequent polishing and sintering respectively improved the surface roughness after milling while polishing and glazing did not improve the roughness after sintering. To have a smooth surface on the milled LMGC, it was proposed that polishing must be applied after milling before sintering (i.e. CAD/CAM-polished-sintered process). The improved surface quality from this procedure was lower than the threshold surface roughness for bacterial plaque retention.

Fabrication of Y-TZP restorations is carried out by CAD/CAM machining of pre-sintered Y-TZP followed by sintering and polishing. Sandblasting is also applied to roughen the cementation surface for improved adhesion with the luting cement. This research investigated the surface quality of CAD/CAM-milled pre-sintered Y-TZP which subsequently underwent sintering, polishing and sandblasting processes with respect to phase transformation, surface roughness and morphology, and removal mechanisms. CAD/CAM milling induced both partial ductile and brittle fracture modes as the dominant material removal mechanism in pre-sintered Y-TZP. Subsequent polishing and sintering processes could not improve the surface roughness after milling respectively. Polishing after sintering did not improve the roughness. However, the simultaneous application of polishing and sintering processes after the CAD/CAM milling significantly produced the surface roughness that met the bacterial plaque retention surface roughness threshold and was therefore recommended (i.e. CAD/CAM-polished-sintered process). In addition, sandblasting the sintered Y-TZP with 110 μm and 250 μm alumina particles produced similar surface roughness but less severe damage was induced by the former than the latter. Therefore, sandblasting with 110 μm was recommended for sintered Y-TZP restorations.

Finally, low-cycle-high-load Hertzian cyclic spherical indentations simulating teeth grinding and clenching in the posterior region where the highest concentrating stresses occur were conducted to study the fatigue behavior of treated LDGC and Y-TZP surfaces. Maximum contact stresses were evaluated as functions of number of cycles and surface treatments using the Hertzian model. The fatigue damage of treated LDGC and Y-TZP surfaces after cyclic indentations was viewed using SEM to understand the relationships among microstructures, surface asperities and crack propagation.

The maximum contact stresses of indented LGDC surfaces reduced significantly with the number of cycles and surface treatments (ANOVA, $p < 0.05$). The smoothest CAD/CAM-

polished-sintered surfaces sustained the highest maximum contact stresses and the least fatigue damage at higher number of cycles. Furthermore, quasi-plastic deformation was dominant on all indented surfaces at a single indentation. At higher indentations, partial cone cracks were formed on all surfaces; radial and transverse cracks were formed on the roughest surfaces. In addition, ring cracks, fretting, pulverization, micro-bridges, surface smearing and wedging and edge chippings were propagated on all surfaces. Therefore, the proposed fatigue mechanism was mechanically assisted growth of surface asperities for treated LDGC surfaces and the rougher the surface, the heavier the induced mechanical damage.

The maximum contact stresses of indented Y-TZP surfaces reduced significantly with number of cycles and surface treatments (ANOVA, $p < 0.05$). The CAD/CAM-polished-sintered surfaces sustained the highest maximum contact stresses. The surface quality influence on the fatigue damage of treated Y-TZP surfaces was dependent on the asperities present. At a single indentation, quasi-plastic deformation was induced on all surfaces. At higher indentations, cyclic indentations led to plastic deformation-induced smoothening process which increased with number of cycles. Therefore, crack surface-roughness-induced closure was the main fatigue mechanism proposed for this material. However, cyclic indentations also led to intergranular fractures in the roughest surfaces and phase transformation in the smoothest CAD/CAM-polished-sintered surfaces. With respect to sandblasted surfaces, cyclic indentations induced more fatigue damage on surfaces abraded with 250 µm alumina grains than 110 µm alumina grains.

The fundamental research conducted in this thesis provides technical insights into the fabrication and application of LDGC and Y-TZP for durable restorations.

# Table of Contents

# List of Figures

# List of Tables

# List of Publications

| **Refereed Journal Papers** | **Status** |
|---|---|
| 1. **A.-R. Alao**, R. Stoll, X.-F. Song, T. Miyazaki, Y. Hotta, Y. Shibata, L. Yin, Surface quality of yttria-stabilized tetragonal zirconia polycrystal in CAD/CAM milling, sintering, polishing and sandblasting processes, Journal of the Mechanical Behavior of Biomedical Materials 65 (2017) 102–116. | Published |
| 2. **A.-R. Alao**, L. Yin, Assessment of elasticity, plasticity and resistance to machining-induced damage of porous pre-sintered zirconia using nanoindentation techniques, Journal of Materials Science & Technology 32 (2016) 402–410. | Published |
| 3. **A.-R. Alao**, L. Yin, Nano-mechanical behaviour of lithium metasilicate glass-ceramic, Journal of the Mechanical Behavior of Biomedical Materials 49 (2015) 162–174. | Published |
| 4. **A.-R. Alao**, L. Yin, Nanoindentation characterization of the elasticity, plasticity and machinability of zirconia, Materials Science & Engineering: A Structural Materials 628 (2015) 181–187. | Published |
| 5. **A.-R. Alao**, L. Yin, Loading rate effect on the mechanical behavior of zirconia in nanoindentation, Materials Science & Engineering: A Structural Materials 619 (2014) 247–255. | Published |
| 6. **A.-R. Alao**, L. Yin, Nano-scale mechanical properties and behavior of pre-sintered zirconia, Journal of the Mechanical Behavior of Biomedical Materials 36 (2014) 21–31. | Published |
| **Submitted Journal Paper** | |
| 7. **A.-R. Alao**, R. Stoll, X.-F. Song, J.R. Abbott, L. Yin, Surface integrity of CAD/CAM-milled and surface-treated lithium metasilicate/disilicate glass-ceramics, Journal of Materials Science: Materials in Medicine. | In review |
| **Refereed Conference Papers** | |
| 8. L. Yin, **A.-R. Alao**, X.-F. Song, R. Stoll, Manufacturing reliable ceramic crowns –The role of abrasive machining in digital dentistry, Proceedings of the ASME International Manufacturing Science and Engineering Conference (MSEC 2016), June 27-July 1, 2016, Virginia Tech, Virginia, USA. | Published |

| | |
|---|---|
| 9. **A.-R Alao**, L. Yin, Machinability determination of dental ceramics using nanoindentation (Conference Abstract), 6th International Conference on Mechanics of Biomaterials and Tissues, December 6-10, 2015, Hawaii, USA. | Published |
| 10. **A.-R Alao**, L Yin, Prediction of the resistance to machining-induced cracking in zirconia by nanoindentation, Recent Advances in Structural Integrity Analysis: Proceedings of the Asian-Pacific Conference on Fracture and Strength/the International Conference on Structural Integrity and Failure (APCF/SIF-2014), December 9–12, 2014, Sydney, Australia, Woodhead Publishing/Elsevier, UK, pp 580–584. | Published |

# Chapter 1

# Introduction

## 1.1 General

Ceramics are widely used in restorative dentistry as implants, crowns and bridges because of their excellent mechanical, aesthetic, and biocompatibility, transformation toughening capability and chemical properties (Kelly, 1997; Rekow and Thompson, 2007; Denry and Holloway, 2010). Depending on the mechanical and aesthetic requirements in dentistry, a variety of dental ceramics are available. These include felspathic porcelains, mica glass ceramics, lithium disilicate glass ceramics (LDGC), and alumina and zirconia-based ceramics. LDGC and yttria-stabilized tetragonal zirconia polycrystal (Y-TZP) have been selected for further investigation in this study because they are the state-of-the-art materials for dental appliications as load-bearing and wear-resistant structures.

LDGC has the highest strength and fracture toughness among the glass ceramics; and excellent chemical durability and aesthetic property (Anusavice and Zhang, 1997; ElBatal et al., 2009; Guess et al., 2010b). The high strength and toughness of LDGC arise from the layered and interlocked lithium disilicate crystals due to the mismatch in thermal coefficients and elastic moduli between lithium disilicate crystals and glassy phases forming compressive stresses which deflect advancing cracks (Apel et al., 2008; Denry, 2013; Denry and Holloway, 2010; Serbena and Zanotto, 2012). It is mainly used for fabricating dental restorations (Höland et al., 2000). Similarly, Y-TZP has high strength and fracture toughness, low thermal conductivity, high ionic conductivity and is biocompatible. Thus, it is widely used in engineering and medicine as thermal barrier coatings, fuel cell electrolytes, pump components, valve seals, bushings/bearings, body implants, hip prostheses, dental crowns and bridges (Chevalier et al., 2009; Miyazaki et al., 2013; Piconi and Maccauro, 1999; Ritzberger et al. 2010; Swain 1985; 2009). The high fracture toughness of Y-TZP is associated with the tetragonal-to-monoclinic ($t \rightarrow m$) phase transformation (Garvin et al., 1975; Hannink and Swain, 1994; Hannink et al., 2000) or ferroelastic domain switching (Cain and Lewis, 1990; Virkar and Matsumoto, 1986), resulting in a high damage tolerance (Kelly and Denry, 2008). Consequently, both LDGC and Y-TZP possess excellent properties enabling the fabrications of crowns and multiple unit bridges in large stress-bearing (posterior) areas with the labside or chairside computer aided design/computer aided manufacturing (CAD/CAM) abrasive machining. In addition, their

restorations may not require veneers especially in areas where a high degree of translucency is not important, thereby minimizing veneering-associated problems (Zhang et al., 2013a). The brittleness of the veneering ceramics and the mismatch in the coefficient of thermal expansion between the veneer and the core generating tensile residual stresses at the interface have been reported to have caused veneered ceramics fractures (Lawn et al., 2002a, 2002b; Taskonak et al., 2005, 2006; Zhao et al., 2012). Finally, their restorations can be conventionally luted.

## 1.2 Problem Statements

### *1.2.1 Mechanical Behavior of LMGC/LDGC and Y-TZP*

CAD/CAM-abrasive machining of LDGC and Y-TZP are done by machining their pre-sintered blocks which are lithium metasilicate glass ceramics (LMGC) and pre-sintered Y-TZP respectively followed by post-machining sintering. Direct machining of their fully sintered blocks (sintered and pressable LDGC and sintered Y-TZP) is also conducted in restorative dentistry (Denry and Holloway, 2010; Denry and Kelly, 2008). In both processing routes, the hard diamond abrasives make numerous and simultaneous indentations and scratches on these brittle materials, inducing inevitably surface/subsurface damage and resulting in poor surface quality and property degradation (Rekow and Thompson, 2005). To minimize machining-induced damage for these materials, there is a need to comprehensively understand the mechanical behavior of these materials which, in turns, provides scientific insights into their machining behavior and mechanical functions. Further, understanding their elastic/plastic deformations, ductility indices, resistances to plasticity and resistances to machining-induced cracking is a crucial prerequisite for evaluating and predicting their machinability.

The materials' behavior in indentation studies using diamond indenters mimics their machining responses in diamond abrasive machining with respect to deformations and fractures (Lawn and Cook, 2012). Thus, the indentation approach lays a foundation mechanics for abrasive machining (Komanduri et al., 1997; Malkin and Hwang, 1996). Particularly, machining forces, cutting speeds and abrasive geometries can be simulated by indentation loads, loading rates and indenter geometries, respectively (Yan et al., 2006). In nanoindentation, loading rates mimic the dynamic feature in abrasive machining. They are manifest on the force-displacement curves as discrete discontinuities and continuous deformation which can be correlated to several phenomena including incipient plasticity, shear banding, dislocation activity, fracture and phase transformation (Schuh, 2006). For LDGC and Y-TZP in pre-sintered, sintered and pressed

states, loading rate effect has not been elaborately studied and linked to their behavior in abrasive machining.

### *1.2.2 CAD/CAM Millling of LMGC/LDGC and Y-TZP*

High strength of LDGC and its brittle glassy phase make the machining of LDGC difficult using the existing chair-side or lab-side dental CAD/CAM technology (Denry and Holloway, 2010). Instead, diamond abrasive machining of LMGC becomes practical (Denry and Holloway, 2010). Similarly, the CAD/CAM machining of sintered Y-TZP induces martensitic $t \rightarrow m$ phase transformation making it more susceptible to ageing, thereby putting it at risk of catastrophic failure (Silva et al., 2010; Zarone et al., 2011). Thus, Y-TZP is often machined in its pre-sintered state (Klocke et al., 1998) which is the key procedure in its dental CAD/CAM processing (Al-Amleh et al. 2010; Denry, 2013; Filser et al., 2003; Rekow and Thompson, 2005; Ritzberger et al., 2010). The CAD/CAM-milled LMGC and pre-sintered and Y-TZP are subsequently sintered to produce LDGC and Y-TZP restorations respectively. Other post-machining processes including polishing and glazing may be added to achieve accurate occlusal fits for masticatory functions while sandblasting with alumina abrasives is used to treat Y-TZP cementation surfaces for improved adhesion (Guess et al., 2010b; Miyazaki et al., 2013; Zhang et al., 2004a). This thesis also investigates the surface quality of CAD/CAM-machined LMGC and pre-sintered Y-TZP and subsequent post-machining surface treatments with respect to phase transformations, surface roughness and morphology and removal mechanisms.

### *1.2.3 Fatigue Behavior of Treated LDGC and Y-TZP Surfaces*

The induced damage during CAD/CAM milling of LMGC and pre-sintered Y-TZP may not be healed in the subsequent sintering process (Rekow and Thompson, 2005; Rekow et al., 2011). This damage serves as stress concentration sites for crack initiation, nucleation and propagation, reducing fatigue strength and lifetimes of restorations. Also, post-machining treatments may have an adverse effect on the fatigue property but this has hitherto not reported. Further, human masticatory function is a cyclic loading process and has been reported to be subject to 1400–1500 cycles/day, with loads as high as 100–800 N at the rate of 1.5 Hz (Rekow and Thompson, 2005; 2007). A number of fatigue studies were done on dental ceramics using the conventional load-to-fracture methods including tension-tension, flexure, shear, torsion or compression (Chevalier et al., 1999; Baran et al., 2001; Zhu et al., 2003, Studart et al., 2007a; 2007b). However, in these methods, exceedingly greater failure loads than the ranges for mastication were reported. Also, the methods reported incorrect stress states, and the crack systems were not

representative of the bulk failures reported clinically (Kelly et al., 2010). Consequently, Hertzian contact tests have been used to study dental fatigue behavior. This form of testing provides a fundamental method for characterizing the failure mechanisms of dental materials in relation to contact conditions simulating oral loading conditions and is characterized by contact load and indenter radius that have direct clinical relevance (Peterson et al., 1998). The contact load simulates occlusal load and the indenter radius simulates cuspal. Hertzian contact tests have been carried out to characterize various failure modes on dental ceramics. Depending on the specimen configurations, applied loads (concentrated or sliding), outer, inner and partial cones, median and radial cracks and quasi-plastic damage can be formed and critical loads have been reported for these cracks (Deng et al., 2002a; Lawn et al., 2001; 2002a; 2002b; 2004; 2007; Peterson et al., 1998). However, the prevailing fatigue failure modes of CAD/CAM-milled LMGC and pre-sintered Y-TZP subject to subsequent surface treatments have not been unraveled. Understanding the response of different surface asperities to fatigue damage is critically important in predicting the clinical success of restorations (Rekow et al., 2011). In addition, in the posterior region, teeth grinding or clenching (bruxism) with a high chewing force up to 800 N often occurs in the oral environment (Rekow and Thompson, 2007). Therefore, the LDGC and Y-TZP restorations must be able to withstand this high cyclic force. The low-cycle-high-load cyclic Hertzian indentation enables the prediction of fatigue property in a short-crack domain within a stress concentration region in which most dental ceramics are vulnerable. This thesis also investigates the low-cycle-high-load cyclic Hertzian indentation of treated LDGC and Y-TZP surfaces with respect to maximum contact stresses as a function of cyclic numbers, and the relations among microstructures, surface asperities and crack propagation.

## 1.3 Aim and Objectives

The overall aim of this project is to investigate fundamental issues in the fabrication of LDGC and Y-TZP restorations for high reliability. This aim can be realized by addressing the following objectives:

1. *To characterize rate effect on nano-scale mechanical behavior of LMGC, sintered and pressed LDGC, pre-sintered and sintered Y-TZP, and link to their behavior abrasive machining responses.*
2. *To partition their deformations into elasticity and plasticity and compare their resistances to plasticity, ductility indices and resistances to machining-induced cracking.*

3. *To fabricate LMGC and pre-sintered Y-TZP with the clinically used CAD/CAM technique and study their machining responses.*
4. *To subject the CAD/CAM-milled LMGC and pre-sintered Y-TZP surfaces to different surface treatments and investigate the surface quality in terms of phase transformations, surface roughness and morphology and material removal mechanisms.*
5. *To investigate the influence of different surface asperities on the fatigue behavior of sintered LDGC and Y-TZP surfaces obtained from the CAD/CAM-milling of LMGC and Y-TZP which are subjected to post-fabrication treatments.*

The research outcomes provide scientific insights into the fabrication of the high-strength LDGC and Y-TZP restorations for prolonged lifetimes.

## 1.4 Thesis Organization

Chapter 1 introduces the thesis highlighting the different ceramics in dental applications and the rationale behind the selection of LDGC and Y-TZP as the research focus of this study. The problems associated with the fabrication of LDGC and Y-TZP ceramics are identified, and the aim and objectives of the study are unambiguously enumerated. Finally, a brief thesis overview is presented in this section.

Chapter 2 presents a detailed literature review related to this research with a particular emphasis on dental ceramics and CAD/CAM systems. In both cases, the emphasis is placed on LDGC and Y-TZP. Part of the work in this chapter will be presented and published in the following conference proceeding:

1. *L. Yin, A.-R. Alao, X.-F. Song, R. Stoll, Manufacturing reliable ceramic crowns–The role of abrasive machining in digital dentistry, Proceedings of the ASME International Manufacturing Science and Engineering Conference (MSEC 2016), June 27–July 1, 2016, Virginia Tech, Virginia, USA.*

Chapter 3 investigates the mechanical behavior of LMGC, sintered and pressable LDGC, pre-sintered and sintered Y-TZP, using nanoindentation and *in situ* scanning probe imaging techniques. It provides a detailed literature review on nanoindentation studies conducted on these materials and the rationale for studying their mechanical behavior in the Introduction. It further details the characterization experiments used in the extraction of their mechanical properties from force-displacement curves using the Oliver-Pharr model. It also presents the

analysis of their indentation-induced deformation mechanisms studied from their indentation imprints and depth cross-sectional profiles. Finally, it discusses the linkage between their studied mechanical behavior and their machining responses during sharp abrasive machining. The bulk of this chapter has been largely reported in the following journal articles:

1. *A.-R. Alao, L. Yin, Nano-scale mechanical properties and behavior of pre-sintered zirconia, J. Mech. Behav. Biomed. Mater. 36 (2014) 21–31.*
2. *A.-R. Alao, L. Yin, Loading rate effect on the mechanical behavior of zirconia in nanoindentation, Mater. Sci. Eng. A–Struct. Mater. 619 (2014) 247–255.*
3. *A.-R. Alao, L. Yin, Nano-mechanical behaviour of lithium metasilicate glass-ceramic, J. Mech. Behav. Biomed. Mater. 49 (2015) 162–174.*

Chapter 4 studies the advanced analysis of mechanical behavior of LMGC, sintered and pressed LDGC, pre-sintered and sintered Y-TZP using nanoindentation techniques. It provides a detailed literature review and the rationale for studying their advanced mechanical behavior in the Introduction. It presents the analysis of their deformations partitioned into elasticity and plasticity, and the extraction of their resistances to plasticity using the Sakai model. It also analyzes their ductility indices and resistances to machining-induced cracking using the Sakai-Nowak model. Finally, it discusses and ranks their machinability theoretically based on this quantitative analysis. The bulk of this chapter has been largely reported in the following journal articles and conference proceedings:

1. *A.-R. Alao, L. Yin, Nanoindentation characterization of the elasticity, plasticity and machinability of zirconia. Mater. Sci. Eng. A–Struct. Mater. 628 (2015) 181–187.*
2. *A.-R. Alao, L. Yin, Assessment of elasticity, plasticity and resistance to machining-induced damage of porous pre-sintered zirconia using nanoindentation techniques, J. Mater. Sci. Technol. 32 (2016) 402–410.*
3. *A.-R. Alao, L. Yin, Prediction of the resistance to machining-induced cracking in zirconia by nanoindentation, Recent Advances in Structural Integrity Analysis: Proceedings of the Asian-Pacific Conference on Fracture and Strength/the International Conference on Structural Integrity and Failure (APCF/SIF-2014), December 9–12, 2014, Sydney, Australia, Woodhead Publishing/Elsevier, UK, pp 580–584.*

Chapter 5 studies the surface quality of CAD/CAM-milled LMGC and subsequently subject to different sintering, polishing and glazing conditions with respect to phase transformations, surface roughness and morphology, and removal mechanisms. A thorough literature review and

reasons for the study are carried out in the Introduction. Detailed experimental procedures are also presented. The fabrication process that produces the lowest surface quality which meets the bacterial plaque retention threshold is proposed for this material. The content of this chapter has been submitted to the following journal:

1. *A.-R. Alao, R. Stoll, X.-F. Song, J.R. Abott, L. Yin, Surface integrity of CAD/CAM-milled and surface-treated lithium metasilicate/disilicate glass-ceramics, J. Mater. Sci.: Mater. Med., in review.*

Chapter 6 studies the surface quality of CAD/CAM-milled pre-sintered Y-TZP that undergoes subsequent sintering, polishing and sandblasting treatments with respect to phase transformations, surface roughness and morphology, and removal mechanisms. A thorough literature review and reasons for the study are carried out in the Introduction. Detailed experimental procedures are also presented. The fabrication process that produces the lowest surface quality which meets the bacterial plaque retention threshold is recommended for this material. The content of this chapter has been published in the following journal:

1. *A.-R. Alao, R. Stoll, X.-F. Song, T. Miyazaki, Y. Hotta, Y. Shibata, L. Yin, Surface quality of yttria-stabilized tetragonal zirconia polycrystal in CAD/CAM milling, sintering, polishing and sandblasting processes, J. Mech. Behav. Biomed. Mater. 65 (2017) 102–116.*

Chapter 7 investigates the fatigue behavior of differently treated LDGC and Y-TZP surfaces produced from CAD/CAM-milled LMGC and pre-sintered Y-TZP respectively as outlined in Chapters 5 and 6. It provides a detailed literature review on fatigue studies of dental ceramics and the rationale for studying the fatigue behavior of these materials in the introduction. It details the experimental procedures for the low-cycle-high-load cyclic Hertzian indentations used in the study. The fatigue mechanisms of treated LDGC and Y-TZP surfaces are proposed.

Chapter 8 presents the concluding remarks for this work highlighting the contributions made to knowledge as well as recommendations for future work.

# Chapter 2

# Literature Review

## 2.1 Introduction

In restorative dentistry, many dental materials are available, including metals, ceramics, polymers and composites. Historically, metals are the oldest restorative materials that have been widely used as crowns, fixed partial dentures (FPFs), and removable partial dentures (RPDs). They are mechanically strong and durable, but are not aesthetically pleasing because of their metallic color. Although, they are often fused with ceramics to improve their aesthetics but there are other associated problems. The intraoral galvanic corrosion may occur due to the potential difference between two dissimilar metals leading to the flow of current between them through intraoral fluids (saliva) that can serve as electrolyte (Bergman et al., 1978; Ciszewski et al., 2007; Horasawa et al., 1999; Sutow et al., 2004; 2006). This can lead to allergic or toxic reactions within the soft or hard tissues of the oral cavity potentially causing intraoral cancer. Therefore, the patients' demand for metal-free restorations with high aesthetic and biocompatible properties has increased over the years. To this end, there has been tremendous growth in the use of dental ceramics in the restorative dentistry. These dental ceramics which are reviewed in this chapter are glass ceramics emphasizing more on LDGC and polycrystalline ceramics with emphasis placed on zirconia. This chapter also reviews dental CAD/CAM systems, CAD/CAM machining effects on LDGC and Y-TZP in pre-sintered and sintered states.

## 2.2. Glass Ceramics

### *2.2.1 Feldspathic Porcelains and Leucite Glass Ceramics*

Introduced in 1774 into dentistry, porcelains are used mostly as veneers fused to prosthetic metals or other ceramics due to their excellent aesthetic properties (Kelly, 1997). Seghi et al. (1990) reported that feldspathic porcelains are low-strength and low-fracture-toughness dental ceramics. But their continuous clinical usage stems from their aesthetic appeals, ability to fit to the prepared tooth and ability to be acid-etched to form micro-mechanically retentive features for the adherence of dental cements (Kelly, 1997). Vita Mark II is an example of feldspathic porcelain for dental use as inlays/onlays and veneers. Due to their high brittleness and large amount of glassy phase, porcelains are more vulnerable to fracture. Therefore, their physical and mechanical properties have been subjected to continual improvements with the addition of

reinforcements like leucite (potassium alumino silicate-$KAlSi_2O_6$), which forms the crystalline phase, to improve their thermal expansion behavior (Kelly, 1997). Despite this reinforcement with the leucite phase, strength improvement is still limited by the intrinsic weakness of the glassy phase (Song and Yin, 2012). Therefore, leucite glass ceramics have been recommended for inlays/onlays, veneers and single crowns. Examples of leucite reinforced glass ceramic available for CAD/CAM machining include ProCAD and Empress™ CAD (Li et al., 2014).

### *2.2.2 Mica Glass Ceramics*

Mica-based glass ceramics are machinable ceramics that allow machining to be performed with conventional cutting tools, thereby facilitating the fabrication of dental restorations (Xiang et al., 2007). Its machinability originates from the weak interfaces between the mica crystals and the glassy matrix that promote local microfracture and material dislodgement during machining (Xu and Jahanmir, 1998). Furthermore, it is reported that these glass ceramics have good physical properties that closely match human enamel in terms of density, thermal conductivity, refractive index and translucency (Dong et al., 2000). Two types of mica-based glass ceramics are being used as dental ceramics: Macor and Dicor. The difference between these two ceramics has its root in their microstructures. Dicor microstructural crystals are composed of about 70% tetrasilicic fluormica ($K_2Mg_6Al_2Si_6O_{20}F_4$) precipitated in a 30% glass matrix whereas Macor consists of fluorine phlogopite ($KMg_3AlSi_3O_{10}F_2$) crystals (Conrad et al., 2007). Mica-based glass ceramics are commercially fabricated by CAD/CAM or melt-cast technology. Mechanical and biological properties of these materials are highly dependent on the composition and the crystalline phase. However, these ceramics suffer from low hardness and insufficient mechanical strength, restricting their dental usage to inlays/onlays and veneers (Montazerian et al., 2008).

### *2.2.3 Alumina Glass Composites*

Alumina glass composites (glass infiltrated alumina or In-Ceram Alumina) was designed for making all-ceramic prostheses to replace the conventional glass ceramics due to failures and brittleness associated with them (Hornberger et al., 1996). Consequently, In-Ceram Alumina has been reported to show some improvements in strength. This strength enhancement can be attributed to the excellent wetting of alumina particles within the infiltrated glassy phase resulting in low porosity, the filling of the glass phase at low triple points (Hornberger et al., 1996). The internal (residual) stresses resulting from the difference in the thermal expansion coefficients between the alumina and the glassy phases also contribute to the strength

enhancement of this composite (Hornberger et al., 1996). The fabrication of the In-Ceram Alumina system is based on a partially-sintered, porous alumina structure infiltrated with molten lanthanum glass and veneered with feldspathic porcelains. In-Ceram Alumina system may contain about 70% alumina, 25% glass phase and 5% porosity by volume. The presence of large alumina crystals, with a high refractive index together with a non-negligible amount of porosity, accounts for the high degree of opacity (Denry and Holloway, 2010).

### *2.2.4 Lithium Metasilicate /Disilicate Glass Ceramics (LMGC/LDGC)*

LDGC was developed as a biomaterial by Professor Hench following his extensive research in the physical chemistry of glasses (Barrett et al., 1980). LDGC is a high aesthetic and strength dental glass ceramic. It consists mainly of lithia ($Li_2O$) and silica ($SiO_2$) with some additives like potassia ($K_2O$), zinc oxide (ZnO), zirconia ($ZrO_2$) and phosphorus pentoxide ($P_2O_5$) to form a $Li_2O$-$SiO_2$-$K_2O$-ZnO-$ZrO_2$-$P_2O_5$ system. The silica has the highest composition of about 70% by weight and $P_2O_5$ serves as the nucleating agent. Laboratory preparation of LDGC involves the melting of an appropriate glass batch at 1,200–1,450 $^oC$ for 4 hours followed by quenching in cold water to form a frit (El-Meliegy and van Noort, 2012). The glass block is then annealed, and crystalized by surface and volume crystallization mechanism (El-Meliegy and van Noort, 2012). During this process two heating cycles are normally applied for crystal nucleation at 480–600 $^oC$ and growth at a higher temperature. After the full crystallization process, the crystalline phase is precipitated in the glass matrix and the main crystalline phase is lithium disilicate crystals. Other metastable phases like lithium orthophosphate ($Li_3PO_4$), lithium orthosilicate ($Li_4SiO_4$) and lithium metasilicate ($Li_2SiO_3$) of much lower volume have been reported to have been formed first during the first crystallization process and are the precursor phases to the formation of lithium disilicate crystals (Iqbal et al., 1998; Höland et al., 2000; ElBatal et al., 2009; Goharian et al., 2010; Yuan et al., 2013). A representative $Li_2O$-$SiO_2$ equilibrium system showing the characteristic lithium orthosilicate, lithium metasilicate and lithium disilicate phases is displayed in Fig. 2.1. The melting points of $Li_2O$ and $SiO_2$ are 1,727 and 1,713 $^oC$ respectively.

Dental crowns and fixed partial dentures (FPDs) can be made easily from LDGC by heat-pressed method or CAD/CAM method. For the CAD/CAM method, LMGC containing metastable lithium metasilicate crystals of approximately 100 MPa strength is machined by the CAM process and then sintered at 850 $^oC$ for full crystallization (Denry and Holloway, 2010; Guess et al., 2010b; Yin and Stoll, 2014). LMGC is obtained by a controlled nucleation and crystallization of the base glass ($SiO_2$-ZnO-$K_2O$-$Li_2O$) through heat treatments with little or no

porosity (Beall, 1992; Cramer von Clausbruch et al., 2000). Its microstructure which consists of 40% lithium metasilicate crystals, of a grain size of 0.5–1 µm and in platelet-shape form, embedded in a glassy phase is shown in Fig. 2.2(a). It is milled directly to generate complex inlay/onlay, single crown and three-unit bridge profiles using chair-side or laboratory dental CAD/CAM systems equipped with diamond abrasive tools (Guess et al., 2010b; Silva et al., 2011). After milling, LMGC prostheses subsequently undergo heat treatments which lead to the formation of the stable, high strength (360–400 MPa) and highly translucent LDGC (Goharian et al., 2010; Höland et al., 2006a; Iqbal et al., 1998; Kracek, 1930; Soares et al., 2003; Yuan et al., 2013; Zheng et al., 2008). The conversion from lithium metasilicate to lithium disilicate crystals is associated with a negligible linear shrinkage of only about 0.2–0.3% (El-Meliegy and van Noort, 2012). The microstructure of sintered LDGC consists of 70% lithium disilicate crystals embedded in a glassy matrix with a grain size measuring 1–1.5 µm in length (Fig. 2.2(b)). An example of the LMGC available for CAD/CAM machining is IPS e.max CAD.

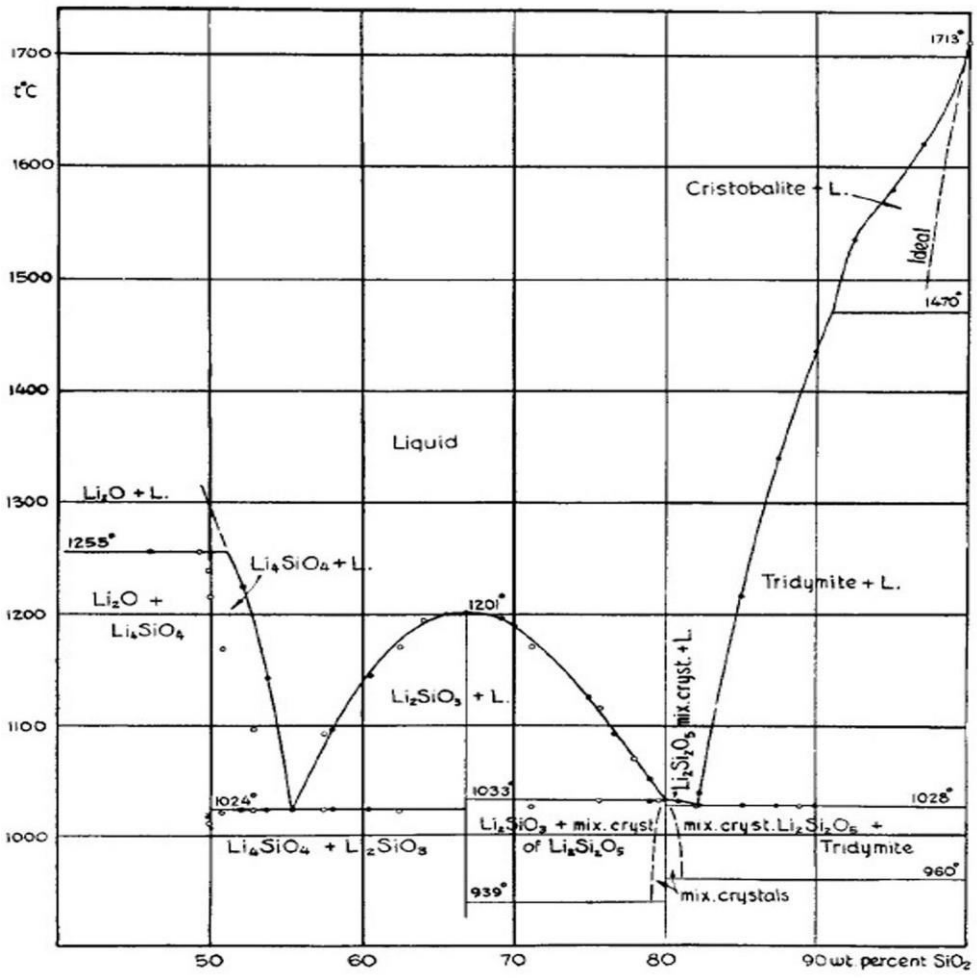


Fig. 2.1. The phase equilibrium diagram for the $Li_2O$-$SiO_2$ system (Kracek, 1930).

For the traditional heat-pressed method, the glass ceramic ingots are placed into a pressing furnace using the viscous flow mechanism and heated to a temperature of 920 $^{o}$C (Höland et al., 2000). The pressed glass ceramic becomes viscous at this temperature and is pressed in the plastic state into a mold to form a dental restoration. The microstructure of the pressed LDGC consists of 70% needle-like lithium disilicate crystals embedded in a glassy matrix with a grain size measuring 3–6 µm in length (Fig. 2.2(c)). IPS e.max Press is a typical pressable LDGC used for dental restorations.

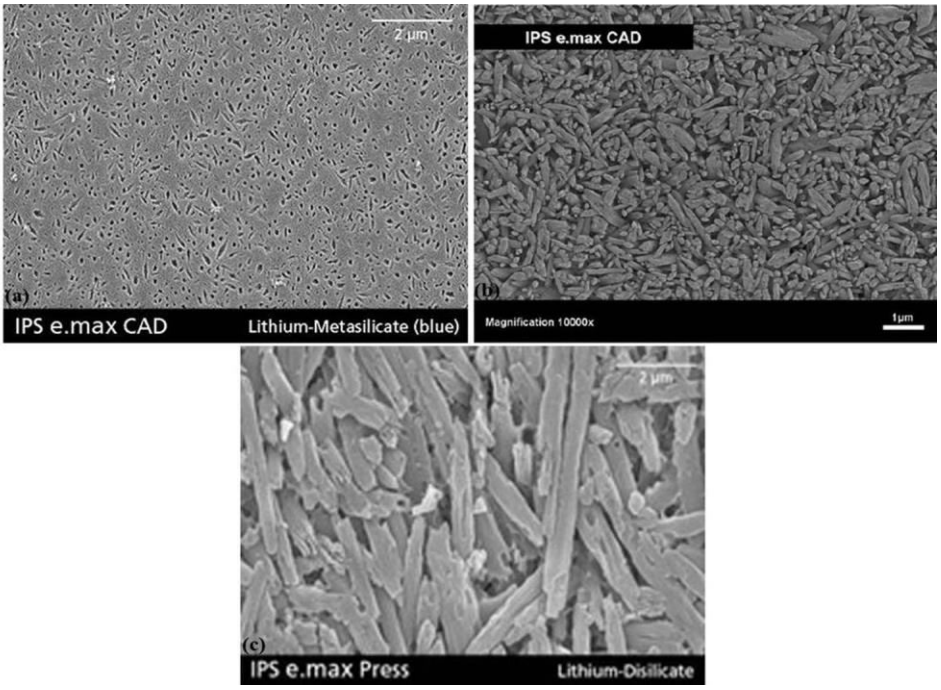


Fig. 2.2. SEM micrographs showing the microstructures of (a) LMGC (Bühler-Zemp and Völkel, 2005a), (b) sintered LDGC (Ritzerberger et al., 2010), and (c) pressable LDGC (Bühler-Zemp and Völkel, 2005a).

As expected, the CAD/CAM and heat-pressed methods give different microstructures resulting in different properties of sintered and pressable LDGC. The higher platelet length, width and thickness in the lithium disilicate crystals of the pressed LDGC account for its slightly higher strength (440 MPa) than the sintered LDGC (360–400 MPa) as shown in Fig. 2.2.

Many studies report that due to lithium disilicate crystals, natural refraction of light and improved flexural strength is possible (Höland et al., 2000). The mechanism for the strength enhancement in LDGC can be explained in terms of the mismatch in the coefficient of thermal expansion between lithium disilicate crystals and the glassy matrix forming tangential compressive stresses (Denry and Holloway, 2010). These stresses around the crystals are

potentially responsible for crack deflection and strength increase. The interlocked microstructure and layered crystals (Fig. 2.2) can also contribute to strengthening. The crack-deflection phenomenon was confirmed by Apel et al. (2008) who reported that cracks only propagated through the residual glass phase that constitutes about 30-40% by volume and not through the lithium disilicate crystals.

A number of studies have been conducted on the strength of CAD/CAM manufactured and heat-pressed LDGC. In comparison with other glass ceramics (feldspathic porcelains, leucite glass ceramics), and resin-based composite, the fracture strength of CAD/CAM LDGC manufactured for inlay FPDs was significantly higher than that of other materials (Bindl et al., 2003). Also, the fracture strength of conventionally (zinc-phosphate) cemented LDGC posterior crowns fabricated with CAD/CAM systems was higher than that of feldspathic porcelains and leucite reinforced glass ceramics (Bindl et al., 2006). In addition, the pressed LDGC was reported to exhibit higher fracture strength than leucite glass ceramic (Albakry et al., 2003; Della et al., 2004; Guazzato et al., 2004).

## 2.3 Polycrystalline Ceramics

### *2.3.1 Alumina and Magnesia-Alumina Ceramics*

Improving the translucency of the alumina dental ceramics, particularly In-Ceram Alumina, requires minimizing the porosity. Therefore, densely-sintered, high-purity alumina (Procera) was developed (Andersson and Odén, 1993). Procera, produced by dry-pressing followed by sintering, contains high crystalline alumina (more than 99.5%) with little or no porosity. As a result of the negligible amount of porosity, this material's translucency has been significantly better than that of In-Ceram Alumina. Also, magnesia-based dental ceramics (In-Ceram Spinell) was introduced as a substitute for the opaque In-Ceram Alumina. In-Ceram Spinell contains a mixture of magnesia and alumina ($MgAl_2O_4$) in the framework to increase translucency (Conrad et al., 2007). In fact, Heffernan et al. (2002) reported that In-Ceram Spinel had the highest amount of relative translucency among all-ceramic cores. However, the addition of $MgAl_2O_4$ to the In-Ceram Spinel compromises the mechanical properties of the ceramic with improved aesthetic feature restricting its usage to the anterior segment (Conrad et al., 2007).

### *2.3.2 Zirconia-Based Ceramics*

Zirconia was discovered in 1789 by Martin Heinrich Klaproth after heating some gems (Piconi and Maccauro, 1999). Zirconium comes from the Arabic word (zargon, meaning-golden in color) derived from the two Persian words zar (gold) and gun (color). Since its discovery, zirconia products have been used in many industries (Piconi and Maccauro, 1999). Tough, wear resistant, refractory zirconia ceramics are used to produce parts in extrusion dynes, valves, port liners for combustion engines; zirconia blades are used to cut Kevlar and magnetic tapes. High temperature ionic conductivity makes zirconia ceramics suitable as solid electrolytes in fuel cells and oxygen sensors (Piconi and Maccauro, 1999).

Zirconia was also introduced as a biomaterial due to its good chemical and dimensional stability, and high mechanical strength and toughness. It was used for the fabrication of prosthetic crowns and FPDs with CAD/CAM technique (Denry and Kelly, 2008). Among all the dental ceramics, zirconia-based ceramics exhibit an unsurpassed fracture toughness and strength due to transformation toughening. Its toughening capability is often explained in terms of the transformation of one crystal structure to another (Garvin et al., 1975). It has three polymorphs, depending on temperature and pressure. At ambient pressure, unalloyed zirconia is monoclinic (*m*) at room temperature up to 1170 $^{o}$C; it is tetragonal (*t*) between 1170 $^{o}$C and 2370 $^{o}$C and cubic above this temperature up to the melting point (2680 $^{o}$C) as shown in the relation below. These polymorphic forms are schematically shown in Fig. 2.3.

$$\text{Orthorhombic} \leftrightarrow \text{monoclinic} \xleftrightarrow{1170^{o}C} \text{tetragonal} \xleftrightarrow{2370^{o}C} \text{cubic} \xleftrightarrow{2680^{o}C} \text{liquid.}$$

Tetragonal zirconia crystal is metastable and adjusts itself to an equilibrium state by transforming to the stable monoclinic structure. This process occurs at about 950 $^{o}$C. The spontaneous reverse transformation ($t \rightarrow m$) is accompanied by a significant increase in volume (about 3-5%) sufficient to lead to a fatal failure. To avoid this catastrophic failure, the retention of the *t*-structure has to be maintained while cooling to room temperature. This retention is often done by alloying pure zirconia with stabilizing oxides (dopants) like calsia (CaO), magnesia (MgO), yttria ($Y_2O_3$), alumina ($Al_2O_3$), ceria ($CeO_2$), europia ($Eu_2O_3$), erbia ($Er_2O_3$), gadolinia ($Gd_2O_3$), scandia ($Sc_2O_3$), lanthania ($La_2O_3$) and ytterbia ($Yb_2O_3$). These processes form zirconia-based ceramics such as yttria-tetragonal zirconia polycrystal (Y-TZP), magnesia partially stabilized zirconia (Mg-PSZ), zirconia-toughened alumina (ZTA), ceria tetragonal zirconia crystals (Ce-TZP) etc. These dopants allow the retention of the *t*-structure at room temperature thereby controlling the stress-induced $t \rightarrow m$ transformation, arresting crack propagation and leading to high toughness (Garvin et al., 1975; Hannink et al., 2000; Lughi and

Sergo, 2010). Mg-PSZ, Y-TZP and ZTA are the commonly used zirconia-based ceramics in the dental industry (Denry and Kelly, 2008). The microstructural features of the major categories of zirconia are shown in Fig. 2.4.

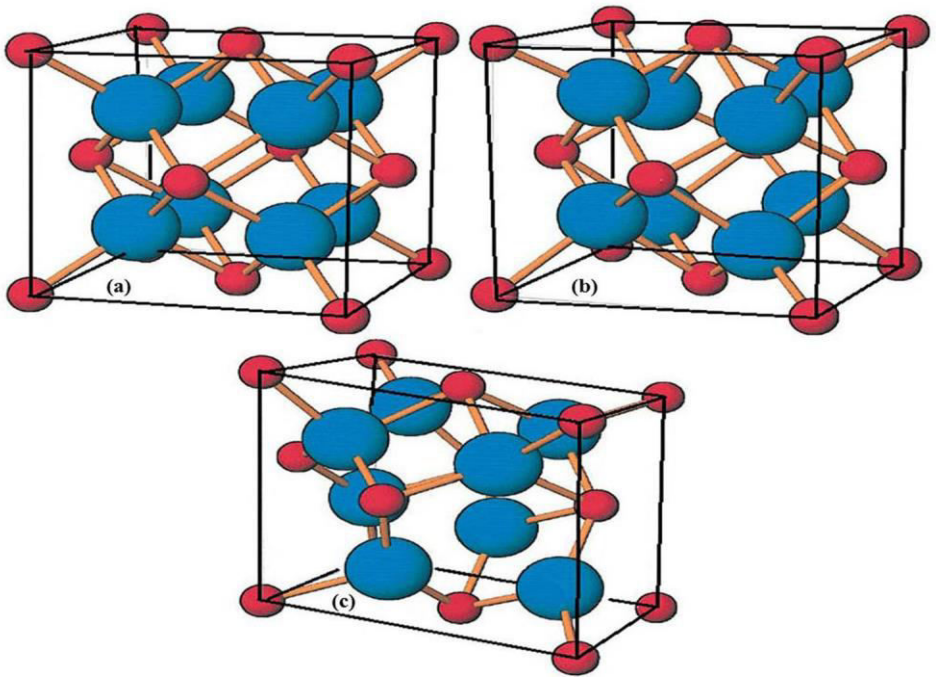


Fig. 2.3. Schematic representation of three polymorphs of zirconia: (a) monoclinic ($P2_1/c$), (b) tetragonal ($P4_2/nmc$), (c) cubic ($Fm\bar{3}m$) (Hannink et al. 2000).

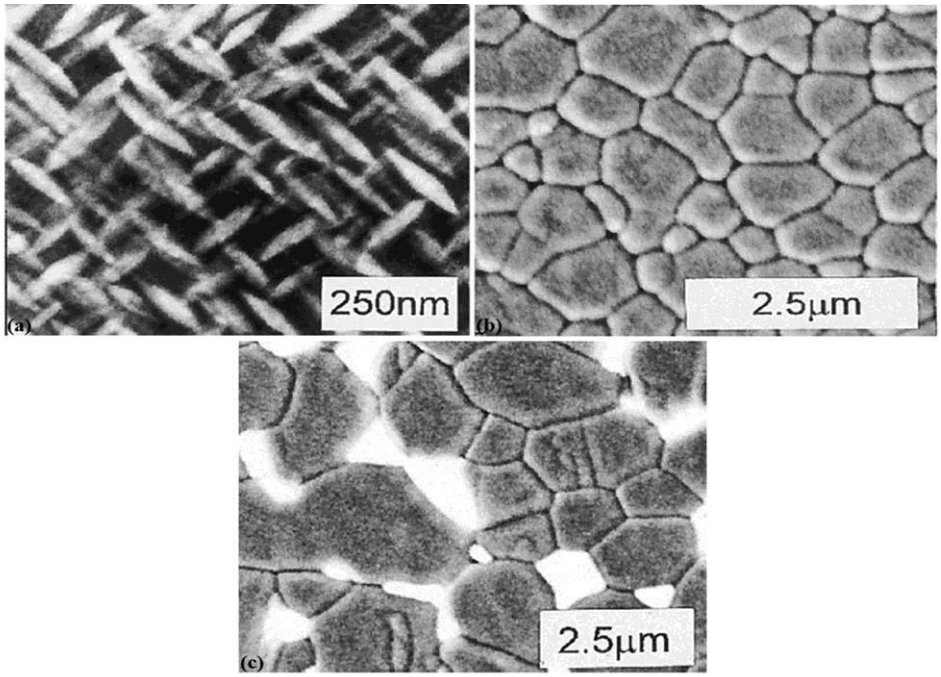


Fig. 2.4. Microstructural features of the three major categories of zirconia-based ceramics: (a) MgPSZ, (b) Y-TZP, and (c) ZTA (Hannink et al. 2000).

However, Y-TZP is the only zirconia-based composite that has reached the status of having a dedicated ISO standard for surgical application (Lughi and Sergo, 2010) rationalizing its selection in this study. A typical $Y_2O_3$-$ZrO_2$ phase equilibrium system showing the Y-TZP region containing *t*-grains only at room temperature and partially stabilized zirconia (PSZ) region consisting of *t* and *c* phases is displayed in Fig. 2.5. The room temperature-retained fraction of *t*-phase is reportedly dependent on grain size and yttria content and the grade of constraint exerted on these two parameters (Picano and Maccauro, 1999). These parameters, in turn, determine the mechanical properties of Y-TZP (Picano and Maccauro, 1999).

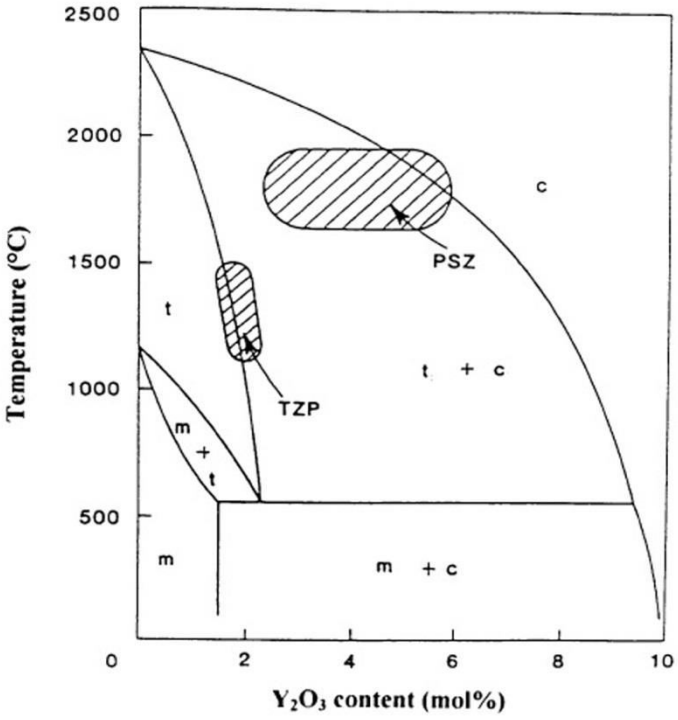


Fig. 2.5. The phase equilibrium diagram for the yttria-zirconia system (Scott, 1975). The *m*, *t*, and *c* represent monoclinic, tetragonal and cubic phases respectively. TZP and PSZ represent tetragonal zirconia polycrystal and partially stabilized zirconia respectively.

Y-TZP exhibits the transformation toughening phenomenon. Piconi and Maccauro (1999) explained the transformation toughening mechanism in zirconia in terms of the dissipation of energy. As shown in Fig. 2.6, the stress field associated with volume expansion due to $t \rightarrow m$ transformation acts in opposite to the stress field that promotes crack propagation. Fracture toughness is enhanced because the energy of the advancing cracks is dissipated in the transformation process as well as in overcoming the compressive stresses due to volume expansion. The crack propagation is thus hindered due to the compressive stress acting on the crack tip. The formation of compressive stresses on the surface strengthens the material (Lawson, 1995; Deville et al., 2006).

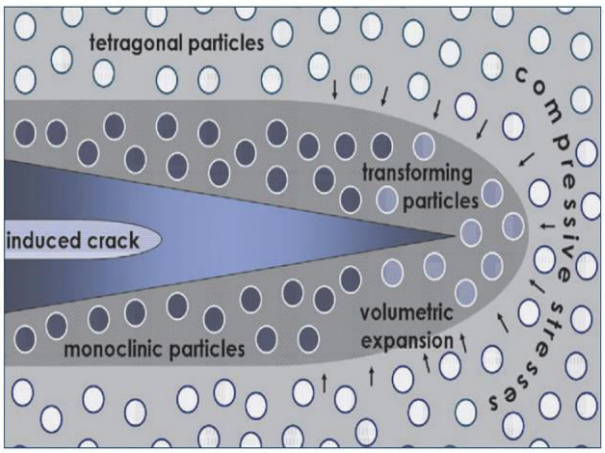


Fig. 2.6. Schematic representation of the mechanism for enhanced fracture toughness due to phase transformation in zirconia (Vagkopoulou et al., 2009).

Another possible source of toughening in Y-TZP is crack-propagation-induced or stress-induced ferroelastic domain switching proposed by Virkar and Matsumoto (1986). Ferroelasticity may occur in PSZ (Fig. 2.5) when, under the action of an external stress, a *c*-phase transforms to a *t*-phase which has about six crystallographically equivalent orientations (Chevalier et al., 2009). These *t*-phase orientations (domains) have the same energy but can switch from one orientation to another when the applied compressive stress exceeds the coercive stress (the stress required for ferroelastic transition) (Cain and Lewis, 1990). In the case of Y-TZP (Fig. 2.5), ferroelasticity may occur on the *t*-phase in which each grain can be a single domain. Then, individual grains or portions within each grain can be switched to a different orientation by an applied stress or in the presence of a propagating crack (Chevalier et al., 2009). The toughening effect relates to this change from one equilibrium state to another equilibrium state unlike in transformation toughening which involves mainly $t \rightarrow m$ transformation. Also, Cain and Lewis (1990) reported the occurrence of ferroelastic transition in Y-TZP at a coercive stress of 1.6 GPa.

The transformation toughening capability of Y-TZP is beneficial to the natural tooth. Natural tooth may contain many cracks in the enamel that do not propagate through the entire tooth (Giordano, 2006). These cracks can be stopped by the unique interface at the enamel-dentin junction (EDJ). The ability to stop cracks as they enter the Y-TZP core structure mimics the effect seen in natural teeth. This effect was reported by Preis et al., (2012). Enamel antagonists showed wear, cracks, fractures, but revealed smooth surfaces when opposed to polished/ground/repolished Y-TZP but ploughed when opposed to ground/repolished/ glazed porcelains.

Tensile stresses from grinding, sandblasting and polishing can trigger *t→m* transformation. Depending on the magnitude and type (tensile or compressive) of induced residual stresses, these operations can either strengthen or degrade the strength of Y-TZP. Tensile residual stresses are more favorable for the occurrence of *t→m* transformation in Y-TZP leading to the degradation of the strength while compressive residual stresses are less favorable to the transformation leading to improved strength (Deville et al., 2006). Therefore, fine grinding, mild sandblasting and polishing can induce compressive residual stresses which can inhibit crack propagation, enhancing the strength and fracture toughness. Increase in the flexural strength in Y-TZP during fine grinding was reported (Curtis et al., 2006; Xu et al. 1997). In addition, coarse grinding was reported to reduce the strength of Y-TZP (Curtis et al., 2006; Denry and Holloway, 2006; Kim et al., 2010; Luthardt et al., 2002a; 2004; Xu et al. 1997). This is because coarse grinding induces in ceramics micro-cracks which exceed the compressive layer produced by the grinding-induced *t→m* transformation (Li and Liao, 1996). The reported micro-crack depth on Y-TZP was 15 μm due to the coarse grinding attributed to the changes in the sharpness of the diamond tool and number of active grains (Luthardt et al., 2004). Machining-induced damage was also reported for high-strength Y-TZP up to 6 μm micro-cracks (Kim et al., 2010).

Increase in the strength of the Y-TZP by mild sandblasting was also reported (Curtis et al., 2006; Guazzato et al., 2005; Karakoca and Yilmaz, 2009; Kosmač et al., 1999; Wang et al., 2008). The authors attributed this increase to the *t→m* transformation which formed the compressive layer on the surface. However, this layer can be removed in the subsequent heat treatment as shown by Guazzato et al. (2005) when sandblasted surfaces were heated leading to reduced strength. They argued that heat treating the sandblasted Y-TZP surfaces reversed the *m*-phase back to the *t*- phase, removing the compressive surface stresses in the process. However, Wang et al. (2008) showed that thermal firing before or after sandblasting had no effect on the strength of Y-TZP. This may be the case if the thermally-induced grain size does not exceed the critical grain size for the occurrence of spontaneous *t→m* transformation. Above this critical grain size, the strength of Y-TZP decreased (Nakamura et al., 2012; Stawawarczyk et al., 2013; Trunec, 2008). Consequently, the thermal firing process should be selected appropriately to avoid grain coarsening larger than the critical size. In addition, severe sandblasting with coarse alumina abrasives induced damage to Y-TZP which reduced its strength (Chintapalli et al., 2013; 2014; Zhang et al., 2004a).

Phase transformation in Y-TZP can also be triggered in humid environment, a phenomenon known as low temperature degradation (LTD)/hydrothermal degradation or ageing. LTD can

lead to strength degradation and micro-cracking in Y-TZP (Chevalier et al., 2007; Lughi and Sergo, 2010). It is a slow *t*→*m* transformation occurring over time at low temperatures when the transformation is not triggered by the local stress produced at the tip of an advancing crack. It roughens the surface mechanically and aesthetically; increasing wear rates with grains pull out. Consequently, it leads to degradation in mechanical properties due to the formation of *m*-structure and once this is formed, reverting back to *t*-phase is almost impossible (Lughi and Sergo, 2010). It is formed by a process known as autocatalysis (Fig. 2.7). In Fig. 2.7(a), the whole microstructure of the sample is composed of *t*-grains with the top surface exposed to water (liquid or vapor). As shown in Fig. 2.7(b), one grain transforming to *m*-structure on the top surface is free to expand provoking an uplift of the surface itself. On the left, right and below, the newly formed monoclinic grain is constrained by the surrounding untransformed material. Since this grain is limited in its expansion, a large compression is implied, $-\sigma_1$, whereas its push against the surrounding materials gives room to a small tensile stress, $+\sigma_1$. In Fig. 2.7(c), when more grains transform to *m*-structure, they are less constrained and the compressive stress diminishes to $-\sigma_2$, whereas they put in larger tensile stress, $+\sigma_2$, in the remaining *t*-structure. Micro-cracks originating from the *t*→*m* transformation facilitate the inward diffusion of water.

A number of studies have been conducted to investigate LTD in Y-TZP. In summary, the characteristic factors responsible for the LTD in Y-TZP are water or water vapor, temperature (most sensitive in the range of 200–300 $^{o}$C), leading to intergranular fracture (Paul et al., 2011). However, some studies have also reported that LTD does not occur below a certain grain size of ≈ 0.3 μm (Guicciardi et al., 2007; Paul et al., 2011) and certain processes (grinding and sandblasting) can enhance LTD resistance due to the occurrence of *t*→*m* transformation (Kosmač et al., 2000; Kim et al., 2010).

## 2.4 Dental CAD/CAM Systems

Conventional fabrication processes of dental crowns and bridges generally involve intraoral abutments, impression, working model, waxing up, casting of metal works, porcelain works, final restorations, luting to the abutments (Miyazaki et al., 2009). These processes are manually operated, labor-intensive, and heavily depended on the art crafts of individual dental clinicians. Also, such methods are unlikely useful for the fabrication of crowns or bridges made of modern dental ceramics. Sophisticated dental CAD/CAM technologies have, therefore, been introduced to restorative dentistry since 1980's. These systems have the capability to produce the entire spectrum of restorations from inlays to full-coverage crowns and multi-unit bridges directly at

the chairside in dental clinics (Andersson and Odén, 1993; Beuer et al., 2009; Miyazaki et al., 2009; Mörmann, 2006; Rekow and Thompson, 2005; Strub et al., 2006; Yin et al., 2006). Also, these systems have been automated not only to realize uniform material quality but also to ensure the standardization of the dental restoration process reducing the manufacturing cost and shortening the fabrication process (Wittneben et al., 2009). Further, they can be used to shape high-strength dental ceramics.

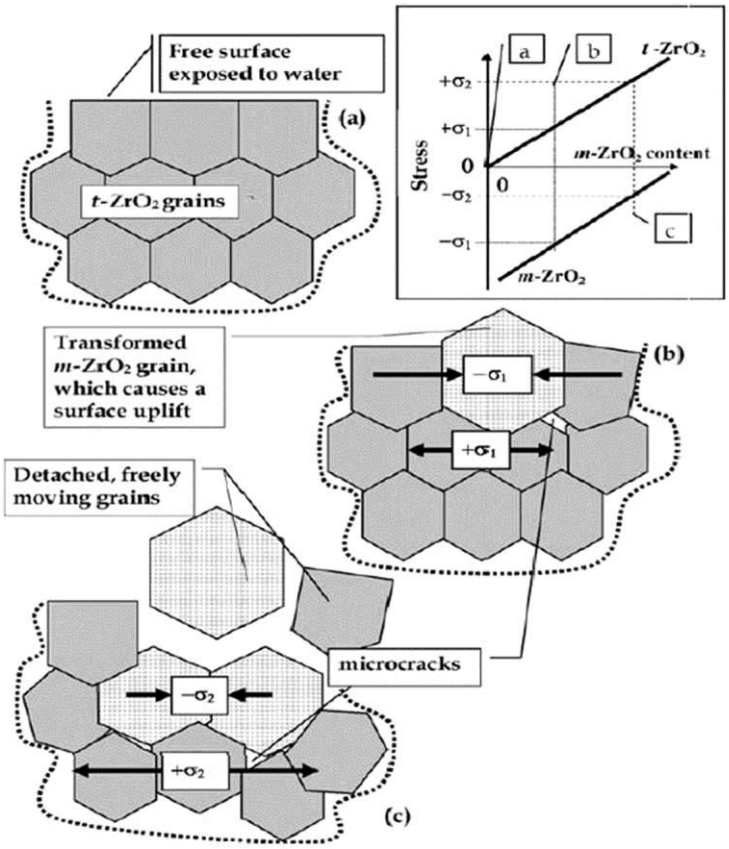


Fig. 2.7. Schematic representation of the mechanics of low temperature degradation by autocatalysis process (Lughi and Sergo, 2010).

Similar to any other CAD/CAM systems applied in manufacturing engineering, dental CAD/CAM systems are also based on data acquisition, data processing and manufacturing (Fig. 2.8). They consist of digital image generation and data acquisition, computer-assisted milling systems and tooling systems (Miyazaki et al., 2009, Yin et al., 2006). For instance, intraoral digitizing (optical impression) is used to replace the conventional impression. CAD is applied for replacing the virtual model/waxup. CAM with NC machining/milling is utilized to generate final restorations. Now it is possible to create a 3D model of the oral cavity directly with advanced computer-aided scanning systems. The digital model can then be used to design the

restoration, such as crowns, bridges and partial denture framework in less than 20 minutes (Miyazaki et al., 2009).

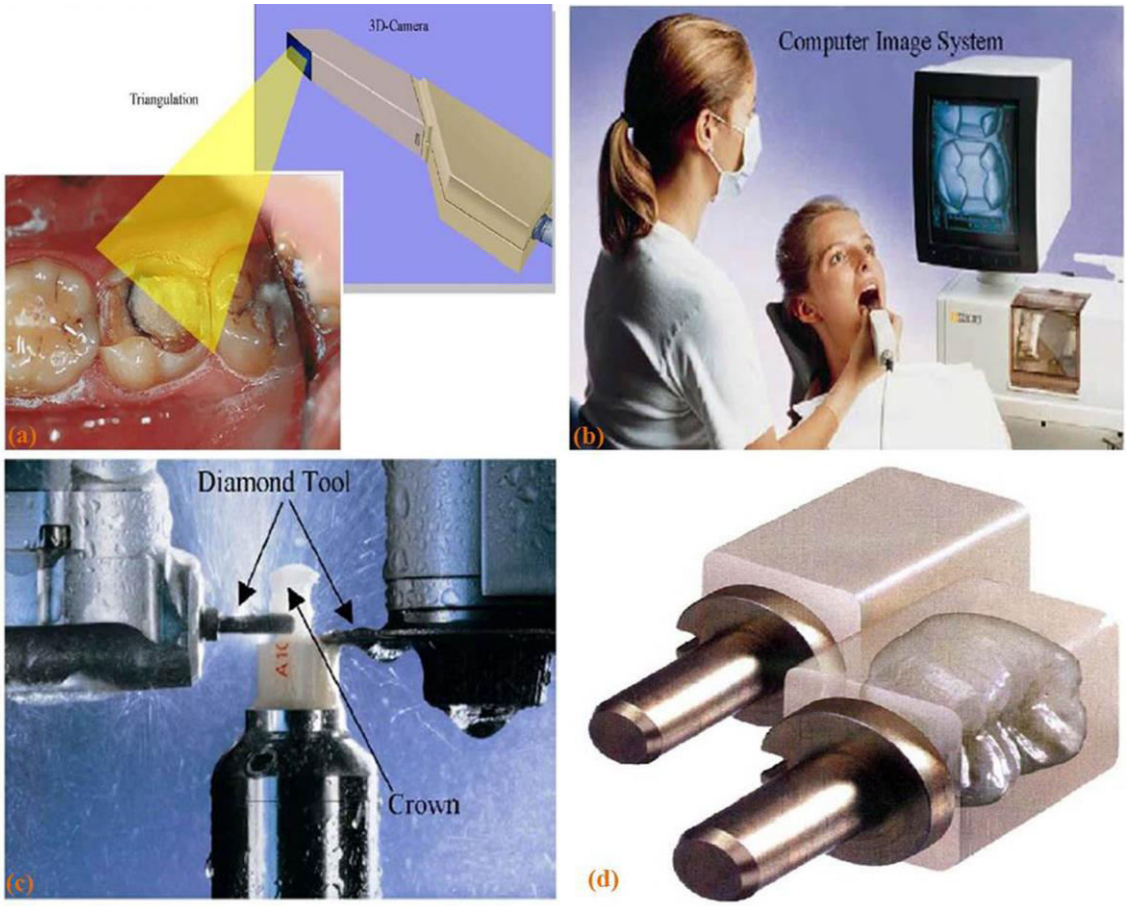


Fig. 2.8. (a) 3D camera for computer–aided optical triangulation system, (b) data acquisition converted into virtual image, (c) computer-aided manufacturing, (d) the manufactured crown from a blank (Yin et al., 2006).

The mechanical/optical digitizers or scanning devices (e.g. contact probes) available in various dental CAD/CAM systems are used for acquiring data. They are used to scan and record the oral environment (tooth prepared, adjacent teeth and occluding tooth geometry) as shown in Fig. 2.8(a) in which a triangulation-based 3D camera is applied. The CAD software then designs the restoration with wireframe design, freeform surface generation or solid modelling (Fig. 2.8(b)) and transforms the virtual model into a specific set of commands that drives the CAM unit (Yin et al., 2006). Once the restoration solid model is established, abrasive machining using diamond tools is commonly involved in milling and grinding of ceramic blocks to generate dental restorative profiles. First, computer-aided process planning (CAPP) needs to be approved. Following is the CAM process in which a diamond milling toolpath needs to be designed to

machine the ceramic block to generate the basic restorative profile. Details of these operations include defining the machining boundaries, options of auto cut, cut single or cut all, selections of machining parameters for multi-axis solids or surface toolpaths, and toolpath capabilities of finishing (Yin et al., 2006). Fig. 2.8(c) shows the CAM process in which two diamond abrasive burs are used. The twin milling units with the two axes of four degrees of freedom for each one are installed for simultaneous processing of restorations with two diamond burs. The machining conditions such as depth of cut, feed rate and cutting speed are automated within most of the systems. Fig. 2.8(d) shows a typical manufactured crown from a blank ceramic.

Commercial dental CAD/CAM systems are classified as chairside or office-based and laboratory-based. Chairside dental CAD/CAM systems provide in-office design and milling, allowing one-appointment restoration fabrication using prefabricated ceramic monoblocks. Today, the most popular chairside system is the Cerec AC (Sirona Dental Systems GmbH, Bensheim, Germany), which was introduced in 1987 by Mörmann (2006) and the first dental system to combine digital scanning with a milling unit. Over the thirty years, the Cerec systems have been significantly evolved. The current version is capable of taking half arch or full arch impressions and creating crowns, veneers and multiple unit bridges. It is equipped with an advanced intraoral 3D scanning device (digitizer) using intense blue light from blue light-emitting diodes and powerful software to create 3D restorative models. This system also enables the milling of a very wide spectrum of all machinable dental ceramics. The milling units have the function of digital closed-loop feed control for extremely sensitive processing of ceramic materials.

Laboratory-based dental CAD/CAM systems are much larger, more expensive, and have more integrated and precise functions in comparison with chairside systems (Beuer et al., 2008; Davidowitz and Kotick, 2011; Strub et al., 2006). These systems are particularly useful for direct grinding or milling of fully sintered, completely dense Y-TZP or alumina ceramic restorations with high strength. Thus, sintering-induced shrinkage can be avoided to obtain high precision of restorations. More advanced laboratory-based CAD/CAM systems are centralized production using machining centers and network systems (Beuer et al., 2008; Strub et al., 2006). In addition, satellite scanners in the dental laboratory can be connected to a production center via the internet. Data sets of restorative models produced in the dental laboratory are sent to the machining center for the manufacture of restorations. These laboratory-based devices or machining centers use 3-axis, 4-axis or 5-axis milling systems using tungsten carbide end milling tools or single-layered electroplated diamond tools (Davidowitz and Kotick, 2011; Miyazaki et al., 2009). For pre-sintered ceramic blocks, dry-milling is generally used to reduce

the machining cost and avoid moisture absorption by the highly porous ceramic (Beuer et al., 2008). For fully sintered high-strength ceramics, wet milling with diamond tools is conducted to reduce the machining heat and machining-induced damage to the ceramic workpiece. Tool wear in machining of these fully sintered ceramics is very severe. The common dental ceramics, their applications in restorative dentistry, mechanical properties and luting systems and the available dental CAD/CAM systems are summarized in Table 2.1.

### *2.4.1 CAD/CAM Machining Effects on LMGC/LDGC, Pre-Sintered and Sintered Y-TZP*

So far, there has been no dedicated dental CAD/CAM system available for the machining of LDGC because its high strength and brittleness of the glassy phase make it difficult for machining (Denry and Holloway, 2010; Li et al., 2014; Ritzberger et al., 2010). As explained previously, the CAD/CAM machining of LMGC, which contains lithium metasilicate crystals, is often carried out using some of the systems listed in Table 2.1 and then sintered to ensure full crystallization into LDGC. Although the sintering process can reduce the extent of mechanical residual stresses from machining but the machining-induced damage is not completely eliminated by this treatment (Denry, 2013). This damage can become fracture origins, reducing the lifespans of LDGC restorations. Thus, this study is undertaken to address fundamental fabrication issues on these two important dental ceramics to prolong their lifetimes using the objectives outlined in Chapter 1.

As reported in Table 2.1, sintered Y-TZP can be machined by some dental CAD/CAM systems. Due to its poor machinability and high hardness, the CAD/CAM systems must be strong, stiff and robust (Denry and Kelly, 2008; Rekow et al., 2011). The effects associated with the machining of the sintered Y-TZP include the generation of micro-cracks with coarse abrasives (Luthardt et al., 2004) and the $t \rightarrow m$ martensitic transformation rendering it susceptible to LTD and putting it at risk of spontaneous failure (Silva et al., 2010; Zarone et al., 2011). Tool wear is also a common feature in the CAD/CAM machining of sintered Y-TZP. Therefore, the CAD/CAM machining of pre-sintered Y-TZP is often preferred to eliminate the $t \rightarrow m$ martensitic transformation and reduce the tool wear (Al-Amleh et al. 2010; Denry, 2013; Rekow and Thompson, 2005; Ritzberger et al., 2010). Some dental CAD/CAM systems for this purpose are also listed in Table 2.1. However, because of the high brittleness of pre-sintered Y-TZP, machining-induced cracking can also occur during its CAD/CAM machining process which is not healable during the subsequent sintering process (Kim et al., 2010). This can compromise the strength of Y-TZP restorations as well as their fatigue property shortening their lifetimes.

Table 2.1. Dental ceramics, CAD/CAM systems, restorative applications, and mechanical property (Denry and Kelly, 2008; Fasbinder et al., 2010; Liu, 2005; Miyazaki et al., 2009).

| Dental ceramic | CAD/CAM system | Restorative application | Conventional cementation | Flexural strength (MPa) |
|---|---|---|---|---|
| Mica glass ceramic (Dicor MCG) | Cerec | Inlays, onlays, veneers | No | <100 |
| Feldspathic porcelain (Vita Mark II) | Cerec, Decsy Scan | Inlays, onlays, veneers, anterior crowns | No | 150 |
| Leucite glass ceramics (ProCAD) | Cerec InLAB, Everest, Decsy Scan | Inlays, onlays, veneers, anterior crowns | No | 150 |
| LMGC (IPS e.max CAD) | Cerec 3, Cerec InLab, Everest | Inlays, onlays, veneers, crowns, bridges | Yes | 130 |
| In-Ceram Spinell (MgO) | Cerec 3, Cerec InLab | Anterior crowns | Yes | 350 |
| In-Ceram Alumina | Cerec 3, Cerec InLab, DCS Precident, Celay | Crowns, anterior bridges | Yes | 500 |
| Alumina | Procera | Crowns, bridges | Yes | 600 |
| In-Ceram Zirconia (ZTA) | Cerec 3, Cerec InLab, DCS Precident | Crowns, bridges | Yes | 750 |
| Pre-sintered Y-TZP (IPS e.max ZirCAD) | DSC Precident, Lava, Everest, Cercon, Cerec | Crowns, bridges | Yes | 50–90 |
| Sintered Y-TZP (IPS e.max ZirCAD) | DCS Precident, Everest, Denzir, Cercon, Katana | Crown, bridges | Yes | >1,000 |

# Chapter 3

# Mechanical Behavior of LMGC, Sintered and Pressable LDGC, Pre-Sintered and Sintered Y-TZP

## 3.1 Introduction

The understanding of the mechanical behavior of LMGC, sintered and pressable LDGC, pre-sintered and sintered Y-TZP is critical in determining their machinability and machining mechanisms. The materials' behavior in indentation studies using diamond indenters mimics their machining responses in diamond abrasive machining with respect to deformations and fractures (Lawn and Cook, 2012). Thus, the indentation approach lays a foundation mechanics for abrasive machining (Komanduri et al., 1997; Malkin and Hwang, 1996). Particularly, machining forces, cutting speeds and abrasive geometries can be simulated by indentation loads, loading rates and indenter geometries, respectively (Yan et al., 2006).

Concerted efforts have been made towards understanding the mechanical behavior of pressable LDGC and sintered Y-TZP. In particular, Hertzian indentation was performed to characterize deformations and fractures for pressable LDGC (Lawn et al., 2004; Zhang and Lawn, 2004; Zhang et al., 2013a) and sintered Y-TZP (Lawn et al., 2002b; Lee et al., 2000; Peterson et al., 1998). The Hertzian indentation is ideal to measure the elastic properties and the elastic-plastic transitions (Oyen and Cook, 2009). In general, sharper indenters, such as Vickers, can induce larger stresses and strains sufficient to displace large material volumes and impose large amounts of shear stresses allowing easy plastic deformation (Lawn and Cook, 2012; Oyen and Cook, 2009). For instance, micro-indentation of pressable LDGC was conducted, in which fractures were observed (Albakry et al., 2003; Apel et al., 2008; Guazzato et al., 2004). Also, Vickers indentations were used to study the plastic behavior of sintered Y-TZP (Alcalá, 2000; Anton and Subhash, 2000; Klecka and Subhash, 2010; Munoz-Tabares et al., 2012). Those microscale indentation studies also demonstrated fracture mechanisms for pressable LDGC and sintered Y-TZP in which critical load thresholds for median/radial crack formation were exceeded. For porous materials, instrumented indentation tests are preferred to conventional micro-indentation in which uncertainties in measuring the diagonal lengths can be problematic (Tricoteaux et al., 2011). However, little is known about the mechanical behavior of LMGC, sintered LDGC and pre-sintered Y-TZP.

As the scale of deformation becomes small in the sub-threshold region, materials can be removed from brittle materials by plastic deformation leaving a crack-free surface (Bifano et al., 1991). The quest for plasticity is of interest in the development of ductile regime machining of brittle materials to reduce machining damage. In abrasive machining, the plastically deformed material removal can produce crack-free surfaces when machining normal forces are progressively diminished to milli-Newtons per diamond grit (Bifano et al., 1991; Ma et al., 2003; Schmidt and Weigl, 2000; Yin et al., 2004). Therefore, nanoindentation techniques are more suitable to characterize the material behavior at milli-Newton loads (Chintapalli et al., 2012; He et al., 2008; Malkin and Hwang, 1996). They can also be used to probe contact hardness, $H_c$, and Young's modulus, $E$, of materials based on the Oliver–Pharr method (1992, 2004).

Nanoindentation techniques were therefore used to characterize the behavior of pressable LDGC (Buchner et al., 2011; Soares and Lepienski, 2004). In those studies, fractures also occurred at several hundreds of milli-Newtons. This indicates that the critical contact loads to initiate fracture were exceeded. Plastic deformation in pressable LDGC was observed in nanoindentation when a milli-Newton (10 mN) peak load was used (Smith et al., 2014). This confirms that the fracture-dominated mode can be changed to the plastic deformation mode by progressively diminishing contact loads (Lawn and Evans, 1977).

Several nano-mechanical studies were conducted on the Y-TZP behaviour influenced by grain size (Guicciardi et al., 2006; Lian et al., 2007), ageing (Catledge et al., 2003; Gaillard et al., 2008; Guicciardi et al., 2007), indentation size effect (Shao et al, 2013) and crystallographic orientation (Gaillard et al., 2009). However, those studies were conducted at constant loading rates which assumed equilibrium deformation conditions. In fact, loading rates can affect the material hardness (Lawn and Cook, 2012), which is an important material design consideration where hardness is taken as a basis for predicting strength, machinability, wear and erosion characteristics.

At the microscale, loading rate effects on the mechanical behavior of alumina, alumina oxynitride, silicon nitride, silicon carbide, sintered Y-TZP and pyrex glass have been investigated in post-threshold indentations in which fractures occurred (Anton and Subhash, 2000; Klecka and Subhash, 2010; Quinn et al., 2002a). It was also found that loading rates influenced the behaviour and properties of bulk metallic glasses in nanoindentation (Burgess et al., 2008; Concustell et al., 2005; Golovin et al., 2001; Greer et al., 2004; Li et al., 2006, Schuh and Nieh, 2003) and silica glasses (Dey et al., 2011; Limbach et al., 2014). The loading rate

effect is manifest on the force-displacement curves as discrete discontinuities and continuous deformation. These can be correlated to several phenomena including shear banding, dislocation activity, fracture and phase transformation (Schuh, 2006). The use of ***in situ*** scanning probe imaging plays a complementary role for the correct interpretation of the force-displacement responses. However, for LMGC, sintered and pressable LDGC, and pre-sintered and sintered Y-TZP, loading rate effect has not been reported in nanoindentation.

Therefore, this chapter reports results of nanoindentation tests conducted on LMGC, sintered and pressable LDGC, pre-sintered and sinteredY-TZP, at a peak load of 10 mN and 0.1–0.2 mN/s loading rates which probe their mechanical properties and behavior. The Oliver–Pharr model was used to extract their contact hardness values and Young's moduli as a function of loading rate. Indentation responses from the force-displacement curves were related to different mechanically-induced deformations assisted by the ***in situ*** scanning probe microscopy and contact mechanics models including strain rate sensitivity, continuum model and pressure-sensitive idealized yield criterion. The studied mechanical behavior of LMGC, sintered and pressed LDGC, and pre-sintered and sintered Y-TZP were used to simulate their responses in abrasive machining process.

## 3.2 Materials

### *3.2.1 LMGC*

LMGC (IPS e.max CAD, Ivoclar Vivadent) blocks can be directly milled using the chair-side or laboratory dental CAD/CAM systems to generate profiles of crowns, bridges, veneers and inlays. It consists of 57–80 wt% $SiO_2$ and 11–19 wt% $Li_2O$ with some additives including 0–13 wt% $K_2O$, 0–11 wt% $P_2O_5$, 0–8 wt% $ZrO_2$, 0–8 wt% ZnO and other colouring oxides to form a $Li_2O$-$SiO_2$-$K_2O$-$P_2O_5$-$ZrO_2$-ZnO system (Bühler-Zemp and Völkel, 2005a). $Li_2O$ and $K_2O$ act as an oxide modifier while ZnO acts as a network forming agent (Beall, 1992; ElBatal et al., 2009). $ZrO_2$ is added to hamper the crystal growth, refine crystals and consequently to improve the material strength (Apel et al., 2007). The addition of $ZrO_2$ to the base glass also increases the glass transition temperature, viscosity, and crystallization temperature leading to a reduction in the crystal growth (Thieme and Rüssel, 2015). $P_2O_5$ is the nucleating agent which reduces the nucleating energy enabling a reduction in the crystallization temperature and a faster attainment of the lithium metasilicate phase (Wen et al., 2007; Zheng et al., 2008).

LMGC can be obtained by melting a base glass consisting of 69.3 wt% $SiO_2$, 15.4 wt% $Li_2O$, 6.05 wt% $K_2O$, 5.28 wt% ZnO and 3.84 wt% $P_2O_5$ at 1,450ºC and annealing at 450ºC (El-Meliegy and van Noort, 2012). The subsequent heat treatment at 480ºC for 1 hour leads to the precipitation of lithium metasilicate crystals (El-Meliegy and van Noort, 2012). For this material, about 40% lithium metasilicate crystals embedded in a glassy phase with the grain size of approximately 0.5–1 µm has been reported (Bühler-Zemp and Völkel, 2005a; El-Meliegy and van Noort, 2012). The material biaxial strength is approximately 130 ± 30 MPa, the Vickers hardness is 5.4 ± 0.1 GPa and the fracture toughness is 1 ± 0.1 MPa $m^{1/2}$ (Bühler-Zemp and Völkel, 2005a). The Poisson's ratio was provided by Ivoclar Vivadent as 0.235.

Samples with dimension 15 mm × 15 mm × 2 mm were obtained from LMGC blocks by metallographical slicing, grinding, lapping and polishing using successively finer diamond abrasives to obtain the optical surface quality for nanoindentation. Fig. 3.1 shows a polished LMGC surface using scanning probe imaging (NT-MDT NTEGRA, Hysitron, USA). The root-mean-square surface roughness, $R_q$, was approximately 6.1 nm from the scanned area of 50 µm × 50 µm. This $R_q$ surface roughness was selected in comparison with other surface roughness parameters because it was used to establish a criterion for the roughness influence on the measured mechanical properties in nanoindentation studies (Miller et al., 2008).

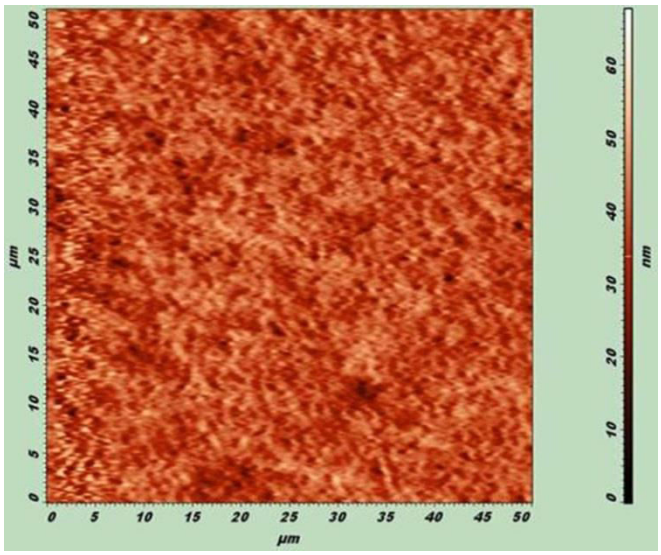


Fig. 3.1. 2D scanning probe image of the polished LMGC.

### *3.2.2 Sintered LDGC*

The studied sintered LDGC was obtained by sintering the LMGC (IPS e.max CAD, Ivoclar Vivadent) in a furnace (MTI GSL1500X) to 850 ºC for 10 minutes at 30 ºC/min heating rate

before naturally cooling to room temperature. In this heat treatment, the metastable lithium metasilicate crystals transformed to lithium disilicate crystals improving the mechanical properties. These sintering conditions agree with the specifications for clinical LDGC restorations (Denry and Holloway, 2010). The material biaxial strength is approximately 360 ± 60 MPa, the Vickers hardness is 5.8 ± 0.1 GPa, the fracture toughness is 2.25 ± 0.25 MPa $m^{1/2}$ (Bühler-Zemp and Völkel, 2005a) and the Poisson's ratio is 0.23 (Ereifej et al., 2011).

Following the sintering process, indentation samples with dimension of 15 mm × 15 mm × 2 mm were obtained using the metallographic procedures described in Section 3.2.1. The indentation samples were scanned using the scanning probe imaging (NT-MDT NTEGRA, Hysitron, USA). Fig. 3.2(a) shows a scanned sintered LDGC surface on which the surface roughness, $R_q$, was 102 nm from the scan area of 50 μm × 50 μm. This indicates that sintered LDGC surfaces became rough due to residual stresses and sintering-induced transformation from lithium metasilicate crystals to lithium disilicate crystals. To meet the sample roughness requirement for nanoindentation, sintered samples were repolished using the same metallographic process for LMGC. After repolishing, sintered LDGC surfaces were rescanned using the scanning probe imaging (NT-MDT NTEGRA, Hysitron, USA). Fig. 3.2(b) shows a scanned repolished sintered LDGC surface, obtaining the surface roughness, $R_q$, of approximately 7.2 nm in the same scan area of 50 μm × 50 μm.

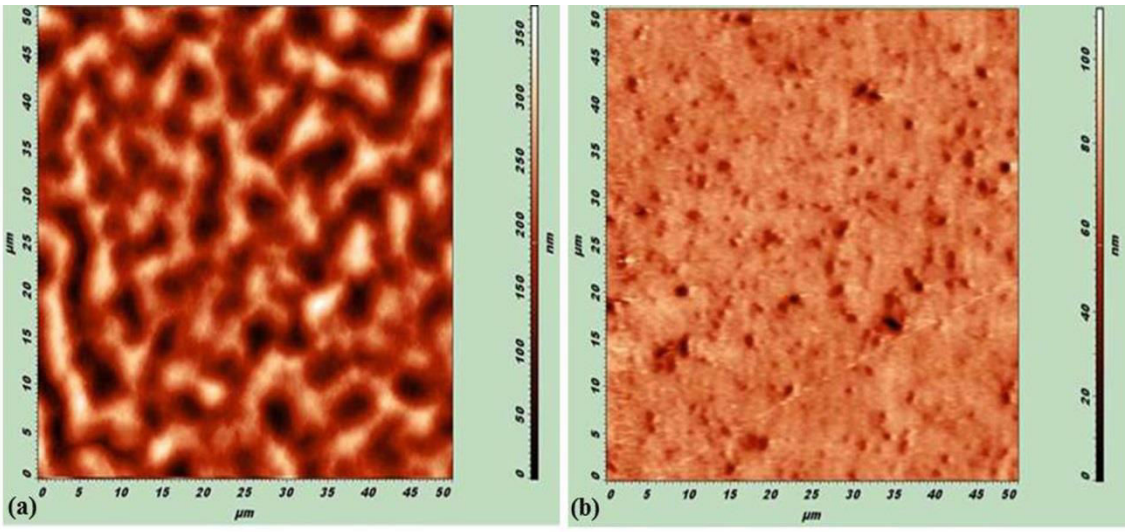


Fig. 3.2. 2D scanning probe images of (a) polished sintered LDGC, (b) sintered and repolished LDGC.

### *3.2.3 Pressable LDGC*

Pressable LDGC (IPS e.max PRESS, Ivoclar Vivadent) basically consists of the same chemical composition as in LMGC but developed as ingots for use with the heat-press technique (Bühler-Zemp and Völkel, 2005b). The ingots were produced by bulk casting and pressing techniques utilizing optimized processing parameters which prevented the formation of pores, pigment or other defects (Bühler-Zemp and Völkel, 2005b). The material biaxial strength is approximately 400 ± 40 MPa, the Vickers hardness is 5.8 ± 0.1 GPa, the fracture toughness is 2.75 ± 0.25 MPa $m^{1/2}$ (Bühler-Zemp and Völkel, 2005b) and the Poisson's ratio is 0.23 (Albakry et al., 2003).

Indentation samples with dimension 15 mm × 15 mm × 2 mm were obtained from pressable LDGC blocks using the metallographic procedures described in Section 3.2.1. Fig. 3.3 shows a polished pressable LDGC surface using the scanning probe imaging (NT-MDT NTEGRA, Hysitron, USA). The surface roughness, $R_q$, was approximately 30.1 nm from the scanned area of 50 µm × 50 µm.

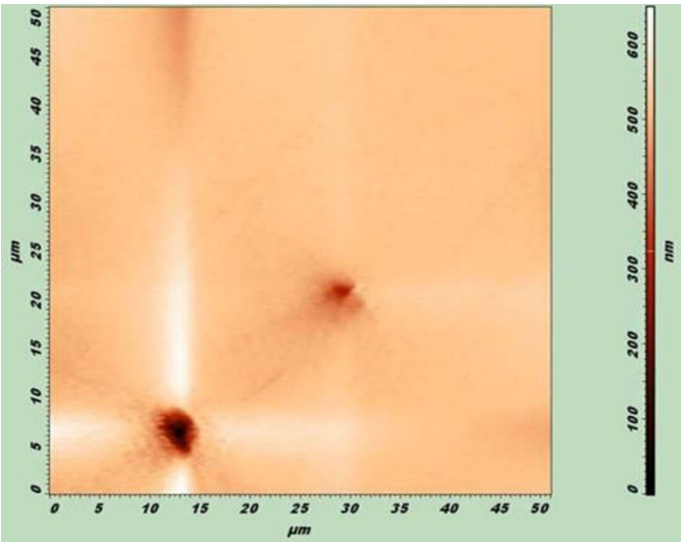


Fig. 3.3. 2D scanning probe image of the polished pressable LDGC.

### *3.2.4 Pre-Sintered Y-TZP*

Pre-sintered Y-TZP (IPS e.max ZirCAD, Ivoclar Vivadent) which is commonly processed chair-side in all dental CAD/CAM systems for crowns and bridges (Denry and Kelly, 2008; Filser et al., 2003) was also studied. This material contains approximately 87–95 wt% $ZrO_2$, 4–6 wt% $Y_2O_3$, 1–5 wt% $HfO_2$ and 0.1–1 wt% $Al_2O_3$ (Ritzberger et al. 2010). $Y_2O_3$ is a stabilizer for retention of tetragonal grains to room temperature while $HfO_2$ binds $ZrO_2$ powders (Denry and

Kelly, 2008). $Al_2O_3$ is added to improve its low temperature degradation resistance. After pre-sintering, the material consisted of 97% tetragonal and 3% monoclinic zirconia (Monaco et al. 2013). Fig. 3.4 shows a fractured specimen microstructure with an isolated or interconnected porous structure and Y-TZP crystals of approximately 300 nm grain size connected to each other by sinter necks using scanning electron microscopy (Jeol JSM5410LV, Japan). The biaxial strength is approximately 50–90 MPa, the density is 3.0–3.21 g/cm$^3$, and the porosity is approximately 47.3–49.3 vol% (Ritzberger et al. 2010). The Poisson's ratio was 0.235 as provided by Ivoclar Vivadent.

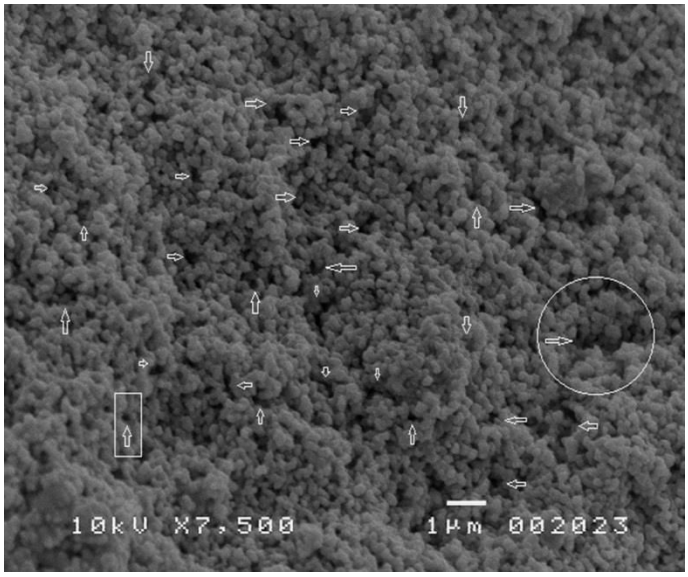


Fig. 3.4. A scanning electron micrograph of the fractured pre-sintered Y-TZP.

Pre-sintered Y-TZP blocks with dimensions of 15 mm × 15 mm × 50 mm were cut into 2 mm thick slices using a low speed diamond saw with tap water as both a coolant and a lubricant. Following established metallographic technique, the top and bottom surfaces of 15 mm × 15 mm of sliced samples were ground using 600-grit alumina abrasives to make the top and bottom surfaces parallel to each other to avoid surface tilting during indentations. Then, samples were ultrasonically bathed in water before polishing. Polishing of the top surfaces was performed using an aluminum polishing jig consisting of a wool cloth polishing lap disc. Diamond pastes with 0.5–1 µm abrasive sizes and water as a polishing lubricant were used to obtain an optical surface quality. The polished surfaces were scanned using scanning probe imaging (NT-MDT NTEGRA, Hysitron, USA) integrated into the nanoindentation system (TriboScope, Hysitron, USA). Fig. 3.5 shows a scanning probe image of a polished pre-sintered zirconia surface with the surface roughness, $R_q$, of approximately 72.3 nm for the scanned area of 50 × 50 µm.

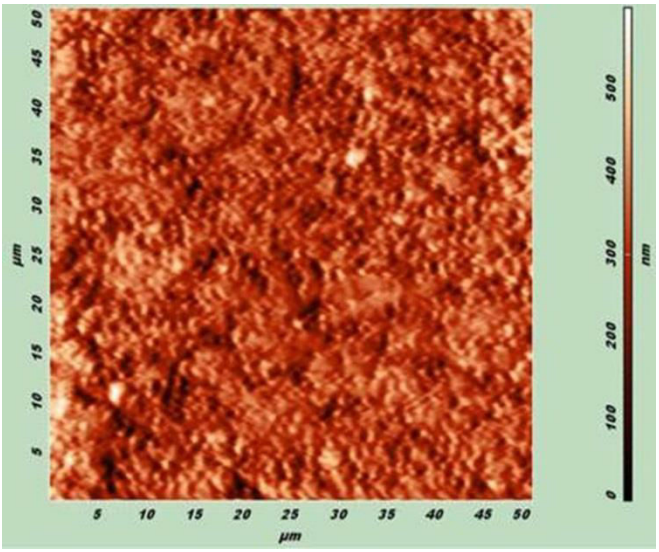


Fig. 3.5. 2D scanning probe image of the polished pre-sintered Y-TZP

### *3.2.5 Sintered Y-TZP*

Sintered Y-TZP was obtained by sintering the pre-sintered Y-TZP (IPS e.max ZirCAD, Ivoclar Vivadent) to 1300°C for two hours at 10°C/min heating rate and then naturally cooled to room temperature. These sintering conditions agree with the specifications for clinical zirconia restorations (Denry and Holloway, 2010). According to the Scott's phase diagram for the $ZrO_2$–$Y_2O_3$ system (Fig 2.5), this sintering condition leads to a structure consisting of tetragonal phase with a small amount of cubic phase (Scott, 1975). The reported density and strength of the sintered Y-TZP are approximately 6.09 g/cm$^3$ and 900 MPa, respectively; the porosity is less than 0.5%; and the fracture toughness is 5.5 MPa m$^{1/2}$ (Ritzberger et al., 2010). The Poisson's ratio of zirconia is 0.3 (Ereifej et al., 2011).

Indentation samples with dimension 15 mm × 15 mm × 2 mm were obtained from sintered Y-TZP using the metallographic procedures described in Section 3.2.4. The samples were scanned using the scanning probe imaging (NT-MDT NTEGRA, Hysitron, USA). Fig. 3.6(a) shows a scanned sintered Y-TZP surface on which the surface roughness, $R_q$, was 102 nm from the 50 µm × 50 µm scan area. This indicates that sintered Y-TZP surfaces became rough due to sintering-induced grain coarsening, shrinkage, residual stresses and monoclinic to tetragonal phase transformation. To meet the sample roughness requirement for nanoindentation, sintered Y-TZP samples were repolished using the same metallographic process for pre-sintered Y-TZP. After repolishing, the surfaces were scanned using the scanning probe imaging. Fig. 3.6(b) shows a scanned repolished sintered zirconia surface, obtaining the surface roughness, $R_q$, of

approximately 7.7 nm in a scan area of 50 μm × 50 μm and an average zirconia grain size of 500 nm.

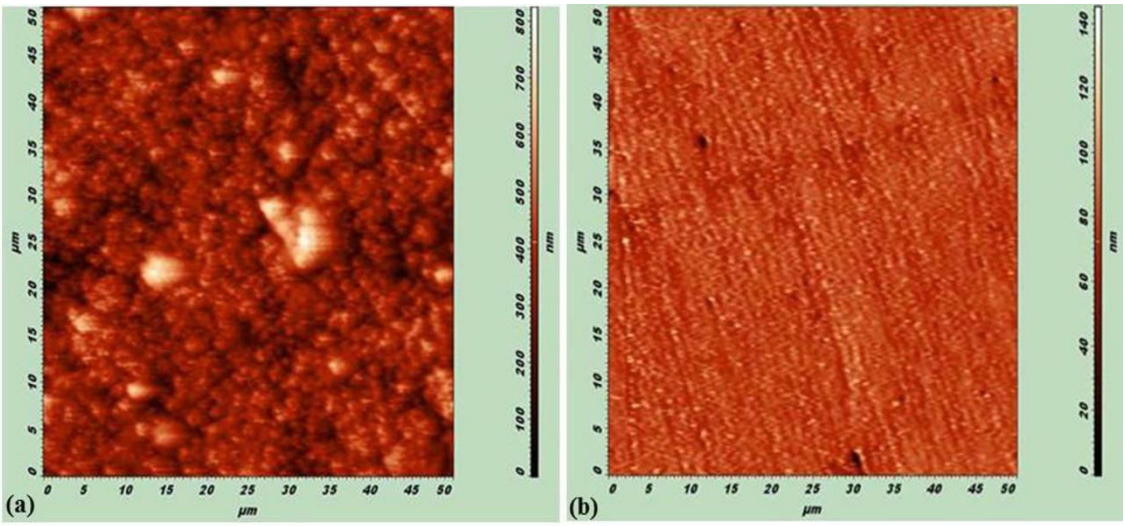


Fig. 3.6. 2D scanning probe images of (a) polished sintered Y-TZP, (b) sintered and repolished Y-TZP.

### 3.3 Nanoindentation Experiments

Nanoindentation testing is a characterization technique for studying materials' mechanical behavior through contact surfaces. It is a depth-sensing indentation test at very small length ranging from nanometer to micrometer that is capable of revealing mechanical properties for a wide variety of materials including ductile, brittle, thin films, layered and natural materials (Pharr, 1998; Oyen and Cook, 2009). High resolution sensors and actuators are used to apply and measure mechanical load and indenter displacement in nanoindentation testing. The load-displacement data measured by this method can then be used to extract properties at the submicron scale, avoiding the need to image the indentation before the determination of materials' mechanical properties. The technique is also ideal for probing local gradients and heterogeneities in natural materials (Oyen and Cook, 2009). Further, no extensive sample preparation is required prior to mechanical testing thus simplifying the experimental set-up. Also, various deformation modes including elastic, plastic, viscous and fracture can be explored from the load-displacement curves depending on the materials properties.

Among the properties routinely measured by nanoindentation testing are contact hardness, $H_c$, and Young's modulus, $E$ (Oliver and Pharr, 1992, 2004). Other properties measured with this technique include fracture toughness (Pharr, 1998; Field et al., 2003; Zhang et al., 2010), and

creep (Lucas and Oliver, 1999; Oyen and Cook, 2003; Fischer-Cripps, 2004). Residual stresses have also been measured by this method (Suresh and Giannakopoulos, 1998; Swadener et al., 2001; Kese and Rowcliffe, 2003; Soares et al., 2004; Zhang et al., 2012).

Nanoindentation experiments were performed using the nanoindentation system (Hysitron, USA) and a Berkovich diamond indenter of approximately 150 nm curvature radius, which is a three-sided pyramid having the same depth-to-projected area ratio as the Vickers indenter. The system has load and depth sensing resolutions of 1 nN and 0.0002 nm, respectively. The Oliver–Pharr method was utilized to determine the mechanical properties. The contact hardness, $H_c$, in a nanoindentation testing is governed by the following expression (Oliver and Pharr, 1992):

$$H_c = \frac{P_{\max}}{A(h_c)} \tag{3.1}$$

where $P_{max}$ is the peak load and $A$ is the residual projected area which is a function of the indenter depth in contact with the sample contact depth, $h_c$. For a perfect Berkovich indenter, $A$ is expressed by (Oliver and Pharr, 1992):

$$A(h_c) = 24.5h_c^2 \tag{3.2}$$

In practice, the indenter tips are not ideally sharp but tip blunting can occur during tests. In this case, $A$ is curve fitted according to the following functional form (Oliver and Pharr, 1992; 2004):

$$A = 24.5h_c^2 + C_1h_c^1 + C_2h_c^{1/2} + C_3h_c^{1/4} + \ldots + C_8h_c^{1/128} \tag{3.3}$$

In Eq. (3.3), the lead term describes a perfect Berkovich indenter whereas other terms represent departure from the Berkovich geometry due to the blunting of the tip. The contact depth, $h_c$, is given by the following expression (Oliver and Pharr, 1992; 2004):

$$h_c = h_{\max} - 0.75\frac{P_{\max}}{S} \tag{3.4}$$

where $h_{max}$ is the maximum penetration depth and $S$ is the contact stiffness defined as the slope of the upper portion of the unloading curve. The unloading curve is best governed by the following equation (Oliver and Pharr, 1992):

$$P = k_2\left(h - h_f\right)^m \tag{3.5}$$

where $k_2$ is the unloading curve constant, $m$ is the unloading exponent, $h$ is the instantaneous depth and $h_f$ is the final depth. The contact stiffness is represented by (Bulychev et al., 1975; Oliver and Pharr, 1992):

$$S = \left(\frac{dP}{dh}\right)_{h=h_{\max}} = mk_2\left(h_{\max} - h_f\right)^{m-1} = \frac{2}{\beta\sqrt{\pi}}E_r\sqrt{A} \tag{3.6}$$

where β is a correction factor which is 1 ± 0.05 (Oliver and Pharr, 2004), and $E_r$ is the reduced modulus including contributions from both the indenter and material. The reduced modulus is given by (Stillwell and Tabor, 1961):

$$\frac{1}{E_r} = \frac{1-\nu^2}{E} + \frac{1-\nu_i^2}{E_i} \tag{3.7}$$

where $E$ and $\nu$ are the Young's modulus and Poisson's ratio of the specimen and $E_i$ and $\nu_i$ are the Young's modulus and Poisson's ratio of the indenter. For the Berkovich diamond indenter, $\nu_i$ = 0.07 and $E_i$ = 1141 GPa (Oliver and Pharr, 1992; 2004). Therefore, the Young's modulus for the specimen can be extracted using the following expression:

$$E = \left(1-\nu^2\right)\left[\frac{1}{E_r} - \frac{\left(1-\nu_i^2\right)}{E_i}\right]^{-1} \tag{3.8}$$

Prior to nanoindentation tests, calibrations were performed on a fused silica indented by the diamond Berkovich tip at a peak load of 3000 μN. At this peak load, the fused silica has indentation modulus and hardness of approximately 69.5 GPa and 9.5 GPa, respectively. These calculated modulus and hardness values were within 0.3% of its known values to assure the precision of the indentation system. Thermal drift corrections were made on the nanoindenter with the maximum drift rate of 0.05 nm/s. The maximum indentation load applied was 10 mN and the loading and unloading rates were 0.1 mN/s, 0.5 mN/s, 1 mN/s and 2 mN/s. No holding time was required. Fig. 3.7 shows the load-time profiles at the loading rates of 0.1 mN/s, 0.5 mN/s, 1 mN/s and 2 mN/s indicating that the indentation loading and unloading times for each indentation were 100, 20, 10 and 5 seconds, respectively.

The contact depth, $h_c$, the maximum penetration depth, $h_{max}$, and the final depth, $h_f$, were determined using Eqs. (3.3)–(3.5) as a function of loading rate. The contact stiffness, $S$, was determined using Eq. (3.6). The contact hardness, $H_c$, and Young's modulus, $E$, were determined using Eqs. (3.1) and (3.8) respectively. The measured properties were determined as a function of loading rate. Six indentations at different locations were performed on the specimens at each loading rate to determine the mean values and standard deviations for each parameter. Single-factor analysis of variance (ANOVA) was applied at a 5% confidence interval to examine the significant loading rate effect on properties. Prior to and after indentation, the indented areas were *in situ* scanned to obtain the surface and indentation patterns using *in situ* scanning probe imaging (NT-MDT NTEGRA, Hysitron, USA). For each indentation imprint, a depth cross-sectional analysis was conducted to investigate the material response underneath the indenter.

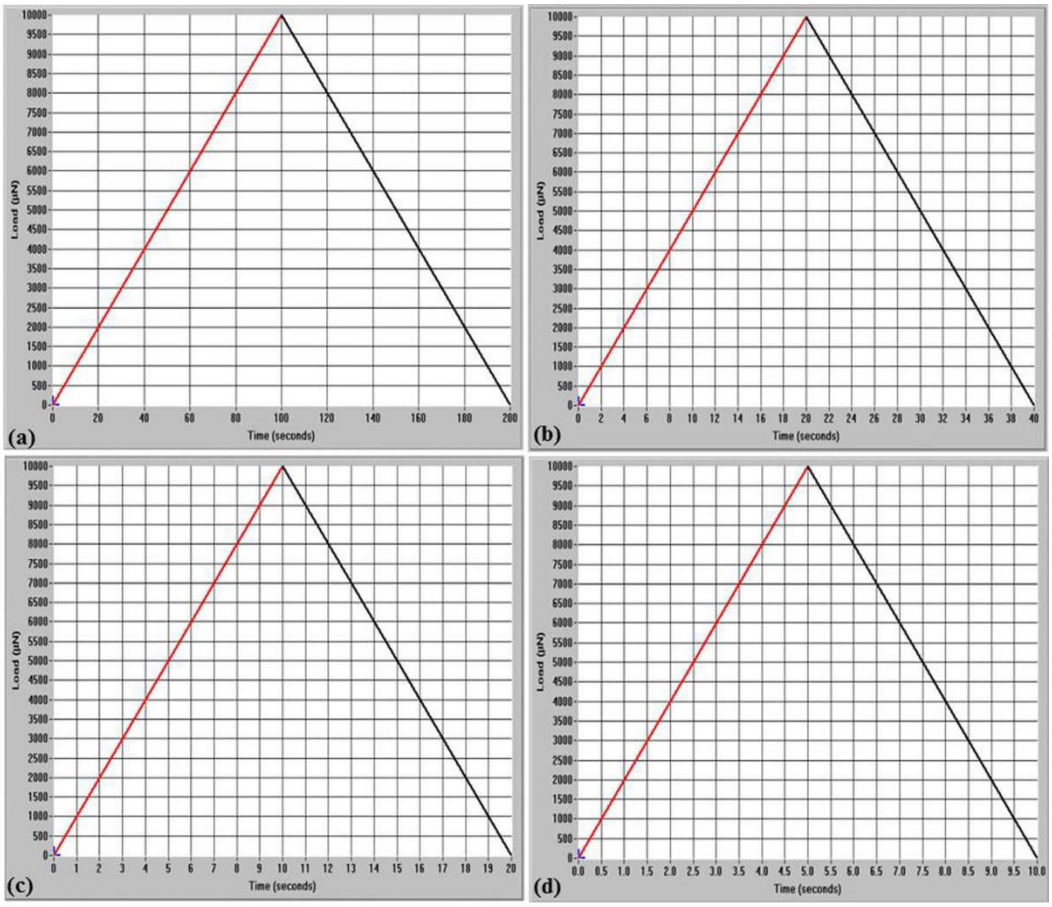


Fig. 3.7. Experimental load-time profiles for nanoindentation testing showing the corresponding loading and unloading times at loading rate (a) 0.1 mN/s, (b) 0.5 mN/s, (c) 1 mN/s, and (d) 2 mN/s.

## 3.4 Results

### *3.4.1 Force-Displacement Curves*

Fig. 3.8 shows force-displacement curves for six indentations on LMGC at 10 mN peak load and loading rates of 0.1 mN/s, 0.5 mN/s, 1 mN/s and 2 mN/s, respectively. At 0.1 mN/s loading rate in Fig. 3.8(a), frequent step-like discontinuities occurred on the loading and unloading curves. At 0.5 mN/s loading rate, fewer ripple-like discontinuities were observed on the loading and unloading curves (Fig. 3.8(b)). At 1 mN/s and 2 mN/s loading rates, there were no evidence of discontinuities in the loading and unloading curves (Fig. 3.8(c) and (d)). Fig. 3.8 indicates that low loading rates promoted extensive discontinuities which may reflect different physical events beneath the indenter, while high indentation rates suppressed them. In addition, the largest dispersion of the force-displacement curves was observed at the lowest loading rate in

Fig. 3.8 (a) in comparison to the reduced dispersions with the increased loading rates in Fig. 3.8(b)–(d).

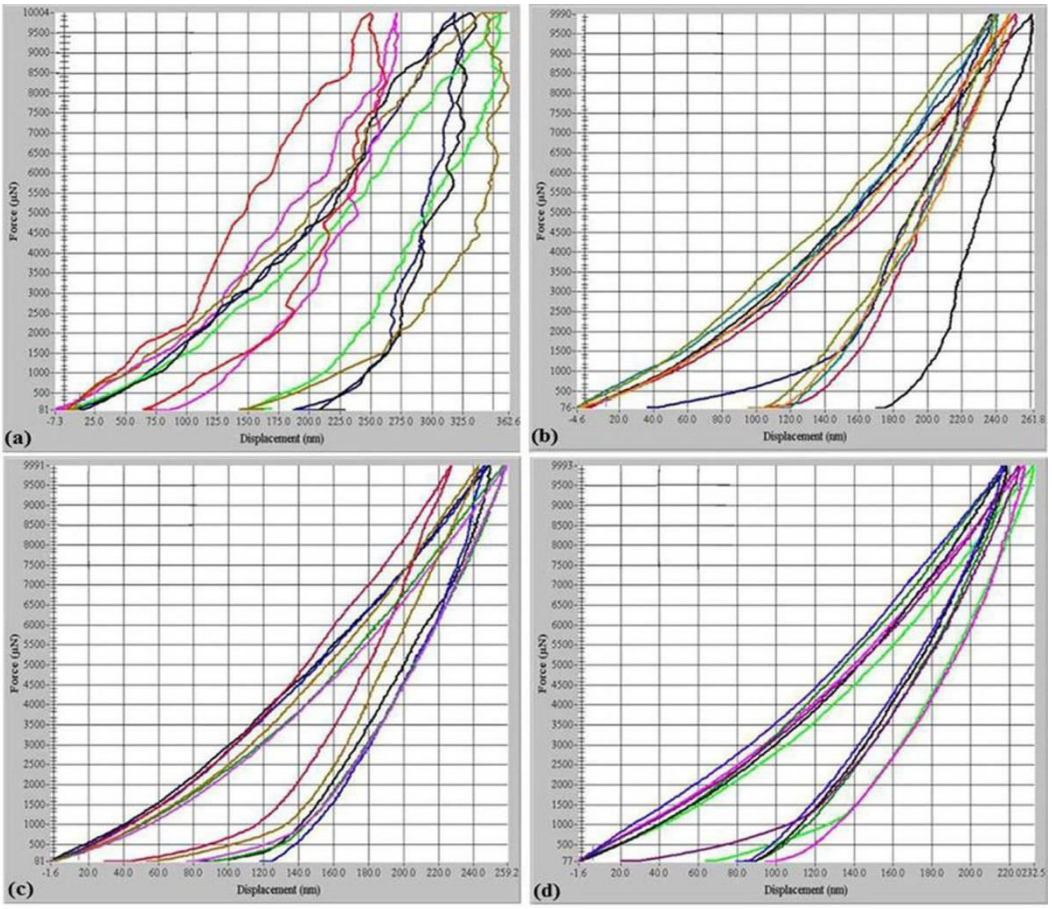


Fig. 3.8. Force-displacement curves for six indentations on LMGC at 10 mN peak load with loading rate (a) 0.1 mN/s, (b) 0.5 mN/s, (c) 1 mN/s, and (d) 2 mN/s.

Fig. 3.9 shows force-displacement curves for six indentations on sintered LDGC at 10 mN peak load and loading rates of 0.1 mN/s, 0.5 mN/s, 1 mN/s and 2 mN/s, respectively. At 0.1 mN/s loading rate in Fig. 3.9(a), frequent ripple-like discontinuities occurred on the loading and unloading curves. At 0.5 mN/s loading rate, fewer ripple-like discontinuities were observed on the loading and unloading curves (Fig. 3.9(b)). At 1 mN/s and 2 mN/s loading rates, there were no evidence of discontinuities in the loading and unloading curves (Fig. 3.9(c) and (d)). As demonstrated in Fig. 3.8 for LMGC, the low loading rates promoted extensive discontinuities reflecting different physical events beneath the indenter, while high indentation rates suppressed the discontinuities. In addition, there was the largest dispersion of the force-displacement curves at the lowest loading rate in Fig. 3.9(a) in comparison to the reduced dispersions with the increased loading rates in Fig. 3.9(b)–(d).

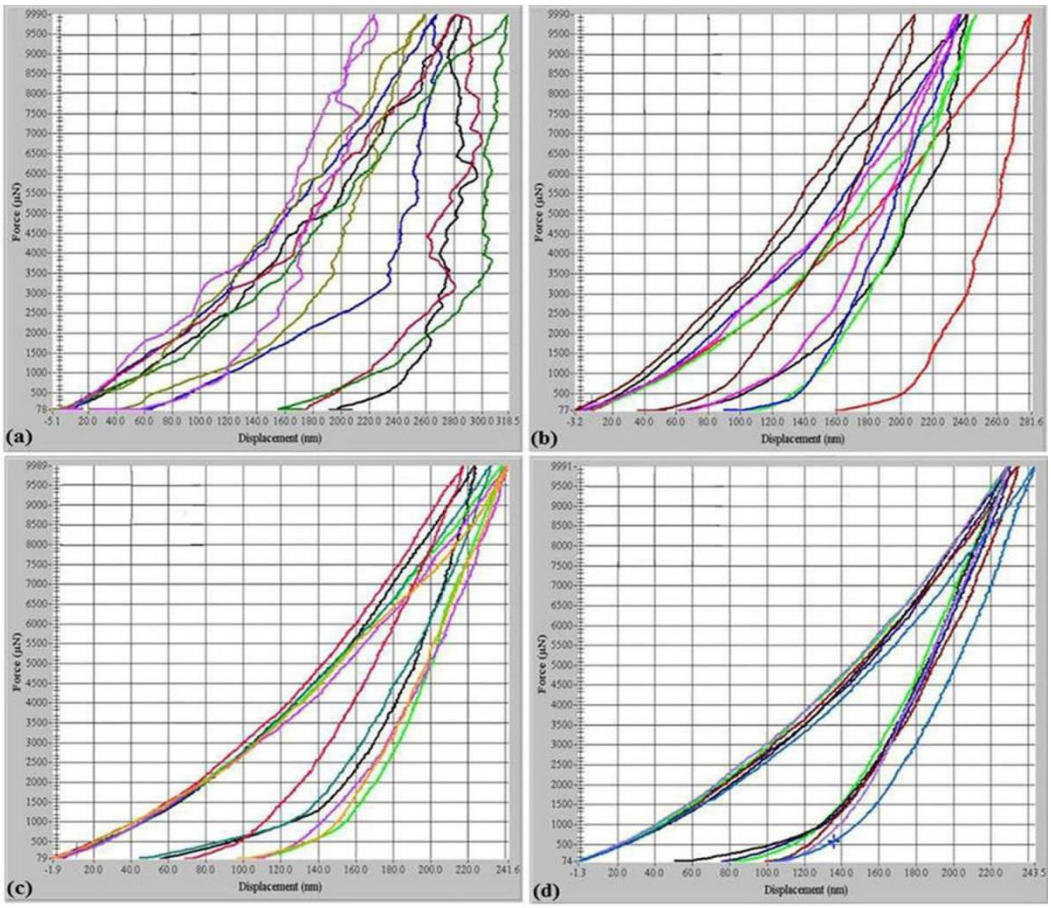


Fig. 3.9. Force-displacement curves for six indentations on sintered LDGC at 10 mN peak load with loading rate (a) 0.1 mN/s, (b) 0.5 mN/s, (c) 1 mN/s, and (d) 2 mN/s.

Fig. 3.10 shows force-displacement curves for six indentations on pressable LDGC at 10 mN peak load and loading rates of 0.1 mN/s, 0.5 mN/s, 1 mN/s and 2 mN/s, respectively. At 0.1 mN/s loading rate in Fig. 3.10(a), frequent ripple-like discontinuities occurred on the loading and unloading curves. At 0.5 mN/s loading rate, fewer ripple-like discontinuities were observed on the loading and unloading curves (Fig. 3.10(b)). At 1 mN/s and 2 mN/s loading rates, there were no evidence of discontinuities in the loading and unloading curves (Fig. 3.10(c) and (d)). This indicates the rate effect on the occurrence of discontinuities in this material with slow rates promoting them and high rates promoting suppressing them. The discrete discontinuities may reflect different physical events beneath the indenter. In addition, the dispersion of the force-displacement curves observed at the lowest loading rate in Fig. 3.10(a) was the largest but it was reduced with the increase in loading rates as shown in Fig. 3.10(b)–(d).

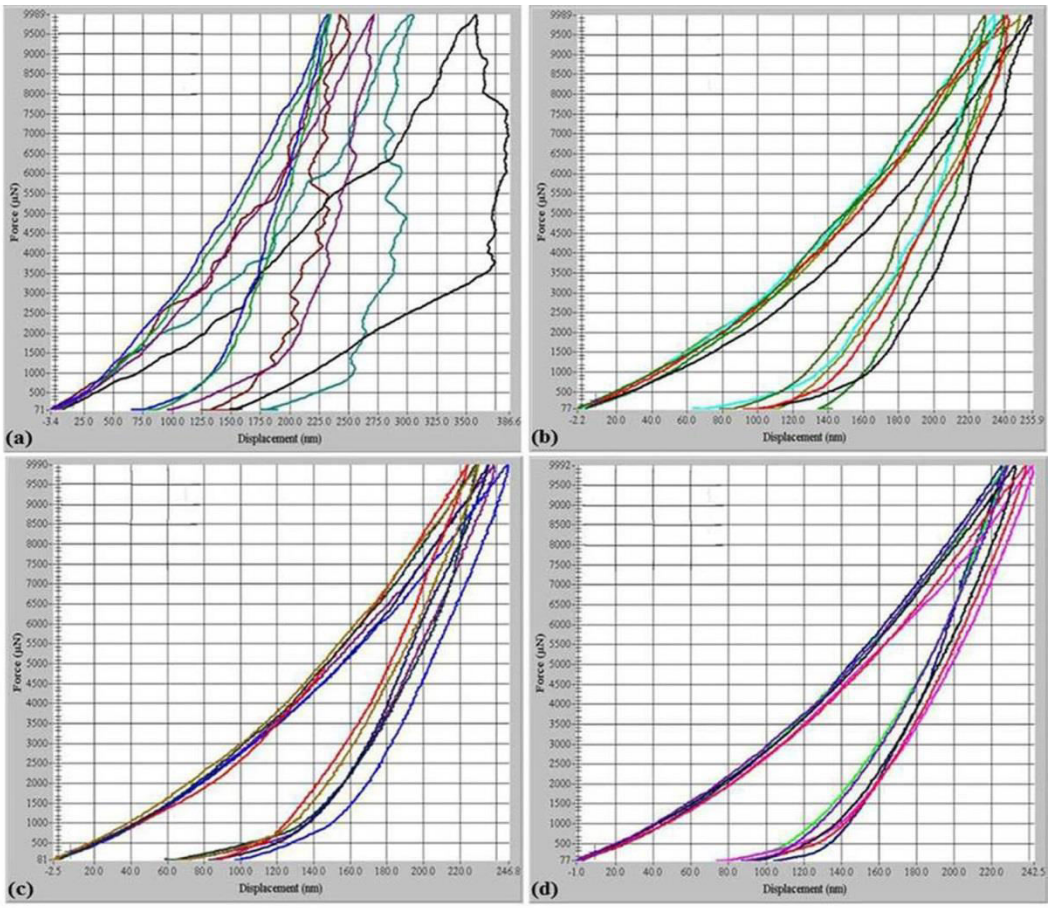


Fig. 3.10. Force-displacement curves for six indentations on pressable LDGC at 10 mN peak load with loading rate (a) 0.1 mN/s, (b) 0.5 mN/s, (c) 1 mN/s, and (d) 2 mN/s.

Fig. 3.11 shows force-displacement curves for six indentations on pre-sintered Y-TZP at each loading rate. Fig. 3.11(a) shows frequent pop-in events (indicated by arrows) on both loading and unloading curves for the six indentations at the loading rate of 0.1 mN/s. Fig. 3.11(b) shows fewer discontinuities observed in the loading curve at the loading rate of 0.5 mN/s. Also, Fig. 3.11(c) and (d) shows few pop-ins only on the loading curves at the loading rates of 1 mN/s and 2 mN/s, respectively. These pop-ins reflect different discrete physical events beneath the indenter tip with slow indentation rates promoting extensive discontinuities while rapid indentation rates partially suppressing the discontinuities.

Fig. 3.12 shows force-displacement curves for six indentations on sintered Y-TZP at loading rates of 0.1 mN/s, 0.5 mN/s, 1 mN/s and 2 mN/s, respectively. At 0.1 mN/s loading rate in Fig. 3.12(a), frequent pop-in events were observed on the loading and unloading curves. At 0.5 mN/s loading rate in Fig. 3.12(b), fewer discontinuities were observed on the loading and unloading curves. In contrast, at 1 mN/s and 2 mN/s loading rates, no evidence of pop-ins in the loading and unloading curves (Fig. 3.12(c) and (d)). Pop-in phenomena on loading and unloading curves

can reflect different physical events beneath the indenter tip. Fig. 3.12 indicates that slow indentation rates promoted extensive discontinuities while rapid indentation rates suppressed the discontinuities. In addition, the largest dispersion was also observed on the force-displacement curves at the lowest loading rate in Fig. 3.12(a). As the loading rate was increased, the dispersion on the force-displacement curves was reduced as shown in Fig. 3.12(b)–(d).

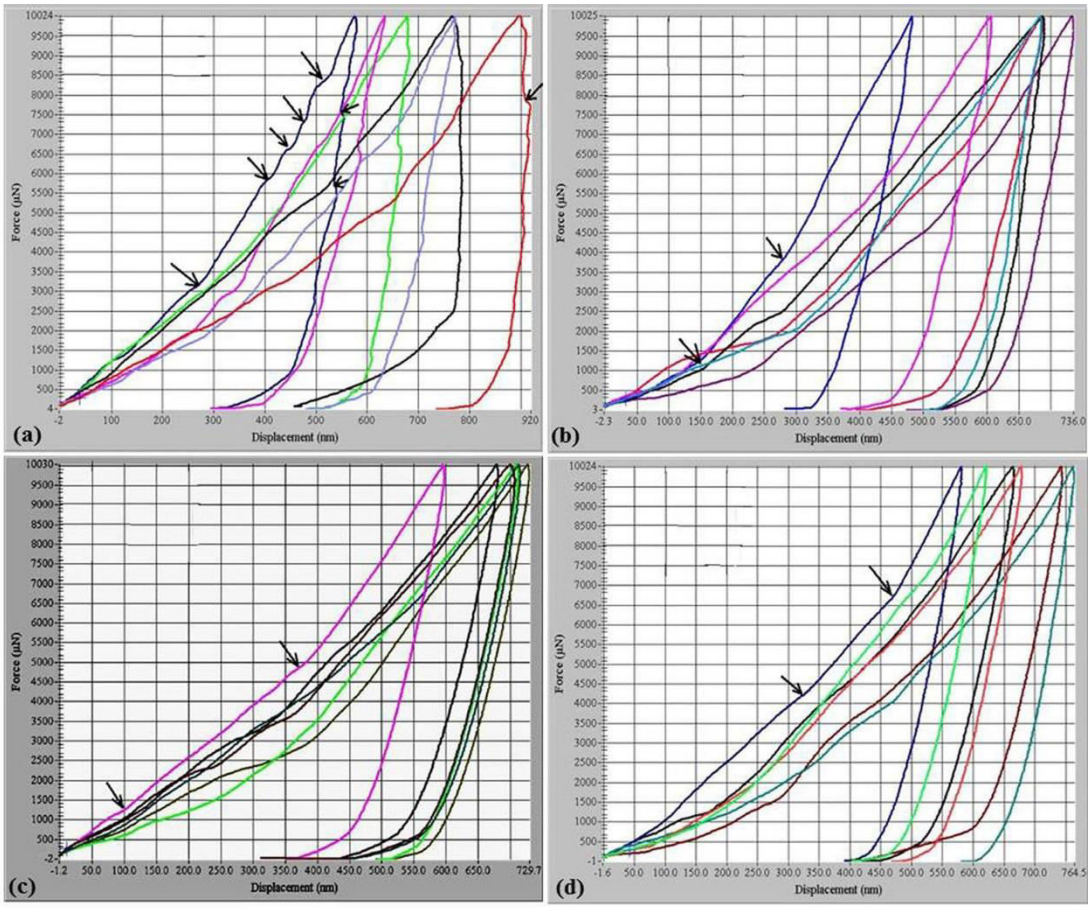


Fig. 3.11. Force-displacement curves for six indentations on pre-sintered Y-TZP at 10 mN peak load with loading rate (a) 0.1 mN/s, (b) 0.5 mN/s, (c) 1 mN/s, and (d) 2 mN/s. Arrows indicate pop-in events.

### *3.4.2 Indentation Displacements*

Fig. 3.13 shows maximum penetration, $h_{max}$, contact, $h_c$, and final $h_f$, penetration depths, versus loading rate for LMGC. Both maximum penetration and contact depths decreased sharply when increasing the loading rate from 0.1 mN/s to 0.5 mN/s. They then decreased steadily with the increase in loading rate from 0.5 mN/s to 2 mN/s. The final depths decreased steadily with the increase in loading rate from 0.1 mN/s to 2 mN/s. Further, the largest maximum penetration, contact and final depths occurred at the lowest loading rate of 0.1 mN/s.

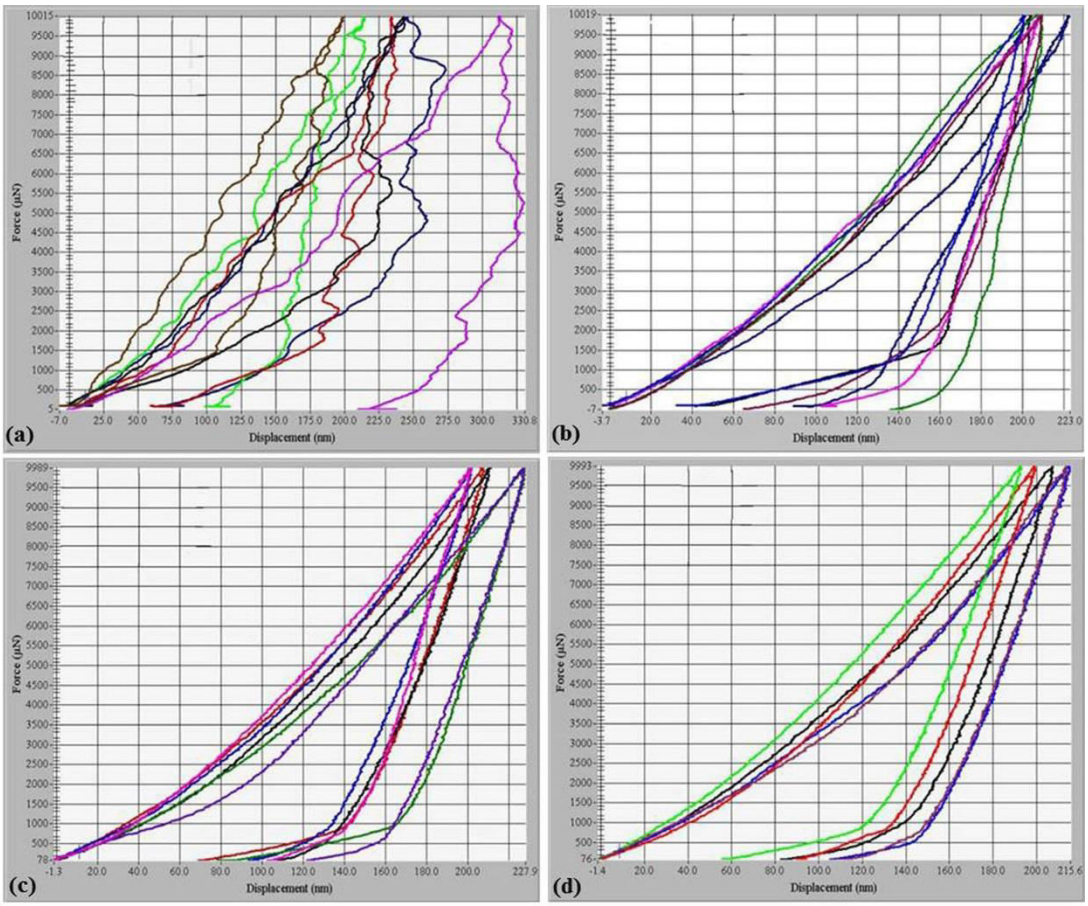


Fig. 3.12. Force-displacement curves for six indentations on sintered Y-TZP at 10 mN peak load with loading rate (a) 0.1 mN/s, (b) 0.5 mN/s, (c) 1 mN/s, and (d) 2 mN/s.

Fig. 3.14 shows maximum penetration, contact and final penetration depths versus loading rate for sintered LDGC. Both maximum penetration and contact depths decreased steadily when increasing the loading rate from 0.1 mN/s to 2 mN/s. The final depths decreased steadily with the increase in loading rate from 0.1 mN/s to 0.5 mN/s. They increased with the increase in loading rate from 0.5 mN/s to 1 mN/s and remained relatively constant with the loading rate increase from 1 mN/s to 2 mN/s. Further, maximum penetration, contact and final depths had their largest values at the lowest loading rate of 0.1 mN/s.

Fig. 3.15 shows maximum penetration, contact and final penetration depths versus loading rate for pressable LDGC. The maximum penetration, contact and final depths decreased sharply when increasing the loading rate from 0.1 mN/s to 0.5 mN/s. They then decreased steadily with the increase in loading rate from 0.5 mN/s to 2 mN/s. The largest maximum penetration, contact and final depths occurred at the lowest loading rate of 0.1 mN/s.

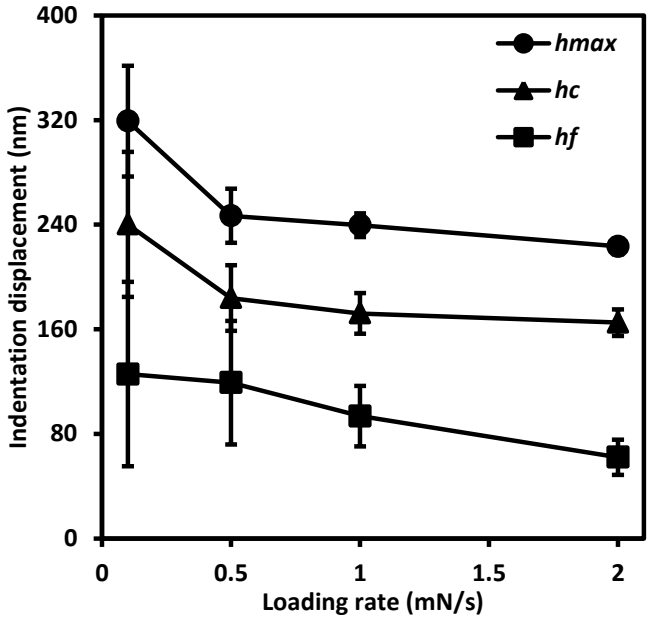


Fig. 3.13. Maximum penetration ($h_{max}$), contact ($h_c$) and final depths ($h_f$) versus loading rate for LMGC. Each data point is the mean value of the six repeated indentations; each error bar corresponds to ± one standard deviation for the six repeated indentations.

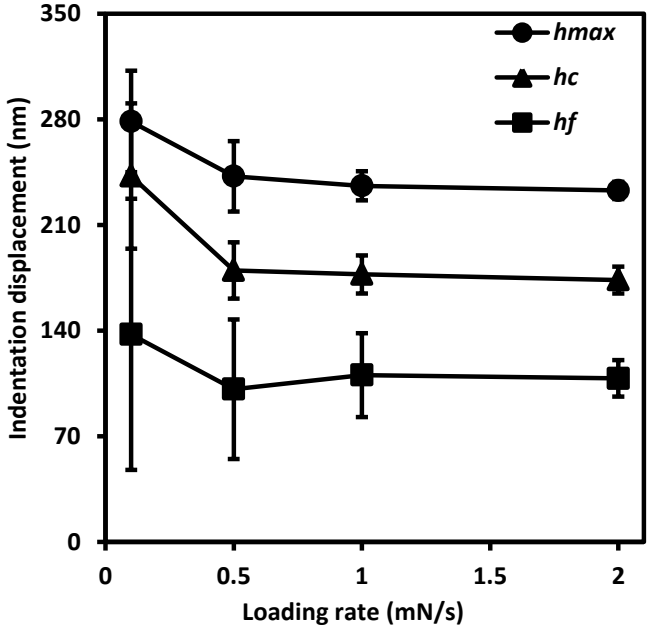


Fig. 3.14. Maximum penetration ($h_{max}$), contact ($h_c$) and final depths ($h_f$) versus loading rate for sintered LDGC. Each data point is the mean value of the six repeated indentations; each error bar corresponds to ± one standard deviation for the six repeated indentations.

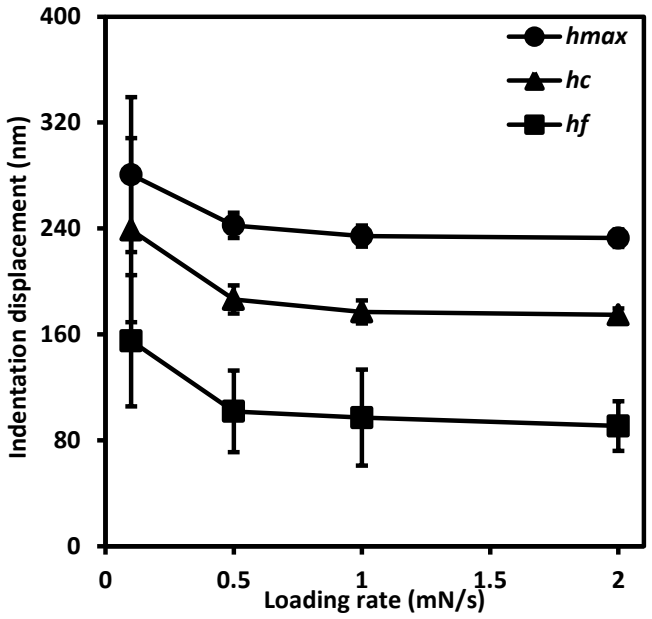


Fig. 3.15. Maximum penetration ($h_{max}$), contact ($h_c$) and final depths ($h_f$) versus loading rate for pressable LDGC. Each data point is the mean value of the six repeated indentations; each error bar corresponds to ± one standard deviation for the six repeated indentations.

Fig. 3.16 shows maximum penetration, contact and final depths versus loading rate for pre-sintered Y-TZP. The maximum penetration depths at the loading rates of 0.1 mN/s, 0.5 mN/s, 1 mN/s and 2 mN/s are 728.93 ± 122.69 nm, 648.15 ± 91.06 nm, 620.85 ± 64.20 nm and 676.47 ± 70.07 nm, respectively. Accordingly, the contact depths are 675.63 ± 146.20 nm, 483.58 ± 202.69 nm, 544.05 ± 67.07 nm and 608.83 ± 71.31 nm, respectively. The final depths are 582.19 ± 185.27 nm, 504.62 ± 117.45 nm, 451.45 ± 68.04 nm and 503.48 ± 73.34 nm, respectively. Both maximum penetration and final depths decreased with increase in loading rate up to 1 mN/s and increased above this loading rate. However, the contact depths decreased as the loading rate increased to 0.5 mN/s but increased above this rate. The largest maximum penetration, contact and final depths occurred at the lowest loading rate of 0.1 mN/s.

Fig. 3.17 shows maximum penetration, contact and final penetration depths versus loading rate for sintered Y-TZP. Both maximum penetration and contact depths decreased with increase in loading rate with the largest maximum penetration and contact depths occurring at the lowest loading rate of 0.1 mN/s. In comparison, final depths increased as the loading rate was increased to 1 mN/s but decreased when the loading rate increased from 1 mN/s to 2 mN/s.

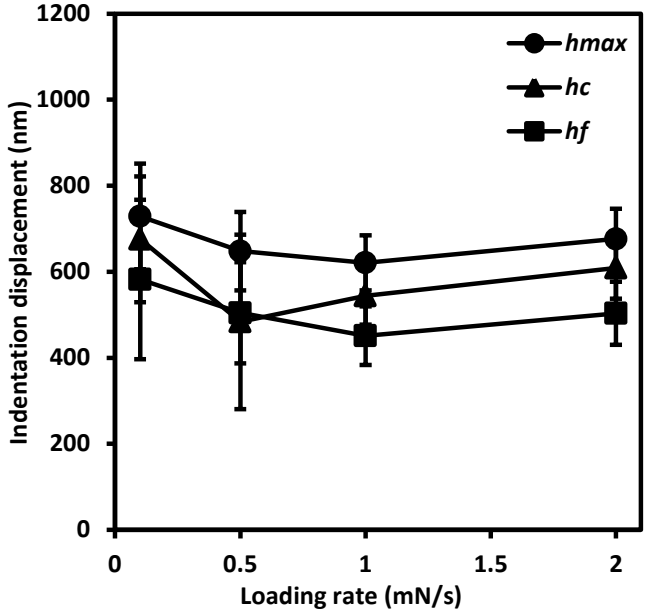


Fig. 3.16. Maximum penetration ($h_{max}$), contact ($h_c$) and final depths ($h_f$) versus loading rate for pre-sintered Y-TZP. Each data point is the mean value of the six repeated indentations; each error bar corresponds to ± one standard deviation for the six repeated indentations.

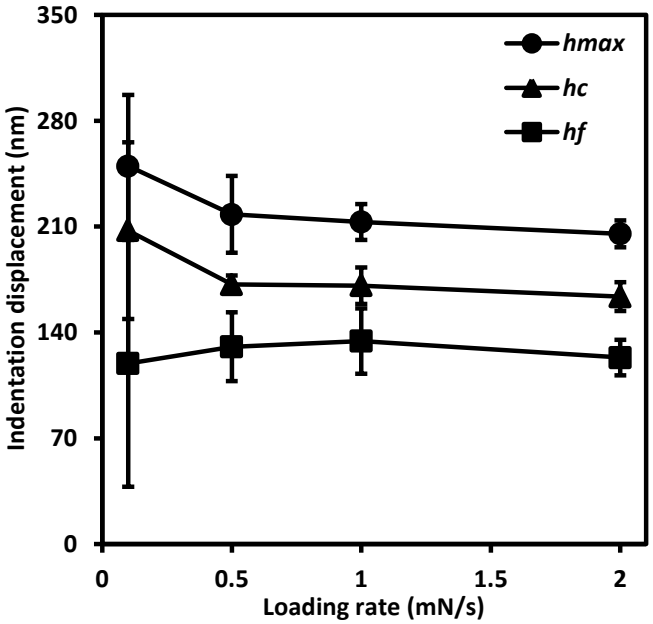


Fig. 3.17. Maximum penetration ($h_{max}$), contact ($h_c$) and final depths ($h_f$) versus loading rate for sintered Y-TZP. Each data point is the mean value of the six repeated indentations; each error bar corresponds to ± one standard deviation for the six repeated indentations.

### *3.4.3 Contact Stiffness*

Fig. 3.18 shows contact stiffness, $S$, versus loading rate for LMGC. The contact stiffness decreased as the loading rate was increased from 0.1 mN/s to 1 mN/s and increased slightly with the loading rate increase from 1 mN/s to 2 mN/s. The single factor ANOVA shows an insignificant loading rate effect on the contact stiffness ($p > 0.05$).

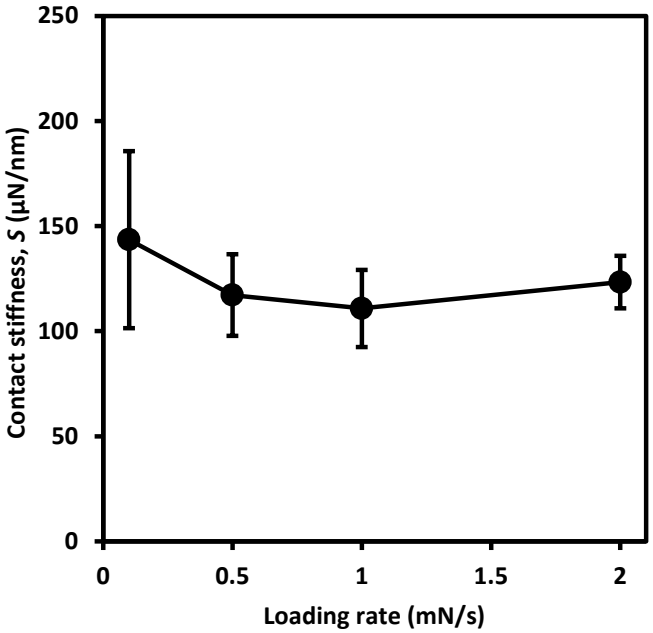


Fig. 3.18. Contact stiffness ($S$) versus loading rate for LMGC. Each data point is the mean value of the six repeated indentations; each error bar corresponds to ± one standard deviation for the six repeated indentations.

Fig. 3.19 shows contact stiffness versus loading rate for sintered LDGC. The mean contact stiffness and its standard deviation at the lowest loading rate of 0.1 mN/s was significantly higher than the mean and standard deviation values at other loading rates. At higher loading rates of 0.5 mN/s, 1 mN/s and 2 mN/s, the contact stiffness was independent of the loading rate.

Fig. 3.20 shows the contact stiffness versus the loading rate for pressable LDGC. The contact stiffness followed the same pattern with the loading rate as in Fig. 3.19 for sintered LDGC.

Fig. 3.21 shows the contact stiffness versus loading rate for pre-sintered Y-TZP. At the lowest loading rate of 0.1 mN/s, the mean contact stiffness doubled the values at the other loading rates while its standard deviation was also very large.

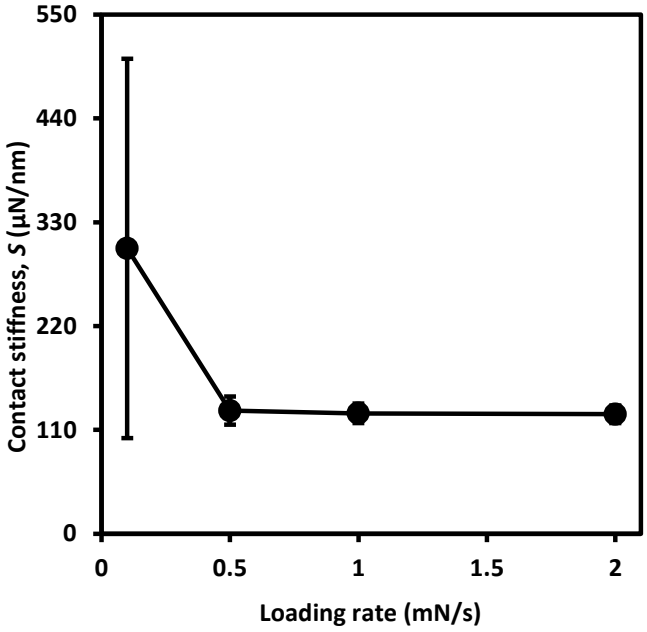


Fig. 3.19. Contact stiffness (*S*) versus loading rate for sintered LDGC. Each data point is the mean value of the six repeated indentations; each error bar corresponds to ± one standard deviation for the six repeated indentations.

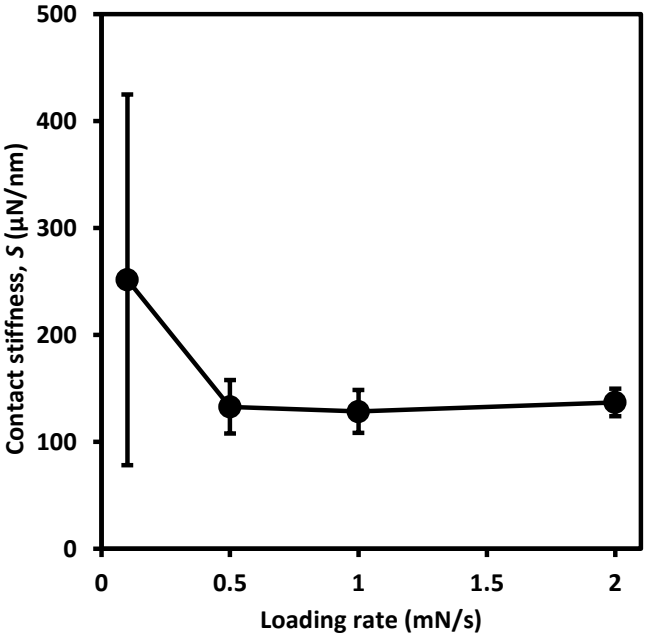


Fig. 3.20. Contact stiffness (*S*) versus loading rate for Pressable LDGC. Each data point is the mean value of the six repeated indentations; each error bar corresponds to ± one standard deviation for the six repeated indentations.

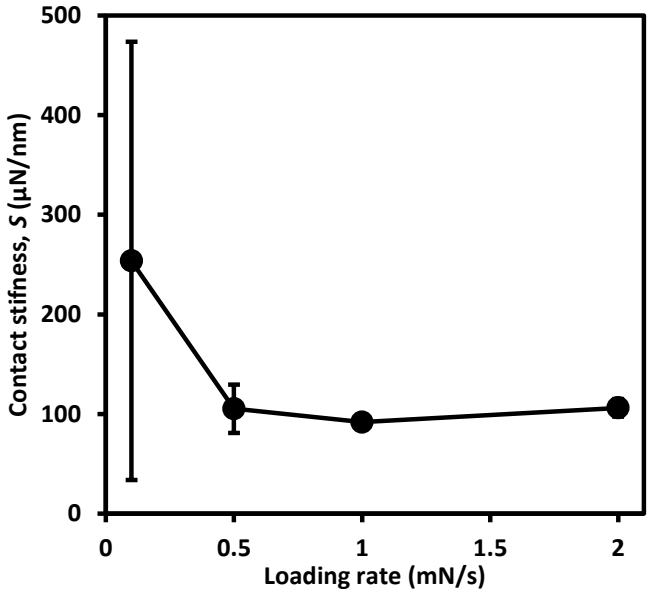


Fig. 3.21. Contact stiffness (*S*) versus loading rate for pre-sintered Y-TZP. Each data point is the mean value of the six repeated indentations; each error bar corresponds to ± one standard deviation for the six repeated indentations.

Fig. 3.22 shows the contact stiffness versus loading rate for sintered Y-TZP. The contact stiffness decreased as the loading rate was increased from 0.1 mN/s to 1 mN/s and remained constant when the loading rate increased from 1 mN/s to 2 mN/s. At the lowest loading rate of 0.1 mN/s, the standard deviation for the contact stiffness was very large.

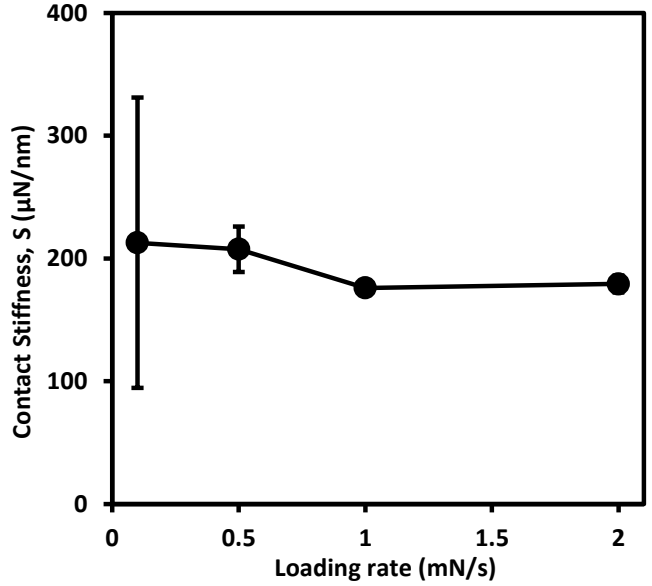


Fig. 3.22. Contact stiffness (*S*) versus loading rate for sintered Y-TZP. Each data point is the mean value of the six repeated indentations; each error bar corresponds to ± one standard deviation for the six repeated indentations.

### *3.4.4 Contact Hardness*

Fig. 3.23 shows indentation contact hardness, $H_c$, versus loading rate for LMGC. The contact hardness increased sharply when increasing the loading rate from 0.1 mN/s to 0.5 mN/s. It then increased steadily with the increased loading rate from 0.5 mN/s to 2 mN/s. The measured means and standard deviations for contact hardness at 0.1 mN/s, 0.5 mN/s, 1 mN/s and 2 mN/s loading rate are 4.64 ± 1.40 GPa, 8.33 ± 1.00 GPa, 8.51 ± 0.97 GPa, and 9.83 ± 0.91 GPa, respectively. The mean contact hardness increased by 112% when increasing the loading rate from 0.1 mN/s to 2 mN/s and was significantly loading-rate dependent ($p < 0.05$).

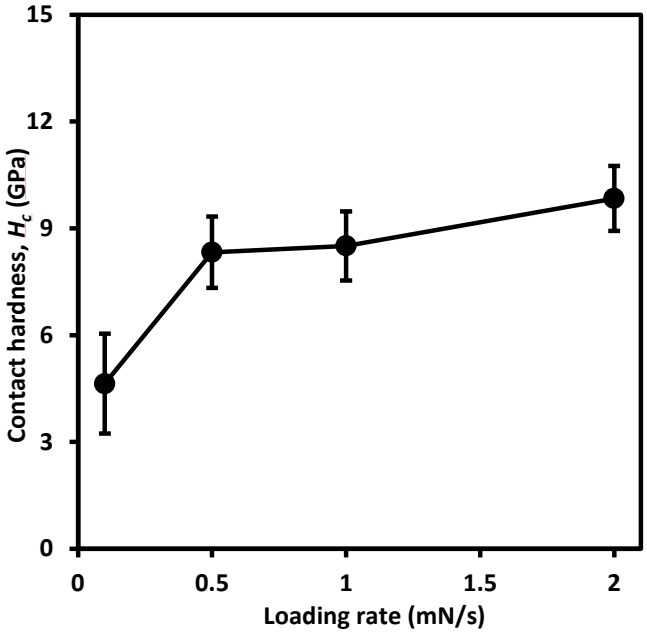


Fig. 3.23. Contact hardness ($H_c$) versus loading rate for LMGC. Each data point is the mean value of the six repeated indentations; each error bar corresponds to ± one standard deviation for the six repeated indentations.

Fig. 3.24 shows indentation contact hardness versus loading rate for sintered LDGC. The contact hardness increased steadily with the increase in loading rate from 0.1 mN/s to 2 mN/s. The measured means and standard deviations for contact hardness at 0.1 mN/s, 0.5 mN/s, 1 mN/s and 2 mN/s loading rate are 5.64 ± 2.03 GPa, 8.30 ± 2.15 GPa, 8.82 ± 1.12 GPa, and 9.07 ± 0.70 GPa, respectively. The mean contact hardness increased significantly by 61% when increasing the loading rate from 0.1 mN/s to 2 mN/s ($p < 0.05$).

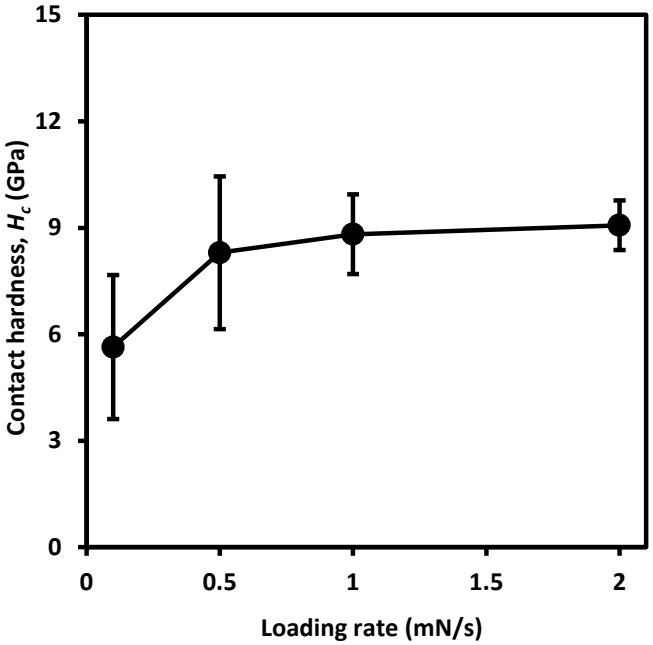


Fig. 3.24. Contact hardness ($H_c$) versus loading rate for sintered LDGC. Each data point is the mean value of the six repeated indentations; each error bar corresponds to ± one standard deviation for the six repeated indentations.

Fig. 3.25 shows indentation contact hardness versus loading rate for pressable LDGC. The contact hardness increased steadily when increasing the loading rate from 0.1 mN/s to 1 mN/s. It then remained constant with the increased loading rate from 1 mN/s to 2 mN/s. The measured means and standard deviations for contact hardness at 0.1 mN/s, 0.5 mN/s, 1 mN/s and 2 mN/s loading rate are 6.71 ± 2.01 GPa, 8.10 ± 0.72 GPa, 8.80 ± 0.68 GPa, and 8.64 ± 0.37 GPa, respectively. The mean contact hardness increased by 31% when increasing the loading rate from 0.1 mN/s to 2 mN/s and was significantly loading-rate dependent ($p < 0.05$).

Fig. 3.26 shows indentation contact hardness versus loading rate for pre-sintered Y-TZP. It increased with the loading rate at 0.1 mN/s to 1 mN/s and decreased with the loading rate when the loading rate changed from 1 mN/s to 2 mN/s. The measured contact hardness values at the loading rates of 0.1 mN/s, 0.5 mN/s, 1 mN/s and 2 mN/s are 0.92 ± 0.35 GPa, 1.20 ± 0.45 GPa, 1.28 ± 0.27 GPa, and 1.04 ± 0.23 GPa, respectively. Single factor ANOVA shows the insignificant effect of the loading rate on the contact hardness ($p > 0.05$).

Fig. 3.27 shows indentation contact hardness versus loading rate for sintered Y-TZP. The contact hardness increased slightly and significantly with the loading rate ($p < 0.05$). The measured means and standard deviations for contact hardness at 0.1 mN/s, 0.5 mN/s, 1 mN/s and 2 mN/s loading rate are 7.61 ± 2.96 GPa, 9.09 ± 1.16 GPa, 9.33 ± 1.02 GPa, and 9.97 ± 0.92

GPa, respectively. Thus, by increasing the loading rate from 0.1 mN/s to 2 mN/s, the mean contact hardness increased by 31%. In addition, the standard deviations decreased with the loading rate. This is in line with the dispersions associated with the force-displacement curves in Fig. 3.12.

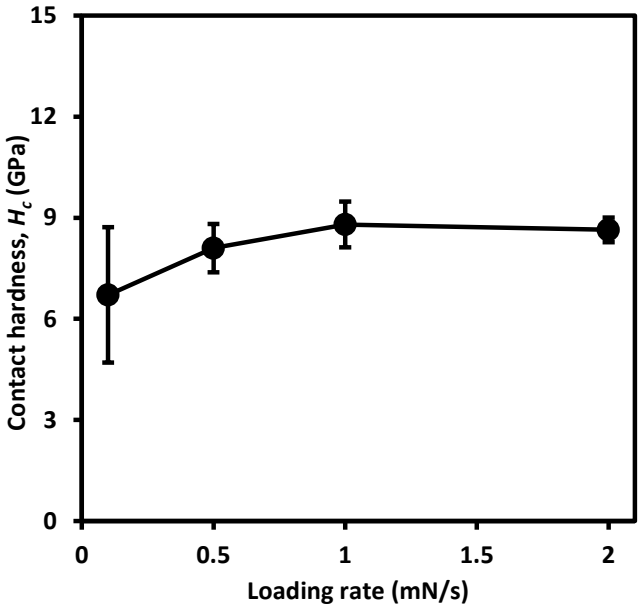


Fig. 3.25. Contact hardness ($H_c$) versus loading rate for pressable LDGC. Each data point is the mean value of the six repeated indentations; each error bar corresponds to ± one standard deviation for the six repeated indentations.

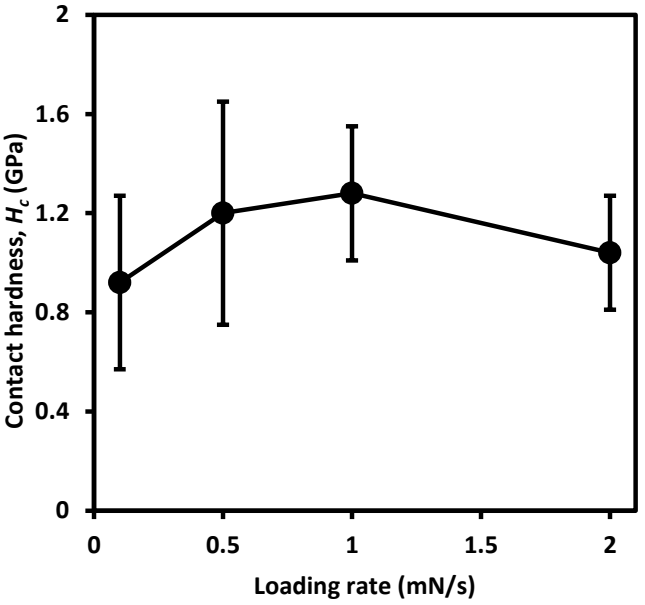


Fig. 3.26. Contact hardness ($H_c$) versus loading rate for pre-sintered Y-TZP. Each data point is the mean value of the six repeated indentations; each error bar corresponds to ± one standard deviation for the six repeated indentations.

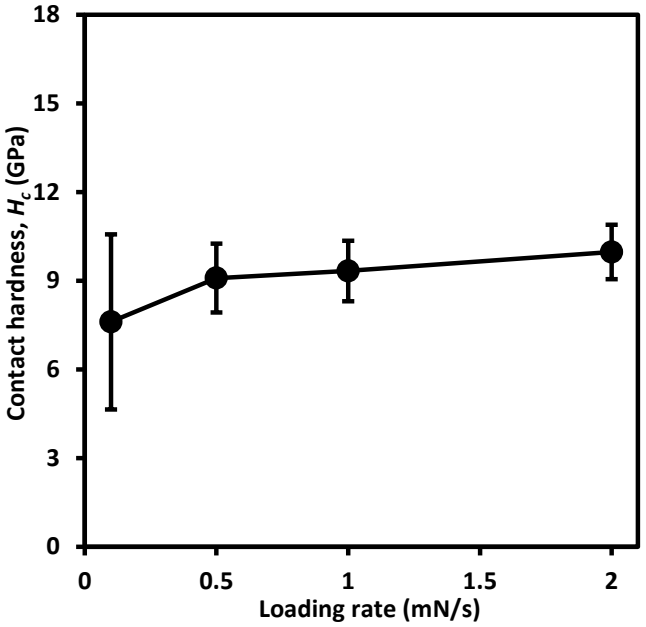


Fig. 3.27. Contact hardness ($H_c$) versus loading rate for sintered Y-TZP. Each data point is the mean value of the six repeated indentations; each error bar corresponds to ± one standard deviation for the six repeated indentations.

### *3.4.5 Young's Moduli*

Fig. 3.28 shows Young's modulus, $E$, versus loading rate for LMGC. The Young's modulus generally increased with the loading rate with a slight turbulence at 1–2 mN/s. The measured Young's modulus means and standard deviations at 0.1 mN/s, 0.5 mN/s, 1 mN/s and 2 mN/s loading rates are 86.62 ± 23.08 GPa, 96.75 ± 10.76 GPa, 93.90 ± 15.22 GPa, and 112.65 ± 7.40 GPa, respectively. The single factor ANOVA shows an insignificant loading rate effect on the Young's modulus ($p > 0.05$).

Fig. 3.29 shows Young's modulus versus loading rate for sintered LDGC. The measured Young's modulus means and standard deviations at 0.1 mN/s, 0.5 mN/s, 1 mN/s and 2 mN/s loading rates are 225.26 ± 165.40 GPa, 118.26 ± 20.78 GPa, 110.24 ± 6.02 GPa, and 111.34 ± 4.74 GPa, respectively. The Young's modulus sharply decreased when increasing the loading rate from 0.1 mN/s to 0.5 mN/s. It remained independent of the loading rate at higher loading rates from 0.5 mN/s to 2 mN/s. At the lowest loading rate of 0.1 mN/s, there is a large scatter in Young's modulus values which follows the same trend as Fig. 3.19.

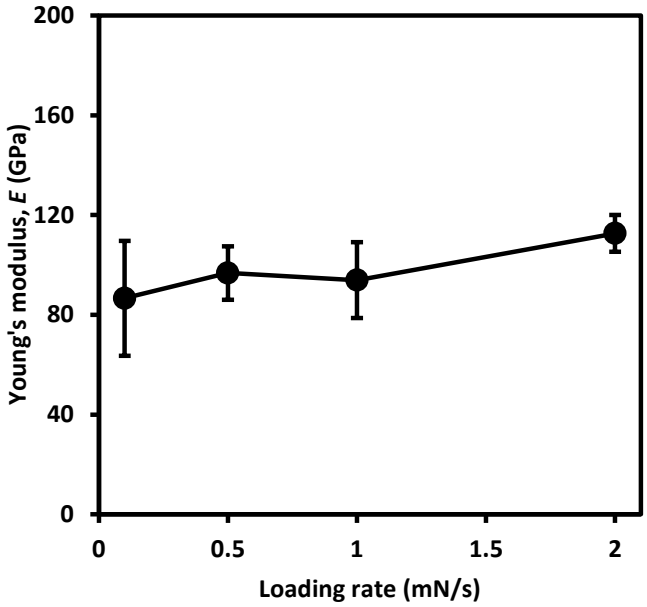


Fig. 3.28. Young's modulus (*E*) versus loading rate for LMGC. Each data point is the mean value of the six repeated indentations; each error bar corresponds to ± one standard deviation for the six repeated indentations.

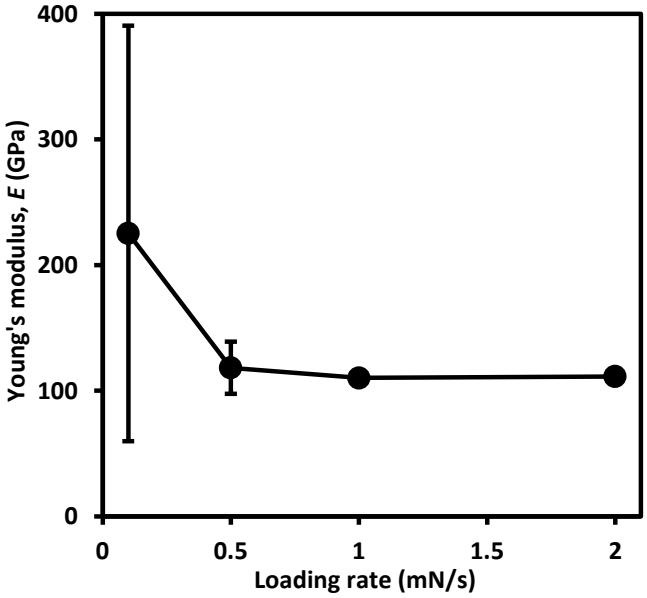


Fig. 3.29. Young's modulus (*E*) versus loading rate for sintered LDGC. Each data point is the mean value of the six repeated indentations; each error bar corresponds to ± one standard deviation for the six repeated indentations.

Fig. 3.30 shows Young's modulus versus loading rate for pressable LDGC. The measured Young's modulus means and standard deviations at 0.1 mN/s, 0.5 mN/s, 1 mN/s and 2 mN/s loading rates are 186.37 ± 132.57 GPa, 110.09 ± 19.24 GPa, 111.33 ± 16.94 GPa, and 118.57 ±

13.24 GPa, respectively. The Young's modulus sharply decreased when increasing the loading rate from 0.1 mN/s to 0.5 mN/s. It remained independent of the loading rate at higher loading rates from 0.5 mN/s to 2 mN/s. At the lowest loading rate of 0.1 mN/s, there is a large scatter in Young's modulus values which follows the same trend as Fig. 3.20.

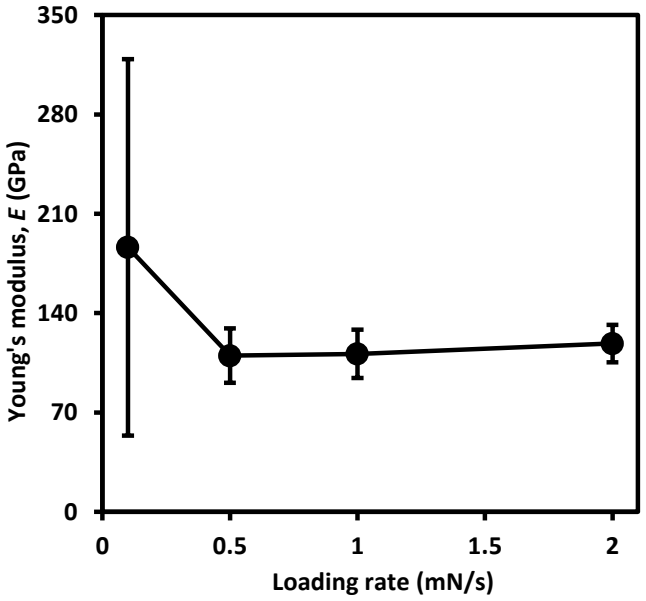


Fig. 3.30. Young's modulus ($E$) versus loading rate for pressable LDGC. Each data point is the mean value of the six repeated indentations; each error bar corresponds to ± one standard deviation for the six repeated indentations.

Fig. 3.31 shows Young's modulus versus loading rate for pre-sintered Y-TZP. The measured Young's modulus values at the loading rates of 0.1 mN/s, 0.5 mN/s, 1 mN/s and 2 mN/s are 61.25 ± 48.51 GPa, 30.66 ± 7.68 GPa, 28.00 ± 2.51 GPa, and 29.23 ± 3.58 GPa, respectively. The Young's modulus decreased rapidly when increasing loading rate from 0.1 mN/s to 1 mN/s and remained relatively constant as the loading rate increased. There is a large scatter in Young's modulus values at the lowest loading rate of 0.1 mN/s, at which the average value is approximately twice the moduli at higher loading rates.

Fig. 3.32 shows Young's modulus versus loading rate for sintered Y-TZP. The measured Young's modulus means and standard deviations at 0.1 mN/s, 0.5 mN/s, 1 mN/s and 2 mN/s loading rates are 158.4 ± 57.13 GPa, 189.55 ± 14.28 GPa, 157.50 ± 11.31 GPa, and 167.32 ± 9.06 GPa, respectively. The standard deviations of Young's moduli decreased with the loading rate, which followed the dispersion trend in the force-displacement curves in Fig. 3.12. Single factor ANOVA shows the insignificant loading rate effect on the Young's modulus ($p > 0.05$).

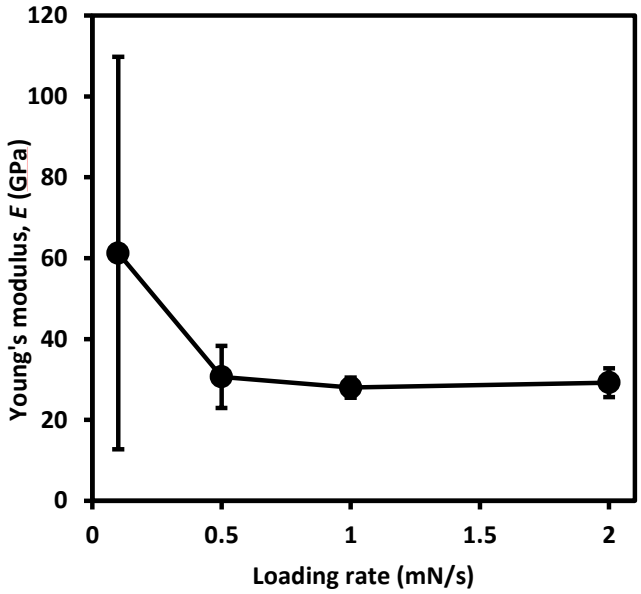


Fig. 3.31. Young's modulus (*E*) versus loading rate for pre-sintered Y-TZP. Each data point is the mean value of the six repeated indentations; each error bar corresponds to ± one standard deviation for the six repeated indentations.

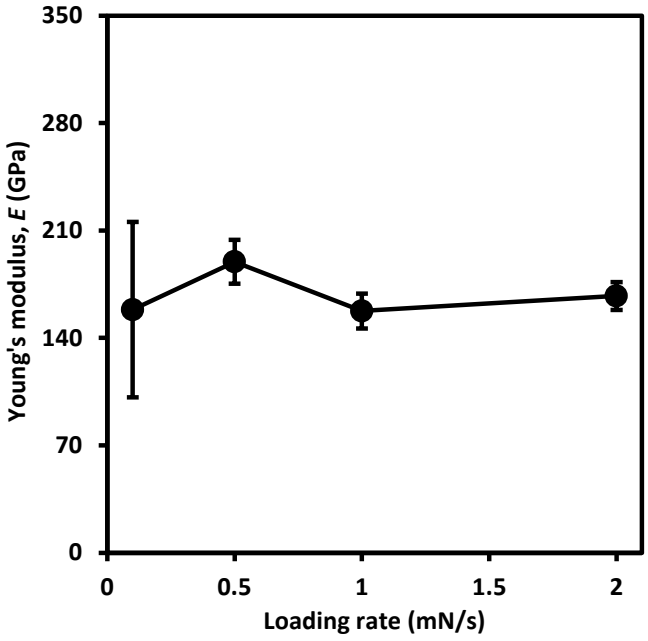


Fig. 3.32. Young's modulus (*E*) versus loading rate for sintered Y-TZP. Each data point is the mean value of the six repeated indentations; each error bar corresponds to ± one standard deviation for the six repeated indentations.

### *3.4.6 Topological Analyses of Indentation Profiles*

Fig. 3.33 shows 3D scanning probe images of the indented imprints at 0.1 mN/s, 0.5 mN/s, 1 mN/s and 2 mN/s loading rates, respectively for LMGC. All indented areas at all loading rates show plastic deformation without any radial cracks along the corners where highest stresses are usually concentrated.

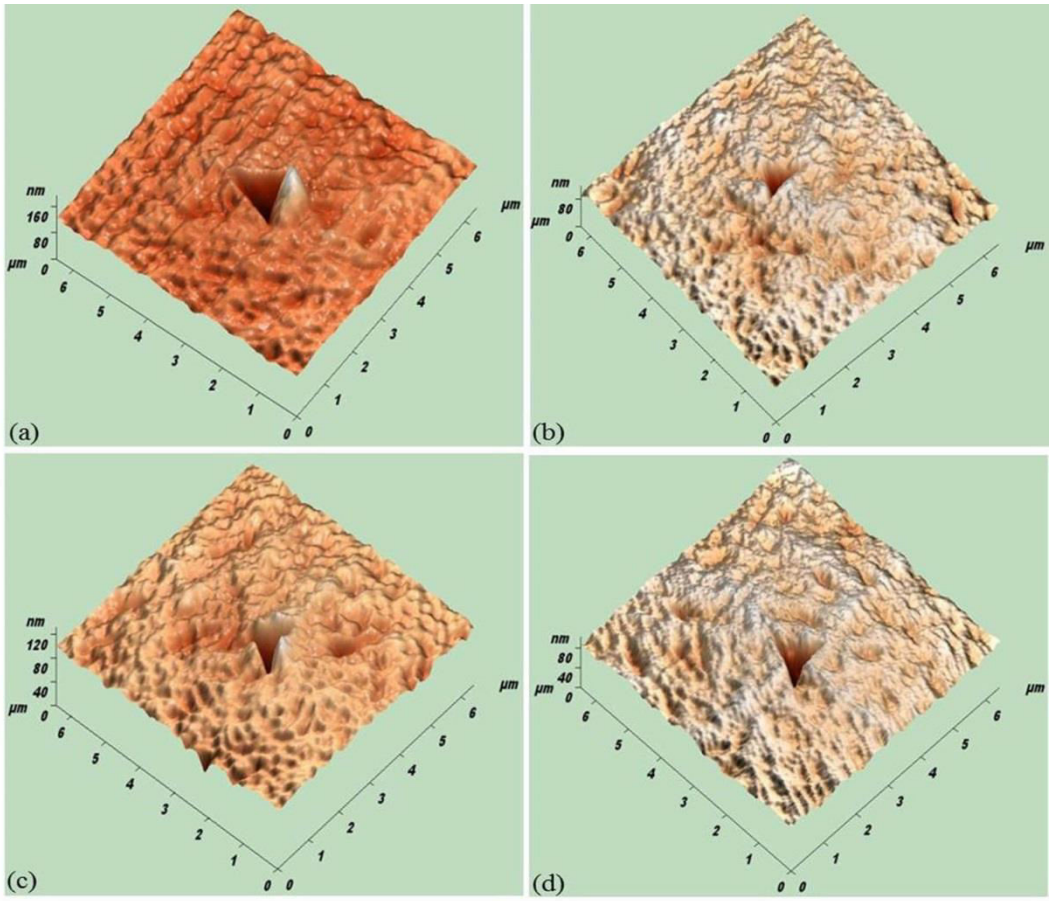


Fig. 3.33. 3D-scanning probe images of nanoindentation impressions for LMGC showing the permanent plastic deformation without the formation of radial cracks in the tensile regions around indent corners at 10 mN peak load and loading rate of (a) 0.1 mN/s, (b) 0.5 mN/s, (c) 1 mN/s and (d) 2 mN/s.

Fig. 3.34 shows 2D scanning probe images of the indented morphologies and their depth cross-sectional profiles at 0.1 mN/s, 0.5 mN/s, 1 mN/s and 2 mN/s loading rates, respectively for LMGC. It shows significant material piling-ups on the indentation contact boundaries at 0.1 mN/s, 0.5 mN/s and 1 mN/s loading rates in Fig. 8(a), (b) and (c), respectively. These piling-up heights corresponded to surface deformation displacements of 64 nm, 9 nm and 6 nm at 0.1 mN/s, 0.5 mN/s and 1 mN/s loading rates, respectively. No visible piling-ups can be found

around the indentation imprint at 2 mN/s loading rate in Fig. 8(d) but only minor sinking-in was observed. These indicate the loading rate-dependent occurrence of the piling-up events for LMGC. Meanwhile, it is reasonable to indicate that the critical loading rate for the suppression of piling-ups in LMGC was approximately 1–2 mN/s.

Fig. 3.35 shows 3D scanning probe images of the indented imprints at 0.1 mN/s, 0.5 mN/s, 1 mN/s and 2 mN/s loading rates, respectively for sintered LDGC. All indented areas at all loading rates show plastic deformation without any radial cracks along the corners where highest stresses are usually concentrated.

Fig. 3.36 shows 2D scanning probe images of the indented morphologies and their depth cross-sectional profiles at 0.1 mN/s, 0.5 mN/s, 1 mN/s and 2 mN/s loading rates, respectively for sintered LDGC. It shows significant material piling-ups on the indentation contact boundaries at 0.1–1 mN/s loading rates respectively (Fig. 3.36(a)–(c)). These piling-up heights corresponded to surface deformation displacements of 44 nm, 9 nm and 5 nm at 0.1 mN/s, 0.5 mN/s and 1 mN/s loading rates, respectively. Neither visible piling-up nor sinking-in can be found around the indentation imprint at 2 mN/s loading rate in Fig. 3.36(d) indicating the loading rate dependence for piling-up occurrence in sintered LDGC. Thus, the critical loading rate for the suppression of piling-ups in sintered LDGC was also 1–2 mN/s.

Fig. 3.37 shows 3D scanning probe images of the indented imprints at 0.1 mN/s, 0.5 mN/s, 1 mN/s and 2 mN/s loading rates, respectively for pressable LDGC. Similar to LMGC and sintered LDGC, all indented areas at all loading rates show plastic deformation without any radial cracks along the corners where highest stresses are usually concentrated.

Fig. 3.38 shows 2D scanning probe images of the indented morphologies and their depth cross-sectional profiles at 0.1 mN/s, 0.5 mN/s, 1 mN/s and 2 mN/s loading rates, respectively for pressable LDGC. It shows significant material piling-ups on the indentation contact boundaries at all loading rates in Fig. 3.38(a)–(d). These piling-up heights corresponded to surface deformation displacements of 38 nm, 25 nm, 12 nm and 10 nm at 0.1 mN/s, 0.5 mN/s, 1 mN/s and 2 mN/s loading rates, respectively. These indicate that within the studied loading rates, piling-up events could not be completely suppressed for pressable LDGC.

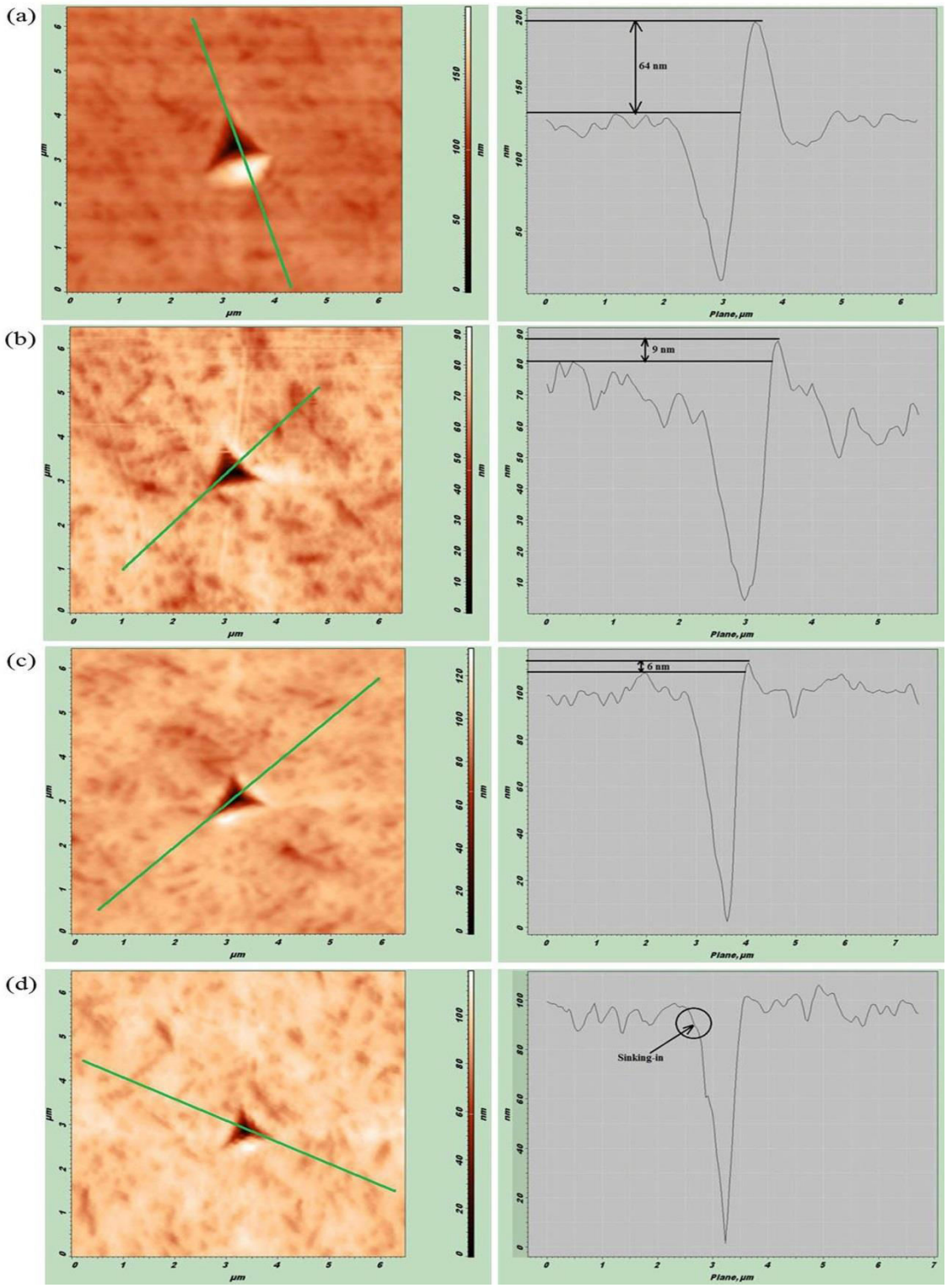


Fig. 3.34. 2D-scanning probe images of nanoindentation impressions and their corresponding depth cross-sectional profiles for LMGC at 10 mN showing piling-ups at loading rate of (a) 0.1 mN/s, (b) 0.5 mN/s, (c) 1 mN/s, respectively; and (d) sinking-in at 2 mN/s. The surface deformation displacements at 0.1 mN/s, 0.5 mN/s, and 1 mN/s are of 64 nm, 9 nm, and 6 nm respectively.

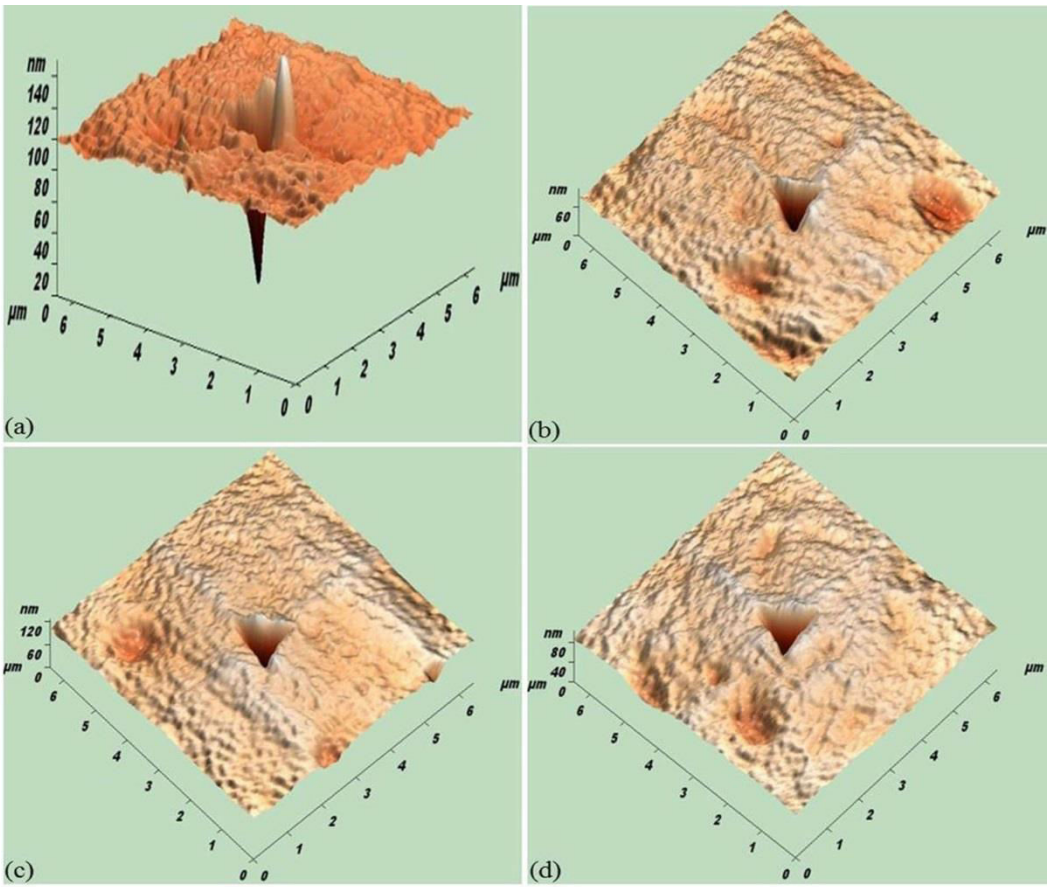


Fig. 3.35. 3D-scanning probe images of nanoindentation impressions of sintered LDGC showing the permanent plastic deformation without the formation of radial cracks in the tensile regions around indent corners at 10 mN peak load and loading rate of (a) 0.1 mN/s, (b) 0.5 mN/s, (c) 1 mN/s and (d) 2 mN/s.

Fig. 3.39 shows the 3D scanning probe images of the indented morphologies at the loading rates of 0.1 mN/s, 0.5 mN/s, 1 mN/s and 2 mN/s, respectively for pre-sintered Y-TZP. Plastic deformation was observed on all indented areas; no radial cracks along the corners where highest stresses are concentrated were observed.

Fig. 3.40 shows 2D scanning probe images of the indented morphologies and their depth cross-sectional profiles at loading rates of 0.1 mN/s, 0.5 mN/s, 1 mN/s and 2 mN/s, respectively for pre-sintered Y-TZP. No significant pile-ups were observed around the indentations. At low loading rates of 0.1 mN/s (Fig. 3.40(a)) and 0.5 mN/s (Fig. 3.40(b)), the cross-section profiles revealed relatively frequent ruptures or collapses as the indenter penetrated the material.

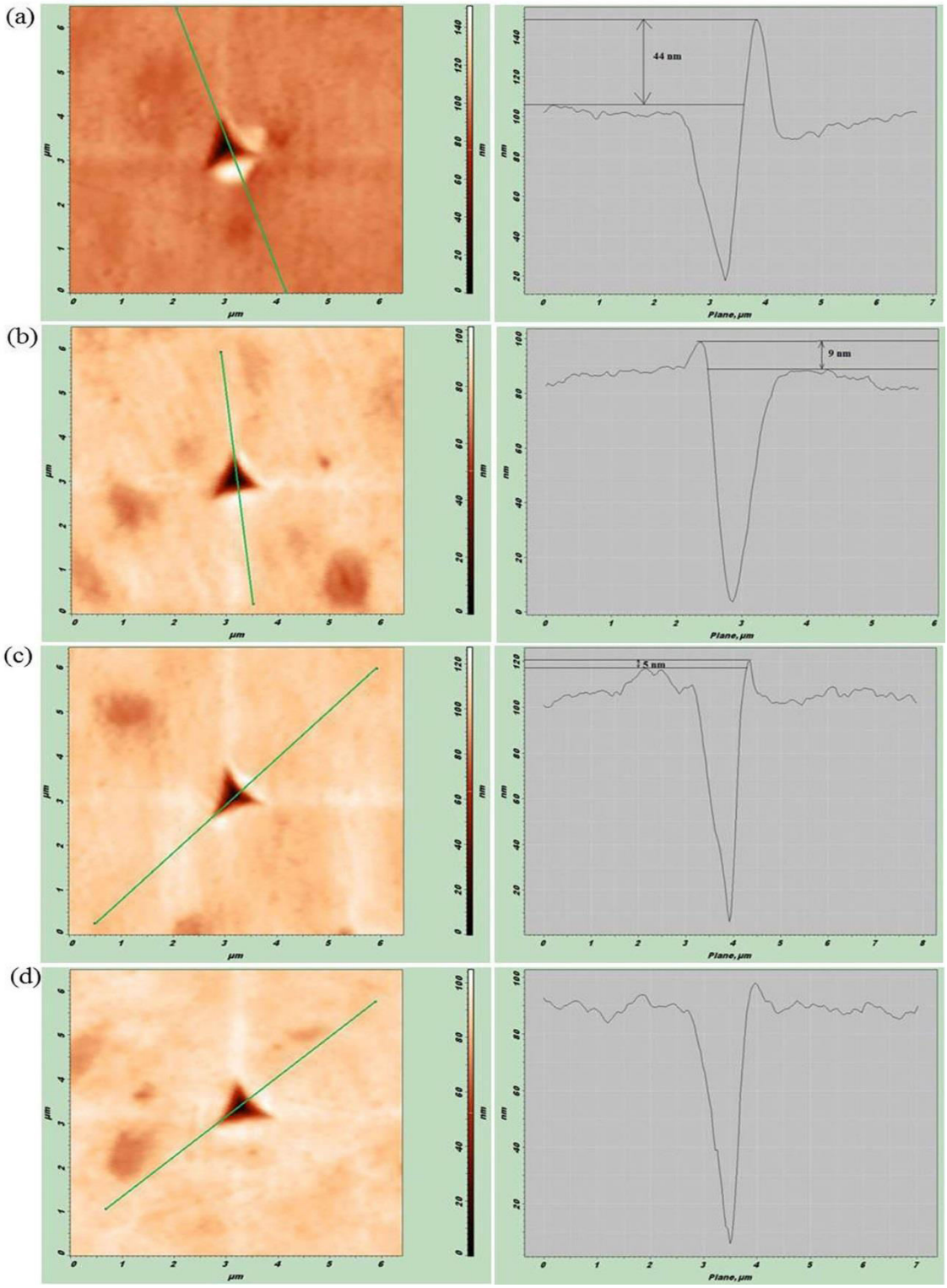


Fig. 3.36. 2D-scanning probe images of nanoindentation impressions and their corresponding depth cross-sectional profiles for sintered LDGC at 10 mN showing piling-ups at loading rate of (a) 0.1 mN/s, (b) 0.5 mN/s, (c) 1 mN/s, respectively; and (d) no piling-up at 2 mN/s. The surface deformation displacements at 0.1 mN/s, 0.5 mN/s, and 1 mN/s are of 44 nm, 9 nm, and 5 nm respectively.

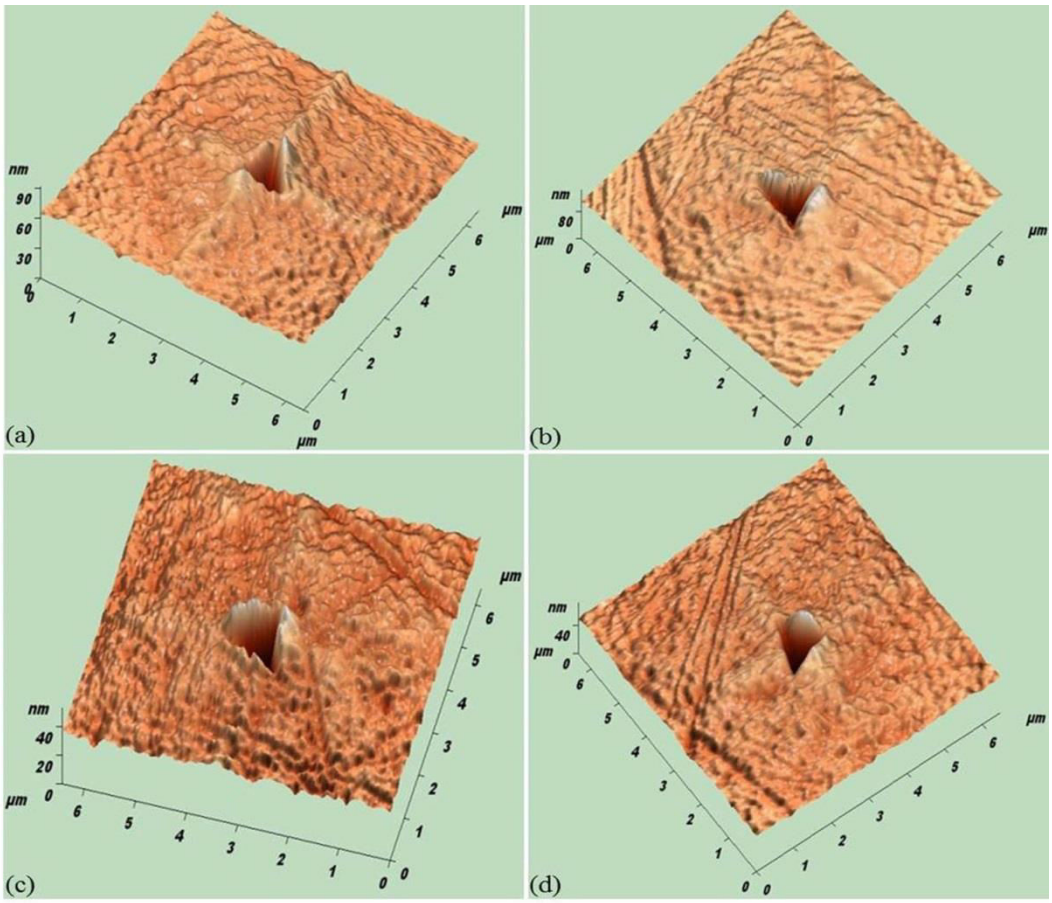


Fig. 3.37. 3D-scanning probe images of nanoindentation impressions of pressable LDGC showing the permanent plastic deformation without the formation of radial cracks in the tensile regions around indent corners at 10 mN peak load and loading rate of (a) 0.1 mN/s, (b) 0.5 mN/s, (c) 1 mN/s and (d) 2 mN/s.

The occurrence of frequent collapses of the indenter at low loading rates may have led to the compaction of the indented profiles. At higher loading rates of 1 mN/s (Fig. 3.40(c)) and 2 mN/s (Fig. 3.40(d)), the indenter collapses due to the reduction in material porosity and the porosity filling might have dominated at these loading rates. Evidence of the pore filling is shown in Fig. 3.40(d) where at the loading rate of 2 mN/s, the cross-sectional profile shows sudden steps on the indentation profile. This is manifested by the sudden change in indentation profile (the circle in Fig. 3.40(d)).

Fig. 3.41 highlights the kink bands observed in the indentation imprint observed in pre-sintered Y-TZP at the loading rate of 1 mN/s, where dislocation-associated parallel kink bands were induced in the vicinity of the indentation.

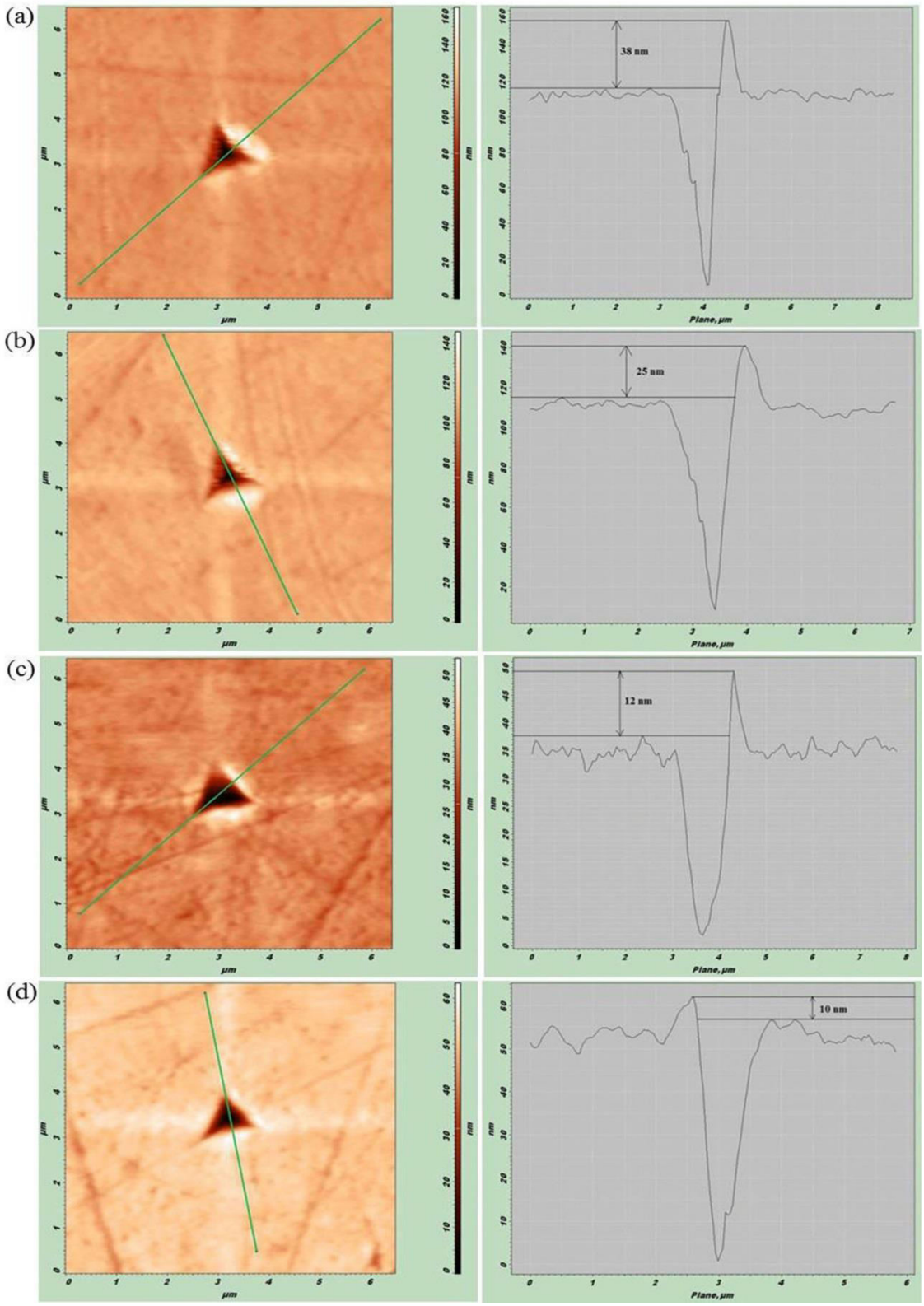


Fig. 3.38. 2D-scanning probe images of nanoindentation impressions and their corresponding depth cross-sectional profiles for pressable LDGC at 10 mN and loading rate of (a) 0.1 mN/s, (b) 0.5 mN/s, (c) 1 mN/s, and (d) 2 mN/s, showing piling-ups and surface deformation displacements of 38 nm, 25 nm, 12 nm, and 10 nm respectively.

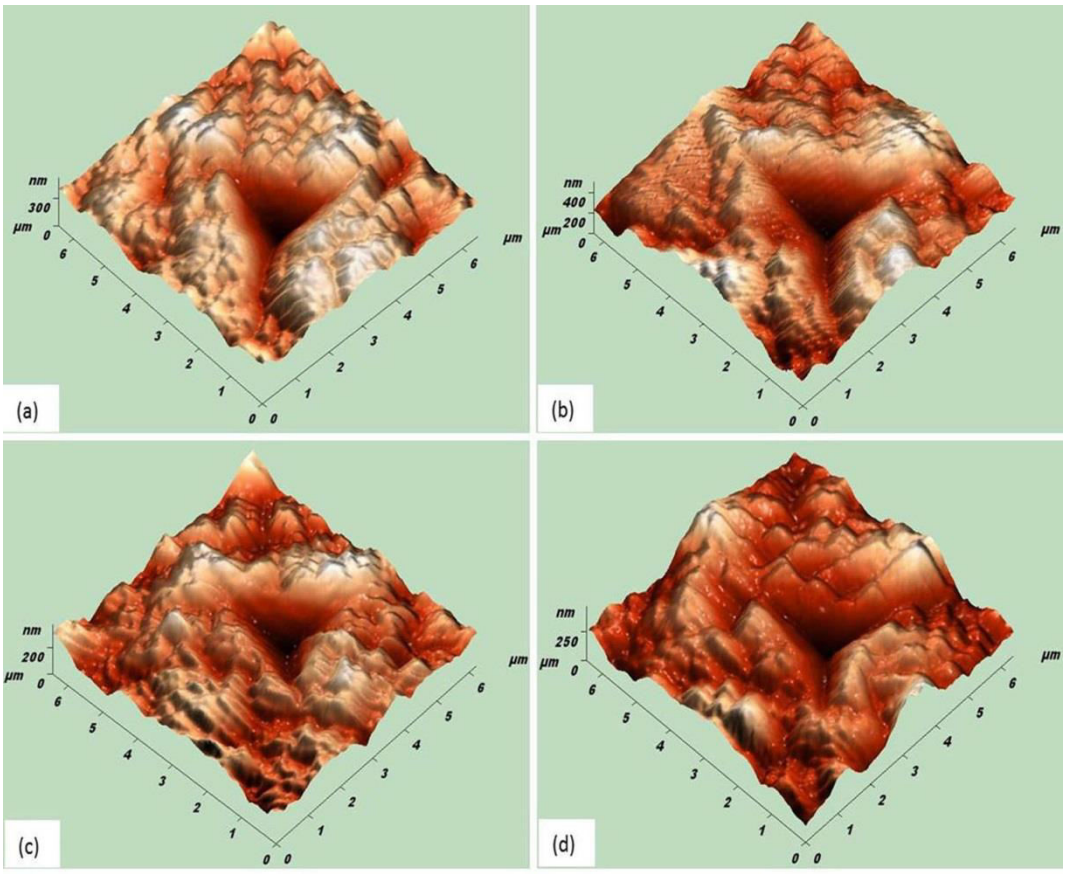


Fig. 3.39. 3D-scanning probe images of nanoindentation impressions of pre-sintered Y-TZP LDGC showing the permanent plastic deformation without the formation of radial cracks in the tensile regions around indent corners at 10 mN peak load and loading rate of (a) 0.1 mN/s, (b) 0.5 mN/s, (c) 1 mN/s and (d) 2 mN/s.

Fig. 3.42 shows 3D scanning probe images of the indented morphologies at 0.1 mN/s, 0.5 mN/s, 1 mN/s and 2 mN/s loading rates, respectively for sintered Y-TZP. Plastic deformation was observed on all indented areas and no radial cracks along the corners where highest stresses are usually concentrated were found.

Fig. 3.43 shows 2D scanning probe images of the indented morphologies and their depth cross-sectional profiles at 0.1 mN/s, 0.5 mN/s, 1 mN/s and 2 mN/s loading rates, respectively for sintered Y-TZP. Significant pileups in Figs. 3.43(a), (b) and (c) were observed around the indentations at 0.1 mN/s, 0.5 mN/s and 1 mN/s loading rates, corresponding to surface deformation displacements of 25 nm, 10 nm and 9 nm, respectively. However, there was no evidence of pileup around the indenter at 2 mN/s loading rate in Fig. 3.43(d). These indicate that the occurrence of the pileup phenomenon for sintered Y-TZP was dependent on the loading rate. It may be taken that the critical loading rate at which pileup events cannot occur in this sintered Y-TZP investigated was 1–2 mN/s.

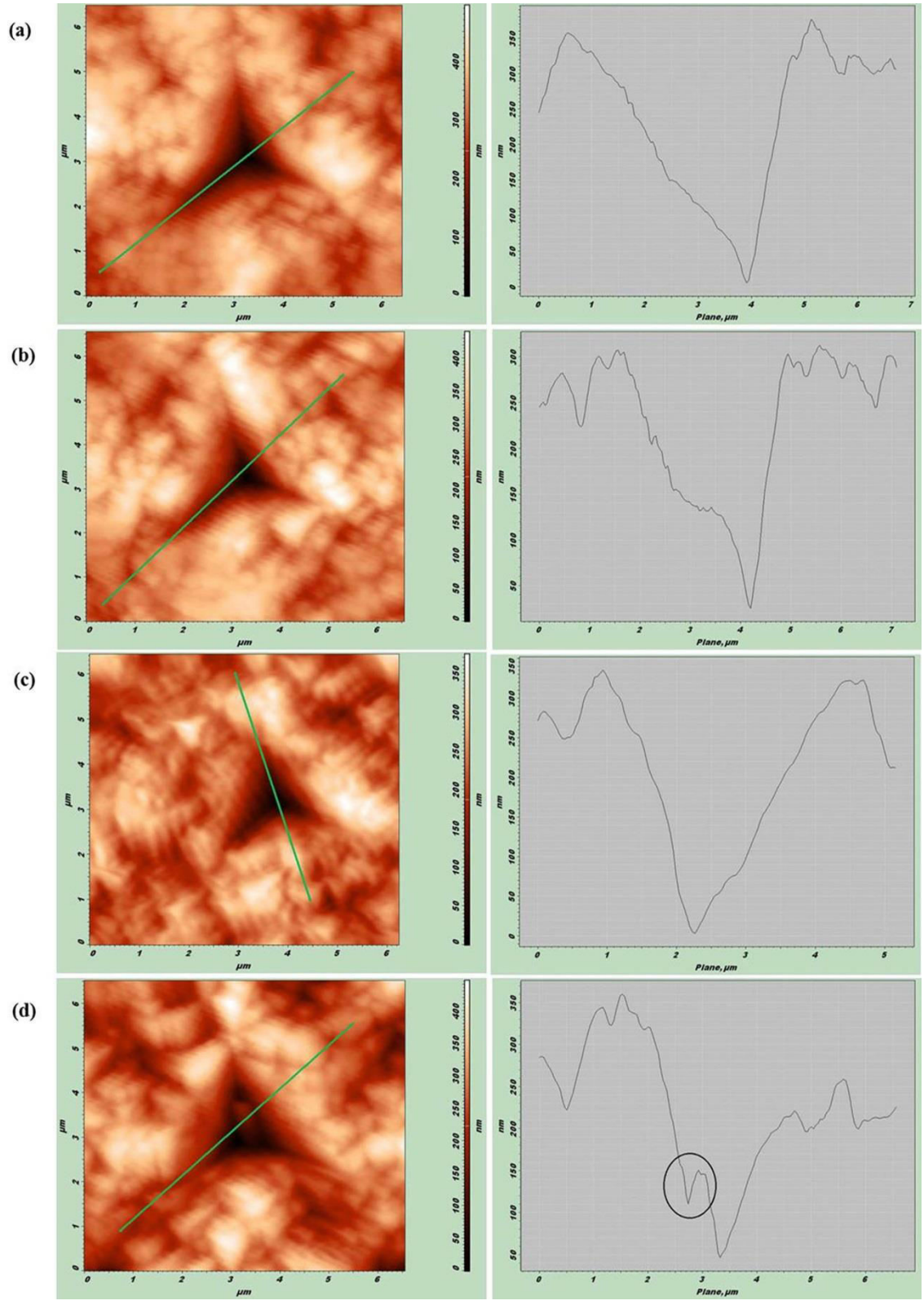


Fig. 3.40. 2D-scanning probe images of nanoindentation impressions and their corresponding depth cross-sectional profiles for presintered Y-TZP at 10 mN and loading rate of (a) 0.1 mN/s, (b) 0.5 mN/s, (c) 1 mN/s, and (d) 2 mN/s.

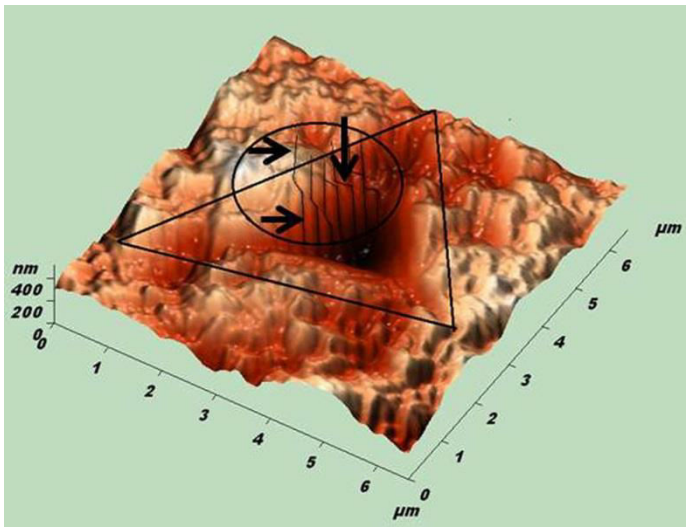


Fig. 3.41. A 3D-scanning probe image of nanoindentation impression of pre-sintered Y-TZP at 10 mN peak load and 1 mN/s loading rate showing the kinking behavior for pre-sintered zirconia. The kinking, buckling and bending of the pre-sintered zirconia grains (represented by the circle) took place in the vicinity of the indentation (represented by the triangle). The horizontal and vertical arrows represent parallel pair dislocations and slip planes respectively.

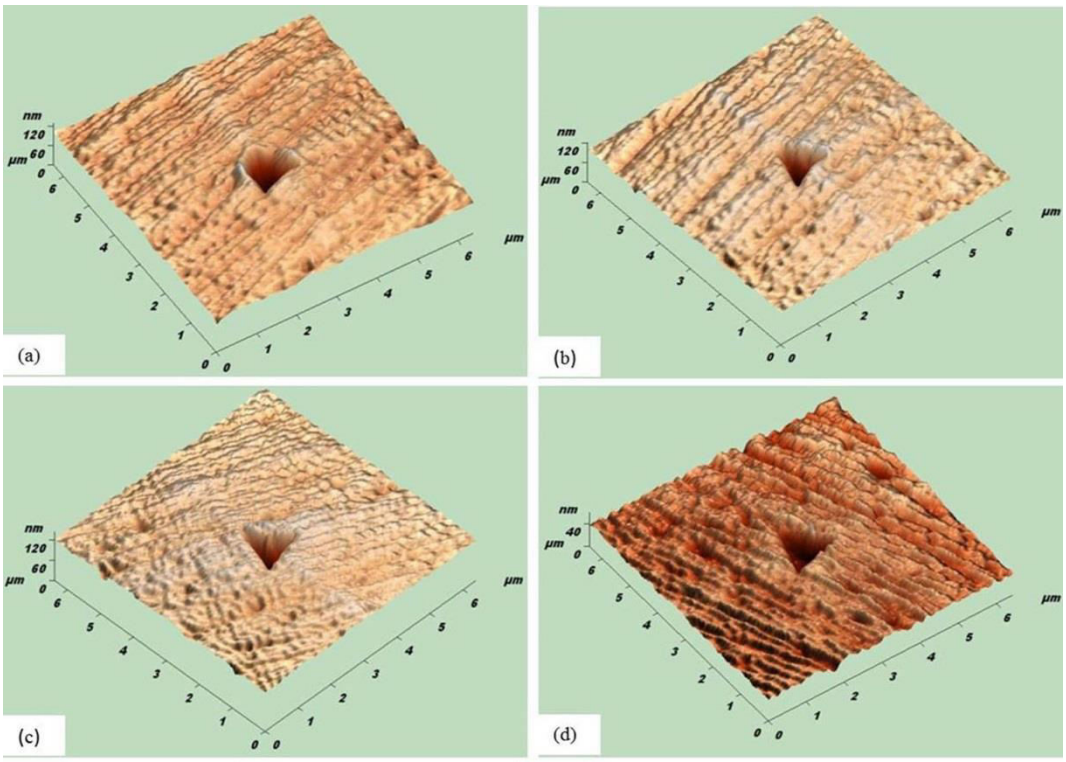


Fig. 3.42. 3D-scanning probe images of nanoindentation impressions of sintered Y-TZP showing the permanent plastic deformation without the formation of radial cracks in the tensile regions around indent corners at 10 mN peak load and loading rate of (a) 0.1 mN/s, (b) 0.5 mN/s, (c) 1 mN/s and (d) 2 mN/s.

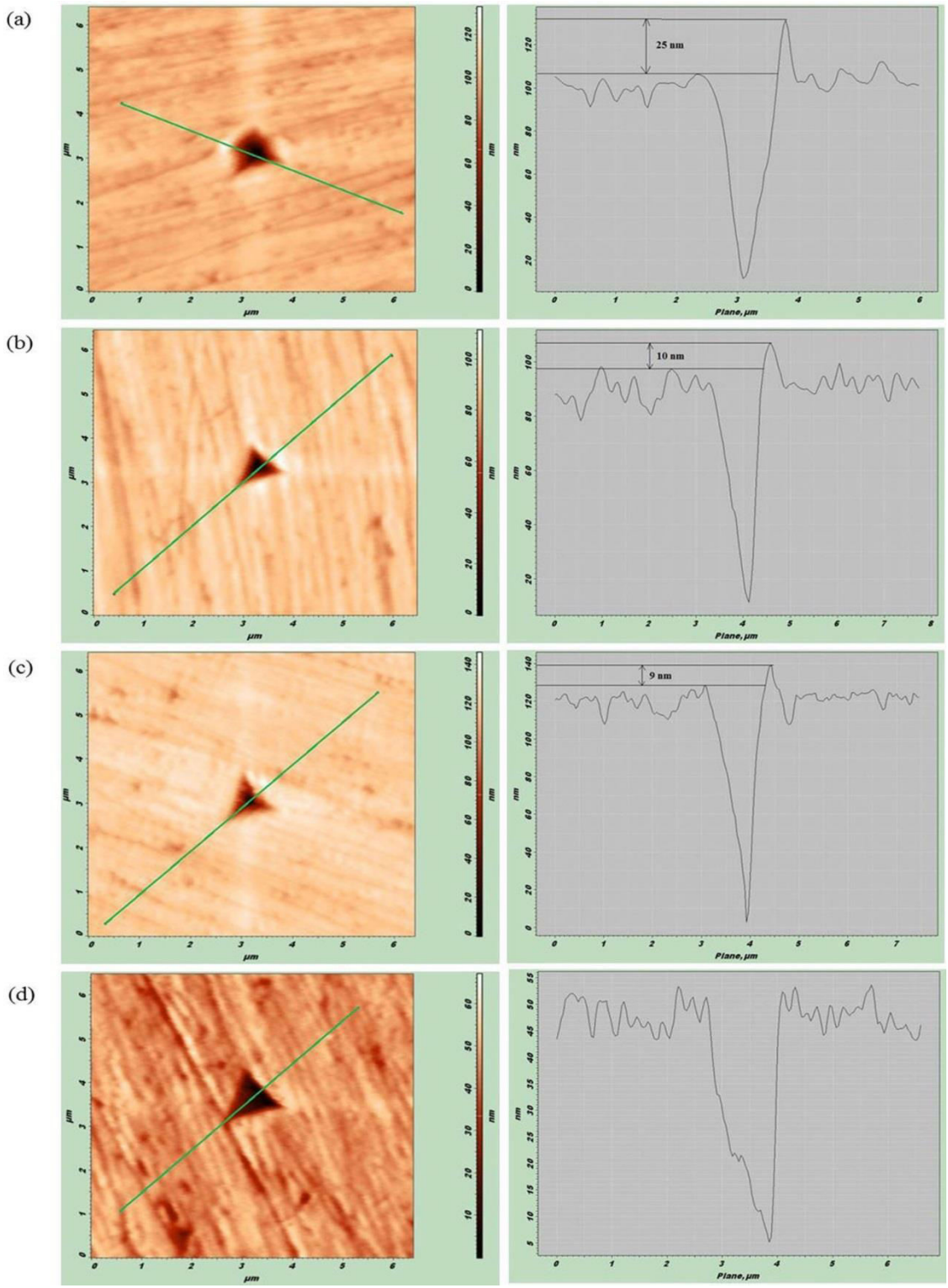


Fig. 3.43. 2D-scanning probe images of nanoindentation impressions and their corresponding depth cross-sectional profiles for sintered Y-TZP at 10 mN showing piling-ups at loading rate of (a) 0.1 mN/s, (b) 0.5 mN/s, (c) 1 mN/s, respectively; and (d) no piling-up at 2 mN/s. The surface deformation displacements at 0.1 mN/s, 0.5 mN/s, and 1 mN/s are 25 nm, 10 nm, and 9 nm respectively.

## 3.5 Discussion

### *3.5.1 LMGC, Sintered and Pressable LDGC*

This is the first study on the nano-mechanical behavior of LMGC, sintered and pressable LDGC using diamond indenter at different loading rates.

The reverse increase of the contact depths with the loading rates in Figs. 3.13–3.15 indicate that the contact areas were enhanced at the lower loading rate. This is consistent with the relation in Eq. (3.3) between the projected area, $A$, and the contact depth, $h_c$, established by Oliver and Pharr, (1992; 2004). These loading-rate downward dependent depths feature the increased contact hardness with the loading rate in Figs. 3.23–3.25, because the contact hardness, $H_c$, is the ratio of the peak load, $P_{max}$, to the projected area (Oliver and Pharr, 1992; 2004). The increase in the contact hardness with increasing loading rate is in line with indentation studies of glasses (Anton and Subhash, 2000; Dey et al., 2011; Shang and Rouxel, 2005), although LMGC, contains lithium metasilicate crystals and glass matrix. And sintered and pressable LDGC contains lithium disilicate crystals embedded in glass matrix.

However, the Young's modulus, $E$, of LMGC in Fig. 3.28 reveals loading rate-independent effect, which is determined from the reduced modulus, $E_r$, in Eq. (3.7) which itself depends on both contact stiffness, $S$, and projected area in Eq. (3.6). The loading rate-independent contact stiffness (Fig. 3.18) affected the Young's modulus to be independent of loading rate even though the contact area was dependent on the loading rate (Fig. 3.13). Different values of the unloading constant, $k_2$, and the unloading exponent, $m$, (Eq. (3.6)) extracted at different loading rates (Fig. 3.8) might have also contributed to the independence of the contact stiffness on the loading rate. The mean and standard deviation of the measured Young's modulus at all loading rates from 24 indentations were 97.48 ± 17.24 GPa. This value is slightly higher than the Young's modulus (75 GPa) reported for LMGC containing 8–10% lithium metasilicate phase using an ultrasonic technique (Mastelaro and Zanotto, 1999). This indicates that the higher volume (40%) lithium metasilicate crystal phase in LMGC in this study improves the mechanical stiffness.

The Young's moduli of sintered and pressable LDGC in Figs. 3.29 and 3.30 are identical following the same trend as their contact stiffness plots in Figs. 3.19 and 3.20. The increase in the Young's moduli at 0.1 mN/s loading rate in Figs. 3.29 and 3.30 has been attributed to the tensile residual stresses that might occur as the indenter penetrated slowly (Alao and Yin,

2014b). This phenomenon is explained clearly in Section 3.5.2. Above this loading rate, the Young's moduli of the two materials were independent of the loading rate. Thus, the mean and standard deviation of the loading rate-independent Young's modulus of sintered LDGC from 18 indentations were 113.28 ± 12.56 GPa, consistent with the reported Young's modulus of 90–100 GPa for sintered LDGC (Bühler-Zemp and Völkel, 2005a; Ereifej et al., 2011). Similarly, the measured mean and standard deviation of the Young's modulus from 18 indentations for pressable LDGC were 113.33 ± 16.11 GPa, in line with the reported value 90–100 GPa for the same material (Albakry et al., 2003; Bühler-Zemp and Völkel, 2005b; Ereifej et al., 2011). It should be noted that the Young's modulus of sintered and pressable LDGC is significantly higher than that of the LMGC due to the resistance to elastic deformation offered by the lithium disilicate crystals compared to lithium metasilicate crystals in LMGC.

The significant piling-ups in Figs. 3.33 and 3.34 observed for LMGC, Figs. 3.35 and 3.36 for sintered LDGC and Figs. 3.37 and 3.38 for pressable LDGC might overestimate their measured contact hardnesses (Figs. 3.23–3.25) and Young's moduli (Figs. 3.28–3.30). This is because the true contact area by the Oliver-Pharr method can be underestimated (Bolshakov and Pharr, 1998). Thus, it is important to investigate the authenticity of the properties measured. For the Oliver-Pharr method to be applicable for piling-up materials, first, the ratio of the final depth, $h_f$, to the maximum depth, $h_{max}$, should be less than 0.7 (i.e. $h_f/h_{max} \leq 0.7$); secondly, the material should moderately strain harden (Bolshakov and Pharr, 1998). For LMGC, the calculated means and standard deviations of the $h_f/h_{max}$ ratios at 0.1 mN/s, 0.5 mN/s, 1 mN/s and 2 mN/s from Fig. 3.13 were 0.38 ± 0.19, 0.48 ± 0.17, 0.39 ± 0.09 and 0.28 ± 0.06, respectively. For sintered LDGC, the calculated $h_f/h_{max}$ ratios at 0.1 mN/s, 0.5 mN/s, 1 mN/s and 2 mN/s from Fig. 3.14 were 0.47 ± 0.28, 0.40 ± 0.17, 0.47 ± 0.10 and 0.47 ± 0.06, respectively. For pressable LDGC, the calculated $h_f/h_{max}$ ratios at 0.1 mN/s, 0.5 mN/s, 1 mN/s and 2 mN/s from Fig. 3.15 were 0.55 ± 0.11, 0.42 ± 0.12, 0.41 ± 0.14 and 0.39 ± 0.08, respectively. Based on the indentation tests conducted, all these $h_f/h_{max}$ ratios were less than the threshold of 0.7 for the three materials. Therefore, the usage of the Oliver-Pharr method fulfilled the first condition.

To verify the second condition of strain hardening, the strain rate sensitivity model can be applied, which relates the contact hardness, $H_c$, to the intrinsic contact hardness, $H_o$, the constant effective strain rate, $\dot{\varepsilon}$, and the strain rate sensitivity, $n$, as (Limbach et al., 2014; Peykov et al., 2012):

$$H_c = H_o \dot{\varepsilon}^n \tag{3.9}$$

For a strain-hardening material, its strain rate sensitivity, $n$, should be greater than 0. Eq. (3.9) can also be rewritten as follows:

$$Log(H_c) = n\,Log\left(\dot{\varepsilon}\right) + LogH_o \tag{3.10}$$

Since the load-controlled instrument was used, the constant loading rate should be converted to the constant effective strain rate. In addition, the application of a constant strain rate over the whole indentation depth allows the formation of a steady-stress state below the indenter after a certain depth is reached (Limbach et al., 2014). Thus, the relationship between the constant strain rate, $\dot{\varepsilon}$, and the constant loading rate, $\dot{P}$, can be described as (Lucas and Oliver, 1999):

$$\dot{\varepsilon} = \frac{1}{2}\frac{\dot{P}}{P_{\max}} \tag{3.11}$$

where $P_{max}$ is the peak load. Accordingly, the constant strain rates at 0.1 mN/s, 0.5 mN/s, 1 mN/s and 2 mN/s were 0.005 $s^{-1}$, 0.025 $s^{-1}$, 0.05 $s^{-1}$, and 0.1 $s^{-1}$, respectively. Figs. 3.44–3.46 shows the log-log plot of the contact hardness, $H_c$, versus the strain rate, $\dot{\varepsilon}$, for LMGC, sintered and pressable LDGC respectively. The corresponding linear correlation equations for LMGC, sintered and pressable LDGC from these figures can be written as Eqs. (3.12)–(3.14) respectively.

$$Log\left(H_c\right) = 0.261\,Log\left(\dot{\varepsilon}\right) + 1.2757 \tag{3.12}$$

$$Log\left(H_c\right) = 0.181\,Log\left(\dot{\varepsilon}\right) + 1.1638 \tag{3.13}$$

$$Log\left(H_c\right) = 0.118\,Log\left(\dot{\varepsilon}\right) + 1.0792 \tag{3.14}$$

The coefficient of determination, $R^2$, for Eq. (3.12)–(3.14) is 93%, 94% and 91% respectively.

Comparing Eq. 3.10 with Eqs. (3.12)–(3.14), we obtain $n$ = 0.261 and Log($H_o$) = 1.2757 for LMGC, $n$ = 0.181 and Log($H_o$) = 1.1638 for sintered LDGC and $n$ = 0.118 and Log($H_o$) = 1.0792 for pressable LDGC. Because $n > 0$ in Eqs. (3.12)–(3.14), it indicates that the three materials were moderately sensitive to strain hardening, indicating the second condition is fulfilled. Thus, the measured contact hardness and Young moduli using the Oliver-Pharr method were not influenced by piling-up effects (Bolshakov and Pharr, 1998).

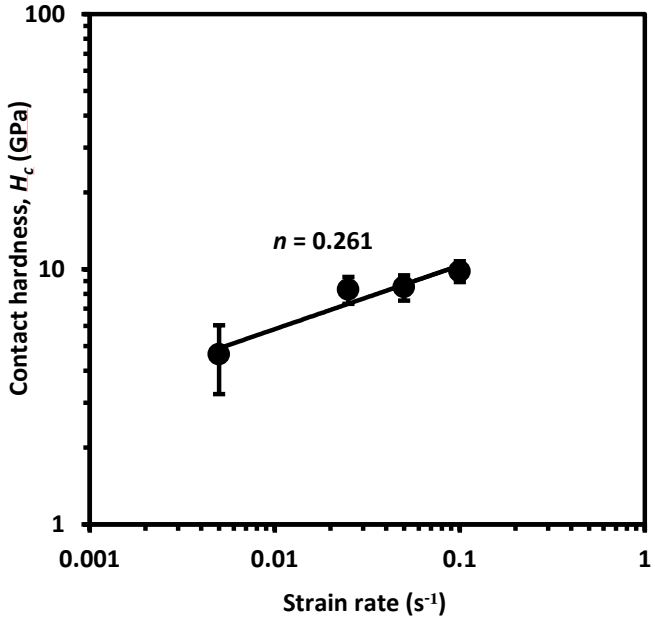


Fig. 3.44. Contact hardness ($H_c$) versus strain rate ($\dot{\varepsilon}$) for LMGC. Each data point is the mean value for six repeated indentations; each error bar corresponds to ± one standard deviation for the six repeated indentations. The linear graph is described by the Eq. (3.12) and the slope of the graph gives the strain-rate sensitivity, $n$ = 0.261.

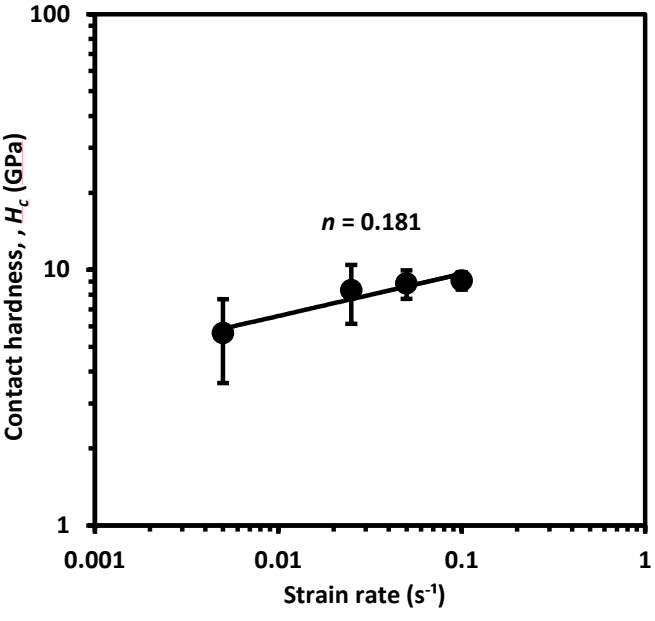


Fig. 3.45. Contact hardness ($H_c$) versus strain rate ($\dot{\varepsilon}$) for sintered LDGC. Each data point is the mean value for six repeated indentations; each error bar corresponds to ± one standard deviation for the six repeated indentations. The linear graph is described by the Eq. (3.13) and the slope of the graph gives the strain-rate sensitivity, $n$ = 0.181.

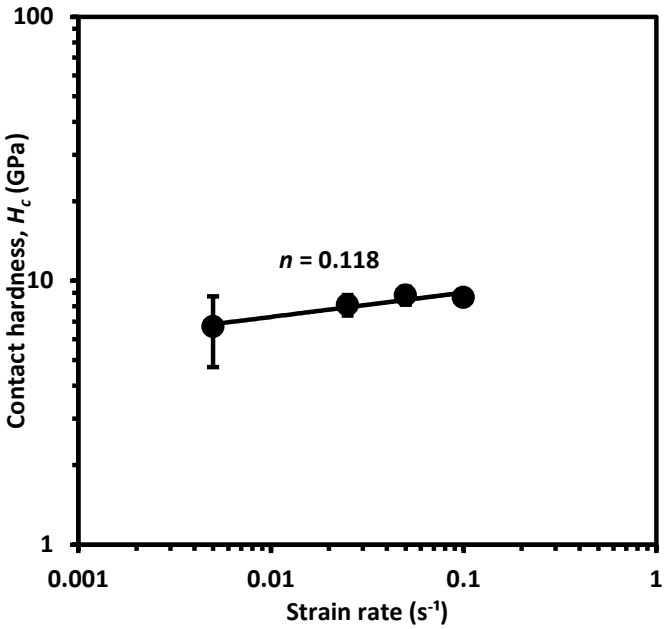


Fig. 3.46. Contact hardness ($H_c$) versus strain rate ($\dot{\varepsilon}$) for pressable LDGC. Each data point is the mean value for six repeated indentations; each error bar corresponds to ± one standard deviation for the six repeated indentations. The linear graph is described by the Eq. (3.14) and the slope of the graph gives the strain-rate sensitivity, $n$ = 0.118.

A minor sinking-in occurred at the highest loading rate in Fig. 3.34(d) because this phenomenon predominates in materials with strain rate sensitivity greater than 0.2 (Alcalà et al., 2000). A similar observation was noted in indentation of annealed Cu-alloys by Zhang et al. (2011), in which two sides of the indentation were relatively flat but the sinking-in effect actually occurred. When a material transits from piling-up to sinking-in, it becomes more elastic (Alcalà et al., 2000). This explains why the Young's modulus at the highest loading rate was slightly higher (Fig. 3.28). Due to higher strain rates at higher loading rates, LMGC may have been subjected to higher pressure (Buchner et al., 2011), resulting in an enhanced Young's modulus (Fig. 3.28). In addition, a recent study suggested that piling-up and sinking-in deformation modes co-existed in materials when the $h_f/h_{max}$ ratio was 0.83 (N'jock et al., 2015). As explained above, the $h_f/h_{max}$ ratios for LMGC at different loading rates were less than 0.83 and both deformations occurred indicating that the proposed criterion is not applicable to pressure sensitive and strain-hardening materials like LMGC.

No sinking-in occurred in sintered and pressable LDGC (Figs. 3.36 and 3.38) because their $n$ values are less than 0.2 (Alcalà et al., 2000). However, the $n$ of pressable LDGC is less than that of sintered LDGC indicating that sintered LDGC is more sensitive to strain hardening than

pressable LDGC. This effect can be seen in Figs. 3.24 and 3.25 in which the contact hardness increased with the loading rate 0.1–2 mN/s by 61% and 31% for sintered and pressable LDGC respectively. Also, the strength of pressable LDGC which is higher than sintered LDGC provides higher resistance to strain rate sensitivity than sintered LDGC. Further, the occurrence of pile-ups in pressable LDGC at all loading rates (Fig. 3.38(a)–(d)) can be attributed to the viscous flow mechanism with which the material was made (Höland et al., 2000). It is envisaged that the pile-up may be suppressed in a higher than the used maximum 2 mN/s loading rate in this study.

From the above analysis, LMGC, sintered and pressable LDGC were strain-rate sensitive. It is of interest to determine their individual intrinsic or loading rate-independent contact hardness free from the strain rate sensitivity. Based on Eqs. (3.12)–(3.14), the intrinsic contact hardness was 18.9 GPa for LMGC which was significantly higher than those of sintered and pressable LDGC which were 14.58 GPa and 12 GPa, respectively. The intrinsic contact hardness of LMGC is about 3.5 times higher than its Vickers hardness (5.4 ± 0.1 GPa) (Bühler-Zemp and Völkel, 2005a). Also, the intrinsic contact hardness values of sintered and pressable LDGC are about 2.5 and 2.1 times higher than their Vickers hardness (5.8 ± 0.1 GPa) respectively (Bühler-Zemp and Völkel, 2005a; 2005b). Hardness is one of the most important mechanical properties of materials. The quantitative scales of hardness are related to the measurement methods at different length scales. In Vickers indentation, loads applied range up to 10 N, much higher than 10 mN applied in nanoindentation applied in this study. Due to the small volume of materials indented, the contact depth during nanoindentation is always much smaller than that in micro-indentation, a phenomenon often attributed to the intrinsic size effect (Lawn and Cook, 2012). For example, a study showed that pressable LDGC exhibited the indentation size effect (Smith et al., 2014). Therefore, as the indentation size diminished from micro- to nano-domain, the intrinsic hardness for LMGC, sintered and pressable LDGC became higher. Also, the more heavily the indent piles up (or sinks-in), the larger the difference between nano-hardness and micro-hardness (Qian et al., 2005).

The notable discrete discontinuities on the loading and unloading curves at lower loading rates (Figs. 3.8(a), 3.9(a) and 3.10(a)) versus the continuous deformation at higher loading rates (Figs. 3.8(d), 3.9(d) and 3.10(d)) need to be analyzed. These discontinuities in LMGC, sintered and pressable LDGC may have occurred by densification, viscous/shear flow or shear band formation (Limbach et al., 2014). Densification in the glass phase of the material involves a collapse of matter into a more close-packed structure, which is associated with the atomic packing density, i.e., the smaller the atomic packing density the larger the indentation-induced

densification can be (Rouxel et al., 2010). In glass, the atomic packing density, the Poisson's ratio and the glass network dimensionality are strongly correlated (Rouxel, 2007). In glass-ceramics with a Poisson's ratio less than 0.25, there is a highly cross-linked network resulting in a low atomic packing density (Rouxel, 2007). Since the Poisson's ratio of LMGC, sintered and pressable LDGC was less than 0.25, indentation-induced densification must have occurred at all loading rates. Meanwhile, the shear flow caused the material piling-up in the vicinity of indentation and it increases with the loading time because it is not kinematically bounded (Rouxel et al., 2010).

The shear band formation is well-known in metallic glasses (Schuh and Nieh, 2003). The resistance against the indenter penetration of in-organic non-metallic glass can be in the form of densification, pile-up/shear flow or shear band formation but a mixed scenario is most probable in reality (Limbach et al. 2014). Evidence of shear band in an in-organic non-metallic glass (soda-lime-silica glass) was reported inside the nanoindentation cavities (Chakraborty et al., 2010). Shear-banding formation was also reported in glass indentation with sharp indenters by Lawn and Cook (2012). For glass-ceramics, shear bands were reported by Fischer-Cripps and Lawn (1996). Shear bands were also shown in Vickers indentation cavities of pressable LDGC (Apel et al., 2008). All these attest to the fact that shear bands can occur in in-organic non-metallic glasses and glass-ceramics. Therefore, at low loading rates, both densification and inhomogeneous shear band-induced piling-ups are the mechanisms for discrete discontinuities occurring on the loading and unloading curves (Figs. 3.8(a), 3.9(a) and 3.10(a)). The assumption of the occurrence of shear band as a plastic deformation mechanism in LMGC, sintered and pressable LDGC is therefore meaningful.

The basic physical process underlying the inhomogeneous shear band-induced piling-up phenomenon in LMGC, sintered and pressable LDGC can be considered as local softening in these materials (Sergueeva et al., 2005). This is because the localization of the shear-band piling-up requires some structural change of the material inside the bands such that they deform faster than in the rest of the material. The shear band consists of a layer of the material with a viscosity (material resistance to gradual deformation by shear, compressive or tensile stress) lower than that of the rest material. Since the induced compressive stress at low loading rate was low; therefore, the viscosity was low. Thus, at lowest loading rates, the material appeared softer with lowest hardness for LMGC (Fig. 3.23), sintered (Fig. 3.24) and pressable LDGC (Fig. 3.25). Increasing the loading rate correspondingly increased the induced compressive stress, leading to the increased imposed strain rate. To accommodate this increased imposed strain rate, multiple shear bands must operate simultaneously (Schuh and Nieh, 2003). The accumulation

of the multiple shear bands inside the material might have given rise to the strain hardening effect of LMGC, sintered and pressable LDGC in Figs. 3.44–3.46 respectively which in turn raised their viscosity. The increased viscosity led to a gradual suppression of discontinuities of LMGC in Fig. 3.8(b)–(d)), sintered LDGC in Fig. 3.9(b)–(d)), and pressable LDGC in Fig. 3.10(b)–(d)). It also led to the reduction of their piling-up heights in Figs. 3.34, 3.36 and 3.38 respectively. Therefore, at higher loading rates, both densification and homogeneous shear bands are the deformation mechanisms in nanoindentation of LMGC, sintered and pressable LDGC.

When the imposed compressive stresses were relaxed during unloading processes, shear bands beneath the indenter might also occur in the densified zone (Limbach et al., 2014; Rouxel et al., 2010). The densified shear zone can be predicted by the continuum model, which is based on the Johnson's spherical cavity model. This model allows the densified shear zone radius in the sub-surface, $c$, to be predicted from the indentation load, $P$, and the yield strength, $\sigma_y$, as follows (Kramer et al., 1999):

$$c = \left( \frac{3P}{2\pi\sigma_y} \right)^{1/2} \tag{3.15}$$

In this study, $P = P_{max}$ = 10 mN. A relationship between the contact hardness, $H_c$, and the yield strength, $\sigma_y$, was established (Tabor, 1951):

$$H_c = C\sigma_y \tag{3.16}$$

where $C$ is a constraint factor which is 3 for materials that exhibit a combination of piling-up and shear-banding phenomenon such as LMGC, sintered and pressable LDGC (Zhang et al., 2011). Thus, the estimated yield strengths for LMGC were 1.55 ± 0.47 GPa, 2.78 ± 0.33 GPa, 2.84 ± 0.32 GPa and 3.28 ± 0.30 GPa at the loading rates of 0.1 mN/s, 0.5 mN/s, 1 mN/s and 2 mN/s, respectively. For the sintered LDGC, the estimated yield strengths were 1.88 ± 0.66 GPa, 2.77 ± 0.72 GPa, 2.94 ± 0.37 GPa and 3.02 ± 0.23 GPa at the loading rates of 0.1 mN/s, 0.5 mN/s, 1 mN/s and 2 mN/s, respectively. For the pressable LDGC, the estimated yield strengths were 2.44 ± 0.67 GPa, 2.70 ± 0.24 GPa, 2.93 ± 0.23 GPa and 2.88 ± 0.12 GPa at the loading rates of 0.1 mN/s, 0.5 mN/s, 1 mN/s and 2 mN/s, respectively. The applicability of Eq. (3.15) to a wide range of materials in nano-contacts was established by Kramer et al. (1999). Further, to ensure that Eq. (3.15) was applicable to LMGC, sintered and pressable LDGC, it was suggested that the Johnson's elastic-plastic analysis is strictly valid for the following expression (Kramer et al., 1999):

$$E \tan\beta / \sigma_y < 40 \tag{3.17}$$

where $E$ is the Young's modulus, $\beta$ is the face angle which is 24.7° for the Berkovich indenter (Sakai et al., 1999). Using the results in this study, the expression in Eq. (3.17) was 27.55 ± 10.77, 16.43 ± 4.11, 15.37 ± 2.91 and 15.98 ± 2.48 at 0.1 mN/s, 0.5 mN/s, 1 mN/s and 2 mN/s, respectively, indicating that Eq. (3.15) was valid for LMGC. For sintered LDGC, the expression in Eq. (3.17) was 35.83 ± 20.52, 21.80 ± 11.23, 17.47 ± 2.27 and 17.06 ± 2.02 at 0.1 mN/s, 0.5 mN/s, 1 mN/s and 2 mN/s, respectively. Also, for pressable LDGC, the expression in Eq. (3.17) was 33.05 ± 20.11, 19.01 ± 4.52, 17.60 ± 3.47 and 18.94 ± 1.99 at 0.1 mN/s, 0.5 mN/s, 1 mN/s and 2 mN/s, respectively. This also indicates that Eq. (3.15) could be valid for sintered and pressable LDGC.

The densified shear zone radii, $c$, for LMGC were estimated as 1.80 ± 0.25 µm, 1.32 ± 0.09 µm, 1.30 ± 0.07 µm, and 1.21 ± 0.06 µm at 0.1 mN/s, 0.5 mN/s, 1 mN/s and 2 mN/s, respectively, as shown in Fig. 3.47. For sintered LDGC, the densified shear zone radii were 1.66 ± 0.28 µm, 1.35 ± 0.20 µm, 1.28 ± 0.07 µm, and 1.26 ± 0.05 µm at 0.1 mN/s, 0.5 mN/s, 1 mN/s and 2 mN/s, respectively, as shown in Fig. 3.48.

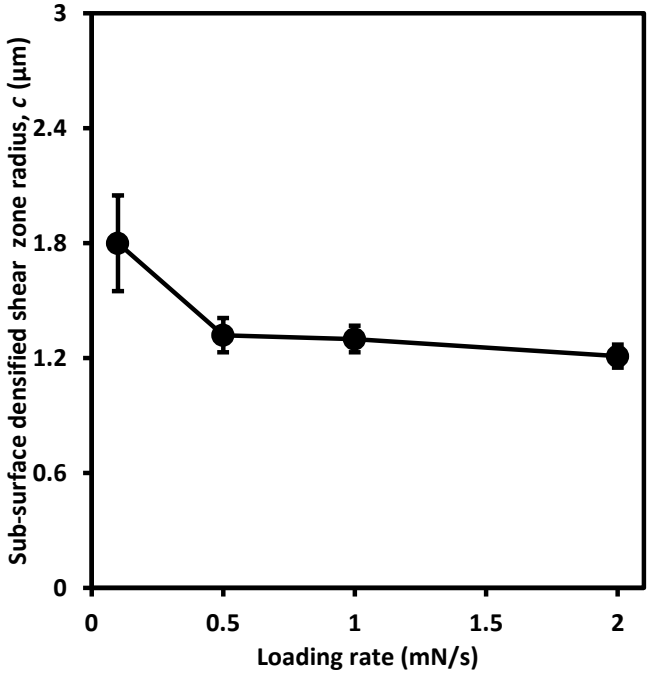


Fig. 3.47. Sub-surface densified shear zone radius (c) versus loading rate for LMGC. Each data point is the mean value for six repeated indentations; each error bar corresponds to ± one standard deviation for the six repeated indentations.

Also, for pressable LDGC, the densified shear zone radii were estimated as 1.51 ± 0.24 µm, 1.33 ± 0.06 µm, 1.29 ± 0.05 µm, and 1.28 ± 0.03 µm at 0.1 mN/s, 0.5 mN/s, 1 mN/s and 2

mN/s, respectively, as shown in Fig. 3.49. Therefore, the largest densified shear zones were predicted at the lowest loading rate for LMGC, sintered and pressable LDGC in Figs. 3.47–3.49 respectively. This rationalized why the largest maximum, final and contact depths occurred at the lowest loading rate for LMGC, sintered and pressable LDGC in Figs. 3.13–3.15 respectively. Further, these predicted largest densified shear zones at the lowest loading rate might be attributed to the discontinuities formed during the unloading processes of LMGC, sintered and pressable LDGC as shown in Figs. 3.8(a), 3.9(a) and 3.10(a) respectively. These discontinuities might be formed by tensile residual stresses which resulted from the mismatch between the plastic zone and the surrounding elastic matrix (Gong et al., 2004). Alao and Yin (2014b) have attributed these discontinuities to the action of tensile residual stresses. Thus, the induced residual stresses might have generated additional shear bands which increased the densified shear zone at the lowest loading rate for these materials.

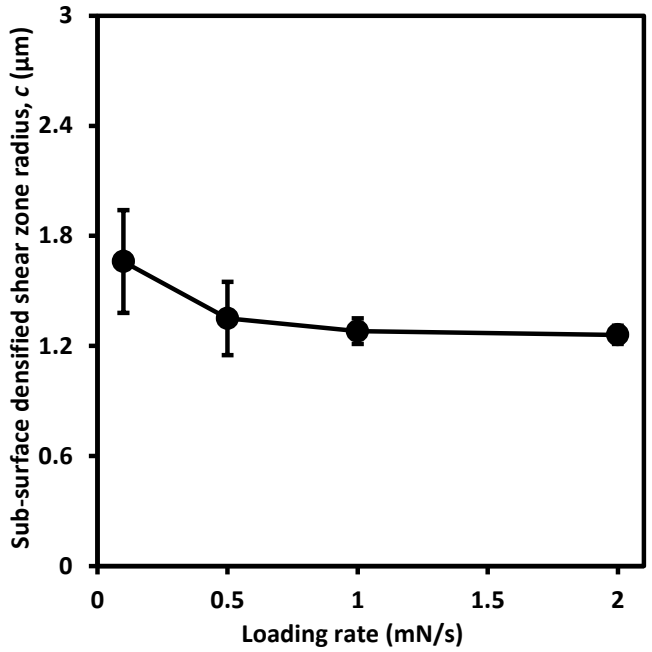


Fig. 3.48. Sub-surface densified shear zone radius (c) versus loading rate for sintered LDGC. Each data point is the mean value for six repeated indentations; each error bar corresponds to ± one standard deviation for the six repeated indentations.

It should be noted that with the current *in situ* scanning probe microscopy assisted nanoindentation techniques, it is unlikely to recognize the glass and crystal phases. It can be used for imaging and measuring surface topography on a fine scale, down to the level of molecules and groups of atoms. It does not contain the phase contract microscopy. Atomic force microscopy with phase detection microscopy or phase detection atomic force microscopy can be

used to detect phases but it is not yet integrated with the current nanoindentation systems. Thus, the indentations made using the *in situ* scanning probe microscopy assisted nanoindentation technique could indent either lithium metasilicate or glassy in the case of LMGC or lithium disilicate or glassy phases in the case of sintered or pressable LDGC. Thus, it is impossible to discern the specific phase at which the indenter penetrated from the polished LMGC (Fig. 3.1), sintered LDGC (Fig. 3.2(b)) and pressable LDGC (Fig. 3.3). A number of authors have proposed grid and statistical indentation methods to characterize mechanical properties for a phase in composites containing multiple phases (Constantinides et al., 2006; Ulm et al., 2007). These techniques can be applied to structural composite materials in which individual phases are easily recognized. The identification of the distinct behavior of the individual phases in LMGC, sintered and pressable LDGC is challenging and needs to be investigated in the future.

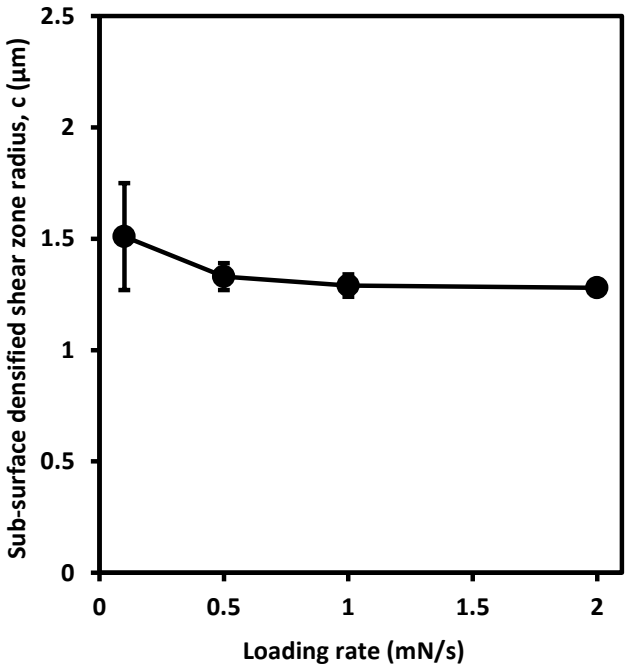


Fig. 3.49. Sub-surface densified shear zone radius (c) versus loading rate for pressable LDGC. Each data point is the mean value for six repeated indentations; each error bar corresponds to ± one standard deviation for the six repeated indentations.

### *3.5.2 Pre-Sintered Y-TZP*

This study has demonstrated the nano-scale mechanical behavior of pre-sintered Y-TZP during sharp indentation. Unlike fully dense ceramics, pre-sintered Y-TZP is highly porous, providing a challenge to surface and materials characterization by nanoindentation.

Measured properties extracted from nanoindentation tests can be influenced by surface roughness (Chung and Yap 2005; Lawn and Cook, 2012; Miller et al. 2008), instrument calibration, thermal drifts, pile-ups and tip rounding (Lawn and Cook, 2012). Thus, it is important to analyze the influence of these factors in this study. There are several established surface roughness criteria capable of minimizing the influence of surface roughness on extracted indentation properties at the micro scale (Chung and Yap, 2005) or for cement paste at the nano scale (Miller et al. 2008). None of these criteria can be directly applied to porous ceramics. However, it has been found that at very shallow indentation depth (typically < 100 nm), nanoindentation hardness data can deviate significantly (Kim et al., 2007b). In this investigation, the average maximum penetration depths for all load-displacement curves in Fig. 3.11 ranged between 620–720 nm, six to seven times deeper than 100 nm. Additionally, during nanoindentation of porous bone materials, it was found that the roughness effects may be small at the contact-depth-to-$R_q$ roughness ratio ($h_c/R_q$) greater or equal to the range of 2.8–4.3 (Donnelly et al., 2006). In this study, the mean contact depths at any loading rate ranged 483–675 nm (Fig. 3.16) and the surface roughness, $R_q$, of the scanned area was 72.3 nm. The contact-depth-to-$R_q$ roughness ratios ($h_c/R_q$) are 6.7–9.3. Therefore, surface roughness did only minimally affect the nanoindentation measurement in this study.

Prior to indenting pre-sintered Y-TZP, series of indents were performed on standard fused silica for load-frame compliance and tip area calibrations. The machine compliance was very small and the area function followed Eq. (3.3). Thermal drift correction was enabled on the nanoindenter and the maximum drift rate was 0.05 nm/s. The maximum drifts for the loading-unloading sequences corresponded to 5 nm, 1 nm, 0.5 nm and 0.25 nm for 0.1 mN/s, 0.5 mN/s, 1 mN/s and 2 mN/s load rates, respectively. These drifts were several orders of magnitudes less than maximum, contact and final depths recorded in Fig. 3.16. Consequently, thermal drifts did not affect the measurement of mechanical properties in nanoindentation. Further, no significant pile-ups were observed in the scanned indentation imprints shown in Figs. 3.39 and 3.40. This indicates that the Oliver–Pharr method can be applied to deconvolute the mechanical properties for this material. In addition, significant tip rounding was not witnessed because indentation area functions followed the first five terms of Eq. (3.3) during the experiments.

This study found that largest maximum penetration, contact and final depths occurred at the lowest loading rate (Fig. 3.16). This indicates that the indented material was more compacted at the low loading rate. This was also supported by the increased contact stiffness (Fig. 3.21) and Young's modulus (Fig. 3.31) at the low loading rate. However, the contact hardness at the low loading rate (Fig. 3.26) did not increase due to enhanced compact contact areas underneath the

diamond indenter. This loading rate-independent hardness is consistent with the observations by Quinn et al. (2002a) where loading rates did not significantly influence micro-indentation hardness values of steel, fully sintered SiC and AlON. To deconvolute the mechanical properties for porous ceramics, Nakamura et al. (2000) suggested the measurement of average values indented at various locations. The loading rate-independent average contact hardness was $H_c$ = 1.11 ± 0.34 GPa from 24 indentations at all loading rates for the pre-sintered Y-TZP. For the Young's modulus, the load-independent average value with a standard deviation is $E$ = 29.32 ± 4.93 GPa from 18 indentations, excluding indentations at 0.1 mN/s. This value is consistent with the Young's modulus extracted for porous Y-TZP having the same relative density of 0.54 (Deng et al., 2002b) as the studied pre-sintered Y-TZP using the pulse-echo method indicating the correctness of the indentation method.

Another significant indentation distinction induced by the loading rate is the remarkable increase in pop-in events on the force-displacement curves at the lower loading rates shown in Fig. 3.11. These discontinuities reflect different discrete physical events beneath the indenter tip.

During the loading processes, the mechanisms for the pop-in events in indenting porous materials such as pre-sintered Y-TZP can be very complex. These discontinuities can be associated with several mechanisms such as fracture, compaction or kink bands. The scanning probe images of nanoindentation impressions shown in Figs. 3.39 and 3.40 confirm no radial cracks in the tensile regions around the indent corners. This indicates that the pop-in events witnessed for this material were not due to fracture.

Frequent pop-in events at the lowest loading rate of 0.1 mN/s is related to the development of localized compaction. This observation can also be supported by the scanning probe indentation imprint image shown in Fig. 3.40(a) revealing frequent collapses as the indenter penetrated slowly. This discontinuity associated with sudden compaction was also observed in indenting highly porous inorganic solids such as plaster (Clément et al. 2013). The prolonged compressive stresses beneath the indenter tips at low loading rates may have resulted in such an occurrence of localized compaction.

Kinking is also responsible for the pop-in events for this material, as observed in the indentation imprint at 1 mN/s loading rate in Fig. 3.41. Kinking is a form of plastic buckling. It is different from slipping or twinning in that it requires the generation of a succession of, more or less, regularly spaced dislocation pairs on many parallel slip planes (Barsoum et al., 2003;

Fraczkiewicz et al., 2006; Sun et al., 2005). Once kinks initiate, it is conceived that they grow athermally until they meet grain boundaries or a free surface (open pores). Regular kink bands are formed at higher deformation stresses because their production and annihilation are believed to be irreversible (Barsoum et al., 2003; Fraczkiewicz et al., 2006; Sun et al., 2005). Further, Luo and Stevens (1999) observed that in the instrumented indentations of dense Y-TZP, the indentation is generated by the elastic-plastic deformation. But for pre-sintered Y-TZP, an additional contribution to the deformation is the porosity filling generated by the high indentation stress beneath the indenter. This additional contribution to the deformation might have promoted the formation of kink bands. Consequently, kinking might be facilitated by the presence of pores in pre-sintered materials underneath the sharp indenter (Sun et al., 2005). The presence of pores might also have caused micro-collapse underneath the indenter resulting in the sudden change of stress-strain behavior of the material (Lu et al., 2006).

During unloading processes, the pop-in events at the lower loading rates (Fig. 3.11(a)) were absent at the higher loading rates (Fig. 3.11(b)–(d)). The reason for the pop-ins may be attributed to the residual stresses generated on the surface during elastic recovery. Residual stresses occur due to the mismatch between the plastic zone beneath the indenter and the surrounding elastic matrix (Gong et al., 2004). During the elastic recovery, residual stresses might have induced additional virtual loads different from the maximum indented load as the indenter was removed from the indented surface. These virtual loads, either tensile or compressive, may have modified the elastic deformation by introducing their own displacements in series with the displacement from the maximum load. As the indenter penetrated the surface slowly, there was sufficient time for the formation of these virtual loads. Consequently, the unloading pop-ins at the lowest loading rate (Fig. 3.11(a)) were due to the action of residual stress producing displacement bursts. At higher loading rates, indentation-induced residual stresses might also occur but their formations were subtle due to the fast unloading rates. The increase in Young's moduli at 0.1 mN/s loading rate (Fig. 3.31) suggests the virtual loads were tensile which superimposed with the maximum load (10 mN) for the material densification and compaction. The absence of pop-in events on the unloading curves at higher loading rates suggests that the influence of residual stresses on Young's moduli at higher loading rates was minimal.

### *3.5.3 Sintered Y-TZP*

This work also demonstrates for the first time that the loading rate has a significant influence on the mechanical behavior of sintered Y-TZP in nanoindentation.

The lowest loading rate resulted in the largest maximum penetration and contact depths (Fig. 3.17). This indicates that contact areas between the indenter and the material were most enhanced at this loading rate. Increasing the loading rate, contact areas reduced, corresponding to the reduction in contact depths (Fig. 3.17). Thus, the decrease in contact area with the increase in loading rate led to higher contact hardness (Fig. 3.27). This loading rate-dependent contact hardness of sintered Y-TZP at the submicron scale has enhanced our understanding of the similar behavior of silicon carbide, zirconia and alumina at the micro scale (Anton and Subhash, 2000; Bhattacharya et al., 2012; Klecka and Subhash, 2010).

However, the measured contact hardness (Fig. 3.27) and Young's moduli (Fig. 3.32) can be overestimated when pile-up is significant. This is because the Oliver-Pharr method does not account for the pile-up phenomenon around the contact boundary which often leads to underestimating the true contact area (Bolshalov and Pharr, 1998). Evidence of the occurrence of pile-up events is manifest in Fig. 3.42(a)–(c) and Fig. 3.43(a)–(c). Therefore, it is important to determine the accuracy of the measured properties with the Oliver-Pharr method. The conditions nullifying the Oliver-Pharr method for indentations with significant pileups are that the $h_f/h_{max}$ ratios must be greater than 0.7 (Bolshalov and Pharr, 1998). The calculated means and standard deviations of $h_f/h_{max}$ ratios at 0.1 mN/s, 0.5 mN/s, 1 mN/s and 2 mN/s loading rates in Fig. 3.12 are 0.45 ± 0.28, 0.63 ± 0.10, 0.63 ± 0.08, and 0.6 ± 0.03, respectively, which are smaller than the threshold of 0.7. Therefore, it is confident that the pileups in the nanoindentation patterns studied (Figs. 3.42 and 3.43) were not a significant factor.

In this study, strain hardening may have occurred, which can be measured by the material's sensitivity to strain hardening using a strain rate sensitivity model as discussed in Section 3.5.1.

Fig. 3.50 reveals $Log(H_c)$ versus $Log(\dot{\varepsilon})$ in which the corresponding linear equation with a coefficient of determination, $R^2$, of 97% is expressed as:

$$Log(H_c) = 0.113\,Log\left(\dot{\varepsilon}\right) + 1.1189 \tag{3.18}$$

where $n$ = 0.113 and $Log(H_o)$ = 1.1189. This indicates that sintered Y-TZP was sensitive to strain hardening at a moderate level. Thus, when $h_f/h_{max} < 0.7$, or materials that moderately work harden, the Oliver-Pharr method gives acceptable results of the contact hardness and Young's moduli in this study (Bolshalov and Pharr, 1998).

In addition, the pileup absence in Fig. 3.43(d) cannot be attributed to the sinking-in effect. The sinking-in phenomenon can predominate in materials with strain rate sensitivity greater than 0.2

(Alcalá et al., 2000). Given that $n$ was less than 0.2 for the sintered Y-TZP, it was unlikely for the sinking-in effect to occur at 2 mN/s loading rate. As this material was moderately sensitive to strain hardening, its intrinsic contact hardness free from strain rate sensitivity, $H_o$, is determined to be 13.15 GPa from Eq. (3.18). This value is consistent with micro-hardness values (13–15 GPa) for zirconia ceramics (Alcalá, 2000; Santos et al., 2009; Ritzberger et al., 2010). This indicates that the strain rate sensitivity model is valid to determine the material intrinsic contact hardness as well as the surface contact hardness at any loading rates.

The loading-rate dependent contact hardness in sintered Y-TZP (Fig. 3.27) may also be attributed to pressure hardening, which can be measured by the material's pressure-hardening sensitivity using a pressure-sensitive idealized yield criterion model (Chen, 1986). This ideal elastic-plastic yield criterion is given as (Chen, 1986):

$$\sigma_Y = \alpha P + \sigma_o \tag{3.19}$$

where $\sigma_o$ is the compressive yield stress at zero pressure, $\alpha$ is the pressure hardening coefficient, $P$ is the confining internal pressure and $\sigma_Y$ is the compressive yield stress due to internal pressures.

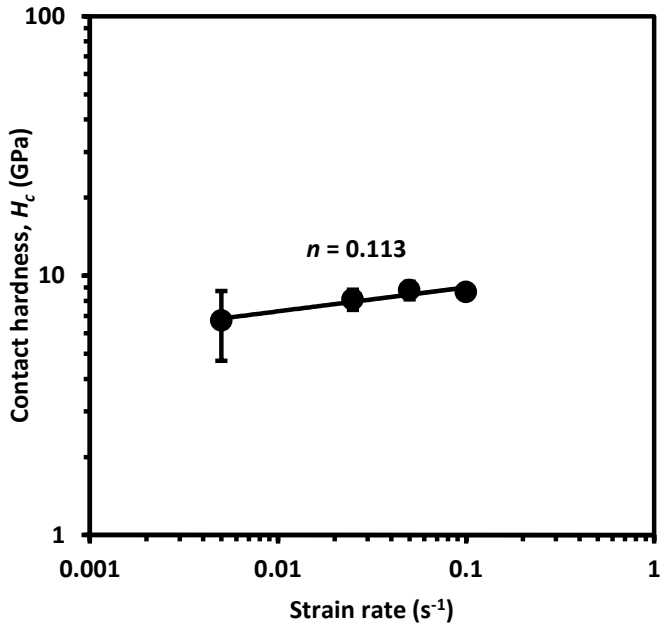


Fig. 3.50. Contact hardness ($H_c$) versus strain rate ($\dot{\varepsilon}$) for sintered Y-TZP. Each data point is the mean value for six repeated indentations; each error bar corresponds to ± one standard deviation for the six repeated indentations. The linear graph is described by the Eq. (3.18) and the slope of the graph gives the strain-rate sensitivity, $n$ = 0.113.

The higher the value of $\alpha$, the greater the material is sensitive to pressure hardening. For materials of an ideal elastic-plastic yielding behavior like sintered Y-TZP, a relationship between the contact hardness and the compressive yield stress has been established in Eq. (3.16), where $C$ approximately equal to 3 (Tabor, 1951). Thus, the means and standard deviations of compressive yield stresses at 0.1 mN/s, 0.5 mN/s, 1 mN/s and 2 mN/s loading rates are estimated to be 2.54 ± 0.99 GPa, 3.03 ± 0.39 GPa, 3.11 ± 0.34 GPa, and 3.32 ± 0.31 GPa, respectively. Fig. 3.51 demonstrates compressive yield stress versus loading rate, $\dot{P}$, in which a linear relation with a coefficient of determination, $R^2$, of 78% was established as

$$\sigma_y = 0.356\dot{P} + 2.68 \tag{3.20}$$

At the zero loading rate in Fig. 3.51, the zero pressure, $\sigma_o$, is estimated to be 2.68 GPa. For pressure-sensitive materials, the intrinsic contact hardness can also be estimated using the following equation (Chen, 1986):

$$H_o = (3+2\alpha)\sigma_o \tag{3.21}$$

where $H_o$ = 13.15 GPa and $\sigma_o$ = 2.68 GPa. Upon substituting these values, the coefficient of pressure hardening, $\alpha$, is 0.953. A comparison between $\alpha$ and $n$ shows that α is about 8.5 times higher than $n$. This indicates that the sintered Y-TZP was more sensitive to pressure hardening than strain hardening. Further, by replacing, $H_c$ in Eq. (3.16) with $H_o$ = 13.15 GPa, the loading rate-independent or intrinsic compressive yield stress, $\sigma_Y$, is 4.38 GPa. This value agrees with the yield strength (4.36 ± 0.13 GPa) determined for sintered Y-TZP by Zeng and Chiu (2001) using a different method. This reconfirms the validation of our applied method and authenticates its results. Substituting, the values of $\sigma_Y$ = 4.38 GPa, $\sigma_o$ = 2.68 GPa, and $\alpha$ = 0.953 in Eq. (3.21), the confining pressure, $P$, is 1.79 GPa.

Unlike the contact hardness, the Young's modulus of sintered Y-TZP (Fig. 3.32) was independent of the loading rate. The reason for this is that the Young's modulus is dependent on both the contact stiffness and the contact area (Eq. 3.6). Even though the contact area decreased with the loading rate (Fig. 3.17), this effect did not affect the Young's modulus because the contact stiffness depends, in a complex manner, on the maximum and final depths and the unloading exponent. As shown in Fig. 3.17, the final depth had a complex relationship with the loading rate and this also influenced the contact stiffness in Fig. 3.22. In addition, Fig. 3.42 has shown that the indentation patterns at all loading rates deformed plastically and did not fracture. The material stiffness was unchanged because plastic deformation involves extremely small defects (Oyen and Cook, 2009). This loading rate-independent Young's modulus buttressed the point that sinking-in process did not occur at the highest loading rate (Fig. 3.43(d)) because the material would have become stiffer at 2 mN/s loading rates if sinking-in had occurred (Alcalá et

al., 2000). Therefore, the mean and standard deviation of the measured Young's modulus at all loading rates from 24 indentations was 168.19 ± 31.20 GPa. This value is consistent with the Young's modulus extracted for sintered Y-TZP by Alcalá (2000) with Vickers indenter under varying applied loads.

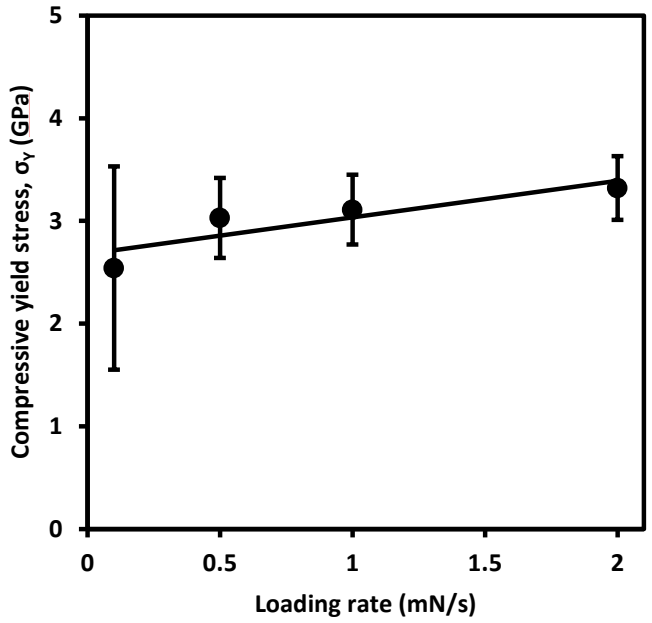


Fig. 3.51. Compressive yield stress ($\sigma_y$) versus loading rate. Each data point is the mean value for the six repeated indentations; each error bar corresponds to ± one standard deviation for the six repeated indentations. The linear graph is described by the Eq. (3.20) and the intercept on the y-axis gives the zero loading rate compressive yield stress, $\sigma_o$ = 2.68 GPa.

Another remarkable indentation distinction observed by changing the loading rate is the dependence of the pop-in formation on the loading rate (Fig. 3.12). These pop-ins were most markedly manifested in the loading-unloading curves at the lowest loading rate. With increase in loading rate, their number decreased and was almost imperceptible at the highest loading rate. The mechanisms of the pop-ins may be associated with fracture, phase transformation, shear bands or dislocation networks (Schuh, 2006). These pop-ins are not due to fracture because there were no radial cracks in the tensile regions around the indent corners in Figs. 3.42 and 3.43.

Further, the $t \rightarrow m$ phase transformation may not responsible for the pop-ins since a critical contact pressure (13.3 GPa) is required to transform $t \rightarrow m$ in polycrystalline Y-TZP with a Berkovich indenter (Gaillard et al., 2009). The contact hardness at any loading rate in Fig. 3.27 is lower than this critical contact pressure for the occurrence of the martensitic $t \rightarrow m$

transformation. If the $t \rightarrow m$ phase transformation might have occurred, the contact pressure would have decreased rather than increased with the loading rate because the $t \rightarrow m$ phase transformation is associated with a volume increase (Catledge et al., 2003; Cattani-Lorente et al., 2011). The densities of tetragonal Y-TZP and monoclinic Y-TZP are 6.09 g/cm$^3$ and 5.68 g/cm$^3$, respectively. The increase in volume could lower the atomic density, resulting in a decrease in contact hardness (Catledge et al., 2003; Cattani-Lorente et al., 2011).

In addition, shear bands cannot be responsible for the pop-ins because shear bands occur in amorphous materials where no dislocations or strain hardening occurs (Schuh 2006). In this study, the sintered Y-TZP is polycrystalline containing grain boundaries and impurities where dislocation motion and interaction can prevail. Also, strain-hardening occurred as evident in Fig. 3.50. Therefore, the observed pop-ins in Fig. 3.12 is due to dislocation nucleation and interactions.

The surface relief in Fig. 3.42 was due to the motion of dislocations (slip lines) or ductile streaks associated with the polishing process prior to nanoindentation. These dislocation networks were also responsible for plastic deformation in the form of material piling up around the indenter's contact boundaries (Figs. 3.42 and 3.43). Dislocation gliding (slip lines) was not observed using scanning probe imaging in this study. However, a similar observation was reported by Gaillard et al. (2009) who used a Berkovich indenter to indent a polycrystalline Y-TZP. They observed dislocation gliding on this material when a cube corner indenter was used to induce larger stresses which favored dislocation motions on respective glide systems of the material. This shows that dislocations were confined around the pileup areas. Each observed pop-in in Fig. 3.12, therefore, represents the activation of a dislocation network.

When a pressure-sensitive material is indented at a low loading rate, a higher internal pressure is required to sustain the impression due to the pressure hardening near the impression (Chen, 1986). In this case, elastic-plastic indentation boundaries were further pushed outward, resulting in material pileups. This process could also lead to surface strain softening of the material, yielding lower contact hardness. As the loading rate was raised, the induced compressive stress increased deforming larger material volume and broadening the plastic zone size (Fig. 3.43(d)). This rationalizes why surface deformation displacements in Fig. 3.43 decreased with the loading rate. Consequently, pressure hardening raised the compressive yield stress (Fig. 3.51) and the contact hardness (Fig. 3.27) as the loading rate increased.

### *3.5.4 Technical Implications of the Studied Mechanical Behavior*

The rate-dependent mechanical behavior of LMGC, sintered and pressable LDGC, pre-sintered and sintered Y-TZP in nanoindentation provides scientific implications for their abrasive machining processes using sharp diamond abrasives. In general, the machining conditions applied in these processes, such as depths of cut, feed rates and machining speeds are dynamically different from nanoindentation environments. For ceramic machining using conventional CNC machines and diamond abrasive tools, machining conditions are ranged with feed rates of approximately 500–20,000 mm/min, depths of cut of approximately 10–50 μm, and milling/grinding speeds of approximately 40–60 m/s (Luthardt et al., 2004; Yin and Huang, 2004). However, indentation models are generally used to simulate abrasive machining (Komanduri et al., 1997). This is because similar deformation and fracture occur in both ceramic machining and indentation processes (Xu et al., 1996; Yin et al., 2004). In fact, in a load-control mode, the indentation load simulates to the machining normal force, the loading/unloading rate simulates to the machining cutting speed and the indenter shape simulates to the cutting tool geometry (Yan et al., 2006). In a depth-control mode, the displacement simulates to the machining depth of cut or undeformed chip thickness and in indentation scratching; the sliding force simulates to the machining cutting force (Yan et al., 2006). Further, indentation absorbed energy was used to simulate the specific cutting energy in abrasive machining (Xu et al., 1996).

In sharp abrasive machining, the cutting edges are geometrically undefined and the material removal is distributed over as many cutting edges as possible. Consequently, many abrasives are involved in the cutting process and the normal force impacted per grit can be very low. Normal machining load per grit can be likened to the peak load in nanoindentation. In this study, the peak load of 10 mN is definitely below the threshold for inducing median/radial cracks. This is evidenced in Figs. 3.33 and 3.34 (LMGC), Figs. 3.35 and 3.36 (sintered LDGC), Figs. 3.37 and 3.38 (pressable LDGC), Figs. 3.39 and 3.40 (pre-sintered Y-TZP) and Figs. 3.42 and 3.43 (sintered Y-TZP) in which permanent impressions were formed. Consequently, if machining is performed on these materials in the plastic region, ductile regime machining can be realized. The specific responses of these materials in abrasive machining processes are addressed as follows.

The inhomogeneous shear band-induced piling-ups at low loading rates in Figs. 3.34(a), 3.36(a) and 3.38(a) for LMGC, sintered and pressable LDGC respectively, indicate that plastically deformed material volumes would flow on the machined surfaces at low cutting speeds. This

flow would lead to increased surface roughness on their machined surfaces since the induced pileup flow from one abrasive can be ground by the next abrasive. Further, an improved strength was reported near the surface area of LMGC at the near-surface area due to the compressive and isotropic micro-residual stresses (Pinto et al., 2007). This improved strength may be compromised if machining is performed at low cutting speeds due to the formation of discontinuities in the unloading processes (Fig. 3.8(a)) which were ascribed to tensile residual stresses (Alao and Yin, 2014b). Crack initiations could also occur by extensions of the subsurface shear bands into the underlying tensile matrix or from the stress concentration sites at the intersections of shear bands (Lawn and Cook, 2012). Therefore, the largest shear zone at the lowest loading rates in Figs. 3.47–3.49 of LMGC, sintered and pressable LDGC respectively can be prone to cracking under tensile residual stresses.

Machining at high deformation rates may lead to the generation of continuous chips due to the accumulation of multiple shear bands which led to strain hardening of LMGC, sintered and pressed LDGC as shown in Figs. 3.8(d), 3.9(d) and 3.10(d) respectively. Strain hardening may be beneficial to biological materials because they can undergo large deformation before failure (Chintapalli et al., 2014a). This indicates that successive deformations can be accommodated by strain hardening in the ductile mode region prior to the occurrence of fracture but their machined surfaces would become hardened. To obtain smooth surfaces, a polishing process may be required. Further, the strain hardening process led to the reduction in plasticity as shown in the reduction of contact depths of LMGC, sintered and pressed LDGC in Figs. 3.13–3.15 respectively. Also, sinking-in effect may occur at high deformation rate in LMGC with a consequence of the increased material's elasticity. Therefore, to avoid the generation of inhomogeneous shear bands at low deformation rates and strain hardening and sinking-in effects at high deformation rates, it is suggested that LMGC should be machined at a moderate deformation rate. In addition, machining at moderate deformation rates is also suggested to be applied to sintered and pressable LDGC to avoid inhomogeneous shear bands at low deformation rates and hardening effects at high deformation rates.

Based on the pre-sintered Y-TZP results, at low loading rates in nanoindentation, it is anticipated that abrasive machining at low speeds, compaction/densification might prevail. However, the extensive discontinuities on the unloading curves (Fig. 3.11) caused by the tensile residual stresses in nanoindentation may predict that there might be tensile residual stresses developed during slow abrasive cutting. It is these residual stresses that cause lateral cracks during indentation elastic recovery or as the cutting tool moves forward during abrasive machining that lead to material removal by brittle fracture (Komanduri et al., 1997). If the

residual tensile stress is larger than the intrinsic theoretical strength of pre-sintered Y-TZP before plastic deformation takes place, brittle fracture occurs (Shimada and Ikawa, 1995). Furthermore, material strength can be degraded by extending the stress-induced median/radial cracks (Malkin and Hwang, 1996). To avoid the formation of heterogeneous compaction bands which could induce tensile residual stresses, application of a high deformation rate to pre-sintered Y-TZP is suggested. In rapid abrasive machining processes porosity filling, which leads to material kinking (Figs. 3.40(d) and 3.41) is expected to dominate. In addition, high deformation rates may induce high hydrostatic pressure sufficient to facilitate ductile regime machining for the pre-sintered Y-TZP. However, the feasibility of ductile machining of pre-sintered Y-TZP needs to be further investigated.

Similar to LMGC, sintered and pressable LDGC, material pileups were also formed around the indenter at low loading rates for sintered Y-TZP as shown in Figs. 3.42 and 3.43. This means that plastically deformed material would also flow on the machined surface during slow abrasive machining. Since the cutting force performs a secondary role of extruding chips from a plastic zone that has been fully developed by the normal force (Shaw, 1995), it is easier to extrude large volume of material from the deformed material at low cutting speed (Shaw, 1995). Discrete slip events in Fig. 3.12(a) also indicate that serrated or discontinuous chips may occur while machining at low speeds. Further, a discontinuous chip from one abrasive can be ground by the next abrasive, increasing the surface roughness. Therefore, slow deformation rates may favor rough machining for sintered Y-TZP. Continuous chips may be removed when machining sintered Y-TZP at a high cutting speed due to the suppression of serrated flow (Fig. 3.12(d). Therefore, this study predicts that high deformation rates may favor small- or submicron-scale material removal processes like ductile machining, fine finishing and polishing for sintered Y-TZP. This assertion may contribute to the realization of ductile machining of Y-TZP at high cutting speeds (Yin and Huang, 2004; Yin et al., 2003).

## 3.6 Conclusions

This work studied the nanoindentation behavior of LMGC, sintered and pressable LDGC, pre-sintered and sintered Y-TZP at different loading rates. The contact hardness values of LMGC, sintered and pressable LDGC increased with the loading rate and their intrinsic contact hardness values based on the strain rate sensitivity model were 18.9 GPa, 14.58 GPa, and 12 GPa respectively. However, the contact hardness of pre-sintered Y-TZP was insignificantly affected by the loading rate with 1.11 GPa ± 0.35 GPa. Further, the contact hardness of sintered Y-TZP was loading rate dependent while its intrinsic hardness based on the strain rate model was 13.15

GPa which was in the range of the published micro-hardness values. Consequently, LMGC revealed the highest intrinsic contact hardness; pre-sintered Y-TZP showed the lowest intrinsic contact hardness while sintered and pressable LDGC and sintered Y-TZP revealed intermediate intrinsic contact hardness values.

The Young's modulus of LMGC revealed loading rate-independent with the value of 97.48 ± 17.24 GPa. However, the Young's moduli of sintered and pressable LDGC and pre-sintered Y-TZP were not single-valued at low loading rates; their loading rate-independent moduli at high loading rates were 113.28 ± 12.56 GPa, 113.33 ± 16.11 GPa, 29.32 ± 4.93 GPa respectively. Further, sintered Y-TZP revealed a significant loading-rate independent Young's modulus of 168.19 ± 31.20 GPa. Therefore, sintered Y-TZP revealed the highest Young's modulus; pre-sintered Y-TZP revealed the lowest modulus while LMGC, sintered and pressable LDGC showed the intermediate moduli.

Discrete discontinuities observed on the force-displacement curves of LMGC, sintered and pressable LDGC at low loading rates were attributed to densification and inhomogeneous shear band-induced pile-ups. The continuous deformation at high loading rates on the force-displacement curves was ascribed to densification and homogeneous shear bands which caused strain hardening effect in the three materials and sinking-in effect in LMGC. In addition, plastic deformation occurred at the tested peak load and all loading rates. The mechanical behavior of the material studied in nanoindentation might reflect material removal mechanisms in small-scale abrasive machining using sharp diamond abrasives. It is suggested that that these materials should be machined at moderate deformation rates to avoid the generation of inhomogeneous shear bands at low deformation rates, and strain hardening at high deformation rates. Also, the sinking-in effect of LMGC which might enhance its elasticity would be avoided if it were machined at moderate deformation rates.

The complex discontinuities on the force-displacement curves of pre-sintered Y-TZP at low loading rates were attributed to indentation-induced microstructural compaction, kink band formation and residual tensile stresses. Pore-filling contributed to the discontinuities observed on the force-displacement curves at high loading rates. The results also indicate that indentations occurred in the plastic region at 10 mN peak load at all loading rates applied. The mechanical properties and behavior of pre-sintered Y-TZP in nanoindentation might reflect material removal mechanisms in small volume abrasive machining using diamond abrasives. To avoid the formation of heterogeneous compaction bands which could induce tensile residual

stresses on pre-sintered Y-TZP, we suggest that a high loading rate should be applied on this material.

Finally, the serrated pop-ins on the force-displacement curves of sintered Y-TZP at low loading rates were attributed to inhomogeneous dislocation networks and indentation-induced microstructural pileups. The suppression of the pop-ins at high loading rates on the force-displacement curves was ascribed to moderate strain and pressure hardening. The results also indicated the plastic feature of sintered Y-TZP at the tested peak load and all loading rates. The mechanical behavior of sintered Y-TZP in nanoindentation might also reflect material removal mechanisms in small volume abrasive machining using diamond abrasives. Therefore, it is suggested that high deformation rates may favor small-scale material removal processes while low deformation rates may produce rough surfaces due to increased pileups.

# Chapter 4

# Advanced Analysis of Mechanical Behavior of LMGC, Sintered and Pressable LDGC, Pre-Sintered and Sintered Y-TZP

## 4.1 Introduction

Instrumented indentation is often used to characterize contact hardness, $H_c$, and plane strain modulus, $E'$, for materials (Ebenstein and Pruitt, 2006; Oliver and Pharr, 1992). The contact hardness is a hybrid parameter encompassing both elastic and plastic behavior of materials (Lawn and Howes, 1981; Sakai, 1999; Sakai and Nakano, 2002; Sakai et al., 1999). The resistance to plasticity, $H_T$, which can be obtained using the Sakai model (Sakai, 1999), measures the material plasticity associated with machinability, strength, wear, fatigue and erosion resistance characteristics (Baik et al., 1995; Quinn et al., 2002b; Yin, 2012; Yin and Huang, 2008; Yin et al., 2003). In particular, the occurrence of plastic deformation can facilitate ductile material removal to minimize machining-induced cracks. Ductile machining is a nano- or micro-abrasive machining process in which material removal mechanism is through plastic deformation and not fractures if the scale of deformation is small.

The Sakai model assumes "springs in series" contributions for elastic and plastic deformations from a single indentation loading curve. It enables the resistance to plasticity to be deconvoluted from contact hardness and plane strain modulus. It was used to characterize resistances to plasticity for several metal and ceramic materials (Oyen, 2006; Sakai and Nakano, 2002; Wei and Lin, 2008) and hard tissues, such as bone (Ferguson, 2009; Oyen, 2006; Wei and Lin, 2008). Further, the model allows a single indentation response to be partitioned into elastic and plastic deformation components (Sakai, 1999). This partitioning provides insights into the dominating material deformation behavior: If the dominant deformation is elastic, the material is more prone to brittle fracture; if the dominant deformation is plastic, the material is more resistant to fracture. Thus, the quantitative distinction of the contributions from elastic and plastic deformations in nanoindentation can predict the material responses to machining and functional processes. The occurrence of an elastic deflection of a material during diamond abrasive machining plays a significant role in controlling the surface quality (Marinescu et al., 2004). Thus, understanding the elastic behavior of the material is helpful for predicting residual stresses induced during indenter withdrawal or traversing cutting tools. In fact, machining-induced residual tensile stresses, which are often locked on the material surface, can cause quality problems (Marinscu et al. 2014). Further, the occurrence of plastic deformation in

machining can also facilitate the material removal in the ductile region to minimise machining-induced micro-cracks. For LMGC, sintered and pressable LDGC, pre-sintered and sintered Y-TZP, little is known about their resistances to plasticity and the respective contributions of elasticity and plasticity to the total deformation during nanoindentation and how these contributions affect their machinability.

Indentation energies are useful parameters in analysing the mechanical behavior of materials (Attaf, 2004; Cheng and Cheng, 1998). The characteristic energy-absorbing or energy-releasing events occurring beneath an indenter are the total energy, $U_t$, the indentation absorbed energy, $U_r$, and the elastic strain energy, $U_e$ (Fig 4.1). The total energy, $U_t$, spent in indenting a material to the peak load is the total area under the loading $p$-$h$ curve, i.e., the area ABDA in Fig. 4.1. The elastic strain energy recovered, $U_e$, is the area of the unloading portion of the $p$-$h$ curve, (i.e., the area CBDC in Fig. 4.1), representing the work restored by the material and associated residual stresses caused by the indenter withdrawal. The indentation absorbed energy, $U_r$, , i.e., the area ABCA in Fig. 4.1, represents the energy dissipated during indentation due to plastic deformation, cracking and crushing processes. Thus, by normalizing $U_e$ and $U_r$ to $U_t$, the respective contribution of elastic strain energy and indentation absorbed energy to the material deformation can be determined. The normalized indentation elastic strain energy, $U_e/U_t$, was linked to the material's deformation recovery capability and the initial unloading stiffness (Jha et al., 2013). Also, the normalized indentation absorbed energy, $U_r/U_t$, was directly related to the contact hardness-to-Young's modulus ratio ($H_c/E$) of materials, providing an alternative method for measuring mechanical properties of materials (Cheng and Cheng, 1998). Further, the $U_r/U_t$ ratio was linked to the ductility index (Cheng and Cheng, 1998; Sakai, 1999), machinability (Xu et al., 1996) and wear resistance of materials (Frutos et al., 2012; Leyland and Mathews, 2000). For LMGC, sintered and pressable LDGC, pre-sintered and sintered Y-TZP, nanoindentation energies and associated properties have not been studied.

Another important issue for LMGC, sintered and pressable LDGC, pre-sintered and sintered Y-TZP is their resistances to machining-induced cracking, $M$. The resistance to machining-induced cracking can be simulated by nanoindentation techniques due to similar micro-fractures generated in both nanoindentation and machining (Sakai and Nowak, 1992; Xu et al., 1996). Sakai and Nowak (1992) reported the resistances to machining-induced cracking in nanoindentation for several ceramics using indentation techniques. However, those studies were conducted at constant loading rates which assumed equilibrium deformation conditions. In many engineering processes, such as grinding, lapping and polishing, loading rates vary; thus, their influences become important.

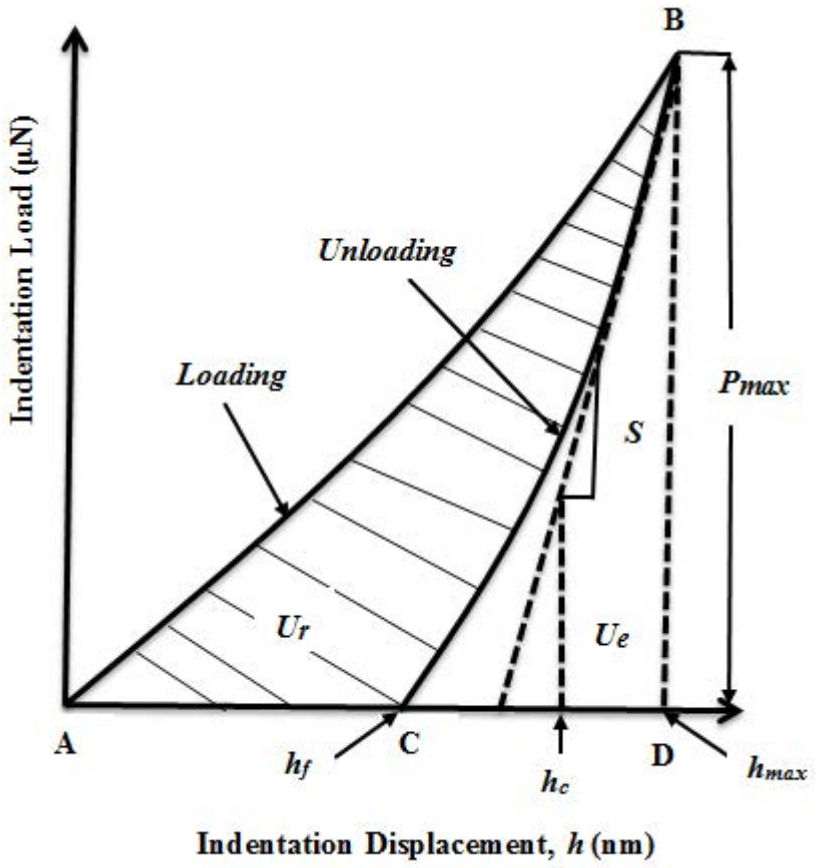


Fig. 4.1. Schematic illustration of an indentation load-displacement curve, in which $U_r$ is the indentation absorbed energy, $U_e$ is the elastic strain energy, $P_{max}$ is the peak load, $h_{max}$ is the maximum depth, $h_c$ is the contact depth, $h_f$ is the final depth, and $S$ is the initial unloading stiffness.

Therefore, this chapter examines loading rate-dependent resistances to plasticity, elastic/plastic displacements/deformation components, normalized elastic strain/indentation absorbed energies, and resistances to machining-induced cracking of LMGC, sintered and pressable LDGC, pre-sintered and sintered Y-TZP. The Sakai's series elastoplastic model (Sakai, 1999) was used to extract their resistances to plasticity from their plane strain moduli and contact hardness values reported in Chapter 3. Their elastic and plastic displacements were extracted from their plane strain moduli and resistances to plasticity respectively. Their resistances to machining-induced damage were calculated based on the Sakai–Nowak model (Sakai and Nowak, 1992) from their fracture energies and their normalized indentation absorbed energies. These properties were used to predict the machinability of these materials.

## 4.2 Mechanical Characterization in Nanoindentation

Nanoindentation tests described previously in Chapter 3 were conducted on LMGC, sintered and pressable LDGC, pre-sintered and sintered Y-TZP using a Hysitron Triboscope (Hysitron, USA). Briefly, a Berkovich diamond indenter of approximately 150 nm tip radius was used. Prior to the nanoindentation tests, the system was calibrated using a fused silica standard. Nanoindentation tests were conducted in a load-control mode at 10 mN peak load and 0.1 mN/s, 0.5 mN/s, 1 mN/s and 2 mN/s loading rates, corresponding to 100, 20, 10 and 5 seconds loading and unloading times, respectively (Fig. 3.7). During indentation, load-displacement curves were automatically recorded for advanced analysis of the mechanical behavior for these materials (Figs. 3.8–3.12). For the Berkovich indenter used, the indentation response for these materials may show either elastic-plastic or viscous-elastic-plastic deformation mode (Oyen and Cook, 2009). However, the viscous behavior could be eliminated through a rapid unloading rate or holding the material at a peak load (Olesiak et al., 2010). Hence, incorporating the peak-load-holding segment into our experiments would necessitate extracting the viscous or creep property (Concustell et al., 2005; Lucas and Oliver, 1999; Oyen and Cook, 2003) for these materials using models such as the Oyen-Cook's (Oyen and Cook, 2003). Therefore, no holding time at a peak load was used in this study (Fig. 3.7), making the analysis purely elastic-plastic.

### *4.2.1 Resistance to Plasticity*

The extraction of the resistance to plastic deformation, $H_T$, using the Sakai model (Sakai, 1999) in nanoindentation techniques has been well-detailed by Alao and Yin (2015b). Briefly, the total contact displacement, $h_t$, at the peak load, $P_{max}$, was assumed to result from elastic and plastic deformations. Consequently, this behavior was modelled as a sum of purely elastic and plastic components in series with the elastic, $h_e$, and plastic, $h_p$, displacements (Sakai, 1999):

$$h_t = h_e + h_p \tag{4.1}$$

For the purely elastic component, the constitutive load-displacement equation can be described as (Sakai, 1999):

$$P_e = \alpha_2 E' h_e^2 \tag{4.2}$$

where $P_e$ is the load in the elastic component, $\alpha_2$ is a geometric constant which is 4.4 for the Berkovich indenter applied in this study (Oyen, 2006), $E'$ is the plane strain modulus, which is expressed as (Oliver and Pharr, 1992):

$$E' = \frac{E}{1-\nu^2} = \left[\frac{1}{E_r} - \frac{\left(1-\nu_i^2\right)}{E_i}\right]^{-1} \tag{4.3}$$

In Eq. (4.3), $E$ and $\nu$ are the Young's modulus and Poisson's ratio of the material and $E_i$ and $\nu_i$ are the Young's modulus and Poisson's ratio of the indenter. For a Berkovich diamond indenter, $\nu_i$ = 0.07 and $E_i$ = 1141 GPa (Oliver and Pharr, 1992). Similarly, the constitutive load-displacement equation for the plastic element can be expressed as (Sakai, 1999):

$$P_p = \alpha_1 H_T h_p^2 \tag{4.4}$$

where $P_p$ is the load in the plastic component, $\alpha_1$ is a non-dimensional constant dependent on the geometry of the indenter, which is 24.5 for the Berkovich indenter (Sakai, 1999), and $H_T$ is the resistance to plasticity. At the peak load, both elastic load and plastic load are equal to the peak load (i.e., $P_e = P_p = P_{max}$). Substituting $h_e$ from Eq. (4.2) and $h_p$ from Eq. (4.4) in Eq. (4.1), then Eq. (4.1) becomes (Sakai, 1999; Oyen, 2006):

$$h_t = \frac{P_{\max}^{1/2}}{\left(\alpha_2 E'\right)^{1/2}} + \frac{P_{\max}^{1/2}}{\left(\alpha_1 H_T\right)^{1/2}} \tag{4.5}$$

The hybrid contact hardness, $H_c$, in nanoindentation tests is expressed as (Oliver and Pharr, 1992):

$$H_c = \frac{P_{\max}}{\alpha_1 (h_c)^2} \tag{4.6}$$

where $h_c$ is the contact depth. Replacing $h_c$ in Eq. (4.6) with $h_t$ in Eq. (4.5), the hybrid contact hardness, $H_c$, becomes (Sakai, 1999; Oyen, 2006):

$$H_c = \frac{1}{\alpha_1 \left( \left(\alpha_2 E'\right)^{\frac{-1}{2}} + \left(\alpha_1 H_T\right)^{\frac{-1}{2}} \right)^2} \tag{4.7}$$

From Eq. (4.7), the resistance to plastic deformation, $H_T$, can then be expressed as thus:

$$H_T = \frac{H_c \alpha_2 E'}{\left[ \left(\alpha_2 E'\right)^{\frac{1}{2}} - \left(\alpha_1 H_c\right)^{\frac{1}{2}} \right]^2} \tag{4.8}$$

At each loading rate, the resistance to plasticity, $H_T$, of LMGC, sintered and pressable LDGC, pre-sintered and sintered Y-TZP was calculated using Eq. (4.8) with their previously reported values of contact hardness and plane strain modulus in Chapter 3.

### *4.2.2 Elastic and Plastic Displacements*

The respective elastic displacement, $h_e$, and plastic displacement, $h_p$, can be obtained as follows from Eqs. (4.2) and (4.4) by using $P_e = P_p = P_{max}$:

$$h_e = \left( P_{\max} \Big/ \alpha_2 E' \right)^{1/2} \tag{4.9}$$

$$h_p = \left( P_{\max} \Big/ \alpha_1 H_T \right)^{1/2} \tag{4.10}$$

The elastic and plastic displacements, $h_e$ and $h_p$, of LMGC, sintered and pressable LDGC, pre-sintered and sintered Y-TZP were calculated from Eqs. (4.9) and (4.10). Their elastic and plastic deformation components were calculated from $h_e/(h_e+h_p)$ and $h_p/(h_e+h_p)$, respectively.

### *4.2.3 Indentation Energies*

In Fig. 4.1, the loading portion of the load-displacement curve is often described by the Meyer's law (Attaf, 2004; Sakai, 1999):

$$P = k_1 h^n \tag{4.11}$$

where $P$ is the instantaneous load, $k_1$ is the loading curve constant, $n$ is the loading exponent and $h$ is the instantaneous depth. The total energy, $U_t$, is obtained by integrating Eq. (4.11) from zero depth to the maximum depth, $h_{max}$:

$$U_t = \int_0^{h_{\max}} P dh = \int_0^{h_{\max}} k_1 h^n dh = \frac{k_1 h_{\max}^{n+1}}{n+1} \tag{4.12}$$

The unloading curve is described by the following expression (Oliver and Pharr, 1992):

$$P = k_2 \left( h - h_f \right)^m \tag{4.13}$$

where $k_2$ is the unloading curve constant, $m$ is the unloading exponent and $h_f$ is the final depth. The elastic strain energy, $U_e$, is obtained by integrating Eq. (4.13) from the final depth to the maximum depth.

$$U_e = \int_{h_f}^{h_{\max}} P dh = \int_{h_f}^{h_{\max}} k_2 \left( h - h_f \right)^m dh = \frac{k_2 \left( h_{\max} - h_f \right)^{m+1}}{m+1} \tag{4.14}$$

Then, the indentation absorbed energy, $U_r$, is expressed by the difference between the total energy and the elastic strain energy.

$$U_r = U_t - U_e \tag{4.15}$$

The normalized indentation elastic strain energy, $U_e/U_t$, of LMGC, sintered and pressable LDGC, pre-sintered and sintered Y-TZP was determined using Eqs. (4.12) and (4.14). Their normalized indentation absorbed energies, $U_r/U_t$, were determined using Eqs. (4.12) and (4.15).

### *4.2.4 Resistance to Machining-induced Cracking*

According to the Sakai–Nowak model (Sakai and Nowak, 1992), the potential strain energy for machining-induced cracking is provided by the elastic strain energy, $U_e$. The total energy consumed during surface cracking is provided by the fracture energy, $R_c$, and the resultant fracture surface area for the mechanically induced $i$-th damage or crack, $\sum_{i=1}^{n} A_i$ . The fracture energy, $R_c$, based on the Irwin's model is given by (Sakai and Nowak, 1992):

$$R_c = \frac{K_{Ic}^2}{E'} \tag{4.16}$$

where $K_{Ic}$ is the fracture toughness and $E'$ is the plane strain modulus. Assuming that all the potential strain energy is converted to the total surface energy, it then follows:

$$U_t - U_r = R_c \sum_{i=1}^{n} A_i \tag{4.17}$$

Substituting $D = U_r/U_t$ into Eq. (4.17), the following equation is obtained:

$$U_t = \frac{R_c}{1-D} \sum_{i=1}^{n} A_i \tag{4.18}$$

The resistance to machining-induced cracking, $M$, defined as the inverse degree of damage for a unit applied work, can be expressed as (Sakai and Nowak, 1992):

$$M = \frac{1}{\left[\sum_{i=1}^{n} A_i\right] \Big/ U_t} = \frac{U_t}{\sum_{i=1}^{n} A_i} = \frac{R_c \sum_{i=1}^{n} A_i}{(1-D)\sum_{i=1}^{n} A_i} = \frac{K_{Ic}^2}{E'(1-D)} \tag{4.19}$$

$M$ reduces naturally to the fracture energy if $D = 0$ and becomes infinite if $D = 1$.

The resistance to machining-induced cracking of LMGC, sintered and pressable LDGC, pre-sintered and sintered Y-TZP was calculated using Eq. (4.19) in which the fracture toughness, $K_{Ic}$, is required. The $K_{Ic}$ values of LMGC, sintered and pressable LDGC were 1 MPa $m^{1/2}$, 2.25 MPa $m^{1/2}$, and 2.75 MPa $m^{1/2}$ respectively (Bühler-Zemp and Völkel, 2005a; 2005b). The $K_{Ic}$ value of pre-sintered Y-TZP was determined by the fracture toughness-relative density plot for porous zirconia using a standard single-edge notched beam method (Deng et al., 2002b). The relative density of the pre-sintered Y-TZP is 0.53 based on its density 3.21 g/$cm^3$ against the fully dense Y-TZP density 6.08 g/$cm^3$ (Alao and Yin, 2014a). This relative density value corresponded to the fracture toughness of approximately 1 MPa $m^{1/2}$ (Deng et al., 2002b). The $K_{Ic}$ value of sintered Y-TZP was 5.5 MPa $m^{1/2}$ (Ritzberger et al., 2010).

### *4.2.5 Statistical Analysis*

Six repeated nanoindentations were conducted to determine the mean values and standard deviations of the properties at each loading rate. Single-factor analysis of variance (ANOVA) was applied at a 5% confidence interval to examine significant effects of loading rate on properties.

## 4.3 Results

### *4.3.1 Resistance to Plasticity*

Fig. 4.2 shows the resistance to plasticity, $H_T$, versus loading rate for LMGC. It increased sharply when increasing the loading rate from 0.1 mN/s to 0.5 mN/s, then increased steadily with the increased loading rate from 0.5 mN/s to 1 mN/s and remained almost constant from 1 mN/s to 2 mN/s. Its values at the loading rates of 0.1 mN/s, 0.5 mN/s, 1 mN/s and 2mN/s were 27.70 ± 10.31 GPa, 93.21 ± 18.64 GPa, 104.17 ± 15.62 GPa, and 102.09 ± 10.21 GPa, respectively. The coefficient of variation (i.e. the ratio of the standard deviation to the mean) ranged from 10–37%. The resistance to plasticity increased by 269% when increasing the loading rate from 0.1 mN/s to 2 mN/s and was significantly loading-rate dependent ($p < 0.05$).

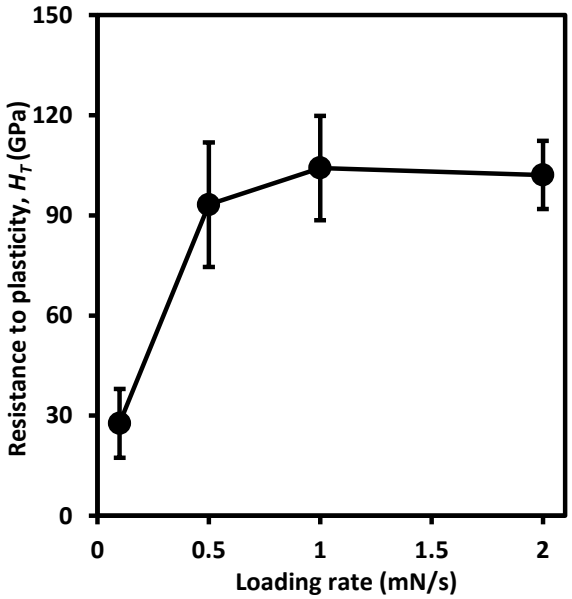


Fig. 4.2. Resistance to plasticity ($H_T$) versus loading rate for LMGC. Each data point is the mean value from six repeated indentations; error bars correspond to ± one standard deviation for the six repeats.

Fig. 4.3 shows the resistance to plasticity versus loading rate for sintered LDGC. It increased sharply when increasing the loading rate from 0.1 mN/s to 0.5 mN/s, then increased steadily with the increased loading rate from 0.5 mN/s to 2 mN/s. Its values at the loading rates of 0.1 mN/s, 0.5 mN/s, 1 mN/s and 2mN/s were 21.85 ± 7.54 GPa, 70.72 ± 18.31 GPa, 77.20 ± 15.44 GPa, and 79.51 ± 15.40 GPa, respectively. The coefficient of variation ranged from 19–35%. The resistance to plasticity increased by 72.5% when increasing the loading rate from 0.1 mN/s to 2 mN/s and was significantly loading-rate dependent ($p < 0.05$).

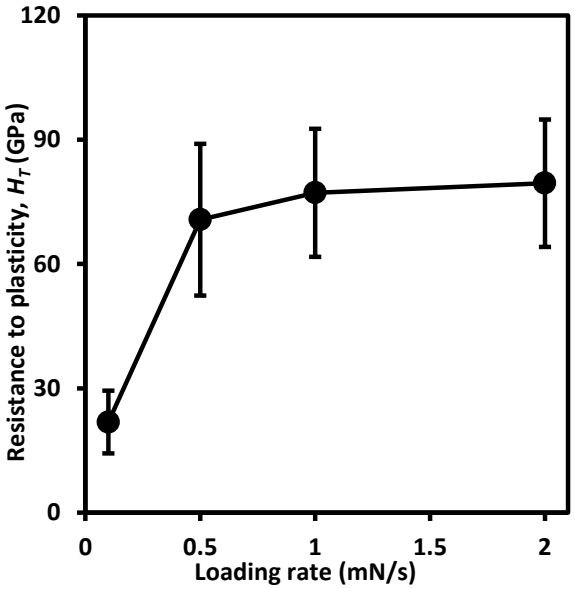


Fig. 4.3. Resistance to plasticity ($H_T$) versus loading rate for sintered LDGC. Each data point is the mean value from six repeated indentations; error bars correspond to ± one standard deviation for the six repeats.

Fig. 4.4 shows the resistance to plasticity versus loading rate for pressable LDGC. It increased steadily with an increase in loading rate from 0.1 mN/s to 1 mN/s, then decreased with the increase in loading rate from 1 mN/s to 2 mN/s. Its values at the loading rates of 0.1 mN/s, 0.5 mN/s, 1 mN/s and 2mN/s were 42.35 ± 12.69 GPa, 68.96 ± 11.03 GPa, 77.62 ± 10.87 GPa, and 61.23 ± 7.96 GPa, respectively. The coefficient of variation ranged from 13–29%. However, the loading rate effect on the resistance to plasticity was insignificant ($p > 0.05$).

Fig. 4.5 shows the resistance to plasticity versus loading rate for pre-sintered Y-TZP. It increased with the loading rate at 0.1 mN/s to 1 mN/s and decreased when the loading rate changed from 1 mN/s to 2 mN/s. Its values at the loading rates of 0.1 mN/s, 0.5 mN/s, 1 mN/s and 2mN/s were 2.66 ± 1.91 GPa, 4.38 ± 2.53 GPa, 5.06 ± 1.58 GPa, and 3.28 ± 0.98 GPa, respectively. The coefficient of variation ranged from 30–72%. However, the loading rate effect on the resistance to plasticity was insignificant ($p > 0.05$).

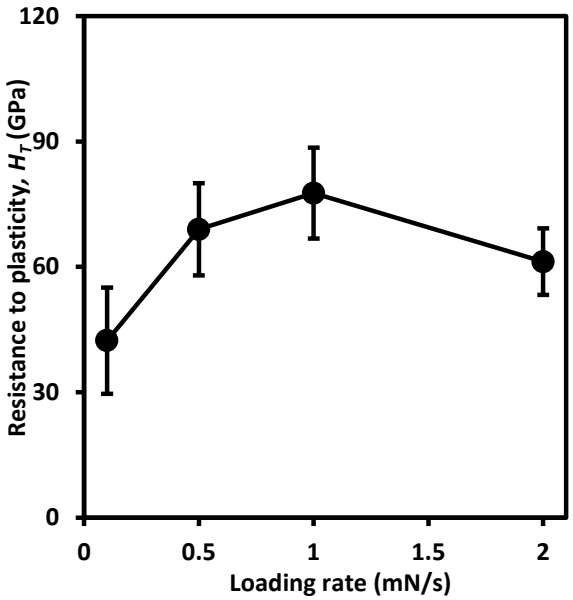


Fig. 4.4. Resistance to plasticity ($H_T$) versus loading rate for pressable LDGC. Each data point is the mean value from six repeated indentations; error bars correspond to ± one standard deviation for the six repeats.

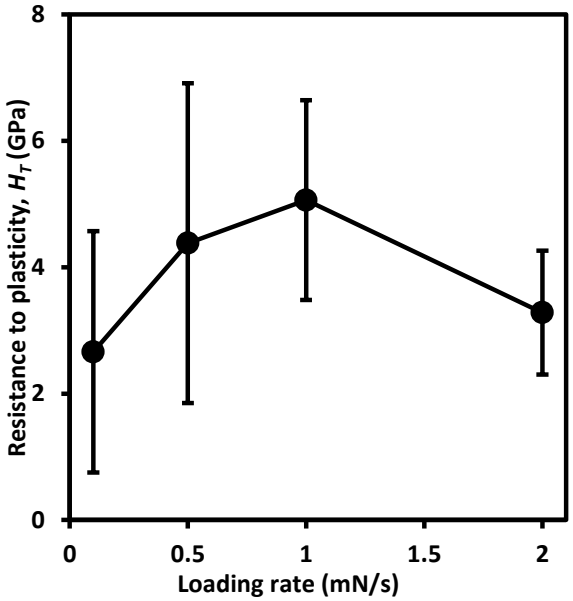


Fig. 4.5. Resistance to plasticity ($H_T$) versus loading rate for pre-sintered Y-TZP. Each data point is the mean value from six repeated indentations; error bars correspond to ± one standard deviation for the six repeats.

Fig. 4.6 shows the resistance to plasticity versus loading rate for sintered Y-TZP. It decreased when the loading rate increased from 0.1 mN/s to 0.5 mN/s and then increased when the loading rate increased from 0.5 mN/s to 2 mN/s. Its values at the loading rates of 0.1 mN/s, 0.5 mN/s, 1

mN/s and 2mN/s were 41.42 ± 30.28 GPa, 35.96 ± 7.66 GPa, 45.89 ± 7.65 GPa, and 49.60 ± 8.74 GPa, respectively. The largest standard deviation of the resistance to plasticity occurred at the loading rate of 0.1 mN/s.. At 0.5–2 mN/s loading rates, the standard deviations remained relatively the same. Overall, the loading rate effect on the resistance to plasticity was insignificant ($p > 0.05$).

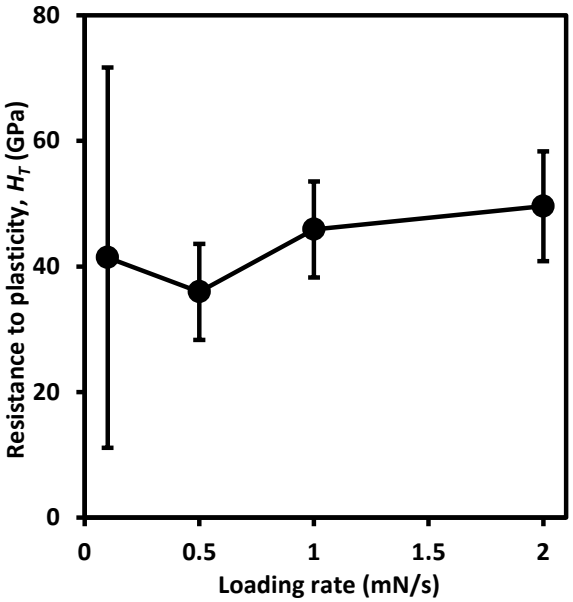


Fig. 4.6. Resistance to plasticity ($H_T$) versus loading rate for sintered Y-TZP. Each data point is the mean value from six repeated indentations; error bars correspond to ± one standard deviation for the six repeats.

### *4.3.2 Elastic and Plastic Displacements*

Fig. 4.7(a) shows elastic, $h_e$, and plastic, $h_p$, displacements versus loading rate for LMGC. The elastic displacement slightly decreased with the loading rate, whereas the plastic displacement decreased significantly with the loading rate. Meanwhile, all elastic displacements are higher than plastic displacements at all loading rates. The power law fittings (solid lines) show the respective dependence of both elastic and plastic displacements on the loading rate, $\dot{P}$, with the following expressions:

$$h_e = 146.40\,\dot{P}^{-0.047} \tag{4.20}$$

$$h_p = 70.66\,\dot{P}^{-0.27} \tag{4.21}$$

The coefficient of determination, $R^2$, for Eqs. (4.20) and (4.21) was 82% and 88.5%, respectively. Fig. 4.7(b) shows elastic and plastic deformation components versus loading rate

for LMGC. The elastic deformation component increased as the loading rate was increased from 0.1 mN/s to 1 mN/s and remained constant when the loading rate was changed from 1 mN/s to 2 mN/s. The plastic deformation components decreased as the loading rate was increased from 0.1 mN/s to 1 mN/s and remained constant as the loading rate was changed to 2 mN/s. At all loading rates, the elastic deformation component was higher than the elastic deformation component indicating the dominant elastic deformation response for LMGC.

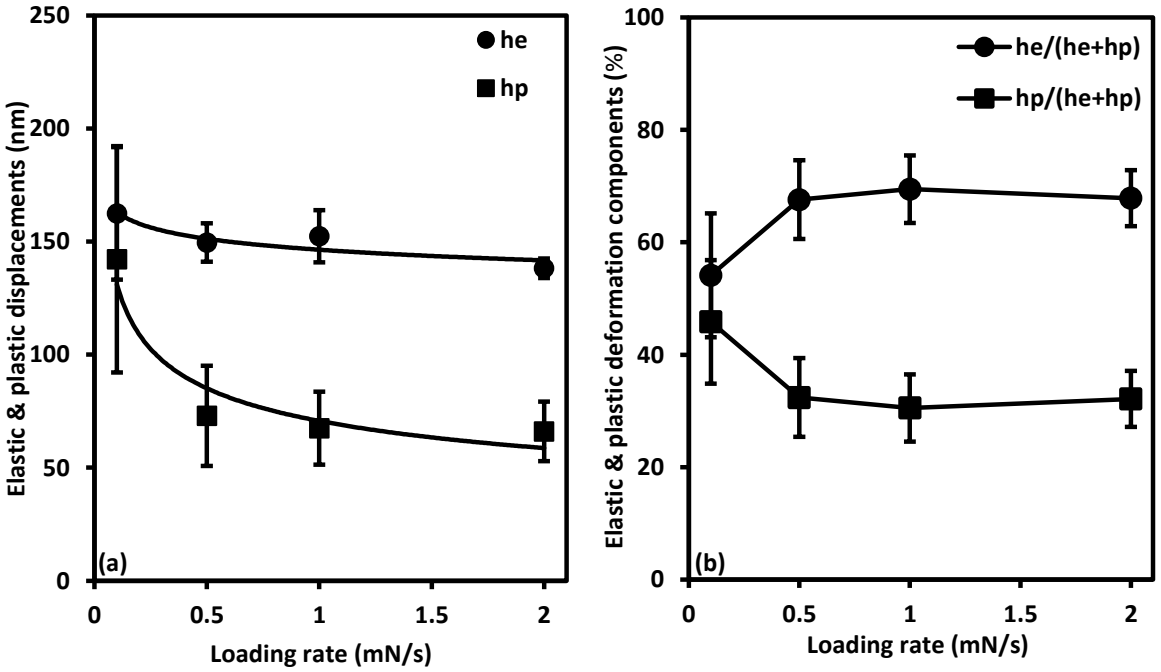


Fig. 4.7. (a) Elastic and plastic displacements ($h_e$ and $h_p$) versus loading rate for LMGC. Solid lines are power law fits to the measured data, (b) Elastic and plastic deformation components, ($h_e/(h_e+h_p)$) and ($h_p/(h_e+h_p)$) versus loading rate. Each data point is the mean value from six repeated indentations; error bars correspond to ± one standard deviation for the six repeats.

Fig. 4.8(a) shows elastic and plastic displacements versus loading rate for sintered LDGC. The elastic displacement increased with the loading rate, whereas the plastic displacement decreased with the loading rate. At 0.1 mN/s low loading rate, the plastic displacement was higher than elastic displacement whereas, at higher loading rates, the elastic displacement dominated. The power law fittings showing the respective dependence of both elastic and plastic displacements on the loading rate are expressed as:

$$h_e = 137.05 \dot{P}^{0.08} \tag{4.22}$$

$$h_p = 81.45 \dot{P}^{-0.29} \tag{4.23}$$

The $R^2$ for Eqs. (4.22) and (4.23) was 86% and 94.3% respectively. Fig. 4.8(b) shows elastic and plastic deformation components versus loading rate for sintered LDGC. Following the same trend as in Fig. 4.8(a), the elastic deformation component increased with the loading rate while the plastic displacement decreased with the loading rate. At 0.1 mN/s loading rate, the plastic deformation component was higher than the elastic deformation component. At higher loading rates, the elastic deformation component dominated.

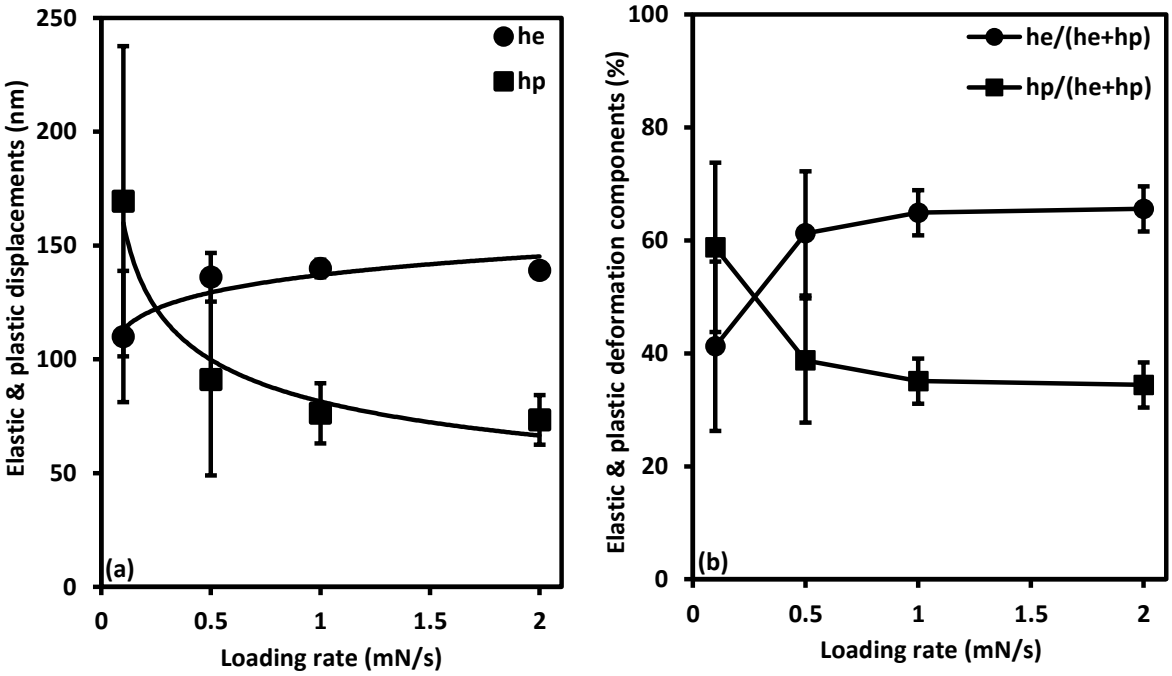


Fig. 4.8. (a) Elastic and plastic displacements ($h_e$ and $h_p$) versus loading rate for sintered LDGC. Solid lines are power law fits to the measured data, (b) Elastic and plastic deformation components ($h_e/(h_e+h_p)$) and ($h_p/(h_e+h_p)$) versus loading rate. Each data point is the mean value from six repeated indentations; error bars correspond to ± one standard deviation for the six repeats.

Fig. 4.9(a) shows elastic and plastic displacements versus loading rate for pressable LDGC. The elastic displacement slightly increased with the loading rate, whereas the plastic displacement significantly decreased with the loading rate. At 0.1 mN/s loading rate, the plastic displacement was slightly higher than elastic displacements whereas at higher loading rates, the elastic displacement dominated. The power law fittings showing the respective dependence of both elastic and plastic displacements on the loading rate are expressed as:

$$h_e = 137.41\dot{P}^{0.04} \tag{4.24}$$

$$h_p = 82.37\dot{P}^{-0.18} \tag{4.25}$$

The $R^2$ for Eqs. (4.24) and (4.25) was 56.3% and 80.4% respectively. Fig. 4.9(b) shows elastic and plastic deformation components versus loading rate for pressable LDGC. The elastic deformation component increased as the loading rate was increased from 0.1 mN/s to 1 mN/s and decreased when the loading rate was changed from 1 mN/s to 2 mN/s. The plastic deformation components decreased as the loading rate was increased from 0.1 mN/s to 1 mN/s and increased further as the loading rate was changed to 2 mN/s. At 0.1 mN/s loading rate, the elastic and plastic deformation components coincided. At higher loading rates, the elastic deformation component was higher than the plastic deformation component indicating the dominant elastic deformation response for pressable LDGC.

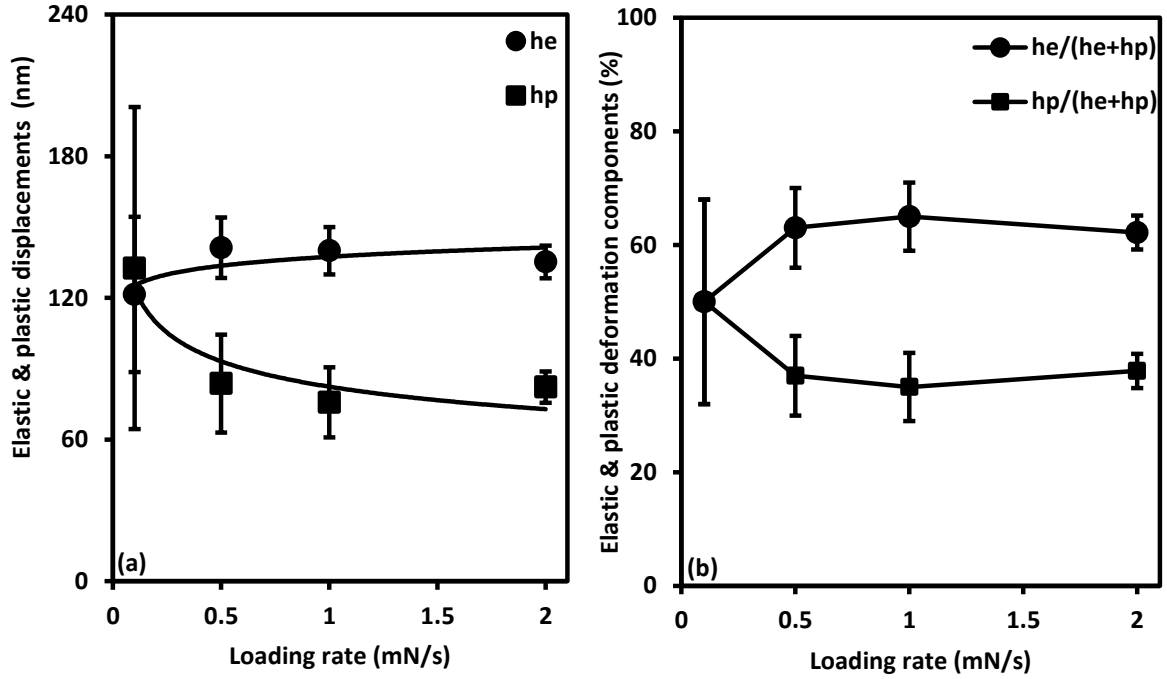


Fig. 4.9. (a) Elastic and plastic displacements ($h_e$ and $h_p$) versus loading rate for pressable LDGC. Solid lines are power law fits to the measured data, (b) Elastic and plastic deformation components ($h_e/(h_e+h_p)$) and ($h_p/(h_e+h_p)$) versus loading rate. Each data point is the mean value from six repeated indentations; error bars correspond to ± one standard deviation for the six repeats.

Fig. 4.10(a) shows elastic and plastic displacements versus loading rate for pre-sintered Y-TZP. The elastic displacement increased with the loading rate, whereas the plastic displacement decreased with the loading rate. Meanwhile, all plastic displacements are higher than elastic displacements at all loading rates. The power law fittings showing the respective dependence of both elastic and plastic displacements on the loading rate are expressed as:

$$h_e = 270.68 \dot{P}^{0.07} \tag{4.26}$$

$$h_p = 338.53 \dot{P}^{-0.12} \tag{4.27}$$

The $R^2$ for Eqs. (4.26) and (4.27) was 82.4% and 55.5% respectively. Fig. 4.10(b) shows elastic and plastic deformation components for pre-sintered Y-TZP. The elastic deformation component increased as the loading rate was increased from 0.1 mN/s to 1 mN/s and decreased when the loading rate was changed from 1 mN/s to 2 mN/s. The plastic deformation components decreased as the loading rate was increased from 0.1 mN/s to 1 mN/s and increased further as the loading rate was changed to 2 mN/s. At all loading rates, the plastic deformation component was higher than the elastic deformation component indicating the dominant plastic deformation response for pre-sintered Y-TZP.

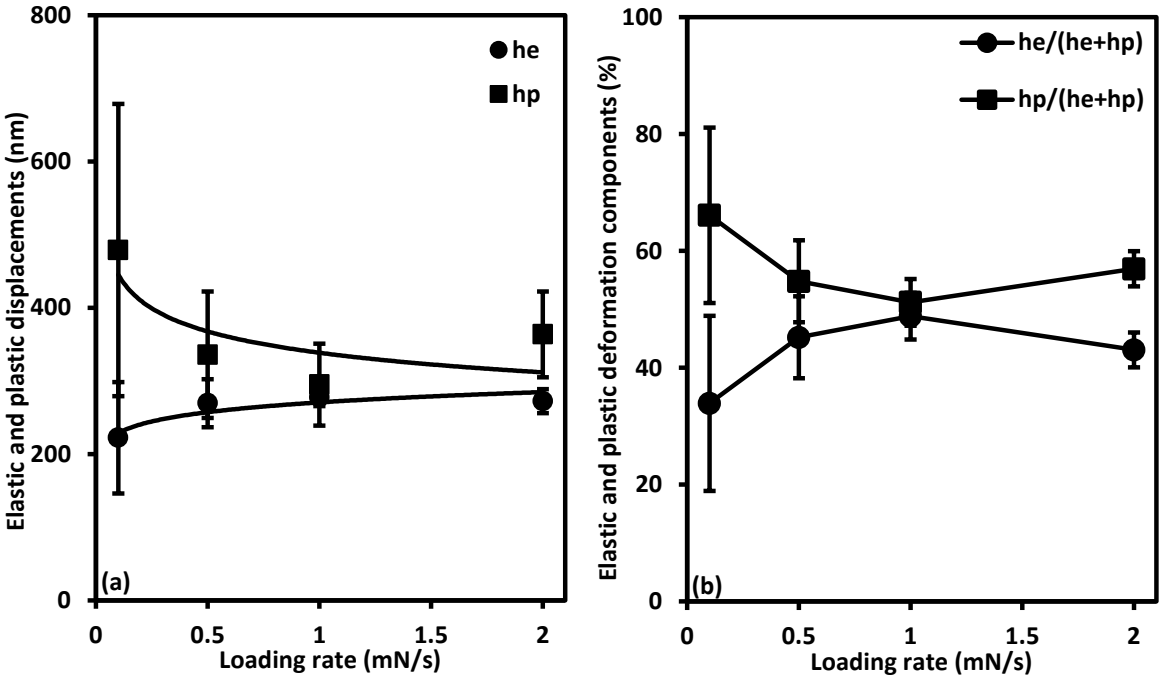


Fig. 4.10. (a) Elastic and plastic displacements ($h_e$ and $h_p$) versus loading rate for pre-sintered Y-TZP. Solid lines are power law fits to the measured data, (b) Elastic and plastic deformation components ($h_e/(h_e+h_p)$) and ($h_p/(h_e+h_p)$) versus loading rate. Each data point is the mean value from six repeated indentations; error bars correspond to ± one standard deviation for the six repeats.

Fig. 4.11(a) shows elastic and plastic displacements versus loading rate for sintered Y-TZP. The elastic displacement remained constant and independent of the loading rate. The plastic

displacement decreased with the loading rate with a regression power law equation as:

$$h_p = 98.03\dot{P}^{-0.12} \tag{4.28}$$

where the experimental data matched the solid line with the $R^2$ of 97.8%. At 0.1 mN/s and 0.5 mN/s loading rates, both the elastic and plastic displacements nearly coincided but at 1 mN/s and 2 mN/s loading rates, the elastic displacement was higher than the plastic displacement for sintered Y-TZP. Fig. 4.11(b) shows elastic and plastic deformation components versus loading rate for sintered Y-TZP. Following the same trend as in Fig. 4.11(a), the elastic deformation components and the plastic deformation components coincided at 0.1 mN/s and 0.5 mN/s loading rates. The elastic deformation component was higher than the plastic deformation component at loading rates of 1 mN/s and 2 mN/s. This indicates that elastic deformation dominated at higher loading rates.

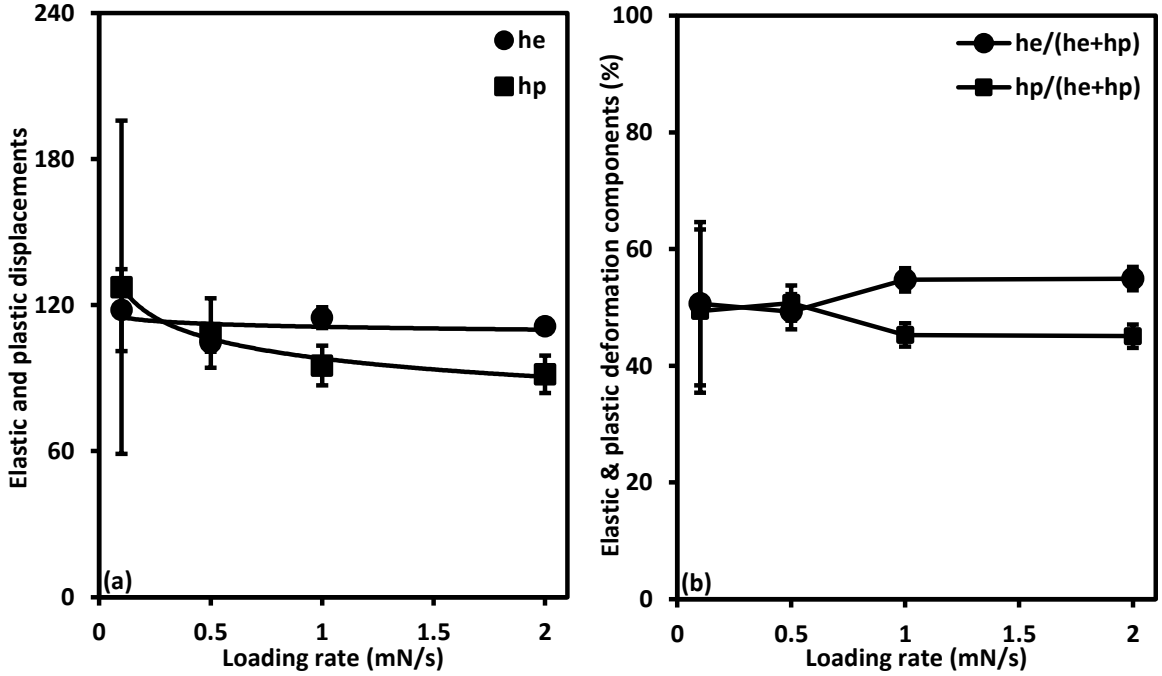


Fig. 4.11. (a) Elastic and plastic displacements ($h_e$ and $h_p$) versus loading rate for sintered Y-TZP. Solid lines are power law fits to the measured data, (b) Elastic and plastic deformation components ($h_e/(h_e+h_p)$) and ($h_p/(h_e+h_p)$) versus loading rate. Each data point is the mean value from six repeated indentations; the error bars correspond to ± one standard deviation for the six repeats.

### *4.3.3 Indentation Energies*

Fig. 4.12 shows normalized elastic strain energy, $U_e/U_t$, and normalized indentation absorbed energy, $U_r/U_t$, versus loading rate for LMGC. The elastic energy decreased with the loading rate

up to 0.5 mN/s and increased afterwards while the absorbed energy exhibited a reciprocal phenomenon. At 0.5 mN/s loading rate, the elastic and absorbed energies coincided. In addition, standard deviations of both $U_e/U_t$ and $U_r/U_t$ reduced when the loading rate increased. ANOVA analysis showed that loading rate did not significantly influence both $U_e/U_t$ and $U_r/U_t$ ($p > 0.05$).

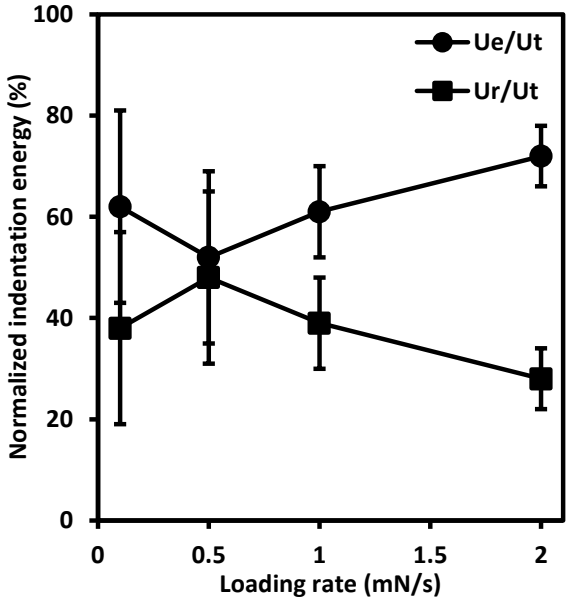


Fig. 4.12. Normalized elastic strain indentation energy ($U_e/U_t$) and normalized indentation absorbed energy ($U_r/U_t$) versus loading rate for LMGC. Each data point is the mean value of six repeated indentations; error bars correspond to ± one standard deviation for the six repeats.

Fig. 4.13 shows normalized elastic strain energy and normalized indentation absorbed energy versus loading rate for sintered LDGC. The elastic energy increased when increasing the loading rate from 0.1–0.5 mN/s and decreased with the loading rate up to 1 mN/s and remained relatively constant afterwards. The absorbed energy decreased when increasing the loading rate from 0.1–0.5 mN/s, then increased with the loading rate up to 1 mN/s and remained relatively constant afterwards. Thus, 1 mN/s loading rate can be considered as the critical loading rate at which the indentation energies were insensitive to the loading rate for sintered LDGC. Further, standard deviations of both $U_e/U_t$ and $U_r/U_t$ reduced when the loading rate increased. ANOVA analysis showed insignificant loading rate influence on both $U_e/U_t$ and $U_r/U_t$ ($p > 0.05$).

Fig. 4.14 shows normalized elastic strain energy and normalized indentation absorbed energy versus loading rate for pressable LDGC. The elastic energy increased with the loading rate from 0.1–2 mN/s while the absorbed energy decreased with the loading rate from 0.1–2 mN/s. In addition, the absorbed energy was slightly higher than the elastic energy at 0.1 mN/s loading rate while the elastic energy dominated at higher loading rates. Also, the standard deviations of

both $U_e/U_t$ and $U_r/U_t$ reduced with the increase in the loading rate. ANOVA analysis found insignificant loading rate effect on both $U_e/U_t$ and $U_r/U_t$ ($p > 0.05$).

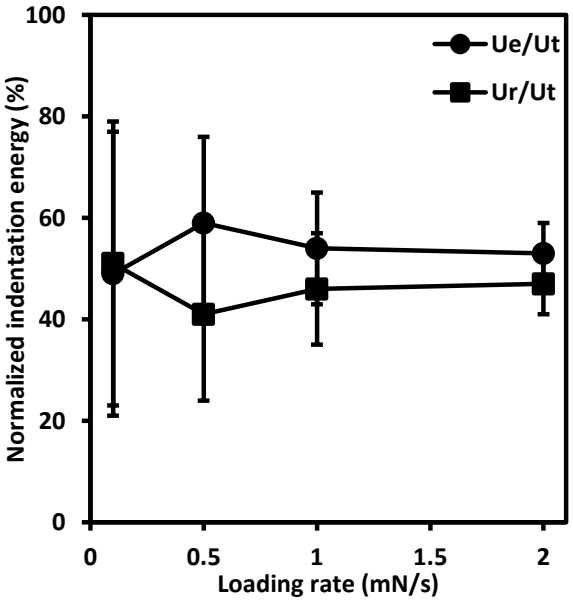


Fig. 4.13. Normalized elastic strain indentation energy ($U_e/U_t$) and normalized indentation absorbed energy ($U_r/U_t$) versus loading rate for sintered LDGC. Each data point is the mean value of six repeated indentations; error bars correspond to ± one standard deviation for the six repeats.

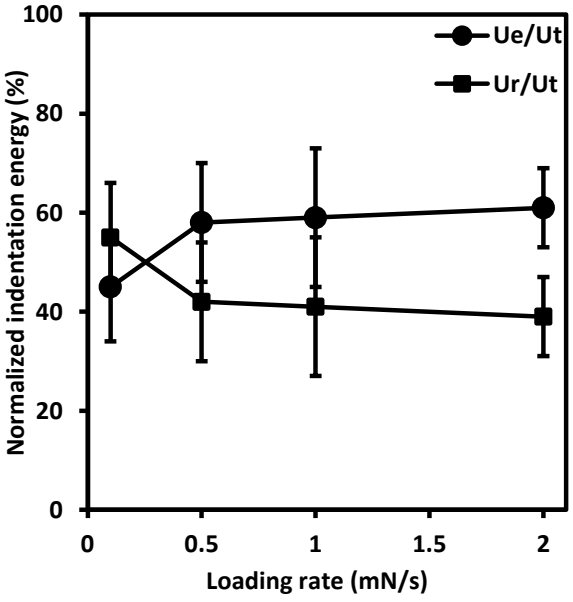


Fig. 4.14. Normalized elastic strain indentation energy ($U_e/U_t$) and normalized indentation absorbed energy ($U_r/U_t$) versus loading rate for pressable LDGC. Each data point is the mean value of six repeated indentations; error bars correspond to ± one standard deviation for the six repeats.

Fig. 4.15 shows normalized elastic strain energy and normalized indentation absorbed energy versus loading rate for pre-sintered Y-TZP. The elastic energy increased with the loading rate up to 1 mN/s and remained relatively constant afterwards while the absorbed energy exhibited a reciprocal phenomenon. Thus, 1 mN/s loading rate can be considered as the critical loading rate at which the indentation energies were insensitive to the loading rate for pre-sintered Y-TZP. This observation can be further confirmed by Fig. 4.10(b) where both elastic and plastic deformation components coincided at 1 mN/s. In addition, standard deviations of both $U_e/U_t$ and $U_r/U_t$ reduced when the loading rate increased. ANOVA analysis showed insignificant loading rate influence on both $U_e/U_t$ and $U_r/U_t$ ($p > 0.05$).

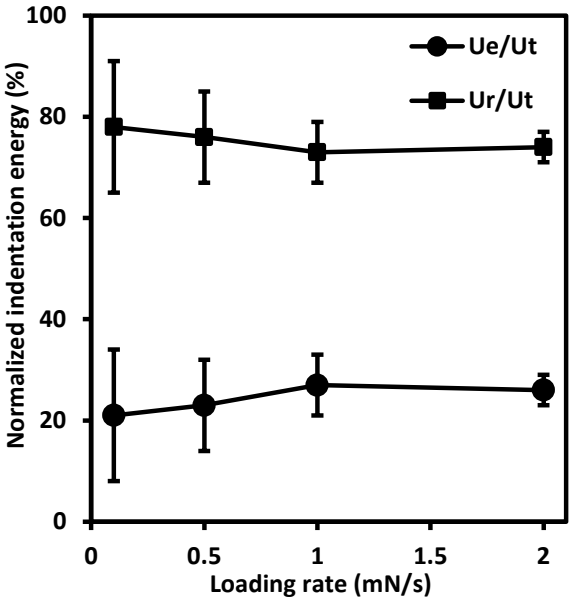


Fig. 4.15. Normalized elastic strain indentation energy ($U_e/U_t$) and normalized indentation absorbed energy ($U_r/U_t$) versus loading rate for pre-sintered Y-TZP. Each data point is the mean value of six repeated indentations; error bars correspond to ± one standard deviation for the six repeats.

Fig. 4.16 shows normalized indentation elastic strain energy and normalized indentation absorbed energy versus loading rate for sintered Y-TZP. The elastic energy decreased with the loading rate up to 0.5 mN/s and remained relatively constant afterwards while the absorbed energy increased as the loading rate was changed from 0.1 mN/s to 0.5 mN/s. From 0.5 mN/s to 2 mN/s, it remained approximately constant. At 0.1 mN/s loading rate, the elastic energy was dominant whereas at higher loading rates the absorbed energy dominated. However, the loading rate effect on both $U_e/U_t$ and $U_r/U_t$ was insignificant ($p > 0.05$).

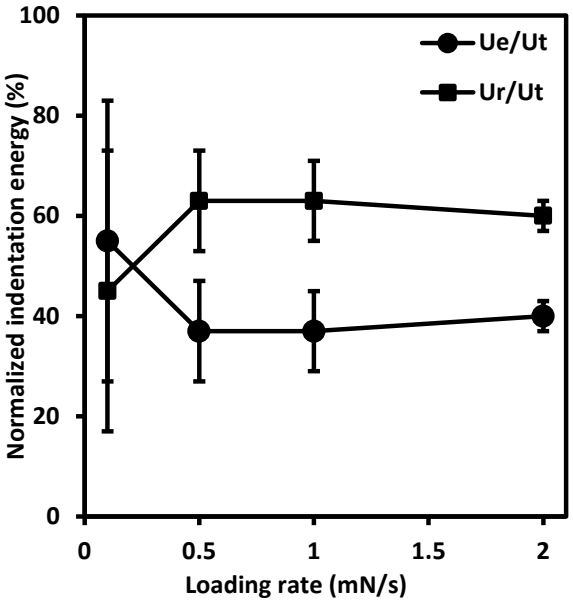


Fig. 4.16. Normalized elastic strain indentation energy ($U_e/U_t$) and normalized indentation absorbed energy ($U_r/U_t$) versus loading rate for sintered Y-TZP. Each data point is the mean value of six repeated indentations; error bars correspond to ± one standard deviation for the six repeats.

### *4.3.4 Resistance to Machining-induced Cracking*

Fig. 4.17 shows the resistance to machining-induced cracking, $M$, versus loading rate for LMGC. Its average and standard deviation values decreased with the loading rate. Its values at the loading rates of 0.1 mN/s, 0.5 mN/s, 1 mN/s and 2mN/s were 22.34 ± 9.55 J/m$^2$, 21.15 ± 8.09 J/m$^2$, 17.37 ± 4.63 J/m$^2$, and 11.73 ± 1.41 J/m$^2$, respectively. Accordingly, the coefficient of variation ranged 12–43%. However, the loading rate influence on the resistance to machining-induced cracking was insignificant ($p > 0.05$).

Fig. 4.18 shows the resistance to machining-induced cracking versus loading rate for sintered LDGC. It increased with the loading rate at 0.1 mN/s to 1 mN/s, and then decreased with the loading rate ranging from 1 mN/s to 2 mN/s. Its values at the loading rates of 0.1 mN/s, 0.5 mN/s, 1 mN/s and 2 mN/s were 56.65 ± 18.71 J/m$^2$, 74.13 ± 21.26 J/m$^2$, 84.77 ± 18.11 J/m$^2$, and 81.71 ± 11.42 J/m$^2$, respectively. The coefficient of variation of these values ranged 14–33% but the loading rate influence was found insignificant ($p > 0.05$).

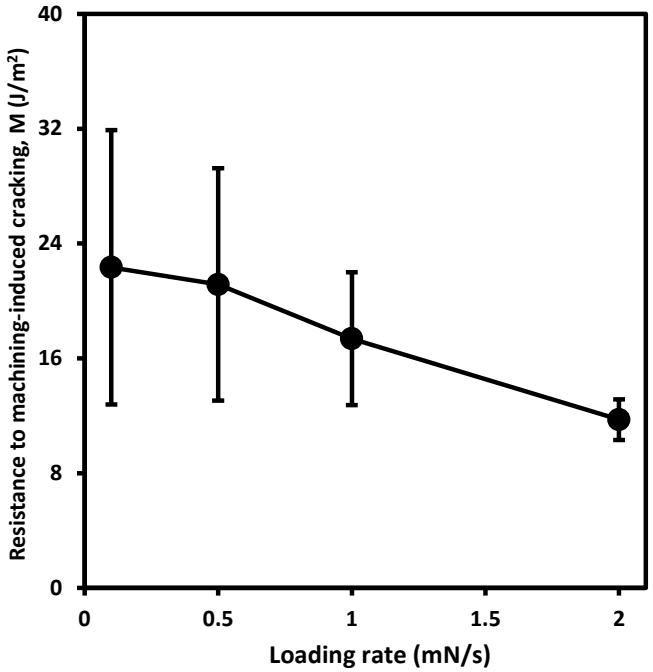


Fig. 4.17. Resistance to machining-induced crack (*M*) versus loading rate for LMGC. Each data point is the mean value of six repeated indentations; error bars correspond to ± one standard deviation for the six repeats.

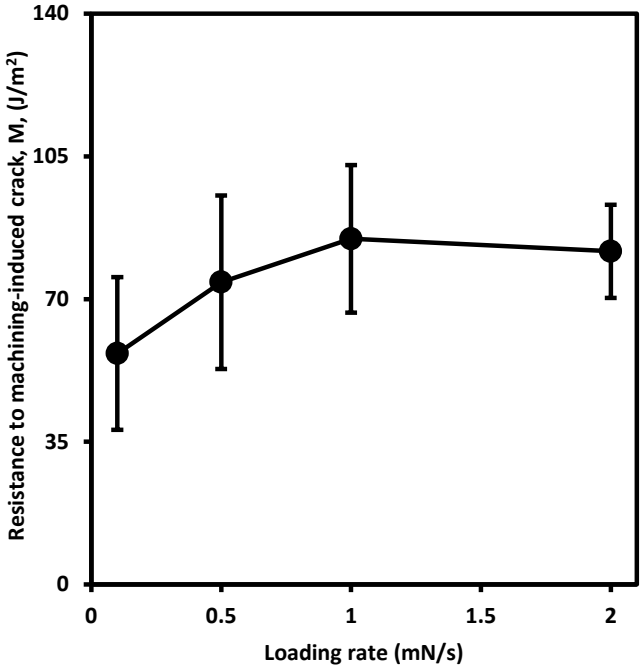


Fig. 4.18. Resistance to machining-induced crack (*M*) versus loading rate for sintered LDGC. Each data point is the mean value of six repeated indentations; error bars correspond to ± one standard deviation for the six repeats.

Fig. 4.19 shows the resistance to machining-induced cracking versus loading rate for pressable LDGC. It increased with the loading rate from from 0.1–1 mN/s, then decreased with the loading rate from 1–2 mN/s mN/s. Its values at the loading rates of 0.1 mN/s, 0.5 mN/s, 1 mN/s and 2mN/s are 111.16 ± 40.34 J/m$^2$, 119.06 ± 34.29 J/m$^2$, 119.81 ± 42.29 J/m$^2$, and 101.01 ± 13.94 J/m$^2$, respectively, which represented the coefficient of variation ranging from 14–36%. The loading rate influence on the resistance to machining-induced cracking was also insignificant ($p > 0.05$).

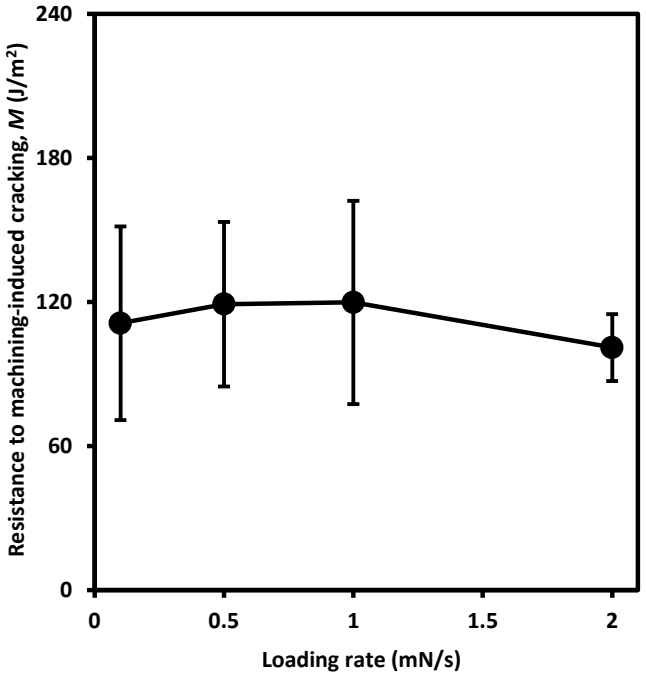


Fig. 4.19. Resistance to machining-induced crack (*M*) versus loading rate for pressable LDGC. Each data point is the mean value of six repeated indentations; error bars correspond to ± one standard deviation for the six repeats.

Fig. 4.20 shows the resistance to machining-induced cracking versus loading rate for pre-sintered Y-TZP. It increased with the loading rate at 0.1 mN/s to 0.5 mN/s, then decreased with the loading rate ranging 0.5–1 mN/s and remained relatively constant with the loading rate from 1–2 mN/s. Its values at the loading rates of 0.1 mN/s, 0.5 mN/s, 1 mN/s and 2mN/s were 117.24 ± 60.15 J/m$^2$, 155.61 ± 52.01 J/m$^2$, 129.20 ± 31.58 J/m$^2$, and 128.90 ± 24.10 J/m$^2$, respectively. For these values, the coefficient of variation ranged 18–51%. Also, the influence of the loading rate on the resistance to machining-induced cracking was insignificant ($p > 0.05$).

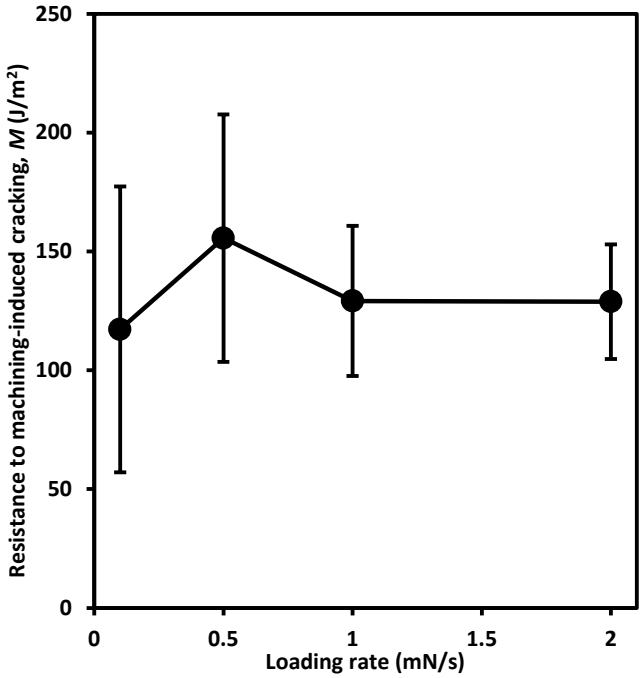


Fig. 4.20. Resistance to machining-induced crack (*M*) versus loading rate for pre-sintered Y-TZP. Each data point is the mean value of six repeated indentations; error bars correspond to ± one standard deviation for the six repeats.

Fig. 4.21 shows the resistance to machining-induced cracking versus loading rate for sintered Y-TZP. It slightly increased with the loading rate at 0.1 mN/s to 1 mN/s and decreased when the loading rate was changed from 1 mN/s to 2 mN/s. Its values at the loading rates of 0.1 mN/s, 0.5 mN/s, 1 mN/s and 2mN/s were 418.75 ± 213.26 J/m$^2$, 426.13 ± 127.11 J/m$^2$, 494.47 ± 123.15 J/m$^2$, and 415.70 ± 52.11 J/m$^2$, respectively. Accordingly, the coefficient of variation ranged 13–51%. The loading rate influence on the resistance to machining-induced cracking was also insignificant ($p > 0.05$).

## 4.4 Discussion

This thesis conducted the first advanced analysis of mechanical behavior of LMGC, sintered and pressable LDGC, pre-sintered and sintered Y-TZP using models developed by Sakai (1999) and Sakai and Nowak (1992). The analyzed properties include resistance to plasticity, elastic and plastic displacements/deformation components, normalized elastic strain and absorbed energies and resistance to machining-induced cracking deconvoluted at a peak load of 10 mN and 0.1–2 mN/s loading rates. These properties are important for machinability prediction of these materials in abrasive machining, such as grinding, lapping and polishing using diamond abrasives.

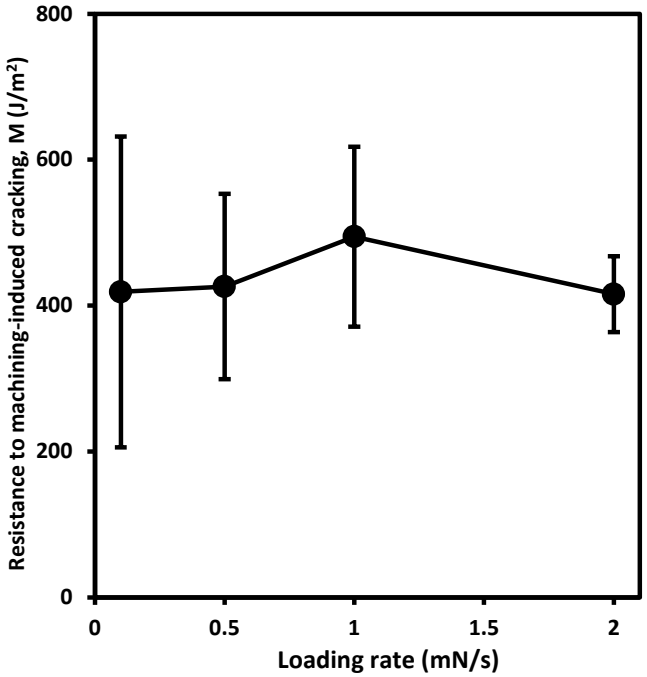


Fig. 4.21. Resistance to machining-induced crack (*M*) versus loading rate for sintered Y-TZP. Each data point is the mean value of six repeated indentations; error bars correspond to ± one standard deviation for the six repeats.

### *4.4.1 LMGC, Sintered and Pressable LDGC*

This study obtained 10–37%, 19–35% and 13–29% coefficients of variation in measured resistances to plasticity of LMGC, sintered and pressable LDGC respectively in Figs. 4.2–4.4. These values are slightly higher than those reported for sintered ceramics in the range of 15–25% (Morena et al., 1986). The higher experimental scatters in the measured resistance to plasticity values of LMGC, sintered and pressable LDGC relative to the sintered ceramics is a direct manifestation of the heterogeneous distribution of microstructural features in LMGC, sintered and pressable LDGC. LMGC contains both lithium metasilicate crystals and glass while LDGC in sintered or pressed form contains lithium disilicate crytstals and glass. Therefore, indentations made on either lithium metasilicate crystals/glass or lithium disilicate crystals/glass would reveal large variation in experimental data since the crystalline phases have generally higher resistance to penetration compared to the amorphous glassy phases. Therefore, higher coefficients of variation are expected to occur in heterogeneous materials than in homogeneous materials.

The resistances to plasticity of LMGC and sintered LDGC showed strong loading-rate dependence (Figs. 4.2 and 4.3) whereas it revealed an independent loading rate effect for

pressable LDGC (Fig. 4.4). This demonstrates an interesting microstructural effect on the deformation mechanisms of these materials in that although, these materials may contain the same constituents but their different crystals sizes and shapes associated with different fabrication methods responded differently to indentations. This effect was also demonstrated for mica glass-ceramic whose microstructure was tailored to different grain sizes by heat treatment which made them to respond differently to indentations (Xu et al., 1996).

It is imperative to determine the loading rate-independent or intrinsic resistance to plasticity for LMGC and sintered LDGC. This can be done using a modified strain rate sensitivity model in which the contact hardness, $H_{c,}$ in Eq. (3.9) is replaced by the resistance to plasticity, $H_T$, and the intrinsic contact hardness, $H_o$, is replaced by the intrinsic resistance to plasticity, $H_{To}$, according to the following equation:

$$H_T = H_{To}\,\dot{\varepsilon}^{\eta} \tag{4.29}$$

The $\eta$ is the modified strain rate sensitivity which is always greater than the strain rate sensitivity, $n$, since $H_T > H_c$ (Sakai, 1999; Oyen, 2006) and $\dot{\varepsilon}$ is the constant effective strain rate which can be obtained from the constant loading rate, $\dot{P}$, according to Eq. (3.11). Eq. (4.29) can be rewritten as:

$$Log(H_T) = \eta\, Log\left(\dot{\varepsilon}\right) + LogH_{T0} \tag{4.30}$$

Figs. 4.22 and 4.23 show the log-log plot of the resistance to plasticity, $H_T$, versus strain rate, $\dot{\varepsilon}$, for LMGC and sintered LDGC respectively. The corresponding linear correlation equations for LMGC and sintered LDGC from these figures can be written as Eqs. (4.31) and (4.32) respectively. The coefficient of determination, $R^2$, of Eqs. (4.32) and (4.33) is 88% and 92% respectively.

$$Log\left(H_T\right) = 0.512\, Log\left(\dot{\varepsilon}\right) + 2.5986 \tag{4.31}$$

$$Log\left(H_T\right) = 0.539\, Log\left(\dot{\varepsilon}\right) + 2.5142 \tag{4.32}$$

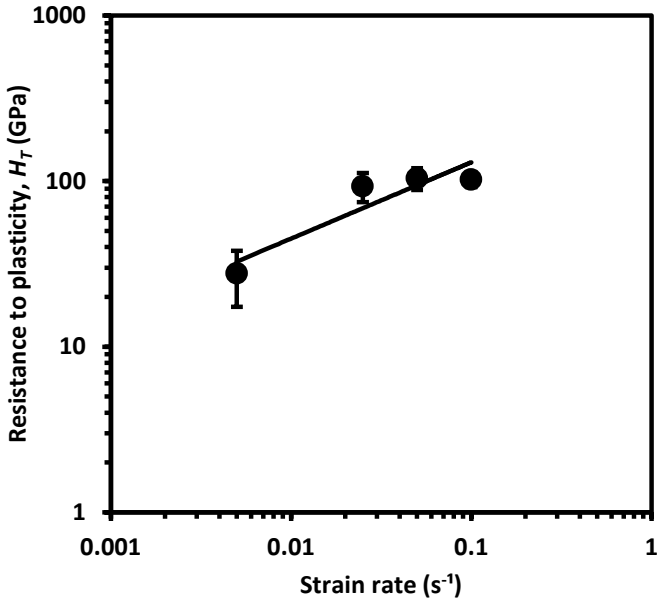


Fig. 4.22. Resistance to plasticity ($H_T$) versus strain rate ($\dot{\varepsilon}$) for LMGC. Each data point is the mean value for six repeated indentations; each error bar corresponds to ± one standard deviation for the six repeated indentations. The linear graph is described by the Eq. (4.31).

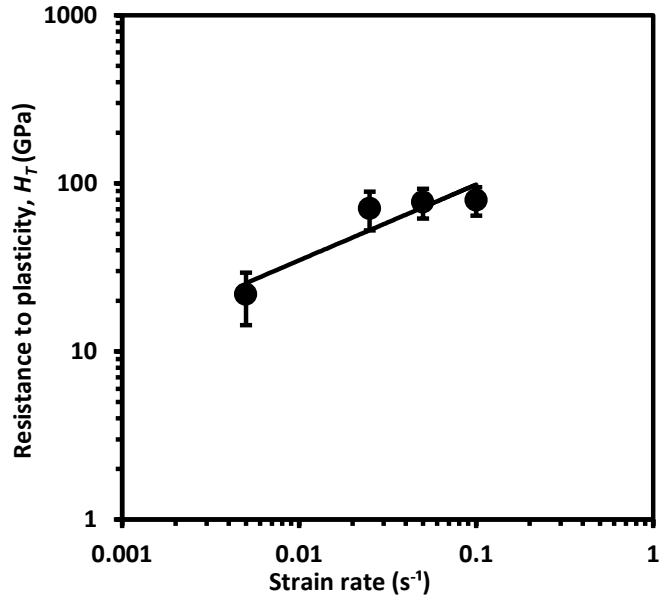


Fig. 4.23. Resistance to plasticity ($H_T$) versus strain rate ($\dot{\varepsilon}$) for sintered LDGC. Each data point is the mean value for six repeated indentations; each error bar corresponds to ± one standard deviation for the six repeated indentations. The linear graph is described by the Eq. (4.32).

Comparing Eq. (4.30) with Eqs. (4.31) and (4.32), we obtain $\eta$ = 0.512 and Log($H_{To}$) = 2.5986 for LMGC, and $\eta$ = 0.539 and Log($H_{To}$) = 2.5142 for sintered LDGC. Accordingly, the intrinsic resistance to plasticity of LMGC and sintered LDGC was 396.83 GPa and 326.72 GPa

respectively. In addition, since the resistance to plasticity of pressable LDGC is independent of loading rate, its value from 24 indentations is 62.54 ± 30.91 GPa. This shows that pressable LDGC is more deformable than sintered LDGC and LMGC. This assertion is consistent with the conclusions that one way to improve the ductility of glass-ceramic is to increase the size of the crystalline phase (Lawn et al., 1994). Further, the resistance to plasticity of LMGC is higher than that of fused silica (350 GPa) (Oyen, 2006) indicating that LMGC is highly brittle whereas that of the sintered LDGC is just a bit lower than fused silica which makes sintered LDGC less brittle than fused silica. However, the resistance of plasticity of pressable LDGC is about 5 times less than fused silica reaffirming that pressable LDGC exhibits better plastic property than sintered LDGC and LMGC.

Deformation partitioning provides insights into the respective contribution of elastic and plastic deformations to the total material deformation and reveals the dominant deformation mechanism. Since elastic deformation components dominated at all loading rates in LMGC (Fig. 4.7(b)), it indicates its dominant deformation mechanism was elastic reconfirming that LMGC is highly brittle. However, for sintered and pressable LDGC, the dominant deformation mechanisms were rate dependent since at low loading rate, the plastic deformation slightly dominated but at higher loading rates, elastic deformation dominated (Figs. 4.8(b) and 4.9(b)). In addition, the dominance of the elastic displacement of LMGC over its plastic displacement in Fig. 4.7(a)) can be ascribed to the dominance of the elastic strain energy over the absorbed energy (Fig. 4.12). This is because the indentation energy is the product of the force (which in the Sakai's model (Sakai, 1999) is the same for both elastic and plastic components in series) and the displacement. Thus, high elastic strain energy produced high elastic displacement while low absorbed energy led to low plastic displacement. The same argument can be extended to the dominance of elastic displacements of sintered and pressable LDGC (Figs. 4.8(a) and 4.9(a)) over their plastic displacements because their elastic strain energies were higher than their absorbed energies (Figs. 4.13 and 4.14) at higher loading rates. In addition, the decrease in plastic displacements with increase in loading rate of LMGC, sintered and pressable LDGC as shown respectively in Figs. 4.7(a), 4.8(a) and 4.9(a) is attributable to strain hardening effect that occurred in these materials which was discussed in Chapter 3 (Alao and Yin, 2015a). Consequently, a material that strain-hardens loses some of its plastic deformation component (Alao and Yin, 2015b).

The normalized indentation elastic strain and indentation absorbed energies are material characteristic parameters (Sakai, 1999). They are independent of peak load, maximum depth and loading rate. For LMGC, sintered and pressable LDGC in Figs. 4.12–4.14, the loading rate-independent normalized indentation absorbed energy from 24 indentations is 38 ± 15%, 45 ±

17% and 48 ± 13% respectively. Again, pressable LDGC reveals better plastic property than sintered LDGC and LMGC indicating that pressable LDGC would be most deformable followed by sintered LDGC and LMGC during abrasive process.

The resistance to machining-induced cracking is another material characteristic parameter (Sakai and Nowak, 1992). This study also obtained 12–43%, 14–33% and 14–36% coefficients of variation in the measured resistances to machining-induced cracking of LMGC, sintered and pressable LDGC in Figs. 4.17–4.19 respectively. As explained before, these scatters were due to the heterogeneous distribution of microstructural features in LMGC, sintered and pressable LDGC. The loading rate independent or intrinsic resistance to machining-induced cracking of LMGC, sintered and pressable LDGC from 24 indentations is 17.69 ± 7.32 J/m$^2$, 74.32 ± 19.95 J/m$^2$ and 112.76 ± 33.17 J/m$^2$ respectively. This indicates that pressable LDGC can resist more machining-induced damage than sintered LDGC and LMGC in nanoindentation. This assertion is attributable to higher fracture toughness and indentation absorbed energy of pressable LDGC in comparison with those of sintered LDGC and LMGC. In the same vein, sintered LDGC can resist higher machining damage than LMGC. The resistance to machining-induced cracking of LMGC is comparable to those of glass and G-carbon (Sakai and Nowak, 1992) making it susceptible to brittle fracture. The resistances to machining-induced cracking of sintered and pressable LDGC are higher than glass, G-carbon, SiC, $Al_2O_3$ and MgO (Sakai and Nowak, 1992).

Based on the results of this study, pressable LDGC can be ranked as the most machinable material among the three glass-ceramics. This is because of its lowest resistance to plasticity, highest normalized indentation absorbed energy and highest resistance to machining-induced cracking. This is followed by sintered LDGC which is ranked more machinable than LMGC due to its lower resistance to plasticity, higher normalized absorbed energy and resistance to machining-induced cracking than the LMGC.

### *4.4.2 Pre-Sintered Y-TZP*

The independent relation between resistance to plasticity and loading rate (Fig. 4.5) reveals high coefficient of variation of 30–72%, which needs to be analyzed. The reason for the large dispersion in the resistance to plasticity values can be attributed to the heterogeneous microstructure of pre-sintered Y-TZP containing about 48% porosity. Consequently, indentations made on different locations with the same loading conditions resulted in variations, considering the statistical distribution of the pores in the surface of the material (Fig. 3.4). For sintered ceramics, the coefficient of variation was established ranging from 15% to 25%

(Morena et al., 1986). For porous ceramics, large error bars were reported. For instance, the contact mean pressure of alumina containing 19% porosity (Ling et al., 2008) revealed 50–85% coefficient of variation at the low penetration depth/load (5 mN) in nanoindentation. The Vickers hardness of NiO-$ZrO_2$ with 20% porosity (Tang and Gong, 2013) also demonstrated above 50% coefficient of variation. Therefore, large data variation is inevitably expected to occur in pre-sintered Y-TZP containing a higher porosity of 48%.

The overlap of the resistance to plasticity values at different loading rates in Fig. 4.5 accounts for its statistical insignificant loading rate independence ($p > 0.05$). This is because within the loading rates applied, there was no significant difference between the indentation sizes or there were not enough impact stresses developed at the high loading rate which could have affected the hardness value (Quinn et al., 2002a). The contact hardness of the pre-sintered Y-TZP applied for the computation of the resistance to plasticity was also loading-rate independent (Alao and Yin, 2014b). Thus, the loading-rate independent resistance to plasticity is also consistent with previous work where the loading rate minimally influenced the measured microhardness of some materials (Quinn et al., 2002a). Nakamura et al. (2000) suggested the average values from multiple indentations at various locations for the determination of mechanical properties for porous ceramics. Thus, the resistance to plasticity for pre-sintered Y-TZP from 24 indentations is 3.82 ± 1.92 GPa. This value approximately agrees with the load-independent indentation-induced resistance to plasticity (3.5 GPa) for porous Y-TZP coatings determined at high loads from 100 mN to 10 N (Latka et al., 2013). This confirms the validity of the use of the Sakai's model (1999) in extracting the resistance to plasticity at the nano scale for this material. The resistance to plasticity for pre-sintered Y-TZP is greater than that of aluminium (0.33 GPa) by 3.49 GPa, and less than that of fused silica (350 GPa) by 346.18 GPa. The small difference in the resistance to plasticity between pre-sintered Y-TZP and ductile aluminum in comparison with the big difference between pre-sintered Y-TZP and brittle fused silica confirms that pre-sintered Y-TZP exhibits quasi-plastic property.

Fig. 4.10(b) shows that plastic deformation was dominant at all loading rates, reconfirming that pre-sintered Y-TZP is quasi-plastic. However, Fig. 4.10(a) shows that this material did not have the single-valued elastic and plastic deformation components at all loading rates. Therefore, it is difficult to compare the elastic and plastic deformation components of pre-sintered Y-TZP with the published data (Oyen, 2006) because the latter were determined at a constant loading rate.

In nanoindentation of elastoplastic materials using sharp indenters like the Berkovich indenter, the loading cycle consists of elastic and plastic deformation portions (Oyen and Cook, 2009). At the elastic-plastic transition point (i.e., the yielding point), the initially sharp Berkovich tip may

inevitably blunt and the geometry of the indenter can be approximated as spherical (Schuh, 2006). With this fortuitous geometry, it is possible to predict the elastic portion using the following Hertzian law (Hertz, 1882; Johnson, 1985; Lawn, 1998):

$$P = \frac{4}{3} E_r R^{1/2} h^{3/2} \tag{4.33}$$

where $P$ is the load, $R$ is the radius of the indenter tip, $E_r$ is the reduced modulus and $h$ is the instantaneous indentation depth. Eq. (4.33) is based on isotropic continuum elasticity and the first point at which the loading curve deviates from it marks the yielding point. At the yield point, which is generally regarded as the first pop-in on the loading cycle for fully dense materials, the indenter travels without a measured increase in the applied load, causing the maximum shear stress, $\tau_{max}$, to occur (Packard and Schuh, 2007). Thus, this maximum shear stress can be estimated by the following relation (Packard and Schuh, 2007):

$$\tau_{\max} = 0.45 \left( \frac{16 P_c E_r^2}{9 \pi^3 R^2} \right)^{1/3} \tag{4.34}$$

where $P_c$ is the critical load to initiate plasticity. While the first pop-in load on the loading cycle corresponds to the $P_c$ for dense materials, it may not be true for porous ceramics. The first pop-in on the loading curve of the porous ceramics may be due to the influences of porosity, roughness, or cracks (Latka et al., 2013). Consequently, the load at the first pop-in on the loading curve of porous ceramics may not represent the yielding critical load. Therefore, in this work, the critical load for pre-sintered Y-TZP was determined using the total elastic contact displacement, $h_e$, calculated from Eq. (4.9). Then the $P_c$ should correspond to the load predicted by the Hertzian law (Eq. (4.33)) at that displacement as presented below:

$$P_c = \frac{4}{3} E_r R^{1/2} h_e^{3/2} \tag{4.35}$$

The dependence of the elastic and plastic displacements on the loading rate in Fig. 4.10(a) can be explained in terms of the maximum shear stress developed using Eq. (4.34) and the indentation energies. Fig. 4.24 shows the maximum shear stress, $\tau_{max}$, versus the loading rate. At the lowest loading rate of 0.1 mN/s, the maximum shear stress was highest, approximately twice the value at 0.5 mN/s loading rate. The maximum shear stress was loading rate-independent above 0.5 mN/s. The high shear stress at the lowest loading rate of 0.1 mN/s caused a quick transition from the elastic deformation to the plastic deformation. This quick elastic-plastic transition led to the low elastic strain energy and the high plastic energy (Fig. 4.15). Since the indentation energy is the product of force and displacement, low elastic strain energy produced low elastic displacement while high plastic energy led to enhanced plastic displacement. As the loading rate increased, the compressive stress between the indenter tip and the material

increased due to the increase in strain rate. This high compressive stress lowered the maximum shear stress to cause yielding. Therefore, the elastic strain energy improved slightly while the plastic energy reduced correspondingly. The higher elastic strain energy led to the larger elastic displacement while the reduced plastic energy lowered the plastic displacement at higher loading rates.

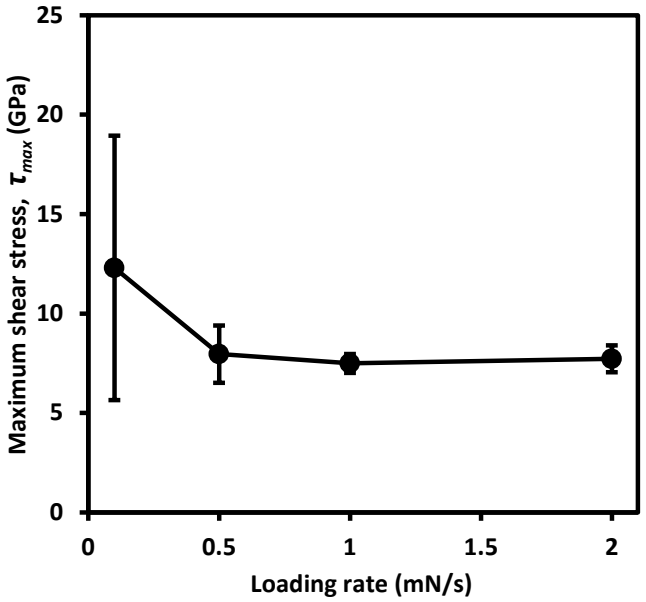


Fig. 4.24. Maximum shear stress ($\tau_{max}$) versus loading rate for pre-sintered Y-TZP. Each data point is the mean value of six repeated indentations; the error bars correspond to ± one standard deviation for the six repeats.

The loading rate independent normalized indentation absorbed energy for pre-sintered Y-TZP (Fig. 4.15) was 0.75 ± 0.08 which is very close to that of copper (≈ 0.9) (Sakai and Nowak, 1992), a well-known ductile material but higher than that of sintered Y-TZP (0.58 ± 016) (Alao and Yin, 2015b). This means that pre-sintered Y-TZP exhibits lower resistance to plastic deformation than sintered Y-TZP during abrasive and erosive contacts. This observation agrees with previous studies where porous hydroxyapatite exhibited higher ductility than sintered hydroxyapatite (He et al., 2008) and highly porous alumina (Latella, et al., 1997) and silicon nitride (Azeggagh et al., 2015) displayed higher ductility than their sintered ones. However, the higher normalized indentation absorbed energy of pre-sintered Y-TZP indicates that it is less resistant to wear than the sintered Y-TZP due to the frictional effect that may be caused by the higher plasticity (Frutos et al., 2012; Leyland and Mathews, 2000).

It is noted that both nanoindentation and nanoscratch tests have been applied to analyse the fundamental deformation and fracture processes that occur during machining (Bhushan and Li,

2003; Jahanmir et al., 1999; Lawn, 1993; Li and Bhushan, 2001). Although nanoindentation is quasi-static, the relative sliding speed between the tool tip and the workpiece in nanoscratching is much smaller than the speeds used in machining (Bhushan and Li, 2003; Jahanmir et al., 1999; Li and Bhushan, 2001). Hence, neither nanoscratching nor nanoindentation can simulate all aspects of the material removal process (Jahanmir et al. 1999). However, as machining is similar to an indentation process, indentation mechanics can predict machining performance with reasonably good accuracy (Xu et al., 1996) and the indentation approach was used to investigate brittle-ductile transitions in ceramics and has provided useful results for tool-workpiece interactions in machining (Malkin and Hwang, 1996; Jahanmir et al., 1999). Another advantage of indentation over nanoscratching is that nanoindentation can provide the energy absorbed during nanoindentation which can be used for predicting the specific cutting energy in machining (Xu et al., 1996). For these reasons, a nanoindentation approach rather than a nanoscratch approach is superior for determining the ceramic machinability.

An important application of the dependence of the elastic displacement on the loading rate can be hypothesized for predicting an improved machinability with a high deformation rate for the material studied. The mechanical responses of pre-sintered Y-TZP to sharp pyramidal indentations at different loading rates can be likened to its abrasive machining behaviour using sharp diamond abrasives at different deformation rates. In machining, many abrasives are involved in the cutting process with each abrasive impacting its own normal force on the workpiece and this normal force per abrasive can be very low (Song and Yin, 2012). This normal load per cutting abrasive in the machining process is similar to the peak load in nanoindentation tests and it is responsible for the elastic/plastic deflections and deformations of the workpiece (Komanduri et al., 1997). It has been analysed that the contact lengths, $L_c$, between abrasives and workpiece materials play a significant role in the machining performance, including surface roughness, cutting forces and cutting efficiency. An expression has been developed relating the contact length to the elastic deflections, $\delta$, of the workpiece and the abrasive wheel caused by the normal grinding force and depth of cut, $a_e$ and the effective wheel diameter, $d_e$ (Qi et al., 1994):

$$L_c^2 = d_e\left(a_e + 4\delta\right) \tag{4.36}$$

As shown in Eq. (4.36), an increase in the elastic displacement of either the workpiece or the abrasive could enhance the elastic deflection which in turn would increase the contact length in abrasive machining. In this study, the elastic displacement increased with the loading rate (Fig. 4.10(a)). Therefore, it is anticipated that the contact length would also increase proportionately with the work-material deformation rate at a constant depth of cut and grinding wheel diameter. The benefits associated with the increase in contact lengths during abrasive machining include

reductions in maximum grinding temperatures, surface roughness and fracture wear of diamond tools (Marinescu et al., 2004). Thus, machining pre-sintered Y-TZP at high deformation rates is predicted to improve its machinability. This assertion complements the previous conclusion of Alao and Yin (2014b) in which the application of high deformation rates was suggested to avoid brittle fracture during machining. However, the practical realization of high-quality abrasive machining of pre-sintered Y-TZP remains future studies.

The loading-rate independent resistance to machining-induced cracking in Fig. 4.20 with variation coefficients (18% to 51%) reflects a characteristic material property for machining. As explained above, the large variation coefficient is attributed to the statistical distribution of the pores on the material surface (Fig. 3.4). Furthermore, to ascertain the correctness of the resistance to machining-induced cracking in Fig. 4.20, a deeper analysis is required to substantiate the authenticity of the used fracture toughness value for the material. Before using the 1 MPa $m^{1/2}$ value (Deng et al., 2002b), we attempted to measure the toughness using Vickers (Zwick/Roell, ZHVμ-S Indentec, UK) indentation fracture method but radial/median cracks were not formed at the indented corners even with the highest load, 19.6 N, on the system (Fig. 4.25). This indicates the unsuitability of the indentation fracture method for the fracture toughness measurement of pre-sintered Y-TZP. In addition, a porosity-fracture toughness relationship was developed to predict the fracture toughness for porous ceramics (Wagh et al., 1993):

$$K_{Ic} = \left(2\gamma_o E_o\right)^{1/2}\left(1-P\right)^{c+0.5} \tag{4.37}$$

where $K_{Ic}$ is the fracture toughness of the porous ceramic, $\gamma_o$ and $E_o$ are the specific fracture energy and the Young's modulus of the fully dense material, $P$ is the porosity. The $c$ is an exponent arising from similar elastic modulus-porosity empirical relationships based on the concept of minimum solid area (Wagh et al., 1993):

$$E = E_o \exp^{(-aP)} \tag{4.38}$$

$$E = E_o\left(1-P\right)^b \tag{4.39}$$

where $E$ is the Young's modulus of the porous ceramics, $E_o$ is the Young's modulus of the fully dense material; $a$ and $b$ are empirical exponents. $E_o$, $a$ and $b$ are determined from experimental results by curve fitting procedure. Accordingly, the $c$ in Eq. (4.37) can be related to either $a$ or $b$ in Eqs. (4.38) and (4.39) (Wagh et al.1993). For porous Y-TZP, these modulus-porosity relationships were reported as (Luo and Stevens, 1999):

$$E = 216\exp^{(-3.69P)} \tag{4.40}$$

$$E = 210.6\left(1-P\right)^{2.96} \tag{4.41}$$

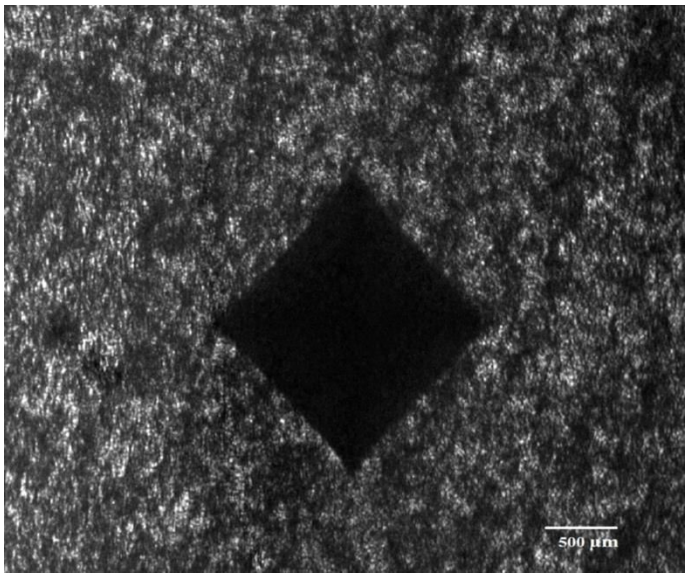


Fig. 4.25. Optical micrograph of a Vickers indentation pattern of pre-sintered Y-TZP at 19.6 N indentation load.

Thus, $a$ = -3.69 and $b$ = 2.96. Determination of the correct exponent to be used as $c$ in Eq. (4.37) between $a$ and $b$ requires knowing the Young's modulus, $E$, of the pre-sintered Y-TZP. Alao and Yin (2014b) reported $E$ for this material in the range of 24.39–34.25 GPa. So, by taking $P$ as 0.483, $E$ in Eq. (4.40) becomes 36.34 GPa which is outside the reported value but it is 29.88 GPa in Eq. (4.41) which is within the reported range. Therefore, the $c$ was taken as 2.96. Substituting $c$ = 2.96, $\gamma_o$ = 168.65 J/m$^2$ (Alao and Yin, 2015b) and $E_o$ = 168.19 GPa (Alao and Yin, 2014a) in Eq. (4.37), the predicted fracture toughness is 0.8 MPa m$^{1/2}$ which is very close to the measured value by Deng et al. (2002b). This agreement confirms the validity of the used fracture toughness for the material. Therefore, the predicted resistance to machining-induced cracking for pre-sintered zirconia from 24 indentations is 132.74 ± 15 J/m$^2$. This predicted resistance to machining-induced cracking is higher than those for sintered ceramics such as glass, SiC, MgO and $Al_2O_3$ (Sakai and Nowak, 1992) but less than sintered Y-TZP (445.44 ± 106.32 J/m$^2$) (Alao and Yin, 2015b).

The low resistance to machining-induced cracking of pre-sintered Y-TZP can be ascribed to its low fracture energy in spite of its high indentation absorbed energy. Rice (1984) clearly pointed out that single (isolated) or multiple (interconnected) pores in polycrystalline ceramics might form equatorial cracks approximately one-half grain deep into the matrix and thus become sharp cracks which could propagate across the grains. Evidence of isolated and interconnected pores is shown in Fig. 3.4 for pre-sintered Y-TZP. Therefore, the low fracture energy and toughness are attributed to the porosity in the material. In addition, the low resistance to machining-induced cracking of this material indicates that during machining, under a small applied normal

force, the sintered necks between grains may easily break and the grains fill the pores leading to the grain/particle coalescence. This coalescence within a localized volume beneath the indenter may lead to the material being compacted or kinked as observed by Alao and Yin (2014b). This assertion is in line with the intragranular microfracture theory provided for the plasticity of porous silicon nitride (She et al., 2003). In addition, the grain/particle coalescence may also explain why the indentation absorbed energy was higher than the elastic strain energy at any loading rate because as the densification increased more energy would be consumed (Fig. 4.15). Finally, the same argument can be extended to the Vickers imprint (Fig. 4.25) in which compaction occurred due to the grain/particle coalescence underneath the indenter without the brittle micro-crack propagation along the indenter's corners.

### *4.4.3 Sintered Y-TZP*

In sintered Y-TZP, the resistance to plasticity was independent of the loading rate (Fig. 4.6). This loading rate-independent resistance to plasticity is consistent with the results of Quinn et al. (2002a) where the loading rate did not influence the resistance to indention-induced plastic deformation of sintered SiC, AlON and steel. The mean and standard deviation (43.22 ± 9.59 GPa) of the resistance to plasticity for zirconia at all loading rates are very close to the resistance to plasticity (48.1 ± 0.8 GPa) extracted with three other tetrahedral pyramidal indenters of face angles of 10°, 22° and 40° for sintered Y-TZP (Sakai and Nakano, 2002). The face angle of the Berkovich indenter used in our study was 24.7° (Sakai et al., 1999). This shows that the resistance to plasticity is independent of the indenter geometry, reconfirming that the resistance to plasticity can be used for representing the plasticity of sintered Y-TZP examined. This study also shows that sintered Y-TZP exhibits mild plastic property since its resistance to plasticity is higher than that of a pure ductile material like aluminium which is 0.33–0.54 GPa (Oyen, 2006; Sakai and Nakano, 2002) but lower than that of a pure fused silica which is 350 GPa (Oyen, 2006).

This study shows that the elastic and plastic deformation components were approximately 50% each at low loading rates (Fig. 4.11(b)). However, the elastic deformation components slightly dominated at high loading rates (Fig. 4.11(b)). This indicates the rate-dependent deformation mechanism for sintered Y-TZP. In addition, the elastic displacement remained constant at all loading rates while the plastic displacement decreased with increase in loading rate (Fig. 4.11(a)). The loading rate-independent elastic displacement can be explained in terms of the maximum shear stress induced at the elastic-plastic transition (yielding point). The maximum shear stress can be estimated by the relation in Eq. (4.34). Fig. 4.26 shows the plot of maximum shear stress, $\tau_{max}$, and loading rate.

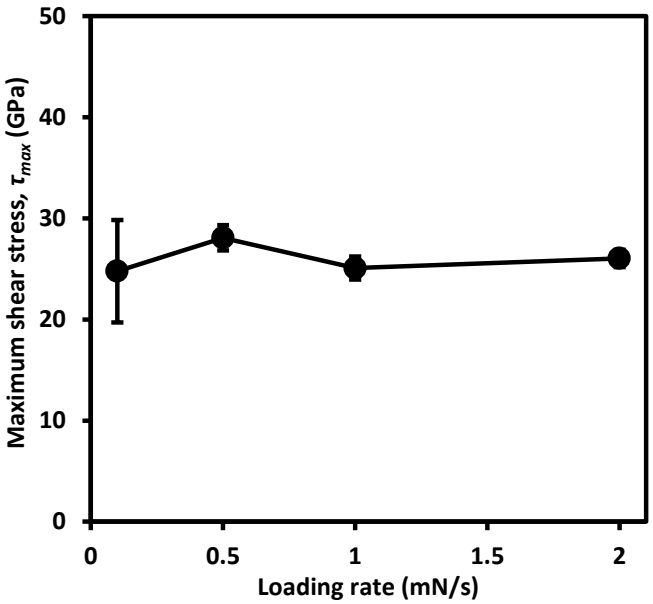


Fig. 4.26. Maximum shear stress ($\tau_{max}$) versus loading rate for sintered Y-TZP. Each data point is the mean value of six repeated indentations; the error bars correspond to ± one standard deviation for the six repeats.

Fig. 4.26 demonstrates that loading rate effect on the maximum shear stress was insignificant indicating that the transition from elastic deformation to plastic deformation was independent of the loading rate for sintered Y-TZP. This means that regardless of the amount of compressive stress applied within the loading rate region investigated, the maximum shear stress generated was constant. The mean and standard deviation (26 ± 3 GPa) of the maximum shear stress at all loading rates reflects that the constancy of the induced maximum shear stress rationalizes why the elastic displacement in Fig. 4.11(a) was constant at all loading rates. Further, the maximum shear stress must be greater than the theoretical shear strength, $\tau_{theor}$, to induce plastic deformation. The material theoretical shear strength can be calculated by (Shaw, 1995):

$$\tau_{theor} = \frac{G}{2\pi} \tag{4.42}$$

where $G$ is the shear modulus expressed by (Callister, 2007):

$$G = \frac{E}{2(1+\nu)} \tag{4.43}$$

where $E$ is the Young's modulus and $\nu$ is the Poisson's ratio. By using $\nu = 0.3$ and the Young's moduli extracted at different loading rates (Alao and Yin, 2014a), the shear modulus for zirconia was 65 ± 12 GPa independent of the loading rate. This value agrees with the shear modulus extracted for sintered TZP (Selçuk and Atkinson, 1997). Based on the $G$ values, the theoretical shear strength estimated for zirconia was 7 ± 1 GPa much lower than the maximum

shear stress. Therefore, sufficient shear stresses were induced by the applied load and loading rates in nanoindentation to initiate the plastic deformation for sintered Y-TZP.

The decrease in plastic displacement (Fig. 4.11(a)) with the increased loading rate can be ascribed to the strain hardening behavior of sintered Y-TZP (Alao and Yin, 2014a). Strain hardening is a reflection of accumulating dislocations inside the material due to the increased strain leading to increased dislocation density and reduced distance between dislocations (Callister, 2007). Therefore, the strain hardening behaviour in sintered Y-TZP at high loading rates weakly hinders the dislocation motion due to the presence of other dislocations since the interactive strains between two dislocations are repulsive. This hindrance in the dislocation motion led to the reduced plastic deformation at higher loading rates. To our best knowledge, this is the first work which quantitatively showed the reduction in the plastic deformation when strain hardening occurred in sintered Y-TZP. This observation reconfirms the assertion that sintered Y-TZP behaves like steel (Garvie et al., 1975).

The dependence of the plastic displacement on the loading rate can be hypothesized that a small material volume can be removed at a high deformation rate by sharp abrasives. During machining, the material removal is distributed over many abrasives with geometrically undefined cutting edges. Each cutting edge induces its own normal force on the material and the induced-normal force per grit is responsible for plastic deformation displacements of the material (Murtagian et al., 2010). Further, this normal force per grit in abrasive machining is likened to the peak load in indentation studies (Murtagian et al., 2010). The indentation response of sintered Y-TZP at different loading rates in Fig. 4.11(a) is schematically shown in terms of the indentation-induced sub-surface elastic and plastic displacements in Fig. 4.27. The plastic deformation depth is linearly correlated to the undeformed chip thickness in grinding (Murtagian et al., 2010). Therefore, as the plastic deformation depth reduces due to increasing loading rate in Fig. 4.27, the undeformed chip thickness would decrease. The decrease in the undeformed chip thickness correspondingly leads to a decrease in the material removal volume. Thus, the smallest material volume is anticipated to be removed at the highest deformation rate studied in this work. Therefore, high deformation rate favours small-scale material removals like ductile regime machining and polishing. This assertion complements our previous study where it was postulated that a small volume material can be removed at a high deformation rate (Alao and Yin, 2014a).

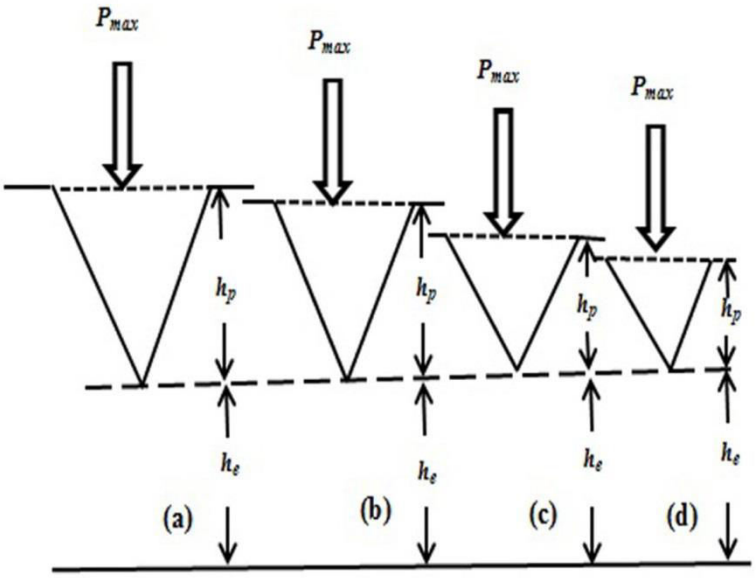


Fig. 4.27. Schematic illustration of the indentation-induced subsurface elastic ($h_e$) and plastic ($h_p$) displacements at a peak load ($P_{max}$) of 10 mN and loading rate of (a) 0.1 mN/s, (b) 0.5 mN/s, (c) 1 mN/s, and (d) 2 mN/s.

The dominance of the normalized absorbed at higher loading rates in Fig. 4.16 can be attributed to the occurrence of strain hardening. This is because at higher loading rates the indentation absorbed energy would consist of work spent in both plastic deformation and strain hardening. The loading rate-independent normalized absorbed energy of sintered Y-TZP at all loading rates was 0.58 ± 0.16. This reconfirms that sintered Y-TZP exhibits partial plastic property. Further, the loading rate-independent resistance to machining-induced cracking in Fig. 4.21 reflects a characteristic machining property for sintered Y-TZP which is 445.44 ± 106.32 J/m$^2$ at all loading rates. This value is higher than the resistances to machining-induced cracking of brittle materials, such as SiC, glass, $Al_2O_3$, and MgO, but less than those of quasi-plastic materials, such as magnesia partially stabilized zirconia and graphite (Sakai and Nowak, 1992). The resistance to machining-induced cracking of sintered Y-TZP studied is also higher than that of pre-sintered Y-TZP (132.74 ± 15 J/m$^2$) due to the higher fracture toughness of the former than the latter. This suggests that sintered Y-TZP can resist mechanical damage than pre-sintered Y-TZP. However, sintered Y-TZP can be less machinable than pre-sintered Y-TZP because it possesses higher resistance to plasticity and lower normalized absorbed energy than pre-sintered Y-TZP.

## 4.5 Conclusions

This study has advanced our understanding of the mechanical behavior of LMGC, sintered and pressable LDGC, pre-sintered and sintered Y-TZP at the nanoscale using nanoindentation and Sakai and Sakai–Nowak models. The resistances to plasticity of LMGC and sintered LDGC revealed significant loading rate dependence and their intrinsic resistances to plasticity based on the modified strain rate sensitivity model were 396.83 GPa and 326.72 GPa respectively. However, the resistances to plasticity of pressable LDGC, pre-sintered and sintered Y-TZP were loading rate independent with means and standard deviations of 62.54 ± 30.91 GPa, 3.82 ± 1.92 GPa and 43.82 ± 9.59 GPa respectively. Consequently, LMGC revealed the highest resistance to plasticity followed by sintered LDGC, pressable LDGC and sintered Y-TZP. Pre-sintered Y-TZP showed the lowest resistance to plasticity ranking it the most quasi-plastic material while LMGC was the most brittle material.

The dominance of the elastic displacement/deformation component of LMGC over its plastic displacement/deformation component at all loading rates indicates the elastic deformation mechanism for the material which reconfirms its high brittleness. This was attributed to the occurrence of higher elastic strain energies at all loading rates than the absorbed energies. For sintered and pressable LDGC, the deformation mechanisms were dynamic with the plastic displacements/deformation components dominating at low loading rates but at higher loading rates, the elastic displacements/deformation components dominated. This behavior was also ascribed to the dominance of their absorbed energies and elastic energies at low and higher loading rates respectively. The decrease in the plastic displacements of LMGC, sintered and pressable LDGC with increase in loading rate was attributable to the strain hardening behavior. The increase in elastic displacement of pre-sintered Y-TZP with the loading rate was due to lower shear stresses developed and the higher elastic strain energy at higher loading rates. The decrease in plastic displacement with the loading rate of pre-sintered Y-TZP was a consequence of higher shear stresses and lower absorbed energy at higher loading rates. At all loading rates, plastic displacements/deformation components dominated over elastic displacements/deformation components, reconfirming the quasi-plastic nature of pre-sintered Y-TZP. The elastic displacement of sintered Y-TZP was loading rate independent because of the constant maximum shear stress generated at all loading rates. Its plastic displacement decreased with the loading rate because of the strain hardening behavior which led to the consumption of more energy, resulting in slightly increased absorbed energy. At lower loading rates, the elastic and the plastic deformation components were 50% each whereas at higher loading rates, the elastic deformation component slightly dominated, indicating the dynamic deformation mechanism for sintered Y-TZP.

Normalized indentation absorbed energies of studied materials were loading rate independent. Consequently, the normalized absorbed energies of LMGC, sintered and pressable LDGC, pre-sintered and sintered Y-TZP were 38 ± 15%, 45 ± 17%, 48 ± 13%, 75 ± 8% and 58 ± 16% respectively. Again, pre-sintered Y-TZP revealed the highest absorbed energy followed by sintered Y-TZP, pressable LDGC, sintered LDGC and then LMGC. Based on this index, pre-sintered Y-TZP is also ranked the most ductile-like material making it more machinable than others while LMGC was the most brittle material. In addition, the resistances to machining-induced cracking of LMGC, sintered and pressable LDGC, pre-sintered and sintered Y-TZP were 17.69 ± 7.32 $J/m^2$, 74.32 ± 19.92 $J/m^2$, 112.76 ± 33.17 $J/m^2$, 132.74 ± 15 $J/m^2$ and 445.44 ± 106.32 $J/m^2$ respectively. This ranks sintered Y-TZP the most resistant to machining-induced cracking material followed by pre-sintered Y-TZP, pressable LDGC and sintered LDGC while LMGC was least resistant to machining-induced cracking.

# Chapter 5

# Surface Quality of CAD/CAM-Milled and Surface-Treated LMGC/LDGC

## 5.1 Introduction

For three decades, CAD/CAM systems have been introduced to dentistry (Miyazaki et al., 2009; 2011; 2013; Mörmann 2006; Rekow 2006). They have capabilities to efficiently produce the entire spectrum of restorations made of ceramics, polymers, metals and composites from inlays/onlays/veneers to crowns and multi-unit bridges at dental clinical chairside or laboratories (Andersson and Odén, 1993; Beuer et al., 2009; Luthardt et al. 2002b; Miyazaki et al., 2009; Mörmann, 2006; Rekow 2006; Rekow and Thompson, 2005; Strub et al., 2006; Yin et al., 2006). These systems have enabled the endurance of the uniform material quality and the standardization of dental restoration processes, reducing manufacturing costs and shortening fabrication times (Wittneben et al., 2009). In particular, they can be used to shape high-strength dental ceramics, such as alumina, LDGC and Y-TZP in posterior regions (Beuer et al. 2008; Miyazaki et al., 2009).

LDGC has the aesthetic appearance and matches well with natural teeth (Anusavice and Zhang, 1997; ElBatal et al., 2009; Höland et al., 2000). Its restorations are often made from LMGC in CAD/CAM milling processes. The milled LMGC blocks are subsequently sintered to ensure restorations to be fully phase-transformed to LDGC for high strength and toughness (Höland et al., 2000). The high strength and toughness of LDGC arise from layered and interlocked lithium disilicate crystals which mismatch the glassy phase with respect to thermal coefficients and elastic moduli (Apel et al., 2008; Denry, 2013; Denry and Holloway, 2010). These result in compressive stresses in LDGC, which can deflect advancing cracks (Alao and Yin, 2015a; Apel et al., 2008; Denry, 2013; Denry and Holloway, 2010; Serbena and Zanotto, 2012). However, the high strength of LDGC and the brittleness of its glassy phase make LDGC very difficult to machine using chairside or labside CAD/CAM-milling systems. Thus, CAD/CAM-milling of weaker LMGC containing metastable lithium metasilicate crystals becomes practical (Alao and Yin, 2015a; Denry, 2013). CAD/CAM-processed single LDGC restorations achieved 100% cumulative survival rate up to two years (Fasbinder et al., 2010) and 96.3% after four years according to the Kaplan-Meier survival analysis (Reich and Schierz, 2013). In contrast, the survival rate for three-unit LDGC partial fixed dentures was 93% up to four years (Reich et al., 2014).

During the CAD/CAM milling of LGMC, surface and subsurface flaws can be easily induced because of the inherent brittle nature of the material and the application of diamond abrasive tools (Denry, 2013; Rekow et al., 2011; Rekow and Thompson, 2005). In milling, diamond abrasives make numerous and simultaneous indentations and scratches on the LGMC material, producing residual damage in the material. The type and extent of damage in CAD/CAM process depend on the machining conditions, microstructure and physical properties, and the coarseness of diamond grains (Dong et al., 2000; Maksoud et al., 1999; Rekow and Thompson, 2005; Sindel et al., 1998; Xu and Jahanmir, 1998; Yin et al. 2007; Song et al., 2016). Consequently, the machining-induced flaws, which may not be healed in the subsequent sintering process, can compromise the strength of the LDGC restorations and shorten their lifespans. Thus, it is critical to minimize the machining-induced flaws in the CAD/CAM-milled LMGC by understanding the indentation mechanics and machining behavior of the material. Therefore, understanding the fundamental responses of LMGC to CAD/CAM milling process is important for restorative quality.

Following the sintering process, LDGC restorations require polishing and glazing (Höland et al., 2006b). Polishing is used for delivering an adequate surface texture to allow for adequate light reflection while glazing is used to seal pores opened on the ceramic surface during the sintering process for bright and smooth surfaces with higher fracture resistance (Boaventura et al., 2013). Polishing and glazing was also applied to CAD/CAM-milled LMGC before sintering (Lin et al., 2012). Hence, sintering, glazing and polishing processes can be applied in an arbitrary manner to CAD/CAM-milled LMGC surface in laboratories or clinics. However, no study has investigated characteristics of CAD/CAM-milled LMGC under different post-machining surface preparation. Therefore, it is highly essential to systematically study the responses of CAD/CAM-milled LMGC and subsequent sintering, glazing and polishing conditions.

Surface quality plays a critical role in controlling the quality and wear and fatigue performance of dental restorations (Denry, 2013; Rekow and Thompson, 2005; Rekow et al., 2011), which includes mechanical properties, phase transformation, surface roughness and morphology (Ulutan and Ozel, 2011). Surface roughness also critically affects cell adhesion, proliferation and protein adsorption (Brunot-Gohin et al., 2013). Intaglio surfaces of restorations are often roughened to improve bonding to adhesives and the rougher intaglio surfaces the better the adhesions (Brunot-Gohin et al., 2013). Occlusal surfaces must be contoured and finished to a high surface luster to reduce fracture risk, bacterial plaque accumulation, tooth stains, and wear on antagonist/adjacent teeth (De Jager et al., 2000; Jefferies, 2007; Kou et al., 2006; Steiner et al., 2015; Whitehead et al., 1995). Further, surface roughness of machined ceramic surfaces can

be used to predict their subsurface damage depth (Li et al., 2008). Studies have reported the surface quality of adjusted LDGC using dental handpieces and diamond burs (Song et al., 2016) and surface-modified LDGC in glazing, grinding and polishing (Boaventura et al., 2013; Kou et al., 2006; Tholt et al., 2006). However, little is known towards the surface quality of CAD/CAM-milled LMGC surfaces subjected to subsequent sintering, glazing and polishing processes.

This chapter aimed to investigate the surface quality of CAD/CAM-milled LMGC and subsequent sintered, polished and glazed LMGC/LDGC surfaces with respect to phase transformation, surface roughness and morphology, and removal mechanisms. X-ray diffraction was used to analyse crystalline phases and phase transformations. Surface roughness was measured in terms of average surface roughness ($R_a$) and maximum height ($R_z$) using a desk-top SEM-assisted morphology analytical software. Scanning electron microscopy (SEM) was applied to analyse removal mechanisms, surface damage and morphology. Finally, an optimal fabrication process for LDGC restorations was proposed to achieve the improved surface quality.

## 5.2 Experimental Procedures

### *5.2.1 Materials*

LMGC blocks of 14.5 mm × 12.4 mm × 18 mm (IPS e.max CAD, Ivoclar Vivadent, Liechtenstein) were selected in this study, which are often used in dental CAD/CAM for all-ceramic LDGC restorations. The chemical composition, microstructure and properties of the LMGC have been reported elsewhere (Alao and Yin, 2015a). Briefly the LMGC can be formed by melting a base glass at 1450 °C consisting of 69.3 wt% $SiO_2$, 15.4 wt% $Li_2O$, 6.05 wt% $K_2O$, 5.28 wt% ZnO and 3.84 wt% $P_2O_5$ and annealing at 450 °C (El-Meliegy and van Noort, 2012). The subsequent annealing of the material at 480°C for 1 h results in precipitated lithium metasilicate crystals (El-Meliegy and van Noort, 2012). The LMGC consists of about 40% lithium metasilicate crystals embedded in a glassy phase with the grain size of approximately 0.5–1 μm (Alao and Yin, 2015a). It has the sufficient biaxial strength of 130 ± 30 MPa, fracture toughness of 1 ± 0.1 MPa $m^{1/2}$ and Vicker's hardness of 5.4 ± 0.1 GPa (Alao and Yin, 2015a).

### *5.2.2 Chairside CAD/CAM Milling*

LMGC blocks were milled using a dental CAD/CAM system (CEREC MC XL, Sirona, Germany) with a step bur 12 S (Ref 6240167, Sirona, Germany) and a cylindrical pointed bur

12 S (Ref 6240159, Sirona, Germany). The step bur consists of a steel shank with three cutting faces with lengths of 3 mm, 3mm, and 6 mm, and diameters of 2.1 mm, 1.7 mm and 1.3 mm, respectively, as shown in Fig. 5.1(a). The cylindrical pointed bur comprises of a steel shank and two cutting faces with lengths of 4 mm and 8 mm and diameters of 2.1 mm and 1.8 mm, respectively, as shown in Fig. 5.1(b). The two burs containing electro-plated diamond abrasives are used to generate flat surfaces as schematically shown in Fig. 5.1(c) in this investigation. The wet milling was conducted following the program recommended by the manufacturer, which simulates surface grinding of crowns, the most challenging step in CAD/CAM process (Luthardt et al., 2004). A new step bur was gold-coated and then observed using scanning electron microscopy (SEM, Jeol JSM5410V, Japan). Fig. 5.2(a) shows the scanning electron micrograph of the step bur morphology. Fig. 5.2(b) demonstrates various abrasive cutting edges on the bur at a higher magnification, clearly revealing the average abrasive grit size of approximately 50–60 μm.

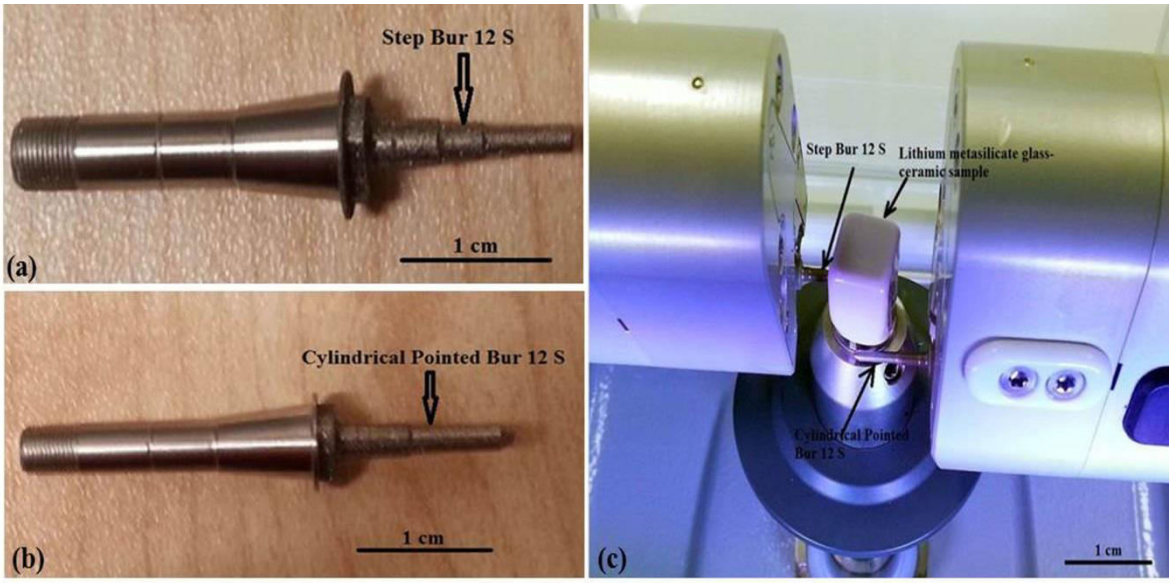


Fig. 5.1. Optical images of (a) a step bur 12 S, (b) a cylindrical pointed bur 12 S, and (c) the usage of the two burs in the chairside CAD/CAM milling system for a LMGC block.

### *5.2.3 Surface Preparation*

After milling, samples were cleaned in acetone and treated under different sintering, polishing and glazing conditions simulating various fabrication processes in clinical practice. These fabrication processes were designated as CAD/CAM-milled, CAD/CAM-polished, CAD/CAM-sintered, CAD/CAM-polished-sintered, CAD/CAM-sintered-polished, CAD/CAM-sintered-glazed, CAD/CAM-polished-sintered-glazed processes as schematically shown in Fig. 5.3.

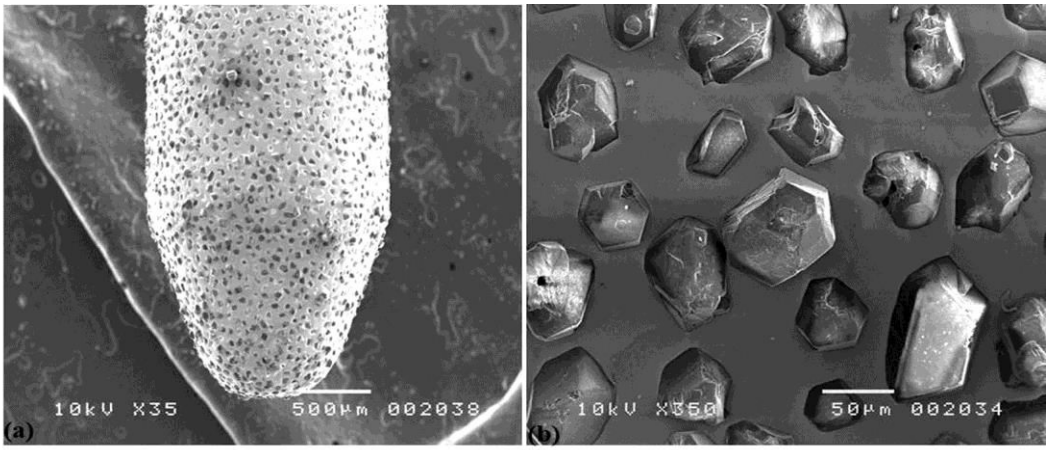


Fig. 5.2. SEM micrographs showing (a) the morphology of the step diamond bur 12 S, (b) diamond abrasives on the bur with the average grit size of approximately 50–60 µm.

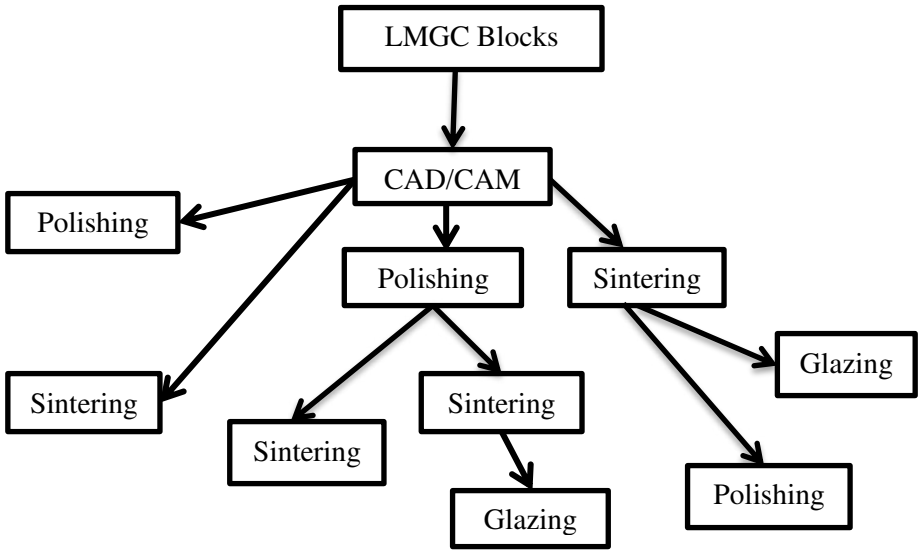


Fig. 5.3. Schematic diagram of all fabrication processes.

Sintering of the milled LMGC samples was carried out in a programed dental furnace (P300, Ivoclar Vivadent, Liechtenstein). The process started the sintering at a stand-by temperature of 403 °C from room temperature. Then, the samples were heated to 770 °C at a heating rate of 60 °C/min and held at the temperature for 10 minutes. After that, they were heated again to 850 °C at a heating rate of 30 °C/min and held for another 10 minutes before cooling to 700 °C. Finally, they were cooled to room temperature.

Polishing was conducted using a clinical dental handpiece with a grey white rubber diamond bur (Exa Cerapol UM, ISO 658.900.114.525.060, Edenta, Switzerland) operated by an experienced dental clinician. The bur contains dispersed diamond abrasives embedded in a

softer elastic matrix (Jefferies, 2007) and is used for intermediate finishing, eliminating scratches and smoothening surfaces recommended by the manufacturer. Fig. 5.4 shows the SEM micrograph of the grey-white bur morphology, revealing the average diamond grit size of approximately 60–70 µm, belonging to the medium-grit-size class of dental burs. Samples were polished at a force of approximately 1 N with the bur rotating at 5,000 rpm to obtain clinically accepted surface quality.


Fig. 5.4. SEM micrograph of the morphology of the grey white rubber diamond bur with the average diamond grit size of approximately 80 µm.

Glazing was conducted by firing samples without the addition of glass beads in the same programed dental furnace for sintering. The process starts the heating of samples at a stand-by temperature of 403 °C. Then samples were reheated to 820 °C at a heating rate 90 °C/min and held for 10 minutes. Then they were heated to 840 °C at 30 °C/min heating rate and holding for 7 minutes. Finally, samples were cooled to 700 °C and then to room temperature.

### *5.2.4 Surface Characterization*

All processed surfaces under each condition were x-ray scanned using an x-ray diffractometer (D/MAX-2500, Rigaku, Japan) to obtain x-ray diffraction patterns. The Cu Kα radiation with 0.15406 nm wave length was used to analyze crystalline phases of each surface. All scans were performed from 10–80° in the 2θ range at 0.02° scanning step to determine the nature of different phases.

Surface roughness for all processed surfaces was characterized in terms of the average surface roughness, $R_a$, and the maximum roughness, $R_z$ which are the most commonly used in practice (De Chiffre et al., 2000) with desktop SEM-assisted morphology analytical software (Phenom-World BV, Netherlands). The software draws lines perpendicular to machining traces and

calculates a profile for each measurement line. Fig. 5.5(a) shows the 3D surface roughness measurement process where measurements were made across three profiles and their average values computed. The cut-off and evaluation lengths were 0.2 mm and 1 mm respectively. Fig. 5.5(b) shows the 2D surface morphology of Fig. 5.5(a). On each surface, three roughness measurements were performed to obtain mean values and standard deviations.

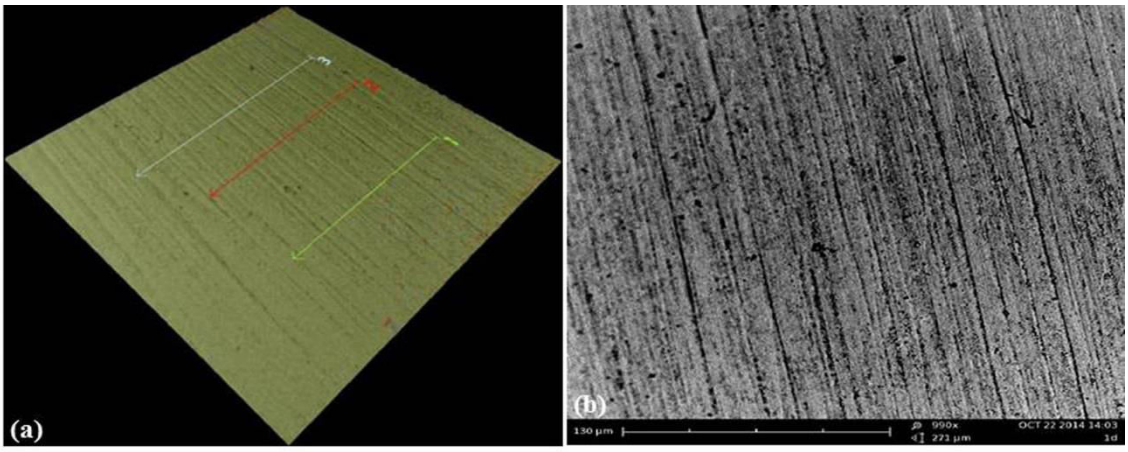


Fig. 5.5. A demonstration of surface roughness measurement using the desktop SEM-assisted morphology analytical software, in which (a) 3D surface roughness measurement with three profiles to be analyzed and (b) 2D surface morphology of (a).

Each surface fabricated in all processes was gold-coated and viewed under SEM (JEOL JSM 5410LV, Tokyo, Japan) to study surface damage, morphology and removal mechanisms.

### *5.2.5 Statistical Analysis*

One-way analysis of variance (ANOVA) was conducted at 5% confidence interval to examine the significance of fabrication processes on the average surface roughness, $R_a$, and the maximum height, $R_z$. Paired $t$ test was also performed at 5% confidence to examine the influence of each surface treatment on surface roughness values.

## 5.3 Results

### *5.3.1 X-ray Diffraction*

X-ray diffraction patterns for all fabrication processes are shown in Fig. 6 in comparison with an un-milled LMGC block from the manufacture. Fig. 5.6(a) shows the x-ray diffraction pattern of the CAD/CAM-milled LMGC surface, which is nearly identical to x-ray patterns of the un-

milled LMGC surface and the CAD/CAM-polished surface. This indicates that CAD/CAM milling and CAD/CAM-polishing did not cause the phase transformation. The main crystalline phase in Fig. 5.6(a) is lithium catena-silicate ($Li_2SiO_3$) or lithium metasilicate crystals. This phase is consistent with the XRD patterns of LMGC published by Alemi et al. (2013) and confirms to the Joint Committee on Powder Diffraction Standards (JCPDS)-file No. 30-0766 for LMGC by Thieme and Rüssel (2015).

Fig. 5.6(b) shows the x-ray diffraction pattern of the CAD/CAM-polished-sintered surface, which is nearly identical to the x-ray diffraction patterns of the CAD/CAM-sintered and CAD/CAM-sintered-polished surfaces. There are lithium disilicate ($Li_2Si_2O_5$) crystals in these materials. These x-ray patterns confirm to lithium disilicate crystals in the JCPDS-file No. 30-0766 (Thieme and Rüssel, 2015). This also reveals that the sintering of CAD/CAM-milled LMGC prior to polishing or post-polishing completely transformed lithium catena-silicate or lithium metasilicate crystals to lithium disilicate crystals.

Fig. 5.6(c) shows the x-ray diffraction pattern of the CAD/CAM-polished-sintered-glazed surface, which is also approximately identical to the x-ray diffraction pattern for the CAD/CAM-sintered-glazed surface. Lithium disilicate crystals are found as the main phase in these two surfaces. This indicates that the sintering of LMGC produced stabilized LDGC and glazing after sintering did not alter crystal phases in polished or unpolished LDGC materials.

### *5.3.2 Surface Roughness*

Fig. 5.7 shows the results of the arithmetic mean roughness, $R_a$, and maximum roughness, $R_z$, versus different surface treatment. The CAD/CAM-milling process produced the coarsest surface roughness with $R_a$ 1.11 ± 0.09 µm and $R_z$ 6.46 ± 0.61 µm while the CAD/CAM-polished-sintered yielded the smoothest surface with $R_a$ 0.12 ± 0.08 µm and $R_z$ 0.89 ± 0.26 µm. The CAD/CAM-polished process produced the moderate roughness with $R_a$ 0.76 ± 0.08 µm and $R_z$ 4.03 ± 0.27 µm, which is similar to the surface with $R_a$ 0.70 ± 0.1 µm; $R_z$ 3.75 ± 0.09 µm produced in CAD/CAM-sintered-glazed process. The improved surfaces were generated in the CAD/CAM-sintered process with $R_a$ 0.58 ± 0.07 µm and $R_z$ 0.89 ± 0.26 µm). It was followed by the CAD/CAM-sintered- polished process ($R_a$ 0.42 ± 0.12 µm; $R_z$ 2.54 ± 0.88 µm), the CAD/CAM-polished-sintered-glazed process ($R_a$ 0.25 ± 0.01 µm; $R_z$ 1.55 ± 0.08 µm).

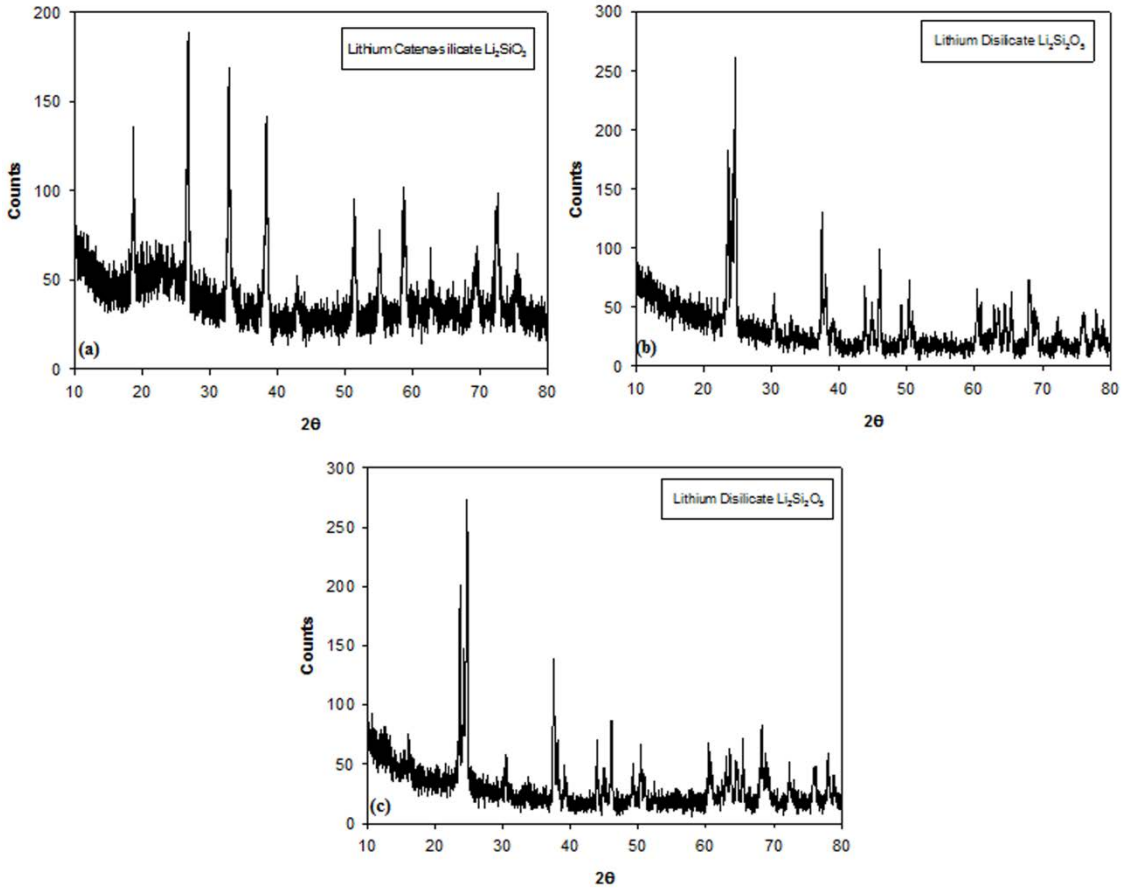


Fig. 5.6. X-ray diffraction patterns of (a) the CAD/CAM-milled surface, which is nearly identical to those of un-milled LMGC and CAD/CAM-polished surfaces, (b) the CAD/CAM-polished-sintered surface, which is approximately identical to those of the CAD/CAM-sintered and CAD/CAM-sintered-polished surfaces, and (c) the CAD/CAM-polished-sintered-glazed, which is approximately identical to that of the CAD/CAM-sintered-glazed surface.

Table 5.1 reveals the result of the one-way ANOVA to determine the influence of different processes on the arithmetic mean roughness, $R_a$. It indicates that $R_a$ was significantly affected by different fabrication processes (ANOVA, $p < 0.05$). Similar analysis was conducted to the maximum roughness height $R_z$, also revealing the significant result (ANOVA, $p < 0.05$).

Table 5.2 shows an example of the paired *t*-test for the significant difference of the arithmetic mean roughness $R_a$ values between the CAD/CAM-milling and CAD/CAM-polished surfaces. It indicates that polishing significantly reduced the $R_a$ values ($p < 0.05$). The same paired *t*-test was also conducted to compare the maximum roughness height $R_z$ values for the two surfaces.

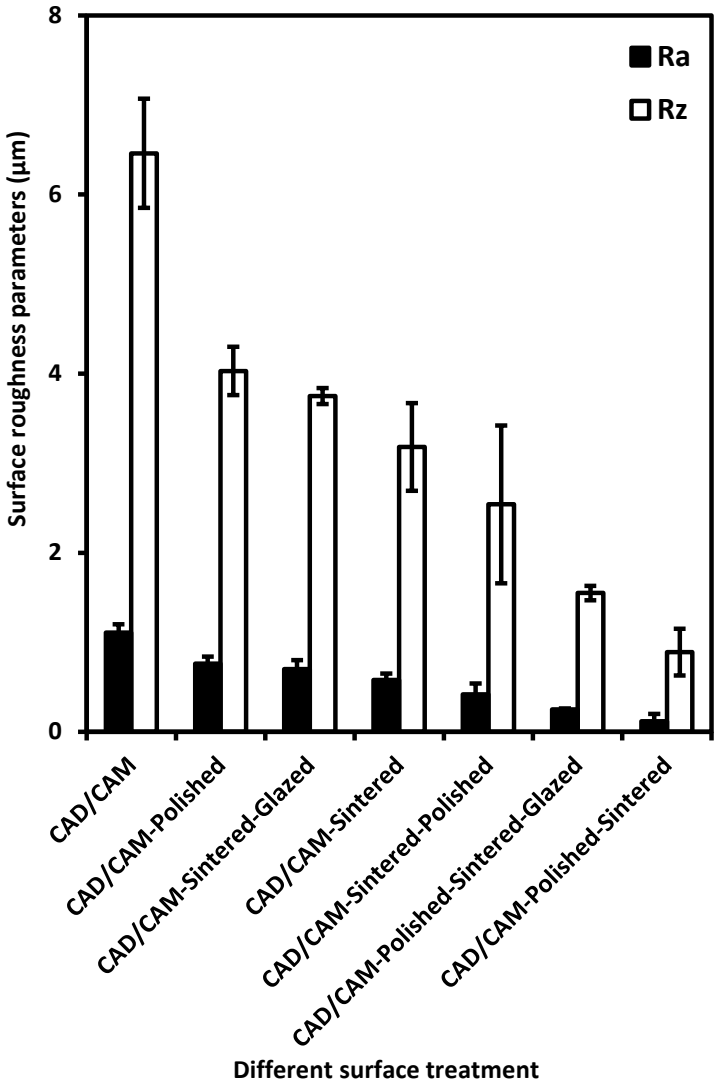


Fig. 5.7. Arithmetic mean roughness, $R_a$, and maximum roughness, $R_z$, versus different surface treatment. Each data point is the mean value of three profiles on each processed surface; the error bars correspond to ± one standard deviation for the three profiles.

Table 5.1. Result of the one-way ANOVA for $R_a$ with respect to different fabrication processes.

| Source of Variation | SS | Df | MS | F | *p*-value | F crit |
|---|---|---|---|---|---|---|
| Between fabrication processes | 2.09 | 6 | 0.34 | 47.02 | 0.00 | 2.85 |
| Within fabrication processes | 0.10 | 14 | 0.01 | | | |
| Total | 2.12 | 20 | | | | |

Table 5.3 summarizes all *p*-values from the paired *t*-tests for $R_a$ and $R_z$ parameters for all fabrication processes. Comparing the CAD/CAM milling process with the CAD/CAM-polishing and CAD/CAM-sintering, both polishing and sintering respectively improved the roughness $R_a$ and $R_z$ values obtained in milling ($p < 0.05$). Further sintering of the polished

surface also significantly reduced both $R_a$ and $R_z$ values ($p < 0.05$). However, further polishing of the sintered surface only significantly improved the $R_a$ values ($p < 0.05$) and did not significantly change $R_z$ values ($p > 0.05$). Glazing did not significantly improve either $R_a$ ($p > 0.05$) or $R_z$ ($p > 0.05$) obtained following the sintering and the polishing-sintering processes.

Table 5.2. An example of a paired *t*-test for $R_a$ values between CAD/CAM-milled and CAD/CAM-polished processes.

| | **CAD/CAM-milled** | **CAD/CAM-polished** |
|---|---|---|
| Mean | 1.11 | 0.76 |
| Variance | 0.01 | 0.01 |
| Observations | 3.00 | 3.00 |
| Pearson correlation | 0.73 | |
| Hypothesized mean difference | 0.00 | |
| Degree of freedom | 2.00 | |
| *t* statistics | 9.80 | |
| *p* (T ≤ t) one-tail | 0.01 | |
| *t* critical one-tail | 2.92 | |
| *p* (T ≤ t) two-tail | 0.01 | |
| *t* critical two-tail | 4.30 | |

Table 5.3. Summary of the *p*-values of all paired *t*-tests for $R_a$ and $R_z$ values of all paired fabrication processes.

| **Surface treatments** | ***p*-value** | |
|---|---|---|
| | **$R_a$ (µm)** | **$R_z$ (µm)** |
| CAD/CAM-milled versus CAD/CAM-polished | $p < 0.05$ | $p < 0.05$ |
| CAD/CAM-milled versus CAD/CAM-sintered | $p < 0.05$ | $p < 0.05$ |
| CAD/CAM-polished versus CAD/CAM-polished-sintered | $p < 0.05$ | $p < 0.05$ |
| CAD/CAM-sintered versus CAD/CAM-sintered-polished | $p < 0.05$ | $p > 0.05$ |
| CAD/CAM-sintered versus CAD/CAM-sintered-glazed | $p > 0.05$ | $p > 0.05$ |
| CAD/CAM-polished-sintered versus CAD/CAM-polished-sintered-glazed | $p > 0.05$ | $p > 0.05$ |

### *5.3.3 Surface Morphology*

Fig. 5.8 shows the milled LMGC surface morphology in the chairside CAD/CAM process. Fig. 5.8(a) shows the machining grooves and traces scratched by diamond abrasives, on which

localized fractures and pulverized/smeared areas caused by shear bands are also formed. Fig. 5.8(b) shows details of irregular fractures and cracks on the milled surface. Fig. 5.8(c) shows higher-magnification details of pulverized/smeared areas where microchips accumulated together on the highly fractured areas. All these SEM micrographs in Fig. 5.8 demonstrate that brittle fracture mode was the dominant material removal mechanism for the CAD/CAM milling of LMGC. Frequent and repeated fractures also caused crystal and glass matrix pulverization, inducing extensive surface defects.

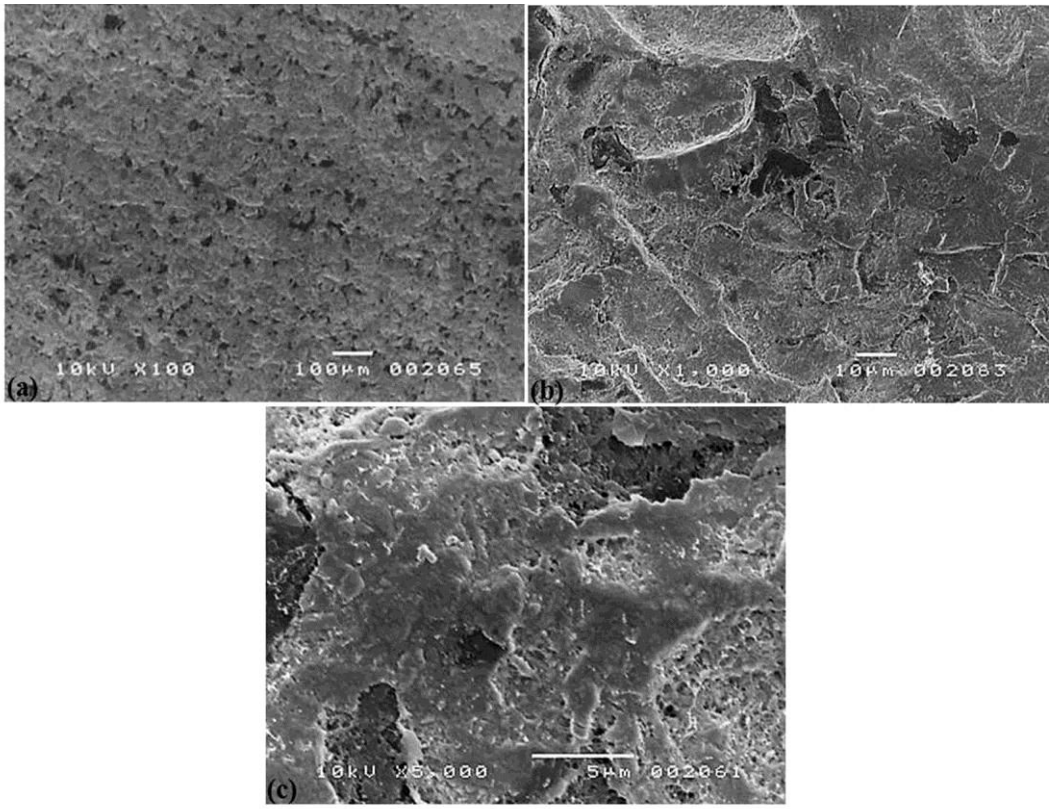


Fig. 5.8. SEM micrographs of the CAD/CAM LMGC surface showing (a) milling traces and fractures and shear band-induced pile-ups leading to the material pulverization, (b) details of surface fractures, and (c) details of pulverized/smeared areas.

Fig. 5.9 shows the LMGC surface morphology produced in the CAD/CAM-polished process. Fig. 5.9(a) shows that the rough milled surface with machining traces and scratches was smoothened, indicating that polishing diminished large scale fractured areas and removed machining traces/scratches. Residual pulverized debris were also observed on the polished surface. Fig. 5.9(b) shows that the surface mainly consisted of glassy networks.

Fig. 5.10 shows the LDGC surface morphology produced in the CAD/CAM-sintered process, on which the large scale fractures on the milled surface in Fig. 5.8 disappeared. Fig. 5.10(a)

shows the bulging of the milled surface due to the lithium catena-silicate or metasilicate–lithium disilicate transformation by the sintering process. The surface looks much smoother than the milled surface, indicating that the sintering-induced phase transformation significantly improved surface roughness. Fig. 5.10(b) shows details of the bulged surface on which microcracks are observed, indicating the sintering cannot completely heal microcracks produced in the CAD/CAM milling.

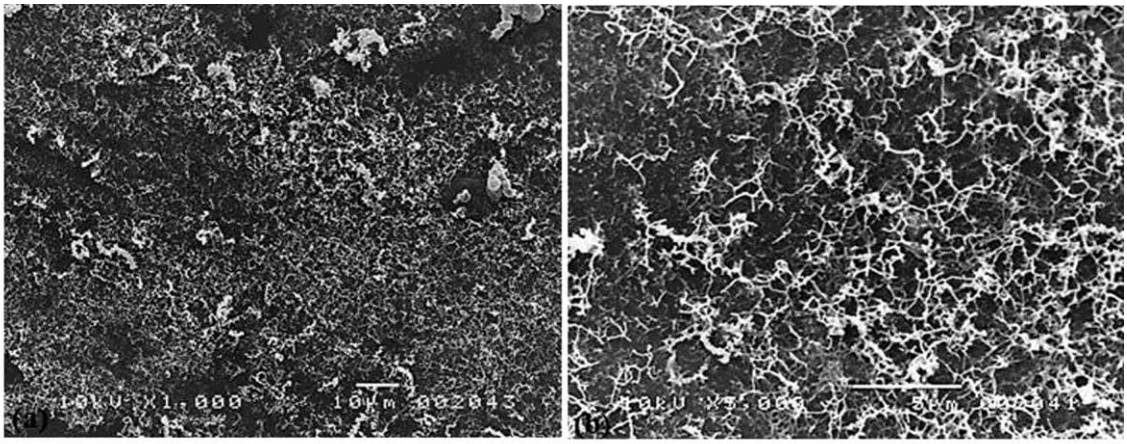

Fig. 5.9. SEM micrographs of the CAD/CAM-polished LMGC surface revealing (a) smoothened milling traces, residual debris and (b) details of glassy networks.

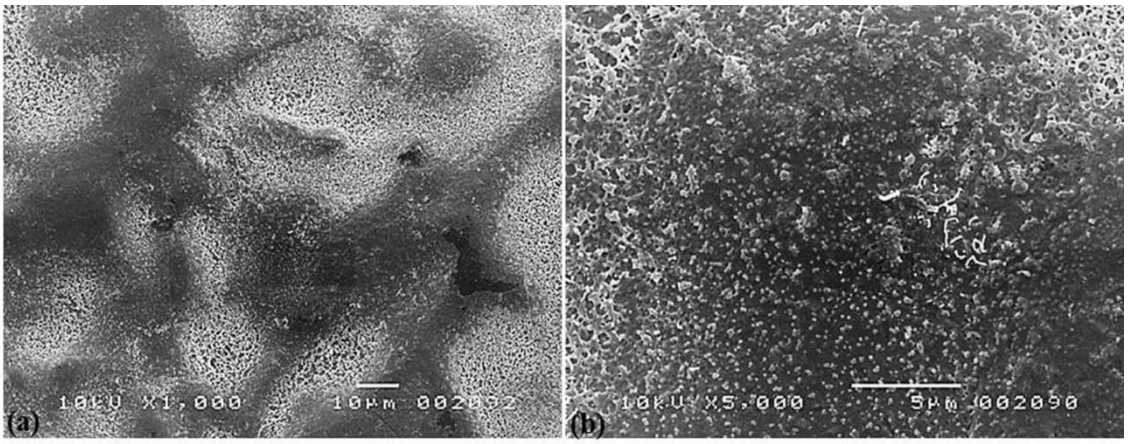


Fig. 5.10. SEM micrographs of the CAD/CAM-sintered LDGC surface showing (a) the bulging of the milled surface and (b) details of the bulged surface.

Fig. 5.11 shows the LDGC surface morphology generated in the CAD/CAM-sintered-glazed process. The glazing-recovery of the bulging of the milled surface due to the lithium metasilicate–lithium disilicate transformation in sintering was observed. Compared with the sintered surface shown in Fig. 5.10, the glazed surface looks smoother. Fig. 5.11(a) shows the

residual pulverized debris in the form of very fine particles on the surface. Fig. 5.11(b) demonstrates details of these powdered debris at the micro or submicro scales.

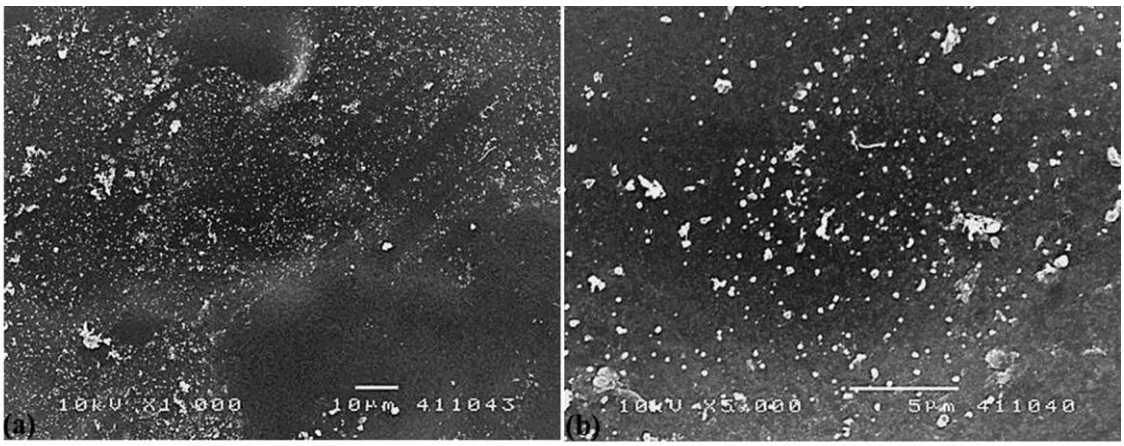


Fig. 5.11. SEM micrographs of the CAD/CAM-sintered-glazed LDGC surface demonstrating (a) residual pulverized debris and (b) details of these powdered debris.

Fig. 5.12 shows the LDGC surface morphology of the CAD/CAM-sintered-polished process. Fig 5.12(a) shows the polishing traces, scratches and fractures on the surface, indicating the polishing after sintering did not significantly improve the poor surface produced in the CAD/CAM milling. Fig. 5.12(b) demosntrates that localised fractures, enlarged debris and smeared areas are also produced.

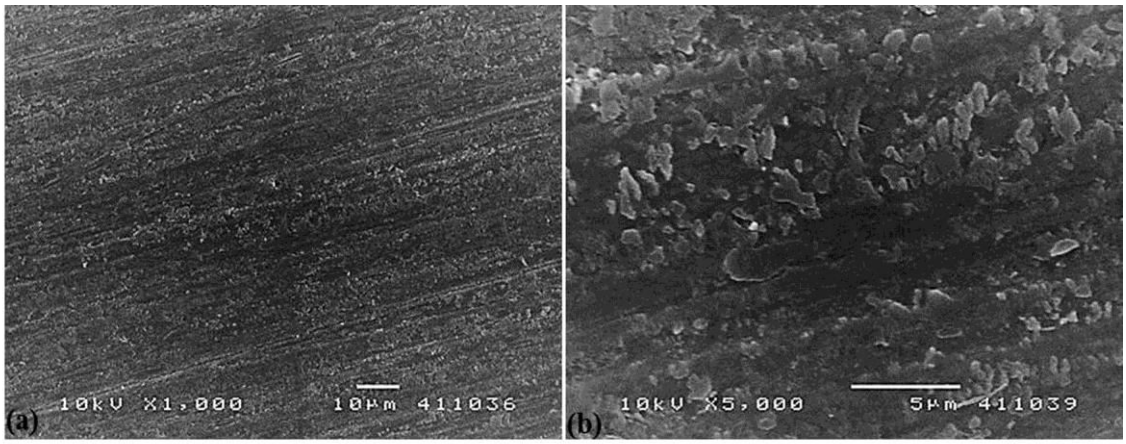


Fig. 5.12. SEM micrographs of the CAD/CAM-sintered-polished LDGC surface showing (a) machining traces, scratches and fractures and (b) details of localized fracture, enlarged debris and smeared area.

Fig. 5.13 shows the LDGC surface morphology of the CAD/CAM-polished-sintered process. Fig. 5.13(a) shows the very smooth surface texture without visible machining traces and the

phase-transformation induced crystal bulging. Fig. 5.13(b) shows surface details at a higher magnification, in which no visible surface defects such as fractures and microracks were observed. This is attributable to the combined action of polishing and sintering processes on the milled CAD/CAM surface.

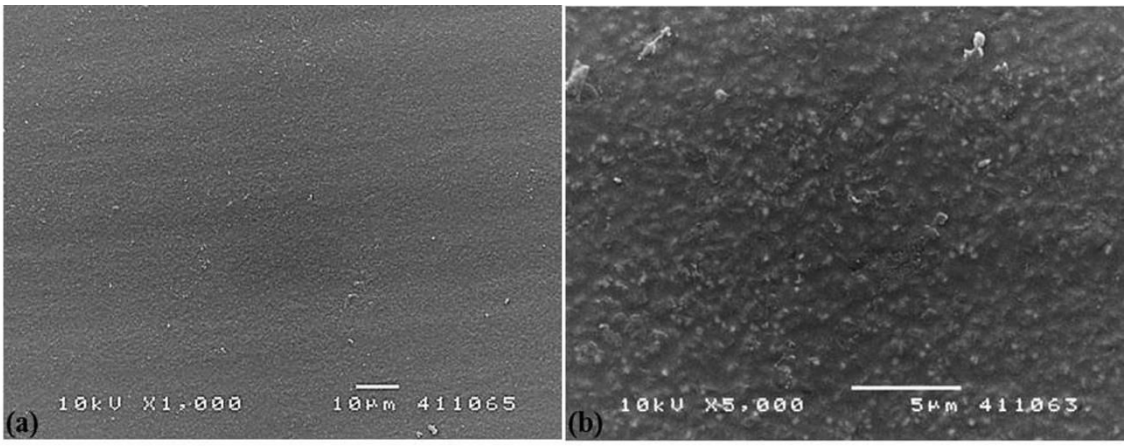


Fig. 5.13. SEM micrographs of the CAD/CAM-polished-sintered LDGC surface revealing (a) the the very smooth surface texture and (b) details of the smooth surface without visible surface defects.

Fig. 5.14 shows the LDGC surface morphology of the CAD/CAM-polished-sintered-glazed process. Fig. 14(a) shows the very fine surface which is very similar to the surface produced in the CAD/CAM-polished-sintered process. Fig. 5.14(b) shows a higher magnification surface image on which no visible surface defects can be observed but only the adhesion of fine particle debris.

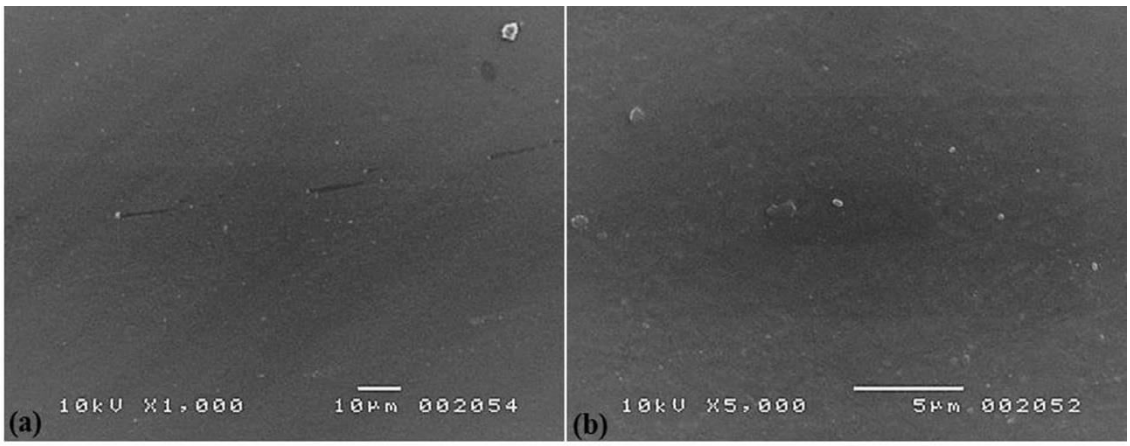


Fig. 5.14. SEM micrographs of the CAD/CAM-polished-sintered-glazed LDGC surface showing (a) the very fine surface similar to the surface in Fig. 5.13(a) and (b) details of the surface with fine particle debris at a higher mignificaiton.

## 5.4 Discussion

This research studied the surface quality of the CAD/CAM-milled and subsequently sintered, polished, and glazed LMGC/LDGC surfaces, which simulate clinical conditions with respect to phase transformation and surface morphology.

Conventional methods for fabricating dental restorations such as lost-wax casting, dough modelling and curing of acrylic resins are not only labor-intensive but also experience-dependent (Miyazaki et al., 2009; 2011; 2013; Mörmann 2006; Rekow 2006). Such methods are also limited to dental materials. Specially, they are unsuitable for the fabrication of crowns and bridges made of dental ceramics (Beuer et al. 2008; Miyazaki et al., 2009; 2011; 2013; Reich et al. 2005; Tinschert et al. 2004). For efficient production of dental restorations made from high-strength ceramics, chairside or laboratory CAD/CAM milling is often carried to the materials in their less strong states. This enables rapid profile generation of restorations and less diamond tool wear (Miyazaki et al. 2013; Miyazaki and Hotta, 2011). However, this process must be followed by the sintering process to strengthen the restorative materials by inducing phase transformations (e.g., LMGC to LDGC) or phase compaction (e.g., porous pre-sintered zirconia to dense sintered zirconia). In this study, x-ray diffraction patterns in Fig. 5.6 proves that lithium catena-silicate or metasilicate crystals in the CAD/CAM and CAD/CAM-polished processes were fully transformed to lithium disilicate crystals after sintering. Further mechanical polishing or thermal glazing of LDGC had no effect on the new phase transformations, indicating that sintering of LMGC produced highly stabilized lithium disilicate crystals in LDGC, which also improved the material strength to 400 GPa (Denry and Holloway, 2010).

Many surface parameters can be used to quantitatively characterize surface quality. Among them, surface roughness is probably the most commonly used method to assess surface textures (De Chiffre et al., 2000). The choice of surface roughness parameters ($R_a$ and $R_z$) in Fig. 5.7 was based on their wide usage in surface texture characterization (De Chiffre, 2000). As shown in Fig. 5.7, the mean surface roughness values generated in different fabrication processes ranged from $R_a$ 1.11–0.12 µm and $R_z$ 6.46–0.89 µm, comparable with those of the ground-polished pressable LDGC ($R_a$ = 0.7 µm) by Kou et al. (2006) and glazed pressable LDGC ($R_a$ = 0.64 ± 0.014 µm) by Boaventura et al. (2013).

The SEM micrographs produced in the CAD/CAM-milling process revealed the brittle fracture mode as the dominant material removal mechanism (Fig. 5.8), which yielded the largest $R_z$ value in Fig. 5.7. Repeated fractures also resulted in the material pulverization, which was the

consequence of the intergranular and/or transgranular micro-cracking due to the localized shear stress field superimposed by hydrostatic compressive stresses induced by diamond abrasives (Zhang and Howes, 1994). The evidence of the transgranular micro-cracking was observed clearly as lithium metasilicate crystals fragmented into micro-sized ceramic grains in Fig. 5.8(c). The pulverized surface in Fig. 5.8(a) emanated from surface and subsurface shear bands reported as the main deformation in nanoindentation of LMGC (Alao and Yin, 2015a). Indentation techniques are often used to simulate the abrasive machining process using very fine diamond abrasives. This is because of the similarity in the indentation-induced and machining-induced micro-mechanical deformations and fractures (Xu et al., 1996). The nano-scale mechanical behavior of LMGC using a diamond indenter revealed the mechanism of shear bands as its plastic deformation mode and suggested the application of moderate speeds in abrasive machining to avoid brittle fracture (Alao and Yin, 2015a). However, it should be noted that while the indentation techniques lay foundation mechanics for abrasive machining, they do not cover all aspects of abrasive machining removal processes (Komanduri et al., 1997; Malkin and Hwang, 1996).

A shear band is a form of the plastic instability that localizes large shear strains in a relatively thin band during a material deformation process (Greer et al., 2013). It can represent the material plastic deformation or serve as crack-initiating sites for the material (Sergueeva et al., 2005). In this study, shear bands might have initiated micro-cracking through extensions of subsurface shear bands into underlying tensile matrices or from stress concentration sites at intersections of shear bands (Alao and Yin, 2015a). Thus, the machining grooves in Fig. 5.8(a) might represent large fragmented shear strains which melted unto the surface due to the machining-induced temperature, roughening the surface (Fig. 5.7).

The polishing of the CAD/CAM-milled LMGC resulted in the reduction of the surface roughness, $R_a$ and $R_z$, in Fig. 5.7. This roughness reduction was statistically significant as evidenced in Tables 5.2 and 5.3. The polishing process smoothened the CAD/CAM-induced milling traces and scratches by the abrasive wear mechanism (Fig. 5.9). This included the transmission of the mechanical energy from abrasives to the material, removing or displacing the material in the process by such a mechanical action (Evans et al., 2003; Jefferies, 2007). Consequently, the polished surface formed debris in Fig. 5.9(a) and produced the glassy networks shown in Fig. 5.9(b).

The sintering of the CAD/CAM-milled LMGC surface (Fig. 5.10) also significantly reduced the surface roughness, $R_a$ and $R_z$, in Fig. 5.7 and Table 5.3. The surface roughness reduction could be ascribed to the phase transformation from lithium catena-silicate or lithium metasilicate to

lithium disilicate crystals (Fig. 5.6). Sintering might have also caused the relaxation of the machining-induced mechanical residual stresses (Zhang and Howes, 1994), thus smoothening the milled surface (Fig. 5.10). Further, sintering may have also generated thermal stresses (Denry, 2013), which might restrict the thermal expansion of the milled surface leading to the bulging of the surface (Fig. 5.10). This may rationalize why the surface improved in the CAD/CAM-sintering process (Fig. 5.10).

However, the thermally-induced stresses during the subsequent glaze-firing after sintering (Fig. 5.11) might have restricted the thermal expansion of the bulged sintered surface. It might cause the necessary hydrostatic compressive stresses to recompact the surface, generating powder debris to increase the surface roughness, as shown in Figs. 5.7 and 5.11. Thus, the significant decrease in the surface roughness of $R_a$ and $R_z$ in the CAD/CAM-sintered process cannot be significantly changed by the following glazing ($p > 0.05$, Table 5.3) because of the bursting of the bulged surface to powders.

The insignificant difference in $R_z$ values ($p > 0.05$) between the surfaces produced in the CAD/CAM-sintered (Fig. 5.10) and CAD/CAM-sintered-polished (Fig. 5.12) processes and the significant difference in their corresponding $R_a$ values ($p < 0.05$) (Table 5.3) needs an indepth analysis. First, it was suggested that the surface feature characterization of dental restorations should be described by more than one surface roughness parameter and the parameters should not only quantify the surface roughness but also provide information on the surface shape (Whitehead et al., 1995). Second, because $R_z$ averages the five highest peak-to-valley values of the surface profile, it was taken as an indicator of the largest surface defect size present (Cook, 2006). It was also used as a measure of the subsurface damage depths in ceramic grinding and lapping processes (Li et al., 2008). Based on the above reasons, $R_z$ is capable of providing better surface characterization texture information than $R_a$. Consequently, polishing after the sintering which transformed LMGC to LDGC did not easily remove the peaks and valleys due to the high strength of transformed LDGC and but only smoothened the average profile to decrease $R_a$ values.

Further, polishing of the sintered surface with the medium grit-sized (60–70 μm) diamond abrasives (Fig. 5.4) might have caused ploughing grooves or scratches (Fig. 5.12), which in some cases were accompanied by Hertzian fracture, localized heat and the creation of smeared surface defects (Jefferies, 2007). To improve this surface roughness, it is required to conduct the second step polishing with finer abrasives, which would not only reduce the roughness but also facilitate the transition from brittle-ductile removal (Schmidt and Weigl, 2000; Yin et al., 2007). In finer abrasive polishing, the interaction of abrasives with the work material is dominated by

normal forces resulting from negative rake angles and small undeformed chip thicknesses in the abrasive –material contact regions (Alao and Konneh, 2012; Evans et al., 2003). These high rake angles permit the necessary hydrostatic pressures/temperatures to enable plastic deformation to occur (Evans et al., 2003). However, the addition of this second step polishing would increase the polishing time and manufacturing cost for restorations (Steiner et al., 2015).

The CAD/CAM-polished-sintered process demonstrated the combined effect of polishing and subsequent sintering on the surface quality (Fig. 5.13), producing the smoothest surface (Fig. 5.7). As explained earlier, polishing of the CAD/CAM-milled LMGC surface reduced the surface roughness by easily removing its CAD/CAM-induced milling traces and scratches as LMGC is much weaker and easier to remove. The immediate sintering complemented the polishing process further to reduce the surface roughness and strengthen the material by transforming LMGC to LDGC. It is worth noting that the surface roughness ($R_a$ = 0.12 ± 0.08 µm) of the CAD/CAM-polished-sintered process was lower than the threshold surface roughness ($R_a$ = 0.20 µm) for bacterial plaque retention (Bollen et al., 1997). This means that bacteria accumulation is unlikely to occur on the surface. Further, the second step polishing with finer grits for structure retention and shininess was not necessarily needed when clinically acceptable optimal surface smoothness was achieved. Thus, the polishing time and cost could be reduced (Alao and Konneh, 2012). This is particularly important in reducing the dental restorative cost.

Meanwhile, the surface produced in the CAD/CAM-polished-sintered process is smoother than that made in the CAD/CAM-polished-sintered-glazed process. The subsequent glazing in the CAD/CAM-polished-sintered-glazed process (Fig. 5.14) resulted in insignificant improved surface roughness $R_a$ ($p > 0.05$) and $R_z$ ($p > 0.05$) values as shown in Table 5.3 and Fig. 5.7. This is in agreement with the reported results that some finishing techniques can obtain surfaces equivalent to glaze-fired ceramic surfaces (Tholt et al., 2006). Further, glazing at a high temperature might have induced thermal deformation in LDGC (Denry and Holloway, 2004) which might not affect the material's mechanical strength (Cattell et al., 2002; Denry and Holloway, 2004; Wen et al., 2007). Nevertheless, Fig. 5.7 shows that glazing increased the surface roughness, which was above the bacterial retention threshold (Bollen et al., 1997), implying the likely bacteria accumulation. Thus, glazing process should be eliminated from the polished-sintered surface.

In comparison of the surface quality produced in all processes, the CAD/CAM-polished-sintered surface quality has met the dental standards, requiring neither fine-grit polishing nor glazing and reducing the manufacturing cost. Therefore, CAD/CAM-polished-sintered process

is proposed for the production of LDGC restorations as schematically described in Fig. 5.15. The CAD/CAM-milling of LMGC first generates rough restorative profiles. Polishing is only conducted on occlusal, facial and lingual surfaces. Then, sintering is applied to strengthen the material via phase transformation to form lithium disilicate crystals which can suppress crack propagation (Apel et al., 2008), leading to improved surface finish that fulfils dental standards. Intaglio surfaces produced in the CAD/CAM-sintered process may be etched in hydrofluoric acid exposing the lithium disilicate crystals which may provide the necessary rough surface suitable for the cementation surface (Borges et al., 2003; Kelly, 1997).

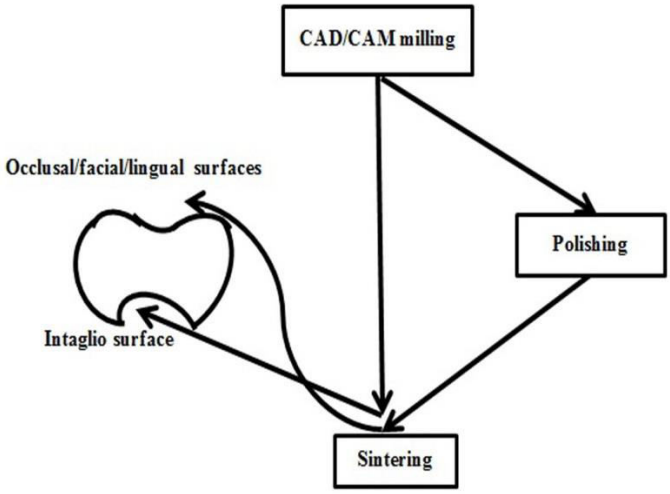


Fig. 5.15. The proposed fabrication procedure for LMGC/LDGC restorations in which the treatments on occlusal/facial/lingual and intaglio (cementation) surfaces meet the threshold surface roughness for bacterial plaque retention and adhesion, respectively.

## 5.5 Conclusions

This work investigated the surface quality of LMGC/LDGC produced in relevant clinical restorative surface processes involving CAD/CAM milling, sintering, polishing and glazing. The CAD/CAM-milling process produced the coarsest surface roughness ($R_a$ and $R_z$) due to extensive brittle cracks and crystal pulverization. Polishing after the CAD/CAM-milling process reduced the improved roughness by wearing the milled traces and scratches through abrasive mechanical actions. Sintering transformed lithium catena-silicate or metasilicate to lithium disilicate crystals to increase the material strength and also lowered the surface roughness produced in milling by reducing milling-induced mechanical residual stresses and generating thermal stresses. The subsequent glaze-firing did not change the stabilized LDGC phase but might have induced additional thermal stresses leading to further deformation. Polishing after

sintering did not significantly improve the surface roughness due to the higher strength of LDGC. Among all processes studies, the CAD/CAM-polished-sintered surface produced the smoothest surface which fulfilled dental conditions in terms of cost effectiveness, time efficiency, and surface quality for occlusal functions and bacterial plaque retention. Further studies will be conducted to determine the reliability of the proposed fabrication process for LDGC restorations and establish the relations between their surface quality and fatigue behavior.

# Chapter 6

# Surface Quality of Y-TZP in CAD/CAM milling, Sintering, Polishing and Sandblasting Processes

## 6.1 Introduction

Y-TZP has high strength and fracture toughness, good biocompatibility, low radioactivity, which make it suitable for applications as load-bearing core structures in crowns and bridges in restorative dentistry (Denry and Kelly, 2008; Manicone et al., 2007; Miyazaki et al., 2013). Recent progress in the processing of Y-TZP materials with high translucency could significantly widen the clinical indications of monolithic zirconia restorations to avoid interface fractures in veneer-core structures (Tong et al., 2016). Generally, pre-sintered or sintered Y-TZP blocks or disks can be shaped to restoration profiles using CAD/CAM technologies (Andersson and Odén, 1993; Beuer et al., 2008; Miyazaki et al., 2009; Mörmann, 2006; Rekow, 2006; Strub et al., 2006; Yin et al., 2006). These digital manufacturing technologies assure the standardization and the uniform material quality of the restorations, reducing their fabrication time and manufacturing cost (Rekow and Thompson, 2005; Wittneben et al., 2009). However, CAD/CAM milling of fully sintered Y-TZP requires machining systems to be extremely strong, robust and stiff because of the high strength, high hardness and low machinability of the material (Alao and Yin, 2014b, Denry and Kelly, 2008; Rekow et al., 2011). Further, machining-induced mechanical stresses in sintered Y-TZP can cause the martensitic tetragonal to monoclinic phase transformation, resulting to low temperature degradation of the restorations and making them susceptible to catastrophic fracture (Silva et al., 2010; Zarone et al., 2011).

To avoid these problems, CAD/CAM milling is more often conducted on pre-sintered Y-TZP in enlarged frameworks to compensate for sintering shrinkages (Filser et al., 2003; Klock et al., 1998). Then, sintering is performed for full crystallization to ensure the diffusion of ions across Y-TZP grain boundaries without the involvement of a liquid phase, achieving the increased mechanical strength (Hallman et al., 2012). In addition, the fabrication process of pre-sintered Y-TZP can decrease the milling time and reduce the cutting tool wear (Al-Amleh et al., 2010; Alao and Yin, 2014b; 2016; Denry, 2013; Filser et al., 2003; Klock et al., 1998; Luthardt et al., 2004; Ritzberger et al., 2010). However, surface and subsurface damages can easily occur in CAD/CAM milled pre-sintered Y-TZP surfaces (Rekow and Thompson, 2005) because of its low damage tolerance and stiffness (Alao and Yin, 2014b; 2016). These damages cannot be

healed in the subsequent sintering process. Therefore, they compromise the strength of the restorations and shorten their lifetimes (Rekow et al., 2011).

To minimize the milling-induced damage and understand the material behavior of zirconia in diamond abrasive processes, indentation studies simulating the abrasive machining behavior (Komanduri et al., 1997; Malkin and Hwang, 1996) have been conducted on pre-sintered Y-TZP (Alao and Yin, 2014b; 2016). These studies have detailed the microstructural compaction (pore closure and opening), and kink band formation in porous Y-TZP during the penetration processes by a diamond indenter (Alao and Yin 2014b). Meanwhile, the machinability of pre-sintered Y-TZP was also determined in terms of its elasticity, plasticity and resistance to machining-induced damage (Alao and Yin, 2016). High deformation rates in indentation corresponding to high cutting speeds in abrasive machining were found to be favourable for the ductile material removal mode for minimization of the machining-induced damage in porous pre-sintered Y-TZP (Alao and Yin, 2014b; 2016). However, indentation mechanics do not cover all aspects of the machining behavior (Komanduri et al., 1997; Malkin and Hwang, 1996). Therefore, it is essential to conduct machining science studies for the understanding of the fundamental responses of pre-sintered Y-TZP to CAD/CAM milling process for high quality of restorations.

Following the sintering process of the CAD/CAM-milled Y-TZP materials, the restorations generally require further surface treatments for improved or roughened surface finishes depending on surface orientations (Denry and Kelly, 2008; Miyazaki et al., 2009; Rekow et al., 2011). In general, exterior surfaces, i.e., occlusal, buccal and lingual surfaces, must be intra/extra-orally polished to obtain occlusal fitness, adequate surface textures and roughness for aesthetic light reflection and bacterial plaque retention (Bollen et al., 1997). Highly polished-sintered Y-TZP surfaces were reported to exhibit bio-tribological properties similar to natural teeth which lowered the antagonist enamel wear (Mitov et al., 2012; Miyazaki et al., 2013; Passos et al., 2014; Preis et al., 2012). Interior intaglio surfaces are normally roughened by chemical etching or sandblasting for strong adhesion of ceramic restorations in the oral environment (Denry and Kelly, 2008; Miyazaki et al., 2009; Rekow et al., 2011). Chemical etching of sintered Y-TZP in hydrofluoric acid is impossible due to the absence of the glassy phase in the materials, which makes adequate roughness and micromechanical bonding possible (Hallmann et al., 2016; Kern, 2009; Monaco, 2013). Therefore, chemical activation for roughening of intaglio surfaces of sintered Y-TZP has to be replaced by mechanical actions, such as sandblasting. Pure alumina particles (Chintappali et al., 2013; Kosmač et al., 1999; 2000; Monaco, 2013), silica coated alumina particles (Kern, 2009) or zirconia particles (Hallman et al., 2016) are all used for the blasting processes. Studies have investigated the

sandblasting effect on the strength of Y-TZP (Chintappali et al., 2014; Curtis et al., 2006; Guazzato et al., 2005; Hallmann et al., 2016; Kosmac et al., 1999; 2000; Passos et al., 2015; Zhang et al., 2004). However, little has been done towards systematic studies of the characteristics of CAD/CAM-milled pre-sintered Y-TZP surfaces under different pre- and post-mechanical and thermal treatments.

Surface quality plays an important role in the mechanical behavior such as wear and fatigue of dental restorations (Denry, 2013, Rekow and Thompson, 2005; Rekow et al., 2011). The quality measures include surface roughness and morphology, phase transformation, mechanical properties of processed surfaces (Ulutan and Ozel, 2011). The surface quality of sintered Y-TZP has been investigated in conventional and high-speed grinding processes (Luthardt et al., 2004; Xu et al., 1997; Yin and Huang, 2004; Yin et al., 2003). However, there lacks comprehensive and systematic examinations of the surface integrity of CAD/CAM-milled pre-sintered Y-TZP surfaces subjected to different sintering, polishing and sandblasting conditions.

Therefore, this Chapter aimed to investigate the surface quality of CAD/CAM-milled pre-sintered Y-TZP and subsequent sintered, polished and sandblasted pre-sintered/sintered Y-TZP surfaces with respect to phase transformation, surface roughness and morphology, and removal mechanisms. X-ray diffraction was used to analyse crystalline phases and phase transformations. Surface roughness was measured in terms of average surface roughness ($R_a$) and maximum height ($R_z$). Scanning electron microscopy (SEM) was applied to analyse removal mechanisms, surface damage and morphology. Finally, an optimized fabrication process for the improved surface quality of Y-TZP restorations was recommended.

## 6.2 Experimental Procedures

### *6.2.1 Materials*

A translucent pre-sintered Y-TZP ceramic disc with 98.5-mm diameter and 14-mm thickness (ZENOSTAR Zr Translucent sun and sun chroma milling disks, Wieland Dental + Technik GmbH & Co. KG, Pforzheim, Germany) was selected in this study. This material is developed for CAD/CAM milling of full contour zirconia crowns and bridges. It comprises about 91% $ZrO_2$, 5% $Y_2O_3$, 2% $HfO_2$, and 0.05% $Al_2O_3$ (Hallman et al., 2012). $Y_2O_3$ acts as stabilizer for the retention of tetragonal grains to room temperature; $HfO_2$ binds $ZrO_2$ powders and $Al_2O_3$ improves its hydrothermal ageing resistance (Denry and Kelly, 2008).

### *6.2.2 CAD/CAM Milling*

The pre-sintered Y-TZP disk was milled using a dental CAD/CAM machine (OCS-11 Hana DIPRO, Digital Process Ltd., Japan) with a tungsten carbide ball end mill with 1-mm diameter (C.K.K Co. Ltd., Japan). The milling process was performed with up and down cuts in dry condition to generate flat surfaces simulating internal surface milling of crowns, which is the most challenging step in CAD/CAM processes (Luthardt et al., 2002; 2004). The rotational speed of the cutter was 30,000 rpm, the feed pitch was 0.1 mm and the feed speed was 1000 mm/min. Fig. 6.1 shows the optical image of the milled disc in which blocks of 10 mm × 12 mm × 14 mm for indentation fatigue testing and multiple milled thin surfaces with thickness of approximately 2.5 mm for surface preparation were produced.

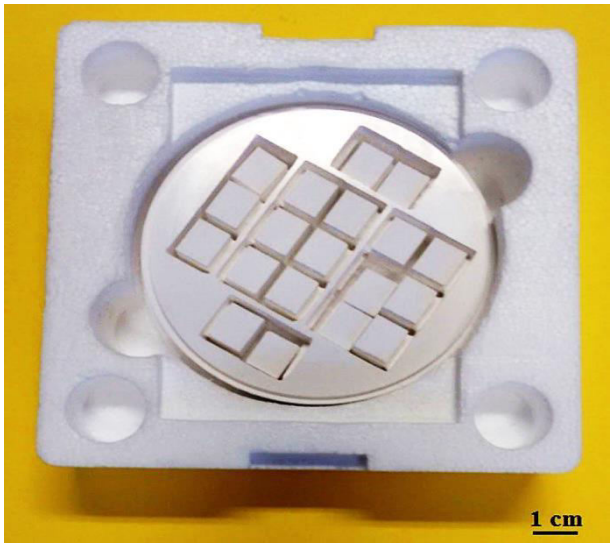


Fig. 6.1. The optical image of the CAD/CAM-milled pre-sintered Y-TZP disc.

### *6.2.3 Surface Preparation*

After milling, the 2.5-mm thin samples were cleaned in acetone and treated under different polishing, sintering and sandblasting conditions simulating various clinical fabrication processes, as shown in Fig. 6.2. These processes were designated as CAD/CAM (i.e., milled by the CAD/CAM machine), CAD/CAM-polished, CAD/CAM-sintered, CAD/CAM-polished-sintered, CAD/CAM-sintered-sandblasted with 110-µm alumina, CAD/CAM-sintered-sandblasted with 250-µm alumina, and CAD/CAM-sintered-polished processes.

Sintering of the milled pre-sintered Y-TZP samples was carried out in a programed dental furnace (Programat S1, Ivoclar Vivadent, Liechtenstein) at a commercial dental laboratory

(John Griffiths Dental Laboratory, Cairns, Australia) following the recommendation of the manufacturer. Program 6 was used to sinter the samples at the temperature of 1530 °C with a duration of 4 h 30 min for heating, temperature holding and cooling processes. This program was recommended for the quick sintering of full-contour zirconia single tooth or bridge restorations as well as zirconia single-tooth and bridge frameworks with higher translucency. The bulk densities of the samples were more than 99% of their theoretical values.

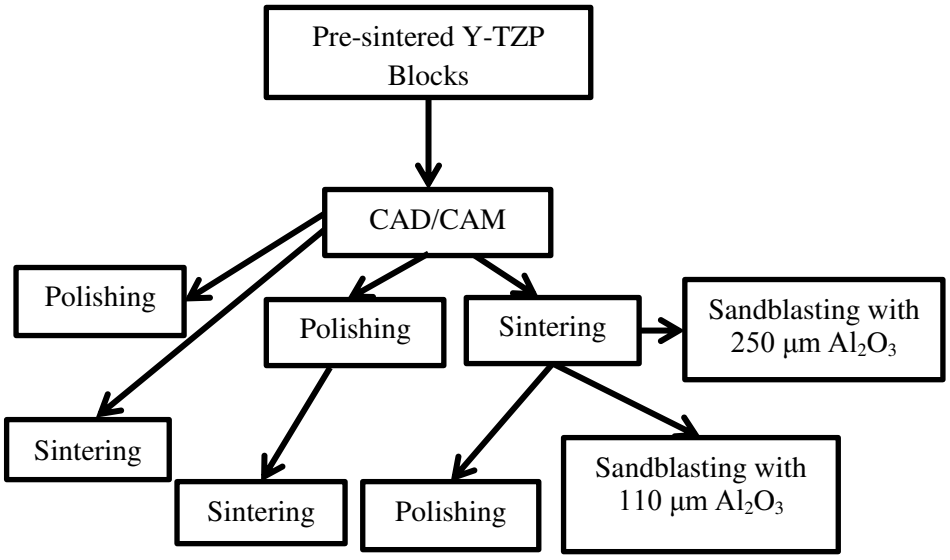


Fig. 6.2. Schematic diagram of all fabrication processes.

Polishing was conducted using a clinical dental handpiece with a grey white rubber diamond bur (Exa Cerapol UM, ISO 658.900.114.525.060, Edenta, Switzerland) by a dental clinician with decades of clinical experience in Australia. The bur contained dispersed diamond abrasives with a medium-grit-size of approximately 60–70 µm embedded in a softer elastic matrix (Jefferies, 2007). This type of the bur is often used for intermediate finishing, eliminating scratches and smoothening surfaces. Samples were polished at the bur rotating speed of 5,000 rpm with a haptic force of approximately 1 N, which is equivalent to the average load applied by a dentist during tooth preparation (Siegel and von Fraunhofer, 1997). The polishing quality was visually examined and approved for clinical satisfaction by experienced dentists.

Sandblasting was conducted using alumina particles impacted perpendicular to their surfaces at a pressure of 2.76 bar and a distance of 10 mm using a sandblaster (Bego, Germany). Both 110 µm and 250 µm alumina grains were blasted, respectively, to reveal the grit size effect on the surface roughness, phase transformation and degree of damage in the treated surfaces.

### *6.2.4 Surface Characterization*

All processed surfaces under each condition were x-ray scanned using an x-ray diffractometer (D/MAX-2500, Rigaku, Japan) to obtain x-ray diffraction patterns. The Cu Kα radiation with 0.15406 nm wave length was used to analyze crystalline phases of each surface. All scans were performed from 10–80° in the 2θ range at 0.02° scanning step to determine the nature of different phases.

Surface roughness of all processed surfaces was characterized under a desktop SEM with assisted morphology analytical software (Phenom-World BV, Netherlands). Prior to the characterization, all tested surfaces were gold-coated. The software enabled to draw lines perpendicular to machining traces and calculate surface profiles for each measurement line. The cut-off and evaluation lengths were 0.2 mm and 1 mm, respectively. Both the average surface roughness, $R_a$, and the maximum roughness, $R_z$ were measured, which are the most commonly used surface parameters in practice (De Chiffre et al., 2000). Three measurements at randomly selected locations on each sample surface (Yin et al., 2003) were performed to obtain mean values and standard deviations.

Each surface fabricated in all processes was also viewed under a high-resolution SEM (JEOL JSM 5410LV, Tokyo, Japan) to study damage morphology and removal mechanisms.

### *6.2.5 Statistical Analysis*

A single factor analysis of variance (ANOVA) was conducted at 5% confidence interval to examine the significance of fabrication processes on the average surface roughness, $R_a$, and the maximum roughness, $R_z$. The paired $t$ test was also performed at 5% confidence to examine the influence of each surface treatment on surface roughness values.

## 6.3 Results

### *6.3.1 X-ray Diffraction*

The x-ray diffraction patterns of all fabrication processes are shown in Fig. 6.3 in comparison with an un-milled pre-sintered Y-TZP blank from the manufacture. Fig. 6.3(a) shows the x-ray diffraction pattern of the CAD/CAM pre-sintered Y-TZP surface, which is approximately similar to those of the unmilled pre-sintered surface and the CAD/CAM-polished surfaces. In Fig. 6.3(a), the main peaks labelling tetragonal $ZrO_2$, (Z1) at the diffraction peak angles, 2θ of

30.2°, 34.9°, 50.4°, 60.2°, 63.5°, and 74.2° correspond to the diffracted plane structures of (111), (200), (220), (311), (222), (400) in tetragonal Y-TZP crystal, respectively (Chintapalli et al., 2013; Denry and Holloway, 2006; Garvin and Nicholson, 1972; Monaco et al., 2013; Toraya et al., 1984). The minor peaks labelling baddeleyite or monoclinic $ZrO_2$, (B) at 2θ of 28.2° and 31.4° correspond to (-111) and (111) planes, respectively (Chintapalli et al., 2013; Garvin and Nicholson, 1972; Monaco et al., 2013; Toraya et al., 1984). This x-ray diffraction pattern indicates that the material contained mainly tetragonal zirconia crystalline phase mixed with baddeleyite or monoclinic zirconia crystal as a minor secondary phase. The similarity among the three x-ray diffraction patterns on the unmilled pre-sintered, CAD/CAM and CAD/CAM-polished surfaces reveals that both the CAD/CAM milling and following polishing processes did not cause the phase transformation.

Fig. 6.3(b) shows the x-ray diffraction pattern of the CAD/CAM-polished-sintered surface. It contained both tetragonal zirconia (Z1) and another tetragonal $ZrO_{1.95}$ phase (Z2) which appeared at 2θ of 28.2°. This indicates that the monoclinic phase in Fig. 6.3(a) was transformed to the tetragonal-$ZrO_{1.95}$ phase by the sintering process since polishing did not cause the phase transformation.

Fig. 6.3(c) shows the x-ray diffraction pattern of the CAD/CAM-sintered surface, which is approximately similar to that of the CAD/CAM-sintered-polished surface. Tetragonal zirconia (Z1) was found as the main phase in these two surfaces. This implies that the sintering process transformed the remaining monoclinic zirconia in the milled pre-sintered material to tetragonal zirconia while polishing did not influence the phase transformation.

Fig. 6.3(d) shows the x-ray diffraction pattern of the CAD/CAM-sintered-sandblasted with 110 µm alumina surface, which is similar to that of the CAD/CAM-sintered-sandblasted with 250 µm alumina surfaces. A strained tetragonal zirconia (Z1) phase associated with the diffraction peak shift and broadening was observed on the two surfaces. Surprisingly, the diffraction peak of monoclinic zirconia (Z2), which is often ascribed to the mechanical action of sandblasting, was not detected in these two surfaces.

### *6.3.2 Surface Roughness*

Fig. 6.4 shows the results of the arithmetic mean roughness, $R_a$, and maximum roughness, $R_z$, versus different surface treatment. The CAD/CAM-sintered-sandblasted with 250 µm alumina particles process produced the roughest surface roughness with $R_a$ 0.55 ± 0.1 µm and $R_z$ 3.41 ± 0.31 µm. It was followed by the CAD/CAM-sintered-sandblasted with 110 µm alumina

particles process with $R_a$ 0.48 ± 0.04 µm and $R_z$ 3.08 ± 0.10 µm. The CAD/CAM-polished-sintered process yielded the smoothest surface with $R_a$ 0.21 ± 0.03 µm and $R_z$ 1.73 ± 0.04 µm. The CAD/CAM-polished process produced the moderate roughness with $R_a$ 0.35 ± 0.02 µm and $R_z$ 2.56 ± 0.04 µm, which is similar to the surface with $R_a$ 0.37 ± 0.02 µm; $R_z$ 2.68 ± 0.15 µm produced in the CAD/CAM process. The increased surface roughness was generated in the CAD/CAM-sintered-polished process with $R_a$ 0.43 ± 0.06 µm and $R_z$ 2.67 ± 0.39 µm, which is similar to the surface of CAD/CAM-sintered process with $R_a$ 0.43 ± 0.04 µm and $R_z$ 2.95 ± 0.03).

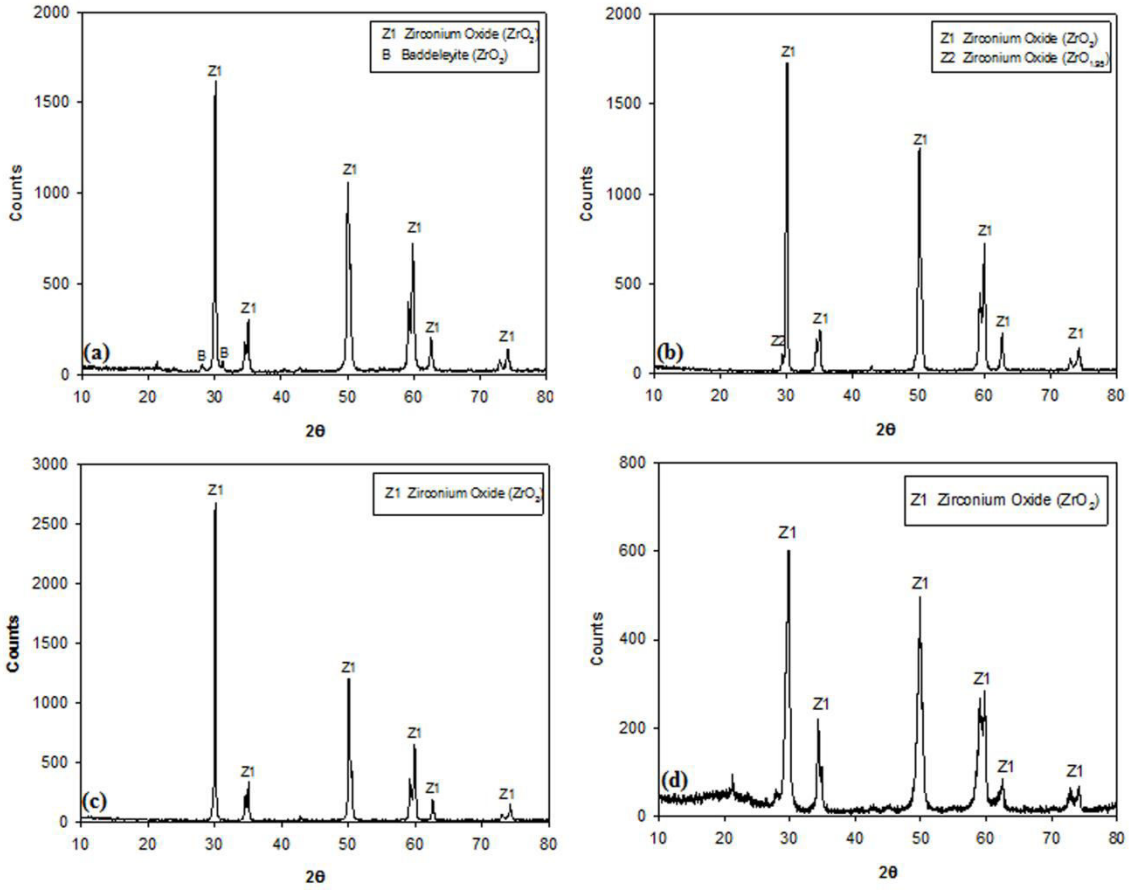


Fig. 6.3. X-ray diffraction patterns of (a) the CAD/CAM-milled surface, which is nearly identical to those of the unmilled pre-sintered and CAD/CAM-polished surfaces, (b) the CAD/CAM-polished-sintered surface, (c) the CAD/CAM-sintered surface, which is approximately identical to that of the CAD/CAM-sintered-polished surface, and (d) the CAD/CAM-sintered-sandblasted surface with 110-µm alumina particles, which is approximately identical to that of the CAD/CAM-sintered-sandblasted surface with 250-µm alumina particles.

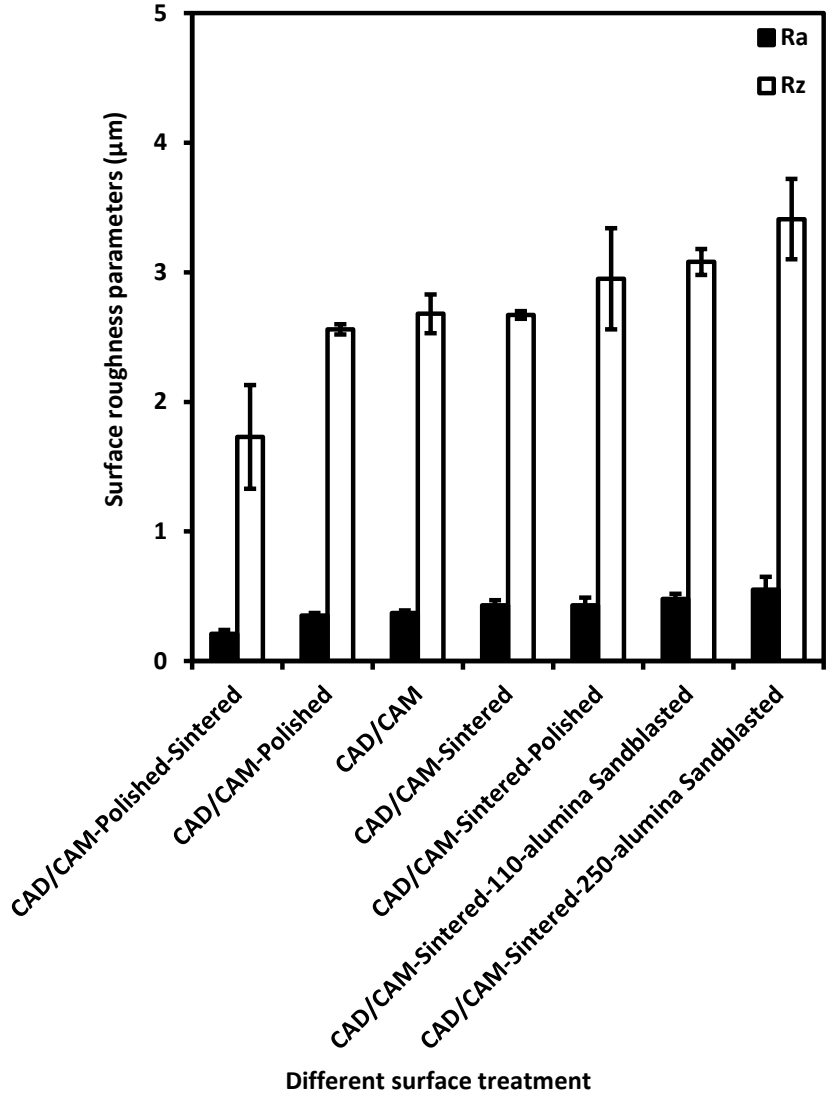


Fig. 6.4. Arithmetic mean roughness, $R_a$, and maximum roughness, $R_z$, versus different surface treatment. Each data point is the mean value of three profiles on each processed surface with the error bars corresponding to ± one standard deviation for the three profiles.

Table 6.1 reveals the result of the one-way ANOVA to determine the influence of different processes on the arithmetic mean roughness, $R_a$. It indicates that $R_a$ was significantly affected by different fabrication processes (ANOVA, $p < 0.05$). Similar analysis was also conducted for the maximum roughness $R_z$, revealing the significant result as well (ANOVA, $p < 0.05$).

Table 6.1 Result of the one-way ANOVA for $R_a$ with respect to different fabrication processes.

| Source of Variation | SS | df | MS | F | *p*-value | F crit |
|---|---|---|---|---|---|---|
| Between fabrication processes | 0.22 | 6 | 0.04 | 13.09 | 0.00 | 2.85 |
| Within fabrication processes | 0.04 | 14 | 0.00 | | | |
| Total | 0.25 | 20 | | | | |

Table 6.2 shows an example of the paired *t*-test for the significant difference of the arithmetic mean roughness $R_a$ values between the CAD/CAM and CAD/CAM-polished surfaces. It indicates that polishing did not significantly reduce the $R_a$ values ($p > 0.05$). The same paired *t*-test was also conducted to compare the maximum roughness height $R_z$ values for the two surfaces. Table 6.3 summarizes all *p*-values from the paired *t*-tests for $R_a$ and $R_z$ parameters for all fabrication processes. Comparing the CAD/CAM process with the CAD/CAM-polishing and CAD/CAM-sintering, neither simply polishing nor sintering significantly improve the roughness $R_a$ and $R_z$ values obtained in milling ($p > 0.05$). In comparison, further sintering of the polished surface significantly improved both $R_a$ and $R_z$ values ($p < 0.05$). However, further polishing of the sintered surface did not significantly improve both $R_a$ and $R_z$ values ($p > 0.05$). Sandblasting of the sintered surfaces with either 110 µm or 250 µm alumina particles did not significantly change both $R_a$ and $R_z$ values ($p > 0.05$). Meanwhile, sandblasting with different grit sizes did not significantly change surface roughness in both $R_a$ and $R_z$ values ($p > 0.05$).

Table 6.2 An example of a paired *t*-test for $R_a$ values between CAD/CAM-milled and CAD/CAM-polished processes.

| | **CAD/CAM-milled** | **CAD/CAM-polished** |
|---|---|---|
| Mean | 0.37 | 0.35 |
| Variance | 0.00 | 0.00 |
| Observations | 3.00 | 3.00 |
| Pearson Correlation | 0.06 | |
| Hypothesized Mean Difference | 0.00 | |
| Degree of freedom | 2.00 | |
| t statistics | 1.01 | |
| P(T<=t) one-tail | 0.21 | |
| t critical one-tail | 2.92 | |
| P(T<=t) two-tail | 0.42 | |
| t critical two-tail | 4.30 | |

### *6.3.3 Surface Morphology*

Fig. 6.5 shows the surface morphology of the CAD/CAM pre-sintered Y-TZP. Fig. 6.5(a) reveals milling traces associated with plastic deformation and scratching-induced fractures by the milling tool. Fig. 6.5(b) shows the details of the fractured area containing micro-chips and cracks on the milled surface. Fig. 6.5(c) shows higher-magnification details of the fractured areas revealing the agglomeration of fractured chips by intragranular or transgranular fracture.

These SEM images indicate that brittle fracture and partial ductile modes were the dominant material removal mechanism for the CAD/CAM milling of pre-sintered Y-TZP.

Table 6.3 Summary of the *p*-values of all paired *t*-tests for $R_a$ and $R_z$ values of all paired fabrication processes.

| Surface treatments | *p*-value | |
|---|---|---|
| | $R_a$ (µm) | $R_z$ (µm) |
| CAD/CAM-milled versus CAD/CAM-polished | $p > 0.05$ | $p > 0.05$ |
| CAD/CAM-milled versus CAD/CAM-sintered | $p > 0.05$ | $p > 0.05$ |
| CAD/CAM-polished versus CAD/CAM-polished-sintered | $p < 0.05$ | $p < 0.05$ |
| CAD/CAM-sintered versus CAD/CAM-sintered-polished | $p > 0.05$ | $p > 0.05$ |
| CAD/CAM-sintered versus CAD/CAM-sintered-110-alumina sandblasted | $p > 0.05$ | $p > 0.05$ |
| CAD/CAM-sintered versus CAD/CAM-sintered-250-alumina sandblasted | $p > 0.05$ | $p > 0.05$ |
| CAD/CAM-sintered-110-alumina sandblasted versus CAD/CAM-sintered-250-alumina sandblasted | $p > 0.05$ | $p > 0.05$ |

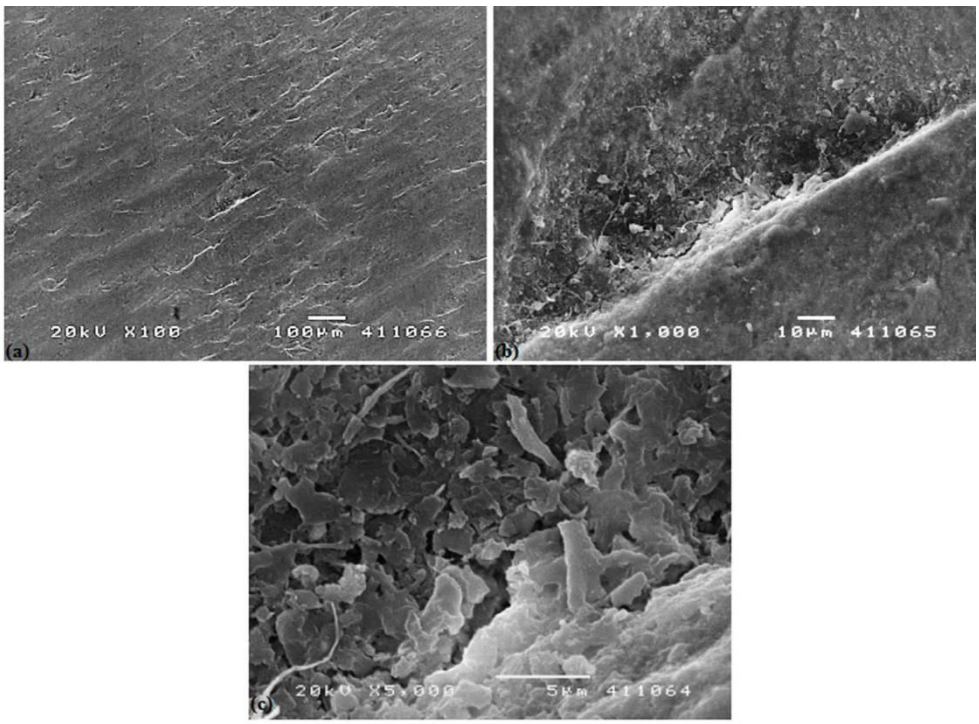


Fig. 6.5. SEM micrographs of the CAD/CAM pre-sintered Y-TZP surface showing (a) milling traces associated with plastic deformation and fractures, (b) details of the fractured area containing micro-chips and cracks, and (c) details of fracture morphology revealing the agglomeration of fractured chips by intragranular or transgranular fracture.

Fig. 6.6 shows the CAD/CAM-polished pre-sintered Y-TZP surface morphology. Fig. 6.6(a) shows the polishing traces characterized by surface irregularities indicating the ineffectiveness of the used polishing abrasives to remove the machining grooves produced in the milled surface. Fig. 6.6(b) shows the details of polishing traces involving such surface defects as delamination, pitting and side flow across scratches. Fig. 6.6(c) shows mainly a rough surface associated with micro-craters and debris.

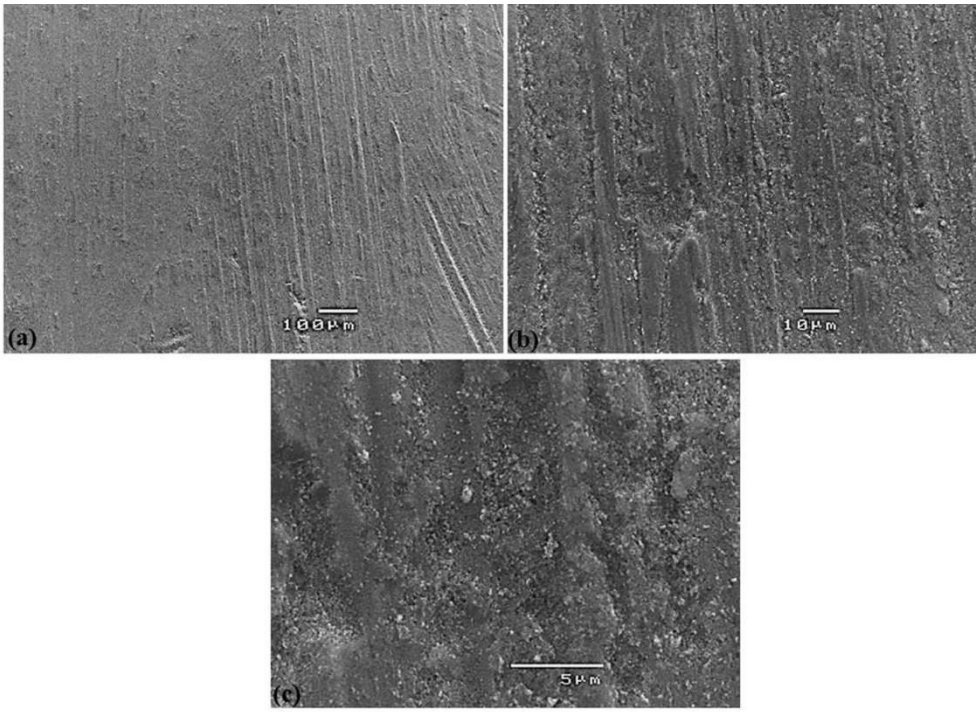


Fig. 6.6. SEM micrographs of the CAD/CAM-polished pre-sintered Y-TZP surface revealing (a) surface irregularities characteristic of polishing traces, (b) details of polishing traces of surface defects such as delamination, pitting and side flow across scratches, and (c) details of a rough surface area associated with micro-craters and debris.

Fig. 6.7 shows the CAD/CAM-sintered Y-TZP surface morphology. Fig. 6.7(a) shows the sintering-induced grain coarsening which was superimposed on the milled surface. Fig. 6.7(b) shows the details of the grain coarsening. Combining the x-ray diffraction results in Fig. 6.3, it is considered that the grain coarsening resulted from the transformation of the monoclinic $ZrO_2$ (B) to tetragonal $ZrO_2$ (Z1) Fig. 6.7(c) shows the details of the transformed surface embedded in the milled surface.

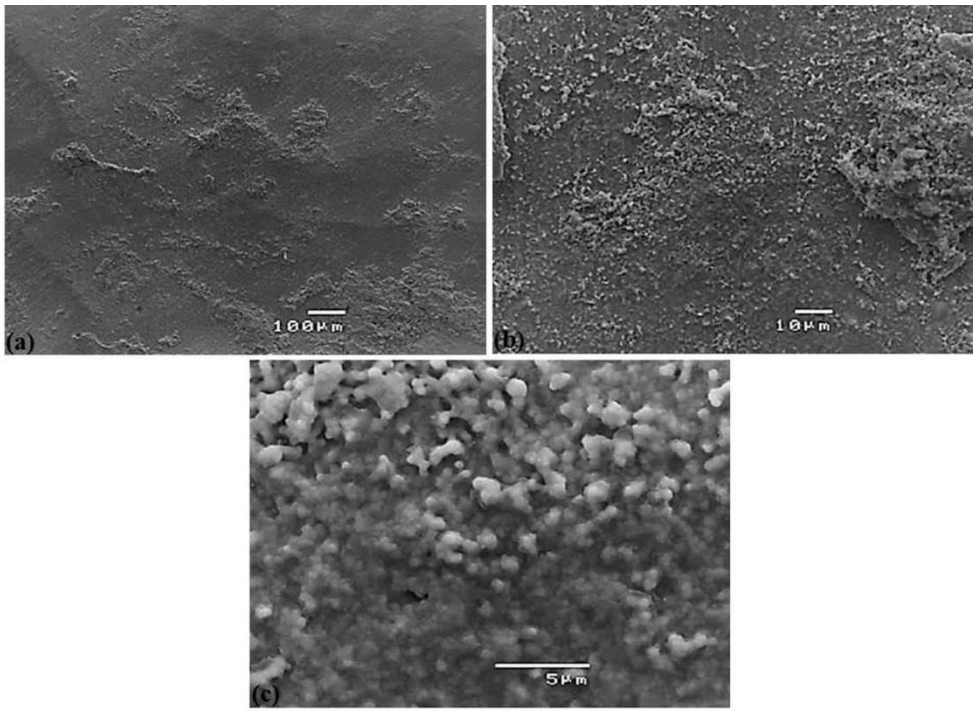


Fig. 6.7. SEM micrographs of the CAD/CAM-sintered Y-TZP surface revealing (a) sintering-induced grain coarsening, (b) details of grain coarsening, and (c) details of the transformed surface embedded in the milled surface.

Fig. 6.8 shows the CAD/CAM-sintered-polished Y-TZP surface morphology. Fig. 6.8(a) shows that some sintering-induced coarse grains in Fig. 6.7(a) were weakly removed by the polishing process. Fig. 6.8(b) shows that the polishing process induced microcracks on the phase-transformed surface. Fig. 6.8(c) shows that the induced fracture was intergranular as microcracks can be seen along the grain boundaries.

Fig. 6.9 shows the CAD/CAM-polished-sintered Y-TZP surface morphology. Fig. 6.9(a) shows the smooth surface texture with no visible milling scratches and the partial removal of sintering-induced grain coarsening formed on the surface. Fig. 6.9(b) shows a higher magnification details revealing little surface defects in comparison with large scale surface defects observed in Figs. 6.5(b), 6.6(b), 6.7(b) and 6.8(b). Also, Fig. 6.9(c) shows plastically deformed layer and little microstructural surface defects like porosity produced during the densification process.

Fig. 6.10 shows the CAD/CAM-sintered-sandblasted Y-TZP surface morphology by 110 µm alumina particles. Fig. 6.10(a) shows the blasted traces with pulverized Y-TZP grains on the surface. Fig. 6.10(b) shows the details of the massive pulverized grains, micro scratches and pitting on the surface which resulted from eroding and impacting from the alumina particles.

Fig. 6.10 (c) shows the higher magnification of the surface revealing ploughing, plastic deformation and pitting on the zirconia surface.

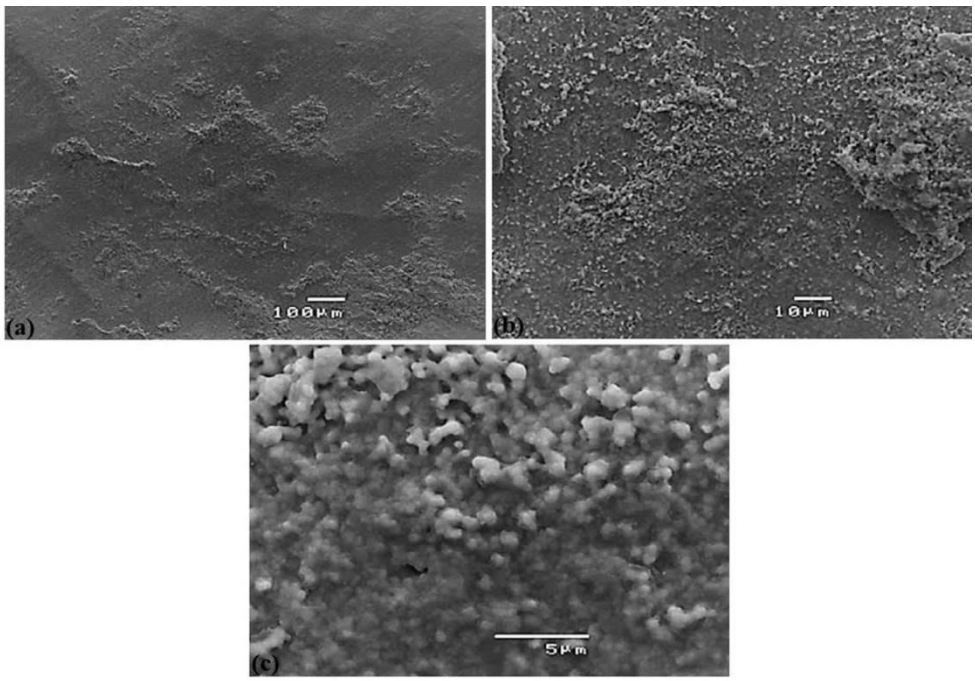


Fig. 6.8. SEM micrographs of the CAD/CAM-sintered-polished Y-TZP surface revealing (a) the weak removal of sintering-induced coarse grains, (b) microcracks induced in the process, and (c) details of induced intergranular microcracks.

Fig. 6.11 shows the CAD/CAM-sintered-sandblasted Y-TZP surface morphology by 250 µm alumina particles. Fig. 6.11(a) shows the rough surface mainly due to the blasting by the alumina particles without the milling traces of the CAD/CAM process. Fig. 6.11(b) reveals the rough surface features consisting of randomly oriented scoring and scratches. Fig. 6.11(c) shows large scale surface defects including deep sharp scratches, micro-craters, pitting and grain pull-out.

## 6.4 Discussion

Owing to the low hardness and strength of the pre-sintered Y-TZP, CAD/CAM milling of the material blanks, i.e., white machining, is first processed in clinical practice (Al-Amleh et al., 2010; Alao and Yin, 2014b; 2016; Denry, 2013; Filser et al., 2003; Klock et al., 1998; Ritzberger et al., 2010). The milled restoration samples are then sintered to their desired dimensions and full strength by inducing phase densification and transformation (Badwal, 1995). This research quantitatively studied the surface quality of the CAD/CAM-milled and subsequently sintered, polished, and sandblasted pre-sintered/sintered Y-TZP surfaces, which

simulate clinical conditions with respect to phase transformation, surface morphology and removal mechanisms.

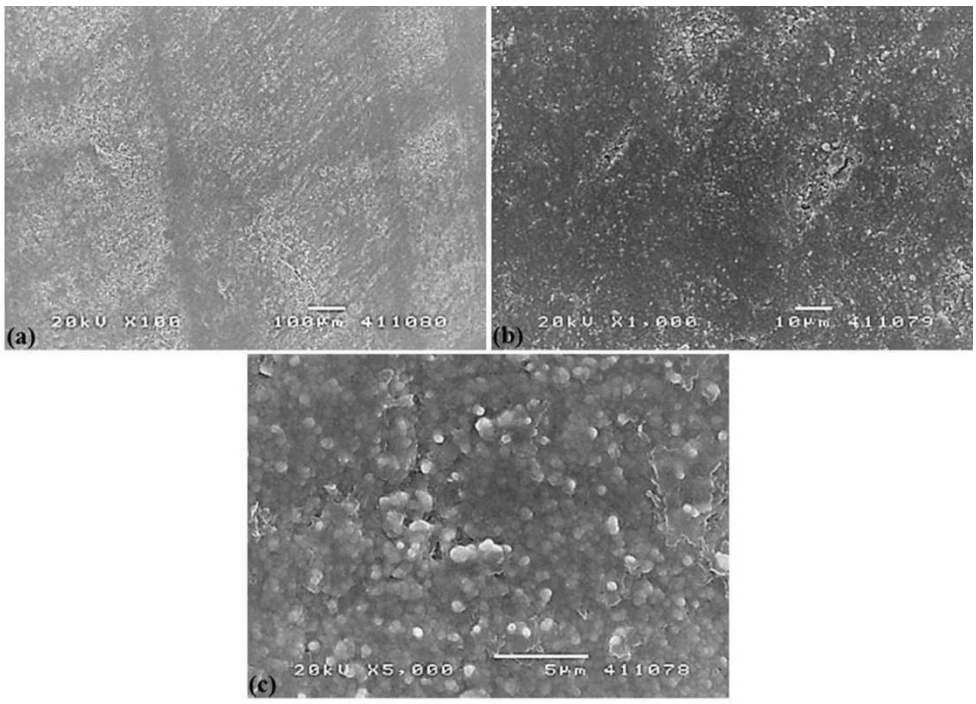


Fig. 6.9. SEM micrographs of the CAD/CAM-polished-sintered Y-TZP surface revealing (a) smooth surface with no visible milling scratches, (b) little surface defects and (c) details involving plastic deformation and little microstructural defects like porosity produced during the densification process.

In this study, the x-ray diffraction patterns in Fig. 6.3(a) showed that both tetragonal (Z1) and baddeleyite/monoclinic (B) $ZrO_2$ were the main crystalline phases in the CAD/CAM and CAD/CAM-polished processes. The monoclinic content was minor, and approximately 3% according to the equation proposed by Garvin and Nicholson (1972) modified by Toraya et al. (1984):

$$V_m = \frac{1.311\left[ I_m\left(\bar{1}11\right) + I_m\left(111\right)\right]}{1.311\left[ I_m\left(\bar{1}11\right) + I_m\left(111\right)\right] + I_t\left(111\right)} \tag{6.1}$$

where $V_m$ is the monoclinic volume content; $I_m$ and $I_t$ are the peak integrated peak intensities of the monoclinic and tetragonal peaks, respectively.

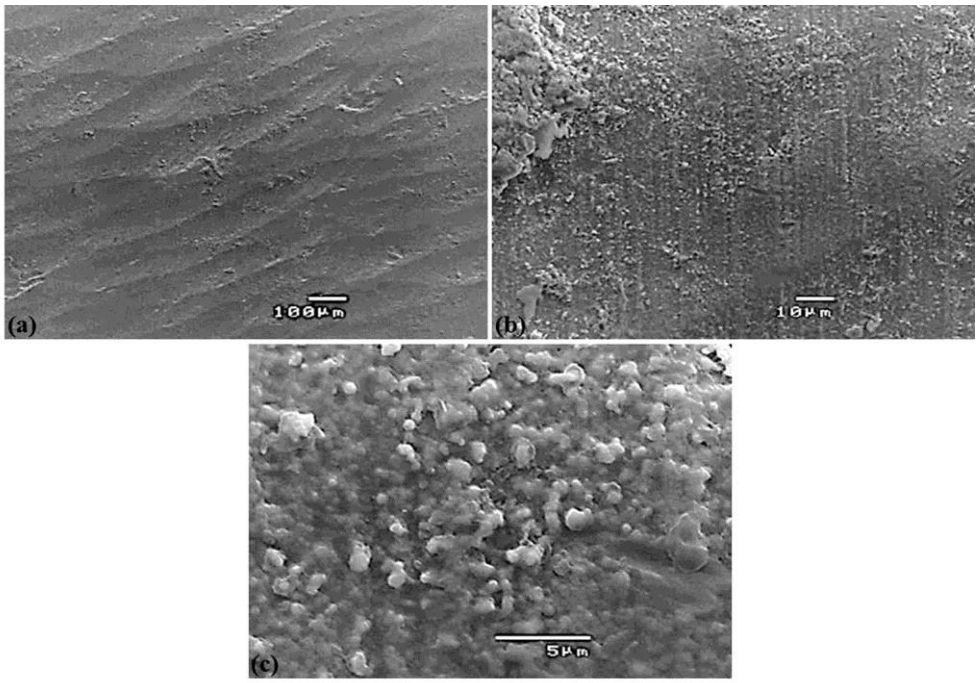


Fig. 6.10. SEM micrographs of the CAD/CAM-sintered-110-µm-alumina sandblasted Y-TZP surface revealing (a) the blasted traces with pulverized Y-TZP grains on the surface, (b) details of the massive pulverized grains, micro scratches and pitting on the surface which resulted from eroding and impacting from the alumina particles, and (c) details revealing ploughing, plastic deformation and pitting on the zirconia surface.

This monoclinic volume content was the same for unmilled pre-sintered Y-TZP samples reported by Monaco et al. (2013), indicating that CAD/CAM milling did not lead to a phase change. Further, polishing after milling did not change the phase, either. However, thermal sintering after CAD/CAM-polished process transformed the monoclinic to tetragonal $ZrO_{1.95}$ (Z2) in Fig. 6.3(b). This tetragonal $ZrO_{1.95}$ (Z2) phase has been referred to as non-stoichiometric tetragonal zirconia or the crystalline oxygen defective tetragonal structure in the literature (Arroyave et al., 2002). The phenomenon behind this transformation is not known yet; however, future studies are envisaged to unravel why this phase occurred. It was reported that this phase was thermodynamically as stable as tetragonal $ZrO_2$ (Ivanoskaya and Frolova, 2007). This suggests that the spontaneous martensitic monoclinic phase transformation may not occur in tetragonal $ZrO_{1.95}$ (Z2) phase except under tensile stresses or humid environment which subjects Y-TZP to low temperature degradation. Further, the complete transformation of monoclinic to tetragonal phase following the sintering process after milling (Fig. 6.3(c)) indicated that fully stabilized tetragonal $ZrO_2$ structures were formed. This is expected because the sintering temperature (1520 °C) was high enough to induce this transformation (Scott, 1975), ensuring the sintered Y-TZP the highest flexural strength of 1281.1 ± 230 MPa (Stawarczyk et al., 2013). Further mechanical polishing of sintered Y-TZP had no effect on the tetragonal phase.

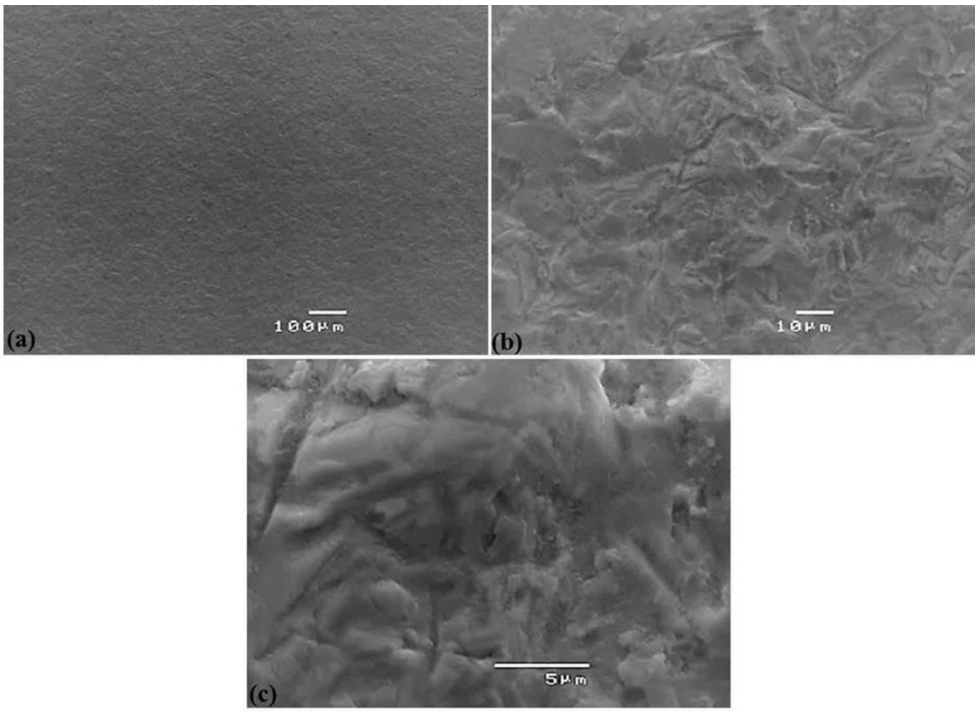


Fig. 6.11. SEM micrographs of the CAD/CAM-sintered-250 µm alumina sandblasted Y-TZP surface revealing (a) the rough surface mainly due to the blasting by the alumina particles without milling traces, (b) rough surface features consisting of randomly oriented scoring and scratches, and (c) large-scale surface defects including deep sharp scratches, micro-craters, pitting and grain pull-out.

Previous studies have claimed that sandblasting of Y-TZP surfaces with 110-µm and 250-µm alumina particles induced mechanical stresses, which transformed the tetragonal to monoclinic phase in sintered Y-TZP (Chintapalli et al., 2013; 2014; Curtis et al., 2006; Guazzato et al., 2005; Kosmac et al., 2000; Monaco et al., 2013; Passos et al., 2015). However, in this study, there was no clear evidence of monoclinic phase in Fig. 6.3(d). The inconsistency between previous and our current studies could be as a consequence of different methods used. In previous studies, the polished-sintered Y-TZP samples were sandblasted in which the polishing removed the compressive layers of the sintering-induced residual stresses, leaving tensile surfaces which can be transformed to monoclinic by sandblasting. In our current study, sintered Y-TZP surfaces were sandblasted after they had been milled using the clinical CAD/CAM process. The CAD/CAM-milling process induced damage (Fig. 6.5) which was further enhanced by sintering (Fig. 6.7). Meanwhile, sintering also converted monoclinic to a strained tetragonal phase (Fig. 6.3(c)). So the amount of strained tetragonal phase produced in sandblasting was less than required to be transformed to monoclinic phase (Denry and Holloway, 2006). Another reason might be that the sandblasting process conditions used in this study introduced surface flaws below the critical transformed depth zone for the monoclinic

phase to occur. These critical transformed depth zones were reported as 12 ± 1 μm and 13 ± 1 μm for 110 μm and 250 μm alumina particles, respectively (Chintapalli et al., 2013). Further, Y-TZP revealed much less susceptibility to stress-induced transformation than a ceria-stabilized zirconia/alumina (CZA) (Sato et al., 2008).

As reported in Table 6.1, each fabrication process significantly affected the surface roughness parameters ($R_a$ and $R_z$) in Fig. 6.4. These surface roughness parameters were selected based on their wide usage in surface texture characterization (De Chiffre et al., 2000). As shown in Fig. 6.4, the mean surface roughness values generated in different fabrication processes ranged from $R_a$ 0.21–0.43 μm and $R_z$ 1.73–2.95 μm, which were in the range of roughness values of ground-polished zirconia published by Miyazaki et al. (2013). In addition, the surface roughness values of CAD/CAM-sintered-sandblasted samples with 110 and 250 μm alumina particles which ranged from $R_a$ 0.48–0.55 μm and $R_z$ 3.08–3.41 μm were also consistent with $R_a$ 0.6 μm reported by Monaco et al. (2013).

The SEM micrographs of the CAD/CAM-milled process revealed partial ductile and brittle fracture modes as the dominant material removal mechanism for this material (Fig. 6.5). These removal modes were consistent with what Luthardt et al. (2004) reported for CAD/CAM machining of sintered Y-TZP, indicating the correctness of the machining removal behavior for pre-sintered Y-TZP in the current study. The brittle fracture which was by intragranular and transgranular fracture in nature can clearly be seen in Fig. 6.5(c) where the Y-TZP grains fragmented into micro-sized chips. This brittle fracture behavior of this material was previously predicted in nanoindentation studies if machining was done at low cutting speeds (Alao and Yin, 2014b; 2016). To ascertain that this material was machined at low cutting speeds, the spindle speed can be converted to the cutting speed in milling by the following expression (Kalpakjian and Schmid, 2013):

$$V = \frac{\pi D N}{60} \tag{6.2}$$

where $V$ is the cutting speed, $D$ is the cutting tool diameter (1 mm) and $N$ is the spindle speed (30,000 rpm). Upon substitution of $D$ and $N$ values in Eq. 2, the cutting speed was 1.57 m/s which was in the low machining speed region when compared to the high machining speed region of 40–160 m/s (Yin and Huang, 2004). Consequently, brittle machining fracture would have occurred because of the likely events of tensile residual stresses causing lateral cracks when the cutting tool traversed the material based on the low cutting speed applied (Alao and Yin, 2014b; 2016).

Simply polishing of the CAD/CAM pre-sintered Y-TZP surface could insignificantly reduce the surface roughness, $R_a$ and $R_z$ as shown in Fig. 6.4 and Tables 6.2 and 6.3. The polishing alone removed the Y-TZP material by abrasion in which polishing abrasives transmitted the mechanical energy to the material, removing or displacing the surface layers (Evans et al., 2003; Jefferies, 2007). The polishing quality is dependent on the type and size of abrasives, polishing medium and polishing conditions applied (Evans et al., 2007). In generally, finer grits produce smoother surfaces. In this study, the applied medium (60–70 µm) grit-size polishing medium produced polishing traces (Fig. 6) and weakly removed the milling traces. This polishing process was accompanied by localized heat, which led to delamination, pitting and micro-craters on the surface (Fig. 6.6(b)).

Meanwhile, simply sintering of the CAD/CAM-milled pre-sintered Y-TZP surface could not significantly reduce the surface roughness, as shown in Fig. 6.4 and Table 6.3. The increased surface roughness could be attributed to the occurrence of sintering-induced grain coarsening (Fig. 6.7) and residual stresses (Denry, 2013). Meanwhile, the shrinkage associated with grain growth and the monoclinic to tetragonal phase transformation as evidenced in Fig. 6.3(c) could have contributed to the increased roughness (Alao and Yin, 2014a; 2015b; Chevalier et al., 2009).

The polishing process did not improve the surface roughness of the sintered Y-TZP surface as demonstrated in Fig. 6.4 and Table 6.3. This is because the applied medium grit abrasives could generate localized heat inducing cracks in the process (Jefferies, 2007), as evident in the polishing-induced intergranular fracture (Fig. 6.8) due to the high strength of sintered Y-TZP. Previous studies have demonstrated that the polishing of sintered Y-TZP surface was difficult (Yin and Huang, 2008) but not impossible if appropriate diamond grit size were used (Kou et al., 2006; Miyazaki et al., 2013). This indicates that the applied medium grit-sized abrasives might have been ineffective for polishing the sintered Y-TZP. It is likely to obtain the improved surface roughness by using finer abrasives. However, it would result in the increased polishing time and manufacturing costs for Y-TZP restorations.

The CAD/CAM-polished-sintered process produced the smoothest surface roughness, $R_a$ = 0.21 ± 0.03 µm and $R_z$ = 1.73 ± 0.04 µm, compared to other fabrication processes in Fig. 6.4. This may be attributed to the simultaneous action of polishing and sintering processes on the CAD/CAM-milled surface (Fig. 6.9). Meanwhile, the mechanical properties of pre-sintered and sintered zirconia materials play critical roles in fabrication processes. In generally, pre-sintered zirconia hardness ranged 0.92 ± 0.35 GPa to 1.28 ± 0.27 GPa (Alao and Yin, 2014b) while sintered zirconia were more than seven times harder, with values of 7.61 ± 2.96 GPa to 9.33 ±

1.02 GPa (Alao and Yin, 2014a). The harder the material, *the harder* it is to remove (Yin, 2012). Thus, the polishing of pre-sintered Y-TZP could have relatively easily removed the milling traces, leaving a tensile surface that was transformed by the sintering process to both tetragonal $ZrO_2$ and tetragonal $ZrO_{1.95}$ (Fig. 6.3(b)). Further, it minimized the roughening effect caused by the sintering-induced grain coarsening. Consequently, the surface roughness was improved (Table 6.3) with plastic deformation formation and little porosity (Fig. 6.9(c)). Both the surface roughness, $R_a$ and $R_z$, produced in the CAD/CAM-polished-sintered process were significantly different from those made in the CAD/CAM-polished process ($p < 0.05$). It is interesting to note the surface roughness $R_a$ = 0.21 ± 0.03 µm met the threshold surface roughness ($R_a$ = 0.2 µm) for bacterial plaque retention (Bollen et al., 1997). This supports its clinical acceptability and indicates the non-retention of bacteria on its surface. Thus, this fabrication process is recommended for the fabrication of Y-TZP restorations from this material.

The quality of intaglios in Y-TZP restorations produced by sandblasting affects adhesive bonding, fit and occlusion (Chintapalli et al., 2013; Curtis et al., 2006; Guazzato et al., 2005; Kosmač et al et al., 1999; 2000; Monaco et al., 2013; Passos et al., 2015; Rekow et al., 2011). The sandblasting process involves the transformation of tetragonal Y-TZP to monoclinic phase, which could strengthen the material if compressive residual stresses are induced. The strength degradation may have also occurred when these compressive residual layers are exceeded by sandblasted flaws (Kosmač et al., 1999; 2000). The extent of transformation, transformed zone and degree of damage depend on the sandblasting conditions applied. Sandblasting with larger abrasives are generally associated with the larger monoclinic phase, transformed zone and damage (Passos et al., 2015; Rekow et al., 2011). In this study, the phase transformation induced by sandblasting was not detected. This may imply that the significant strength degradation might not occur in this material sandblasted with 110-µm alumina particles because mild sandblasting-induced flaws are not detrimental to the strength of Y-TZP (Chintapalli et al., 2013; Kosmač et al., 1999; 2000). The sandblasting-induced flaws in Fig. 6.10 show the occurrence of erosive wear through chipping which levelled the milled surface and sintering-induced grain coarsening, causing ploughing, plastic deformation and pitting on the surface. The similar morphological behavior of the sintered Y-TZP sandblasted using the same grit-sized alumina particles was reported, which was attributed to the strong affinity between alumina and zirconia grains under the induced impact energy (Chintapalli et al., 2013; Kosmač et al., 1999; 2000).

However, sandblasting with 250-µm alumina abrasives induced deep sharp scratches, pitting, grain pull-out and micro-craters (Fig. 6.11) due to the induced high impact energy. The similar behavior was also reported by Chintapalli et al. (2013). These flaws will act as stress

concentration sites for fracture initiation and propagation, greatly compromising the strength of the studied sintered Y-TZP. This is because of the lack of the sandblasting-induced phase transformation (Fig. 6.3(d)) to generate compressive stresses to counteract the sandblasted-induced defects. Consequently, the flaws will affect the long-term property of the material, making the restorations vulnerable to catastrophic failure. Based on these reasons, the sandblasting of this material using 110-μm alumina particles is therefore recommended.

Different from industrial products produced and evaluated using standardized procedures and processes, the quality of ceramic restorations heavily relies on the clinician's experience and visual examinations at different dental clinics. Many dental supplies provide different CAD/CAM systems, milling tools, polishing media, sandblasting machines/abrasives/particle sizes, and sintering furnaces/conditions. However, there lack international standards, which can address best practices for use of dental materials and best operating procedures for reliable restorations (Hayashi et al., 2014; Sakaguchi, 2005). Further, dental education, clinical training and practices in different countries and regions are very different. All these can induce variabilities in quality control for ceramic restorations. Although our study simulated most clinical procedures in zirconia restorations, it is unlikely to cover all practical variabilities applied at different dental clinics. Nevertheless, our quantitative results will provide dental clinicians the scientific insights into the surface quality control for reliable zirconia restorations.

## 6.5 Conclusions

This work studied the surface quality of pre-sintered/sintered Y-TZP produced in dental restorative surface processes including CAD/CAM-milling, sintering, polishing and sandblasting. The sintering-induced monoclinic-tetragonal phase transformation was found by x-ray diffraction while the sandblasting-induced phase transformation was not detected. The CAD/CAM milling produced a rough surface due to the partial ductile deformation and brittle fracture modes of material removal mechanisms. Simply polishing after the CAD/CAM milling process could not reduce the surface roughness because simply displacing the material by mechanical action could not significantly wear away the milling traces. Simply sintering after the CAD/CAM milling process also roughened the surface due to the induced grain coarsening, shrinkage associated with the grain growth and phase transformation. Polishing after sintering did not improve the surface mainly due to the higher strength of sintered Y-TZP. In comparison, the smoothest surface was produced in CAD/CAM milling, polishing and sintering process which met the dental surface quality and bacterial plaque retention and was thus recommended for fabricating dental Y-TZP restorations. Sandblasting with 110-μm alumina abrasives was also recommended due to less severe damage induced compared to 250-μm alumina abrasives.

# Chapter 7

# Fatigue Behavior of Treated LDGC and Y-TZP Surfaces

## 7.1 Introduction

High-strength LDGC and Y-TZP are excellent ceramics for dental crowns and bridges (Guess et al., 2010b; Silva et al., 2011). LDGC is a highly aesthetic ceramic requiring no porcelain veneer whereas full-contour Y-TZP restorations fabricated from pure and highly translucent Y-TZP requiring no veneering were recently incorporated into the restorative dentistry (Beuer et al., 2012; Miyazaki et al., 2013; Silva et al., 2010). Therefore, the chipping of porcelains and complications arising from the performance of the veneering process in improving the aesthetic property of these ceramics can be circumvented. Thus, LDGC and Y-TZP with acceptable aesthetics are suitable as monolithic restorations and are applied in the posterior region of the mouth (Zhang et al., 2013a) where the concentrating stresses are greatest (Höland et al., 2000; Rekow and Thompson, 2005; 2007; Studart et al., 2007).

The fabrication of LDGC and Y-TZP restorations follow similar trend with the current CAD/CAM technology. LDGC restorations are manufactured by CAD/CAM-milling of the intermediate lithium metasilicate glass-ceramic (LMGC) which is easier to machine and then sintered ensuring full crystallization into lithium disilicate crystals (Alao and Yin, 2015 Denry and Holloway, 2010; Li et al., 2014; Ritzberger et al., 2010). Similarly, the pre-sintered Y-TZP is CAD/CAM-milled and then sintered into Y-TZP restorations (Alao and Yin, 2014b; 2016; Denry and Kelly, 2008; Filser et al., 2003; Li et al., 2014; Ritzberger et al., 2010). The CAD/CAM-milling process may initiate crack sites in both LMGC and pre-sintered Y-TZP which may not be completely healed in the following sintering process thereby compromising the strengths of LDGC and Y-TZP restorations (Rekow and Thompson, 2005; Rekow et al., 2011). Other post-fabrication processes like grinding, polishing and sandblasting can potentially exacerbate the existing crack sites or introduce additional initiation sites (Rekow and Thompson, 2005).

A further consequence of the CAD/CAM-induced damage on these ceramic restorations is the failure associated with their long-term fatigue performance. During mastication, mechanical fatigue occurs by the cyclic movement of the lower jaw governed by different muscle groups in different cycle periods (Kosmač et al., 2008). Consequently, the ceramic restorations have to withstand masticatory forces ranging from 100–800 N, at 1500 cycles per day and a frequency

of up to 1.5 Hz at contacts between the opposing cusps of characteristic radii from 2–4 mm during mastication, chewing, teeth grinding/clenching processes (Peterson et al., 1998; Rekow and Thompson, 2007). So, the damage induced during fabrication, preparation and post-fabrication processes can be exacerbated during repetitive occlusal contact leading to the premature clinical failure of ceramic restorations. Therefore, the knowledge of the fatigue behaviour of dental ceramics is critical to their clinical long-term performance.

Fatigue is a process involving initiation, nucleation, coalescence and propagation of cracks. The greatest fatigue damage occurs in the oral posterior region where the greatest concentrating stresses propagate cracks along the tensile field (Zhang et al., 2013b). Traditional load-to-failure tests are amenable to long-crack tests obtaining rising (*R*-curve) toughness values for ceramics (Kelly et al., 2010). However, these tests do not report the correct stress state; the reported crack systems are not compatible with the bulk clinical failure and the reported failure loads far exceed the clinical acceptable ranges for mastication, swallowing and bruxism (Kelly et al., 2010). Another major shortcoming of long-crack tests is the restriction in their capacity for extrapolation down to the microstructural scale (Padture and Lawn, 1995; Pajares et al., 1995; Peterson et al., 1998). Consequently, they are not favourably sensitive to short-crack properties like strength and wear (Padture and Lawn, 1995).

Hertzian contact test can characterize the fatigue damage of dental ceramics because it provides a simple means to quantify the failure mechanisms within the critical short-crack domain (Pajares et al., 1995; Lawn, 1998; Lawn et al., 2001). In this domain, the strength of dental ceramics is most vulnerable (Guiberteau et al., 1993, Zhang et al., 2004b). This test consists of indenting simplified flat geometries with a contacting sphere (Lawn, 1998). The contacting sphere can be made of either a hard steel/tungsten carbide to represent biting on a hard object or polymer to represent chewing on soft food (Lawn, 1998). This way, the oral loading conditions which have direct clinical relevance are simulated: the contact loads and indenter radius simulate the occlusal loads and cuspal curvature respectively (Peterson et al., 1998). The loads can be static, dynamic or cyclic. Static fatigue involves the application of constant stress or strain; dynamic fatigue involves applying constant stressing or straining rate and cyclic fatigue represents application of time-varying stress/strain. The failure modes associated with each loading system are different from one another with the cyclic loads inducing the most severe damage on dental ceramics (Zhang et al., 2013b).

Several failure modes have been reported which usefully identify failures observed clinically on dental ceramic crowns and bridges. The near-surface damage from a model flat layer structures is used to simulate occlusal contact surface cracks in which the sphere is in normal contact with

the ceramics of large thickness. These cracks include outer, inner and partial cones and quasi-plastic deformation (Lawn et al. 2001; Peterson et al., 1998; Zhang et al., 2013b). The outer cone cracks initiate from the top surface outside the contact circle where the Hertzian tensile stress is maximum and grows steadily with time under static load by slow crack growth mechanism leading to tooth chipping (Deng et al., 2002a; Zhang et al., 2013b). The inner cones appear after a prolonged cyclic load and are driven by hydraulic pumping of fluid into surface micro-cracks while partial cones develop in sliding loading by the tangential load component which skews the tensile stress field at the trailing contact edge (Zhang et al., 2013b). The quasi-plastic deformation is also initiated below the contact when the maximum shear stress in the Hertzian near field exceeds half the yield stress (Deng et al., 2002a). It leads to damage accumulation, micro-crack coalescence and accelerated wear. In cyclic loading, radial-median cracks can evolve beneath the accumulated plastic damage zone (Zhang et al., 2013b). In addition, the analogous contact fatigue tests on bilayer structures in which the ceramic is bonded unto a compliant substrate have been used to simulate the fatigue behavior of a dental ceramic crown bonded unto dentine (Deng et al. 2002a; Lawn et al., 2002a; 2004; Zhang and Lawn, 2004; 2005; Zhang et al., 2004a; 2004b; 2013b). At the cementation surface beneath the contact, radial cracks pop-in spontaneously from the starting flaws when the maximum tensile stress equals the bulk flexural strength (Deng et al. 2002a; Lawn et al., 2002a; 2004; Zhang and Lawn, 2004; 2005; Zhang et al., 2004a; 2004b; 2013b). They are highly deleterious in strength losses, barely undetectable in opaque ceramics resulting in their bulk failure (Lawn et al., 2002b; 2004).

Several failure modes may compete in dental ceramics. A mode that dominates under any given set of conditions may be superseded under a different set of conditions. Consequently, failure modes in dental ceramics can be influenced by loads, load types, environment, indenter radius, and material type (Zhang et al., 2005). Most failure modes associated with monolayer structures have been reported in the literature with Hertzian fatigue tests performed on top polished surfaces while only in few cases are tests conducted on top surfaces abraded with 600 silicon carbide grit to introduce controlled flaw density for cone crack initiation (Bhowmick et al., 2005; Zhang et al., 2005). Further, in some cases, the cementation surfaces have been ground, polished or sandblasted to introduce controlled flaws for the initiation of radial cracking in bilayer systems (Guess et al., 2010a; Zhang and Lawn, 2005; Zhang et al., 2004a). However, no studies have reported the prevailing fatigue mechanisms for CAD/CAM-milled LMGC and pre-sintered Y-TZP subjected to subsequent surface conditions including sintering, polishing, sandblasting and glazing. These treatments introduce uncontrolled flaw densities on the sintered LDGC and Y-TZP surfaces. Therefore, understanding the fatigue behavior of these two dental ceramics conditioned to different surface treatments in the low-cycle-high-load cyclic Hertzian

indentations become an important step in the clinical success of LDGC and Y-TZP restorations (Rekow et al., 2011).

This chapter aimed to investigate the fatigue behavior of differently treated LDGC and Y-TZP surfaces in low-cycle-high-load cyclic indentations mimicking teeth clenching or grinding. The top CAD/CAM-milled LMGC surfaces underwent various sintering, polishing and glazing conditions simulating various clinical surfaces as enumerated in Chapter 5. Similarly, the top CAD/CAM-milled pre-sintered Y-TZP surfaces were subjected to various sintering, polishing and sandblasting conditions used in dental practice as documented in Chapter 6. Maximum contact stresses were evaluated as functions of number of cycles and different surfaces of the two materials using the Hertzian model. The fatigue damage of differently treated LDGC and Y-TZP surfaces after cyclic indentations was viewed using SEM to understand the relationships among microstructures, surface asperities and crack propagation. Finally, the fatigue mechanisms of LDGC and Y-TZP subjected to differently treated surfaces were proposed.

## 7.2 Hertzian Contact Fatigue Characterization of Dental Ceramics

### *7.2.1 Mechanics of Cone and Quasi-Plastic Cracks*

The mechanism underlying the formation of cone and quasi-plastic cracks involves crack initiation and propagation process. The cone crack evolves from a ring crack from the top surface outside the elastic contact when the maximum Hertzian tensile stress is reached and then propagates downwards into a stable, truncated cone configuration (Deng et al., 2002). This formation occurs at a critical load ($P_C$) which is expressed by (Lawn 1998):

$$\frac{P_C}{r} = \frac{AK_{Ic}^2}{E} \tag{7.1}$$

where $K_{Ic}$ is the fracture toughness; $E$ is the elastic modulus, $r$ is the radius of indenter and $A$ is a dimensionless constant Auerbach's law expressed as (Lawn 1998):

$$A = \frac{4\pi^2 k}{3I_*^2} \tag{7.2}$$

The value of $A$ has been established as 8600 (Lawn et al., 2001). Consequently, the prediction of $P_C$ can be obtained much easier from material properties and indenter size. Thus, at a given indenter size, tough dental ceramics will have higher $P_C$ values than brittle ceramics.

Quasi-plastic damage occurs when the maximum shear stress in the Hertzian near field exceeds half of the yield stress ($Y$) with the $Y$ determined from the Tabor relation (Lawn, 1998). It occurs at a critical yielding load ($P_Y$) (Rhee et al., 2001):

$$\frac{P_Y}{r^2} = DH\left(\frac{H}{E}\right)^2 \tag{7.3}$$

where $H$, $E$ and $r$ are the hardness, elastic modulus, indenter radius respectively and $D$ is a dimensionless constant expressed by (Rhee et al., 2001):

$$D = \left(1.1\frac{\pi}{c'}\right)^3\left[\frac{3\left(1-\nu^2\right)}{4}\right]^2 \tag{7.4}$$

The value of $D$ has been quantitatively established as 0.85 (Rhee et al., 2001). Again the prediction of $P_Y$ can be made easier from material properties and indenter size. Therefore, at a given indenter size, hard dental ceramics will have higher $P_R$ values than soft ceramics. A parameter derived from the $P_Y/P_C$ ratio can usefully indicate material's index for brittleness or quasi-plasticity. If this $P_Y/P_C$ is greater than 1, the material is brittle; if it is less than 1, it is quasi-plastic (Rhee et al., 2001). However, these critical loads, $P_C$ and $P_Y$, can be reduced greatly during cyclic fatigue by the time-cumulative slow crack growth mechanisms (Lawn et al., 2007; Zhang et al., 2005; 2009). Additional contribution to the reduction of $P_Y$ in cyclic fatigue is the mechanical driving forces which arise from residual stresses within a precursor quasi-plasticity zone (Zhang et al., 2005).

### *7.2.2 Mechanics of Cone and Quasi-Plastic Cracks*

Radial cracks develop on the lower portion of the ceramic at the cementation and connecting surfaces respectively. Specifically, radial cracks become the dominant fracture mode in a thin ceramic bonded on a thick substrate and are consequences of the ceramic layer flexure on a compliant substrate (Lawn et al., 2001; 2002b). In addition, it is said that radial cracks tend to close-up during unloading, making their detection in translucent ceramics difficult (Zhang et al., 2013b). But they lead to deleterious strength loss because they are formed first prior to the induction of cone or quasi-plastic damage in thin bilayers (Lawn et al., 2004). In translucent ceramics, their effect is noticed when delamination or bulk failure has occurred (Lawn et al., 2002b; 2004).

The radial crack pops in spontaneously from a starting flaw in the inner ceramic surface when the maximum tensile stress in this ceramic equals the ceramic bulk flexural stress at critical load ($P_R$) given by (Lawn et al., 2001; 2002b):

$$P_R = B\frac{\sigma_c d^2}{\log\left(E_c/E_s\right)} \tag{7.5}$$

where $B$ is a dimensionless coefficient, $E_c$ and $E_s$ are the ceramic and substrate elastic moduli respectively, $\sigma_c$ is the ceramic flexural stress and $d$ is the ceramic thickness. The value of $B$ was reported as 1.35 (Zhang and Lawn, 2004; Zhang et al., 2009). Eq. (2.5) is valid within $1< E_c/E_s < 100$. Thus, strong dental ceramics will have higher $P_R$ values than weak ceramics. However, the $P_R$ would increase with an increase in loading rate in dynamic fatigue and decrease with test duration time (Zhang and Lawn, 2004). It would also reduce in cyclic fatigue causing cracks to spread steadily over extended time due to the slow crack growth mechanism and mechanical driving forces in quasi-plasticity (Lawn et al., 2007; Zhang et al., 2005; 2009). Also, it is reported that the $P_R$ is insensitive to tangential and sliding loadings since the Hertzian normal contact produces radial crack geometry and critical loads similar to what obtains in sliding and inclined directions (Lee et al., 2001). However, they can be avoided by keeping the net layer thickness sufficiently large, preferably at $d > 1.5$ mm (Lawn et al., 2004).

## 7.3 Experimental Procedures

### *7.3.1 Materials*

The materials investigated include LDGC and Y-TZP whose details have been previously reported in Chapters 5 and 6 respectively. The surfaces of these materials were subjected to different treatments which simulate varying surface conditions in dental clinical practice. These surface treatments subjected the materials to different surface asperities providing different residual stress distributions.

As reported in Chapter 5, the CAD/CAM-milled LMGC surfaces were subjected to different sintering, polishing and glazing conditions. These processes were then designated as CAD/CAM-sintered, CAD/CAM-polished-sintered, CAD/CAM-sintered-polished, CAD/CAM-sintered-glazed and CAD/CAM-polished-sintered-glazed. Prior to the fatigue indentation tests, the smoothest surface roughness was produced in the CAD/CAM-polished-sintered process followed by the CAD/CAM-polished-sintered-glazed process and then CAD/CAM-sintered-polished and then CAD/CAM-sintered processes. The roughest surface roughness was produced in the CAD/CAM-sintered-glazed process. The mechanical properties of sintered LDGC are: Vickers hardness, $H_v$ is 5.8 ± 0.1 GPa, Young's modulus, $E$ is 95 ± 5 GPa and fracture toughness, $K_{Ic}$ is 2.25 ± 0.25 MPa $m^{1/2}$ and biaxial strength is 360 ± 60 MPa (Bühler-Zemp and Völkel, 2005a).

The CAD/CAM-milled pre-sintered Y-TZP surfaces were also treated with different sintering, polishing and sandblasting conditions as presented in Chapter 6. These were then designated as CAD/CAM-sintered, CAD/CAM-polished-sintered, CAD/CAM-sintered-polished, CAD/CAM-110-µm alumina sandblasted and CAD/CAM-250-µm alumina sandblasted processes. Prior to the fatigue tests, the smoothest surface roughness was produced in the CAD/CAM-polished-sintered process followed by the CAD/CAM-sintered-polished process and then CAD/CAM-sintered and then CAD/CAM-sintered-sandblasted with 110 µm alumina particles processes. The roughest surface roughness was generated in the CAD/CAM-sintered-sandblasted with 250 µm alumina process (Chapter 6). The mechanical properties of sintered Y-TZP are: Vickers hardness is 13 GPa, Young's modulus is 210 GPa and fracture toughness is 5.5 MPa $m^{1/2}$ and flexural strength is 1281.1 ± 230 MPa (Alao and Yin, 2014a; Ritzberger et al., 2010; Stawarczy et al., 2013).

### *7.3.2 Hertzian Indentation Fatigue Tests*

For each treated LDGC and Y-TZP surface, three specimens were prepared for the fatigue tests, making a total of 15 specimens each for LDGC and Y-TZP ceramics. The specimens were subjected to the Hertzian fatigue tests using tungsten carbide spherical indenter with a curvature radius of 2.5 mm. This indenter radius fell within the cuspal radii (2–4 mm) for posterior teeth in the oral zone (Peterson et al., 1998). Fig. 7.1(a) shows a typical sample and the indenter placed inside the aluminium sleeve with a steel base before the fatigue test. Hertzian cyclic fatigue tests were carried out on treated LDGC and Y-TZP surfaces which served as their frictional tensile surfaces for evaluating the surface quality effect on their fatigue behavior. The specimen and the indenter were coupled together as shown in Fig. 7.1(b) and mounted on the underside of the crosshead on the universal testing machine (United STM–50KN Testing System) as shown in Fig. 7.1(c). The machine was programmed to apply cyclic loads ranging from 50 N to a maximum load of 800 N at a frequency of 0.1 Hz on the treated surfaces. The applied frequency conformed to the chewing profile during mastication (Steiner et al., 2009, Yin et al., 2013). In addition, the machine applied 1, 10, 100, 1000 and 3000 low indentation cycles to enable the ensuing damage patterns to be examined as a function of number of cycles. Also, the total contact times at 1, 10, 100, 1000 and 3000 indentation cycles corresponded to 10, 10, 1000, 10000 and 30000 s respectively.

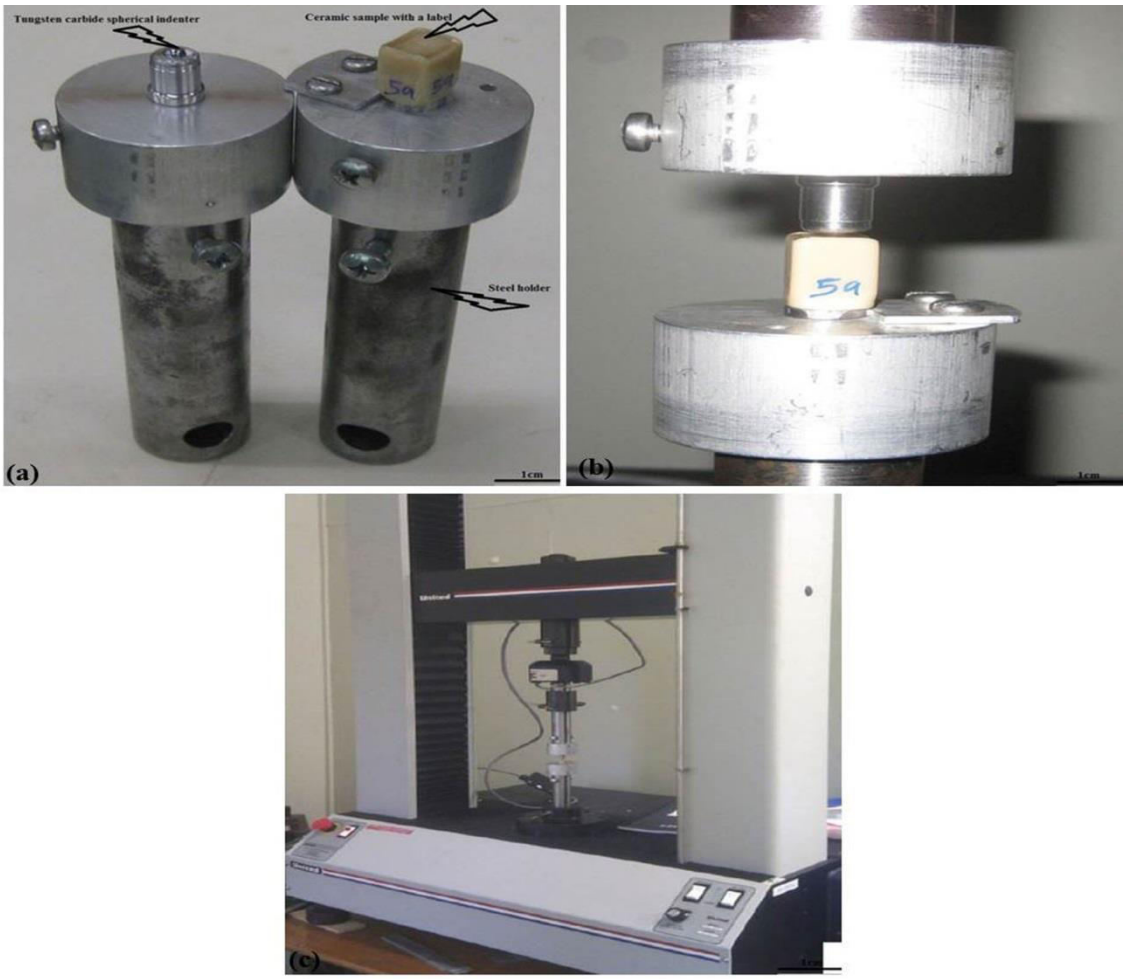


Fig. 7.1. Optical images of (a) the tungsten carbide spherical indenter and a typical ceramic sample positioned inside the aluminum sleeve which is positioned inside a steel base, (b) the coupling of the indenter and sample on the universal testing machine, and (c) the fatigue experimental setup.

### *7.3.3 Surface Characterization*

The maximum contact stress, $\sigma_{max}$, of each treated LDGC and Y-TZP surface under the Hertzian fatigue test was measured using an optical microscope. It was calculated using the Hertzian equation assuming an elastic contact of a sphere on a flat surface (Budinski and Budinski, 2010):

$$\sigma_m = \frac{1.5P_{\max}}{\pi a^2} \tag{7.6}$$

where $P_{max}$ is the maximum load and $a$ is the contact radius. The contact radius of each treated LDGC and Y-TZP surfaces was calculated from the optical image of the indentation-induced residual imprint (Guiberteau et al., 1993). Fig. 7.2 shows examples of indented surfaces of LDGC (Fig. 7.2(a)) and Y-TZP (Fig. 7.2(b)) in which four lines representing contact diameters

were drawn and converted to the image scale bar. Then, the average contact diameter was calculated from the four lines from which the average contact radius was obtained.

Some samples were selected from each surface-treated LDGC and Y-TZP after 1, 10, 100, 1000 and 3000 indentation cycles and examined under SEM (Jeol JSM5410LV, Tokyo, Japan) for ensuing damage evolution. Prior to this SEM examination, the samples were gold-coated, making their surfaces conductive to allow high quality images to be taken.

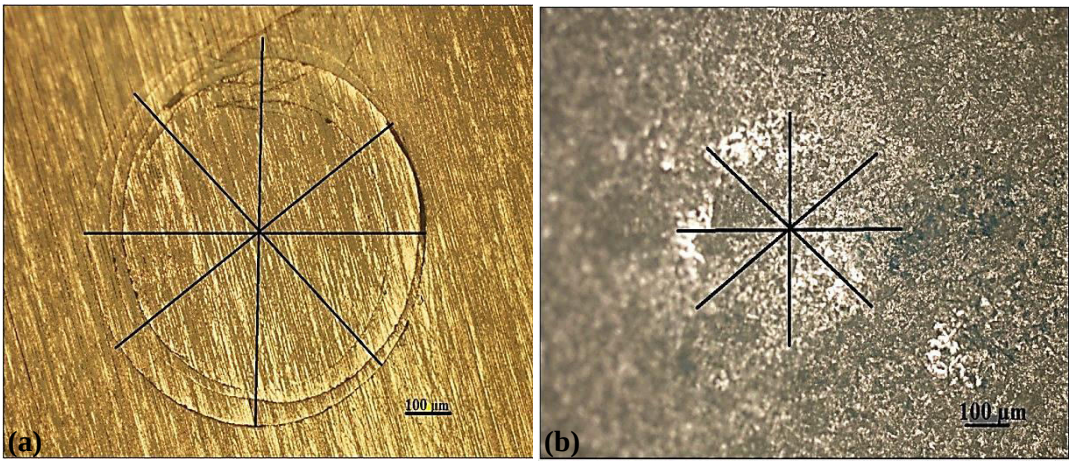


Fig. 7.2. Optical images of indented surfaces used in the computation of contact radius for the maximum contact stress (a) LDGC and (b) Y-TZP.

### *7.3.4 Statistical Analysis*

A two-factor analysis of variance (ANOVA) with replication was applied at 5% confidence interval to examine significant effects of surface treatments and number of cycles on maximum contact stresses of indented LDGC and Y-TZP surfaces in this study.

## 7.4 Results

### *7.4.1 Maximum Contact Stresses*

Fig. 7.3 shows the maximum contact stress versus number of cycles for differently treated LDGC surfaces. All maximum contact stresses decreased with the increase in number of cycles for all treated surfaces, indicating that the contact areas became larger with higher number of cycles. Table 7.1 summarises the maximum contact stresses obtained at different number of cycles for differently treated LDGC surfaces. By increasing the number of cycles from 1 to 3000, the average maximum contact stresses decreased by 60%, 52%, 64%, 50%, 55% for

CAD/CAM-sintered, CAD/CAM-polished-sintered, CAD/CAM-sintered-polished, CAD/CAM-sintered-glazed and CAD/CAM-polished-sintered-glazed processes respectively. The maximum contact stresses of the CAD/CAM-sintered-polished process were highest at 1 and 10 cycles but at 100, 1000 and 3000 cycles, the CAD/CAM-polished-sintered process gave the highest maximum contact stresses. Table 7.2 shows that not only did the different surface treatments have a significant influence on measured maximum contact stresses ($p < 0.05$) but also number of cycles significantly affected them ($p < 0.05$).

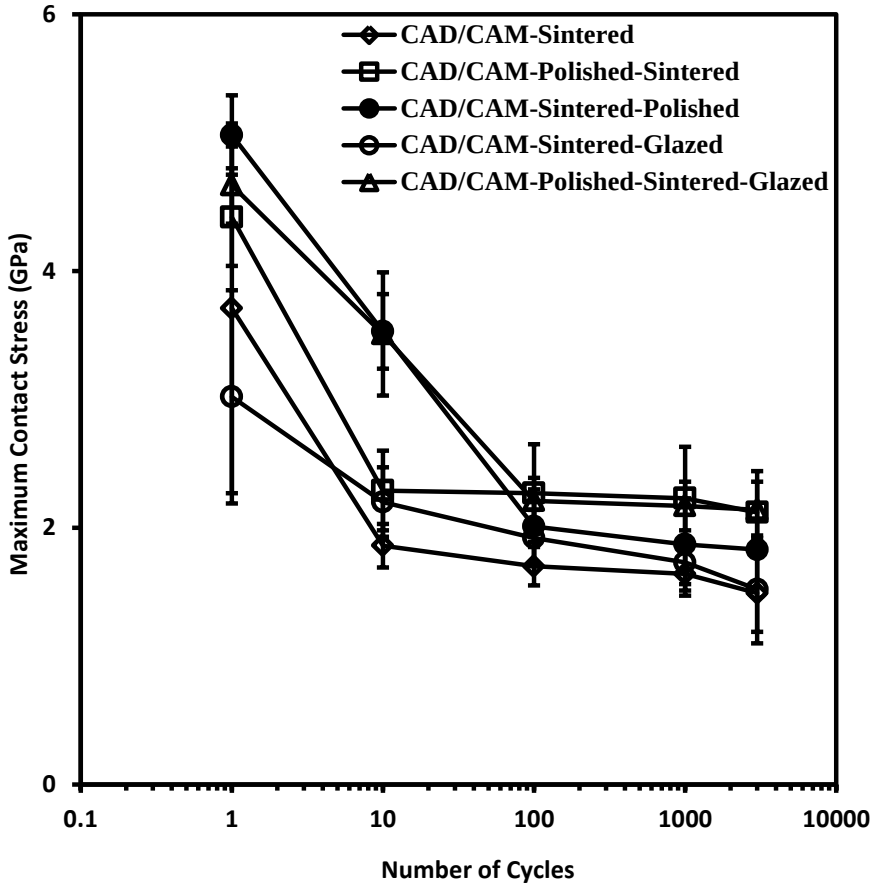


Fig. 7.3. The maximum contact stress versus number of cycles for differently treated LDGC surfaces.

Fig. 7.4 shows the maximum contact stress versus number of cycles for differently treated Y-TZP surfaces. All maximum contact stresses decreased with the increase in number of cycles for all the treated surfaces, indicating that the contact areas became larger with higher number of cycles. Table 7.3 summarises the maximum contact stresses obtained at different number of cycles for differently treated Y-TZP surfaces. By increasing the number of cycles from 1 to 3000, the average maximum contact stresses decreased by 74%, 71%, 69%, 71%, 77% for CAD/CAM-sintered, CAD/CAM-polished-sintered, CAD/CAM-sintered-polished, CAD/CAM-110-µm alumina sandblasted and CAD/CAM-250-µm alumina sandblasted processes

respectively. The maximum contact stresses of the CAD/CAM-250-µm alumina sandblasted processes were highest at 1 cycle but at higher cycles of 10, 100, 1000 and 3000 the CAD/CAM-polished-sintered process gave the highest maximum contact stresses. Table 7.4 shows that different applied surface treatments and number of cycles had significant influences on measured maximum contact stresses ($p < 0.05$).

Table 7.1. Maximum contact stress values obtained at different number of cycles for differently treated LDGC surfaces.

| Surface treatment/number of cycles | Maximum contact stress (GPa) | | | | |
|---|---|---|---|---|---|
| | **1** | **10** | **100** | **1000** | **3000** |
| CAD/CAM-sintered | 3.71±1.44 | 1.86±0.17 | 1.70±0.15 | 1.64±0.17 | 1.49±0.30 |
| CAD/CAM-polished-sintered | 4.42±0.38 | 2.29±0.31 | 2.27±0.38 | 2.23±0.40 | 2.12±0.32 |
| CAD/CAM-sintered-polished | 5.06±0.31 | 3.53±0.29 | 2.01±0.29 | 1.87±0.36 | 1.83±0.04 |
| CAD/CAM-sintered-glazed | 3.02±0.83 | 2.20±0.27 | 1.92±0.22 | 1.73±0.17 | 1.52±0.42 |
| CAD/CAM-polished-sintered-glazed | 4.67±0.30 | 3.50±0.48 | 2.21±0.18 | 2.17±0.19 | 2.11±0.22 |

Table 7.2. Two-way ANOVA with replication for the influence of different surface treatments and number of cycles on the maximum contact stress of indented LDGC surfaces.

| Source of Variation | SS | Df | MS | F | *p*-value | F crit |
|---|---|---|---|---|---|---|
| Surface treatments | 57.96 | 4 | 14.49 | 76.39 | 0.00 | 2.56 |
| Number of Cycles | 10.55 | 4 | 2.64 | 13.90 | 0.00 | 2.57 |
| Interaction | 7.47 | 16 | 0.47 | 2.46 | 0.01 | 1.85 |
| Within | 9.49 | 50 | 0.19 | | | |
| Total | 85.46 | 74 | | | | |

Table 7.3. Maximum contact stress values obtained at different number of cycles for differently treated Y-TZP surfaces.

| Surface treatment/number of cycles | Maximum contact stress (GPa) | | | | |
|---|---|---|---|---|---|
| | **1** | **10** | **100** | **1000** | **3000** |
| CAD/CAM-sintered | 6.47±0.84 | 5.40±0.53 | 3.29±0.70 | 1.81±0.40 | 1.69±0.52 |
| CAD/CAM-polished-sintered | 6.13±0.49 | 5.94±0.63 | 5.31±0.48 | 2.40±0.20 | 1.78±0.12 |
| CAD/CAM-sintered-polished | 5.66±0.44 | 3.52±0.85 | 3.28±0.86 | 2.31±0.13 | 1.75±0.20 |
| CAD/CAM-sintered-110 sandblasted | 5.97±1.04 | 4.89±0.93 | 3.74±1.73 | 2.21±0.16 | 1.76±0.09 |
| CAD/CAM-sintered-250 sandblasted | 6.96±1.13 | 3.84±0.90 | 2.98±0.22 | 2.29±0.28 | 1.75±0.20 |

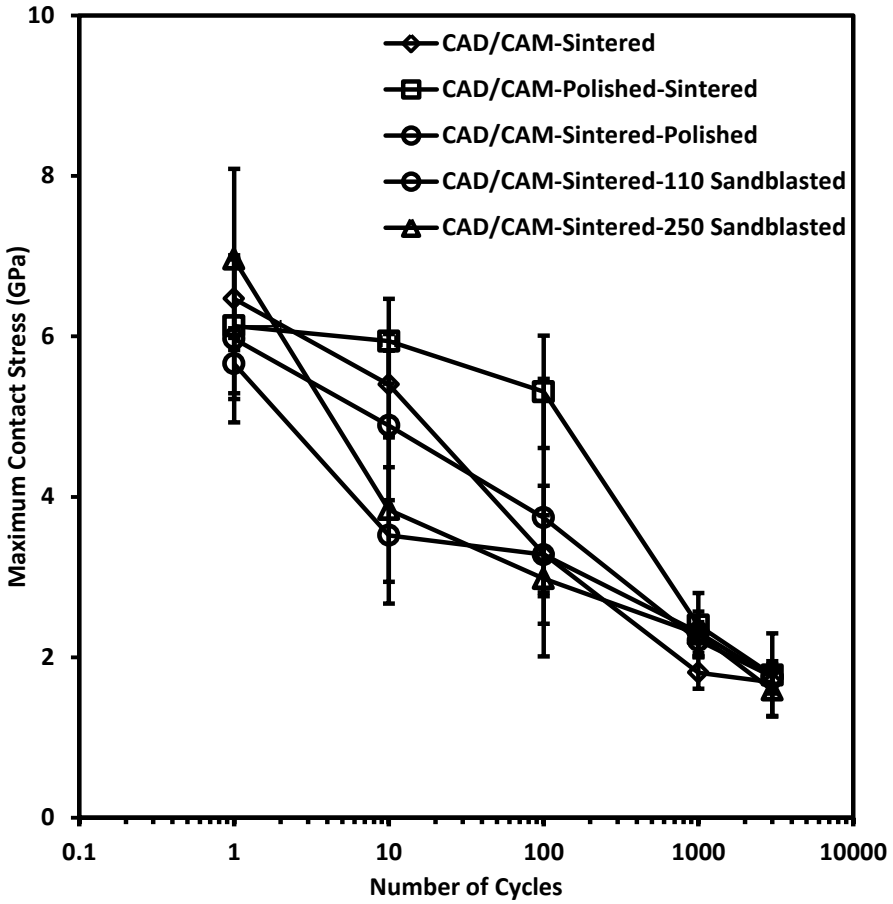


Fig. 7.4. The maximum contact stress versus number of cycles for differently treated Y-TZP surfaces.

Table 7.4. Two-way ANOVA with replication for the influence of different surface treatments and number of cycles on the maximum contact stress of indented Y-TZP surfaces.

| Source of Variation | SS | Df | MS | F | *p*-value | F crit |
|---|---|---|---|---|---|---|
| Surface treatments | 8.39 | 4 | 2.10 | 4.43 | 0.00 | 2.56 |
| Number of cycles | 205.14 | 4 | 51.29 | 108.24 | 0.00 | 2.56 |
| Interaction | 18.25 | 16 | 1.14 | 2.41 | 0.01 | 1.85 |
| Within | 23.69 | 50 | 0.47 | | | |
| Total | 255.47 | 74 | | | | |

### *7.4.2 Indented Morphologies of Treated LDGC Surfaces*

Fig. 7.5 shows SEM micrographs of the CAD/CAM-sintered LDGC surface at 800 N and 1 indentation. Fig. 7.5(a) reveals the shallow Hertzian ring crack formed on the milling-induced rough surface. Fig. 7.5(b) provides the details of ring crack and wedged area. Fig. 7.5(c) demonstrates that the wedged area consist of ring, fretting and pulverized cracks. Fig. 7.5(d)

shows details of wedged cracks. Fig. 7.5(e) shows the formation of fretting and pulverized debris with micro-debris size up to 7 µm in the wedged area and a crack width of 11µm.

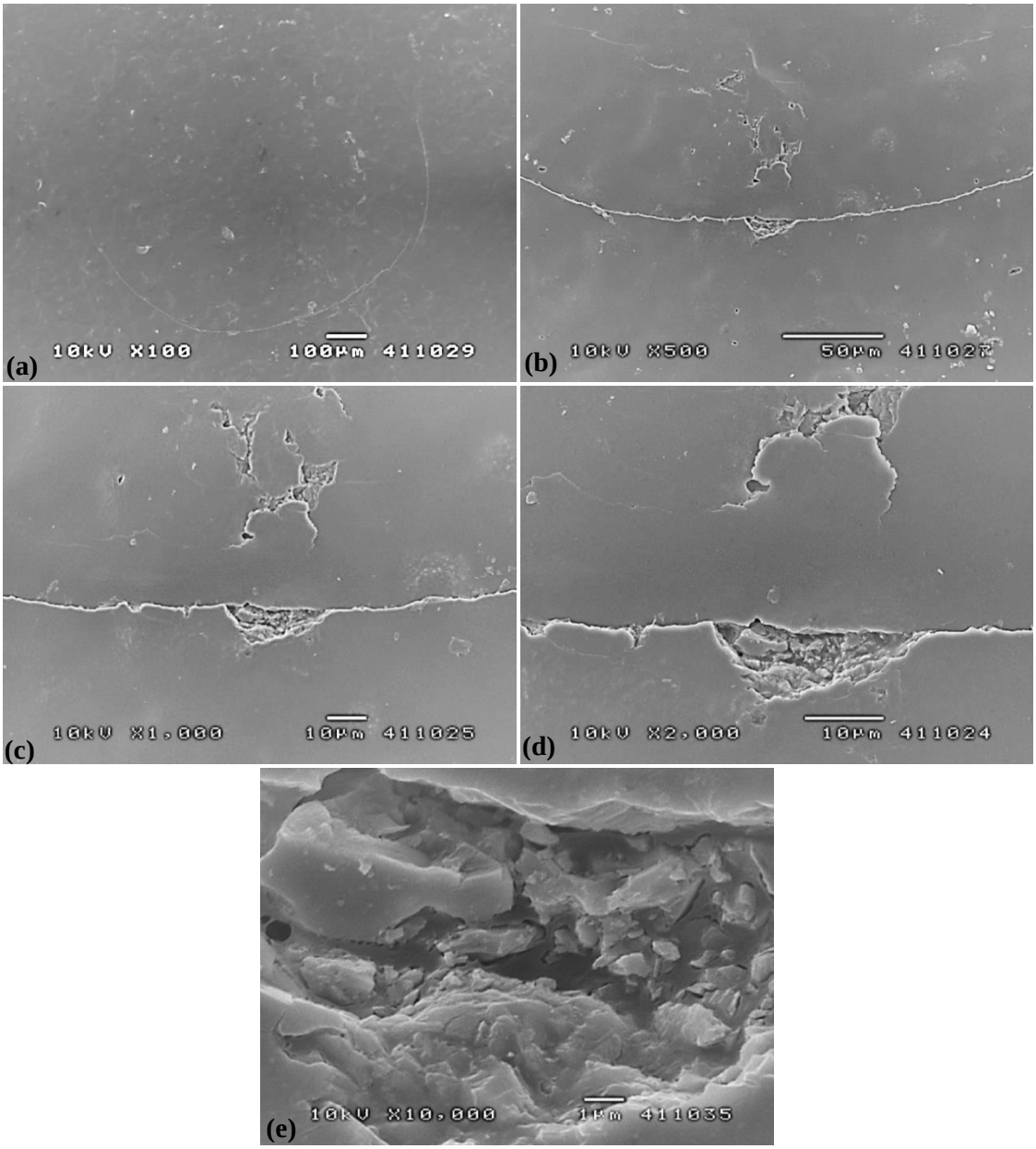


Fig. 7.5. SEM micrographs of the CAD/CAM-sintered LDGC surface at 800 N and 1 indentation showing (a) the shallow Hertzian ring crack, (b) details of ring crack and wedged area, (c) wedged cracks consisting of ring crack, fretting and pulverization, (d), details of wedged cracks and (e) the formation of fretting and pulverized debris in the wedged area.

Fig. 7.6 shows SEM micrographs of the CAD/CAM-polished-sintered LDGC surface at 800 N and 1 indentation. Fig. 7.6 (a) reveals the shallow Hertzian ring crack formed on the smooth surface. Fig. 7.6(b) details the ring crack and the debris removed. Fig. 7.6(c) shows the meandering micro-crack path with crack width of 0.6 µm and micro-debris size of about 1 µm.

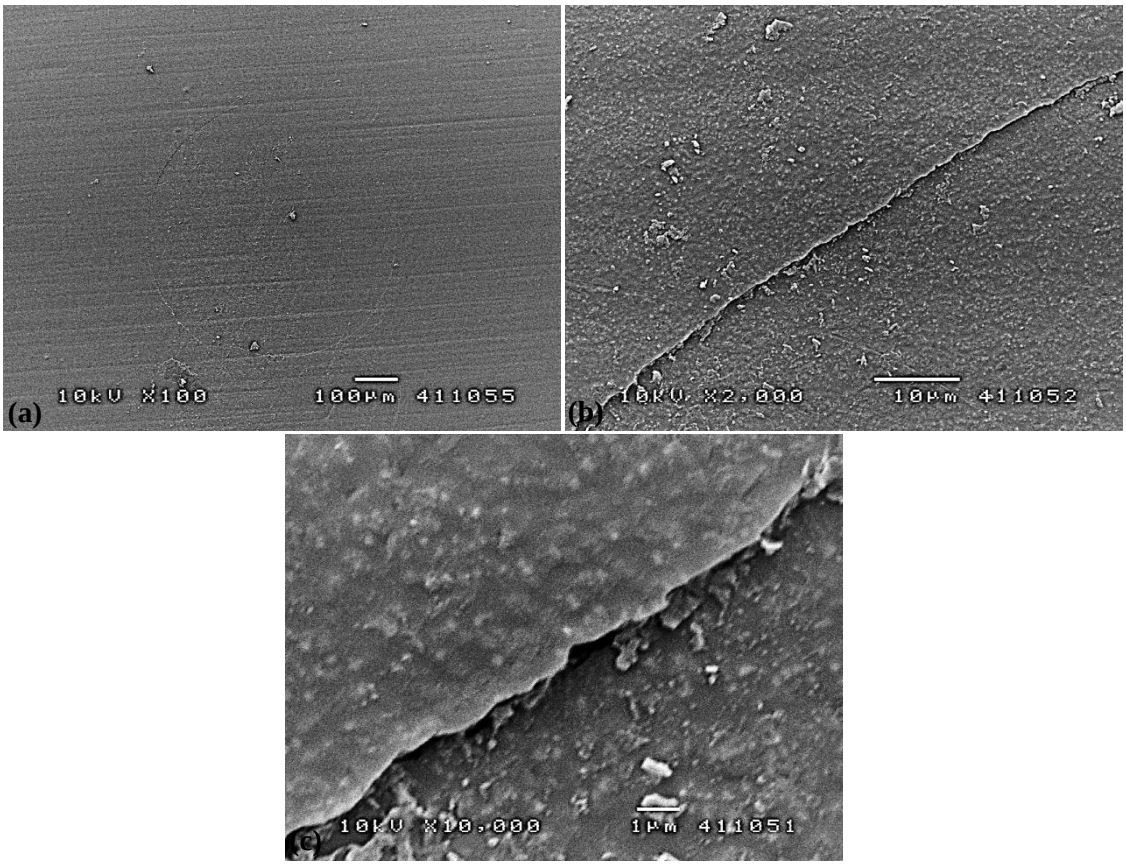


Fig. 7.6. SEM micrographs of the CAD/CAM-polished-sintered LDGC surface at 800 N and 1 indentation revealing (a) the shallow Hertzian ring crack, (b) details of ring crack, and (c) meandering micro-crack path and micro-debris.

Fig. 7.7 shows SEM micrographs of the CAD/CAM-sintered-polished LDGC surface at 800 N and 1 indentation. Fig. 7.7(a) reveals the shallow Hertzian ring crack and the smeared surface. Fig. 7.7(b) demonstrates details of the ring crack and smeared area. Fig. 7.7(c) shows micro-bridges with width of about 3 µm and enlarged smeared fracture in the ring crack.

Fig. 7.8 shows SEM micrographs of the CAD/CAM-sintered-glazed LDGC surface at 800 N and 1 indentation. Fig. 7.8(a) reveals the shallow Hertzian ring crack on the milling-induced rough and pulverized surface. Fig. 7.8(b) shows details of the ring crack and residual pulverized debris. Fig. 7.8(c) meandering micro-crack path with crack width of 0.8 µm and micro-pulverized debris size of about 2 µm.

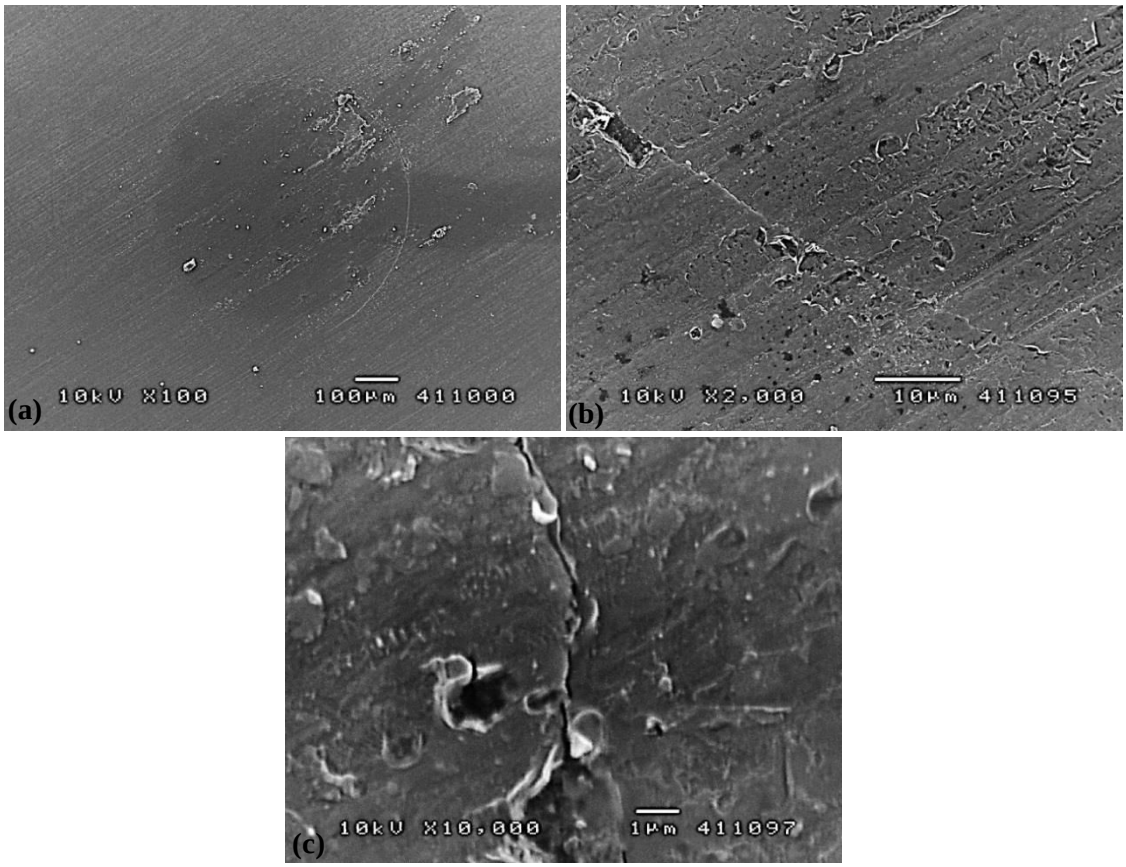


Fig. 7.7. SEM micrographs of the CAD/CAM-sintered-polished LDGC surface at 800 N and 1 indentation revealing (a) the shallow Hertzian ring crack, (b) details of the ring crack and smeared area, and (c) micro-bridges and enlarged smeared fracture in the ring crack.

Fig. 7.9 shows SEM micrographs of the CAD/CAM-polished-sintered-glazed LDGC surface at 800 N and 1 indentation. Fig. 7.9(a) reveals the shallow Hertzian ring cracks formed on the smooth surface in which the indentation-induced smeared area occurred inside the ring. Fig. 7.9(b) details of the ring crack and smeared area. Fig. 7.9(c) shows the meandering micro-crack path with a crack width of 1 µm and peeled smeared debris of size of about 5 µm.

Fig. 7.10 shows SEM micrographs of the CAD/CAM-sintered LDGC surface at 800 N and 10 indentations. Fig. 7.10(a) reveals the overall Hertzian ring cracks that were also formed on the milling-induced rough surface. Fig. 7.10(b) details the ring cracks and wedged area. Fig. 7.10(c) shows details of the ring crack and materials removed. Fig. 7.10(d) and (e) shows the meandering crack path with width of about 1 µm and micro-pulverized debris of size of about 3 µm.

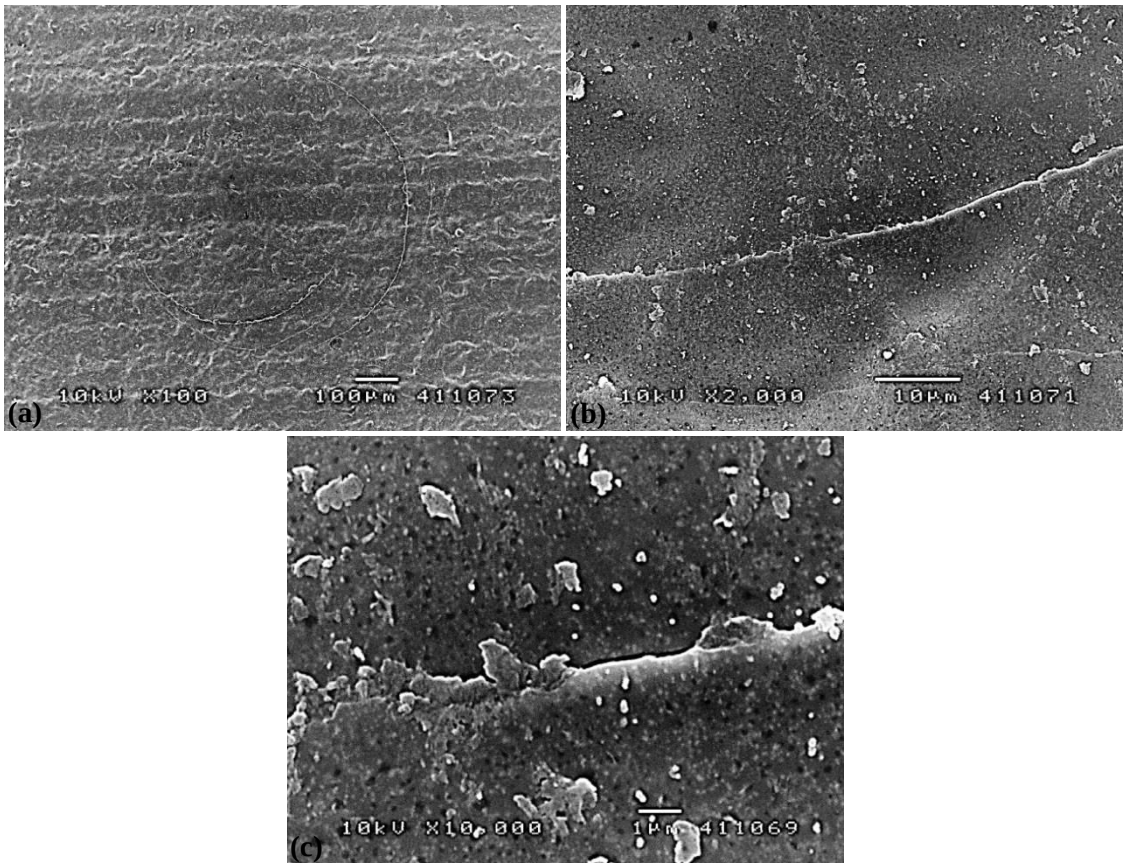


Fig. 7.8. SEM micrographs of the CAD/CAM-sintered-glazed LDGC surface at 800 N and 1 indentation revealing (a) the shallow Hertzian ring crack, (b) details of the ring crack and residual pulverized debris, and (c) meandering micro-crack path and micro- pulverized debris.

Fig. 7.11 shows SEM micrographs of the CAD/CAM-polished-sintered LDGC surface at 800 N and 10 indentations. Fig. 7.11(a) reveals the overall Hertzian cracks with the internal smearing of the smooth surface. Fig. 7.11(b) demonstrates the details of the ring cracks in which pulverized debris were removed. Fig. 7.11(c) shows concentric micro-crack paths with a maximum crack width of about 1 µm. It also shows the removal of some pulverized debris.

Fig. 7.12 shows SEM micrographs of the CAD/CAM-sintered-polished LDGC surface at 800 N and 10 indentations. Fig. 7.12(a) reveals the overall Hertzian cracks, smearing and debris. Fig. 7.12(b) and (c) demonstrates the details of ring cracks and smeared area. Fig. 7.12(d) and (e) shows the formation of fretting debris and pulverization with a crack width of about 2.6 µm and micro-debris in the wedged area.

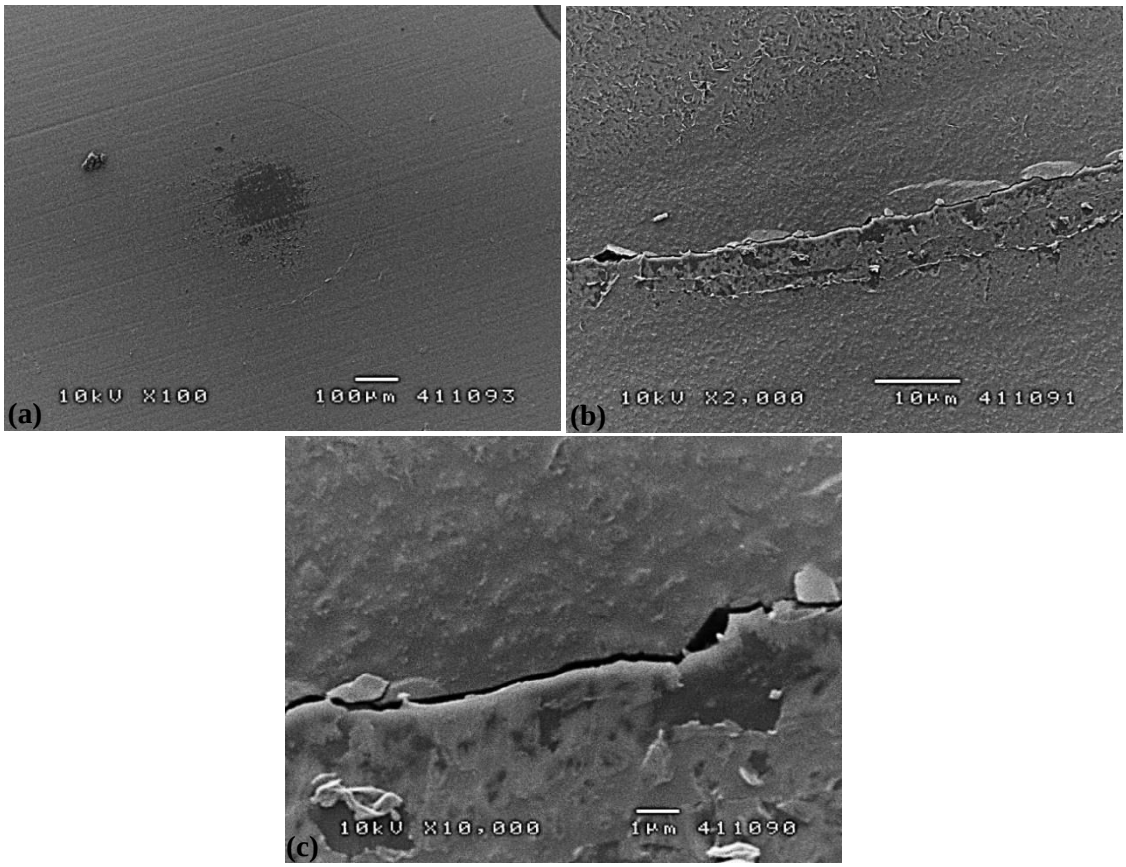


Fig. 7.9. SEM micrographs of the CAD/CAM-polished-sintered-glazed LDGC surface at 800 N and 1 indentation revealing (a) the shallow Hertzian ring cracks, (b) details of the ring crack and smeared area, and (c) meandering micro-crack path and peeled smeared debris.

Fig. 7.13 shows SEM micrographs of the CAD/CAM-sintered-glazed LDGC surface at 800 N and 10 indentations. Fig. 7.13(a) reveals the overall Hertzian cracks and wedged area on the milling-induced rough and pulverized surface. Fig. 7.13(b) demonstrates that the wedged areas consist of ring crack, fretting and pulverizations. Fig. 7.13(c) details the wedged crack having a crack width of about 50 µm. Fig. 7.13(d) and (e) displays the formation of fretting and pulverized debris of size up to 1µm in the wedged area.

Fig. 7.14 shows SEM micrographs of the CAD/CAM-polished-sintered-glazed LDGC surface at 800 N and 10 indentations. Fig. 7.14(a) reveals the overall Hertzian ring cracks formed on the smooth surface with peeled-off layer. Fig. 7.14(b) demonstrates the details of the ring crack and smeared area. Fig. 7.14 (c) shows the meandering micro-crack path with a crack width of 1 µm, peeled smeared layer.

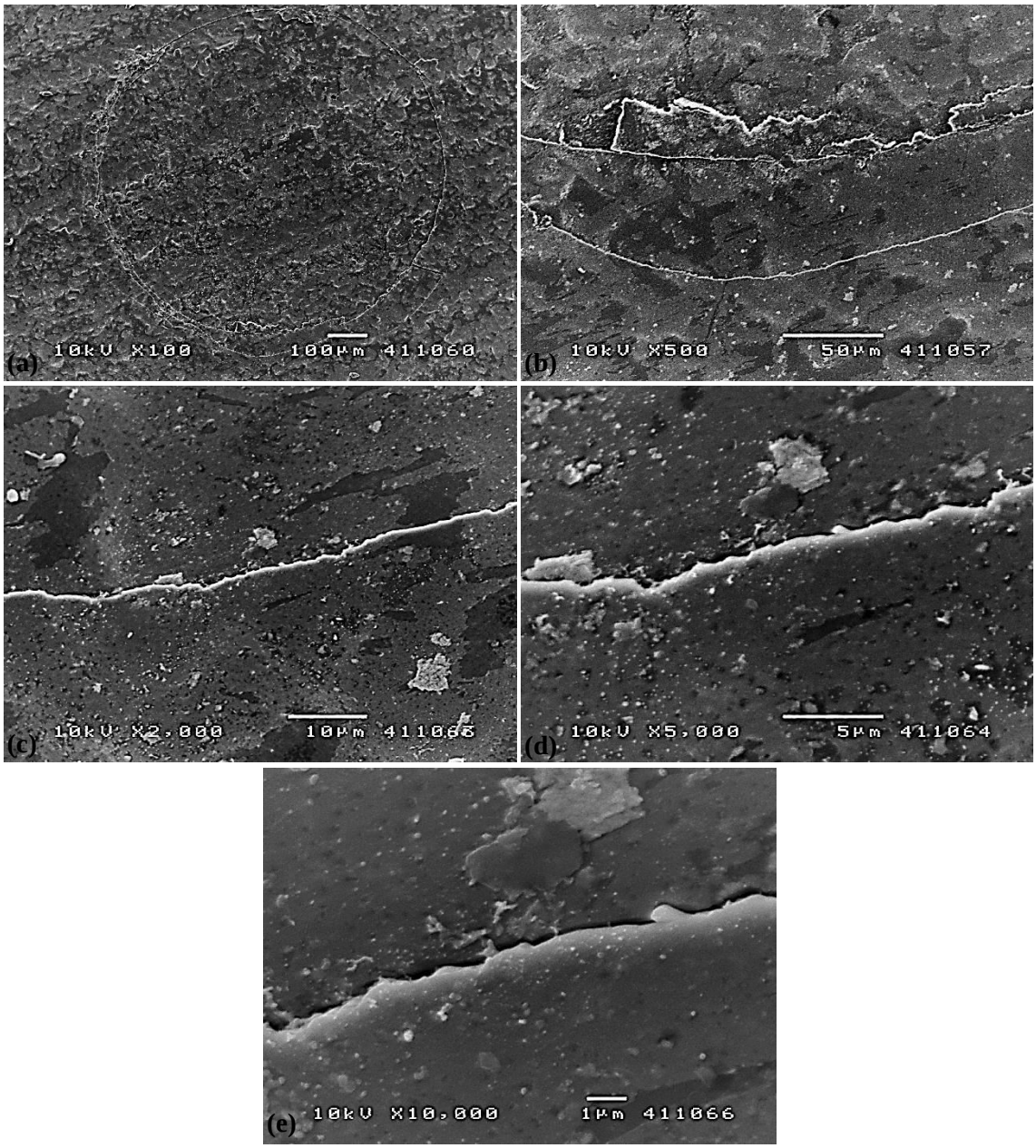


Fig. 7.10. SEM micrographs of the CAD/CAM-sintered LDGC surface at 800 N and 10 indentations revealing (a) the overall Hertzian ring cracks, (b) details of the ring crack and wedged area, (c) details of the ring crack, (d) meandering crack path and micro-pulverized debris and (e) the enlarged view of (d).

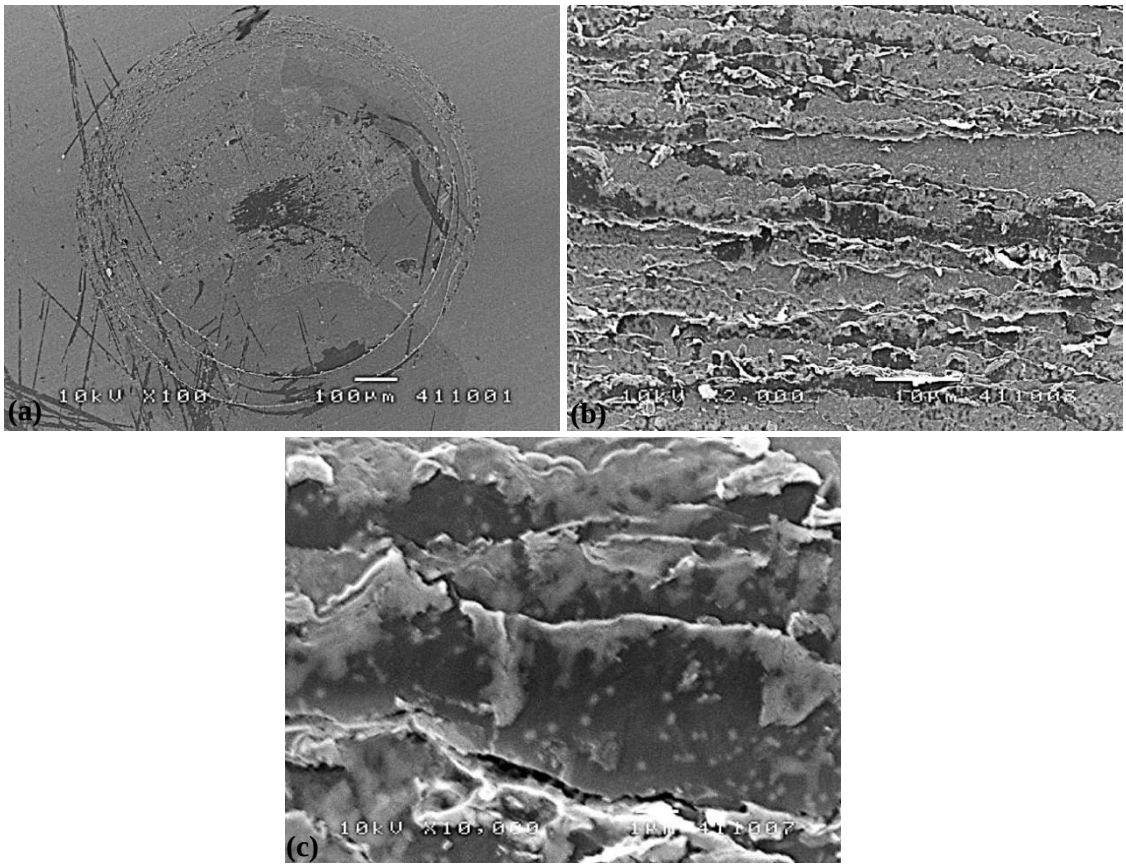


Fig. 7.11. SEM micrographs of the CAD/CAM-polished-sintered LDGC surface at 800 N and 10 indentations revealing (a) the overall Hertzian cracks, (b) details of the ring cracks, and (c) concentric micro-crack paths with the removal of pulverized debris.

Fig. 7.15 shows SEM micrographs of the CAD/CAM-sintered LDGC surface at 800 N and 100 indentations. Fig. 7.15(a) reveals the overall ring cracks, inner edge chippings and wedged area formed on the milling-induced rough surface. Fig. 7.15(b) demonstrates continued and discontinued ring cracks and chipped edge resulting into a fractured surface. Fig. 7.15(c) shows the large-scale fractured surface with a width of about 200 μm. Fig. 7.15(d) and (e) show the details of the fractured defects as the formation of deep micro-craters and the removal of pulverized debris.

Fig. 7.16 shows SEM micrographs of the CAD/CAM-polished-sintered LDGC surface at 800 N and 100 indentations. Fig. 7.16(a) reveals the overall ring cracks, internal smearing and wedged area on the smooth surface. Fig. 7.16(b) and (c) demonstrates the propagation of ring cracks and the formation of fretting debris inside the wedged area. Fig. 7.16(d) shows the formed fretting debris in the wedged areas of approximately 21 μm in width. Fig. 7.16(e) provides the details of the fretting and pulverized debris.

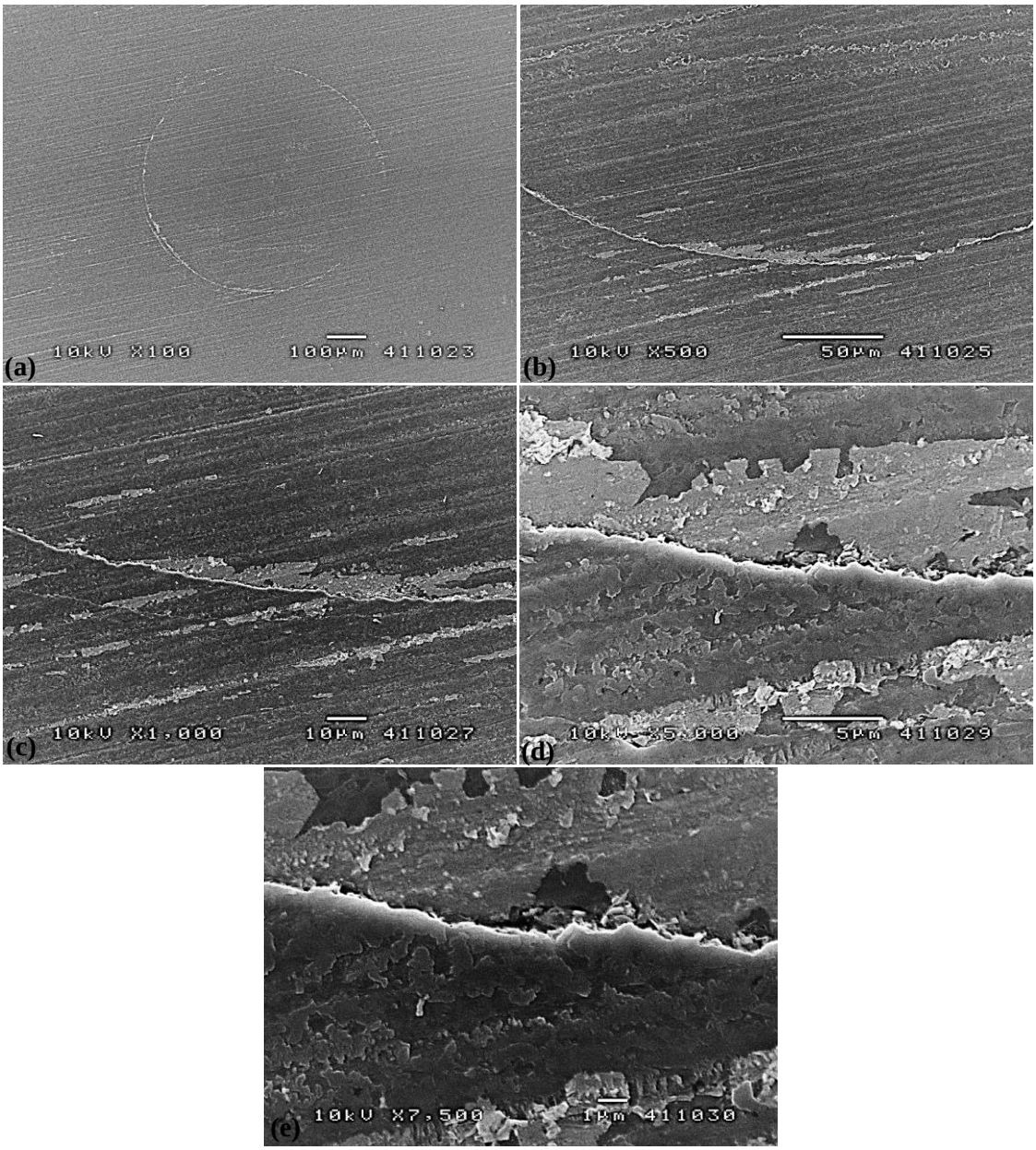


Fig. 7.12. SEM micrographs of the CAD/CAM-sintered-polished LDGC surface at 800 N and 10 indentations revealing (a) the overall ring cracks, (b) details of the ring crack, (c) the enlarged view of (b), (d) meandering crack path and micro-pulverized debris and (e) the enlarged view of (e).

Fig. 7.17 shows SEM micrographs of the CAD/CAM-sintered-polished LDGC surface at 800 N and 100 indentations. Fig. 7.17(a) reveals the overall ring cracks, fragmentations, smearing and debris. Fig. 7.17(b) demonstrates the propagation of ring cracks, the smeared surface and the fretting debris. Fig. 7.17(c) shows the formation of fretting debris and pulverization in the wedged area of about 8 µm in width.

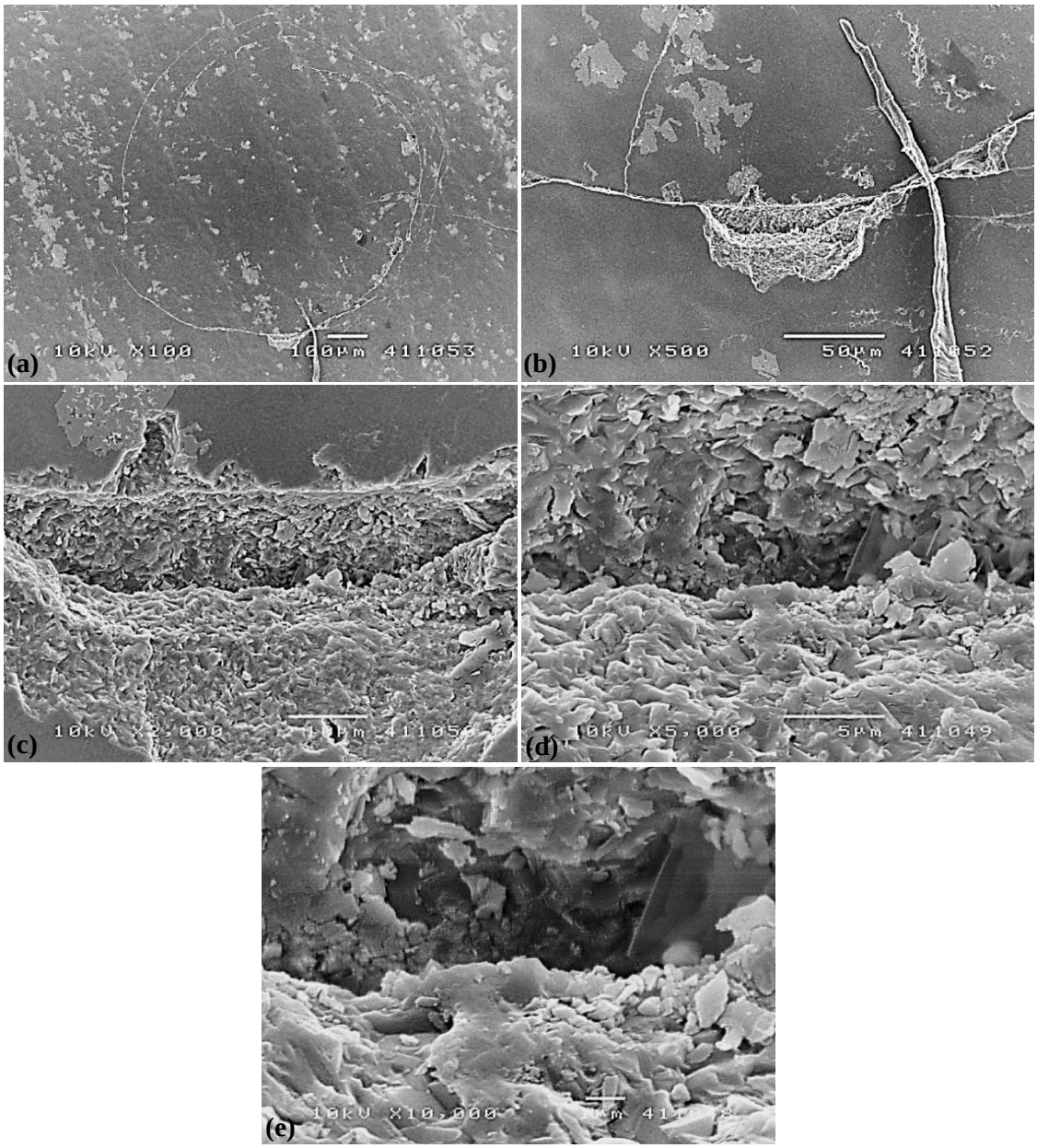


Fig. 7.13. SEM micrographs of the CAD/CAM-sintered-glazed LDGC surface at 800 N and 10 indentations revealing (a) the overall Hertzian cracks, (b) wedged cracks consisting of ring cracks, fretting and pulverization, (c) details of wedged cracks, (d) the formation of fretting and pulverized debris in the wedged area and (e) the enlarged view of (d).

Fig. 7.18 shows SEM micrographs of the CAD/CAM-sintered-glazed LDGC surface at 800 N and 100 indentations. Fig. 7.18(a) reveals the overall Hertzian ring cracks and wedged area on the milling-induced rough and pulverized surface. Fig. 7.18(b) demonstrates continuous and discontinuous ring cracks, fragmented area and fretting debris. Fig. 7.18(c) shows the radial crack formation outside of the ring crack. The cumulative effect of all these cracks resulted in the formation of a large-scale fractured surface observed in Fig. 7.18(d) and (e).

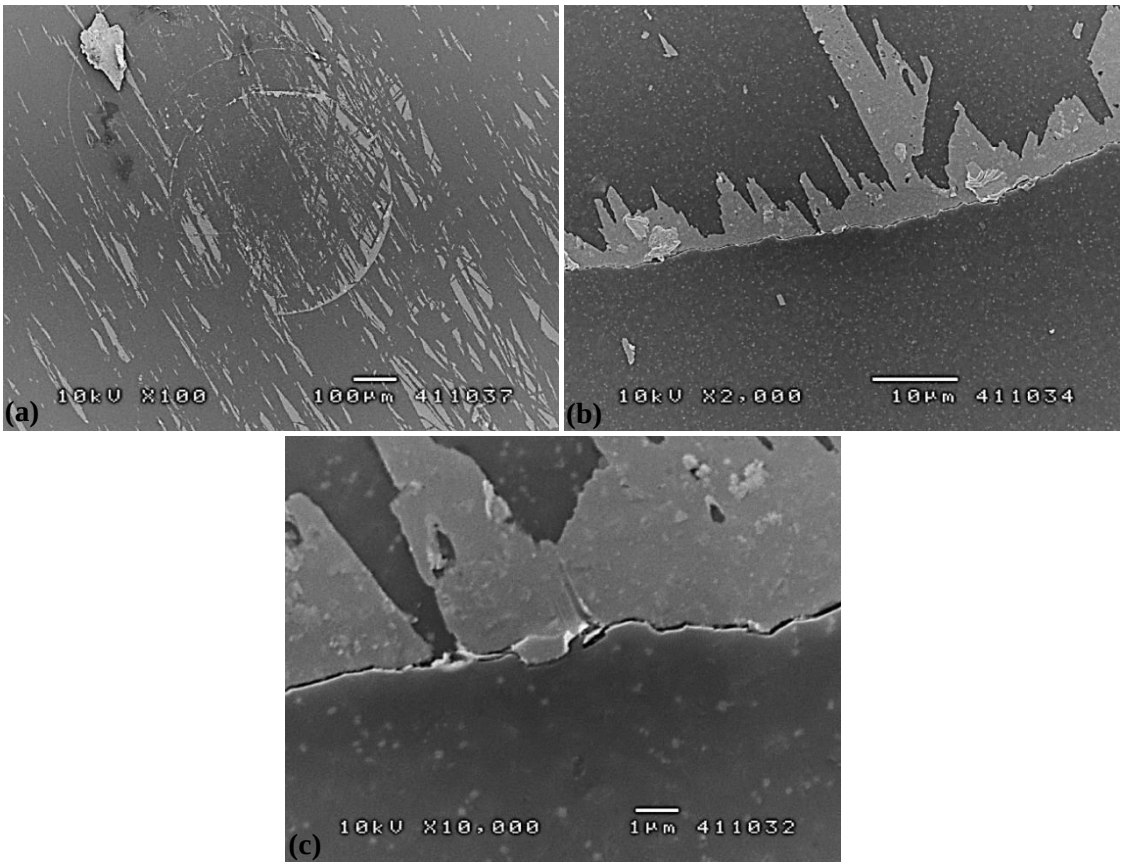


Fig. 7.14. SEM micrographs of the CAD/CAM-polished-sintered-glazed LDGC surface at 800 N and 10 indentations revealing (a) the overall Hertzian ring cracks, (b) details of the ring crack and smeared area, and (c) meandering micro-crack path and peeled smeared debris.

Fig. 7.19 shows SEM micrographs of the CAD/CAM-polished-sintered-glazed LDGC surface at 800 N and 100 indentations. Fig. 7.19(a) reveals the overall Hertzian ring cracks formed on the smooth surface. Fig. 7.19(b) and (c) demonstrates the propagation of ring cracks and the formation of the fretting debris in the wedged areas. Fig. 7.19(d) and (e) shows that the wedged area of approximately 5 µm in width.

Fig. 7.20 shows SEM micrographs of the CAD/CAM-sintered LDGC surface at 800 N and 1000 indentations. Fig. 7.20(a) reveals the overall Hertzian ring cracks, large-scale edge chipping, material removal and radial crack formed on the milling-induced rough surface. Fig. 7.20(b) demonstrates details of the ring crack penetrating into the subsurface and chipped edge crack with 300 µm in width. Fig. 7.20 (c) shows large-scale chipped edge, material removal and micro-craters. Fig. 7.20(d) and (e) reveals large-scale fractured surface.

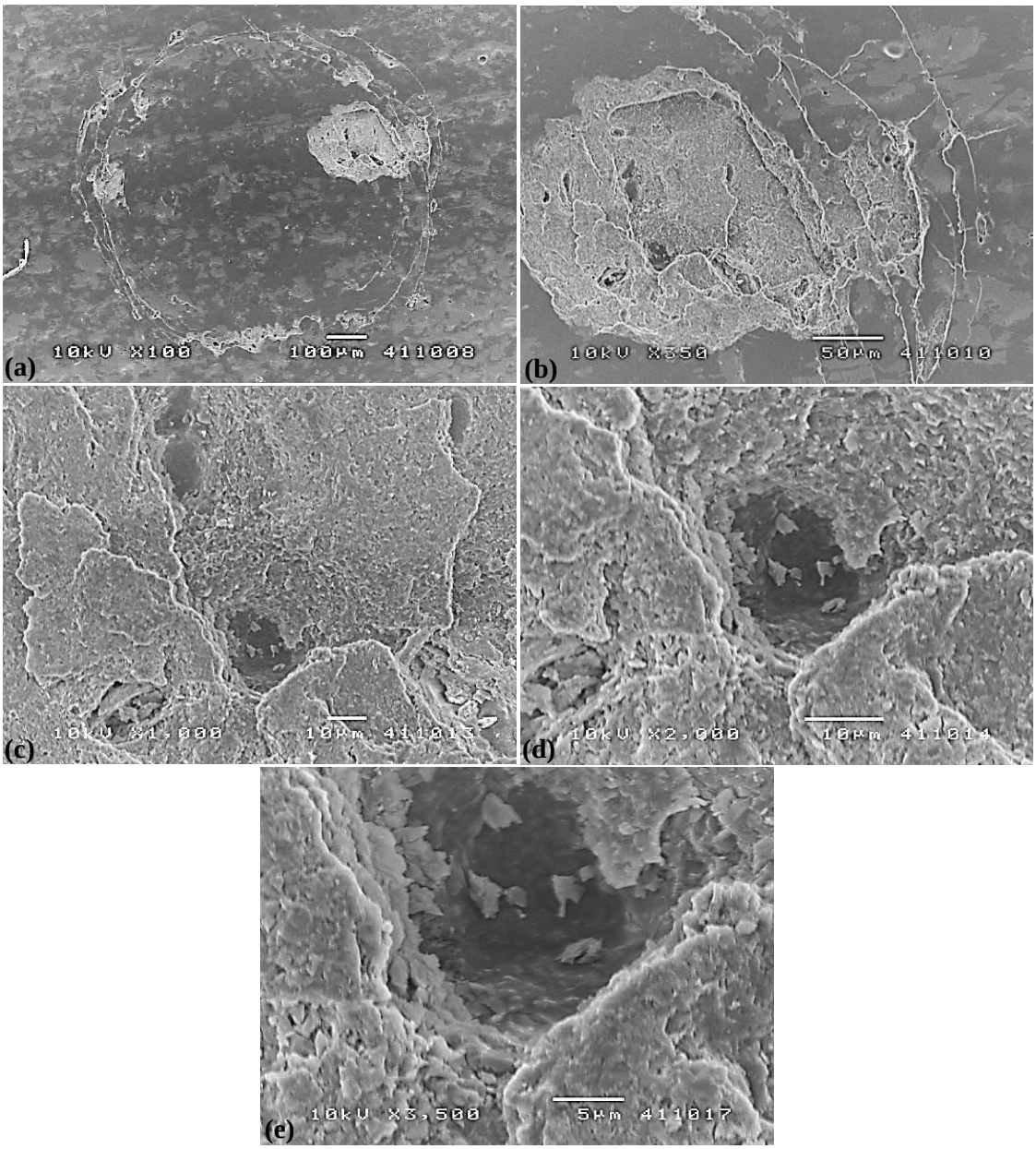


Fig. 7.15. SEM micrographs of the CAD/CAM-sintered LDGC surface at 800 N and 100 indentations revealing (a) the overall ring cracks with inner edge chipping, (b) ring cracks and the chipped edge (c) the large-scale fractured surface, (d) details of the fracture defects and (e) deep micro-craters and debris.

Fig. 7.21 shows SEM micrographs of the CAD/CAM-polished-sintered LDGC surface at 800 N and 1000 indentations. Fig. 7.21(a) reveals the overall Hertzian ring cracks, material removal and inner edge chipping on the smooth surface. Fig. 7.21(b) demonstrates details of the ring crack penetrating on the surface and chipped edge crack of 100 µm in width. Fig. 7.21(c) shows large-scale chipped edge, material removal and micro-craters. Fig. 7.21(d) and (e) displays the large-scale fractured surface resulting from edge chipping.

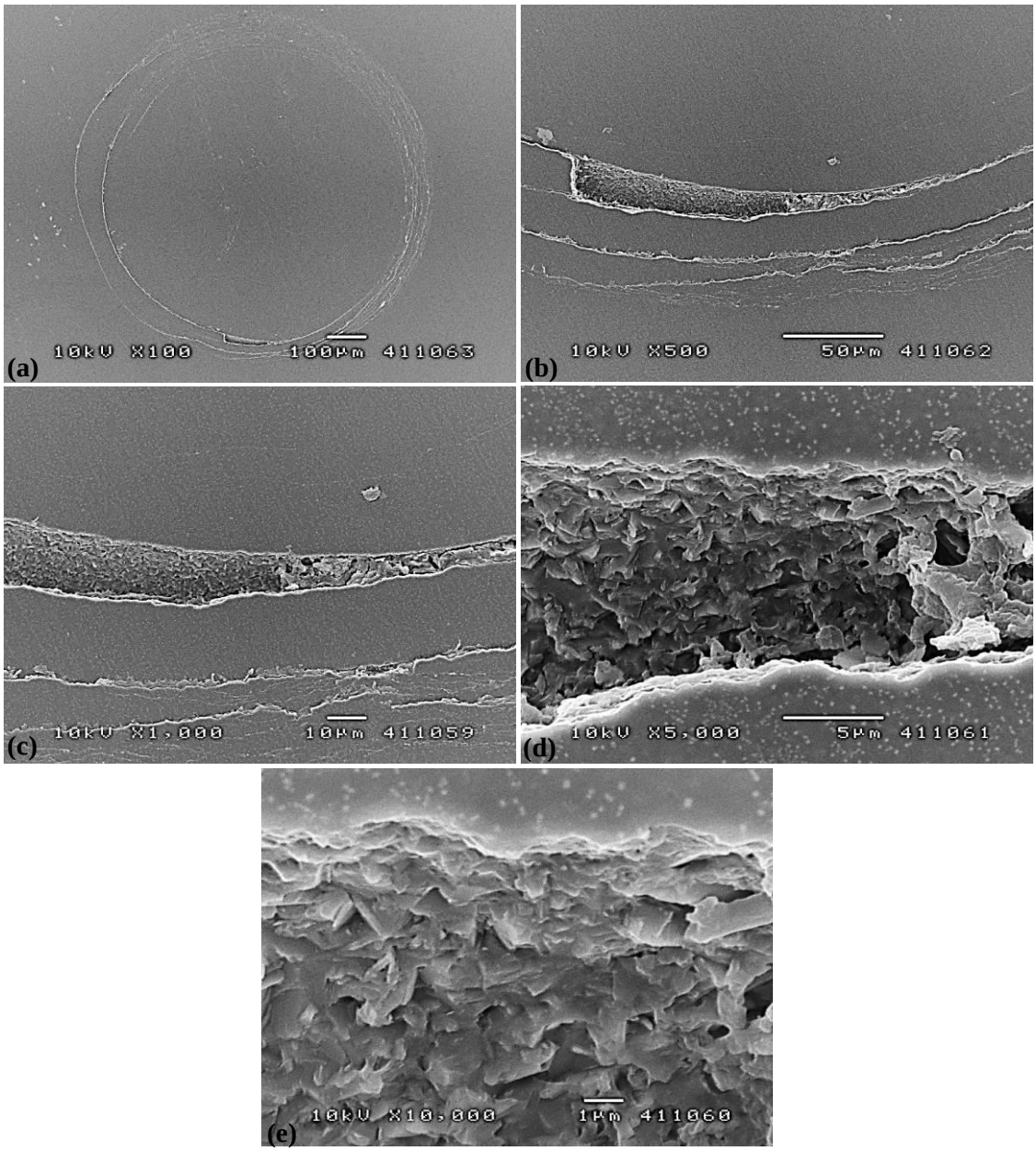


Fig. 7.16. SEM micrographs of the CAD/CAM-polished-sintered LDGC surface at 800 N and 100 indentations revealing (a) the overall ring cracks, (b) ring cracks and wedged area, (c) the enlarged view of (b), (d) the formation of fretting debris in the wedged areas and (e) details of the fretting debris and pulverization.

Fig. 7.22 shows SEM micrographs of the CAD/CAM-sintered-polished LDGC surface at 800 N and 1000 indentations. Fig. 7.22(a) reveals the overall Hertzian ring cracks, fragmentations, wedged area on the smeared surface. Fig. 7.22(b) demonstrates the wedged area as ring cracks penetrating the surface and fretting debris. Fig. 7.22(c) shows details of wedged area with a crack width of 20 µm fretting debris. Fig. 7.22(d) and (e) shows the formation of fretting debris in the wedged area.

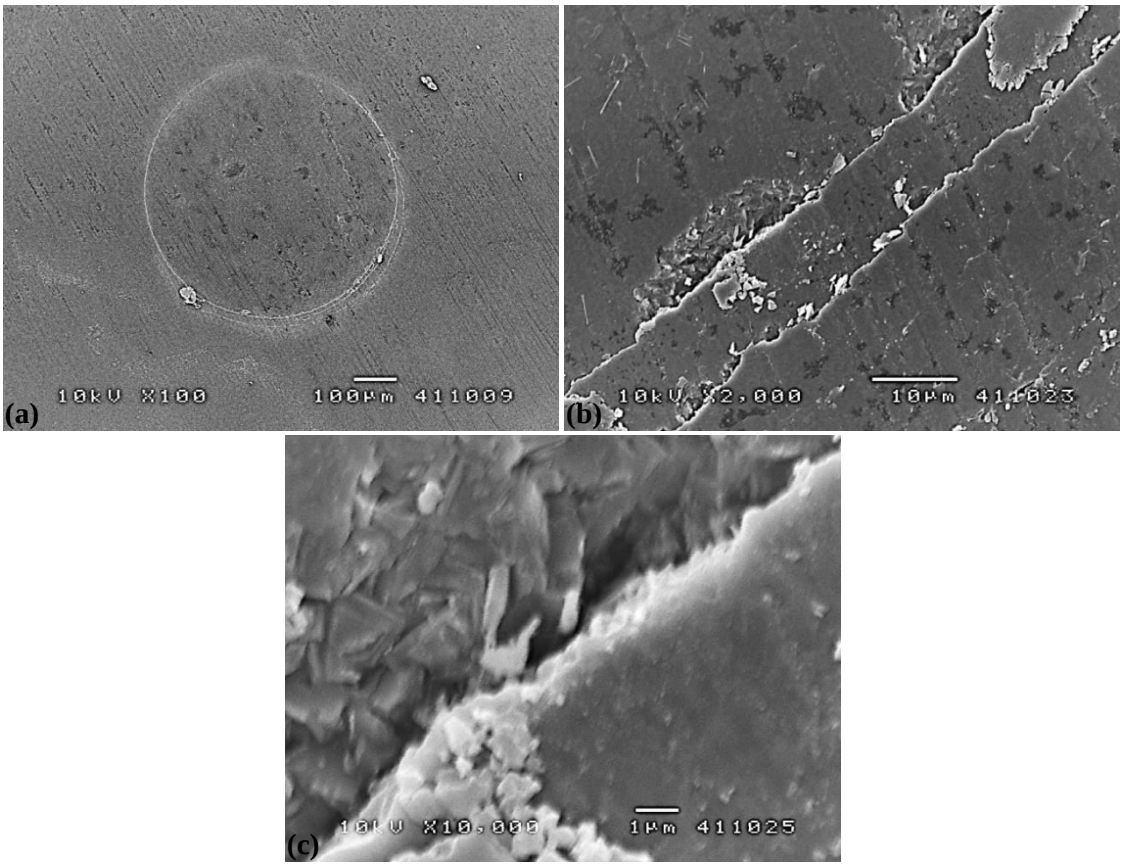


Fig. 7.17. SEM micrographs of the CAD/CAM-sintered-polished LDGC surface at 800 N and 100 indentations revealing (a) the overall Hertzian cracks, (b) details of the ring cracks, smeared area and fretting debris, and (c) the formation of fretting debris and pulverization.

Fig. 7.23 shows SEM micrographs of the CAD/CAM-sintered-glazed LDGC surface at 800 N and 1000 indentations. Fig. 7.23(a) reveals the overall Hertzian ring cracks with inner and outer edge chippings on the milling-induced rough and pulverized surface. Fig. 7.23(b) and (c) demonstrates ring and transverse cracks and wedged area of approximately 100 µm in width. Fig. 7.23(d) shows the wedged area and the sub-surface penetration of transverse crack. Fig. 7.23(e) demonstrates the formation of fretting debris in the wedged area.

Fig. 7.24 shows SEM micrographs of the CAD/CAM-polished-sintered-glazed LDGC surface at 800 N and 1000 indentations. Fig. 7.24(a) reveals the overall Hertzian ring cracks, fragmentations, debris on the smooth surface. Fig. 7.24(b) demonstrates continued and discontinued ring cracks and fretting debris. Fig. 7.24(c) shows details of wedged area of approximately 20 µm in width. Fig. 7.24(d) and (e) reveals the formation of fretting debris in the wedged area.

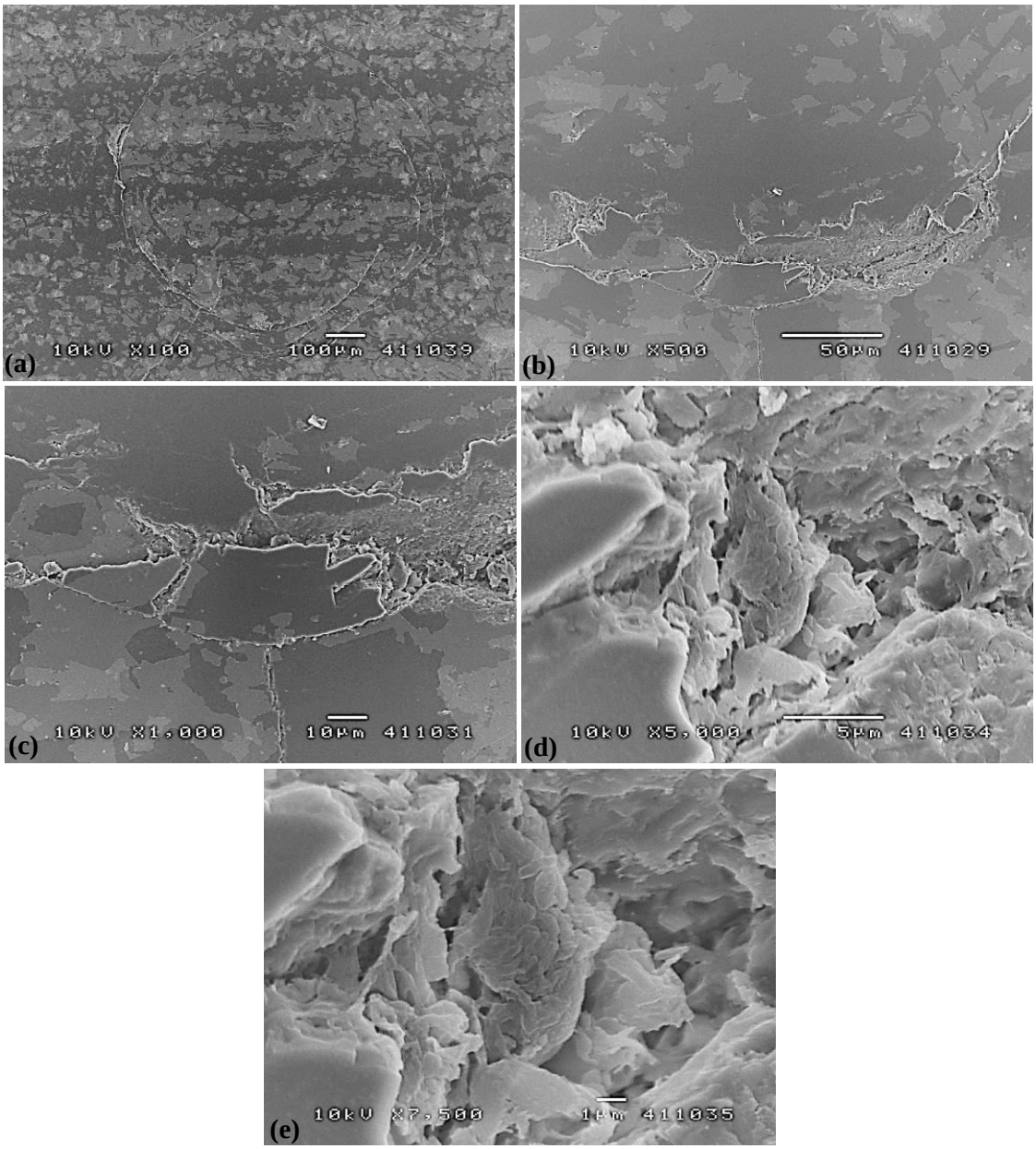


Fig. 7.18. SEM micrographs of the CAD/CAM-sintered-glazed LDGC surface at 800 N and 100 indentations revealing (a) the overall Hertzian ring cracks, (b) ring cracks, fragmentation and fretting debris, (c) the formation of radial crack outside the ring crack, (d) large-scale fragmented surface and (e) the enlarged view of (d).

Fig. 7.25 shows SEM micrographs of the CAD/CAM-sintered LDGC surface at 800 N and 3000 indentations. Fig. 7.25(a) reveals the overall Hertzian ring cracks with large-scale outer edge chippings on the milling-induced rough surface. Fig. 7.25(b) demonstrates large-scale chipped edge of approximately 400 µm in width, material removal and micro-craters. Fig. 7.25(c) shows the large-scale fractured surface. Fig. 7.25(d) and (e) displays the fretting and pulverized debris in the edge-chipped area.

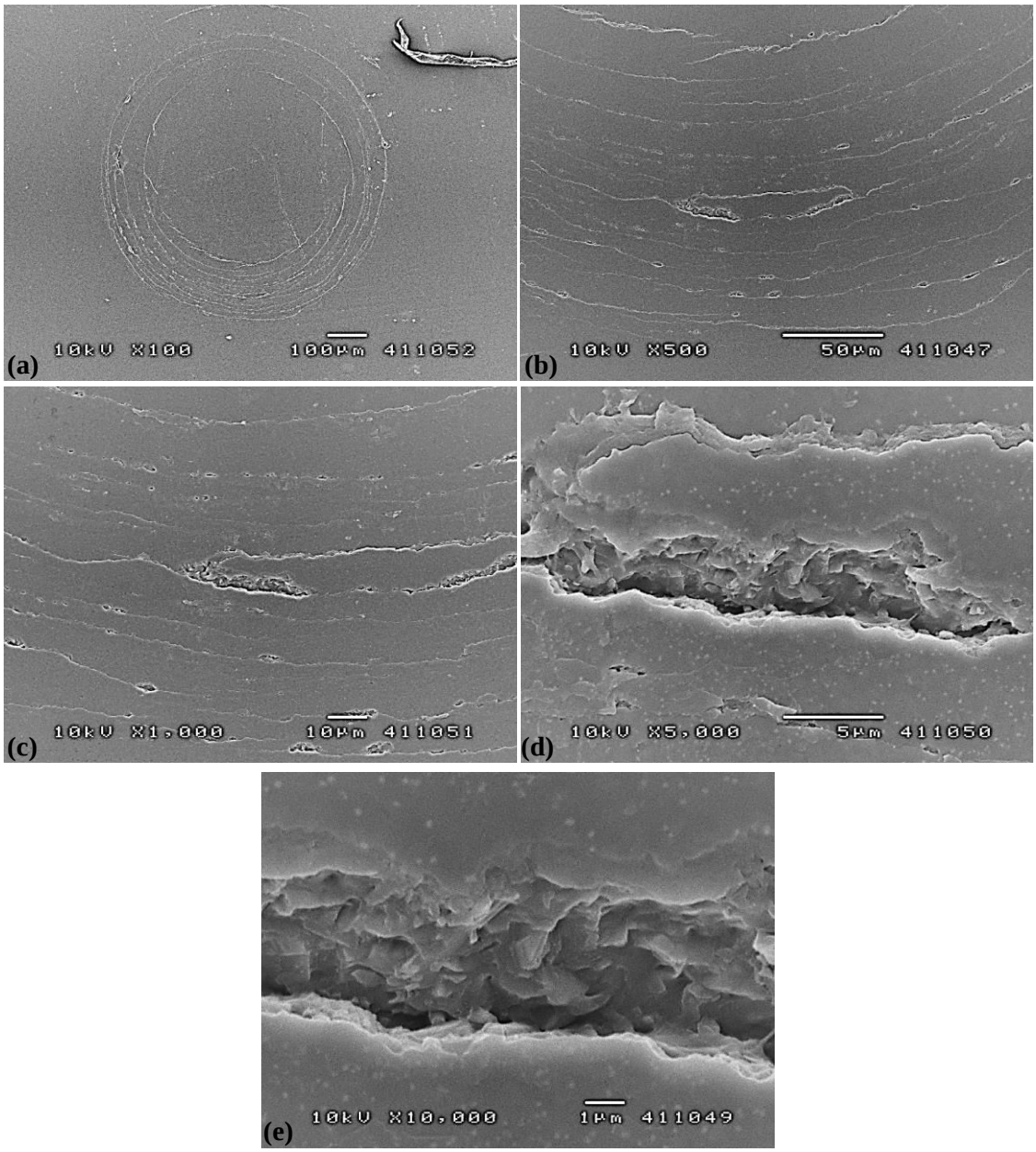


Fig. 7.19. SEM micrographs of the CAD/CAM-polished-sintered-glazed LDGC surface at 800 N and 100 indentations revealing (a) the overall Hertzian ring cracks, (b) ring cracks and wedged area, (c) the enlarged view of (b), (d) the wedged area and (e) the enlarged view of (d).

Fig. 7.26 shows SEM micrographs of the CAD/CAM-polished-sintered LDGC surface at 800 N and 3000 indentations. Fig. 7.26(a) reveals the overall Hertzian ring cracks with large-scale outer edge chipping on the smooth surface. Fig. 7.26(b) demonstrates large-scale chipped edge, material removal, micro-craters and ring cracks. Fig. 7.26(c) shows details of the edge chipping of approximately 143 µm in width. Fig. 7.26(d) and (e) reveals the large-scale fretting and pulverization in the edge-chipped area.

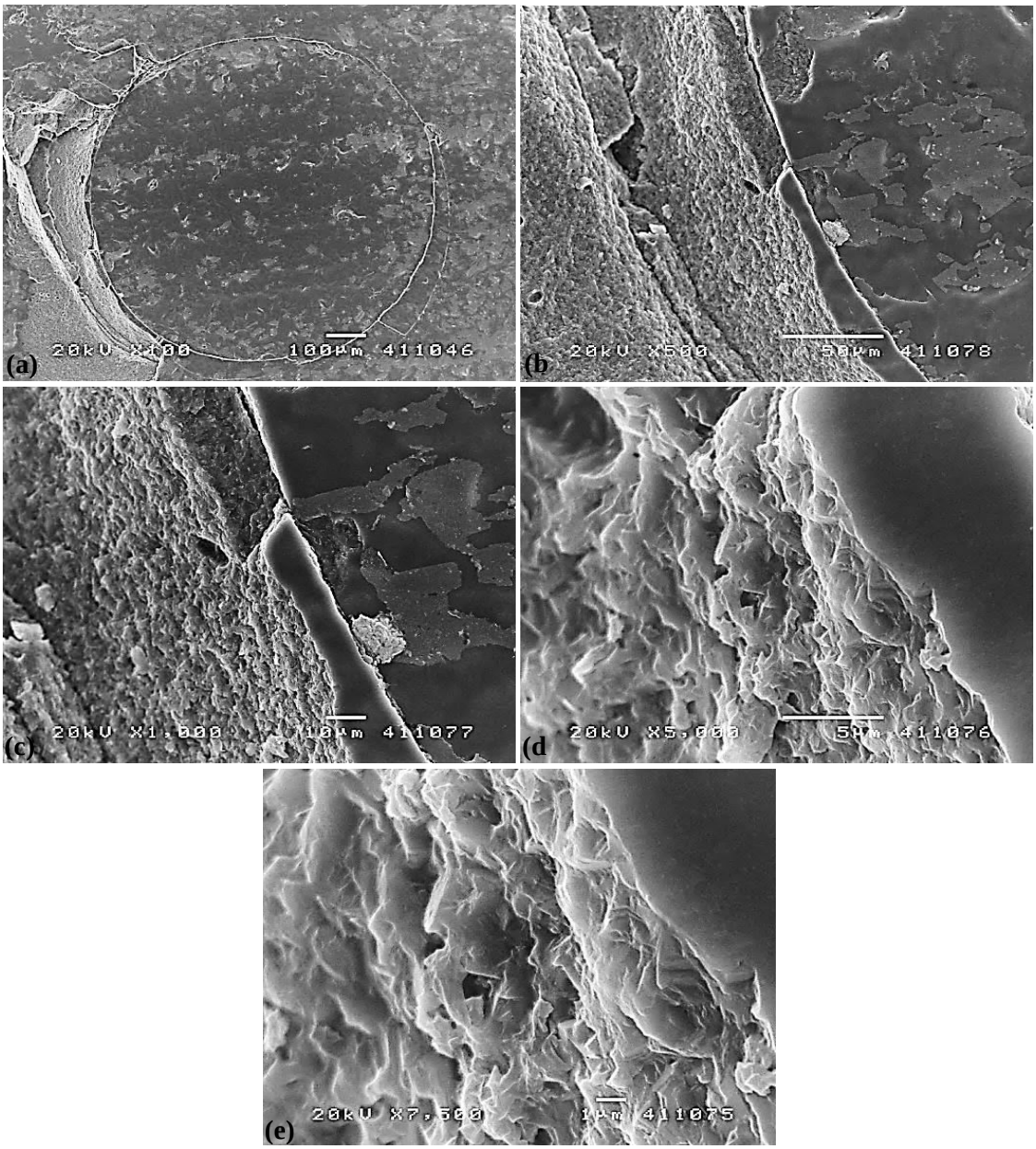


Fig. 7.20. SEM micrographs of the CAD/CAM-sintered LDGC surface at 800 N and 1000 indentations revealing (a) the overall Hertzian ring cracks with edge chipping, (b) details of the ring and chipped edge cracks, (c) large-scale chipped edge, material removal and micro-craters, (d) large-scale fractured surface and (e) the enlarged view of (d).

Fig. 7.27 shows SEM micrographs of the CAD/CAM-sintered-polished LDGC surface at 800 N and 3000 indentations. Fig. 7.27(a) reveals the overall Hertzian ring cracks with large-scale inner edge chipping and wedged area on the smeared surface. Fig. 7.27(b) demonstrates large-scale chipped edge, material removal, micro-craters. Fig. 7.27(c) shows details of edge chipping of approximately 150 µm in width. Fig. 7.27(d) and (e) shows the large-scale fretting and pulverization in the edged-chipped area.

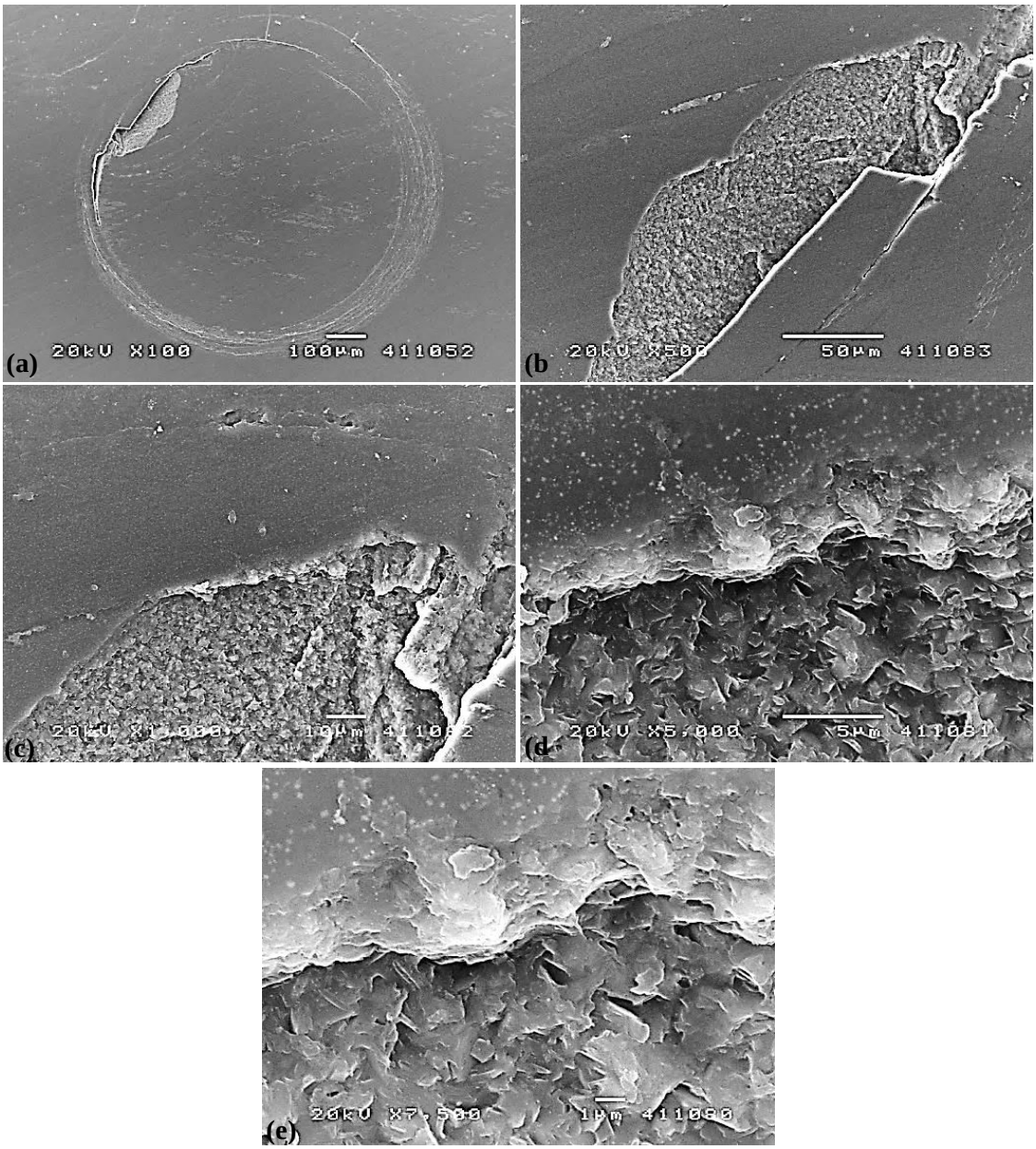


Fig. 7.21. SEM micrographs of the CAD/CAM-polished-sintered LDGC surface at 800 N and 1000 indentations revealing (a) the overall Hertzian ring cracks with inner edge chipping, (b) details of the ring and chipped edge cracks, (c) large-scale chipped edge, material removal and micro-craters, (d) the large-scale fractured surface and (e) the enlarged view of (d).

Fig. 7.28 shows SEM micrographs of the CAD/CAM-sintered-glazed LDGC surface at 800 N and 3000 indentations. Fig. 7.28(a) reveals the overall Hertzian ring cracks with large-scale inner and outer edge chippings on the milling-induced rough and pulverized surface. Fig. 7.28(b) demonstrates large-scale inner chipped edge of approximately 250 µm in width which has penetrated into the material's sub-surface leading to the large-scale micro-craters and material removal. Fig. 7.28(c) shows the sub-surface penetration of large-scale outer chipped edge of approximately 140 µm in width leading to large-scale micro-craters and material

removal. Fig. 7.28(d) displays the detailed large-scale fractured surface of the outer edge chipping. Fig. 7.28(e) displays the detailed large-scale fractured surface of the inner edge chipping.

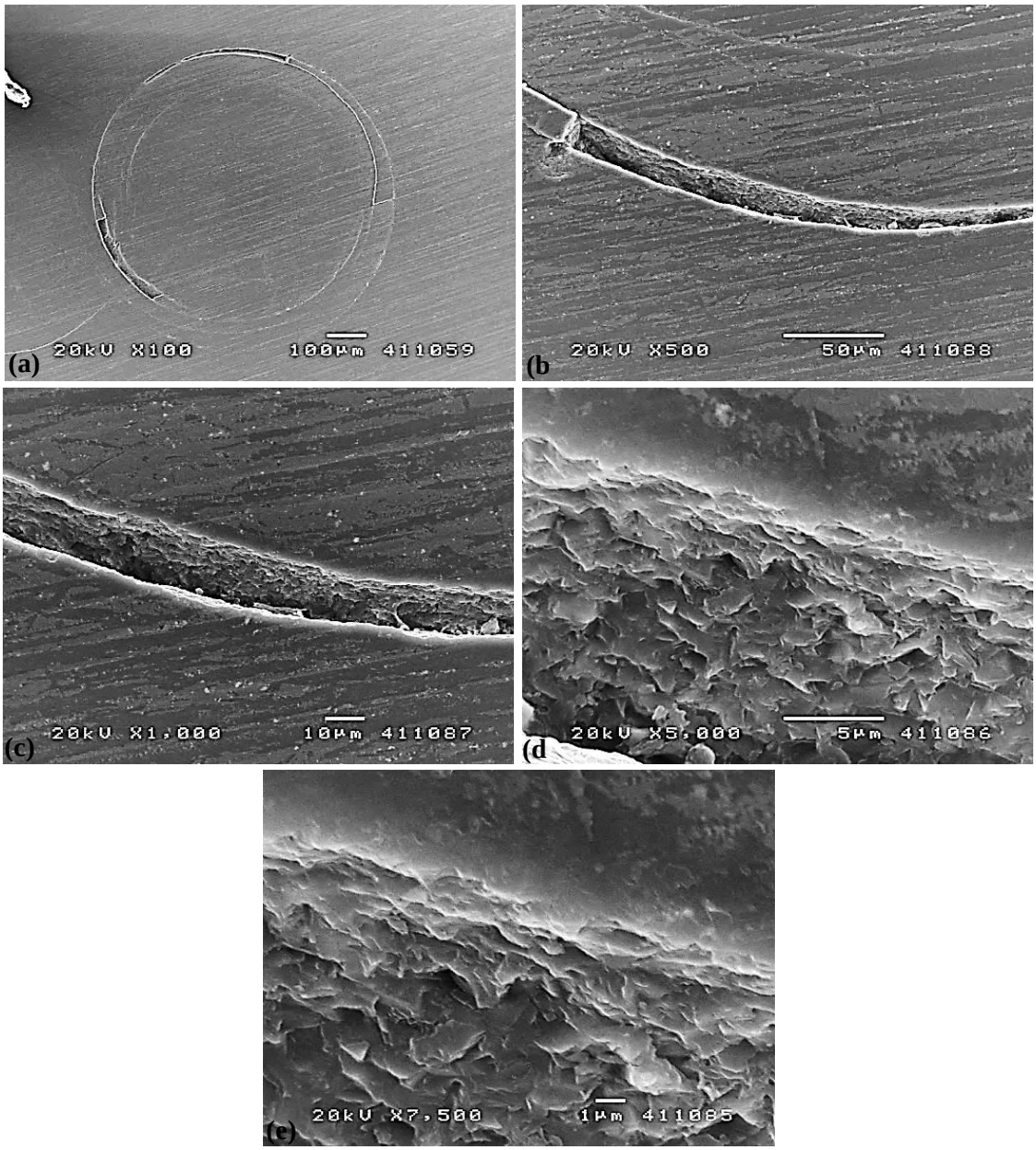


Fig. 7.22. SEM micrographs of the CAD/CAM-sintered-polished LDGC surface at 800 N and 1000 indentations revealing (a) the overall Hertzian ring cracks, (b) ring cracks and fretting debris, (c) details of wedged area, (d) the formation of fretting debris in the wedged area and (e) the enlarged view of (d).

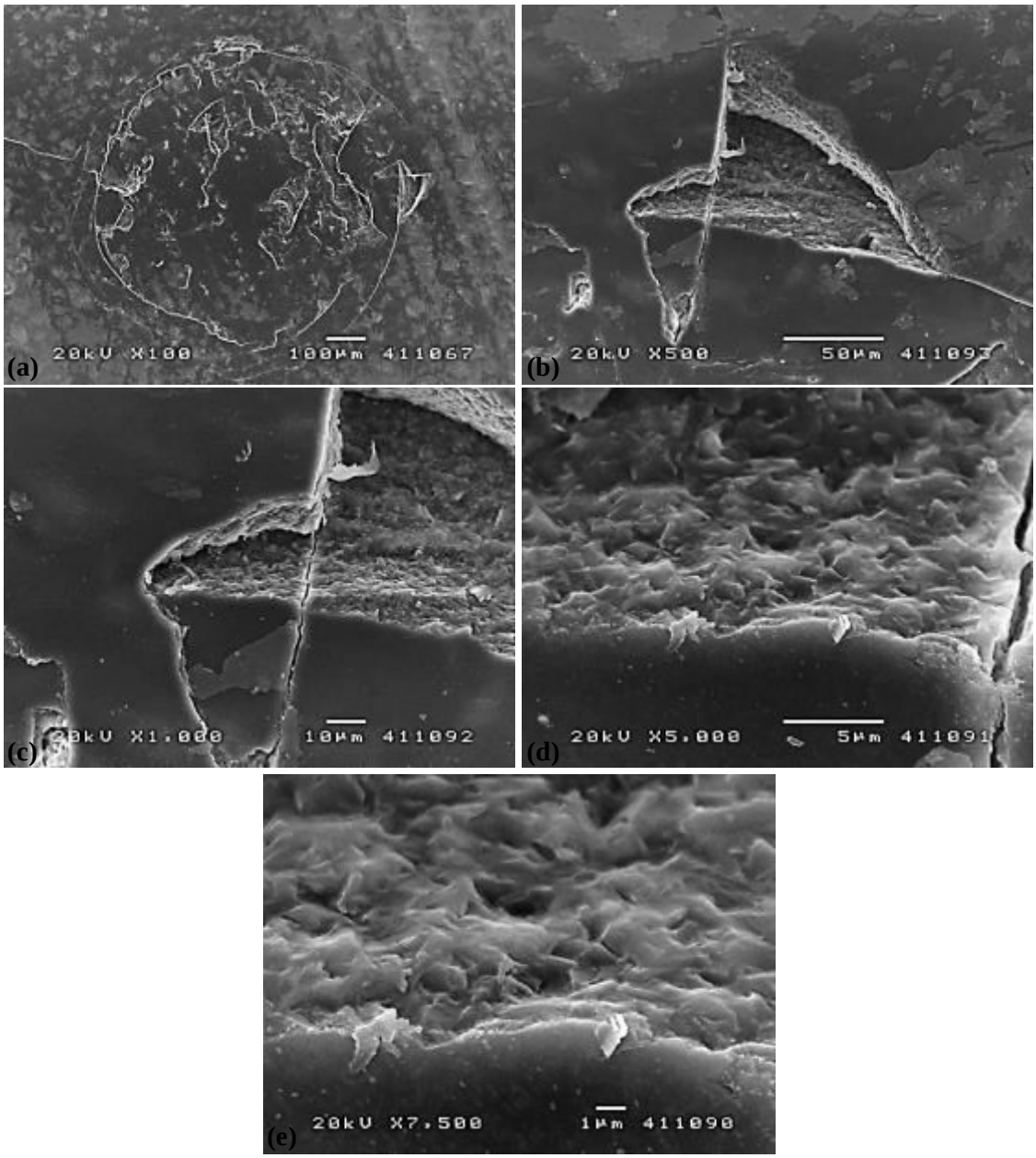


Fig. 7.23. SEM micrographs of the CAD/CAM-sintered-glazed LDGC surface at 800 N and 1000 indentations revealing (a) the overall Hertzian ring cracks with inner and outer edge chippings, (b) ring and transverse cracks and wedged area, (c) the enlarged view of (b), (d) wedged area and transverse crack and (e) the formation of fretting debris in the wedged area.

Fig. 7.29 shows SEM micrographs of the CAD/CAM-polished-sintered-glazed LDGC surface at 800 N and 3000 indentations. Fig. 7.29(a) reveals the overall Hertzian ring cracks with large-scale inner edge chipping and wedged area on the smooth surface. Fig. 7.29(b) demonstrates ring cracks, wedged and smeared areas. Fig. 7.29(c) shows the formation of the fretting debris in the wedged areas of about 80 µm crack in width. Fig. 7.29(d) and (e) displays the large-scale fractured surface with the propagation of a transversing crack.

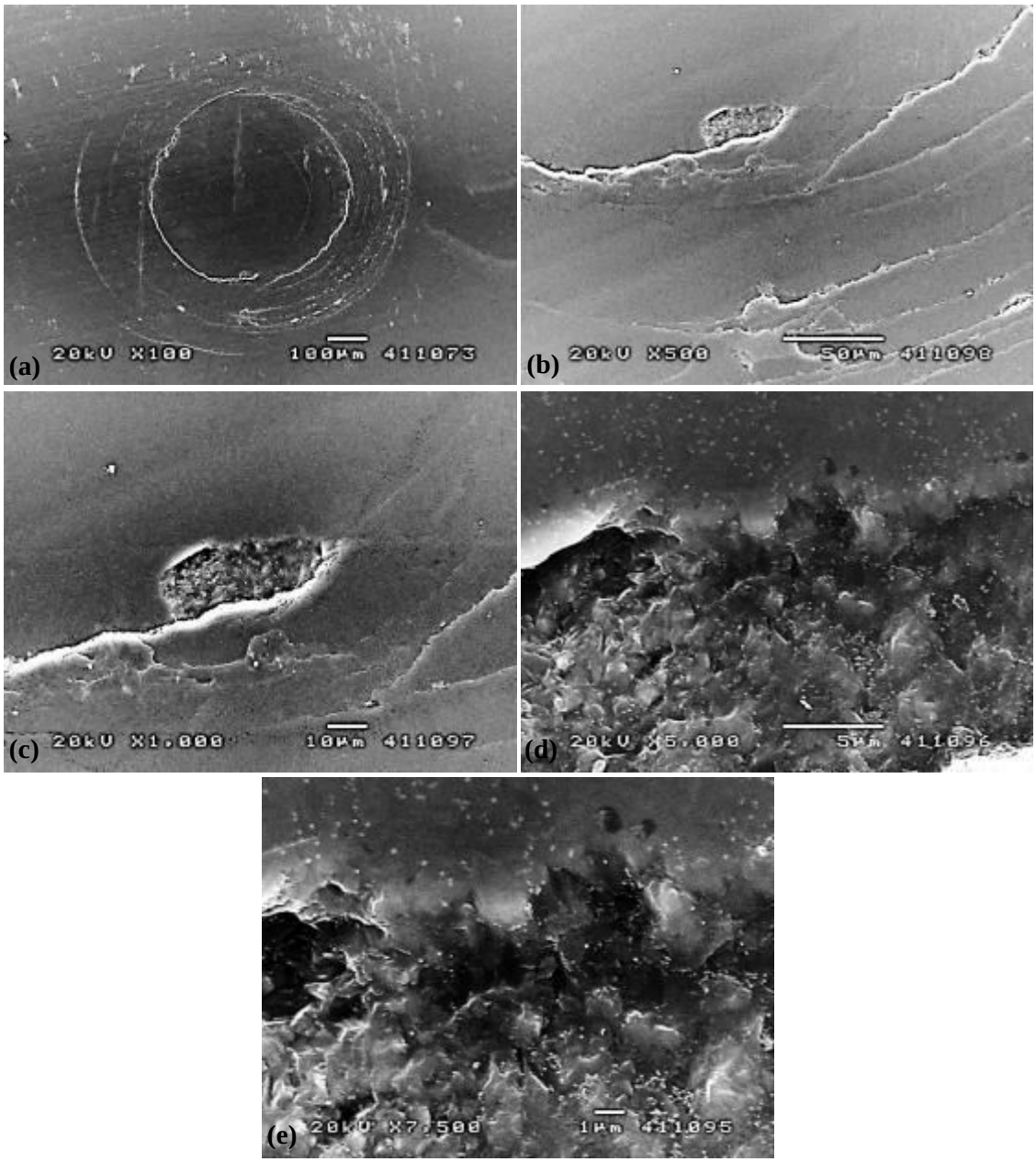


Fig. 7.24. SEM micrographs of the CAD/CAM-polished-sintered-glazed LDGC surface at 800 N and 1000 indentations revealing (a) the overall Hertzian ring cracks, (b) continued and discontinued ring cracks and fretting debris, (c) details of wedged area, (d) the formation of fretting debris in the wedged area and (e) the enlarged view of (d).

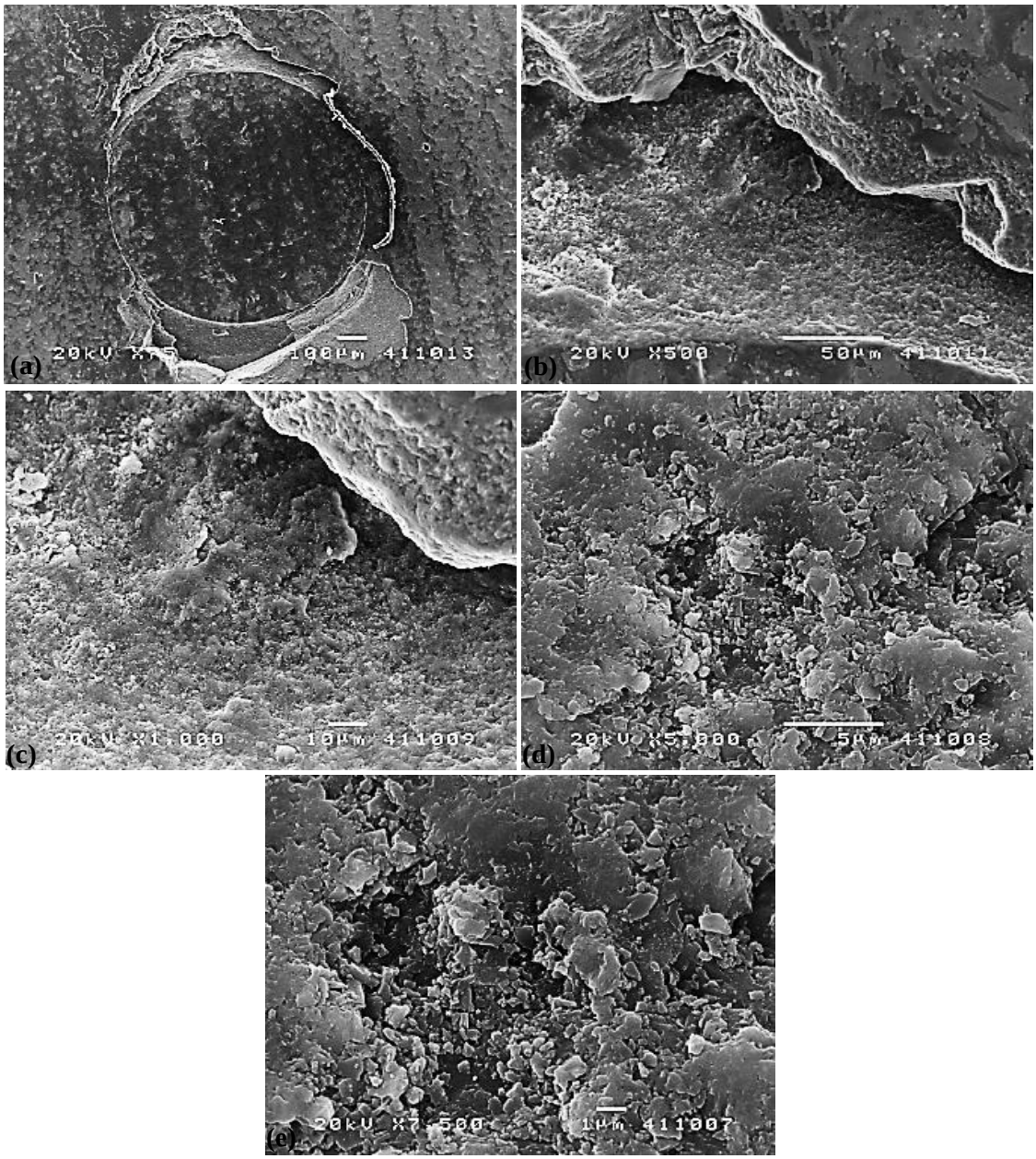


Fig. 7.25. SEM micrographs of the CAD/CAM-sintered LDGC surface at 800 N and 3000 indentations revealing (a) the overall Hertzian ring cracks with large-scale outer edge chippings, (b) large-scale chipped edge, material removal and micro-craters, (c) the large-scale fractured surface, (d) fretting and pulverized debris and (e) the enlarged view of (d).

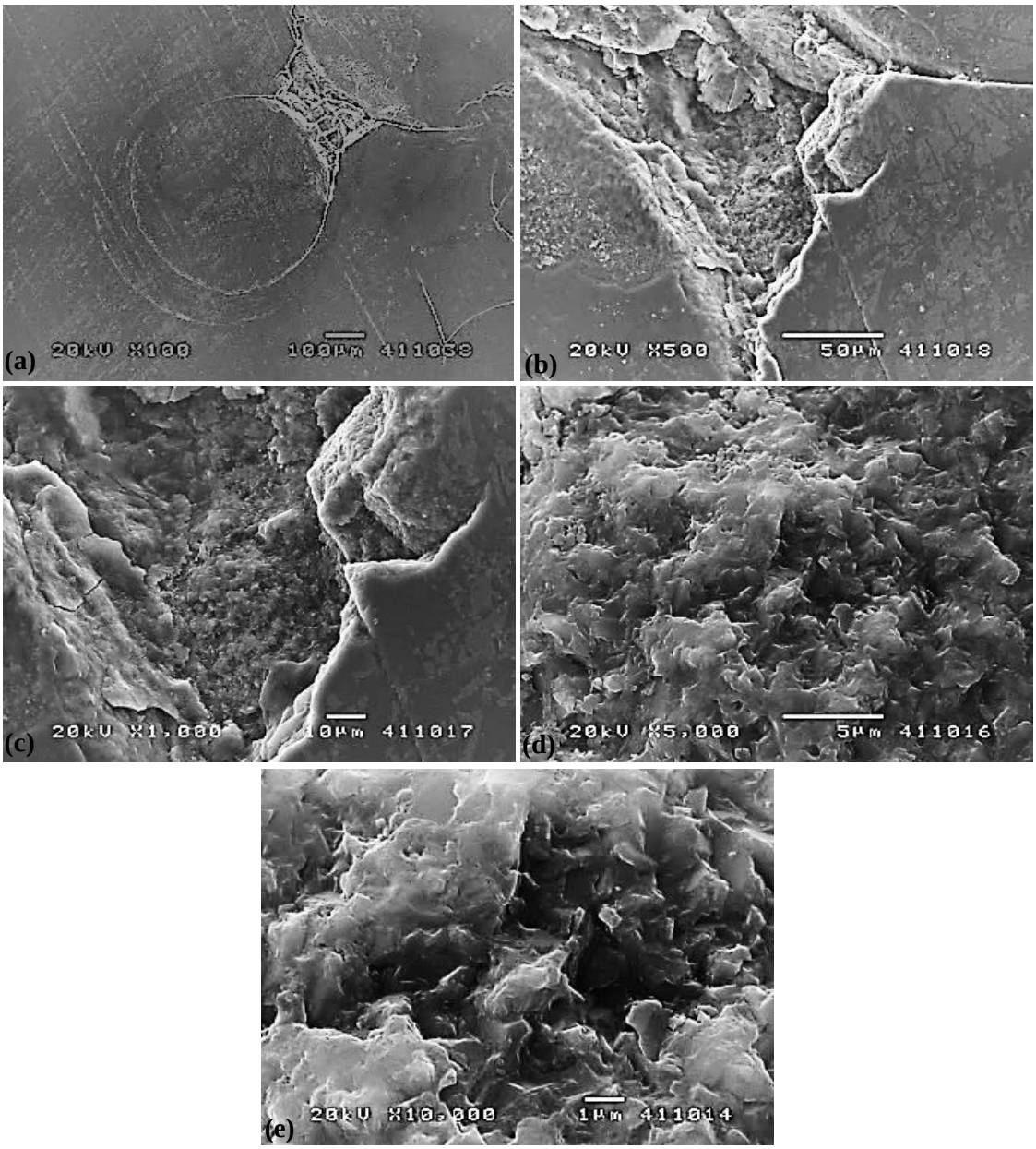


Fig. 7.26. SEM micrographs of the CAD/CAM-polished-sintered LDGC surface at 800 N and 3000 indentations revealing (a) the overall Hertzian ring cracks with large-scale outer edge chipping, (b) large-scale chipped edge, material removal, micro-craters and ring cracks, (c) details of the edge chipping, (d) large-scale fractured surface and (e) the enlarged view of (d).

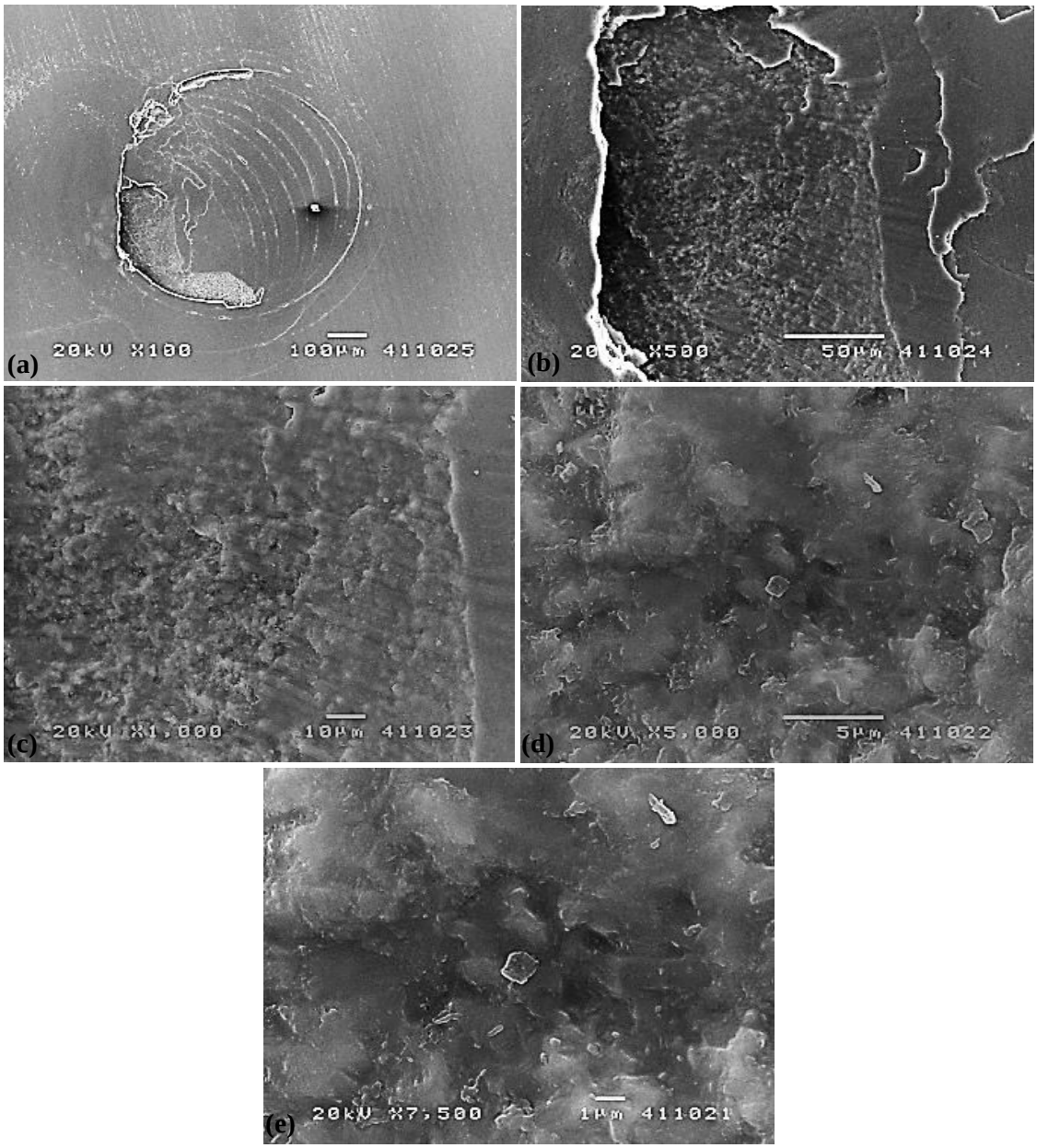


Fig. 7.27. SEM micrographs of the CAD/CAM-sintered-polished LDGC surface at 800 N and 3000 indentations revealing (a) the overall Hertzian ring cracks with large-scale inner edge chipping, (b) large-scale chipped edge, material removal, micro-craters, (c) fractured surface, (d) large-scale fractured surface and (e) the enlarged view of (d).

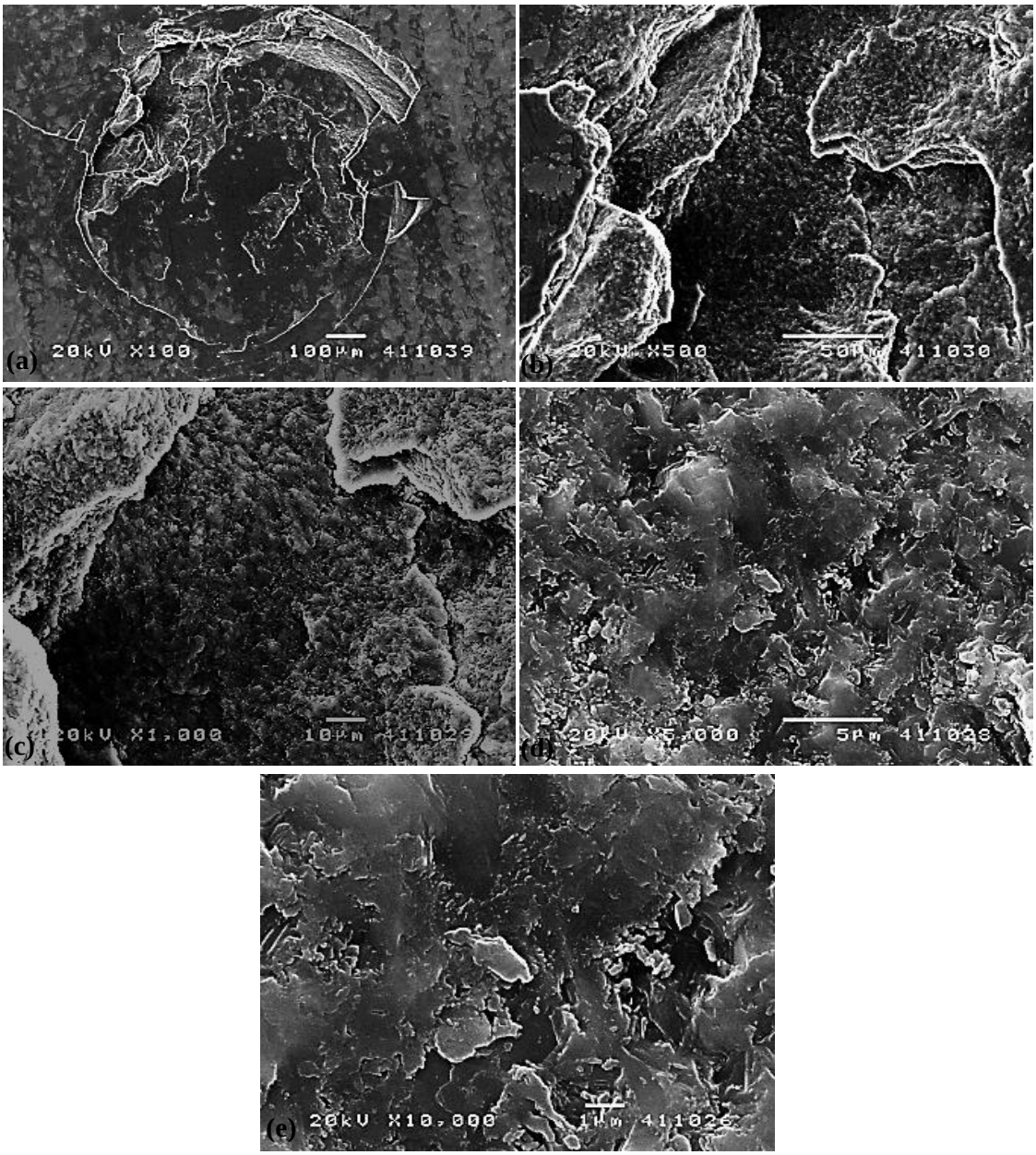


Fig. 7.28. SEM micrographs of the CAD/CAM-sintered-glazed LDGC surface at 800 N and 3000 indentations revealing (a) the overall Hertzian ring cracks with large-scale inner and outer edge chippings, (b) large-scale inner chipped edge, material removal, micro-craters, (c) large-scale outer chipped edge, material removal, micro-craters, (d) large-scale fractured surface of the inner edge chipping and (e) large-scale fractured surface of the outer edge chipping.

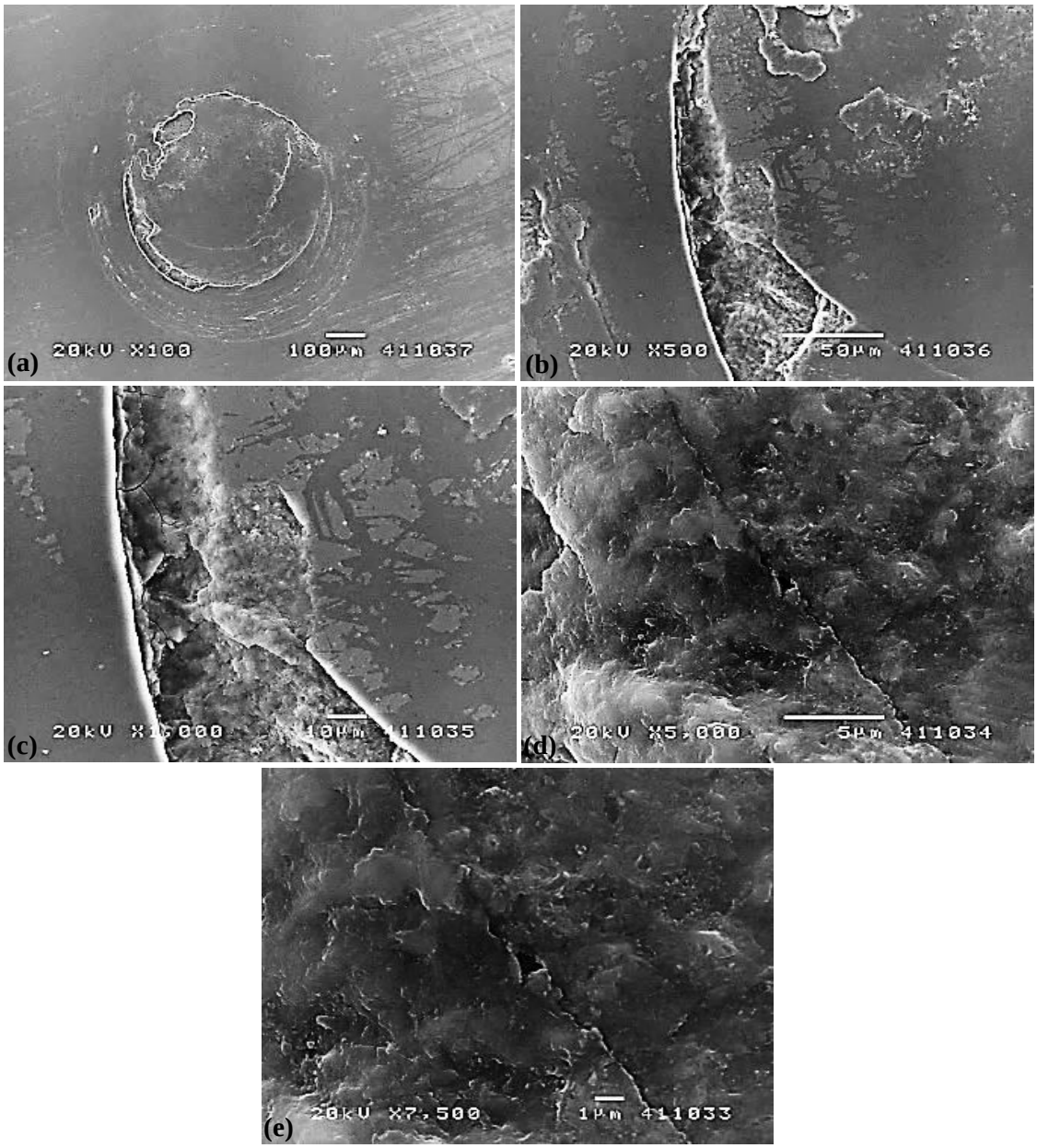


Fig. 7.29. SEM micrographs of the CAD/CAM-polished-sintered-glazed LDGC surface at 800 N and 3000 indentations revealing (a) the overall Hertzian ring cracks with large-scale inner edge chipping, (b) ring cracks and the wedged area, (c) the formation of the fretting debris in the wedged areas, (d) the large-scale fractured surface with a propagating crack and (e) the enlarged view of (d).

### *7.4.3 Indented Morphologies of Treated Y-TZP Surfaces*

Fig. 7.30 shows SEM micrographs of the CAD/CAM-sintered Y-TZP surface at 800 N and 1 indentation. Fig. 7.30(a) reveals the overall indentation pattern on the miling- and sintering-induced rough surface. Fig. 7.30(b) and (c) demonstrates the sintering-induced grain coarsening on the milled surface. Fig. 7.30(d) and (e) shows details of the transformed tetragonal surfaces.

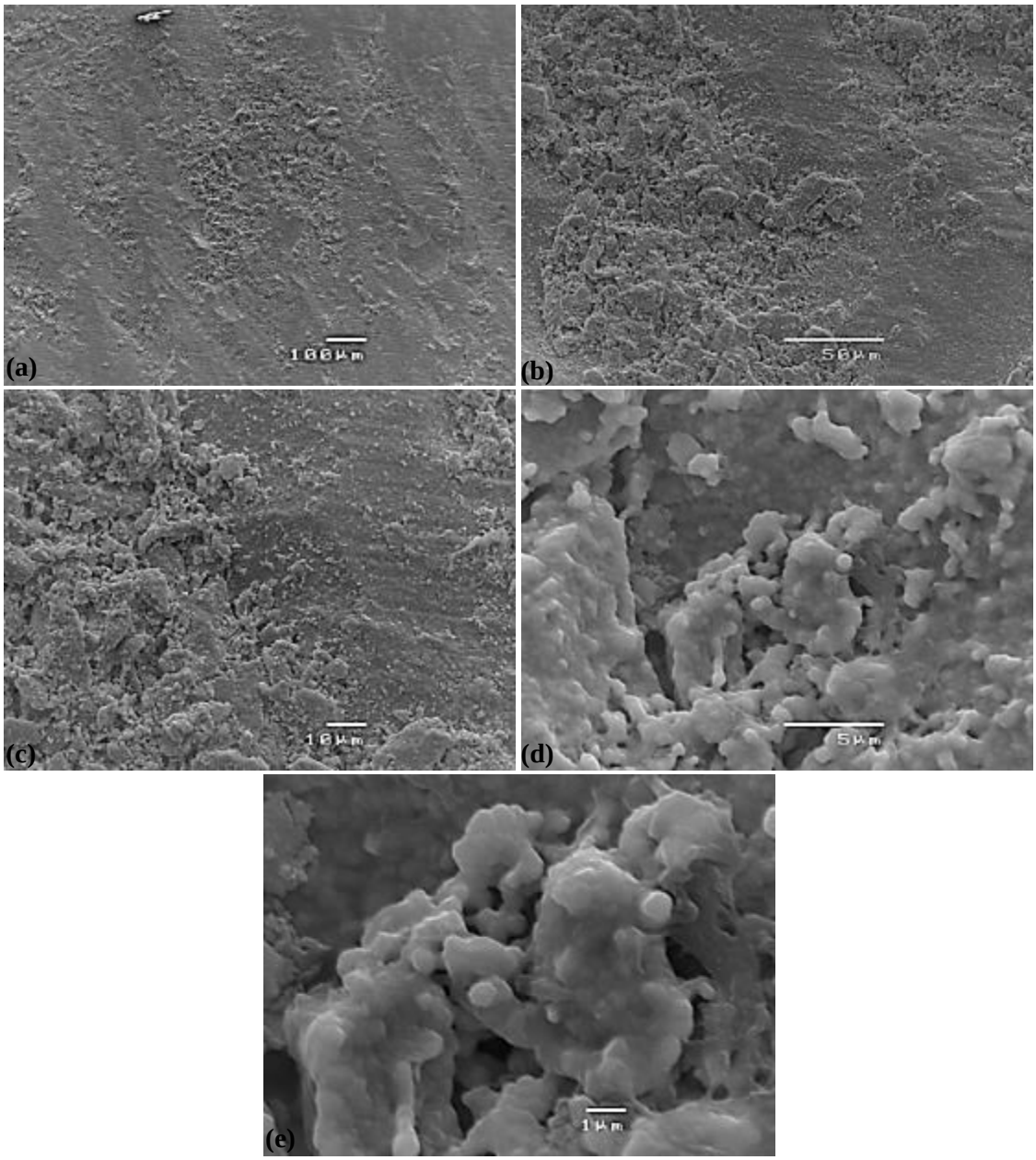


Fig. 7.30. SEM micrographs of the CAD/CAM-sintered Y-TZP surface at 800 N and 1 indentation revealing (a) the overall indentation pattern, (b) the sintering-induced grain coarsening on the milled surface, (c) the enlarged view of (b), (d) details of the transformed surface, and (e) the enlarged view of (d).

Fig. 7.31 shows SEM micrographs of the CAD/CAM-polished-sintered Y-TZP surface at 800 N and 1 indentation. Fig. 7.31(a) reveals the overall indentation pattern on the smooth surface in which the sintering-induced grain coarsening was partially removed. The morphologies across the two opposite sides represent the two dots used to discern the indentation pattern due to its shallowness before taking the SEM images. Fig. 7.31(b) and (c) demonstrates the indentation-induced plastic deformation around the milling-induced surface defect. Fig. 7.31(d) and (e)

shows details of surface defects like microstructural porosity produced during the densification process.

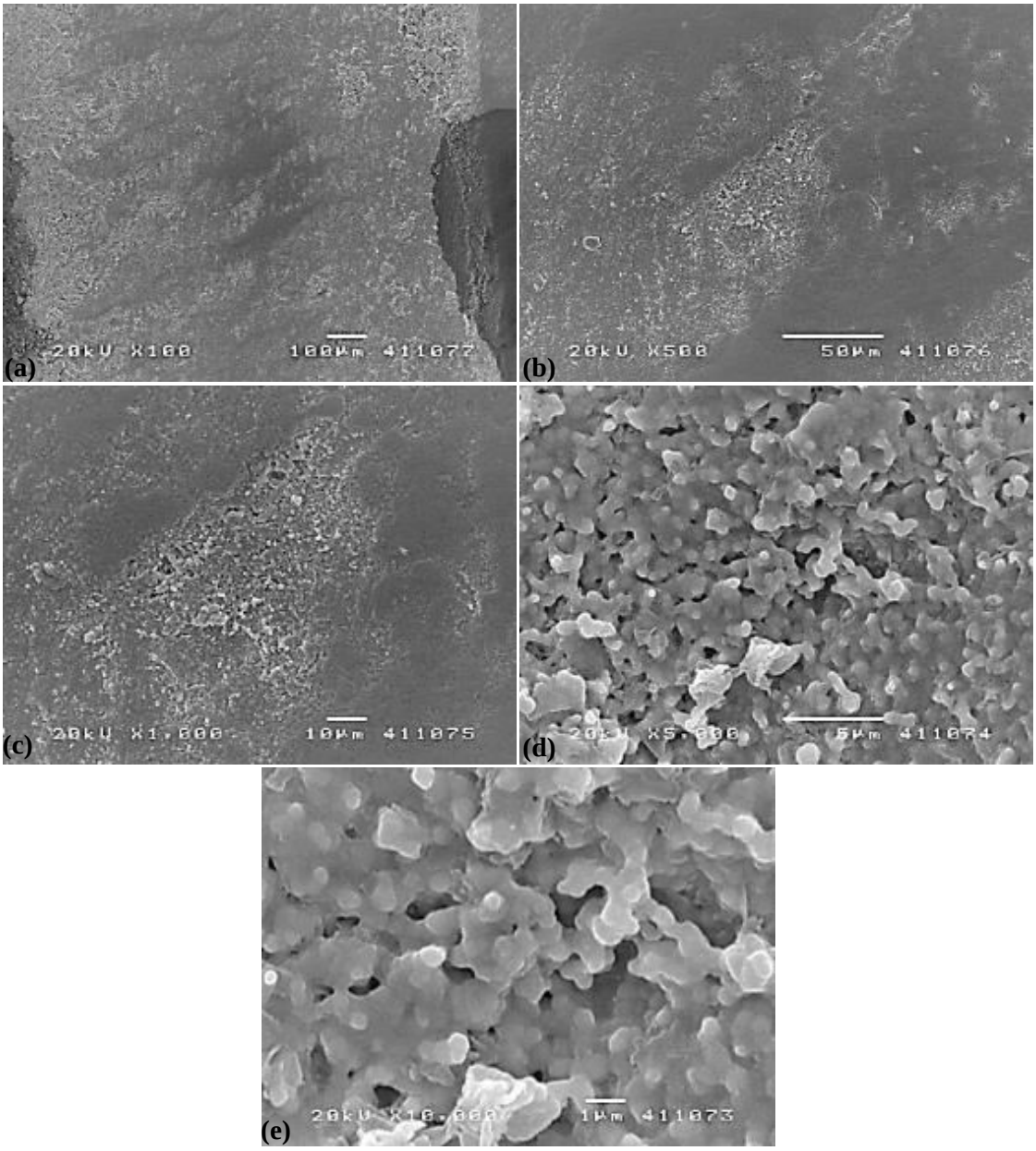


Fig. 7.31. SEM micrographs of the CAD/CAM-polished-sintered Y-TZP surface at 800 N and 1 indentation revealing (a) the overall indentation pattern, (b) the indentation-induced plastic deformation around the milling-induced surface defect, (c) the enlarged view of (b), (d) details of surface defects like microstructural porosity produced during the densification process, (e) the enlarged view of (d).

Fig. 7.32 shows SEM micrographs of the CAD/CAM-sintered-polished Y-TZP surface at 800 N and 1 indentation. Fig. 7.32(a) reveals the overall indentation pattern on the rough surface due

to sintering-induced coarsened grains that were weakly removed by the polishing process. Fig. 7.32(b) demonstrates indentation-induced plastic deformation and micro-craters and surface defects from the milling process which were unremoved by the polishing process. Fig. 7.32(c) shows details of plastic deformation and surface defects. Fig. 7.32(d) and (e) displays the indentation-induced smoothened surface and fracture from the milling process.

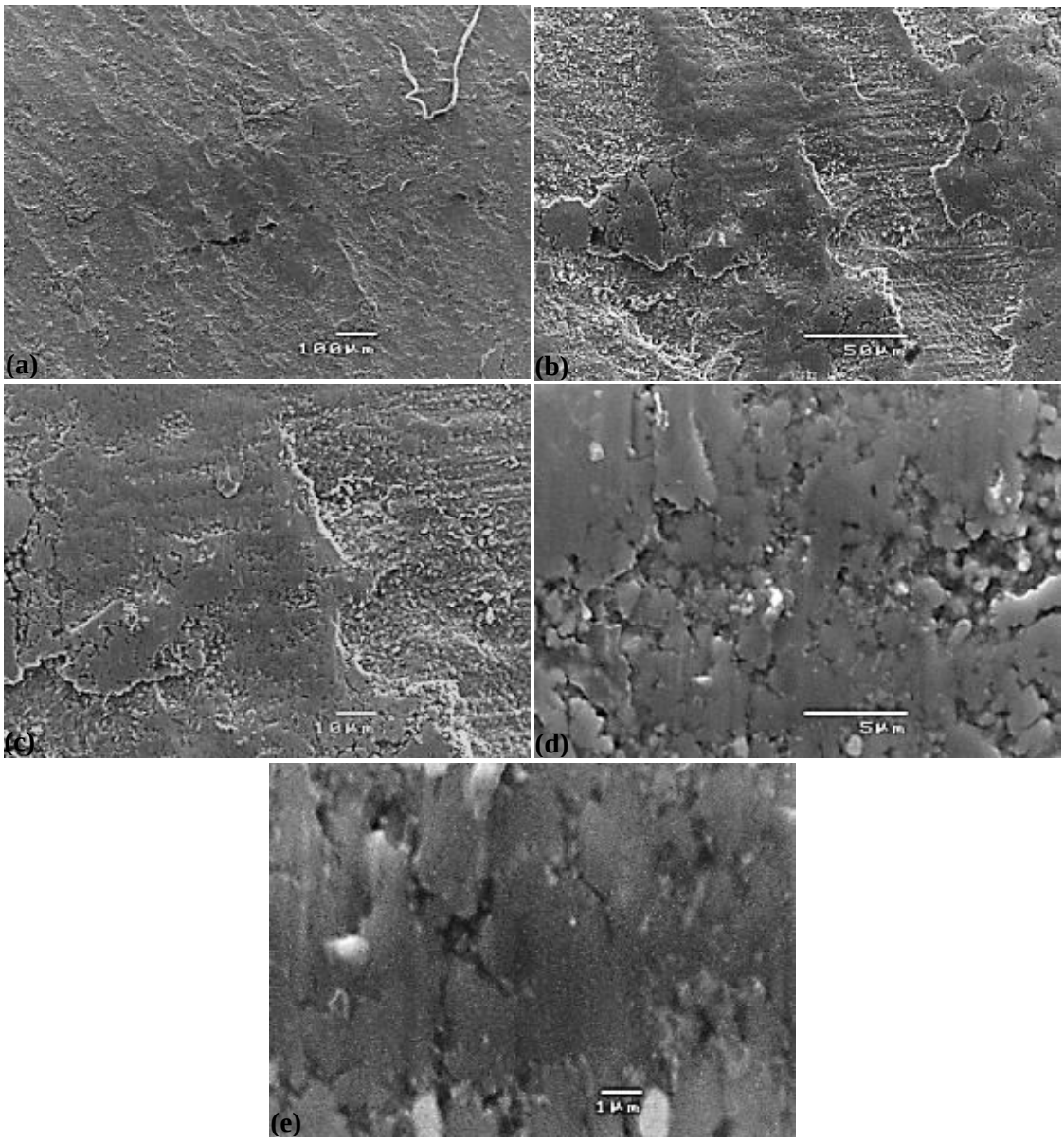


Fig. 7.32. SEM micrographs of the CAD/CAM-sintered-polished Y-TZP surface at 800 N and 1 indentation revealing (a) the overall indentation pattern, (b) indentation-induced plastic deformation and micro-cracks and surface defects from the milling process, (c) details of plastic deformation and surface defects, (d) the indentation-induced smoothened surface and fracture from the milling process, (e) the enlarged view of (d).

Fig. 7.33 shows SEM micrographs of the CAD/CAM-sintered-110 µm alumina sandblasted Y-TZP surface at 800 N and 1 indentation. Fig. 7.33(a) reveals the overall indentation pattern on sandblasting-induced rough surface. Fig. 7.33(b) and (c) demonstrates indentation-induced plastic deformation and surface defects from the milling and sandblasting processes. Fig. 7.33(d) shows plastic surface and the milled and sandblasted fracture. Fig. 7.33(e) shows that the sandblasting-induced fracture is intragranular.

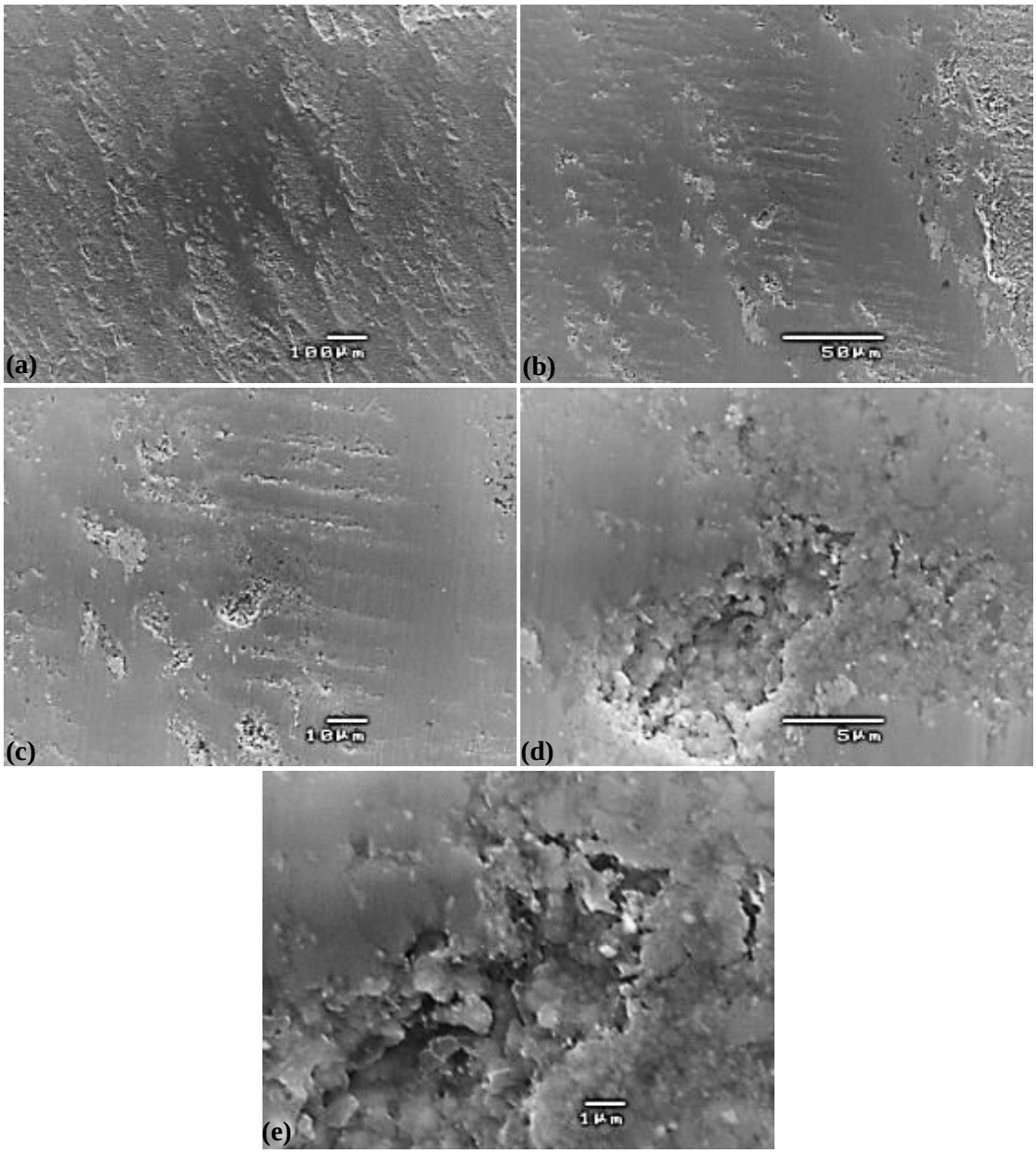


Fig. 7.33. SEM micrographs of the CAD/CAM-sintered-110 µm alumina sandblasted Y-TZP surface at 800 N and 1 indentation revealing (a) the overall indentation pattern, (b) indentation-induced plastic deformation and micro-cracks and surface defects from the milling and sandblasting processes, (c) the enlarged view of (b), (d) plastic surface and the milled and sandblasted fracture, (e) the intragranular fracture.

Fig. 7.34 shows SEM micrographs of the CAD/CAM-sintered-250 µm alumina sandblasted Y-TZP surface at 800 N and 1 indentation. Fig. 7.34(a) reveals the overall indentation pattern on on sandblasting-induced rough surface. Fig. 7.34(b) and (c) demonstrates little indentation-induced plastic deformation, randomly oriented scoring and scratches. Fig. 7.34(d) shows large-scale surface defects including deep sharp scratches, micro-craters, pitting and grain pull-out. Fig. 7.34(e) displays the detailed scoring morphology.

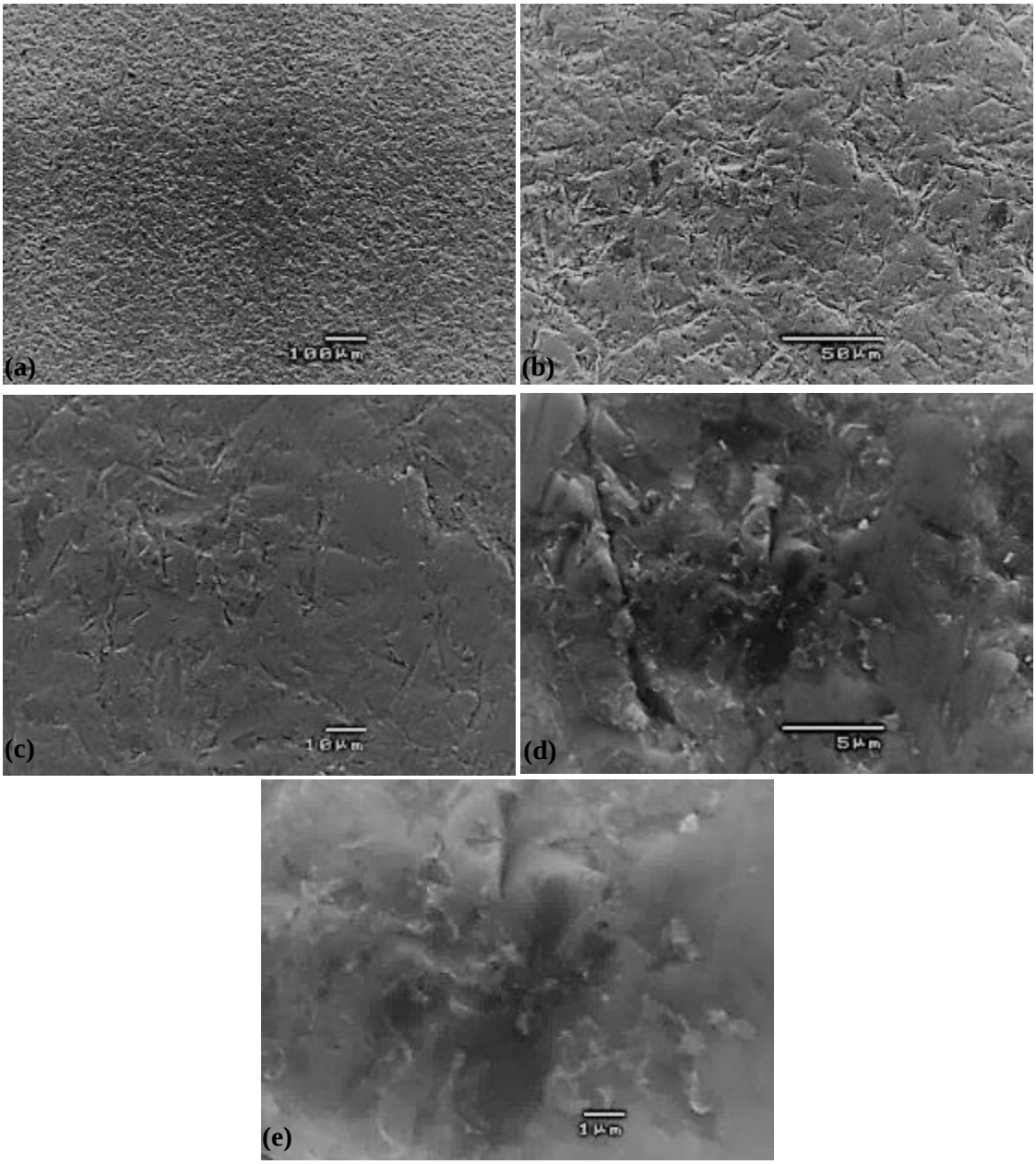


Fig. 7.34. SEM micrographs of the CAD/CAM-sintered-250 µm alumina sandblasted Y-TZP surface at 800 N and 1 indentation revealing (a) the overall indentation pattern, (b) little indentation-induced plastic deformation, randomly oriented scoring and scratches, (c) the enlarged view of (b), (d) large-scale surface defects including deep sharp scratches mocro-craters, pitting and grain pull-out, and (e) the detailed scoring morphology.

Fig. 7.35 shows SEM micrographs of the CAD/CAM-sintered Y-TZP surface at 800 N and 10 indentations. Fig. 7.35(a) reveals the overall indentation pattern on the milling- and sintering-induced rough surface. Fig. 7.35(b) demonstrates the indentation-induced plastic deformation around the milling-induced surface defect. Fig. 7.35(c) shows plastic deformation and sintering-induced grain coarsening on the milled surface. Fig. 7.35(d) displays the sintering-induced grain coarsening. Fig. 7.35(e) shows details of the transformed tetragonal surface.

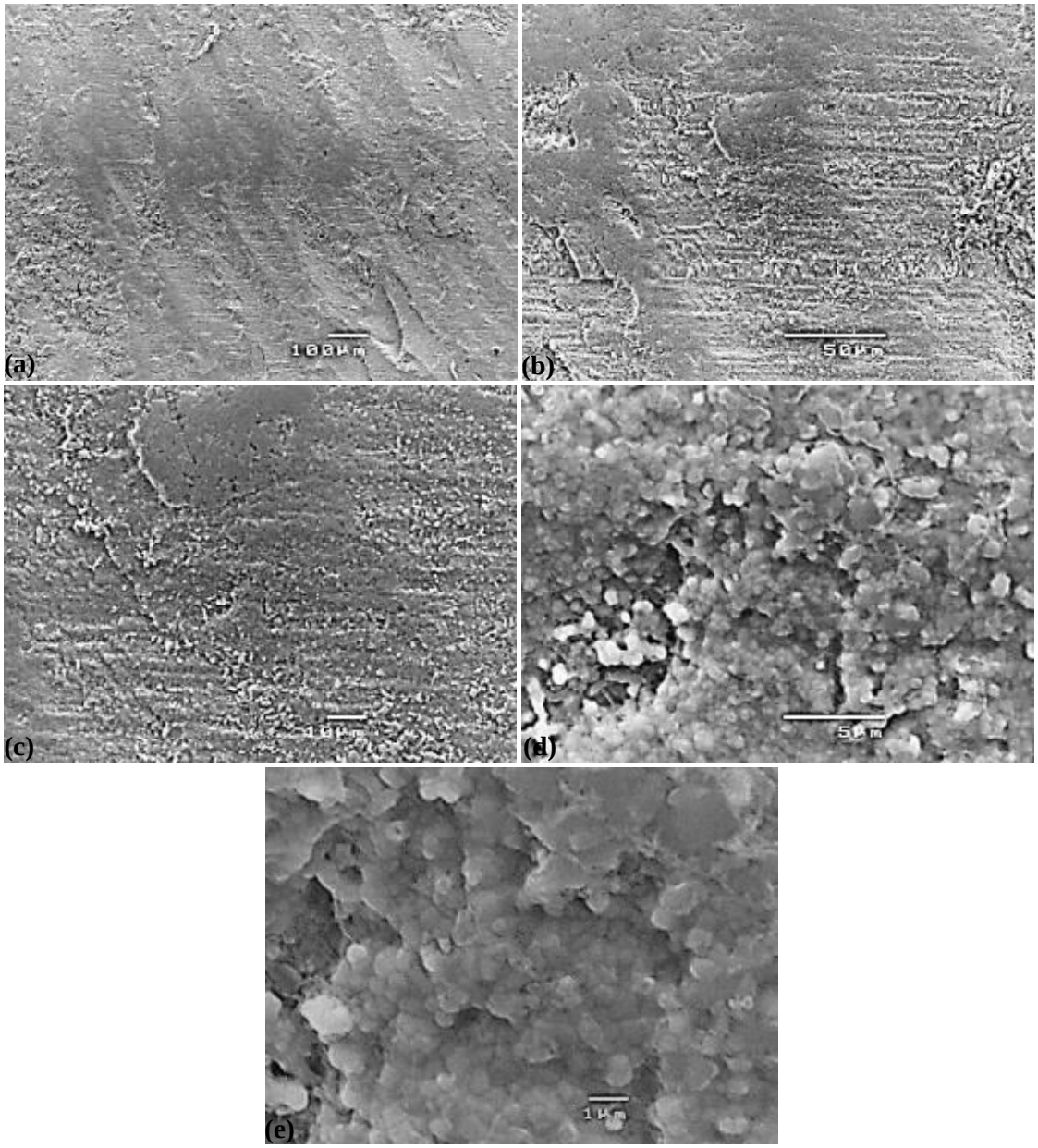


Fig. 7.35. SEM micrographs of the CAD/CAM-sintered Y-TZP surface at 800 N and 10 indentations revealing (a) the overall indentation pattern, (b) the indentation-induced plastic deformation around the milling-induced surface defect, (c) plastic deformation and sintering-induced grain coarsening on the milled surface, (d) the sintering-induced grain coarsening, and (e) details of the transformed surface.

Fig. 7.36 shows SEM micrographs of the CAD/CAM-polished-sintered Y-TZP surface at 800 N and 10 indentations. Fig. 7.36(a) reveals the overall indentation pattern on the smooth surface in which the sintering-induced grain coarsening was partially removed. Fig. 7.36(b) and (c) demonstrates the indentation-induced plastic deformation around the milling-induced surface defect. Fig. 7.36(d) and (e) shows the milling-induced intragranular fracture.

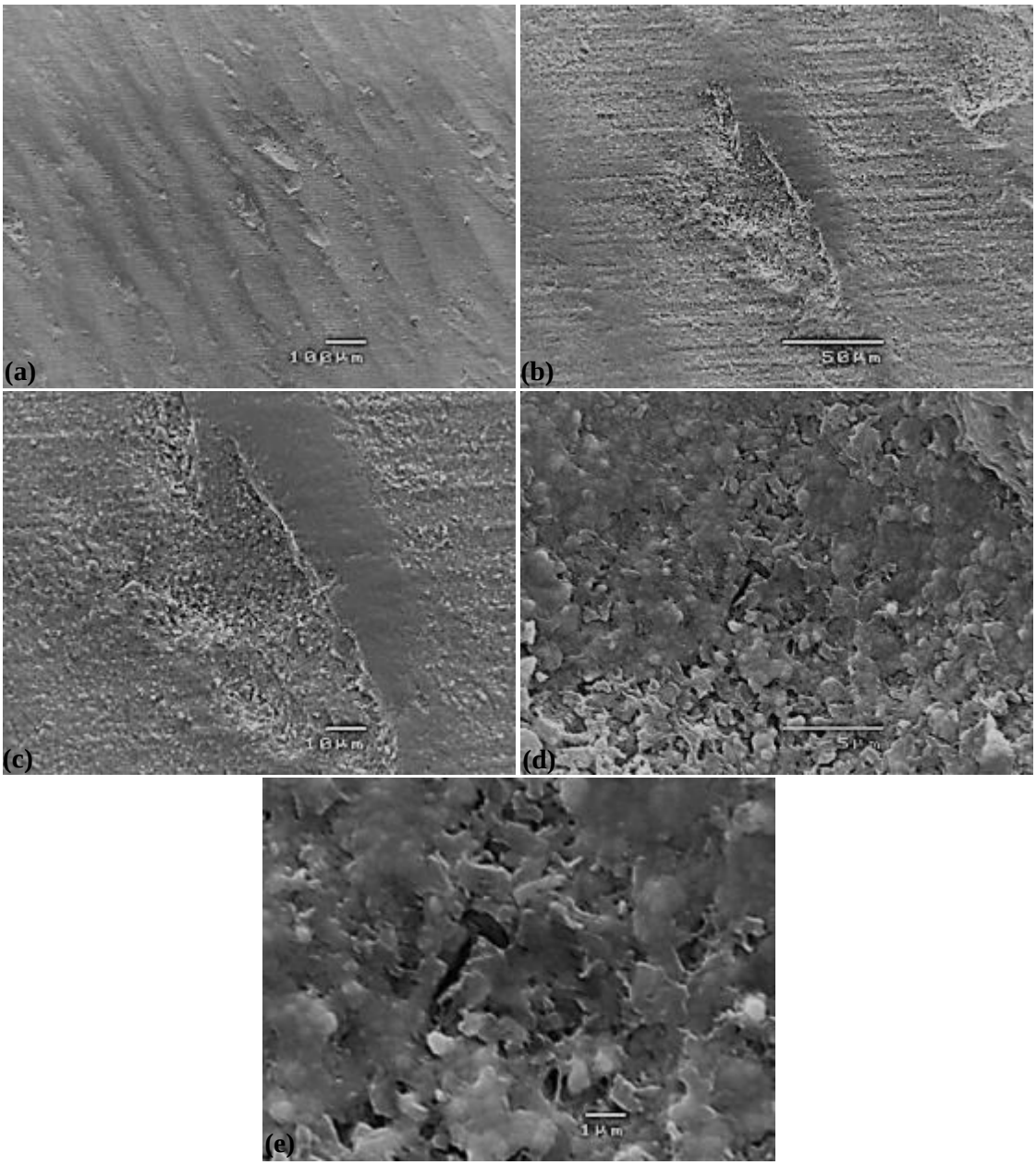


Fig. 7.36. SEM micrographs of the CAD/CAM-polished-sintered Y-TZP surface at 800 N and 10 indentations revealing (a) the overall indentation pattern, (b) the indentation-induced plastic deformation around the milling-induced surface defect, (c) the enlarged view of (b), (d) the milling-induced intragranular fracture, and (e) the enlarged view of (d).

Fig. 7.37 shows SEM micrographs of the CAD/CAM-sintered-polished Y-TZP surface at 800 N and 10 indentations. Fig. 7.37(a) reveals the overall indentation pattern on the rough surface due to sintering-induced coarsened grains that were weakly removed by the polishing process. Fig. 7.37(b) demonstrates indentation-induced plastic deformation and micro-craters and surface defects from the milling process. Fig. 7.37(c) shows details of plastic deformation and surface defects. Fig. 7.37(d) and (e) displays the indentation-induced smoothened surface, polishing traces and fracture from the milling process.

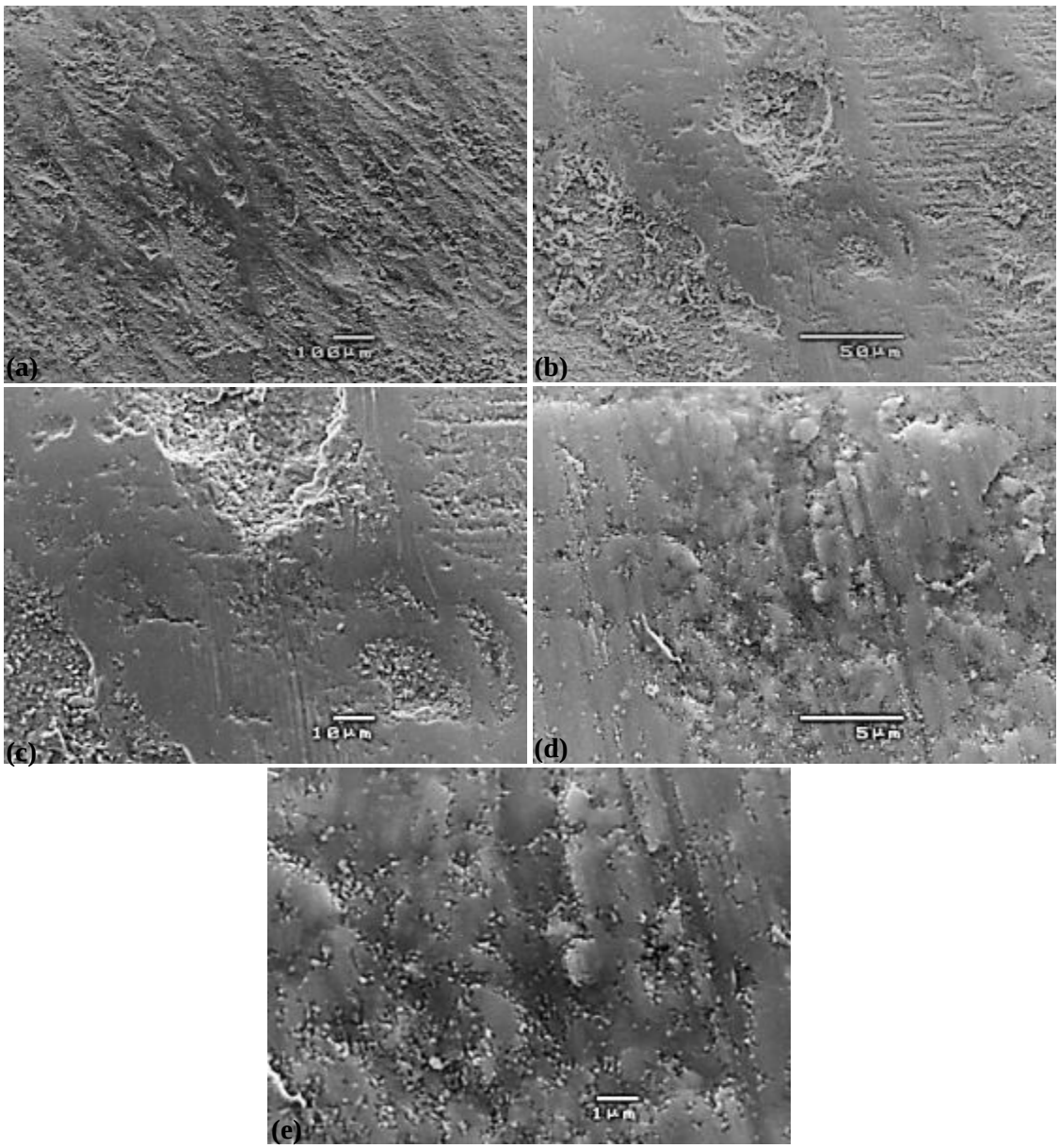


Fig. 7.37. SEM micrographs of the CAD/CAM-sintered-polished Y-TZP surface at 800 N and 10 indentations revealing (a) the overall indentation pattern, (b) indentation-induced plastic deformation and micro-cracks and surface defects from the milling process, (c) details of plastic deformation and surface defects, (d) the indentation-induced smoothened surface, polishing traces and fracture from the milling process, and (e) the enlarged view of (d).

Fig. 7.38 shows SEM micrographs of the CAD/CAM-sintered-110 µm alumina sandblasted Y-TZP surface at 800 N and 10 indentations. Fig. 7.38(a) reveals the overall indentation pattern on sandblasting-induced rough surface. Fig. 7.38(b) demonstrates indentation-induced plastic deformation and surface defects from the milling and sandblasting processes. Fig. 7.38(c) shows the smooth surface due to the indentation-induced plastic deformation. Fig. 7.38(d) displays the milled and sandblasted fractured surface. Fig. 7.38(e) shows indentation-induced smeared surface and intragranular fracture.

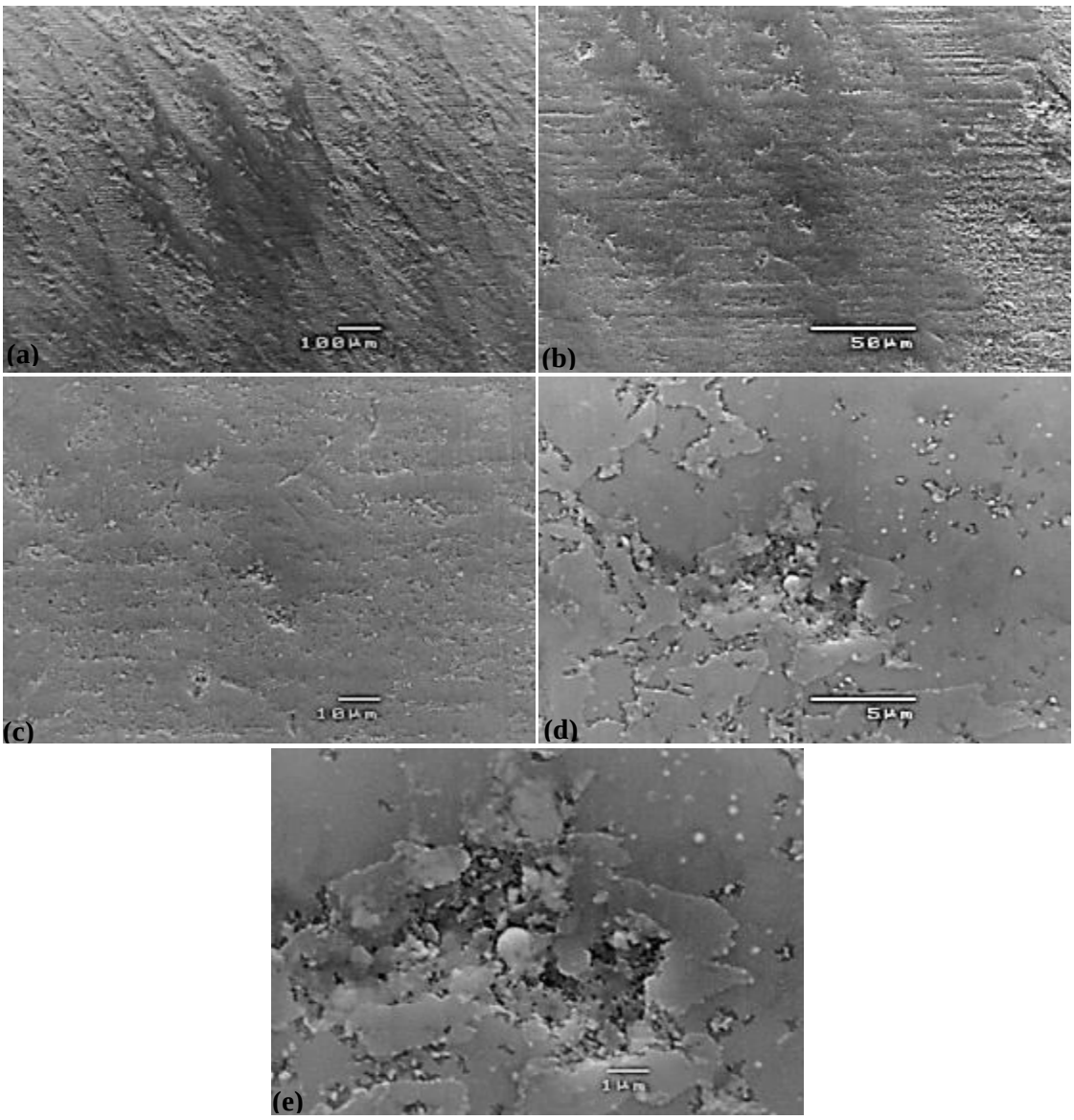


Fig. 7.38. SEM micrographs of the CAD/CAM-sintered-110 µm alumina sandblasted Y-TZP surface at 800 N and 10 indentations revealing (a) the overall indentation pattern, (b) indentation-induced plastic deformation and micro-cracks and surface defects from the milling and sandblasting processes, (c) the smooth surface due to the indentation-induced plastic deformation, (d) the milled and sandblasted fractured surface, and (e) indentation-induced smeared surface and intragranular fracture.

Fig. 7.39 shows SEM micrographs of the CAD/CAM-sintered-250 µm alumina sandblasted Y-TZP surface at 800 N and 10 indentations. Fig. 7.39(a) reveals the overall indentation pattern on sandblasting-induced rough surface. Fig. 7.39(b) and (c) demonstrates little indentation-induced plastic deformation, randomly oriented scoring and scratches. Fig. 7.39(d) shows large-scale surface defects including deep sharp scratches, micro-craters, pitting and grain pull-out. Fig. 7.39(e) displays the detailed scoring.

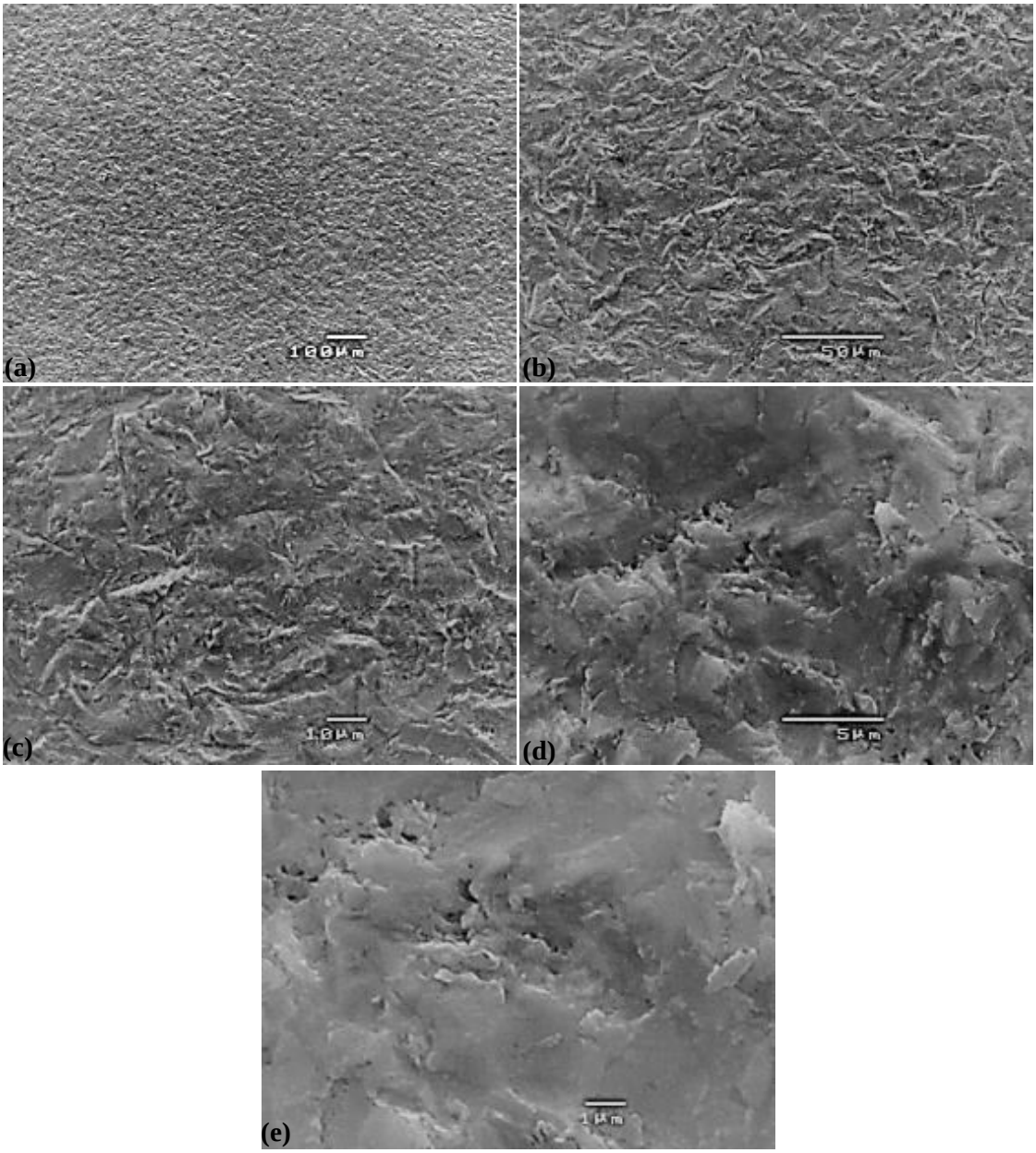


Fig. 7.39. SEM micrographs of the CAD/CAM-sintered-250 µm alumina sandblasted Y-TZP surface at 800 N and 10 indentations revealing (a) the overall indentation pattern, (b) little indentation-induced plastic deformation, randomly oriented scoring and scratches, (c) the enlarged view of (b), (d) large-scale surface defects including deep sharp scratches, micro-craters, pitting and grain pull-out, and (e) the detailed scoring.

Fig. 7.40 shows SEM micrographs of the CAD/CAM-sintered Y-TZP surface at 800 N and 100 indentations. Fig. 7.40(a) reveals the overall indentation on the miling- and sintering-induced rough surface. Fig. 7.40(b) demonstrates the indentation-induced plastic deformation around the milling-induced surface defect. Fig. 7.40(c) shows plastic deformation and sintering-induced grain coarsening on the milled surface. Fig. 7.40(d) displays the sintering-induced grain coarsening. Fig. 7.40(e) shows details of the transformed tetragonal surface.

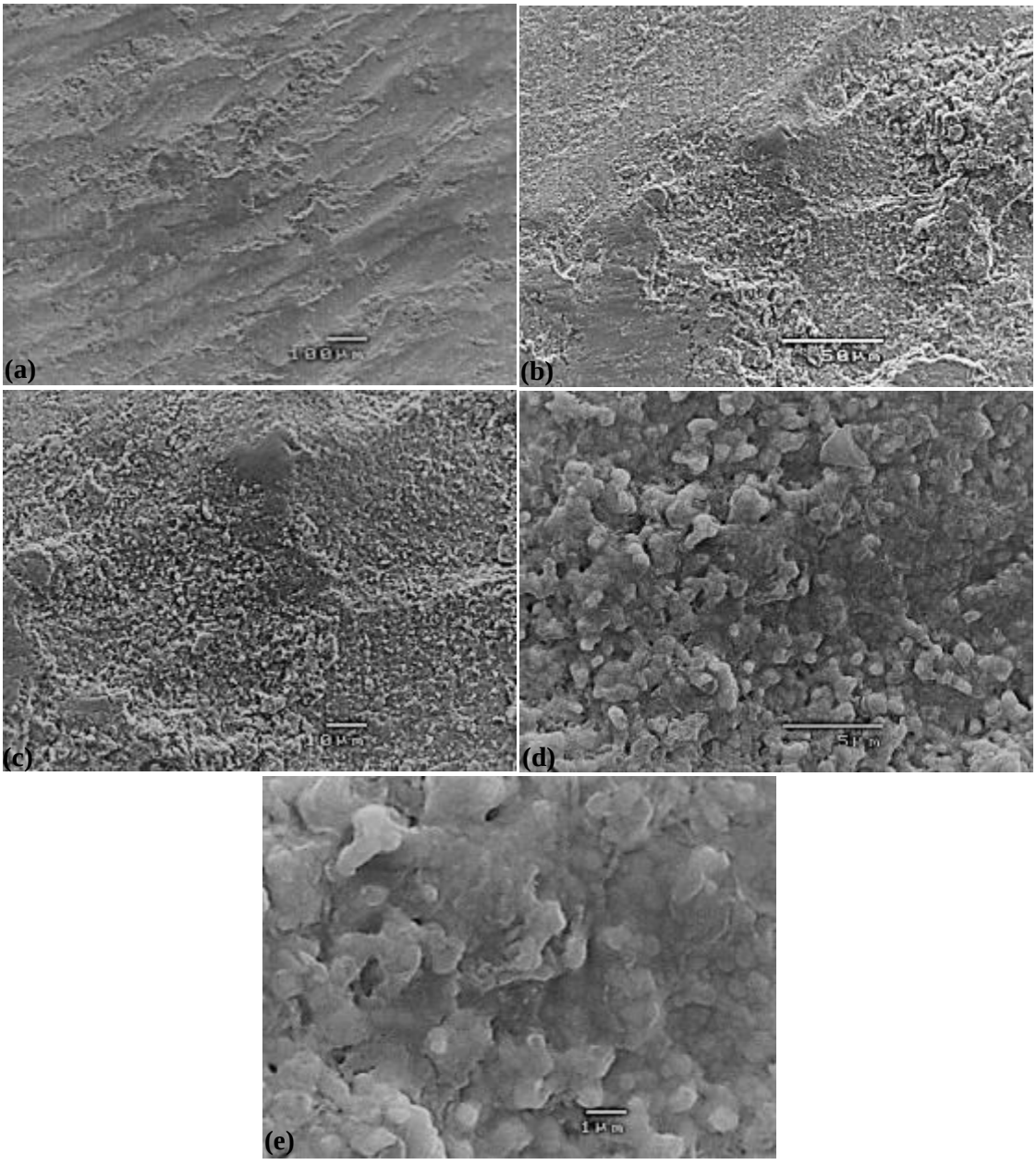


Fig. 7.40. SEM micrographs of the CAD/CAM-sintered Y-TZP surface at 800 N and 100 indentations revealing (a) the overall indentation, (b) the indentation-induced plastic deformation around the milling-induced surface defect, (c) plastic deformation and sintering-induced grain coarsening on the milled surface, (d) the sintering-induced grain coarsening, and (e) details of the transformed surface.

Fig. 7.41 shows SEM micrographs of the CAD/CAM-polished-sintered Y-TZP surface at 800 N and 100 indentations. Fig. 7.41(a) reveals the overall indentation pattern on the smooth surface in which the sintering-induced grain coarsening was partially removed. Fig. 7.41(b) and (c) demonstrates the fracture of the milling grooves due to the indentation. Fig. 7.41(d) and (e) displays plastic deformation and milling-induced intragranular fracture.

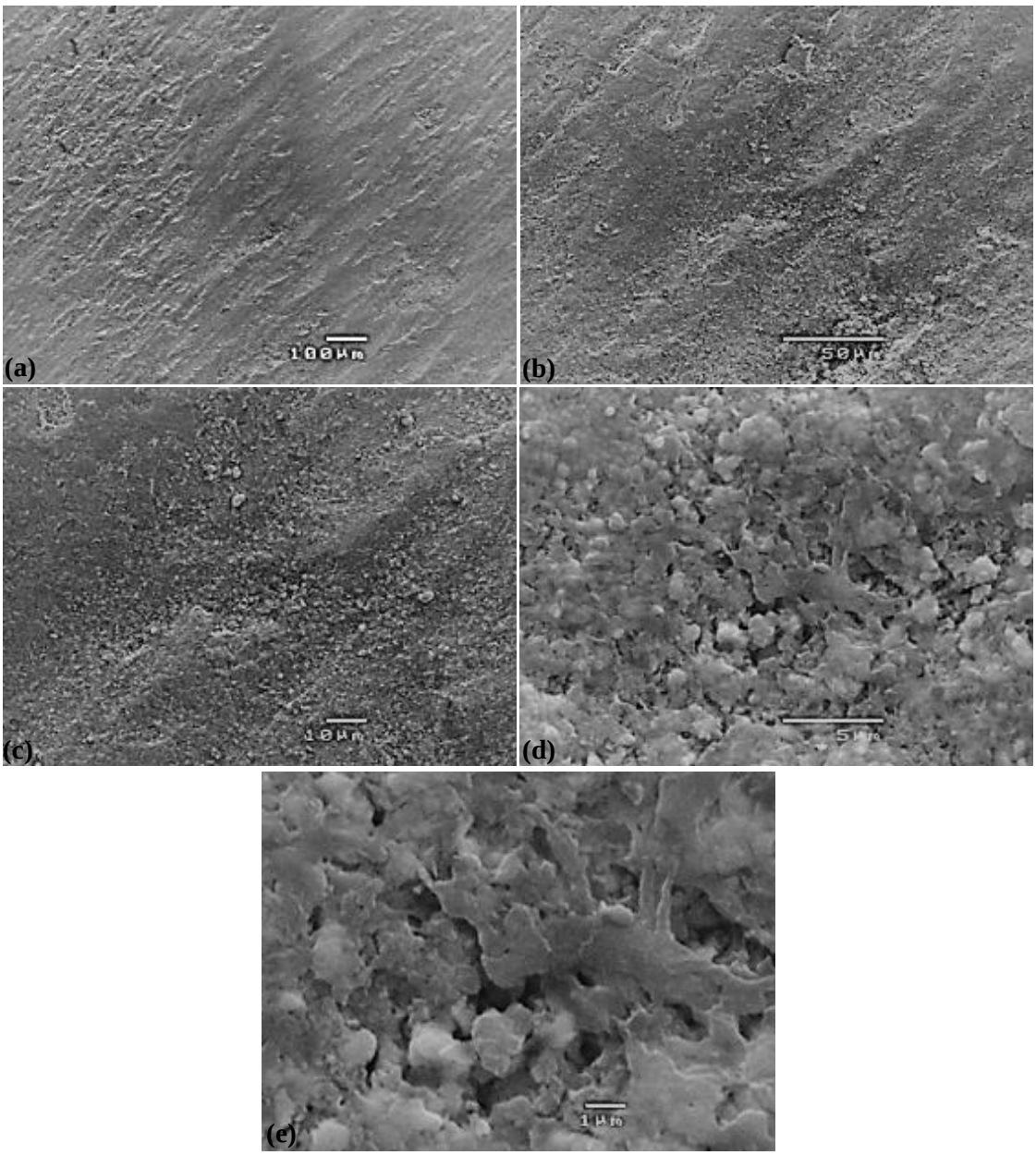


Fig. 7.41. SEM micrographs of the CAD/CAM-polished-sintered Y-TZP surface at 800 N and 100 indentations revealing (a) the overall indentation pattern, (b) the fracture of the milling grooves, (c) the enlarged view of (b), (d) plastic deformation and milling-induced intragranular fracture, and (e) the enlarged view of (d).

Fig. 7.42 shows SEM micrographs of the CAD/CAM-sintered-polished Y-TZP surface at 800 N and 100 indentations. Fig. 7.42(a) reveals the overall indentation pattern on the rough surface due to sintering-induced coarsened grains that were weakly removed by the polishing process. Fig. 7.42(b) and (c) demonstrates indentation-induced plastic deformation and surface defects from the milling process exacerbated by the sintering process. Fig. 7.42(d) shows indentation-induced smoothened surface and milling-induced fracture. Fig. 7.42(e) displays the fractured surface.

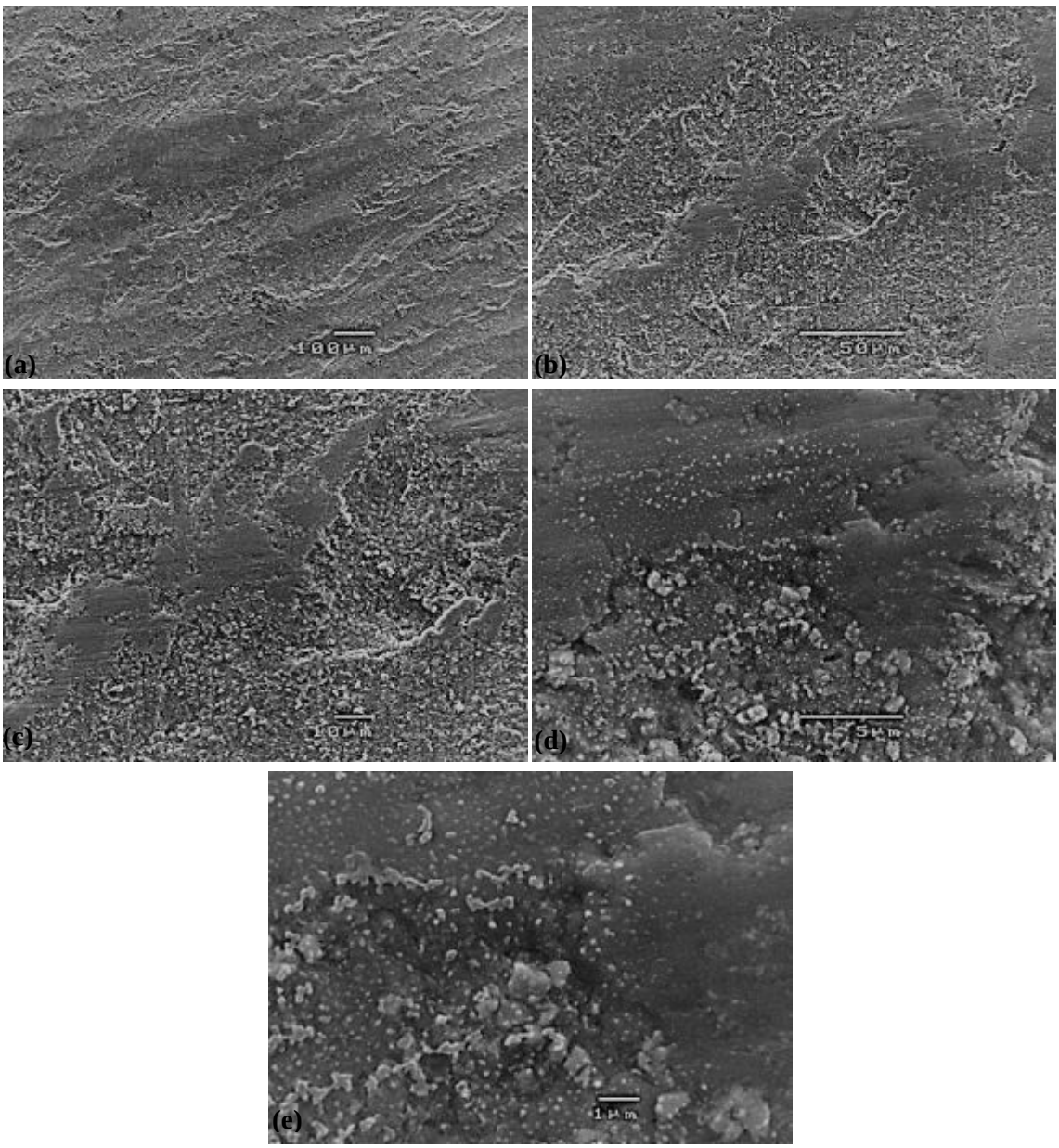


Fig. 7.42. SEM micrographs of the CAD/CAM-sintered-polished Y-TZP surface at 800 N and 100 indentations revealing (a) the overall indentation pattern, (b) indentation-induced plastic deformation and micro-cracks and surface defects from the milling process, (c) the enlarged view of (b), (d) indentation-induced smoothened surface and fracture from the milling process, and (e) the fractured surface.

Fig. 7.43 shows SEM micrographs of the CAD/CAM-sintered-110 µm alumina sandblasted Y-TZP surface at 800 N and 100 indentations. Fig. 7.43(a) reveals the overall indentation pattern on sandblasting-induced rough surface. Fig. 7.43(b) demonstrates indentation-induced plastic deformation and surface defects from the milling and sandblasting processes. Fig. 7.43(c) shows the smooth surface due to the indentation-induced plastic deformation and the sanblasted surface. Fig. 7.43(d) displays the indentation-induced smeared surface. Fig. 7.43(e) shows the detailed smearing of alumina and zirconia grains.

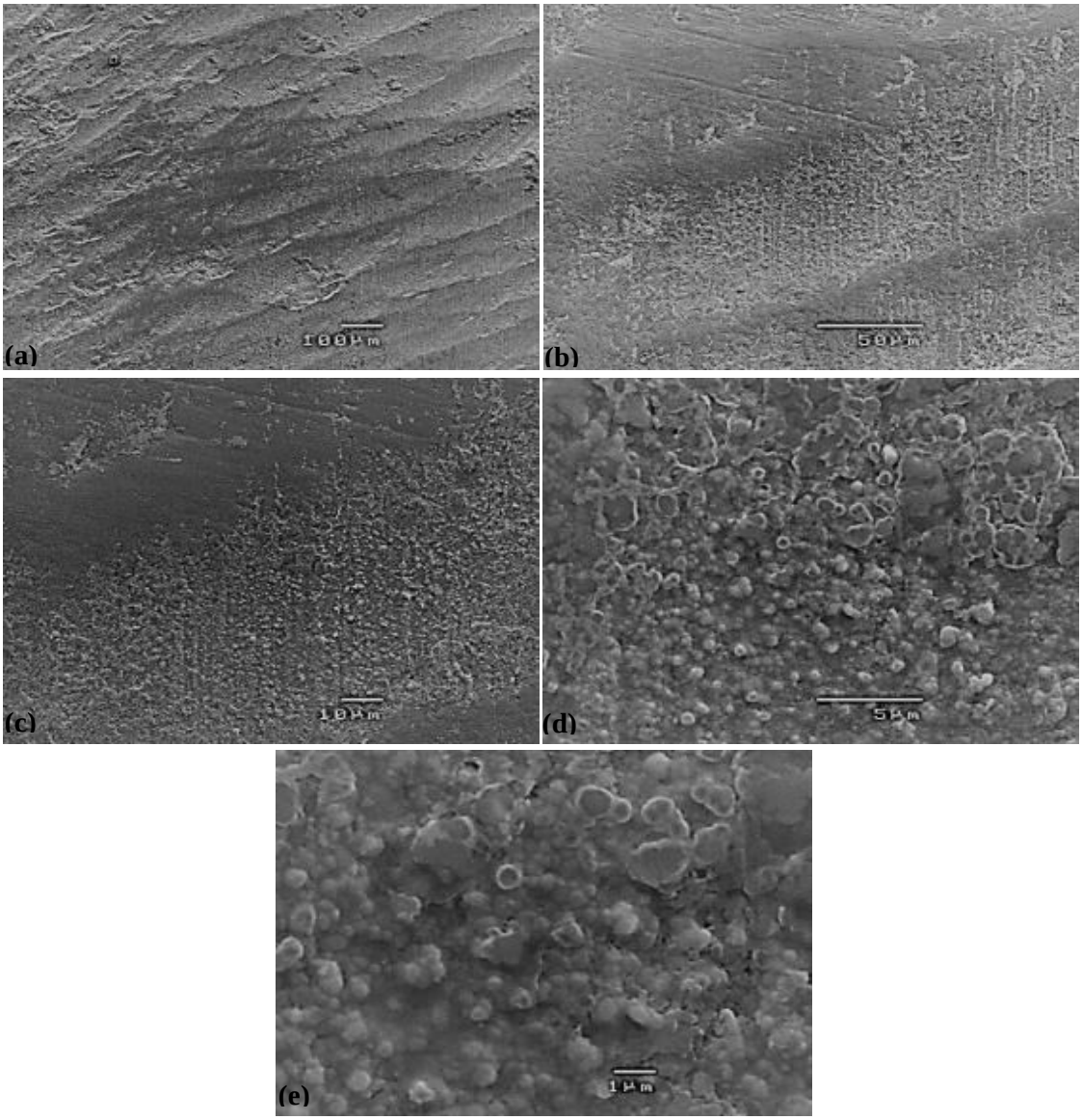


Fig. 7.43. SEM micrographs of the CAD/CAM-sintered-110 µm alumina sandblasted Y-TZP surface at 800 N and 100 indentations revealing (a) the overall indentation pattern, (b) indentation-induced plastic deformation and surface defects from the milling and sandblasting processes, (c) the smooth surface due to the indentation-induced plastic deformation and the sanblasted surface, (d) the indentation-induced smeared surface, and (e) the detailed smearing of alumina and zirconia grains.

Fig. 7.44 shows SEM micrographs of the CAD/CAM-sintered-250 µm alumina sandblasted Y-TZP surface at 800 N and 100 indentations. Fig. 7.44(a) reveals the overall indentation pattern on sandblasting-induced rough surface. Fig. 7.44(b) and (c) demonstrates little indentation-induced plastic deformation, randomly oriented scoring and scratches. Fig. 7.44(d) shows large-scale surface defects including deep sharp scratches, micro-craters, pitting and grain pull-out. Fig. 7.44(e) displays the deep sandblasted scoring and pitting.

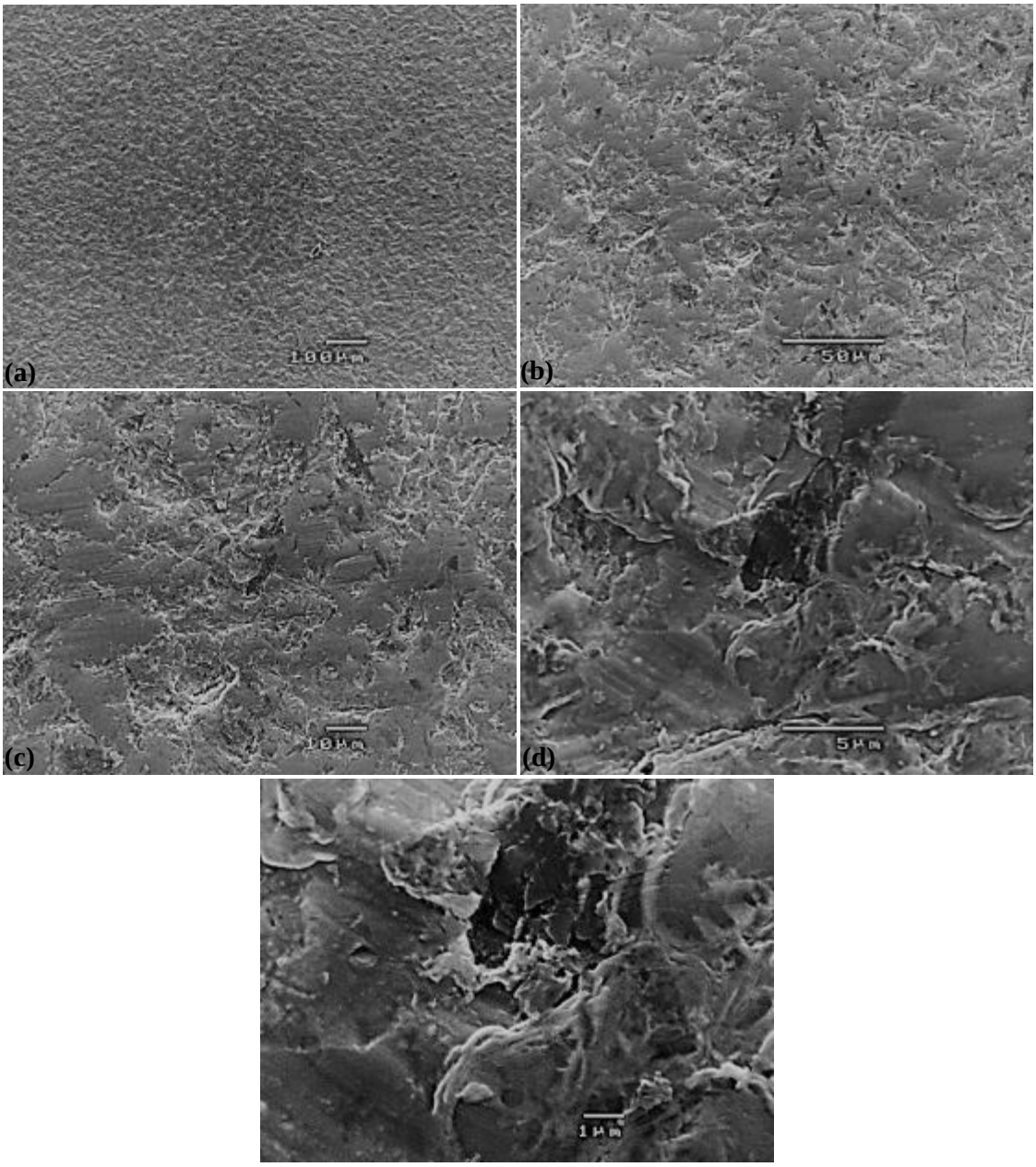


Fig. 7.44. SEM micrographs of the CAD/CAM-sintered-250 µm alumina sandblasted Y-TZP surface at 800 N and 100 indentations revealing (a) the overall indentation pattern, (b) little indentation-induced plastic deformation, randomly oriented scoring and scratches, (c) the enlarged view of (b), (d) large-scale surface defects including deep sharp scratches, micro-craters, pitting and grain pull-out, and (e) the deep sandblasted scoring and pitting.

Fig. 7.45 shows SEM micrographs of the CAD/CAM-sintered Y-TZP surface at 800 N and 1000 indentations. Fig. 7.45(a) reveals the overall indentation pattern on the miling- and sintering-induced rough surface. Fig. 7.45(b) demonstrates the indentation-induced plastic deformation around the milling-induced surface defect. Fig. 7.45(c) shows the plastically deformed surface covering the sintering-induced grain coarsening on the milled surface. Fig. 7.45(d) and (e) displays details of the plastically deformed and smeared layers.

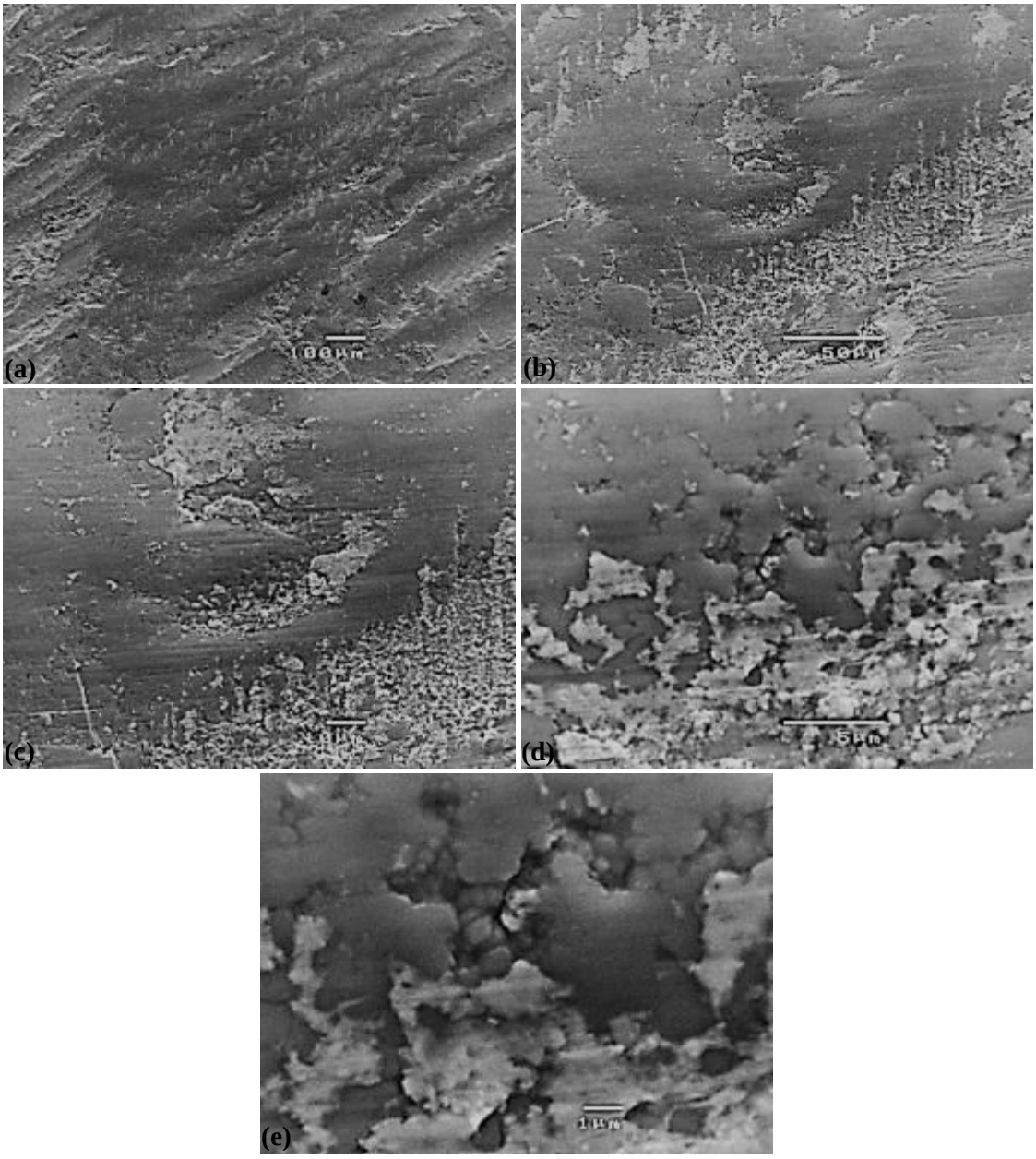


Fig. 7.45. SEM micrographs of the CAD/CAM-sintered Y-TZP surface at 800 N and 1000 indentations revealing (a) the overall indentation pattern, (b) the indentation-induced plastic deformation around the milling-induced surface defect, (c) the plastically deformed surface covering the sintering-induced grain coarsening on the milled surface, (d) details of the plastically deformed and smeared layers, and (e) enlarged view of (d).

Fig. 7.46 shows SEM micrographs of the CAD/CAM-polished-sintered Y-TZP surface at 800 N and 1000 indentations. Fig. 7.46(a) reveals the overall indentation pattern on the smooth surface in which the sintering-induced grain coarsening was partially removed. Fig. 7.46(b) and (c) demonstrates the indentation-plastic deformation and milling-induced surface defect. Fig. 7.46(d) displays the plastic deformation and milling-induced intragranular fracture. Fig. 7.46(e) shows the milling-induced intragranular fracture.

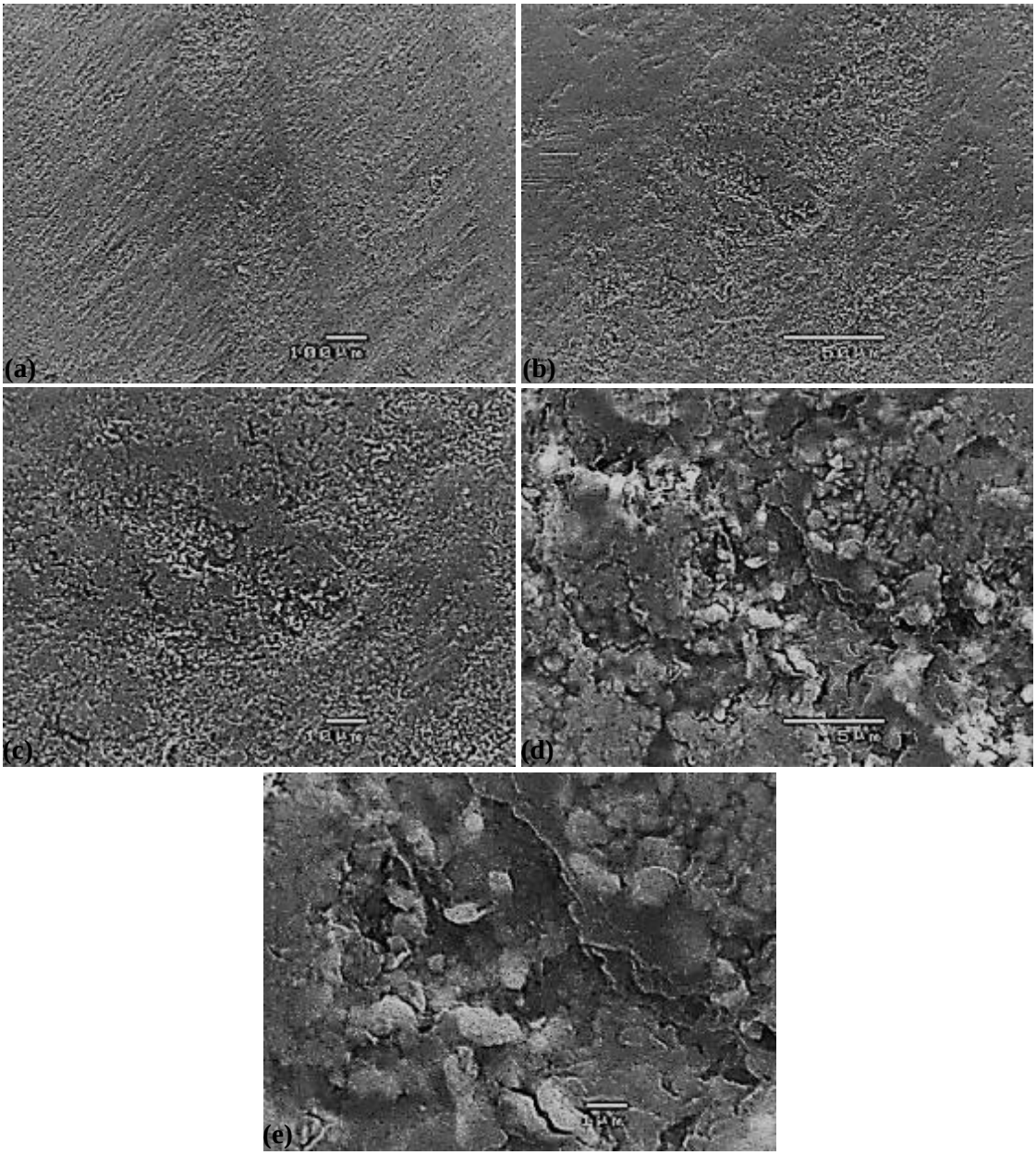


Fig. 7.46. SEM micrographs of the CAD/CAM-polished-sintered Y-TZP surface at 800 N and 1000 indentations revealing (a) the overall indentation pattern, (b) the plastic deformation and milling-induced surface defect, (c) the enlarged view of (b), (d) plastic deformation and milling-induced intragranular fracture, and (e) the milling-induced intragranular fracture.

Fig. 7.47 shows SEM micrographs of the CAD/CAM-sintered-polished Y-TZP surface at 800 N and 1000 indentations. Fig. 7.47(a) reveals the overall indentation pattern on the rough surface due to sintering-induced coarsened grains that were weakly removed by the polishing process. Fig. 7.47(b) and (c) demonstrates the plastically deformed surface covering the surface defects from the milling process. Fig. 7.47(d) shows indentation-induced smoothened surface and fractured surface from the milling process. Fig. 7.47(e) displays the plastically deformed and intergranular smeared layers.

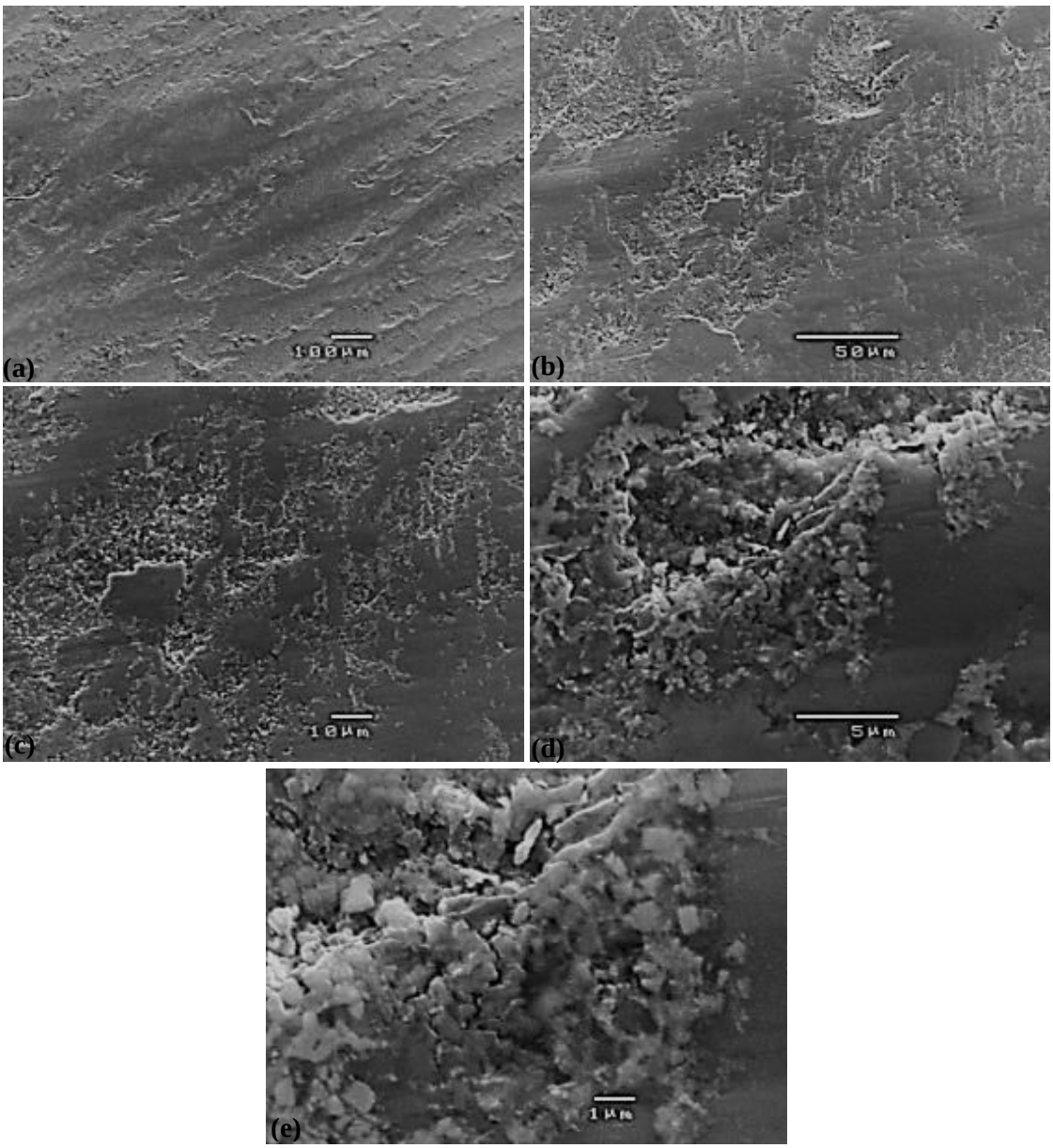


Fig. 7.47. SEM micrographs of the CAD/CAM-sintered-polished Y-TZP surface at 800 N and 1000 indentations revealing (a) the overall indentation pattern, (b) the plastically deformed surface covering the surface defects from the milling process, (c) the enlarged view of (b), (d) indentation-induced smoothened surface and fractured surface from the milling process, and (e) the plastically deformed and intragranular smeared layers and micro-cracks.

Fig. 7.48 shows SEM micrographs of the CAD/CAM-sintered-110 µm alumina sandblasted Y-TZP surface at 800 N and 1000 indentations. Fig. 7.48(a) reveals the overall indentation pattern on sandblasting-induced rough surface. Fig. 7.48(b) and (c) demonstrates indentation-induced plastic deformation and surface defects from the milling and sandblasting processes. Fig. 7.48(d) shows the indentation-induced smeared surface. Fig. 7.48(e) displays the detailed smearing of alumina and zirconia grains with intergranular fracture.

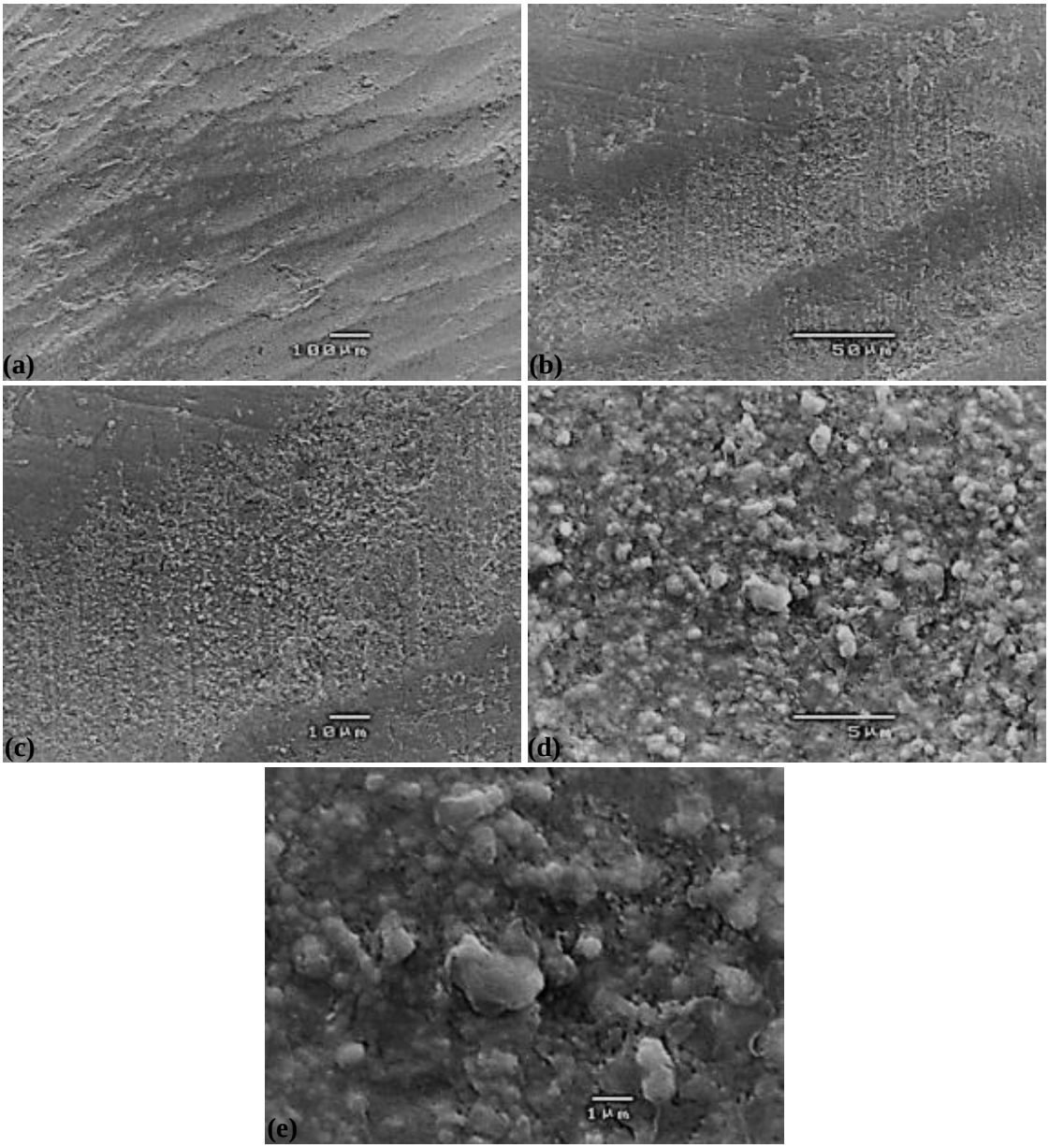


Fig. 7.48. SEM micrographs of the CAD/CAM-sintered-110 µm alumina sandblasted Y-TZP surface at 800 N and 1000 indentations revealing (a) the overall indentation pattern, (b) indentation-induced plastic deformation and surface defects from the milling and sandblasting processes, (c) the enlarged view of (b), (d) the indentation-induced smeared surface, and (e) the detailed smearing of alumina and zirconia grains with intergranular fracture.

Fig. 7.49 shows SEM micrographs of the CAD/CAM-sintered-250 µm alumina sandblasted Y-TZP surface at 800 N and 1000 indentations. Fig. 7.49(a) reveals the overall indentation pattern on sandblasting-induced rough surface. Fig. 7.49(b) and (c) demonstrates the indentation-induced plastically deformed layer spreading over the randomly oriented scoring and scratches. Fig. 7.49(d) shows plastically deformed layer and large-scale sandblasted scoring, micro-craters, pitting and grain pull-out. Fig. 7.49(e) displays the deep sandblasted scoring and pitting.

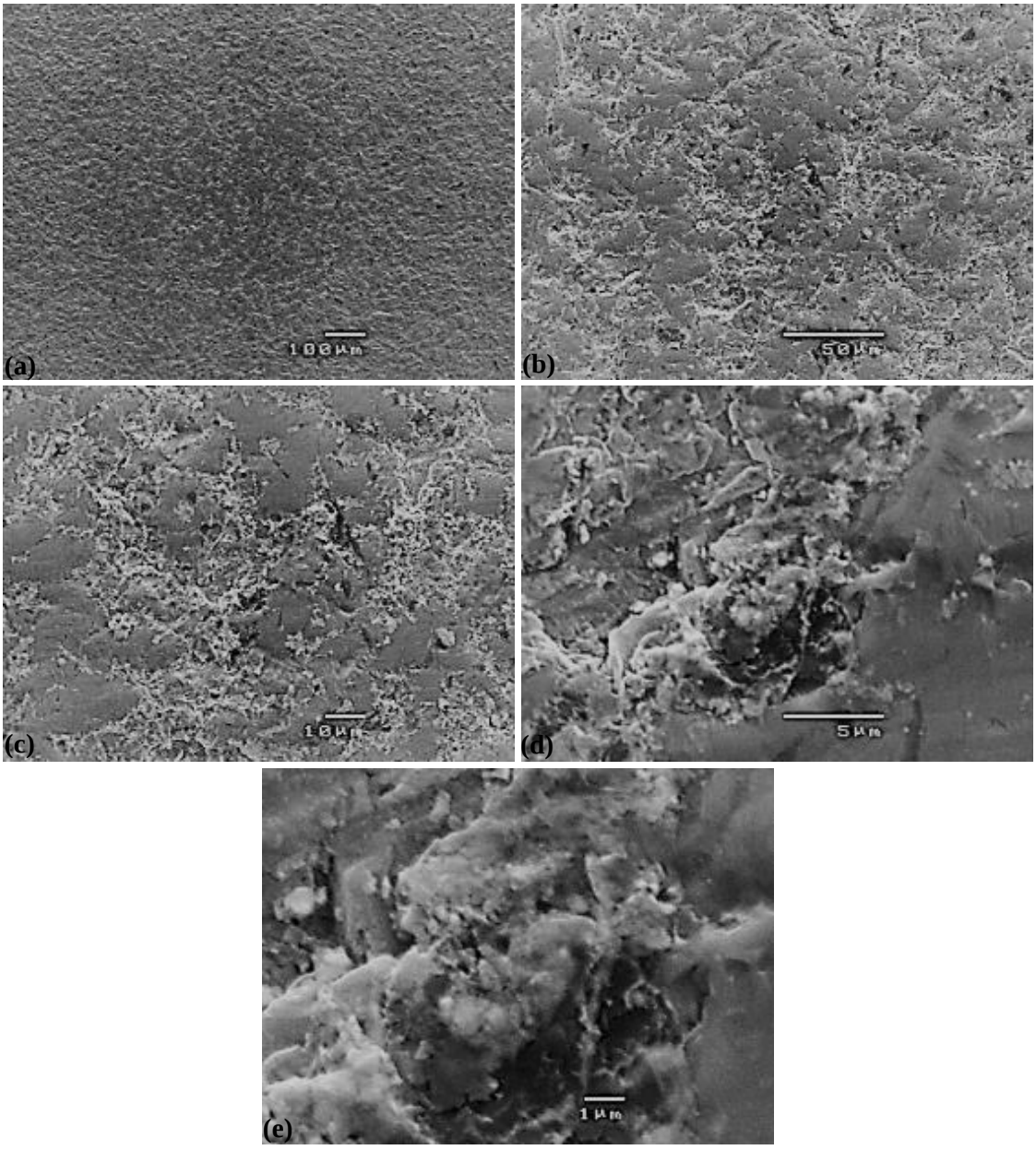


Fig. 7.49. SEM micrographs of the CAD/CAM-sintered-250 µm alumina sandblasted Y-TZP surface at 800 N and 1000 indentations revealing (a) the overall indentation pattern, (b) the indentation-induced plastic deformation, randomly oriented scoring and scratches, (c) the enlarged view of (b), (d) plastically deformed layer and large-scale sandblasted scuring, micro-craters, pitting and grain pull-out, and (e) the deep sandblasted scoring and pitting.

Fig. 7.50 shows SEM micrographs of the CAD/CAM-sintered Y-TZP surface at 800 N and 3000 indentations. Fig. 7.50(a) reveals the overall Hertzian indentation pattern on the miling- and sintering-induced rough surface. Fig. 7.50(b) demonstrates the indentation-induced plastic deformation around the milling-induced surface defects. Fig. 7.50(c) shows the plastically deformed surface covering the sintering-induced grain coarsening on the milled surface. Fig. 7.50(d) and (e) displays details of the plastically deformed layer and intragranular fractured particles.

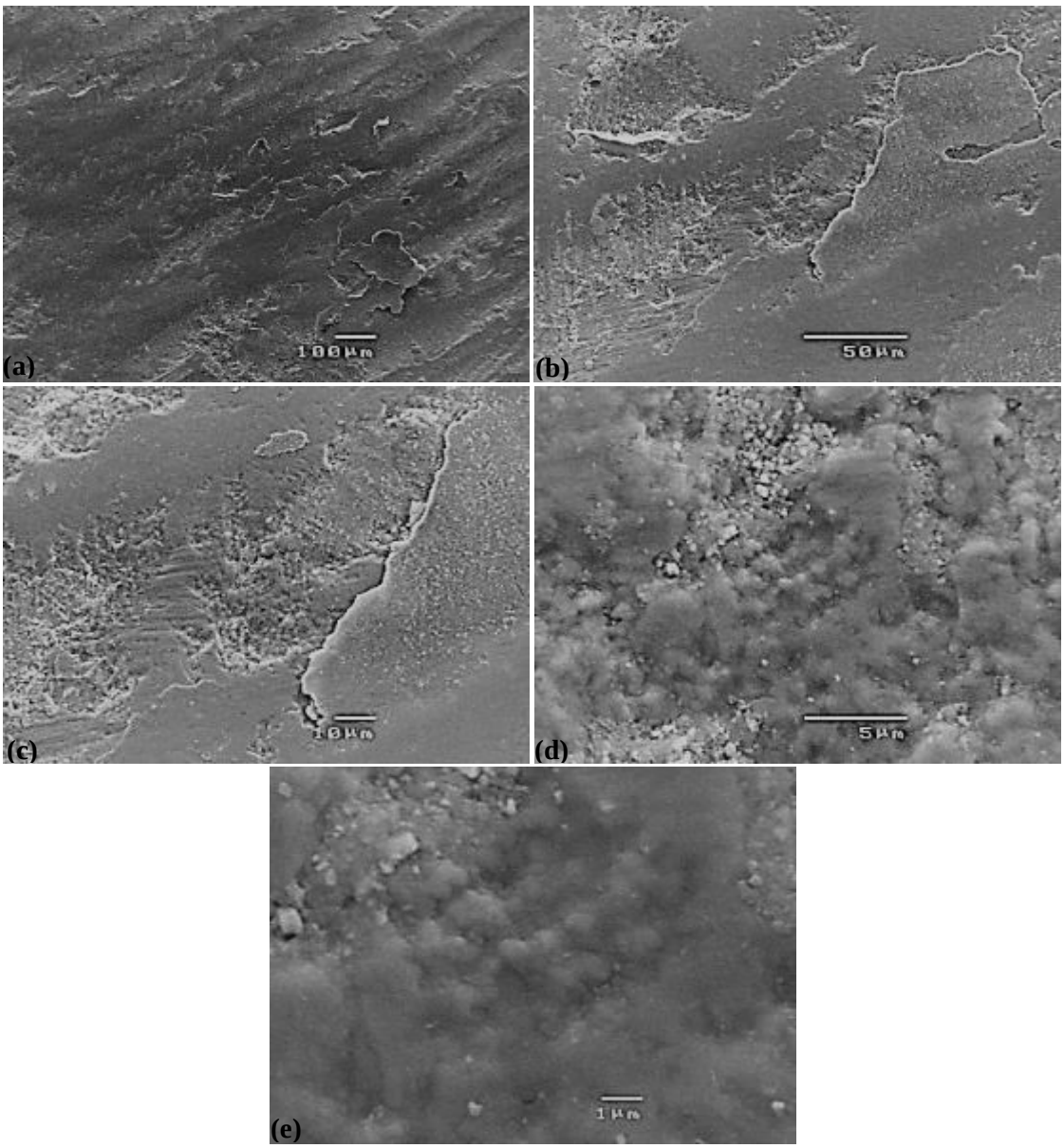


Fig. 7.50. SEM micrographs of the CAD/CAM-sintered Y-TZP surface at 800 N and 3000 indentations revealing (a) the overall indentation pattern, (b) the indentation-induced plastic deformation around the milling-induced surface defect, (c) the plastically deformed surface covering the sintering-induced grain coarsening on the milled surface, (d) details of the plastically deformed layer and intragranular fractured particles, and (e) enlarged view of (d).

Fig. 7.51 shows SEM micrographs of the CAD/CAM-polished-sintered Y-TZP surface at 800 N and 3000 indentations. Fig. 7.51(a) reveals the overall indentation pattern on the smooth surface in which the sintering-induced grain coarsening was partially removed. Fig. 7.51(b) demonstrates the plastic deformation and peripheral damage traces uplifting the contact edge. Fig. 7.51(c) shows micro-cracking within the peripheral damage traces. Fig. 7.51(d) and (e) displays indentation-induced intergranular fracture by grain pull-out.

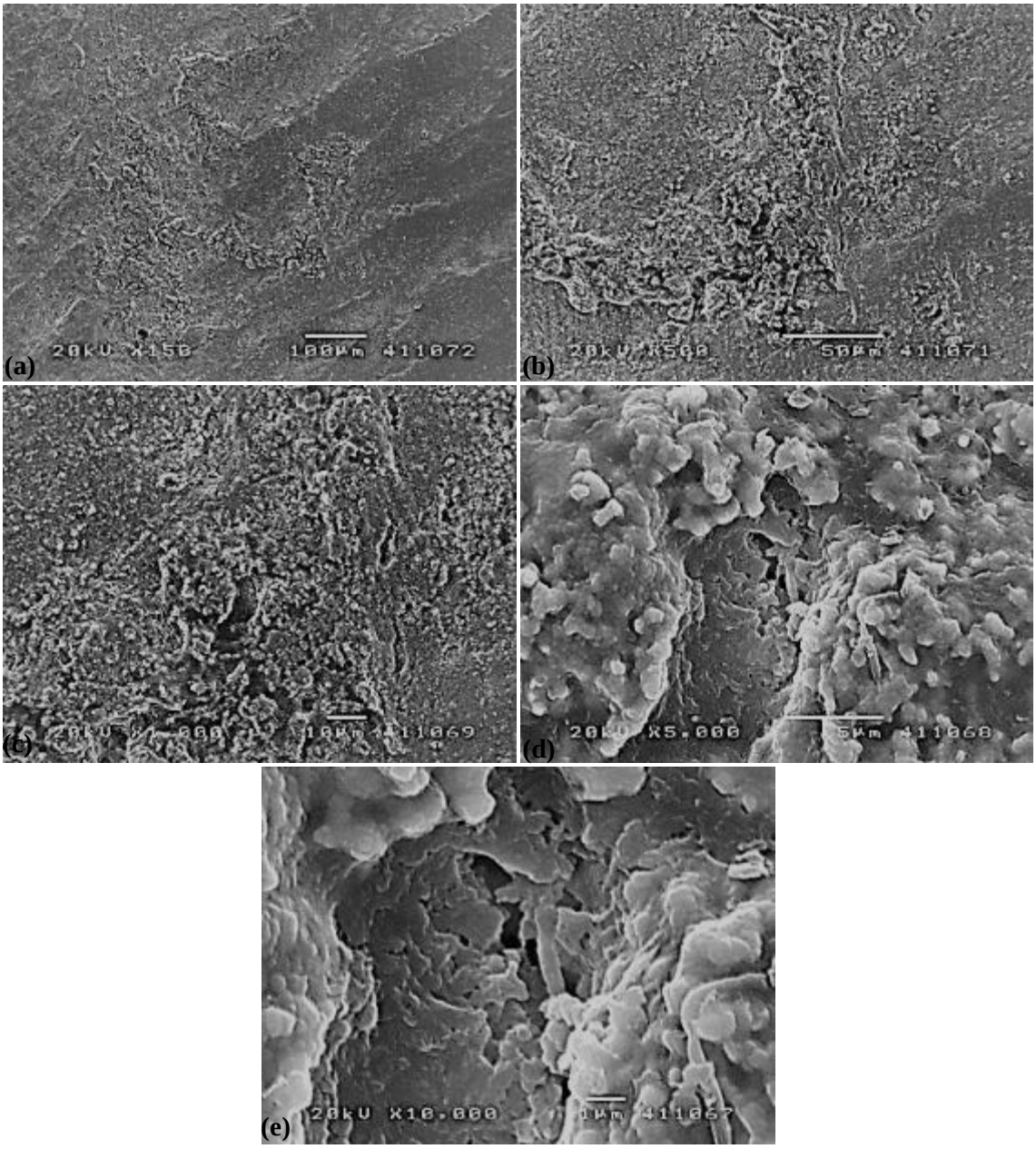


Fig. 7.51. SEM micrographs of the CAD/CAM-polished-sintered Y-TZP surface at 800 N and 3000 indentations revealing (a) the overall indentation pattern, (b) the plastic deformation and surface rumpling micro-cracking characteristic of phase transformation (Lee et al., 2000), (c) micro-cracking within the surface rumpling, (d) indentation-induced intragranular fracture by grain pull-out, and (e) the enlarged view of (d).

Fig. 7.52 shows SEM micrographs of the CAD/CAM-sintered-polished Y-TZP surface at 800 N and 3000 indentations. Fig. 7.52(a) reveals the overall indentation pattern on the rough surface due to sintering-induced coarsened grains that were weakly removed by the polishing process. Fig. 7.52(b) and (c) demonstrates the plastically deformed surface covering the surface defects from the milling process. Fig. 7.52(d) and (e) shows indentation-induced smoothened surface and smeared surfaces from the milling process.

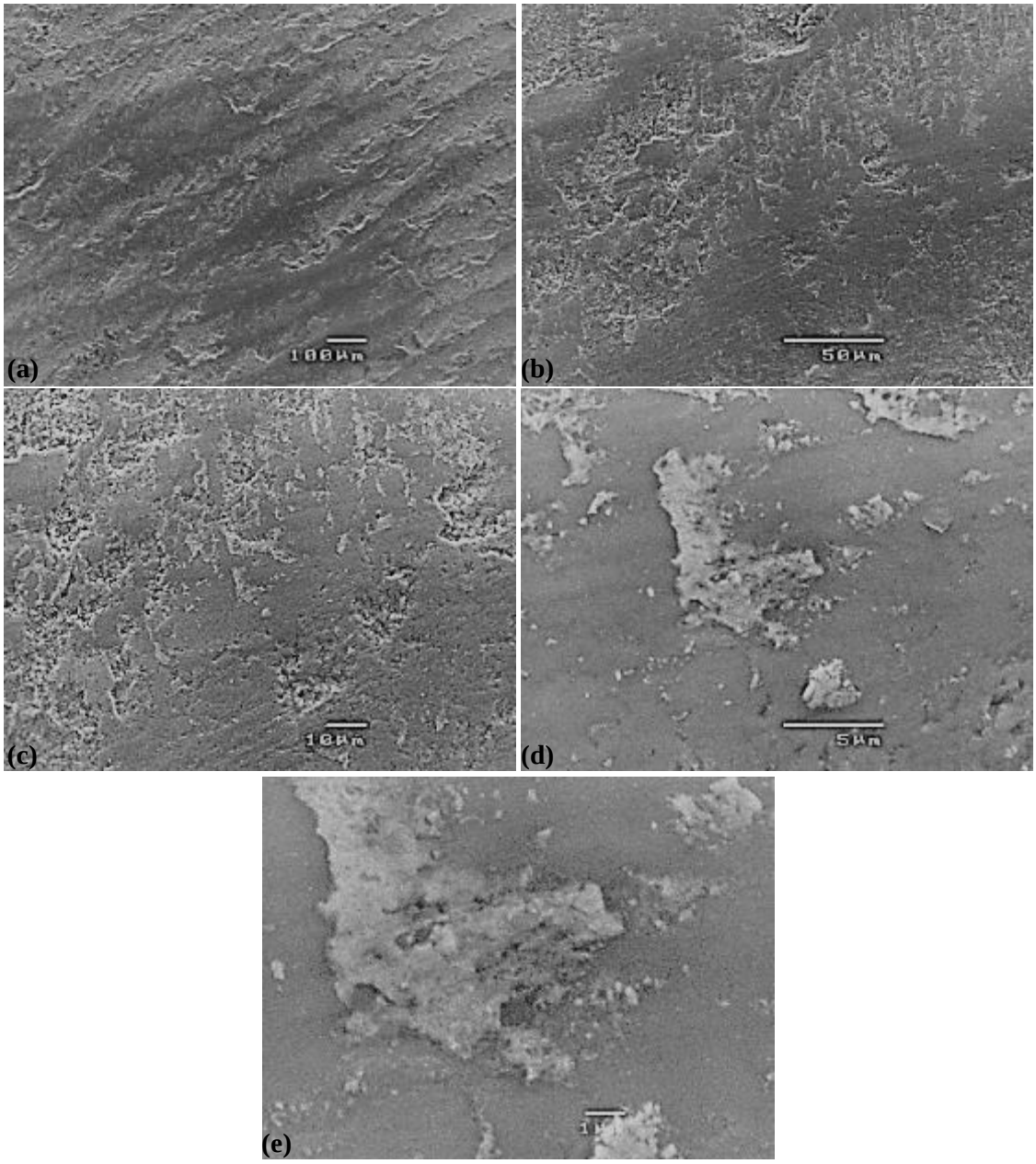


Fig. 7.52. SEM micrographs of the CAD/CAM-sintered-polished Y-TZP surface at 800 N and 3000 indentations revealing (a) the overall indentation pattern, (b) the plastically deformed surface covering the surface defects from the milling process, (c) the enlarged view of (b), (d) indentation-induced smoothened surface and smeared surfaces from the milling process, and (e) the enlarged view of (d).

Fig. 7.53 shows SEM micrographs of the CAD/CAM-sintered-110 µm alumina sandblasted Y-TZP surface at 800 N and 3000 indentations. Fig. 7.53(a) reveals the overall indentation pattern on sandblasting-induced rough surface. Fig. 7.53(b) and (c) demonstrates massive indentation-induced plastic deformation and surface defects from the milling and sandblasting processes. Fig. 7.53(d) and (e) shows the plastically deformed surface, pitting and intragranular fracture of alumina and zirconia grains leading to the surface wedging.

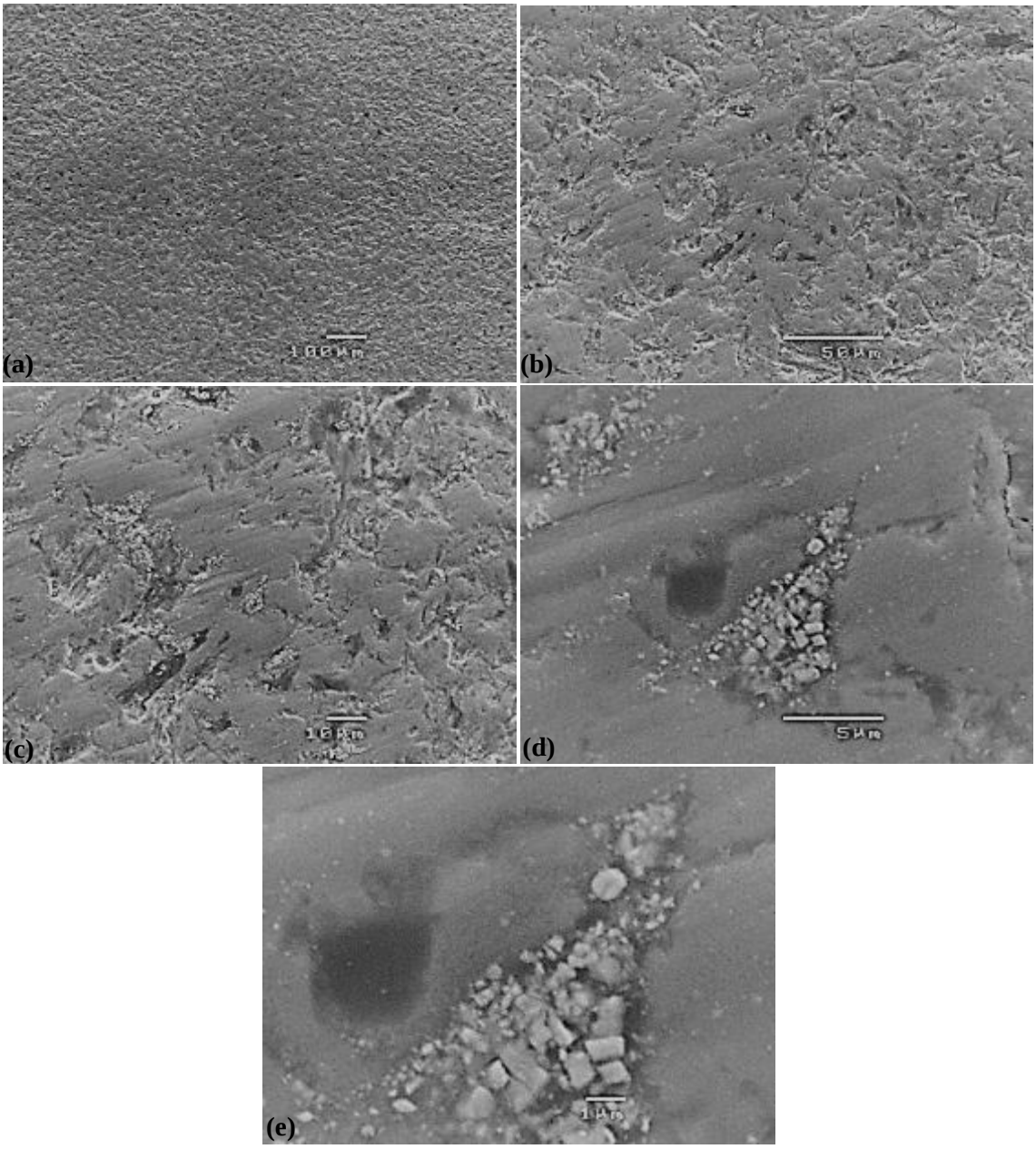


Fig. 7.53. SEM micrographs of the CAD/CAM-sintered-110 µm alumina sandblasted Y-TZP surface at 800 N and 3000 indentations revealing (a) the overall indentation pattern, (b) massive indentation-induced plastic deformation and surface defects from the milling and sandblasting processes, (c) the enlarged view of (b), (d) the plastically deformed surface, pitting and intragranular fracture of alumina and zirconia grains (e) the enlarged view of (d).

Fig. 7.54 shows SEM micrographs of the CAD/CAM-sintered-250 µm alumina sandblasted Y-TZP surface at 800 N and 3000 indentations. Fig. 7.54(a) reveals the overall indentation pattern on sandblasting-induced rough surface. Fig. 7.54(b) and (c) demonstrates massive indentation-induced plastic deformation, randomly oriented scoring and scratches. Fig. 7.54(d) shows plastically deformed layer and large-scale sandblasted scoring, micro-craters, pitting and grain pull-out. Fig. 7.54(e) displays the deep sandblasted scoring and pitting.

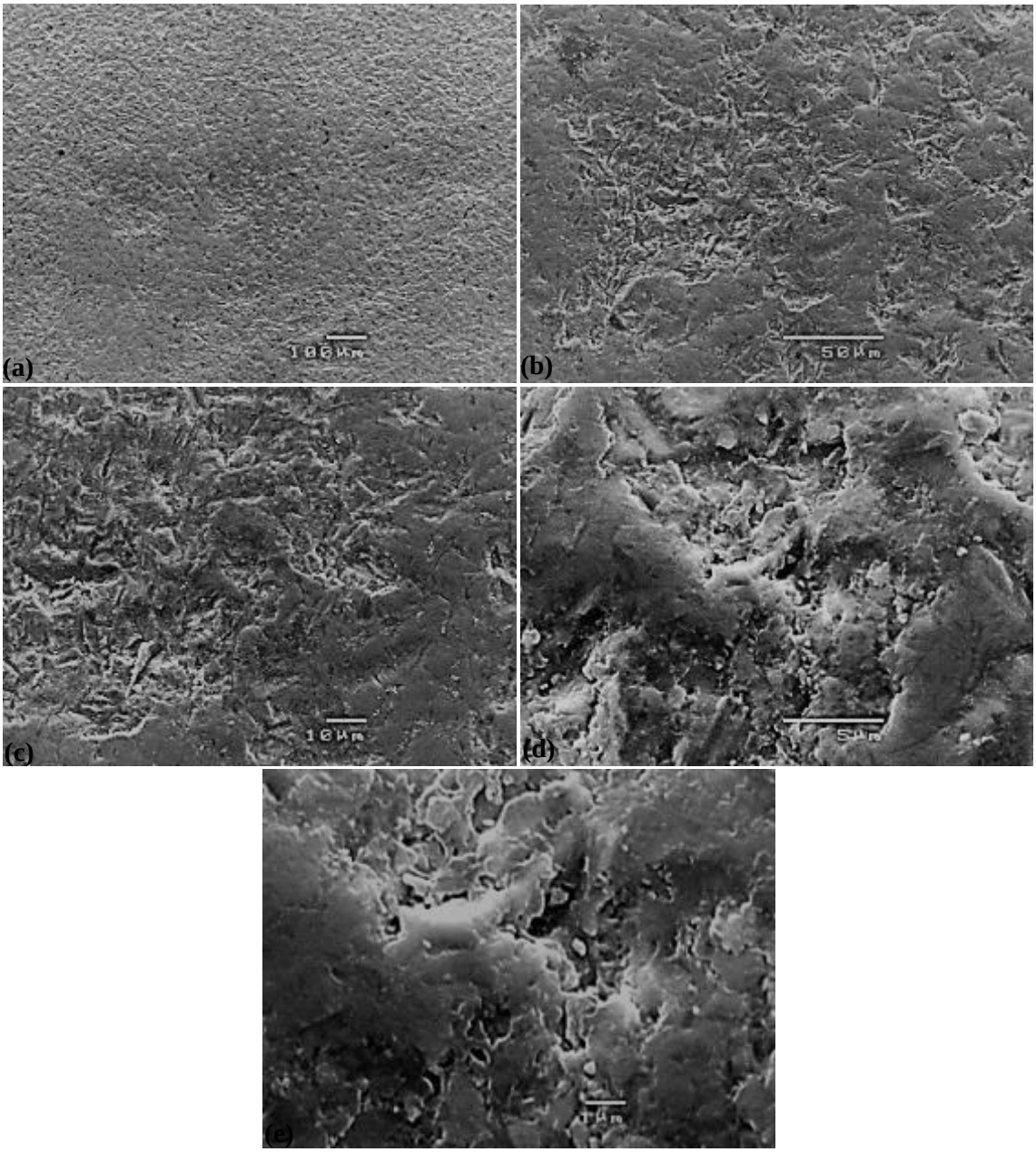


Fig. 7.54. SEM micrographs of the CAD/CAM-sintered-250 µm alumina sandblasted Y-TZP surface at 800 N and 3000 indentations revealing (a) the overall indentation pattern, (b) the indentation-induced plastic deformation, randomly oriented scoring and scratches, (c) the enlarged view of (b), (d) plastically deformed layer and large-scale sandblasted scoring, micro-craters, pitting and grain pull-out, and (e) the deep sandblasted scoring and pitting.

## 7.5 Discussion

This thesis presents results of low-cycle-high-load cyclic fatigue behavior of two high-strength monolithic dental ceramics, LDGC and Y-TZP, using Hertzian spherical indentations. The low-cycle-high-load fatigue tests enable the prediction of the fatigue property within the short-crack domain in which the strength of dental ceramics is most vulnerable (Guiberteau et al., 1993; Yin et al., 2013). Also, this is the first attempt at understanding the behavior of these important materials from the perspective of the influence of different clinically simulated surfaces on the fatigue damage of these two dental materials. The morphologies of the indentation-induced damage of treated LDGC and Y-TZP surfaces were examined using optical microscope to understand the nature of Hertzian cracks and SEM to understand the interrelationships among microstructures, surface asperities and crack propagation.

### *7.5.1 Maximum Contact Stresses*

The maximum contact stresses of treated LDGC (Fig. 7.3) and Y-TZP (Fig. 7.4) surfaces were extracted based on the assumption of the elastic contact of the indenter. To determine whether this indenter's elastic condition in maximum contact stress measurements for these two materials was met, the following condition should be valid (Guiberteau et al., 1993):

$$\sigma_m \leq 0.4H_v \tag{7.7}$$

where $H_v$ is the Vickers hardness of the tungsten carbide indenter which is 20 GPa (Guiberteau et al., 1993). Consequently, the measured maximum contact stresses should be less than 8 GPa to avoid permanent deformation of the indenter. As revealed in Fig. 7.3 and Table 7.1, the maximum contact stresses of indented LDGC surfaces at all cycles were less than 8 GPa indicating the validity of the indenter's elastic deformation. Similarly, Eq. (7.7) was also valid for the maximum contact stress measurements of indented Y-TZP since no maximum contact stresses exceeded 8 GPa in Fig. 7.4 and Table 7.3.

The results presented in Fig. 7.3 and Table 7.1 showed that regardless of the applied surface treatments, the maximum contact stresses of treated LDGC surfaces were reduced by at least 50% at 3000 cycles. However the CAD/CAM-polished-sintered process which was the proposed fabrication method for LDGC restorations based on its lowest surface roughness in Chapter 5 sustained the highest maximum contact stress at higher cycles of 100–3000 indicating its better fatigue property than other processes at high cycles.

Similarly, Fig. 7.4 and Table 7.3 showed that the maximum contact stresses of surface-treated Y-TZP were decreased by at least 69% at 3000 cycles irrespective of the applied surface treatments. However the CAD/CAM-polished-sintered process which was the recommended

fabrication method for Y-TZP restorations based on its lowest surface roughness in Chapter 6 also sustained the highest maximum contact stress at higher cycles of 10–3000 indicating its better fatigue property than other processes.

### *7.5.2 Indented Morphologies of Treated LDGC Surfaces*

Hertzian ring cracks produced on all treated LDGC surfaces at 1 indentation in Figs. 7.5(a), 7.6(a), 7.7(a), 7.8(a) and 7.9(a) can be an indication of incipient cone cracking or quasi-plasticity. To determine the responsible mechanism for the ring crack formation, the critical loads for cone cracks and quasi-plastic deformation are required since the simultaneous occurrence of both modes is impossible (Peterson et al., 1998). Thus, the critical load, $P_C$, for cone cracks can be predicted by the Eq. (7.1). By using the properties listed in Section 7.3.1, the $P_C$ for cone crack of sintered LDGC was 1146 N which was higher than the maximum applied load (800 N) indicating that cone cracks were not formed outside the ring cracks.

Also, the occurrence of quasi-plastic deformation can be predicted at a critical yielding load ($P_Y$) by the Eq. (7.3). By applying the properties in Section 7.3.1, the $P_Y$ for quasi-plastic deformation was 115 N which was less than the experimental applied maximum load (800 N) indicating the formation of quasi-plastic deformation below the Hertzian stress fields. Therefore, the fatigue mechanism of all treated LDGC surfaces at 1 indentation was mechanical in origin caused by attrition of frictional tractions at micro-cracks interfaces similar to was observed in mica glass-ceramic (Cai et al., 1994; Peterson et al., 1998). This is consistent with the results of Coldea et al. (2014) where quasi-plasticity was formed before cone cracks in a single-cycle indentation of LDGC. Thus, the downward propagation of ring cracks into cone cracks could be suppressed by deflection along the weak frictional tractions away from the tensile stress trajectories and into the compressive stress state (Padture and Lawn, 1995; Pajares et al., 1995).

The critical load for cone cracks, $P_C$, in Eq. (7.1), can be greatly reduced during cyclic fatigue loading by the time-cumulative slow crack growth mechanisms (Lawn et al., 2007; Zhang et al., 2005; 2009). Similarly, the quasi-plastic deformation critical load, $P_Y$, in Eq. (7.3) can immensely reduce in cyclic loadings due to the action of mechanical driving forces which arise from residual stresses within a precursor quasi-plasticity zone forming median-radial cracks (Zhang et al., 2005). Thus, the induced radial cracks accelerate material removal by the rapid coalescence of adjacent faults forming median cracks which eventually lead to the strength loss (Deng et al., 2002a; Jung et al., 2000; Lawn et al., 2001; 2002b; 2004; 2007). This might explain why the maximum contact stresses of all the treated LDGC surfaces (Fig. 7.3) reduced with the number of cycles.

At higher cycles of 10–3000, surface damage occurred predominantly in an annular region delineated by the inner and outer contact circles at the minimum and maximum contact loads as shown in Figs. 7.10–7.29. These segmented concentric ring cracks have been attributed to the formation of partial cone cracks developed by cyclic loads, skewing the frictionally assisted tensile stress field at the trailing edge contact (Guiberteau et al., 1993; Kim et al., 1999; 2007a; Rekow et al., 2011; Yin et al., 2013; Zhang et al., 2013b). This indicates that cone cracks were in fact formed at higher cycles. In addition, radial cracks were induced at 100 indentations on the roughest CAD/CAM-sintered-glazed process (Fig. 7.18(c)). Radial cracks may not occur in monolayer configurations of sufficiently large net thickness greater than 1.5 mm (Deng et al., 2002a; Lawn et al., 2002b; 2004; Zhang et al., 2004a). The induction of radial cracks in Fig. 7.18(c) with sample thickness of several orders greater than 1.5 mm (Fig. 7.1) can be ascribed to their sensitivity to starting surface flaws and number of cycles (Jung et al., 2000). In addition, it is worth noting that the same roughest surfaces were induced with transverse cracks at 1000 indentations in Fig. 7.23(c) and (d) which hitherto have not been reported.

Surface asperities played a critical role in the fatigue damage of treated LDGC surfaces with smooth surfaces producing less damage than rough surfaces. The fatigue damage at 1 indentation on CAD/CAM-sintered, CAD/CAM-sintered-polished and CAD/CAM-sintered-glazed surfaces (Figs. 7.5, 7.7 and 7.8) with higher roughness values showed ring cracks, fretting, pulverization and micro-bridges. The damage on indented smooth CAD/CAM-polished-sintered and CAD/CAM-polished-sintered-glazed surfaces (Figs. 7.6 and 7.9) showed surface ring cracks of lower crack widths with the CAD/CAM-polished-sintered surfaces producing the lowest crack width. At 10 indentations, more fatigue damage was noticed on indented rough CAD/CAM-sintered, CAD/CAM-sintered-polished and CAD/CAM-sintered-glazed surfaces (Figs. 7.10, 7.12 and 7.13) with the formation micro-pulverization, fretting debris and large scale wedging. In contrast, the fatigue damage on indented smooth CAD/CAM-polished-sintered and CAD/CAM-polished-sintered-glazed surfaces (Figs. 7.11 and 7.14) was restricted to concentric ring cracks and pulverization, surface smearing and peeling. The lowest crack width was still produced on the indented smoothest CAD/CAM-polished-sintered surfaces. Further, at 100 indentations, edge chipping, large-scale fractures, micro-craters, fragmentations and wedging were formed on indented rough CAD/CAM-sintered, CAD/CAM-sintered-polished and CAD/CAM-sintered-glazed surfaces (Figs. 7.15, 7.17 and 7.18). However, the damage formed on indented smooth CAD/CAM-polished-sintered and CAD/CAM-polished-sintered-glazed surfaces revealed wedging and pulverization (Figs. 7.16 and 7.19).

At 1000 indentations, the fatigue damage metamorphosed into full blown edge chippings in all treated LDGC surfaces, with the higher surface roughness corresponding to the more severe induced damage. The indented rough CAD/CAM-sintered and CAD/CAM-sintered-glazed surfaces were greatly fatigued with the formation of large-scale fractured surfaces and transverse cracks which penetrated unto the subsurface (Figs. 7.20 and 7.23). The indented smooth CAD/CAM-polished-sintered surface revealed localized fracture (Fig. 7.21) and wedging in CAD/CAM-sintered-polished and CAD/CAM-polished-sintered-glazed surfaces (Figs. 7.22 and 7.24). Further, at 3000 indentations, the indented rough CAD/CAM-sintered, CAD/CAM-sintered-polished and CAD/CAM-sintered-glazed surfaces were severely damaged with the formation of large-scale edge chippings, fractured surfaces and micro-craters (Figs. 7.25, 7.27 and 7.28). The edge chippings in the indented smooth CAD/CAM-polished-sintered and CAD/CAM-polished-sintered-glazed surfaces were less severe (Figs. 7.26 and 7.29). However, a transverse cracking propagated through the fractured surface of the indented CAD/CAM-polished-sintered-glazed process (Fig. 7.29(e)) but no such cracking existed in the fractured subsurface of the CAD/CAM-polished-sintered process (Fig. 7.26(e)) indicative of a better fatigue resistance in the latter surface than in the former surface.

The underlying fatigue mechanism proposed in this thesis for the low-cycle-high-load spherical cyclic indentations of treated LDGC surfaces is mechanically assisted growth of surface asperities. First, cyclic fatigue enhances cone cracking by slow extension of cone cracks leading to edge chipping (Peterson et al., 1998; Zhang et al., 2013a; 2013b). Edge chippings were observed at 3000 cycles on all treated surfaces in Figs. 7.25–7.29. Next, quasi-plastic deformation was also enhanced in cyclic loadings by the rapid coalescence of micro-cracks into dangerous median-radial cracks as evident in Fig. 7.18(c) resulting in mechanical fatigue and accelerated wear in Figs. 7.20–7.29. Therefore, the proposed fatigue mechanism is schematically illustrated in Fig. 7.55. A single cycle indentation of treated LDGC surfaces leaves a deformed residual surface area in the form of ring crack with a contact diameter, $2a_1$. Subsequent indentations enlarge the deformed surface area with larger contact diameters, $2a_2$, with the formation of more concentric ring cracks leading to stress concentrations along the edges. Further indentations across these stress concentrating sites produce weak cleavage planes which in turn lead to the mechanical damage which depends on the surface roughness, the rougher the surface, the heavier the mechanical damage.

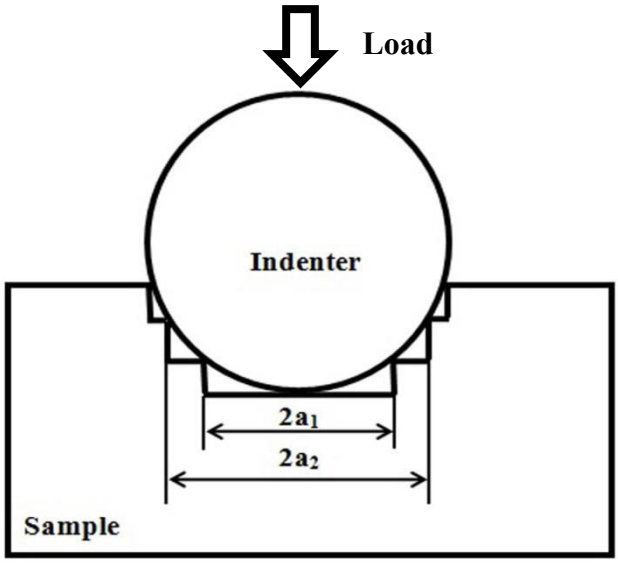


Fig. 7.55. The proposed fatigue mechanism for surface-treated sintered LDGC.

Within the limitation of this study, the smoothest CAD/CAD-polished-sintered surface were least damaged in low-cycle-high-load spherical cyclic fatigue tests in comparison to other treated surfaces and it is therefore the favored process reinforcing our position in Chapter 5.

### *7.5.3 Indented Morphologies of Treated Y-TZP Surfaces*

Similar analyses to determine the prevailing mechanism of the indentation patterns of all treated Y-TZP surfaces at 1 indentation in Figs. 7.30(a), 7.31(a), 7.32(a), 7.33(a) and 7.34(a) were performed. By applying Eq. (7.1) for $P_C$ and Eq. (7.3) for $P_Y$, and the properties in Section 7.3.1, it shows that the $P_C$ was 3097 N which was several orders greater than the maximum experimental load (800 N) but the $P_Y$ was 265 N which was less than 800 N. This indicates that quasi-plastic deformation was formed on all treated Y-TZP surfaces consistent with the mechanism reported in the literature for the material (Coldea et al., 2014; Padture and Lawn, 1995; Pajeres et al., 1995; Peterson et al., 1998; Zhang et al., 2004b). Thus, the fatigue mechanism of all treated Y-TZP surfaces at 1 indentation was also mechanical in nature indicative of compression-shear driving force within the microstructure (Fischer-cripps and Lawn, 1996; Jung et al., 2000; Lawn et al., 2004, Peterson et al., 1998).

Relative to the indented LDGC surfaces, the damage in indented Y-TZP surfaces was slight indicating higher resistance to fatigue damage in the latter than the former. This can also be ascribed to higher fracture strength and toughness of Y- TZP than LDGC. Therefore, at higher number of cycles of 10–3000, no concentric ring cracks was observed in Figs. 7.35–7.54 suggesting the non-occurrence of partial cone cracks, although such cracking may be anticipated

at extreme high-load, high-cycle indentations (Coldea et al., 2014; Guess et al., 2010a; Padture and Lawn, 1995; Peterson et al., 1998). Consequently, the quasi-plastic deformation was revealed for all treated Y-TZP surfaces in Figs. 7.35–7.54. The induced plastic deformation tended to smoothen the milling-induced surface defects in the CAD/CAM-sintered surfaces as shown in Figs. 7.35(b), 7.40(b), 7.45(b) and 7.50(b), the degree of smoothening increasing with the number of cycles. However, for areas not smoothened, the cyclic indentations led to smeared surfaces (Fig. 7.45(d)) at 1000 indentations and intragranular fractures at 3000 indentations (Fig. 7.50(d)). Similarly, the induced plastic deformation tended to smoothen the milling-induced surface defects in the CAD/CAM-polished-sintered surfaces as shown in Figs. 7.36(b), 7.41(b), 7.46(b) and 7.51(b), the extent of smoothening increasing with the number of cycles. The peripheral surface damage traces in Fig. 7.51(b) showing micro-cracking was characteristic of martensitic tetragonal to monoclinic phase transformation (Lee et al., 2000; Pajares et al., 1995). These micro-cracks were an indication of a strong buildup of residual stresses within the transformation zone (Pajares et al., 1995). Therefore, the induced phase transformation might have led to grain pull-out (Fig. 7.51(e)) due to volume dilatation of monoclinic structure (Denry and Holloway, 2006).

For CAD/CAM-sintered-polished surfaces, the induced plastic deformation also tended to smoothen the milling-induced surface defects (Figs. 7.37(b), 7.42(b), 7.47(b) and 7.52(b)), the degree of smoothening increasing with the number of cycles. However, for areas not covered by the plastic deformation-induced smoothening process, the cyclic indentations led to intergranular smeared surface (Fig. 7.47(d)) at 1000 indentations and smeared surface (Fig. 7.52(d)) at 3000 indentations. In addition, the induced plastic deformation tended to smoothen the milling- and sandblasting-induced surface defects in the CAD/CAM-sintered-110 μm alumina sandblasted surfaces as shown in Figs. 7.38(b), 7.43(b), 7.48(b) and 7.53(b), the degree of smoothening increasing with the number of cycles. For uncovered areas in the smoothening process, the cyclic indentations led to granular smearing at 100 indentations (Figs. 7.43(e)), smeared surface with intergranular fracture at 1000 indentations (Fig. 7.48(d)) and intragranular fractures and wedging at 3000 indentations (Fig. 7.50(d)). For CAD/CAM-sintered-250 μm alumina sandblasted surfaces, the induced plastic deformation also tempted to smoothen the milling-induced surface defects (Figs. 7.39(b), 7.44(b), 7.49(b) and 7.54(b)), the extent of smoothening increasing with the number of cycles. The increase in number of cycles led to indentation-enhanced growth of sandblasted scoring and pitting as observed in Figs. 7.44(e), 7.49(e) and 7.54(e) for 100, 1000 and 3000 indentations respectively.

The influence of surface asperities on the indentation-induced fatigue damage of treated Y-TZP surfaces was almost imperceptible at 1 indentation.This can be seen by comparing indented

(Fig. 7.30(b)) with unindented (Fig. 6.7(b)) CAD/CAM-sintered surfaces; indented (Figs. 7.31(b)) with unindented (Fig. 6.9(b)) CAD/CAM-polished-sintered surfaces; and indented (Fig. 7.32(a)) with unindented (Fig. 6.8(a)) CAD/CAM-sintered-polished surfaces. Similarly, no significant differences were observed in indented (Fig. 7.33(a)) and unindented (Fig. 6.10(a)) CAD/CAM-sintered-110 µm alumina sandblasted surfaces and indented (Fig. 7.34(b)) and unindented (Fig. 6.11(b)) CAD/CAM-sintered-250 µm alumina sandblasted surfaces. This indicates that single cycle indentation did not damage the Y-TZP surfaces.

At higher 10–3000 cycles, the surface asperity effect on the fatigue damage of treated Y-TZP surfaces became pronounced. The plastic deformation-induced smoothening processes occurred on all indented treated Y-TZP surfaces regardless of surface asperities (Figs. 7.35–7.54). However, the phase transformation might occur on the smoothest CAD/CAM-polished-sintered surface (Fig. 7.51(b) and intragranular fracture and smeared surfaces on the smoother CAD/CAM-sintered-polished surface (Fig. 7.52(d)). The rough CAD/CAM-sintered surfaces were induced with intragranular fractures (Fig. 7.50(d)). This indicates the surface asperity-dependent response for the fatigue behaviour of treated Y-TZP surfaces.

With respect to the roughest CAD/CAM-sintered-110 µm alumina sandblasted and CAD/CAM-sintered-250 µm alumina sandblasted surfaces, fatigue damage was more severe in the latter than the former. This is because indentation-assisted growth of sandblasted scoring and pitting occurred in CAD/CAM-sintered-250 µm alumina sandblasted (Fig. 7.54(d)) surfaces while smearing, intragranular fractures and wedging only occurred in CAD/CAM-sintered-110 µm alumina sandblasted surfaces (Fig. 7.53(d)). The occurrence of wedging in the CAD/CAM-sintered-110 µm alumina sandblasted surfaces (Fig. 7.53(d)) can shield advancing crack behind the crack tip serving as an extrinsic toughening mechanism in ceramic materials (Ritchie, 1999). Therefore, sandblasting the Y-TZP surfaces with 110 µm alumina grains is recommended because of its inherent better fatigue property. This recommendation complements the conclusion arrived at in Chapter 6.

The fatigue mechanism proposed in this thesis for the low-cycle-high-load spherical cyclic indentations of treated Y-TZP surfaces is thus explained. Cyclic fatigue damage in Y-TZP surfaces occurs due to the degradation of the extrinsic toughening mechanisms responsible for the enhancement of the initial strength (Ritchie, 1999; Studart et al., 2007). This assertion was observed in Fig. 7.4 in which the maximum contact stresses were reduced with increasing number of cycles for all treated Y-TZP surfaces. In addition, indentation-induced quasi plastic deformation was formed all treated Y-TZP surfaces in Figs. 7.30–7.54, smoothening larger areas with higher cycles due to the increasing contact areas. This plastic deformation-induced smoothening process led to the closure of some surface defects as previously explained.

Therefore, the crack surface roughness-induced closure was the fatigue mechanism for the treated Y-TZP surfaces (Ritchie, 1999). This surface contact shield resulted from the creation of plastic deformation zones from physical contact between the contacting surfaces (Ritchie, 1999). This is the first attempt at reporting this fatigue mechanism for this ceramic material. For areas not covered by the smoothening process, intragranular fracture, smearing, wedging and assisted growth of scoring and pitting were induced by cyclic indentations.

The surface uplift in Fig. 7.51 which was intuitively attributed to tetragonal-monoclinic phase transformation might reduce the strength of the CAD/CAM-polished-sintered surfaces but may improve the ageing degradation for this process. This is because water may penetrate through the pulled-out grain (Fig. 7.51(d)) but the intrusion of water may be hindered by the indentation-induced subsurface microscopic shear faults which coalesce shielding progressive propagation (Pajares et al., 1995). In addition, monoclinic surfaces could enhance ageing resistance for Y-TZP (Kosmač et al., 2000; 2008; Kim et al., 2010). For other processes in which intragranular fracture, wedging and indentation-induced sandblasted assisted scoring and pitting were induced (Figs. 7.50, 7.52–7.54), water may penetrate through the defective surfaces slowly transforming them to monoclinic surfaces leading auto-catalytically to failure (Lughi and Sergo 2010). Based on this intuitive reasoning, the smoothest CAD/CAM-polished-sintered process should exhibit the best resistance to low-cycle-high-load spherical cyclic fatigue in line with the recommendations made in Chapter 6 for the same process. To confirm this conclusion, further studies investigating the influence of surface asperities on the strength, wear and ageing properties of Y-TZP surfaces are required.

## 7.6 Conclusions

The chapter investigated the low-cycle-high-load spherical cyclic indentations of two high-strength dental ceramics, LDGC and Y-TZP, allowing the study of their fatigue behaviour within the short-crack domain to which their strengths are most vulnerable. It also addressed the fatigue behavior of these ceramics when conditioned to different surface treatments which simulated various dental clinical surfaces, facilitating the study of the interrelationships among microstructures, surface asperities and crack propagation.

The maximum contact stresses of indented LGDC surfaces reduced significantly with number of cycles which also depended on surface conditions with the smoothest CAD/CAM-polished-sintered surfaces sustaining the highest maximum contact stresses. Also, surface asperities played a major role in the fatigue damage of treated LDGC surfaces with smooth surfaces producing less damage than rough surfaces. The degree of fatigue damage increased with increasing number of cycles. Furthermore, quasi-plastic deformation was dominant at a single

indentation and at higher indentations, partial cone cracks were formed on all surfaces; radial and transverse crack were formed on the roughest CAD/CAM-sintered-glazed surfaces. Also, ring cracks, fretting, pulverization, micro-bridges, surface smearing and wedging and edge chippings were propagated on all surfaces. Therefore, the mechanically assisted growth of the surface flaws was the fatigue mechanism for all treated surfaces and the rougher the surface was, the heavier would be the induced mechanical damage. This augments the superior fatigue resistance of the smoothest CAD/CAM-polished-sintered process for producing LDGC restorations in Chapter 5.

The maximum contact stresses of indented Y-TZP surfaces reduced significantly with the number of cycles which also depended on surface conditions with CAD/CAM-polished-sintered surfaces sustaining higher maximum contact stresses than other surfaces. Also, the influence of surface integrity on the fatigue damage of treated Y-TZP surfaces was dependent of the asperities present. At a single indentation, the quasi-plastic deformation was induced in all surfaces; at higher indentations, this led to plastic deformation-induced smoothening process which increased with the number of cycles. Therefore, crack surface-roughness-induced closure was the main fatigue mechanism for all treated surfaces. However, the cyclic indentations also led to intergranular fractures in CAD/CAM-sintered surfaces, intergranular and smeared surfaces in CAD/CAM-sintered-polished surfaces and phase transformation in CAD/CAM-polished-sintered surfaces. With respect to sandblasted surfaces, cyclic indentations induced more damage on surfaces abraded with 250 µm alumina grains by enhancing the sandblasted scoring and pitting than 110 µm alumina grains which produced wedging serving as an extrinsic toughening mechanism.

The reliability of the proposed CAD/CAM-polished-sintered process for LDGC and Y-TZP restorations based on the lowest surface roughness criterion was intuitively established by the superior fatigue property in comparison to other processes. For long-term success of LDGC and Y-TZP restorations, more studies should investigate the influence of surface asperities on their strengths, wear and ageing behavior.

# Chapter 8

# Conclusions and Recommendations

This PhD thesis studied several key issues involved in the fabrication of two state-of-the-art high strength ceramics, LDGC and Y-TZP for dental restorations. The conclusions and recommendations for future studies are summarized below.

## 8.1 Conclusions

### *8.1.1 Mechanical Behavior*

This thesis characterized the mechanical behavior of LMGC, sintered and pressable LDGC, pre-sintered and sintered Y-TZP. Nanoindentation tests were conducted at several loading rates on these ceramics to understand the rate effect on the mechanical properties and the induced deformations. Their deformation modes were observed using *in situ* scanning probe microscope and Oliver-Pharr, strain rate sensitivity, pressure-sensitive idealized yield criterion and continuum models. This nano-mechanical characterization usefully provides scientific insights into the machining behavior during fabrication because of the mechanical similarity in both indentations and machining responses with respect to deformations and fractures. The LMGC revealed the highest intrinsic contact hardness of 18.9 GPa; the pre-sintered Y-TZP showed the lowest intrinsic contact hardness of 1.11 GPa ± 0.35 GPa. The sintered and pressable LDGC and sintered Y-TZP revealed intermediate intrinsic contact hardness values of 14.58 GPa, 12 GPa and 13.15 GPa respectively. Also, the sintered Y-TZP revealed the highest Young's modulus of 168.19 ± 31.20 GPa; the pre-sintered Y-TZP revealed the lowest modulus of 29.32 ± 4.93 GPa. The LMGC, sintered and pressable LDGC showed the intermediate moduli of 97.48 ± 17.24 GPa, 113.28 ± 12.56 GPa and 113.33 ± 16.11 GPa respectively.

A number of deformation mechanisms were observed. In particular, the plastic deformation mechanisms for LMGC, sintered and pressable LDGC were densification, shear bands and strain hardening. It was therefore recommended that these materials should be machined at moderate deformation rates to avoid the generation of inhomogeneous shear bands at low deformation rates, and strain hardening at high deformation rates. In addition, the sinking-in effect which might enhance the elasticity in LMGC at high deformation rates could be avoided if it were machined at moderate deformation rates. In addition, the plastic deformation mechanisms for pre-sintered Y-TZP were compaction and kink bands. In fact, the discovery of

kink band formation inside the nanoindentation cavity *in situ* was the first study reported, to my best knowledge, for this material. Based on this observation, it was recommended that this material should be machined at high deformation rate to avoid the formation of heterogeneous compaction bands which could induce tensile residual stresses. Further, the plastic deformation mechanisms of sintered Y-TZP were ascribed to dislocation initiation and interactions. Also, the thesis also reported for the first time that sintered Y-TZP was more sensitive to pressure hardening than strain hardening. Based on this observation, it was recommended that high deformation rates might favor small-scale material removal processes while low deformation rates might produce rough surfaces due to increased pileups. In addition, a new method to extract the yield stress of pressure-sensitive materials in nanoindentation using sharp indenters like Berkovich was developed without the need for spherical indenters.

### *8.1.2 Advanced Mechanical Behavior*

The thesis further partitioned the mechanical behavior of LMGC, sintered and pressable LDGC, pre-sintered and sintered Y-TZP into elasticity and plasticity using Sakai and Sakai–Nowak models to reveal the dominant deformation mechanisms. In addition, their resistances to plasticity, ductility indices and resistances to machining-induced cracking were extracted providing a quantitative basis to rank these ceramics in terms of their machinability. The LMGC revealed the highest resistance to plasticity of 396.83 GPa; the pre-sintered Y-TZP showed the lowest resistance to plasticity of 3.82 ± 1.92 GPa. The sintered Y-TZP, pressable and sintered LDGC revealed the intermediate resistances to plasticity of 43.82 ± 9.59 GPa, 62.54 ± 30.91 GPa and 326.72 GPa respectively. Consequently, the LMGC was the most brittle materials while the pre-sintered Y-TZP was the most quasi-plastic material.

The dominant deformation mechanism for LMGC was elastic confirming its high brittleness. However, deformation mechanisms for sintered and pressable LDGC and sintered Y-TZP were dynamic with the plastic deformation components dominating at low loading rates and at higher loading rates, the elastic deformation components dominated. In addition, the plastic deformation dominated in pre-sintered Y-TZP over elastic deformation, confirming its quasi-plastic nature. It was also quantitatively demonstrated for the first time that the plastic deformation in sintered Y-TZP reduced when strain hardening occurred similar to the metallic deformation during the strain hardening process.

Normalized absorbed energies of LMGC, sintered and pressable LDGC, pre-sintered and sintered Y-TZP were 38 ± 15%, 45 ± 17%, 48 ± 13%, 75 ± 8% and 58 ± 16% respectively.

Again, pre-sintered Y-TZP revealed the highest absorbed energy followed by sintered Y-TZP, pressable LDGC, sintered LDGC and then LMGC. This index also ranked pre-sintered Y-TZP as the most ductile-like material making it more machinable than others while LMGC was the most brittle material. In addition, the resistances to machining-induced cracking of LMGC, sintered and pressable LDGC, pre-sintered and sintered Y-TZP were 17.69 ± 7.32 J/m$^2$, 74.32 ± 19.92 J/m$^2$, 112.76 ± 33.17 J/m$^2$, 132.74 ± 15 J/m$^2$ and 445.44 ± 106.32 J/m$^2$ respectively. This ranked sintered Y-TZP the most resistant to machining-induced cracking material followed by pre-sintered Y-TZP, pressable LDGC and sintered LDGC while LMGC was least resistant to machining-induced cracking.

### *8.1.3 CAD/CAM-Milled and Surface Treatments*

The thesis also examined the surface integrity of LMGC/LDGC produced in relevant clinical restorative surface processes involving CAD/CAM-milling, sintering, polishing and glazing with respect to phase transformation, surface roughness and morphology, and removal mechanisms. The CAD/CAM-milling process produced the roughest surfaces ($R_a$ and $R_z$) due to extensive brittle cracks and crystal pulverization. Polishing after the CAD/CAM-milling process reduced the improved roughness by wearing the milled traces and scratches through abrasive mechanical actions. Sintering transformed lithium metasilicate to lithium disilicate crystals to increase the material strength and also lowered the surface roughness produced in milling by reducing milling-induced mechanical residual stresses and generating thermal stresses. The subsequent glaze-firing did not change the stabilized LDGC phase but might have induced additional thermal stresses leading to further deformation. Polishing after sintering did not significantly improve the surface roughness due to the higher strength of LDGC. Among all processes studies, the CAD/CAM-polished-sintered surface produced the smoothest surface which fulfilled dental conditions in terms of cost effectiveness, time efficiency, and surface quality for occlusal functions and bacterial plaque retention and was proposed.

The thesis further studied the surface integrity of pre-sintered/sintered Y-TZP produced in dental restorative surface processes including CAD/CAM-milling, sintering, polishing and sandblasting. The CAD/CAM-milled process produced a rough surface due to the formation of partial ductile mode and brittle fracture. Polishing after the CAD/CAM-milling could not reduce the surface by displacing the material by mechanical action without significantly wearing away the milled surface. Sintering after the CAD/CAM-milling roughened the surface due to the induced grain coarsening, shrinkage associated with grain growth and phase transformation. Polishing after sintering did not improve the surface mainly due to the higher strength of sintered Y-TZP. However, the smoothest surface was produced in CAD/CAM-polished-sintered

process which met the dental surface quality and bacterial plaque retention and was thus recommended for fabricating dental Y-TZP restorations from this studied material. Finally, sandblasting this material with 110 µm alumina abrasives was also recommended due to less severe damage induced than 250 µm alumina abrasives.

### *8.1.4 Fatigue Behavior of Treated Surfaces*

The thesis finally investigated the low-cycle-high-load spherical cyclic indentations of two high-strength dental ceramics, LDGC and Y-TZP, allowing the study of their fatigue behavior within the short-crack domain to which their strengths are most vulnerable. It also addressed the fatigue behavior of these ceramics when conditioned to different surface treatments which simulated various dental clinical surfaces, facilitating the study of the interrelationships among microstructures, surface asperities and crack propagation.

The maximum contact stresses of indented LGDC surfaces reduced significantly with number of cycles which also depended on surface conditions with the smoothest CAD/CAM-polished-sintered surfaces sustaining the highest maximum contact stresses. Also, surface asperities played a major role in the fatigue damage of treated LDGC surfaces with smooth surfaces producing less damage than rough surfaces. The degree of fatigue damage increased with increasing the number of cycles. Furthermore, quasi-plastic deformation was dominant at a single indentation and at higher indentations, partial cone cracks were formed on all surfaces; radial and transverse crack were formed on the roughest CAD/CAM-sintered-glazed surfaces. Also, rings cracks, fretting, pulverization, micro-bridges, surface smearing and wedging and edge chippings were propagated on all surfaces. Therefore, the mechanically assisted growth of the surface flaws was the fatigue mechanism for all treated surfaces and the rougher the surface was, the heavier would be the induced mechanical damage. This augments the superior fatigue resistance of the smoothest CAD/CAM-polished-sintered process for producing LDGC restorations.

The maximum contact stresses of indented Y-TZP surfaces reduced significantly with the number of cycles which also depended on surface conditions with CAD/CAM-polished-sintered surfaces sustaining higher maximum contact stresses than other surfaces. Also, the influence of surface quality on the fatigue damage of treated Y-TZP surfaces was dependent of the asperities present. At a single indentation, the quasi-plastic deformation was induced in all surfaces; at higher indentations, the cyclic indentations led to plastic deformation-induced smoothening process which increased with the number of cycles. Therefore, crack surface-roughness-induced closure was the main fatigue mechanism for all treated surfaces. However, the cyclic

indentations also led to intergranular fractures in CAD/CAM-sintered surfaces, intergranular and smeared surfaces in CAD/CAM-sintered-polished surfaces and phase transformation in CAD/CAM-polished-sintered surfaces. With respect to sandblasted surfaces, cyclic indentations induced more damage on surfaces abraded with 250 μm alumina grains by enhancing the sandblasted scoring and pitting than 110 μm alumina grains which produced wedging serving as an extrinsic toughening mechanism.

## 8.2 Recommendations for Future Studies

Further nanoindentation studies are recommended to be conducted on LMGC, sintered and pressable LDGC identifying the distinct deformation behavior of individual phases in these ceramics. As suggested in Chapter 3, these phases are lithium metasilicate crystals and glassy phase in LMGC, and lithium disilicate crystals and glassy phase in sintered and pressable LDGC. Further, multi-cycling nanoindentation tests at various peak loads, loading rates and indenter angles are recommended to be conducted on LMGC, sintered and pressable LDGC, pre-sintered and sintered Y-TZP. This is necessary to understand fracture and phase transformation mechanisms providing extra information to their observed deformation mechanisms reported in Chapters 3 and 4. Furthermore, scratching tests at increasing loads are recommended to be performed on LMGC and pre-sintered Y-TZP to reveal the transition from ductile to brittle mode facilitating ductile mode machining for these materials. In addition, nanoindentation cyclic loadings (nanoindentation fatigue) experiments at different geometries, loading rates and loads are recommended to be conducted on LDGC and Y-TZP to demonstrate their behavior while chewing sharp or blunt objects.

Practical realization of ductile mode machining of LMGC and pre-sintered Y-TZP is also recommended to be investigated as suggested in Chapters 5 and 6. This can be done by conducting experiments revealing the ductile conditions for depths of cut, feed rates and cutting speeds which can be incorporated in the design of dental CAD/CAM systems for these materials since the machining conditions are automated. In addition, future studies are recommended to unravel why the monoclinic phase transformed to tetragonal $ZrO_{1.95}$ phase for pre-sintered Y-TZP in Chapter 6.

Finally, the reliability of the proposed CAD/CAM-polished-sintered process for LDGC and Y-TZP restorations based on the lowest surface roughness criterion was intuitively established by the superior fatigue property in comparison to other processes in Chapter 7. For the long-term success of LDGC and Y-TZP restorations, further studies should investigate the influence of surface asperities on their strengths, wear and ageing behavior. Also, for the long-term stability

of LDGC and Y-TZP restorations, subcritical crack parameters can be evaluated for the treated LDGC and Y-TZP surfaces in Chapter 7. Also, thermal cycling experiments using mouth-motion chewing simulator are recommended to simulate the physiological ageing behavior experienced by the LDGC and Y-TZP in clinical practice.

# References


Al-Amleh, B., Lyons, K., Swain, M., 2010. Clinical trials in zirconia: a systematic review. J. Oral Rehabil. 37, 641–652.

Alao, A.-R., Konneh, M., 2012. Surface finish prediction models for precision grinding of silicon. Int. J. Adv. Manuf. Technol. 58, 949–967.

Alao, A.-R., Stoll, R., Song, X.-F., Miyazaki, T., Hotta, Y., Shibata, Y., Yin, L., 2017. Surface quality of yttria-stabilized tetragonal zirconia polycrystal in CAD/CAM milling, sintering, polishing and sandblasting processes. J. Mech. Behav. Biomed. Mater. 65, 102–116.

Alao, A.-R., Yin, L., 2014a. Loading rate effect on the mechanical behavior of zirconia in nanoindentation. Mater. Sci. Eng. A–Struct. Mater. 619, 247–255.

Alao, A.-R., Yin, L., 2014b. Nano-scale mechanical properties and behavior of pre-sintered zirconia. J. Mech. Behav. Biomed. Mater. 36, 21–31.

Alao, A.-R., Yin, L., 2014c, Prediction of the resistance to machining-induced cracking in zirconia by nanoindentation, Recent Advances in Structural Integrity Analysis: Proceedings of the Asian-Pacific Conference on Fracture and Strength/the International Conference on Structural Integrity and Failure (APCF/SIF-2014), December 9–12, 2014, Sydney, Australia, Woodhead Publishing/Elsevier, UK, pp 580–584.

Alao, A.-R., Yin, L., 2015a. Nano-mechanical behavior of lithium metasilicate glass-ceramic. J. Mech. Behav. Biomed. Mater. 49, 162–174.

Alao, A.-R., Yin, L., 2015b. Nanoindentation characterization of the elasticity, plasticity and machinability of zirconia. Mater. Sci. Eng. A–Struct. Mater. 628, 181–187.

Alao, A.-R., Yin, L., 2016. Assessment of elasticity, plasticity and resistance to machining-induced damage of porous pre-sintered zirconia using nanoindentation techniques. J. Mater. Sci. Technol. 32, 402–410.

Albakry, M., Guazzato, M., Swain, M.V., 2003. Biaxial flexural strength, elastic moduli, and x-ray diffraction characterization of three pressable all-ceramic materials. J. Prosthet. Dent. 89, 374–380.

Alcalá, J., 2000. Instrumented micro-indentation of zirconia ceramics. J. Am. Ceram. Soc. 83, 1977–1984.

Alemi, A., Khademinia, S., Joo, S.W., Dolatyari, M., Bakhtiari, A., 2013. Lithium metasilicate nanomaterials: optical properties and density functional theory calculations. Int. Nano Lett. 3, 1–11.

Andersson, M., Odén, A., 1993. A new all-ceramic crown. A dense-sintered, high-purity alumina coping with porcelain. Acta Odontol. Scand. 51, 59–64.

Anton, R.J., Subhash, G., 2000. Dynamic Vickers indentation of brittle materials. Wear, 239, 27–35.

Anusavice, K.J., Zhang, N.-Z., 1997. Chemical durability of Dicor and lithia-based glass-ceramics. Dent. Mater. 13, 13–19.

Apel, E., Deubener, J., Bernard, A., Höland, M., Müller, R., Kappert, H., Rheinberger, V., Höland, W., 2008. Phenomena and mechanisms of crack propagation in glass-ceramics. J. Mech. Behav. Biomed. Mater. 1, 313–325.

Apel, E., van't Hoen, C., Rheinberger, V., Höland, W., 2007. Influence of $ZrO_2$ on the crystallization and properties of lithium disilicate glass-ceramics derived from a multi-component system. J. Eur. Ceram. Soc. 27, 1571–1577.

Arroyave, R., Kaufman, L., Eager, T.W., 2002. Thermodynamic modelling of the Zr-O system. Calphad, 26, 95–118.

Attaf, M.T., 2004. Connection between the loading curve models in elastoplastic indentation. Mater. Lett. 58, 3491–3498.

Azeggagh, N., Joly-Pottuz, L., Nélias, D., Chevalier, J., Omori, M., Hashida, T., 2015. Hertzian contact damage in silicon nitride ceramics with different porosity contents. J. Eur. Ceram. Soc. 35, 2269–2276.

Badwal, S.P.S., 1995. Grain boundary resistivity in zirconia-based materials: Effect of sintering temperatures and impurities. Solid State Ionics 76, 67–80.

Baik, D.S., No, K.S., Chun, J.S., Yoon, Y.J., Cho, H.Y. 1995. A comparative evaluation method of machinability for mica-based glass-ceramics. J. Mater. Sci. 30, 1801–1806.

Baran, G., Boberick, K., McCool, J., 2001. Fatigue of restorative materials. Crit. Rev. Oral Biol. Med. 12, 350–360.

Barrett, J.M., Clark, D.E., Hench, L.L., 1980. Glass-ceramic dental restoration, US Patent 4,189,325.

Barsoum, M.W., Zhen, T., Kalidindi, S.R., Radovic, M., Murugaiah, A., 2003. Fully reversible, dislocation-based compressive deformation of $Ti_3SiC_2$ to 1 GPa. Nat Mater. 2, 107–111.

Beall, G.H., 1992. Design and properties of glass-ceramics. Annu. Rev. Mater. Sci. 22, 91–119.

Bergman, M., Ginstrup, O., Nilner, K., 1978. Potential and polarization measurements in vivo of oral galvanism. Scand. J. Dent. Res. 86, 135–145.

Beuer, F., Schweiger, J., Edelhoff, D., 2008. Digital dentistry: an overview of recent developments for CAD/CAM generated restorations. Brit. Dent. J. 204, 505–511.

Beuer, F., Schweiger, J., Eichberger, M., Kappert, H.F., Gernet, W., Edelhoff, D., 2009. High-strength CAD/CAM-fabricated veneering material sintered to zirconia copings- A new fabrication mode for all-ceramic restorations. Dent. Mater. 25, 121–128.

Beuer, F., Stimmelmayr, M., Gueth, J.-F., Edelhoff, D., Naumann, M., 2012. In vitro performance of full-contour zirconia single crowns. Dent. Mater. 28, 449–456.

Bhattacharya, M., Chakraborty, R., Dey, A., Mandal, A.K., Mukhopadhyay, A.K., 2012. Improvement in nanoscale contact resistance of alumina. Appl. Phys. A–Mater. 107, 783–788.

Bhowmick, S., Zhang, Y., Lawn, B.R., 2005. Competing fracture modes in brittle materials subject to cyclic loading in liquid environments: Bilayer structures. J. Mater. Res. 20, 2792–2800.

Bhushan, B., Li, X.D., 2003. Nanomechanical characterisation of solid surfaces and thin films. Int. Mater. Rev. 48, 125–164.

Bifano, T.G., Dow, T.A., Scattergood, R.O., 1991. Ductile-regime grinding: A new technology for machining brittle materials. J. Eng. Ind. Trans. ASME, 113, 184–189.

Bindl, A., Lüthy, H., Mörmann, W.H., 2003. Fracture load of CAD/CAM-generated slot-inlay FPDs. Int. J. Prosthodont. 16, 653–660.

Bindl, A., Lüthy, H., Mörmann, W.H., 2006. Strength and fracture pattern of monolithic CAD/CAM-generated posterior crowns. Dent. Mater. 22, 29–36.

Boaventura, J.M.C., Nishida, R., Elossais, A.A., Lima, D.M., Reis, J.M.S.N., Campos, E.A., de Andrade, M.F., 2013. Effect finishing and polishing procedures on the surface roughness of IPS Empress 2 ceramic. Acta Odontol. Scand. 71, 438–443.

Bollen, C.M.L., Lambrechts, P., Quirynen, M., 1997. Comparison of surface roughness of oral hard materials to the threshold surface roughness for bacterial plaque retention: A review of the literature. Dent. Mater. 13, 258–269.

Bolshakov, A., Pharr, G.M., 1998. Influences of pileup on the measurement of mechanical properties by load and depth sensing indentation techniques. J. Mater. Res. 13, 1049–1058.

Borges, G.A., Sophr, A.M., de Goes, M.F., Sobrinho, L.C., Chan, D.C.N., 2003. Effect of etching and airborne abrasion on the microstructure of different dental ceramics. J. Prosthet. Dent. 89, 479–488.

Brunot-Gohin, C., Duval, J.-L., Azogui, E.-E., Jannetta, R., Pezron, I., Laurent-Maquin, D., Gangloff, S.C., Egles, C., 2013. Soft tissue adhesion of polished versus glazed lithium disilicate ceramic for dental applications. Dent. Mater. 29, e205–e212.

Bühler-Zemp, P., Völkel, T., 2005a. IPS e.max CAD Scientific documentation. Ivoclar Vivadent. 1–16.

Bühler-Zemp, P., Völkel, T., 2005b. IPS e.max Press Scientific documentation. Ivoclar Vivadent. 1–24.

Buchner, S., Lepienski, C.M., Soares Jr, P.C., Balzaretti, N.M. 2011. Effect of high pressure on the mechanical properties of lithium disilicate glass. Mater. Sci. Eng. A–Struct. Mater. 528, 3921–3924.

Budinski, K.G., Budinski, M.K., 2010. Engineering Materials: Properties and Selection, ninth ed. Pearson, New Jersey.

Bulychev, S.I., Alekhin, V.P., Shorshoroy, M.Kh., Ternovskii, A.P., Shnyrev, V.N., 1975. Determining Young's modulus from the indenter penetration diagram. Zavod. Lab. 41, 1137–1140.

Burgess, T., Laws, K.J., Ferry, M., 2008. Effect of loading rate on the serrated flow of a bulk metallic glass during nanoindentation. Acta Mater. 56, 4829–4835.

Cai, H., Kalceff, M.A.S., Hooks, B.M., Lawn, B.R., 1994. Cyclic fatigue of a mica-containing glass-ceramic at Hertzian contacts. J. Mater. Res. 9, 2654–2661.

Cain, M.G., Lewis, M.H., 1990. Evidence of ferroelasticity in y-tetragonal zirconia polycrystals. Mater. Lett. 9, 309–312.

Callister Jr., W.D., 2007. Materials Science and Engineering: An Introduction, seventh ed. John Wiley and Sons, Inc., New York.

Catledge, S.A., Cook, M., Vohra, Y.K., Santos, E.M., Mcclenny, M.D., Moore, K.D., 2003. Surface crystalline phases and nanoindentation hardness of explanted zirconia femoral heads. J. Mater. Sci.–Mater. Med. 14, 863–867.

Cattell, M.J., Palumbo, R.P., Knowles, J.C., Clarke, R.L., Samarawickrama, D.Y.D., 2002. The effect of veneering and heat treatment on the flexural strength of Empress® 2 ceramics. J. Dent. 30, 161–169.

Cattani-Lorente, M., Scherrer, S.S., Ammann, P., Jobin, M., Wiskott, A., 2011. Low temperature degradation of a Y-TZP dental ceramic. Acta Biomater. 7, 858–865.

Chakraborty, R., Dey, A., Mukhopadhyay, A.K., 2010. Loading rate effect on nanohardness of soda-lime-silica glass. Metall. Mater. Trans. A 41A, 1301–1312.

Chen, I.-W., 1986. Implications of transformation plasticity in $ZrO_2$-containing ceramics: II, elastic-plastic indentation. J. Am. Ceram. Soc. 69, 189–194.

Cheng, Y.-T., Cheng, C.-M., 1998. Relationship between hardness, elastic modulus, and the work of indentation. Appl. Phys. Lett. 73, 614–616.

Chevalier, J., Gremillard, L., Deville, S. 2007. Low-temperature degradation of zirconia and implications for biomedical implants. Annu. Rev. Mater. Res. 37, 1–32.

Chevalier, J., Gremillard, L., Virkar, A.V., Clarke, D.R., 2009. The tetragonal-monoclinic transformation in zirconia: Lessons learned and future trends. J. Am. Ceram. Soc. 92, 1901–1920.

Chevalier, J., Olagnon, C., Fantozzi, G. 1999. Subcritical crack propagation in 3Y-TZP ceramics: Static and cyclic fatigue. J. Am. Ceram. Soc. 82, 3129–3138.

Chintapalli, R.K., Jimenez-Pique, E., Marro, F.G., Yan, H., Reece, M., Anglada, M., 2012. Spherical instrumented indentation of porous nanocrystalline zirconia. J. Eur. Ceram. Soc. 32, 123–132.

Chintapalli, R.K., Marro, F.G., Jimenez-Pique, E., Anglada, M., 2013. Phase transformation and subsurface damage in 3Y-TZP after sandblasting. Dent. Mater. 29, 566–572.

Chintapalli, R.K., Breton, S., Dastjerdi, A.K., Barthlat, F., 2014a. Strain rate hardening: A hidden but critical mechanism for biological composites. Acta Biomater. 10, 5064–5073.

Chintapalli, R.K., Rodriguez, A.M., Marro, F.G., Anglada, M., 2014b. Effect of sandblasting and residual stress on strength of zirconia for restorative dentistry applications. J. Mech. Behav. Biomed. Mater. 29, 126–137.

Chung, S.M., Yap, A.U.J., 2005. Effects of surface finish on indentation modulus and hardness of dental composite restoratives. Dent. Mater. 21, 1008–1016.

Ciszewski, A., Baraniak, M., Urbanek-Brychczyńska, M., 2007. Corrosion by galvanic coupling between amalgam and different chromium-based alloys. Dent. Mater. 23, 1256–1261.

Clément P, Meille S, Chevalier J, Olagnon C., 2013. Mechanical characterization of highly porous inorganic solids materials by instrumented micro-indentation. Acta Mater. 61, 6649–6660.

Coldea, A., Swain, M.V., Thiel, N., 2014. Hertzian contact response and damage tolerance of dental ceramics. J. Mech. Behav. Biomed. Mater. 34, 124–133.

Concustell, A., Sort, J., Alcalá, G., Mato, S., Gebert, A., Eckert, J., Baró. M.D., 2005. Plastic deformation and mechanical softening of $Pd_{40}Cu_{30}Ni_{10}P_{20}$ bulk metallic glass during nanoindentation. J. Mater. Res. 20, 2719–2725.

Conrad, H.J., Seong, W.J., Pesun, I.J., 2007. Current ceramic materials and systems with clinical recommendations: A systematic review. J. Prosthet. Dent. 98, 389–404.

Constantinides, G., Ravichandran, K.S., Ulm, F.-J., Van Vliet, K.J., 2006. Grid indentation analysis of composite microstructure and mechanics: Principles and validation. Mater. Sci. Eng. A–Struct. Mater. 430, 189–202.

Cook, R.F., 2006. Strength and sharp contact fracture of silicon. J. Mater. Sci. 41, 841–872.

Cramer von Clausbruch, S., Schweiger, M., Höland, W., Rheinberger, V., 2000. The effect of $P_2O_5$ on the crystallization and microstructure of glass ceramics in the $SiO_2$-$Li_2O$-$K_2O$-ZnO-$P_2O_5$ system. J. Non-Cryst. Solids 263–264, 388–394.

Curtis, A.R., Wright, A.J., Fleming, G.J.P., 2006. The influence of surface modification techniques on the performance of Y-TZP dental ceramic. J. Dent. 34, 195–206.

Davidowitz, G., Kotick, P.G., 2011. The use of CAD/CAM in dentistry, Dent. Clin. North Am. 55, 559–570.

De Chiffre, L., Lonardo, P., Trumpold, H., Lucca, D.A., Goch, G., Brown, C.A., Raja, J., Hansen, H.N., 2000. Quantitative characterization of surface texture. CIRP Ann-Manuf. Technol. 49, 635–652.

De Jager, Feilzer, A.J., Davidson, C.L., 2000. The influence of surface roughness on porcelain strength, Dent. Mater. 16, 381–388.

Della, B.A., Mecholsky Jr., J.J., Anusavice, K.J., 2004. Fracture behavior of lithia disilicate- and leucite-based ceramics. Dent. Mater. 10, 956–962.

Deng, Y., Lawn, B.R., Lloyd, I.K., 2002a. Characterization of damage modes in dental ceramic bilayer structures. J. Biomed. Mater. Res. (Appl. Biomater.) 63, 137–145.

Deng, Z.-Y., Yang, J.-F., Beppu, Y., Ando, M., Ohji, T., 2002b. Effect of agglomeration on mechanical properties of porous zirconia fabricated by partial sintering. J. Am. Ceram. Soc., 85, 1961–1965.

Denry, I., 2013. How and when does fabrication damage adversely affect the clinical performance of ceramic restorations? Dent. Mater. 29, 85–96.

Denry, I., Holloway, J.A., 2004. Effect of post-processing heat treatment on the fracture strength of a heat-pressed dental ceramic. J. Biomed. Mater. Res. Part B: Appl. Biomater. 68B, 174–179.

Denry, I., Holloway, J.A., 2006. Microstructural and crystallographic surface changes after grinding zirconia-based dental ceramics. J. Biomed. Mater. Res. Part B. Appl. Biomater. 76B, 440–448.

Denry, I., Holloway, J.A., 2010. Ceramics for dental application: A review. Materials 3, 351–368.

Denry, I., Kelly, J.R., 2008. State of the art of zirconia for dental applications. Dent. Mater. 24, 299–307.

Deville, S., Chevalier, J., Gremillard, L., 2006. Influence of surface finish and residual stresses on the ageing sensibility of biomedical grade zirconia. Biomaterials 27, 2186–2192.

Dey, A., Chakraborty, R., Mukhopadhyay, A.K., 2011. Enhancement in nanohardness of soda-lime-silica glass. J. Non-Cryst. Solids 357, 2934–2940.

Dong, X., Yin, L., Jahanmir, S., Ives, L.K., Rekow, E.D., 2000. Abrasive machining of glass-ceramics with a dental handpiece. Mach. Sci. Technol. 4, 209–233.

Donnelly, E., Baker, S.P., Boskey, A.L., van der Meulen, C.H., 2006. Effects of surface roughness and maximum load on the mechanical properties of cancellous bone measured by nanoindentation. J. Biomed. Mater. Res. 77A, 426–435.

Ebenstein, D.M., Pruitt, L.A., 2006. Nanoindentation of biological materials. Nano Today 1, 26–33.

El-Meliegy, E., van Noort, R., 2012. Glasses and glass ceramics for medical applications. Springer, New York.

Elbatal, F. H., Azooz, M. A., Hamdy, Y.M., 2009. Preparation and characterization of some multicomponent silicate glasses and their glass-ceramics derivatives for dental applications. Ceram. Int. 35, 1211–1218.

Ereifej, N., Rodrigues, F.P., Silikas, N., Watts, D.C., 2011. Experimental and FE shear-bonding strength at core/veneer interfaces in bilayered ceramics. Dent. Mater. 27, 590–597.

Evans, C.J., Paul, E., Dornfeld, D., Lucca, D.A., Byrne, G., Tricard, M., Klocke, F., Dambon, O., Mullany, B.A., 2003. Material removal mechanisms in lapping and polishing. CIRP Ann-Manuf. Technol. 52, 611–633.

Fasbinder, D.J., Dennison, J.B., Heys, D., Neiva, G. 2010. A clinical evaluation of chairside lithium disilicate CAD/CAM crowns: A two-year report. J. Am. Dent. Assoc. 141 (Suppl. 2), 10s-14s.

Ferguson, V.L., 2009. Deformation partitioning provides insight into elastic, plastic and viscous contributions to bone material behavior. J. Mech. Behav. Biomed. Mater. 2, 364–374.

Field, J.S., Swain, M.V., Dukino, R.D., 2003. Determination of fracture toughness from the extra penetration produced by indentation-induced pop-in. J. Mater. Res. 18, 1412–1419.

Filser, F., Kocher, L.J., Gauckler, L.J., 2003. Net-shaping of ceramic components by direct ceramic machining. Assembly Autom. 23, 382–390.

Fischer-Cripps, A.C., 2004. A simple phenomenological approach to nanoindentation creep. Mater. Sci. Eng. A 385, 74–82.

Fischer-Cripps, A.C., Lawn, B.R., 1996. Indentation stress-strain curves for "quasi-ductile" ceramics. Acta Mater. 44, 519–527.

Fraczkiewicz, M., Zhou, A.G., Barsoum, M.W., 2006. Mechanical damping in porous $Ti_3SiC_2$. Acta Mater. 54, 5261−5270.

Frutos, E., Cuevas, A., Gonzàlez-Carrasco, J.L., Martin, F., 2012. Characterization of the elastic-plastic behavior of intermetallic coatings growth on medical stainless steel by instrumented ultramicroindentation, J. Mech. Behav. Biomed. Mater. 16, 1–8.

Gaillard, Y., Anglada, M., Jiménez-Piqué, E., 2009. Nanoindentation of yttria-doped zirconia: Effect of crystallographic structure on deformation mechanisms. J. Mater. Res. 24, 719–727.

Gaillard, Y., Jiménez-Piqué, E., Soldera, F., Mücklich, F., Anglada, M., 2008. Quantification of hydrothermal degradation in zirconia by nanoindentation. Acta Mater. 56, 4206–4216.

Garvin, R.C., Hannink, R.H., Pascoe, R.T., 1975. Ceramic steel? Nature 258, 703–704.

Garvin, R.C., Nicholson, P.S., 1972. Phase analysis in zirconia systems. J. Am. Ceram. Soc. 55, 303–305.

Giordano, R., 2006. Materials for chairside CAD/CAM-produced restorations. J. Am. Dent. Assoc. 137(Suppl. 9), 14–21.

Goharian, P., Nemati, A., Shabanian, M., Afshar, A., 2010. Properties, crystallization mechanism and microstructure of lithium disilicate glass-ceramic. J. Non-Cryst. Soilds 356, 208–214.

Golovin, Y.I., Ivolgin, V.I., Khonik, V.A., Kitagawa, K., Tyurin, A.I., 2001. Serrated plastic flow during nanoindentation of a bulk metallic glass. Scr. Mater. 45, 947–952.

Gong, J., Miao, H., Peng, Z., 2004. Analysis of the nanoindentation data measured with a Berkovich indenter for brittle materials: effect of the residual stress. Acta Mater. 52, 784–793.

Greer, A.L., Castellero, A., Madge, S.V., Walker, I.T., Wilde, J.R., 2004. Nanoindentation studies of shear banding in fully amorphous and partially devitrified metallic alloys. Mater. Sci. Eng. A–Struct. Mater. 375–377, 1182–1185.

Greer, A.L., Cheng, Y.Q., Ma, E., 2013. Shear bands in metallic glasses. Mater. Sci. Eng. R 74, 71–132.

Guazzato, M., Albakry, M., Ringer, S.P., Swain, M.V., 2004. Strength, fracture toughness and microstructure of a selection of all-ceramic materials. Part I. Pressable and alumina glass-infiltrated ceramics. Dent. Mater. 20, 441–448.

Guazzato, M., Quach, L., Albakry, M., Swain, M.V., 2005. Influence of surface and heat treatments on the flexural strength of Y-TZP dental ceramic. J. Dent. 33, 9–18.

Guess, P.C., Zhang, Y., Kim, J.-W., Rekow, E.D., Thompson, V.P., 2010a. Damage and reliability of Y-TZP after cementation surface treatment. J. Dent. Res. 89, 592–596.

Guess, P.C., Zavenalli, R.A., Silva, N.R.F.A., Bonfante, E.A., Coelho, P.G., Thompson, V.P., 2010b. Monolithic CAD/CAM lithium disilicate versus veneered Y-TZP crowns: Comparison of failure modes and reliability after fatigue. Int. J. Prosthodont. 23, 434–442.

Guiberteau, F., Padture, N., Cai, H., Lawn, B.R., 1993. Indentation fatigue: A simple cyclic Hertzian test for measuring damage accumulation in polycrystalline ceramics. Philos. Mag. A 68, 1003–1016.

Guicciardi, S., Shimozono, T., Pezzotti, G., 2006. Nanoindentation characterization of sub-micrometric Y-TZP ceramics. Adv. Eng. Mater. 8, 994–997.

Guicciardi, S., Shimozono, T., Pezzotti, G., 2007. Ageing effects on the nanoindentation response of sub-micrometric 3Y-TZP ceramics. J. Mater. Sci. 42, 718–722.

Hallman, L., Ulmer, P., Reusser, E., Louvel, M., Hämmerle, C.H.F., 2012. Effect of dopants and sintering temperature on microstructure and low temperature degradation of dental Y-TZP-zirconia. J. Eur. Ceram. Soc. 32, 4091–4104.

Hallman, L., Ulmer, P., Wille, S., Polonskyi, O., Köbel, S., Trottenberg, T., Bornholdt, S., Haase, F., Kersten, H., Kern, M., 2016. Effect of surface treatments on the properties and morphological change of dental zirconia. J. Prosthet. Dent. 115, 341–349.

Hannink, R.H.J., Kelly, P.M., Muddle, B.C., 2000. Transformation toughening in zirconia-containing ceramics. J. Am. Ceram. Soc. 83, 461–487.

Hannink, R.H.J., Swain, M.V., 1994. Progress in transformation toughening of ceramics. Annu. Rev. Mater. Sci. 24, 359–408.

Hayashi, M., Haapasalo, M., Imazato, S., Lee, Jae, I., Momoi, Y., Murakami, S., Whelton, H., Wilson N., 2014. Dentistry in the 21st century: Challenges of a globalising world. Int. Dent. J. 64, 333–342.

He, L.-H., Standard, O.C., Huang, T.T.Y., Latella, B.A., Swain, M.V., 2008. Mechanical behavior of porous hydroxyapatite. Acta Biomater. 4, 577–586.

Heffernan, M.J., Aquilino, S.A., Diaz-Arnold, A.M., Haselton, D.R., Stanford, C.M. Vargas, M.A., 2002. Relative translucency of six all-ceramic systems. Part I: core materials. J. Prosthet. Dent. 88, 4–9.

Hertz, H.H., 1882. On the contact of elastic solids. J. Reine Angew. Math. 92, 156–171.

Höland, W., Apel, E., van't Hoen, Ch., Rheinberger, V., 2006a. Studies of crystal phase formations in high-strength lithium disilicate glass-ceramics. J. Non-Cryst. Soilds 352, 4041–4050.

Höland, W., Rheinberger, V., Apel, E., van't Hoen, C., Höland, M., Dommann, A., Obrecht, M., Mauth, C., Graf-Hausner, U., 2006b. Clinical applications of glass-ceramics in dentistry. J. Mater. Sci: Mater. Med. 17, 1037–1042.

Höland, W., Schweiger, M., Frank, M., Rheinberger, V., 2000. A comparison of the microstructure and properties of the IPS Empress®2 and IPS Empress®glass-ceramics. J. Biomed. Mater. Res. Part B: Appl. Biomater. 53, 297–303.

Horasawa, N., Takahashi, S., Marek, M., 1999. Galvanic interaction between titanium and gallium alloy or dental amalgam. Dent. Mater. 15, 318–322.

Hornberger, H., Marquis, P. M., Christiansen, S., Strunk, H. P., 1996. Microstructure of a high strength alumina glass composite. J. Mater. Res. 11, 855–858.

Iqbal, Y., Lee, W.E., Holland, D., James, P.F., 1998. Metastable phase formation in the early stage of crystallization of lithium disilicate glass. J. Non-Cryst. Solids 224, 1–16.

Ivanoskaya, M.I., Flolova, E.V., 2007. Nature and conditions of formation of structural defects in zirconium(IV) oxide in the course of its preparation from zirconium hydroxide. Russ. J. Gen. Chem. 77, 524–531.

Jahanmir, S., Xu, H.H.K., Ives, L.K., 1999. Mechanism of materials removal in abrasive machining of ceramics. In: Jahanmir, S., Koshy, P., Ramulu, M., (Eds.), Machining of Ceramics and Composites, Marcel Dekker, New York, pp. 11–84.

Jefferies, S.R., 2007. Abrasive finishing and polishing in restorative dentistry: A state-of-the-art review. Dent. Clin. North Am. 51, 379–397.

Jha, K.K., Zhang, S., Suksawang, N., Wang, T.-L., Agarwal, A., 2013. Work-of-indentation as a means to characterize indenter geometry and load-displacement response of a material. J. Phys. D: Appl. Phys. 46, 415501.

Johnson, K.L., 1985. Contact Mechanics, first ed. Cambridge University Press, Cambridge, UK.

Jung, Y.-G., Peterson, I.M., Kim, D.K., Lawn, B.R. 2000. Lifetime-limiting strength degradation from contact fatigue in dental ceramics. J. Dent. Res. 79, 722–731.

Kalpakjian, S., Schmid, S., 2013. Manufacturing Engineering and Technology, seventh ed. Pearson, New Jersey, USA.

Karakoca, S., Yilmaz, H., 2009. Influence of surface treatments on surface roughness, phase transformation, and biaxial flexural strength of Y-TZP. J. Biomed. Mater. Res. Part B. Appl. Biomater. 91B, 930–937.

Klecka, M.A., Subhash, G., 2010. Rate-dependent indentation response of structural ceramics. J. Am. Ceram. Soc. 93, 2377–2383.

Kelly, J.R., 1995. Perspectives on strength. Dent. Mater. 11, 103–110.

Kelly, J.R., 1997. Ceramics in restorative and prosthetic dentistry. Annu. Rev. Mater. Sci. 27, 443–468.

Kelly, J.R., Denry, I., 2008. Stabilized zirconia as a structural ceramic: An overview. Dent. Mater. 24, 289–298.

Kelly, J.R., Rungruanganunt, P., Hunter, B., Vailati, F., 2010. Development of a clinically validated bulk failure test for ceramic crowns. J. Prosthet. Dent. 104, 228–238.

Kern, M., 2009. Resin bonding to oxide ceramics for dental restorations. J. Adhes. Sci. Technol. 23, 1097–1111.

Kese, K., Rowcliffe, D.J., 2003. Nanoindentation method for measuring residual stress in brittle materials. J. Am. Ceram. Soc. 86, 811–816.

Kim, J.-W., Covel, N.S., Guess, P.C., Rekow, E.D., Zhang, Z. 2010. Concerns of hydrothermal degradation in CAD/CAM zirconia. J. Dent. Res. 89, 91–95.

Kim, J.-W., Kim, J.-H., Thompson, V.P., Zhang, Y., 2007a. Sliding contact fatigue damage in layered ceramic structure. J. Dent. Res. 86, 1046–1050.

Kim, J.-Y, Kang S.-K, Lee, J.-J, Jang, J.-I, Lee, Y.-H., 2007b. Influence of surface-roughness on indentation size effect. Acta Mater. 55, 3555–3562.

Klocke, F., Gerent, O., Schippers, C., 1998. Green machining of advanced ceramics, in: Jahanmir S., Ramulu M., Koshy P. (Eds.), Machining of ceramics and composites. Marcel Dekker, New York, pp. 1–10.

Kosmač, T., Oblak, C., Jevnikar, P., Funduk, N., Marion, L., 1999. The effect of surface grinding and sandblasting on the flexural strength and reliability of Y-TZP zirconia ceramic. Dent. Mater. 15, 426–433.

Kosmač, T., Oblak, Č., Jevnikar, P., Funduk, N., Marion, L., 2000. Strength and reliability of surface treated Y-TZP dental ceramics. J. Biomed. Mater. Res. Part B: Appl. Biomater. 53, 304–313.

Kosmač, T., Oblak, C., Marion, L, 2008. The effects of dental grinding and sandblasting on ageing and fatigue behaviour of dental zirconia (Y-TZP) ceramics. J. Eur. Ceram. Soc. 28, 1085–1090.

Komanduri, R., Lucca, D.A., Tani, Y., 1997. Technological advances in fine abrasive processes. CIRP Ann-Manuf. Technol. 46, 545–596.

Kou, W., Molin, M., Sjögren, G., 2006. Surface roughness of five different dental ceramic core materials after grinding and polishing. J. Oral Rehabil. 33, 117–124.

Kracek, F.C., 1930. The binary system $Li_2O$-$SiO_2$. J. Phys. Chem. 34, 2641–2650.

Kramer, D., Huang, H., Kriese, M., Robach, J., Nelson, J., Wright, A., Bahr, D., Berberich, W.W., 1999. Yield strength predictions from the plastic zone around nanocontacts. Acta Mater. 47, 333–343.

Latella, B.A., O'Connor, B.H., Padture, N.P., Lawn, B.R., 1997. Hertzian contact damage in porous alumina ceramics. J. Am. Ceram. Soc. 80, 1027–1031.

Latka, L., Chicot, D., Cattini, A., Pawlowski, L., Ambroziak, A., 2013. Modeling of elastic modulus and hardness determination by indentation of porous yttria stabilized zirconia coatings. Surf. Coat. Technol. 220, 131–139.

Lawn, B., 1993. Fracture of Brittle Solids, second edition. Cambridge University Press, Cambridge, UK.

Lawn, B.R., 1998. Indentation of ceramics with spheres: A century after Hertz. J. Am. Ceram. Soc. 81, 1977–1994.

Lawn, B.R., Bhowmick, S., Bush, M.B., Qasim, T., Rekow, E.D., Zhang, Y., 2007. Failure modes in ceramic-based layer structures: A basis for materials design of dental crowns. J. Am. Ceram. Soc. 90, 1671–1683.

Lawn, B.R., Cook, R.F., 2012. Probing material properties with sharp indenters: a retrospective. J. Mater. Sci. 47, 1–22.

Lawn, B.R., Deng, Y., Lloyd, I.K., Janal, M.N., Rekow, E.D., Thompson, V.P., 2002a. Materials design of ceramic-based layer structures for crowns. J. Dent. Res. 81, 433–438.

Lawn, B.R., Deng, Y., Miranda, P., Pajares, A., Chai, H., Kim, D.K., 2002b. Overview: Damage in brittle layer structures from concentrated loads. J. Mater. Res. 17, 3019–3036.

Lawn, B.R., Deng, Y., Thompson, V.P., 2001. Use of contact testing in the characterization and design of all-ceramic crownlike layer structures: A review. J. Prosthet. Dent. 86, 495–510.

Lawn, B.R., Evans, A.G., 1977. A model for crack initiation in elastic/plastic indentation fields. J. Mater. Sci. 12, 2195–2199.

Lawn, B.R., Howes, V.R., 1981. Elastic recovery at hardness indentations. J. Mater. Sci. 16, 2745–2752.

Lawn, B.R., Padture, N.P., Cai, H, Guiberteau, F., 1994. Making ceramics "ductile". Science, 263, 1114–1116.

Lawn, B.R., Pajares, A., Zhang, Y., Deng, Y., Polack, M.A., Lloyd, I.K., Rekow, E.D., Thompson, V.P., 2004. Materials design in the performance of all-ceramic crowns. Biomaterials 25, 2885–2892.

Lawson, S., 1995. Environmental degradation of zirconia ceramics. J. Eur. Ceram. Soc. 15, 485–502.

Lee, C.-S., Kim, D.K., Sánchez, J., Miranda, P., Pajares, A., Lawn, B.R., 2002. Rate effects in critical loads for radial cracking in ceramic coatings. J. Am. Ceram. Soc. 85, 2019–2024.

Lee, S.K., Tandon, R., Readey, M.J., Lawn, B.R., 2000. Scratch damage in zirconia ceramics. J. Am. Ceram. Soc. 83, 1428–1432**.**

Leyland, A., Mathews, A., 2000. On the significance of the H/E ratio in wear control: a nanocomposite coating approach to optimised tribological behaviour, Wear 246, 1–11.

Li, K., Liao, W., 1996. Surface/subsurface damage and the fracture strength of ground ceramics. J. Mater. Process. Technol., 57, 207–220.

Li, R.W.K., Chow, T.W., Matinlinna, J.P., 2014. Ceramic dental biomaterials and CAD/CAM technology: State of the art. . J. Prosthodont. Res. 58, 208–216.

Li, S., Wang, Z., Wu, Y., 2008. Relationship between subsurface damage and surface roughness of optical materials in grinding and lapping processes. J. Mater. Process. Technol. 205, 34–41.

Li, W.H., Zhang, T.H., Xing, D.M., Wei, B.C., Wang, Y.R., Dong, Y.D., 2006. Instrumented indentation study of plastic deformation in bulk metallic glasses. J. Mater. Res. 21, 75–81.

Li, X.D., Bhushan, B., 2001. Micro/nanomechanical and tribological studies of bulk and thin-film materials used in magnetic recording heads. Thin Solid Films 398, 313–319.

Lian, J., Garay, J.E., Wang, J., 2007. Grain size and grain boundary effects on the mechanical behavior of fully stabilized zirconia investigated by nanoindentation. Scr. Mater. 56, 1095–1098.

Limbach, R., Rodrigues, B.P., Wondraczek, L., 2014. Strain-rate sensitivity of glasses. J. Non-Cryst. Solids 404, 124–134.

Lin, W.-S., Harris, B.T., Morton, D., 2012. Trial insertion procedure for milled lithium disilicate restorations in the precrystallized state. J. Prosthet. Dent., 107, 59–62.

Ling, Z., Wang, X., Ma, J., 2008. The response of porous $Al_2O_3$ probed to nanoindentation. Mater. Sci. Eng. A–Struct. Mater. 483–484, 285–288.

Liu, P.-R., 2005. A panorama of dental CAD/CAM restorative system. Compend. Contin. Educ. Dent. 26, 507–512.

Lu, X.-J., Wang, X., Xiao, P., 2006. Nanoindentation and residual stress measurements of yttria-stabilized zirconia composite coatings produced by electrophoretic deposition. Thin Solid Films 494, 223–227.

Lucas, B.N., Oliver, W.C., 1999. Indentation power-law creep of high-purity indium. Metall. Mater. Trans. A 30A, 601–610.

Lughi, V., Sergo V., 2010. Low temperature degradation-aging- of zirconia: A critical review of the relevant aspects in dentistry. Dent. Mater. 26, 807–820.

Luo, J. Stevens, R., 1999. Porosity-dependence of elastic moduli and hardness of 3Y-TZP ceramics. Ceram. Int. 25, 281–286.

Luthardt, R.G., Holzhüter, M.S., Rudolph, H., Herold, V., Walter, H., 2004. CAD/CAM-machining effects on Y-TZP. Dent. Mater. 20, 655–662.

Luthardt, R.G., Holzhüter, M., Sandkuhl, O., Herold, V., Schnapp, J.D., Kuhlisch, E., Walter, M., 2002a. Reliability and properties of ground Y-TZP-zirconia ceramics. J. Dent. Res. 81, 487–491.

Luthardt, R., Weber, A., Rudolph, H., Schöne, C., Quaas, S., Walter, M., 2002b. Design and production of dental prosthetic restorations: basic research on dental CAD/CAM technology. Int. J. Comput. Dent. 5, 165–176.

Ma, X.-P., Li, G.-X., Shen, L., Jin, Z.-H., 2003. Ductile-mode material removal of a mica-glass-ceramic. J. Am. Ceram. Soc. 86, 1040–1042.

Maksoud, T.M.A., Mokbel, A.A., Morgan, J.E., 1999. Evaluation of surface and sub-surface cracks of ground ceramic. J. Mater. Process. Technol. 88, 222–243.

Malkin, S., Hwang, T.W., 1996. Grinding mechanisms for ceramics. CIRP Ann-Manuf. Technol. 45, 569–580.

Manicone, P.F., Iommetti, P.R., Raffaelli, L., 2007. An overview of zirconia ceramics: basic properties and clinical applications. J. Dent. 35, 819–826.

Marinescu, I.D., Rowe, W.B., Dimitrov, B., Inasaki, I., 2004. Tribology of Abrasive Machining Processes, first ed. William Andrew Inc., New York.

Miller, M., Bobko, C., Vandamme, M., Ulm, F.-J., 2008. Surface roughness criteria for cement paste nanoindentation. Cement Concrete Res. 38, 467–476.

Mitov, G., Heintze, S.D., Walz, S., Woll, K., Muecklich, F., Pospiech, P., 2012. Wear behavior of dental Y-TZP ceramic against natural enamel after different finishing procedures. Dent. Mater. 28, 909–918.

Miyazaki, T., Hotta, Y., 2011, CAD/CAM systems available for the fabrication of crowns and bridge restorations. Aust. Dent. J. 56, 97s–106s.

Miyazaki, T., Hotta, Y., Kunii, J., Kuriyama, S., Tamaki, Y., 2009. A review of dental CAD/CAM: current status and future perspectives from 20 years of experience. Dent. Mater. J. 28, 44–56.

Miyazaki, T., Nakamura, T., Matsumura, H., Ban, S., Kobayashi, T. 2013. Current status of zirconia restoration. J. Prosthodont. Res. 57, 236–261.

Mörmann, W.H., 2006. The evolution of the CEREC system. J. Am. Dent. Assoc. 137, 7s–13s.

Monaco, C., Tucci, A., Esposito, L., Scotti, R., 2013. Microstructural changes produced by abrading Y-TZP in presintered and sintered conditions. J. Dent. 41, 121–126.

Montazerian, M., Alizadeh, P., Yekta, B.E., 2008. Pressureless sintering and mechanical properties of mica glass–ceramic/Y-PSZ composite. J. Eur. Ceram. Soc. 28, 2687–2692.

Morena, R., Lockwood, P.E., Fairhurst, C.W., 1986. Fracture toughness of commercial dental porcelains. Dent. Mater. 2, 58–62.

Munoz-Tabares, J.A., Jiménez-Piqué, E., Reyes-Gasga, J., Anglada, M., 2012. Microstructural changes in 3Y-TZP induced by scratching and indentation. J. Eur. Ceram. Soc. 32, 3919–3927.

Murtagian, G.R., Hecker, R.L., Liang, S.Y., Danyluk, S. 2010. Plastic deformation depth modelling on grinding of gamma titanium aluminides. Int. J. Adv. Manuf. Technol. 49, 89–95.

N'jock, M.Y., Chicot, D., Ndjaka, J.M., Lesage, J., Decoopman, X., Roudet, F., Mejias, A., 2015. A criterion to identify sinking-in and piling-up in indentation of materials. Int. J. Mech. Sci. 90, 145–150.

Nakamura, K., Adolfsson, E., Milleding, P., Kanno, T., Örtengren, U., 2012. Influence of grain size and veneer firing process on the flexural strength of zirconia ceramics. Eur. J. Oral. Sci. 120, 249–254.

Nakamura, T., Qian, G., Berndt, C.C., 2000. Effects of pores on mechanical properties of plasma-sprayed ceramic coatings. J. Am. Ceram. Soc. 83, 578–584.

Olesiak, S.E., Oyen, M.L., Ferguson, V.L., 2010. Viscous-elastic-plastic behavior of bone using Berkovich nanoindentation. Mech. Time-Depend. Mater. 14, 111–124.

Oliver, W.C., Pharr, G.M., 1992. An improved technique for determining hardness and elastic modulus using load and displacement sensing indentation experiments. J. Mater. Res. 7, 1564–1583.

Oliver, W.C., Pharr, G.M., 2004. Measurement of hardness and elastic modulus by instrumented indentation: Advances in understanding and refinements to methodology. J. Mater. Res. 19, 3–20.

Oyen, M.L., 2006. Nanoindentation hardness of mineralized tissues. J. Biomech. 39, 2699–2702.

Oyen, M.L., Cook, R.F., 2003. Load-displacement behavior during sharp indentation of viscous-elastic-plastic materials. J. Mater. Res. 18, 139–150.

Oyen, M.L., Cook, R.F., 2009. A Practical guide for analysis of nanoindentation data. J. Mech. Behav. Biomed. Mater. 2, 396–407.

Packard, C.E., Schuh, C.A., 2007. Initiation of shear bands near a stress concentration in metallic glass. Acta Mater. 55, 5348–5358.

Padture, N.P., Lawn, B.R., 1995. Contact fatigue of a silicon carbide with a heterogeneous grain structure. J. Am. Ceram. Soc. 78, 1431–1438.

Pajares, A., Wei, L., Lawn, B.R., 1995. Damage accumulation and cyclic fatigue in Mg-PSZ at Hertzian contacts. J. Mater. Res. 10, 2613–2625.

Passos, S.P., Linke, B., Major, P.W., Nychka, J.A., 2015. The effect of air-abrasion and heat treatment on the fracture behavior of Y-TZP. Dent. Mater. 31, 1011–1021.

Passos, S.P., Torrealba, Y., Major, P., Linke, B., Flores-Mir, C., Nychka, J.A., 2014. In vitro wear behavior of zirconia opposing enamel: A systematic review. J. Prosthodont. 23, 593–601.

Paul, A., Vaidhyanathan, B., Binner, J.G.P., 2011. Hydrothermal aging behavior of nanocrystalline Y-TZP ceramics. J. Am. Ceram. Soc. 94, 2146–2152.

Peterson, I.M., Pajares, A., Lawn, B.R., Thompson, V.P., Rekow, E.D., 1998. Mechanical characterization of dental ceramics by Hertzian contacts. J. Dent. Res. 77, 589–602.

Peykov, D., Martin, E., Chromik, R.R., Gauvin, R., Trudeau, M., 2012. Evaluation of strain rate sensitivity by constant load nanoindentation. J. Mater. Sci. 47, 7189–7200.

Pharr, G.M., 1998. Measurement of mechanical properties by ultra-low load indentation. Mater. Sci. Eng. A–Struct. Mater. 1–2, 151–159.

Piconi, C., Maccauro, G., 1999. Zirconia as a ceramic biomaterial. Biomaterials 20, 1–25.

Pinto, H., Ito, L., Crovace, M., Ferreira, E.B., Fauth, F., Wroblewski, T., Zanotto, E.D., Pyzalla, A.R., 2007. Surface and bulk residual stresses in $Li_2O.2SiO_2$ glass-ceramics. J. Non-Cryst. Solids 353, 2307–2317.

Preis, V., Behr, M., Handel, G., Schneider-Feyrer, S., Hahnel, S., Rosentritt, M., 2012. Wear performance of dental ceramics after grinding and polishing treatments. J. Mech. Behav. Biomed. Mater. 10, 13–22.

Qi, H.S., Mills, B., Rowe, W.B., 1994. An analysis of real contact length in abrasive machining processes using contact mechanics. Wear 176, 137–141.

Qian, L., Li, M., Zhou, Z., Yang, H., Shi, X., 2005. Comparison of nano-indentation hardness to microhardness. Surf. Coat. Tech. 195, 264–271.

Quinn, G.D., Patel, P.J., Lloyd, I., 2002a. Effect of loading rate upon conventional ceramic microindentation hardness. J. Res. Natl. Inst. Stand. Technol. 107, 299–306.

Quinn, J.B., Yen, J., Katz, R.N., Lloyd I.K., 2002b. Subjective ceramic machinability and material properties. Mach. Sci. Technol. 6, 291–299.

Reich, S., Endres, L., Weber, C., Wiedhahn, K., Neumann, P., Schneider, O., Rafai, N., Wolfart, S., 2014. Three-unit CAD/CAM-generated lithium disilicate FDPs after a mean observation time of 46 months. Clin. Oral Invest. 17, 2171–2178.

Reich, S., Schierz, O., 2013. Chair-side generated posterior lithium disilicate crowns after four years. Clin. Oral Invest. 17, 1765–1772.

Reich, S., Wichmann, M., Nkenke, E., Proeschel, P., 2005. Clinical fit of all-ceramic three-unit fixed partial dentures, generated with three different CAD/CAM systems. Eur. J. Oral Sci. 113, 174–179.

Rekow, D., Thompson, V.P., 2005. Near-surface damage-a persistent problem in crowns obtained by computer-aided design and manufacturing. Proc. Inst. Mech. Eng. H. 219, 233–243.

Rekow, D., Thompson, V.P., 2007. Engineering long term clinical success of advanced ceramic prostheses. J. Mater. Sci:-Mater. Med. 18, 47–56.

Rekow, E.D., 2006. Dental CAD/CAM systems: A 20-year success story. J. Am. Dent. Assoc. 137, 5s–6s.

Rekow, E.D., Silva, N.R.F.A., Coelho, P.G, Zhang, Y., Guess, P., Thompson, V.P., 2011. Performance of dental ceramics: Challenges for improvements. J. Dent. Res. 90, 937–952.

Rhee, Y.-W., Kim, H.-W., Deng, Y., Lawn, B.R., 2001. Contact-induced damage in ceramic coatings on compliant substrates: fracture mechanics and design. J. Am. Ceram. Soc. 84, 1066–1072.

Rice, R.W., 1984. Pores as fracture origins in ceramics. J. Mater. Sci. 19, 895–914.

Ritchie, R.O., 1999. Mechanisms of fatigue-crack propagation in ductile and brittle solids. Int. J. Fract. 100, 55–83.

Ritzberger, C., Apel, E., Höland, W., Peschke, A., Rheinberger, V.M., 2010. Properties and clinical application of three types of dental glass-ceramics and ceramics for CAD-CAM technologies. Materials 3, 3700–3713.

Rouxel, T., 2007. Elastic properties and short-to medium-range order in glasses. J. Am. Ceram. Soc. 90, 3019–3039.

Rouxel, T., Ji, H., Guin, J.P., Augereau, F., Rufflè, B., 2010. Indentation deformation mechanism in glass: Densification versus shear flow. J. Appl. Phys. 107, 094903 (5pp).doi: 10.1063/1.3407559.

Sakaguchi, R. L., 2005. Review of the current status and challenges for dental posterior restorative composites: clinical, chemistry, and physical behavior considerations. Summary of discussion from the Portland Composites Symposium (POCOS) June 17–19, 2004, Oregon Health & Science University, Portland, Oregon. Dent. Mater. 21, 3–6.

Sakai, M., 1999. The Meyer hardness: A measure for plasticity. J. Mater. Res. 14(9), 3630–3639.

Sakai M, Nakano, Y., 2002. Elastoplastic load-depth hysteresis in pyramidal indentation. J. Mater. Res. 17, 2161–2173.

Sakai, M., Nowak, R., 1992. Fracture toughness and brittleness of ceramic materials. In: Bannister M.J. (Ed), Ceramics-Adding the value, Australian Ceramic Society (Austceram 92), Melbourne, Australia 2, 922–931.

Sakai, M, Shimizu, S., Ishikawa, T., 1999. The indentation load-depth curve of ceramics. J. Mater. Res. 14, 1471–1484.

Santos, C., Teixeira, L.H.P., Daguano, J.K.M.F., Rogero, S.O., Strecker, K., Elias, C.N., 2009. Mechanical properties and cytotoxicity of 3Y-TZP bioceramics reinforced with $Al_2O_3$ particles. Ceram. Int. 35, 709–718.

Sato, H., Yamada, K., Pezzotti, G., Nawa, M., Ban, S., 2008. Mechanical properties of dental zirconia ceramics changed with sandblasting and heat treatment. Dent. Mater. J. 27, 408–414.

Schmidt, C., Weigl, P., 2000. Machinability of IPS Empress 2 framework ceramic: potential for ceramic dentures. J. Biomed. Mater. Res. (Appl. Biomater.) 53, 348–352.

Schuh, C.A., 2006. Nanoindentation studies of materials. Mater. Today, 9, 32–40.

Schuh, C.A., Nieh, T.G., 2003. A nanoindentation study of serrated flow in bulk metallic glasses. Acta Mater. 51, 87–99.

Scott, H.G. 1975. Phase relationships in the zirconia-yttria system. J. Mater. Sci. 10, 1527–1535.

Seghi, R.R., Daher, T., Caputo A., 1990. Relative flexural strength of dental restorative ceramics. Dent. Mater. 6, 181–184.

Selçuk, A., Atkinson, A., 1997. Elastic properties of ceramic oxides used in solid oxide fuel cells (SOFC). J. Eur. Ceram. Soc. 17, 1523–1532.

Serbena, F.C., Zanotto, E.D., 2012. Internal residual stresses in glass-ceramics: A review. J. Non-Cryst. Solids 358, 975–984.

Sergueeva, A.V., Mara, N.A., Kuntz, J.D., Lavernia, E.J., Mukherjee, A.K., 2005. Shear band formation and ductility in bulk metallic glass. Philos. Mag. 85, 2671–2687.

Shang, H., Rouxel, T., 2005. Creep behavior of soda-lime glass in the 100–500K temperature range by indentation creep test. J. Am. Ceram. Soc. 88, 2625–2628.

Shao, L., Jiang, D., Gong, J.H., 2013. Nanoindentation characterization of the hardness of zirconia dental ceramics. Adv. Eng. Mater. 15, 704–707.

Shaw, M.C., 1995. Precision finishing. CIRP Ann-Manuf. Technol. 44, 343–348.

She, J., Yang, J.-F., Beppu, Y., Ohji, T., 2003. Hertzian contact damage in a highly porous silicon nitride ceramic. J. Eur. Ceram. Soc. 23, 1193–1197.

Shimada, S., Ikawa, N., 1995. Brittle-ductile phenomena in microindentation and micromachining. CIRP Ann-Manuf. Technol. 44, 523–526.

Siegel, S.C., von Fraunhofer, J.A., 1997. Effect of handpiece load on the cutting efficiency of dental burs. Mach. Sci. Technol. 1, 1–14.

Silva, N.R.F.A., Sailer, I., Zhang, Y., Coelho, P.G., Guess, P.C., Zembic, A., Kohal, R.J., 2010. Performance of Zirconia for dental health. Materials 3, 863–896.

Silva, N.R.F.A., Thompson, V.P., Valverde, G.B., Coelho, P.G., Powers, J.M., Farah, J.W., Esquivel-Upshaw, J., 2011. Comparative reliability analyses of zirconium oxide and lithium disilicate restorations in vitro and in vivo. J. Am. Dent. Assoc. 142, 4s–9s.

Sindel, J., Petschelt, A., Grellner, F., Dierken, C., Greil, P. 1998. Evaluation of subsurface damage in CAD/CAM machined dental ceramics. J. Mater. Sci: Mater. Med. 9, 291-295.

Smith, C.M., Jiang, D., Gong, J., Yin, L., 2014. Determination of the mechanical behavior of lithium disilicate glass ceramics by nanoindentation & scanning probe microscopy. Mater. Chem. Phys. 148, 1036–1044.

Soares Jr., P.C., Lepienski, C.M., 2004. Residual stress determination on lithium disilicate glass-ceramic by nanoindentation. J. Non-Cryst. Solids 348, 139–143.

Soares Jr., P.C., Zanotto, E.D., Fokin, V.M., Jain, H., 2003. TEM and XRD study of early crystallization of lithium disilicate glasses. J. Non-Cryst. Solids 331, 217–227.

Song, X.-F., Ren, H.-T., Yin, L., 2016. Machinability of lithium disilicate glass ceramic in *in vitro* dental diamond bur adjusting process. J. Mech. Behav. Biomed. Mater. 53, 78–92.

Song, X.-F., Yin, L., 2012. Surface morphology and fracture in handpiece adjusting of a leucite-reinforced glass ceramic with coarse diamond burs. Mater. Sci. Eng. A–Struct. Mater. 534, 193–202.

Stawarczyk, B., Özcan, M., Hallmann, L., Ender, A., Mehl, A., Hämmerlet, C.H.F., 2013. The effect of zirconia sintering temperature on flexural strength, grain size, and contrast ratio. Clin. Oral Invest. 17, 269–274.

Steiner, R., Beier, U.S., Heiss-Kisielewsky, I., Engelmeier, R., Dumfahrt, H., Dhima, M., 2015. Adjusting dental ceramics: An in vitro evaluation of the ability of various ceramic polishing kits to mimic glazed dental ceramic surface. J. Prosthet. Dent. 113, 616 –622.

Strub, J.R., Rekow, E.D., Witkowski, S. 2006. Computer-aided design and fabrication of dental restorations: Current systems and future possibilities. J. Am. Dent. Assoc. 137, 1289-1296.

Studart, A.R., Filser, F., Kocher, P., Gauckler, L.J., 2007a. Fatigue of zirconia under cyclic loading in water and its implications for the design of dental bridges. Dent. Mater. 23, 106–114.

Studart, A.R., Filser, F., Kocher, P., Gauckler, L.J., 2007b. *In vitro* lifetime of dental ceramics under cyclic loading in water. Biomaterials 28, 2695–2705.

Sun, Z.M., Murugaiah, A., Zhen, T., Zhou, A., Barsoum, M.W., 2005. Microstructure and mechanical properties of porous $Ti_3SiC_2$. Acta Mater. 53, 4359–4366.

Suresh, S., Giannakopoulos, E., 1998. A new method for estimating residual stresses by instrumented sharp indentation. Acta Mater. 46, 5755–5767.

Sutow, E.J., Maillet, W.A., Hall, G.C., 2006. Corrosion potential variation of aged dental amalgam restorations over time. Dent. Mater. 22, 325–329.

Sutow, E.J., Maillet, W.A., Taylor, J.C., Hall, G.C., 2004. In vivo galvanic currents of intermittently contacting dental amalgam and other metallic restorations. Dent. Mater. 20, 823–831.

Swadener, J.G., Taljat, B., Pharr G.M., 2001. Measurement of residual stress by load and depth sensing indentation with spherical indenters. J. Mater. Res. 16, 2091–2102.

Swain, M.V., 1985. Inelastic deformation of MgPSZ and its significance for strength-toughness relationship of zirconia toughened ceramics. Acta Metall. 33, 2083–2091.

Swain, M.V., 2009. Unstable cracking (chipping) of veneering porcelain on all-ceramic crowns and fixed partial dentures. Acta Biomater. 5, 1668–1677.

Tabor, D., 1951. The hardness of Metals, first ed. Oxford University Press, London.

Tang, Q., Gong, J., 2013. Effect of porosity on the microhardness testing of brittle ceramics: A case study on the system of NiO–$ZrO_2$. Ceram. Int. 39, 8751–8759.

Taskonak, B., Mecholsky, J.J.Jr., Anusavice, K.J., 2005. Residual stresses in bilayer in dental ceramics. Biomaterials 26, 3235–3241.

Taskonak, B., Mecholsky, J.J.Jr., Anusavice, K.J., 2006. Fracture surface analysis of clinically failed fixed partial dentures. J. Dent. Res. 85, 277–281.

Thieme K., Rüssel, C., 2015. Nucleation and growth kinetics and phase analysis in zirconia-containing lithium disilicate glass. J. Mater. Sci. 50, 1488–1499.

Tholt, B., Miranda-Júnior, W.G., Prioli, R., Thompson, J., Oda, M., 2006. Surface roughness in ceramics with different finishing techniques using atomic force microscope and profilometer. Oper. Dent. 31–4, 442–449.

Tinschert, J., Natt, G., Hassenpflug, S., Spiekermann, H., 2004. Status of current CAD/CAM technology in dental medicine. Int. J. Comput. Dent. 7, 25–45.

Tong, H., Tanaka, C.B., Kaizer, M.R., Zhang, Y., 2016. Characterization of three commercial Y-TZP ceramics produced for their high-translucency, high-strength and high-surface area. Ceram. Int. 42, 1077–1085.

Toraya, H., Yoshimura, M., Shigeyuki, S., 1984. Calibration curve for quantitative analysis of the monoclinic-tetragonal $ZrO_2$ systems by X-ray diffraction. J. Am. Ceram. Soc. 67, C119–C121.

Tricoteaux, A., Rguiti, E., Chicot, D., Boilet, L., Descamps, M., 2011. Influence of porosity on the mechanical properties of microporous β-TCP bioceramics by usual and instrumented Vickers microindentation. J. Eur. Ceram. Soc. 31, 1361–1369.

Trunec, M., 2008. Effect of grain size on mechanical properties of 3Y-TZP ceramics. Ceram-Silikaty 52, 165–171.

Ulm, F.-J., Vandamme, M., Bobko, C., Ortega, J.A., Tai, K., Ortiz, C., 2007. Statistical indentation techniques for hydrated nanocomposites: Concrete, bone, and shale. J. Am. Ceram. Soc. 90, 2677–2692.

Ulutan, D., Ozel, T., 2011. Machining induced surface integrity in titanium and nickel alloys: A review. Int. J. Mach. Tools Manuf. 51, 250–280.

Vagkopoulou, T., Koutayas, S.Q., Koidis, P., Strub, J.R., 2009. Zirconia in dentistry: Part 1. Discovering the nature of an upcoming bioceramic. Eur. J. Esth Dent. 4, 2–23.

Virkar, A.V., Matsumoto, R.L.K., 1986. Ferroelastic domain switching as a toughening mechanism in tetragonal zirconia. J. Am. Ceram. Soc. 69, C224–C226.

Wagh, A.S., Singh, J.P., Poeppel, R.B., 1993. Dependence of ceramic fracture properties on porosity. J. Mater. Sci. 28, 3589–3593.

Wang, H., Aboushelib, M.N., Feilzer, A.J., 2008. Strength influencing variables on CAD/CAM zirconia frameworks. Dent. Mater. 24, 633–638.

Wei, P.J., Lin, J.F., 2008. Determination for elasticity and plasticity from time-dependent nanoindentations. Mater. Sci. Eng. A–Struct. 496, 90–97.

Wen, G., Zheng, X., Song, L., 2007. Effects of $P_2O_5$ and sintering temperature on microstructure and mechanical properties of lithium disilicate glass-ceramics. Acta Mater. 55, 3583–3591.

Whitehead, S.A., Shearer, A.C., Watts, D.C., Wilson, N.H.F., 1995. Comparison of methods for measuring surface roughness of ceramic. J. Oral Rehabil. 22, 421–427.

Wittneben, J.-G., Wright, R.F., Weber, H.-P. Gallucci, G.O. 2009. A systematic review of the clinical performance of CAD/CAM single-tooth restorations. Int. J. Prosthodont. 22, 466-471.

Xiang, Q., Liu, Y., Sheng, X., Dan, X., 2007. Preparation of mica-based glass-ceramics with needle-like fluorapatite. Dent. Mater. 23, 251–258.

Xu, H.H.K., Jahanmir, S., 1998. Effect of microstructure on damage tolerance in grinding dental glass-ceramics. J. Mater. Res. 13, 2231–2236.

Xu, H.H.K., Jahanmir, S., Lewis, L.K., 1997. Effect of grinding on strength of tetragonal zirconia and zirconia-toughned alumina. Mach. Sci. Technol. 1, 49–66.

Xu, H.H.K., Smith, D.T., Jahanmir, S., 1996. Influence of microstructure on indentation and machining of dental glass-ceramics. J. Mater. Res. 11, 2325–2337.

Yan, J., Takakashi, H., Gai, X., Harada, H., Tamaki, J., Kuriyagawa, T., 2006. Load effects on the phase transformation of single-crystal silicon during nanoindentation tests. Mater. Sci. Eng. A-Struct. 423, 19–23.

Yin, L., 2012. Property-process relations in clinical abrasive adjusting of dental ceramics. J. Mech. Behav. Biomed. Mater. 16, 55–65.

Yin, L., Alao, A.-R., Song, X.-F., Stoll, R., 2016. Manufacturing reliable ceramic crowns –The role of abrasive machining in digital dentistry, Proceedings of the ASME International Manufacturing Science and Engineering Conference (MSEC 2016), June 27-July 1, 2016, Virginia Tech, Virginia, USA.

Yin, L., Han, Y.-G., Song, X.-F., Wang, H., 2007. Effect of diamond burs on process and damage involving in vitro dental resurfacing of a restorative porcelain. J. Phys. D: Appl. Phys. 40, 5291–5300.

Yin, L., Huang, H., 2004. Ceramic response to high speed grinding. Mach. Sci. Technol. 8, 21–37.

Yin, L., Huang, H., 2008. Brittle materials in nano-abrasive fabrication of optical mirror-surfaces. Precis. Eng. 32, 336–341.

Yin, L., Jahanmir, S., Ives, L.K., 2003. Abrasive machining of porcelain and zirconia with a dental handpiece. Wear 255, 975–989.

Yin, L., Song, X.F., Song, Y.L., Huang, T., Li, J., 2006. An overview of in vitro abrasive finishing & CAD/CAM of bioceramics in restorative dentistry. Int. J. Mach. Tools Manuf. 46, 1013–1026.

Yin, L., Stoll, R., 2014. Ceramics in restorative dentistry, in: Low, I.M. (Ed.), Advances in Ceramic Matrix Composites. Woodhead Publishing Limited, Cambridge, UK, pp 624–655.

Yin, L., Vancoille, E.Y.J., Ramesh, K., Huang, H., 2004. Surface characterization of 6H-SiC (0001) substrates in indentation and abrasive machining. Int. J. Mach. Tools Manuf. 44, 607–615.

Yuan, K., Wang, F., Gao, J., Sun, X., Deng, Z., Wang, H., Chen, J., 2013. Effect of sintering time on the microstructure, flexural strength and translucency of lithium disilicate glass-ceramics. J. Non-Cryst. Solids 362, 7–13.

Zarone, F., Russo, S., Sorrentino, R., 2011. From porcelain-fused-to-metal to zirconia: Clinical and experimental considerations. Dent. Mater. 27, 83–96.

Zhang, B., Howes, T.D., 1994. Material-removal mechanisms in grinding ceramics. CIRP Ann-Manuf. Technol. 43, 305–308.

Zhang, P., Li, S.X., Zhang, Z.F., 2011. General relationship between strength and hardness. Mater. Sci. Eng. A–Struct. Mater. 529, 62–73.

Zhang, T., Feng, Y., Yang, R., Jiang, P., 2010. A method to determine fracture toughness using cube-corner indentation. Scr. Mater. 62, 199–201.

Zhang, Y., Allahkarami, M., Hanan, J.C. 2012. Measuring residual stress in ceramic zirconia-porcelain crowns by nanoindentation. J. Mech. Behav. Biomed. Mater. 6, 120–127.

Zhang, Y., Bhowmick S., Lawn, B.R. 2005. Competing fracture modes in brittle materials subject to concentrated cyclic loading in liquid environments: Monoliths. J. Mater. Res. 20, 2021–2029.

Zhang, Y., Kim, J.-W., Bhowmick, S., Thompson, V.P., Rekow, E.D., 2009. Competition of fracture mechanisms in monolithic dental ceramics: Flat model system. J. Biomed. Mater. Res. Part B: Appl. Biomater. 88B, 402–411.

Zhang, Y., Kim, J.-W., Kim, J.-H., Lawn, B.R., 2008. Fatigue damage in ceramic coatings from cyclic contact loading with a tangential component. J. Am. Ceram. Soc. 91, 198–202.

Zhang, Y., Lawn, B.R., 2004. Long-term strength of ceramics for biomedical applications. J. Biomed. Mater. Res. Part B: Appl. Biomater. 69B, 166–172.

Zhang, Y., Lawn, B.R. 2005. Fatigue sensitivity of Y-TZP to microscale sharp-contact flaws. J. Biomed. Mater. Res. Part B: Appl. Biomater. 72B, 388–392.

Zhang, Y., Lawn, B.R., Rekow, E.D., Thompson, V.P., 2004a. Effect of sandblasting on the long-term performance of dental ceramics. J. Biomed. Mater. Res. Part B: Appl. Biomater. 71B, 381–386.

Zhang, Y., Lee, J.J.-W., Srikanth, R., Lawn, B.R., 2013a. Edge chipping and flexural resistance of monolithic ceramics. Dent. Mater., 29, 1201–1208.

Zhang, Y., Pajares, A., Lawn, B.R. 2004b. Fatigue and damage tolerance of Y-TZP ceramics in layered biomechanical systems. J. Biomed. Mater. Res. Part B: Appl. Biomater. 71B, 166–171.

Zhang, Y., Sailer, I., Lawn, B.R., 2013b. Fatigue of dental ceramics. J. Dent. 41, 1135–1147.

Zhao, K., Pan, Y., Guess, P.C., Zhang, X.-P., Swain, M.V., 2012. Influence of veneer application on fracture behavior of lithium-disilicate-based ceramic crowns. Dent. Mater. 28, 653–660.

Zheng, X., Wen, G., Song, L., Huang, X.X., 2008. Effects of $P_2O_5$ and heat treatment on crystallization and microstructure in lithium disilicate glass ceramics. Acta Mater. 56, 549–558.

Zhu, P., Lin, Z., Chen, G., Kiyohiko, I., 2004. The predictions and applications of fatigue lifetime in alumina and zirconia ceramics. Int. J. Fatigue 26, 1109–1114.